Transactions of the ASME®

# Journal of Applied Mechanics

Published Quarterly by The American Society of Mechanical Engineers

VOLUME 59 • NUMBER 3 • SEPTEMBER 1992



**Transactions of the ASME, Journal of Applied Mechanics** (ISSN 0021-8936) is published quarterly (Mar., June, Sept., Dec.) for $165.00 per year by The American Society of Mechanical Engineers, 345 East 47th Street, New York, NY 10017. Second class postage paid at New York, NY and additional mailing office. POSTMASTER: Send address changes to Transactions of the ASME, Journal of Applied Mechanics, c/o THE AMERICAN SOCIETY OF MECHANICAL ENGINEERS, 22 Law Drive, Box 2300, Fairfield, NJ 07007-2300.
**CHANGES OF ADDRESS** must be received at Society headquarters seven weeks before they are to be effective. Please send old label and new address.
**PRICES:** To members, $40.00, annually; to nonmembers, $165.00.
Add $20.00 for postage to countries outside the United States and Canada.

**INDEXED** by Applied Mechanics Reviews and Engineering Information, Inc.
Canadian Goods & Services Tax Registration #126148048

473 In Memoriam

474 Reviewers

TECHNICAL PAPERS

477 Limit Analysis of a Stochastically Inhomogeneous Plastic Medium With Application to Plane Contact Problems
R. P. Nordgren

485 Numerical Analysis of Plane-Strain Tension Test for Rate-Dependent Solids
P. Tuğcu

491 An Analysis of Shear Localization During Bending of a Polycrystalline Sheet
R. Becker

497 On the Use of Approximation Methods for Microcrack Shielding Problems
H. Cai and K. T. Faber

502 An Interlaminar Shear Stress Continuity Theory for Both Thin and Thick Composite Laminates
Xianqiang Lu and Dahsin Liu

510 The Influence of Inclusion Shape on the Overall Viscoelastic Behavior of Two-Phase Composites
Y. M. Wang and G. J. Weng

519 Regular Pyramid Punch Problem
G.G. Bilodeau

524 Analysis of a Crack Bridged by a Single Fiber
G. Meda and P. S. Steif

530 On Interface Crack Growth in Composite Plates
K.-F. Nilsson and B. Storåkers

539 Mori-Tanaka Estimates of the Overall Elastic Moduli of Certain Composite Materials
Tungyang Chen, George J. Dvorak, and Yakov Benveniste

547 Interfacial Slippage of a Unidirectional Fiber Composite Under Longitudinal Shearing
Hong Teng and A. Agah-Tehrani

552 Analysis of Thermal Conduction Effects on Thermoelastic Temperature Measurements for Composite Materials
S. A. Dunn

559 Influence of Porosity on Plane Strain Tensile Crack-Tip Stress Fields in Elastic-Plastic Materials: Part I
W. J. Drugan and Y. Miao

568 The Complementary Potentials of Elasticity, Extremal Properties, and Associated Functionals
Gerald Wempner

572 Equilibrium Configurations of Cantilever Beams Subjected to Inclined End Loads
S. Navaee and R. E. Elling

580 Unilaterally Supported Plates on Elastic Foundations by the Boundary Element Method
E. J. Sapountzakis and J. T. Katsikadelis

587 Modified Mixed Variational Principle and the State-Vector Equation for Elastic Bodies and Shells of Revolution
Charles R. Steele and Yoon Young Kim

596 Scattering of an Impact Wave by a Crack in a Composite Plate
S. K. Datta, T. H. Ju, and A. H. Shah

604 A General Algorithm for the Numerical Solution of Hypersingular Boundary Integral Equations
M. Guiggiani, G. Krishnasamy, T. J. Rudolphi, and F. J. Rizzo

615 An Investigation of Dynamic Pulse Buckling of Thick Rings
N. G. Pegg

622 Initial Development of Microdamage Under Impact Loading
Yilong Bai, Zhong Ling, Limin Luo, and Fujiu Ke

628 A Theory for Transverse Deflection of Poroelastic Plates
Larry A. Taber

635 Two-Dimensional Rigid-Body Collisions With Friction
Yu Wang and Matthew T. Mason

643 A Projection Method Approach to Constrained Dynamic Analysis
W. Blajer

650 Eigenvalue Inclusion Principles for Distributed Gyroscopic Systems
B. Yang

657 Auto and Cross-Bispectral Analysis of a System of Two Coupled Oscillators With Quadratic Nonlinearities Possessing Chaotic Motion
Charles Pezeshki, Steve Elgar, R. Krishna, and T. D. Burton

664 Lyapunov Exponents and Stochastic Stability of Coupled Linear Systems Under Real Noise Excitation
S. T. Ariaratnam and Wei-Chau Xie

(Contents continued on Inside Back Cover)

## CONTENTS (CONTINUED)

### BRIEF NOTES


A Follower Load Buckling Problem for Rectangular Plates 674
**Eric Reissner and Frederick Y. M. Wan**

Instability of Generalized Equilibria of Pseudodissipative Systems 676
**J. A. Walker**

A Note on Determining the Initial Velocity of a Modal Field 677
**Q. Zhou, T. G. Zhang, and T. X. Yu**

On the Bending of Rectangular Plates With Two Opposite Edges Simply Supported 679
**James R. Hutchinson**

Energy Dissipated in Planar Collision 681
**W. J. Stronge**

Unilateral Contract of a Springboard and a Fulcrum 682
**M. Kuipers and A. A. F. van de Ven**

Slewing Motion Control of a Very Flexible Elastic Beam 684
**J. W. Eischen, L. Silverberg, and H. L. Wang**

687 Absence of One Nodal Diameter Critical Speed Modes in an Axisymmetric Rotating Disk
**Anthony A. Renshaw and C. D. Mote, Jr.**

688 Nonuniqueness in Elastoplastic Frames
**W. A. M. Alwis**

690 Some Remarks on the Solutions of a Concentrated Torque and Double Forces on an Elastic Half-Space
**T. Chen**

692 Configuration of a Bent Tape of Curved Cross-Section
**K. Schulgasser**

693 The Dynamics of a Nonharmonically Excited System Having Rigid Amplitude Constraints
**Pi-Cheng Tung**

696 Viscoelastic Damping Calculations Using a p-Type Finite Element Code
**C. J. Wilson, P. Carnevali, R. B. Morris, and Y. Tsuji**


### DISCUSSION


700 **Predicting Rebounds Using Rigid-Body Dynamics, by Charles E. Smith—Discussion by Raymond M. Brach**


### ERRATUM


627 **On A Crack Terminating at a Slipping Interface Between Two Materials, by V. M. Gharpuray, J. Dundurs, and L. M. Keer and published in the December 1991 issue of the Journal of Applied Mechanics**


### ANNOUNCEMENTS AND SPECIAL NOTES


**663** First SES-ASME-ASCE Joint Meeting—Announcement and Call for Papers

**614** Symposium on High-Performance Computing for Flight Vehicles—Announcements

**523** Second International Conference on Vibration Problems of Mathematical Elasticity and Physics—Announcement and Call for Papers

**634** Change of Address Form

**701** Books Received by the Office of the Technical Editor

**702** Worldwide Mechanics Meetings List

**704** Information for Authors

# Julius Miklowitz

1919–1992

Julius Miklowitz, Professor of Applied Mechanics, Emeritus, at the California Institute of Technology, died on March 15, 1992 after many years of struggle with the debilitating effects of multiple sclerosis. He was 72 years old. He is survived by his wife Gloria and two sons, Dr. Paul S. Miklowitz and Dr. David J. Miklowitz.

Miklowitz was a leader in studies on wave propagation in elastic solids and waveguides. He developed analytical techniques to study scattering and diffraction of elastic waves and to obtain the transient response of beams, plates, and shells for a variety of time-varying loading conditions.

Miklowitz earned his B.S. degree in Mechanical Engineering from the University of Michigan in 1943. During World War II he conducted research at the Westinghouse Research Laboratory where his work focused on the inelastic behavior and fracture of metals and polymers for a broad spectrum of rates and types of loading. In 1949 he became Associate Professor of Mathematics and Engineering at the New Mexico Institute of Mining and Technology. From 1951 to 1955 he was a consultant in solid mechanics and wave propagation in solids at the Naval Undersea Warfare Center. Miklowitz came to Cal Tech in 1956 as Associate Professor of Applied Mechanics. He was named Professor of Applied Mechanics in 1962 and Professor Emeritus in 1985.

As he related on occasion, Julius found his way into the subject of waves in solids quite accidentally early in his career. In experiments with plexiglass tension specimens, a few of the specimens in these static tests broke suddenly and in a brittle manner in two places. Simple wave analysis, discussed in one of his first papers published in this Journal (Vol. 20, 1953, pp. 120–130), showed that the second fracture was created through a series of reflections of the unloading wave, generated by the first fracture, from the ends of the remaining clamped part of the specimen. This paper was one of the early works in an area, dynamic fracture, which has remained of interest through the years.

Julius was a master in the application of Fourier transform techniques to solve elastic wave propagation problems. He developed to a fine art the capability to lift from complicated mathematical expressions those defining parts that are directly related to significant physical effects.

Later in his career Julius became totally fascinated, perhaps obsessed, with finding analytical elastodynamic solutions to the quarter-space problem and to related corner problems with unmixed conditions. He made significant progress and for this particular class of problems his work pushed to the limit the use of classical techniques of applied mathematics.

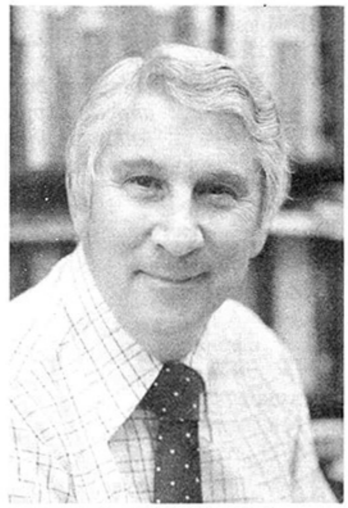

(Photo: Bob Paz, California Institute of Technology)

**Julius Miklowitz, Ph.D.**

Miklowitz was the author of more than 50 technical papers. His book, *Theory of Elastic Waves and Waveguides*, was published in 1978. The book presents a comprehensive treatment of the propagation of waves in elastic solids. It deals with time-harmonic as well as transient wave motion, and discusses waves in waveguides and scattering and diffraction problems. He was a member of the Board of Editors of *WAVE MOTION* since its inception.

Julius was actively involved with the Applied Mechanics Division throughout his career. He served on the Executive Committee of the Applied Mechanics Division from 1970 until 1976.

In all of his work Julius projected an infectious enthusiasm. Many will remember the tall speaker at meetings of the Applied Mechanics Division—presenting an invited lecture or a contributed paper, holding forth on the intricate details of Fourier transform applications to elastic wave propagation problems.

Julius Miklowitz was a gentleman and a scholar in the finest applied mechanics tradition. He will be remembered fondly by his students, colleagues, and friends.

J. D. Achenbach
Northwestern University

# Limit Analysis of a Stochastically Inhomogeneous Plastic Medium With Application to Plane Contact Problems[1]

**R. P. Nordgren**[2]
Department of Civil Engineering
Rice University
Houston, TX 77251
Fellow ASME

*The lower and upper bound theorems of plastic limit analysis are extended to a stochastically inhomogeneous medium. The extended theorems provide bounds on the mean safety factor against plastic collapse. A three-parameter yield function is treated by introducing a spatial correlation function for uniaxial yield strength. Application of the stochastic upper-bound theorem is made to the plane problem of a truncated wedge under contact pressure. The results apply to the design of arctic structures against local ice pressure.*

## Introduction

For many problems in the mechanics of solids, the material may be considered to be homogeneous. For other problems, the effect of inhomogeneity is important enough to be considered in the material model. Of special concern are problems involving yield or failure over regions of weakness. In particular, ice and rock generally are inhomogeneous and may fail in this manner. If the inhomogeneity is irregular and random in nature, then a stochastic description of material strength is required.

The present paper treats an elastic/perfectly plastic material with stochastically inhomogeneous yield strength. For a body of this material, the first and second collapse theorems of limit analysis are extended to give lower and upper bounds on the *mean* safety factor against plastic collapse under a given load system. The theorems are specialized to a three-parameter yield function which quadratically relates mean shear stress at yield to mean normal stress. Such a yield function appears to be suitable for ice and rock. The uniaxial compressive yield strength is considered to be the basic random variable for the material. The spatial fluctuations in this yield strength field are described by a homogeneous, isotropic correlation function. The three parameters in the yield function are determined in terms of the uniaxial compressive strength by deterministic scaling rules.

[1]Presented at the Eleventh U.S. National Congress of Applied Mechanics, The University of Arizona, May 21–25, 1990.

[2]Formerly at Shell Development Company, Houston, Texas, where this research was sponsored.

Contributed by the Applied Mechanics Division of THE AMERICAN SOCIETY OF MECHANICAL ENGINEERS for publication in the ASME JOURNAL OF APPLIED MECHANICS.

Discussion on this paper should be addressed to the Technical Editor, Professor Leon M. Keer, The Technological Institute, Northwestern University, Evanston, IL 60208, and will be accepted until four months after final publication of the paper itself in the JOURNAL OF APPLIED MECHANICS.

Manuscript received by the ASME Applied Mechanics Division, June 12, 1990; final revision, Jan. 4, 1991. Associate Technical Editor: R. M. McMeeking.

Application of the stochastic upper-bound theorem is made to the plane problem of a truncated wedge under uniform contact pressure. This problem is of technical interest for the determination of local ice pressure on offshore arctic structures. The problem was treated by Nordgren (1988) for a homogeneous, elastic/perfectly plastic material with the three-parameter quadratic yield function. In addition to exact rigid/plastic plane solutions, upper bounds on the contact pressure were obtained for both plane problems and three-dimensional problems. The upper bounds for plane problems were found using constant velocity fields in triangular regions. For the stochastically inhomogeneous plane wedge, the straight line rigid-plastic and plastic-plastic boundaries are replaced by zigzag boundaries. In a realization of the stochastic material, the zigzag directions are chosen to minimize the upper bound on the mean safety factor. The minimization is carried out both analytically and by numerical simulation with optimization by the method of dynamic programming. The analytical approach depends on new statistical results for the minimum of several correlated random variables with normal and lognormal distributions.

Numerical results for the truncated wedge problem are obtained for a special one-parameter correlation function believed to be applicable to multiyear sea ice. In some cases the upper-bound mean safety factor is lower than the upper-bound safety factor for the corresponding homogeneous material with yield strength taken equal to the mean yield strength of the stochastic model. Thus, contact pressure may be reduced by consideration of stochastic inhomogeneity.

The calculated upper bound on the mean safety factor decreases with increasing length of the loaded boundary, which may be considered as indicating a "size effect." The actual mean safety factor also is expected to decrease with increasing loaded length. The calculation of a lower bound on the mean safety factor could confirm this conjecture.

Some caution is in order in applying the present results to ice and rocks since the proofs of the theorems of limit analysis depend on Drucker's postulate of a stable plastic material. In particular, this postulate is not satisfied for pressure-sensitive materials that yield by frictional sliding on microfissures.

Further, in applications that involve the calculation of structural loads from the stochastic bound theorems, the mean safety factor may not be indicative of the maximum load condition. Information on the variance of the safety factor also is required. In some cases, estimates of the variance can be calculated along with the bounds on the mean safety factor.

## Correlation Function for Yield Strength

The stochastic inhomogeneity of yield strength will be characterized by a correlation function using a formulation given by Yaglom (1962). The correlation function relates the correlation coefficient for yield strength at two points to the distance between the points. A one-parameter form for the correlation function will be introduced as a special case. Before considering the correlation function, we review the formulation of the three-parameter quadratic yield function and extend it to a stochastically inhomogeneous material.

**Yield Function.** Following the notation of Nordgren (1988) and earlier work, the three-parameter yield function can be written as

$$f = aJ_2 + bI_1 + cI_1^2 - 1, \tag{1}$$

where $a$, $b$, and $c$ are strength parameters, and $I_1$ and $J_2$ are stress invariants given in terms of the principal stresses ($\sigma_1$, $\sigma_2$, $\sigma_3$) as

$$I_1 = \sigma_1 + \sigma_2 + \sigma_3, \quad J_2 = \frac{1}{6}\left[(\sigma_1 - \sigma_2)^2 + (\sigma_2 - \sigma_3)^2 + (\sigma_3 - \sigma_1)^2\right]. \tag{2}$$

The parameters $a$, $b$, $c$ in the yield function (1) are considered to be random fields in three dimensions. The statistical properties of $a$, $b$, $c$ are to be determined from experimental data on yield strength. The usual experiments are compression tests on circular cylindrical specimens with and without confining pressure. In an unconfined uniaxial compression test with yield stress $q$, the yield condition ($f = 0$) from (1) gives the relation

$$\frac{1}{3}aq^2 - bq + cq^2 = 1. \tag{3}$$

Let $\bar{q}$ be the mean value of $q$ as obtained from experimental data. Let $\bar{a}$, $\bar{b}$, $\bar{c}$ be the values of $a$, $b$, $c$ that best fit the yield function (1) to the experimental data and satisfy (3) with $q = \bar{q}$. Then, for any value of uniaxial yield stress $q$, we assume that the strength parameters $a$, $b$, $c$ are related to $q$ by the scaling rules

$$a/\bar{a} = c/\bar{c} = (\bar{q}/q)^2, \quad b/\bar{b} = \bar{q}/q, \tag{4}$$

which satisfy (3). The scaling rules (4) imply that yield curves in the $\sqrt{J_2}$, $I_1$-plane are geometrically similar. It is difficult to verify this by direct experiment; however, the scaling rules do appear to be consistent with experimental data on ice strength.

**Correlation Function.** The uniaxial compressive yield strength $q$, is considered to be a random field in three dimensions with mean $\bar{q}$ and fluctuations $\xi$, i.e.,

$$q(x) = \bar{q} + \xi(x), \quad x \equiv (x_1, x_2, x_3), \tag{5}$$

where $x_i$ are rectangular Cartesian coordinates. For a stochastically isotropic and homogeneous medium, the correlation coefficient $B(x, x')$ for the fluctuation field $\xi(x)$ at the two points $x$ and $x'$ depends only on the distance $r$ between the two points, i.e.,

$$B(x,x') \equiv E[\xi(x)\xi(x')] = B(r). \tag{6}$$

Using results from Yaglom (1962), the correlation function can be written as

$$B(r) = \int_0^\infty \frac{\sin\lambda r}{\lambda r}\, dG(\lambda), \tag{7}$$

where $G(\lambda)$ is a nondecreasing bounded function of $\lambda$ for $\lambda \geq 0$.

As a useful special case, we consider the function

$$G(\lambda) = -B_0 e^{-\lambda h}(\lambda + 1/h)/h, \tag{8}$$

for which (7) gives

$$B(r) = \frac{B_0}{1 + r^2/h^2}. \tag{9}$$

Here, $B_0 = B(0)$ is the variance of the strength fluctuations $\xi$ and the parameter $h$ sets the length scale for the fluctuations. The special correlation function (9) can be fit to experimental strength data from specimens with known separation distance.

## Stochastic Collapse Theorems

The first and second collapse theorems of limit analysis furnish lower and upper bounds on the collapse load for an elastic/perfectly plastic body under surface stress and body force. Here the collapse theorems will be extended to a stochastically inhomogeneous, elastic/perfectly plastic medium. The stochastic collapse theorems give lower and upper bounds on the mean safety factor, i.e., the factor by which a given set of loads is multiplied to cause collapse. Knowledge of the statistical distribution and spatial correlation of the yield strength parameters is required in order to apply the stochastic collapse theorems.

We will follow Koiter (1960) and state the collapse theorems of limit analysis in terms of the safety factor. Consider a body loaded by body force vector $X_i$ and surface stress vector $\sigma_i^*$ on a portion $S_\sigma$ of the surface $S$. The displacement vector $u_i$ is prescribed to be zero on the remainder of the surface $S_u$. The *safety factor* for this load system is defined as the positive multiplier $n$ such that $n\sigma_i$ and $nX_i$ constitute a limit load system, i.e., a load system for which the body cannot support a further increase in load.

**Stochastic Lower-Bound Theorem.** The first (lower-bound) theorem of limit analysis states that a body will not collapse if an equilibrium stress field $n_L\sigma_{ij}$ can be found for the loads $n_L\sigma_i^*$ and $n_LX_i$ such that the yield function satisfies $f(n_L\sigma_{ij}) \leq 0$ throughout the body. Therefore, $n_L$ is a lower bound on the safety factor $n$.

The first collapse theorem is proved indirectly by Koiter (1960) using Drucker's (1951) stability postulate. The proof extends to a deterministic inhomogeneous material upon consideration that parameters in the yield function depend on position in the inhomogeneous body. To formulate the theorem mathematically, let $n^*$ be the solution of

$$f(n^*\sigma_{ij}) = 0 \tag{10}$$

for a given stress tensor $\sigma_{ij}$. Thus, $n^*$ depends implicitly on the yield parameters and therefore is a function of position in the inhomogeneous body. If the stress field $\sigma_{ij}$ satisfies the equations of equilibrium and stress boundary conditions, then, by the first collapse theorem, a lower bound on $n$ may be written as

$$n_L = \min_x\{n^*(x)\}. \tag{11}$$

Furthermore, one may adjust the stress field $\sigma_{ij}$ so as to maximize $n_L$ in (11), subject to (10), the equilibrium equations, and the stress boundary conditions.

For a stochastically inhomogeneous material, $n_L$ from (11) is a random variable that depends on the stochastic properties of the yield parameters through (10). Then, the mean value of $n_L$ is given by

$$\bar{n}_L = E[\min_x\{n^*(x)\}], \tag{12}$$

where the mean $E[\ldots]$ is taken with respect to the random strength parameters in the yield function which enter through the solution of (10) for $n^*$. Since $n_L$ is a lower bound on $n$ for each realization of the stochastically inhomogeneous body, it follows that $\overline{n}_L$ is a lower bound on the mean safety factor $\overline{n}$.

For the three-parameter yield function (1), by (10) and the scaling rules (4), it follows that

$$n^*(x) = [q(x)/\overline{q}]\{-\overline{b}I_1 + [(\overline{b}^2 + 4\overline{c})I_1^2 + 4\overline{a}J_2]^{\frac{1}{2}}\}/[2(\overline{a}J_2 + \overline{c}I_1^2)], \quad (13)$$

which may be useful in applications.

**Stochastic Upper-Bound Theorem.** The second (upper-bound) theorem of limit analysis can be stated in a number of ways. Here, we follow Koiter (1960) and state that an upper bound $n_U$ on the safety factor $n$ is determined by the equation

$$n_U\left[\int_{S_\sigma} \sigma_i v_i^0 dS + \int_V X_i v_i^0 dV\right] = \int_V F(\dot{\epsilon}_{ij}^0)dV + \int_{S_D} F_S(\delta v_i^0)dS, \quad (14)$$

where $v_i^0$ is a kinematically admissible velocity field such that $v_i^0 = 0$ on $S_u$ and the strain rate tensor is given by

$$\dot{e}_{ij}^0 = \frac{1}{2}(v_{i,j}^0 + v_{j,i}^0). \quad (15)$$

In (14), $F$ is the energy dissipation rate per unit volume and $F_S$ is the energy dissipation rate per unit area of a surface $S_D$ across which $v_i^0$ has a jump discontinuity $\delta v_i^0$. Further, the left-hand side of (14) must be positive and there may be additional restrictions on $v_i^0$ for certain yield functions, e.g., $\dot{e}_{kk}^0 = 0$ for the Mises yield function. Specific expressions for $F$ and $F_S$ are available for the three-parameter yield function (1) as will be discussed in what follows. The upper-bound theorem is proved indirectly by Koiter (1960) using Drucker's (1951) stability postulate. The proof can be seen to hold for a deterministic inhomogeneous material. In this case, the material strength parameters in the energy dissipation functions $F$ and $F_S$ vary with position in the body.

Next, the upper-bound theorem will be extended to a stochastically inhomogeneous medium in which the yield strength parameters are random fields in three dimensions. For this material, the mean value of $n_U$, denoted by $\overline{n}_U$, is determined from (14) as

$$\overline{n}_U\left[\int_{S_\sigma} \sigma_i v_i^0 dS + \int_V X_i v_i^0 dV\right] = E\left[\int_V F(\dot{e}_{ij}^0)dV\right] + E\left[\int_{S_D} F_S(\delta v_i^0)dS\right], \quad (16)$$

where the mean $E[\ldots]$ is taken with respect to the random fields for the yield strength parameters and the integrals on the right-hand side are considered as the limits of appropriate sums. The relation between $q$ and the energy dissipation rates $F$ and $F_S$ must be established for a particular yield function as will be considered next for the three-parameter quadratic yield function. Since $n_U$ is an upper bound on $n$ for all realizations of the random strength parameter fields, it follows that $\overline{n}_U$ is an upper bound on the mean safety factor $\overline{n}$.

For the three-parameter yield function (1), Nordgren (1988) verified earlier results that, under certain mild restrictions, the energy dissipation rates are given by

$$F = \frac{1}{6c}\left\{(b^2+4c)^{\frac{1}{2}}\left[18\frac{c}{a}\dot{\epsilon}_{ij}\dot{\epsilon}_{ij} + (\dot{e}_{kk})^2\right]^{\frac{1}{2}} - b\dot{e}_{kk}\right\}, \quad (17)$$

$$F_S = \frac{1}{6c}\left\{(b^2+4c)^{\frac{1}{2}}\left[\delta v_n^2 + 3\frac{c}{a}(3\delta v_t^2 + 4\delta v_n^2)\right]^{\frac{1}{2}} - b\delta v_n\right\}, \quad (18)$$

where $\epsilon_{ij}$ is the deviatoric strain tensor defined as

$$\epsilon_{ij} = e_{ij} - \frac{1}{3}\delta_{ij}e_{kk}, \quad (19)$$

and $\delta v_n$ and $\delta v_t$ are the magnitudes of the velocity discontinuity normal and tangential to the surface of discontinuity $S_D$.

Let $\overline{F}$ and $\overline{F}_S$ be the energy dissipation functions (17) and (18) with $a$, $b$, $c$ replaced by $\overline{a}$, $\overline{b}$, $\overline{c}$. Then, by (17), (18), and (4), $F$ and $F_S$ scale according to

$$F/\overline{F} = F_S/\overline{F}_S = q/\overline{q}. \quad (20)$$

Therefore, (16) can be written as

$$\overline{n}_U\left[\int_{S_\sigma} \sigma_i v_i^0 dS + \int_V X_i v_i^0 dV\right] = E\left[\int_V q(x)\overline{F}(\dot{e}_{ij}^0)dV + \int_{S_D} q(x)\overline{F}_S(\delta v_i^0)dS\right]/\overline{q}, \quad (21)$$

where now the mean $E[\ldots]$ is taken with respect to the random field $q(x)$. In applications, minimization of $\overline{n}_U$ is achieved by selecting the velocity field $v_i^0$ as will be illustrated next in an example.

## Contact Pressure on a Truncated Plane Wedge

Nordgren (1988) obtained upper bounds on the average contact pressure acting on a truncated wedge of homogeneous elastic/perfectly plastic material obeying the three-parameter yield function (1). For plane problems, the upper bound compared favorably with an exact solution for a rigid/perfectly plastic material obtained by the method of characteristics. Both plane stress and plane strain were considered as well as a three-dimensional contact problem. The assumed velocity field for application of the upper-bound theorem to the plane problem consisted of two triangular regions of constant velocity, $ABD$ and $BCD$, as shown in Fig. 1. The magnitude of the velocities and position of the rigid-plastic boundaries $AB$ and $BC$ were obtained by an optimization calculation for each particular case. These same optimal values are assumed to apply here as a base case for application of the stochastic upper-bound theorem to the inhomogeneous wedge.

**Zigzag Boundary.** In order to take advantage of the inhomogeneity in yield strength, the straight-line segments of the rigid-plastic boundary are replaced by zigzag lines, as shown in Fig. 1. On each subsegment of the boundary, the branch of the zigzag that minimizes the energy dissipation is to be chosen for each realization of the stochastic material. For example, in Fig. 1 one may replace the subsegment $AG$ by either $AEG$ or $AFG$. We will calculate the effect of this optimal replacement strategy on the upper bound on the mean contact pressure. The alternate system of zigzag paths in the inset of Fig. 1 will be considered later.

The mean value of the minimum energy dissipation is required in the stochastic upper-bound theorem (21). The integral over $S_D$ in (21) can be expressed as the sum of integrals over subsegments of the zigzag boundaries of the plastic regions. Further, the $\overline{F}_S$ term is constant and can be removed from each integral leaving the $q(x)$ term. The integral of $q(x)$ represents the average yield strength on the zigzag subsegment. Either zigzag branch can be chosen so as to minimize the mean of this $q$ integral for each subsegment. Since the average yield strength for the two zigzag branches are correlated, we have the problem of finding the mean of the minimum of two *correlated* random variables. Before discussing this minimization problem, we consider the calculation of the correlation

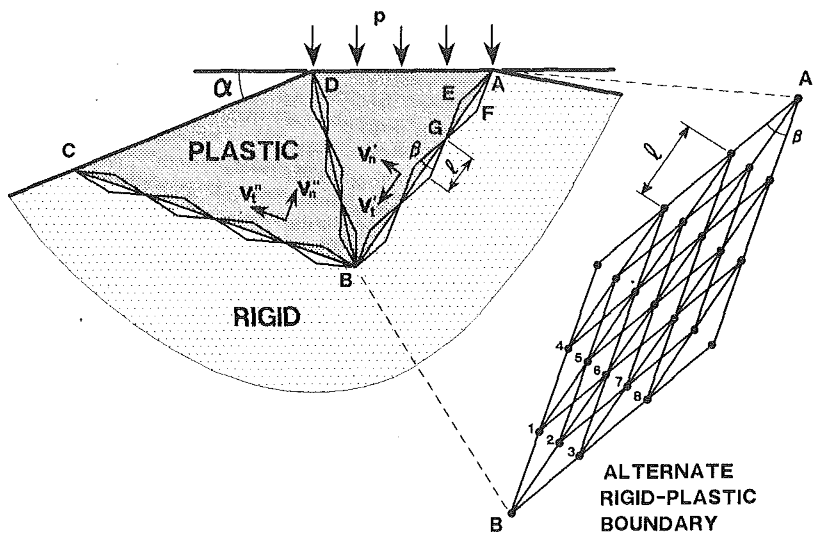


Fig. 1 Velocity field for upper-bound on contact stress in the plane contact problem. Alternate zigzag paths for rigid-plastic boundary.

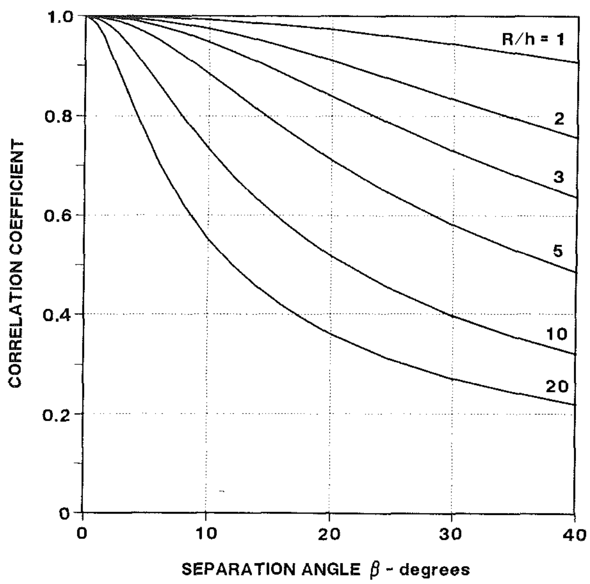


Fig. 2 Correlation coefficient of average strength on two lines of length $R$ with a common end point versus separation angle $\beta$ and $R/h$ for the special correlation function (9)

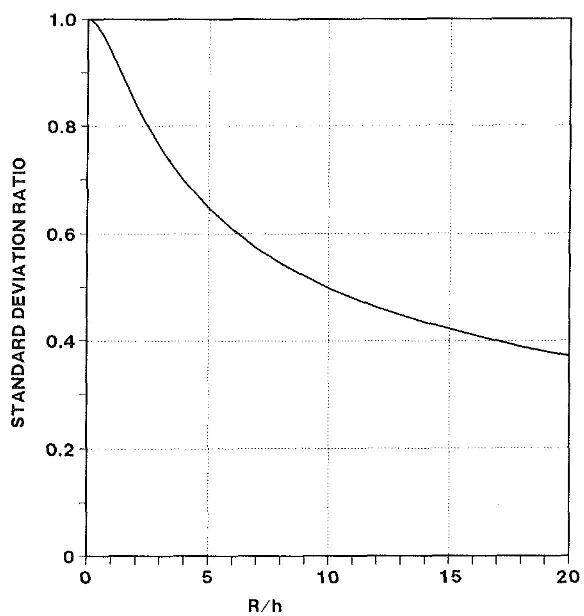


Fig. 3 Ratio of standard deviation of average strength on a line of length $R$ to standard deviation of strength versus $R/h$ for the special correlation function (9)

coefficient for average yield strength on the two branching zigzags.

This correlation coefficient can be obtained for the special correlation function (9) from results developed in the Appendix. These results for the correlation coefficient of a random field along two line segments of length $R$ with separation angle $\beta$ are shown in Fig. 2. For the zigzags $AEG$, $AFG$, we have $R \approx l$ for $\beta \ll 1$, where $2l$ is the length of $AG$. The result is a good approximation since the correlation on $AF$ and $AE$ dominates over the neglected strength correlation on $AF$ and $FG$ and $EG$ for $\beta \ll 1$. Further, the variance in the strength along $AFG$ and $AEG$ is given approximately by Fig. 3 with $R \approx 2l$ for $\beta \ll 1$. Results shown in Fig. 3 also are developed in the Appendix.

Results for the minimum of several *uncorrelated*, normal random variables are given by Gumbel (1958). The minimization problem for *correlated* random variables is solved in the Appendix for both the normal and lognormal distributions. From the results obtained there, Fig. 4 gives the mean of the minimum of 2, 3, 4, and 5 correlated normal variates with the same distribution. The mean of the minimum is normalized on the standard deviation of a single variate. The correlation coefficient is assumed to be identical for all pairs of variates. Figures 5 and 6 give the mean of the minimum of two and three correlated lognormal variates, respectively. Here the mean of the minimum is normalized on the mean of a single variate.

In view of the form of the right-hand side of (21), the effect of taking the mean minimum strength on the zigzag branches for each subsegment of the rigid-plastic boundary is to reduce the upper bound on the mean safety factor, obtained using mean strength properties in Nordgren's (1988) deterministic analysis, by the *branch factor* which is defined as the ratio of the mean of the minimum strength to the mean strength as obtained from Fig. 4 or 5. This assumes that the subsegments for all three segments ($AB$, $BC$, and $BD$ in Fig. 1) are the same length which can be arranged approximately for large contact areas which have several subsegments for each main segment. To improve the upper bound, the minimum energy dissipation

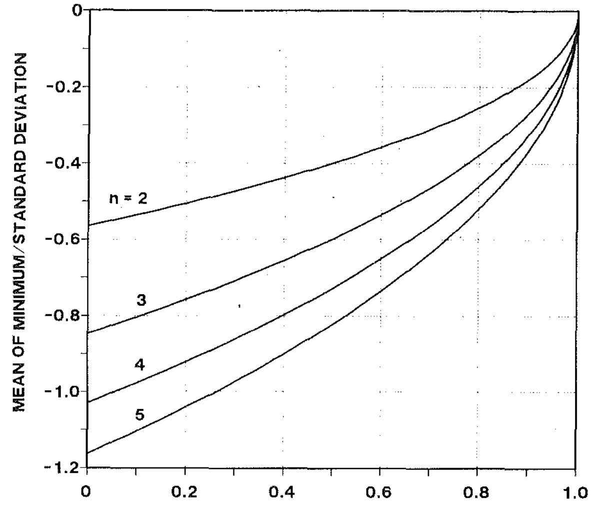


Fig. 4 Mean of the minimum of $n$ correlated normal variates with mean zero and the same standard deviation

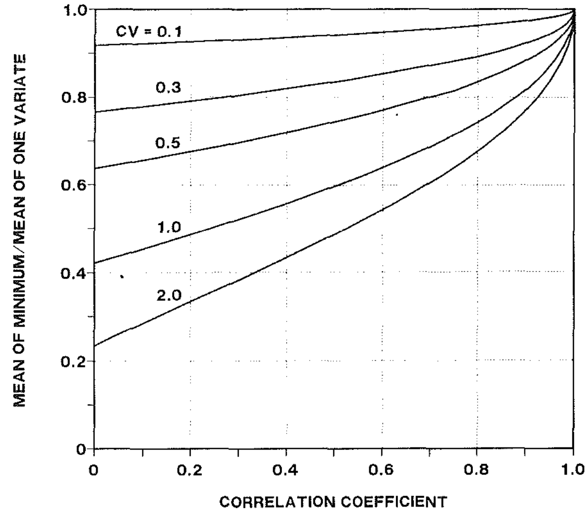


Fig. 6 Mean of the minimum of three correlated lognormal variates with the same mean and coefficient of variation $CV$

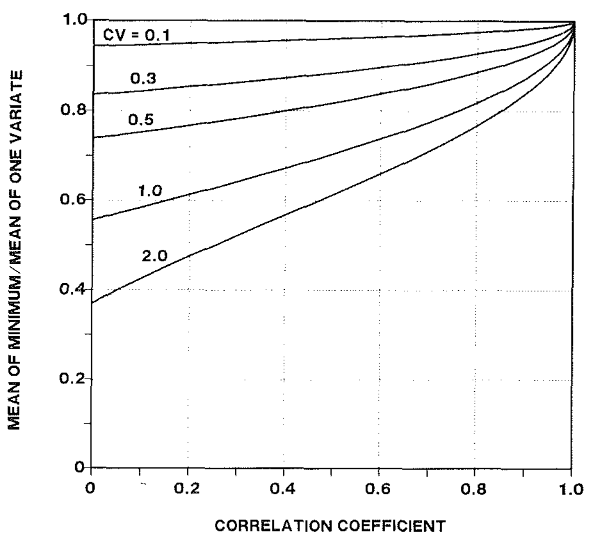


Fig. 5 Mean of the minimum of two correlated lognormal variates with the same mean and coefficient of variation $CV$

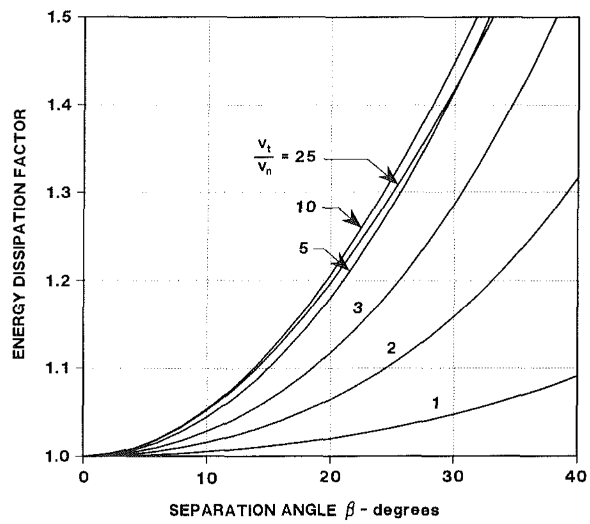


Fig. 7 Energy dissipation factor for zigzag rigid-plastic boundary versus separation angle $\beta$ for various velocity ratios

rate on each segment of the rigid-plastic boundary could be calculated separately.

In calculating the energy dissipation on the zigzags, account must be taken of the change in velocity components due to the inclination of the zigzags. On the rigid-plastic boundary segment $AB$ in Fig. 1, the normal and tangential components of velocity discontinuity are $v_n'$ and $v_t'$, respectively. On the zigzag boundary segment $AF$, which is inclined to $AG$ at an angle $1/2\beta$, the velocity discontinuity components are

$$\{\delta v_n\}_{AF} = v_n' \cos \frac{1}{2}\beta + v_t' \sin \frac{1}{2}\beta,$$

$$\{\delta v_t\}_{AF} = -v_n' \sin \frac{1}{2}\beta + v_t' \cos \frac{1}{2}\beta. \quad (22)$$

On the zigzag boundary segment $FG$, the velocity discontinuity components are given by (22) with $1/2\beta$ replaced by $-1/2\beta$. The energy dissipation rate for segments $AF$ and $FG$ then can be calculated from (18) and compared with the rate for $AG$. The increased length of $AFG$ over $AG$ is accounted for in the comparison. The ratio of the energy dissipation rate on $AFG$ to that on $AG$, called the *energy dissipation factor*, as calculated from (18), is shown in Fig. 7 for various ratios of tangential velocity to normal velocity ($v_t/v_n$) and values of the yield parameters $\bar{a}$, $\bar{b}$, $\bar{c}$ typical for ice.[3] The results are not very sensitive to the yield parameters. The cancellation of first-order terms in $\beta$ accounts for the quadratic variation of the energy dissipation factor at low values of $\beta$. In the cases considered by Nordgren (1988), values of $v_t/v_n$ are typically in the range 3 to 25. Thus, the maximum values of the energy dissipation factor (at $v_t/v_n \simeq 10$) can be used in general calculations of an upper bound. The energy dissipation factor for the zigzag boundary segment $AFG$ also applies to the zigzag boundary segment $AEG$ in Fig. 1. For the deterministic material, use of the zigzag boundaries increases the upper bound on the collapse pressure in proportion to the energy dissipation factor.

In applying the foregoing results, the separation angle $\beta$ and the length $l$ of the zigzags in Fig. 1 should be selected to minimize the upper bound, i.e., to minimize the product of the energy dissipation factor and the branch factor. A low

[3] In the notation of Nordgren (1988), the yield parameters are determined from $Q_1/Q_0 = 1.5$ and $P_1/Q_0 = 2$, where $Q_0 = q$ and $Q_1$, $P_1$ are the maximum confined strength and the corresponding confining pressure in a conventional triaxial test.

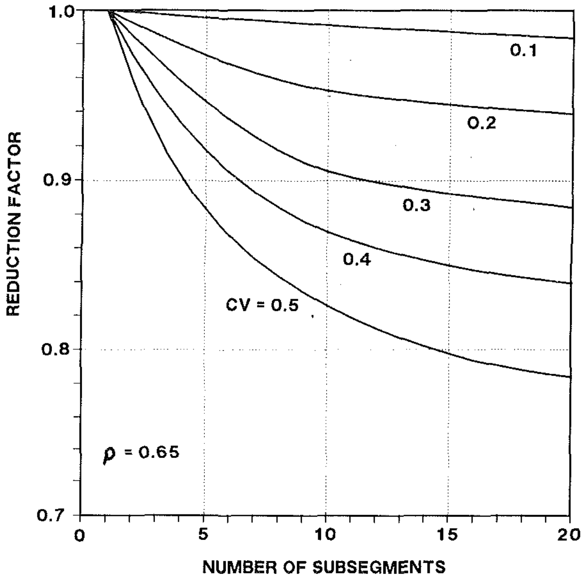


**Fig. 8 Reduction factor for upper bound on mean contact pressure versus number of subsegments on each segment of the rigid-plastic boundary for various values of the coefficient of variation $CV$ of strength for a branch. Lognormal distribution for strength with correlation coefficient $\rho = 0.65$, $\beta = 18$ deg.**

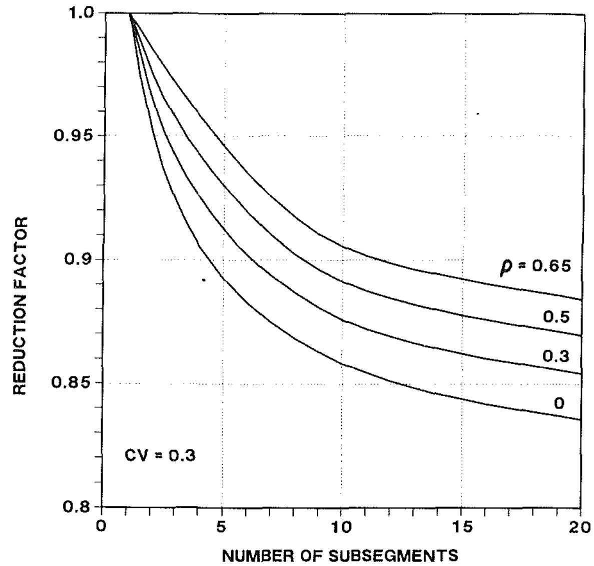


**Fig. 9 Reduction factor for upper bound on mean contact pressure versus number of subsegments on each segment of the rigid-plastic boundary for various values of the correlation coefficient $\rho$ with $\beta = 18$ deg and lognormal distribution for strength with coefficient of variation $CV = 0.3$ for each branch**

value of $\beta$ is desirable to reduce the dissipation factor (Fig. 7), whereas a high value of $\beta$ reduces the correlation coefficient (Fig. 2) which reduces the branch factor (Figs. 4 and 5). The optimal value of $\beta$ usually lies in the range 10 deg to 20 deg. Similarly, low values of $l$ reduce the standard deviation (Fig. 3 with $R \simeq 2l$), whereas high values of $l$ reduce the correlation coefficient (Fig. 2 with $R \simeq l$). The reduction of both the standard deviation and the correlation coefficient reduce the mean of the minimum (Figs. 4 and 5). The optimal value of $l/h$ usually lies in the range 5 to 15.

As seen from Fig. 5, a coefficient of variation (standard deviation ÷ mean) in uniaxial yield strength of approximately 0.3 or more is required to obtain a reduction in the upper bound $\bar{n}_U$ when a energy dissipation factor of 1.1 (Fig. 7) is considered.

In addition to the two zigzag branches for each subsegment, the original subsegment itself can be included and the minimum of the three branches taken. However, the correlation coefficient is higher for the case of three branches, since the angle between two of the pairs of lines now is $\beta/2$ rather than $\beta$. Thus, calculations with Figs. 4 or 6 show that the upper bound $\bar{n}_U$ is not lowered significantly by this three-branch approach.

**Alternate Boundary.** In a further attempt to lower the upper bound on the mean safety factor, we consider a more complicated set of zigzag boundaries with multiple branches as shown in the inset to Fig. 1 for the segment $AB$. The segments $BC$ and $BD$ have a similar set of multiple branches. We seek the zigzag boundary path from $A$ to $B$ which minimizes the energy dissipation with respect to all possible paths. The path may branch at each of the nodal points indicated in the inset, e.g., at point 6 the path may branch to points 1, 2, or 3. On the inclined branches of the path, the effect of the energy dissipation factor (Fig. 7) must be accounted for. Also, the separation angle $\beta$ and the subsegment length $l$ are optimized as before.

The mean of the minimum energy dissipation on the multiple branches has been found by a Monte Carlo simulation calculation. For each realization of the stochastic material, correlated yield strengths are generated for all possible branches using methods developed in the Appendix. The optimal path and the minimum energy dissipation are found by the method of dynamic programming as given by Bellman and Dreyfus (1962). This method substantially reduces the search effort required to find the minimizing path.

Results of the simulation are presented in Figs. 8 and 9, where the *reduction factor* is defined as the ratio of the mean minimum energy dissipation over the multiple branches to the mean energy dissipation over the straight segment. In both figures, the energy dissipation factor is taken as 1.1. In Fig. 8, the correlation coefficient, $\rho$, for strength on the subsegments is held at the value 0.65, while the coefficient of variation for strength on the subsegments, $CV$, is varied as a parameter. Values of $\rho$ above 0.65 cannot be simulated by the method of the Appendix for large values of $CV$. In Fig. 9, $CV$ is held at the value 0.3, while $\rho$ is varied as a parameter. The reduction factor for energy dissipation from the multiply branched rigid-plastic boundary again is an approximation to the mean upper bound $\bar{n}_U$ for cases of several subsegments per segment. Now the reduction factor decreases with increasing number of subsegments. Thus, the model indicates a "size effect" in that the upper bound on mean contact pressure decreases with increasing contact area (for constant subsegment length $l$).

In obtaining the numerical results by simulation, it was observed that the variance of the calculated safety factor also decreases with increasing contact area. Although this is only an estimate of the actual variance in the safety factor, the result may be of interest in problems where maximum loading is important. For sufficiently large contact areas, the mean safety factor may give an adequate indication of the maximum load.

Strictly speaking, the foregoing results are valid only for the state of plane stress in a thin plate where variations in strength across the plate thickness are negligible. The results also may be a useful approximation for the state of plane strain, if the body is considered to be composed of a stack of plates. Each plate is analyzed independently by the foregoing stochastic approach. The neglected interaction between the plates is expected to be small if the plate thickness is taken to be on the order of the correlation length parameter $h$ in (9). For a more accurate treatment of plane strain as well as three-dimensional problems, it appears necessary to generalize the concept of multiple alternate branches in applying the extended upper-bound theorem.

## Conclusion

The collapse theorems of limit analysis have been extended to a stochastically inhomogeneous material. For the problem of contact pressure on a truncated wedge, the stochastic upper-bound theorem leads to a reduction in the upper bound on mean collapse pressure from the deterministic treatment using mean yield strength. Numerical results show that the upper bound on mean collapse pressure decreases as the contact area increases, which indicates a "size effect."

Application of the stochastic lower-bound theorem to the contact problem remains to be explored. Other applications of stochastic limit analysis appear to be possible.

## References


Bellman, R. E., and Dreyfus, S. E., 1962, *Applied Dynamic Programming*, Princeton University Press, Princeton, New Jersey.

Drucker, D. C., 1951, "A More Fundamental Approach to Plastic Stress-Strain Relations," *Proc. 1st U.S. Natl. Cong. Appl. Mech.*, ASME, New York, pp. 487–491.

Gumbel, E. J., 1958, *Statistics of Extremes*, Columbia University Press, New York.

Koiter, W. T., 1960, "General Theorems for Elastic-Plastic Solids," *Progress in Solid Mechanics*, Vol. 1, I. N. Sneddon and R. Hill, eds., North-Holland, Amsterdam, pp. 167–221.

Nordgren, R. P., 1988, "Plastic Analysis of Ice Contact Problems," ASME Journal of Applied Mechanics, Vol. 55, pp. 73–80.

Parzen, E., 1967, *Modern Publishing Theory and Its Applications*, John Wiley and Sons, New York.

Yaglom, A. M., 1962, *An Introduction to the Theory of Stationary Random Functions*, translated and edited by R. A. Silverman, Prentice-Hall, Englewood Cliffs, New Jersey.


## APPENDIX

For application of the stochastic upper-bound theorem to the plane problem of contact pressure on a truncated wedge, certain mathematical results are required. These results will be derived here. For background on the deviations, see Gumbel (1958), Parzen (1967), and Yaglom (1962).

**Average Strength on Line Segments.** Let $\hat{q}(R)$ be the average uniaxial compressive strength (or any other isotropic, homogeneous random field) over a line segment of length $R$ between points $P_0$ and $P_1$. Using (5) we have

$$\hat{q}(R) \equiv \frac{1}{R}\int_{P_0}^{P_1}[\overline{q}+\xi(s)]ds = \overline{q} + \lim_{n\to\infty}\frac{1}{n}\sum_{m=1}^{n}\xi(mR/n), \quad \text{(A1)}$$

where $s$ is the arc length along $P_0P_1$. The mean value of $\hat{q}_R$ on $P_0P_1$ is simply the mean strength $\overline{q}$. Thus, using (6) and (A1), the variance is given by

$$\sigma_R^2 \equiv E[(\hat{q}_R-\overline{q})^2] = \frac{1}{R^2}\int_0^R\int_0^R B(s-s')dsds'. \quad \text{(A2)}$$

By a similar limit process, the covariance in the average strength over the lines $P_0P_1$ and $P_0P_2$ with lengths $R_1$ and $R_2$ and separation angle $\beta$ is found to be

$$\lambda_{12} \equiv E\left[\left(\frac{1}{R_1}\int_{P_0}^{P_1}\xi(s_1)ds_1\right)\left(\frac{1}{R_2}\int_{P_0}^{P_2}\xi(s_2)ds_2\right)\right],$$

$$= \frac{1}{R_1R_2}\int_0^{R_1}\int_0^{R_2}B(r_{12})ds_1ds_2, \quad \text{(A3)}$$

where

$$r_{12} = [s_1^2+s_2^2-2s_1s_2\cos\beta]^{\frac{1}{2}}.$$

For the special correlation function (9) with $R_1 = R_2 \equiv R$, the variance (A2) and covariance (A3) reduce to

$$\sigma_R^2 = B_0(h/R)\{2\arctan(R/h) - (h/R)\ln[1+(R/h)^2]\}, \quad \text{(A4)}$$

$$\lambda_{12} = B_0(h/R)^2\int_0^{\pi/4}\ln[1+(R/h)^2(1-\sin 2\theta\cos\beta)/\cos^2\theta]/[1-\sin 2\theta\cos\beta]d\theta. \quad \text{(A5)}$$

The integral in (A5) can be evaluated by numerical quadrature. Results for the standard deviation $\sigma_R$ and the correlation coefficient, $\rho_R = \lambda_{12}/\sigma_R^2$, obtained from (A4) and (A5) are shown in Figs. 3 and 2, respectively.

**Minimum of Correlated Random Variables.** The two correlated random variables $y_1$, $y_2$ can be generated from uncorrelated random variables $x_1$, $x_2$ by the formulas

$$y_1 = x_1+\alpha x_2, \quad y_2 = x_2+\alpha x_1, \quad \text{(A6)}$$

where $\alpha$ is a constant. Similar formulas apply for three or more correlated variables. If $x_1$, $x_2$ have mean $m$ and variance $\sigma^2$, then $y_1$, $y_2$ have mean, variance, and covariance

$$\overline{y} \equiv E[y_i] = (1+\alpha)m,$$
$$\sigma_y^2 \equiv \mathrm{Var}[y_i] = (1+\alpha^2)\sigma^2, \quad \text{(A7)}$$
$$\lambda \equiv \mathrm{Cov}[y_1,y_2] = 2\alpha\sigma^2.$$

Then the correlation coefficient is

$$\rho_y \equiv \lambda/\sigma_y^2 = 2\alpha/(1+\alpha^2), \quad \text{(A8)}$$

which can be solved for $\alpha$ as

$$\alpha = \rho_y/[1+\sqrt{1-\rho_y^2}]. \quad \text{(A9)}$$

We define the random variable $z$ as

$$z \equiv \min(y_1,y_2). \quad \text{(A10)}$$

The cumulative distribution function for $z$ is given by

$$F(z) = 2\iint H[y_2-y_1]H[z-y_1]g(y_1,y_2)dy_1dy_2, \quad \text{(A11)}$$

where $H[\ldots]$ is the unit step function and $g(y_1, y_2)$ is the joint probability density function (p.d.f.) for $y_1$ and $y_2$. Once $F(z)$ is evaluated, the p.d.f. for $z$ follows by differentiation. The formulas can be generalized to $n$ correlated $y_i$ variates with minimum $z_n$.

**Normal Distribution.** If $x_1$, $x_2$ are independent normal variates, then $y_1$, $y_2$ are (correlated) normal variates, as seen from the definition (A6) and their joint p.d.f. is

$$g(y_1,y_2) = \frac{1}{2\pi\sigma_y^2\sqrt{1-\rho_y^2}}\exp\left\{-\frac{(y_1-\overline{y})^2-2\rho_y(y_1-\overline{y})(y_2-\overline{y})+(y_2-\overline{y})^2}{2\sigma_y^2(1-\rho_y^2)}\right\}. \quad \text{(A12)}$$

In this case, the p.d.f. for the variate $z$ is determined from (A11) as

$$f(z) \equiv \frac{dF}{dz} = \frac{1}{\sqrt{2\pi}\sigma_y}\exp\left\{-\frac{(z-\overline{y})^2}{2\sigma_y^2}\right\}\mathrm{erfc}\left\{\sqrt{\frac{1-\rho_y}{1+\rho_y}}\frac{(z-\overline{y})}{\sqrt{2}\sigma_y}\right\}. \quad \text{(A13)}$$

From $f(z)$, the mean and variance of $z$ are found to be

$$\overline{z} = \overline{y} - \sigma_y\sqrt{1-\rho_y}/\sqrt{\pi}, \quad \sigma_z^2 = \sigma_y^2[1+(1-\rho_y)/\pi]. \quad \text{(A14)}$$

The dependence of the mean $\overline{z}$ on the correlation coefficient $\rho_y$ is shown in Fig. 4 as the case $n = 2$. The standard deviation $\sigma_z$ depends weakly on $\rho_y$, varying from 1.148 to 1.0 as $\rho_y$ varies from 0 to 1.

In a similar manner, we have considered the generalized case of $n$ correlated normal random variables $(y_1, y_2, \ldots, y_n)$ all with the same mean $\overline{y}$, variance $\sigma_y^2$, and pairwise correlation coefficients $\rho_y$. The minimum of $(y_1, y_2, \ldots, y_n)$ is denoted by $z_n$. Closed formulas for the mean $\overline{z}_n$ have been obtained for $n$

= 3, 4, 5 and these results also are shown in Fig. 4. For the case of $n$ uncorrelated variables ($\rho_y = 0$), our results agree with Gumbel (1958).

**Lognormal Distribution.** For the lognormal distribution, a slightly different approach is required. Let $u_1$, $u_2$ be the random variables defined by

$$u_1 = \exp\{y_1\}, \quad u_2 = \exp\{y_2\}, \qquad \text{(A15)}$$

where $y_1$, $y_2$ are the correlated normal variates defined by (A6) in which $x_1$, $x_2$ again are independent normal variates with mean $m$ and variance $\sigma^2$. Thus, $u_1$ and $u_2$ are correlated lognormal variates. Expressions for the mean, variance, and covariances of $u_1$, $u_2$ can be derived with the aid of the moment generating function for $x_1$, $x_2$, namely

$$\psi(t) = \exp\left\{mt + \frac{1}{2}\sigma^2 t^2\right\} = \int_{-\infty}^{\infty} e^{xt} g(x)\,dx, \qquad \text{(A16)}$$

where $g(x)$ is the normal p.d.f. for $x_1$, $x_2$. Then, the mean and variance of $u_1$, $u_2$ are given by

$$\bar{u} = \exp\left\{(1+\alpha)m + \frac{1}{2}(1+\alpha^2)\sigma^2\right\},$$

$$\sigma_u^2 = \exp\{2(1+\alpha)m + 2(1+\alpha^2)\sigma^2\} - \bar{u}^2. \qquad \text{(A17)}$$

The correlation coefficient for $u_1$, $u_2$ is found to be

$$\rho_u \equiv \mathrm{Cov}[u_1, u_2]/\sigma_u^2 = [\exp\{2\alpha\sigma^2\} - 1]\bar{u}^2/\sigma_u^2. \qquad \text{(A18)}$$

It follows from the preceding equations that

$$\bar{y} = \ln\bar{u} - \frac{1}{2}\ln[1 + (\sigma_u/\bar{u})^2], \quad \sigma_y^2 = \ln[1 + (\sigma_u/\bar{u})^2],$$

$$\rho_y = \ln[1 + \rho_u(\sigma_u/\bar{u})^2]/\ln[1 + (\sigma_u/\bar{u})^2], \qquad \text{(A19)}$$

which serve to determine $\bar{y}$, $\sigma_y$, and $\rho_y$ for given $\bar{u}$, $\sigma_u$, and $\rho_u$. Then, $m$, $\sigma$, and $\alpha$ can be determined from (A7) and (A9). For the lognormal case, the p.d.f. for the variate $z$ is determined from (A11) as

$$f(z) \equiv \frac{dF}{dz}$$

$$= \frac{1}{\sqrt{2\pi} z\sigma_y} \exp\left\{-\frac{(\ln z - \bar{y})^2}{2\sigma_y^2}\right\} \mathrm{erfc}\left\{\sqrt{\frac{1-\rho_y}{1+\rho_y}}\frac{(\ln z - \bar{y})}{\sqrt{2}\sigma_y}\right\}. \qquad \text{(A20)}$$

The mean and variance of $z$ are found to be given by

$$\frac{\bar{z}}{\bar{u}} = \mathrm{erfc}\left\{\frac{1}{2}\left\langle \ln\left[\frac{1 + (\sigma_u/\bar{u})^2}{1 + \rho_u(\sigma_u/\bar{u})^2}\right]\right\rangle^{\frac{1}{2}}\right\},$$

$$\sigma_z^2 = (\sigma_u^2 + \bar{u}^2)\,\mathrm{erfc}\left\{\left\langle \ln\left[\frac{1 + (\sigma_u/\bar{u})^2}{1 + \rho_u(\sigma_u/\bar{u})^2}\right]\right\rangle^{\frac{1}{2}}\right\} - \bar{z}^2 \qquad \text{(A21)}$$

Figure 5 shows the dependence of the mean ratio $\bar{z}/\bar{u}$ on the correlation coefficient $\rho_u$ for various values of the coefficient of variation $\sigma_u/\bar{u}$.

Further, we have considered the related case of three correlated lognormal random variables ($u_1$, $u_2$, $u_3$) with the same mean $\bar{u}$ and variance $\sigma_u^2$, and identical pairwise correlation coefficients $\rho_u$. The minimum of ($u_1$, $u_2$, $u_3$) is denoted by $z_3$. An expression for the mean $\bar{z}_3$ has been obtained, and results are shown in Fig. 6 which is similar to Fig. 5.

# Numerical Analysis of Plane-Strain Tension Test for Rate-Dependent Solids

**P. Tuğcu**
Faculty of Applied Science,
Universite de Sherbrooke,
Sherbrooke, Quebec J1K 2R1
Canada

*The plane-strain tension test is analyzed numerically for a material with strain and strain-rate hardening characteristics. The effect of the prescribed rate of straining is investigated for an additive logarithmic description of the material strain-rate sensitivity. The dependency to the imposed strain rate so introduced is shown to have a significant effect on several features of the load-elongation curve such as the attainment of the load maximum, the onset of localization, and the overall engineering strain.*

## 1 Introduction

The plastic instability in plane-strain tension of a rate-dependent material is similar to the axisymmetric case where an almost homogeneous deformation state is followed by the formation of a diffuse neck due some sort of material or geometric inhomogeneity. Compared to the rate-independent behavior, differences in the deformation history arise mainly due to the stabilizing influence of the material strain-rate sensitivity, manifested by a larger overall engineering strain due to a retarded neck growth. The increase in uniform elongation for a rate-dependent solid is of particular interest in general, since the behavior of the metals is inherently rate-dependent at high speeds of deformation. One area of particular interest is the sheet metal forming processes, for which the search for improved predictability continues as commercial operations involve increasingly higher speeds.

In this study, a rectangular elastic-viscoplastic specimen under plane-strain loading conditions is analyzed where the isotropic hardening flow theory relations are generalized for rate-dependent behavior. Like in the axisymmetric case reported in Tuğcu (1989), an additive logarithmic representation is chosen to describe the dependence of the viscoplastic strain rate, on the state variables in the current state. This in turn brings in the prescribed rate of straining as an important factor affecting the deformation history of the specimen, contrary to the separable power law such as employed in Becker and Needleman (1986). The traditionally employed limit strain definition for forming limit curves of strain-rate-dependent solids is also questioned in favor of a unified definition with the rate-independent case on physical grounds.

The numerical results were generated using a finite element method for the entire deformation history of a specimen. An initial thickness inhomogeneity is prescribed to initiate the localization process corresponding to a zero angle of neck orientation, which also represents the diffuse neck instability mode for the whole range of the biaxial tensile strain domain in sheet-metal-forming limit curves. The final mode of failure in plane-strain tension, however, often involves shear band formation which cannot be predicted with the analysis given here (Needleman and Tvergaard, 1984; Becker and Needleman, 1986). Overall elongation levels to fracture are nevertheless compared qualitatively on the basis of neck development.

## 2 Analysis

The field equations for the finitely deformed elastic-viscoplastic solid are based on a Langrangian formulation, where the initial undeformed configuration with volume $V$ and surface $S$ is taken as a reference. In this reference, state material points are identified by convected coordinates $x^i$. The position vector of a material point in the initial and current configurations are denoted by $\mathbf{r}(x^j)$ and $\mathbf{R}(x^j)$, respectively. The base vectors $\mathbf{g}_k$ and $\mathbf{G}_i$ in the reference and current configurations are given by

$$\mathbf{g}_i = \frac{\partial \mathbf{r}}{\partial x^i}, \; \mathbf{G}_i = \frac{\partial \mathbf{R}}{\partial x^i}. \tag{1}$$

The metric tensors in the reference and current configurations are $g_{ij} = \mathbf{g}_i \cdot \mathbf{g}_j$ and $G_{ij} = \mathbf{G}_i \cdot \mathbf{G}_j$, respectively. The displacement vector from the undeformed configuration is denoted by $\mathbf{u}$.

The nominal traction vector $\mathbf{F}$, defined as the load per unit area $dS$ of the undeformed configuration, is obtained from

$$F^j = n_i(\tau^{ij} + \tau^{ik} u^j_{,k}) = n_k q^{ij} \tag{2}$$

where $\tau^{ij}$ and $q^{ij}$ denote the contravariant components, respectively, of the symmetric Kirchhoff stress-tensor defined with respect to the deformed base vectors $\mathbf{G}_i$, and the nonsymmetric nominal stress tensor defined with respect to the undeformed base vectors $\mathbf{g}_i$. In (2), $\mathbf{n} = n_i \mathbf{g}^i$ represents the area

Contributed by the Applied Mechanics Division of THE AMERICAN SOCIETY OF MECHANICAL ENGINEERS for publication in the JOURNAL OF APPLIED MECHANICS.

Discussion on this paper should be addressed to the Technical Editor, Prof. Leon M. Keer, The Technological Institute, Northwestern University, Evanston, IL 60208, and will be accepted until four months after final publication of the paper itself in the JOURNAL OF APPLIED MECHANICS.

Manuscript received by the ASME Applied Mechanics Division, Aug. 1, 1990; final revision, Apr. 19, 1991. Associate Technical Editor: R. M. McMeeking.

and orientation of the material element in the reference configuration and a comma denotes covariant differentiation with respect to the undeformed metric. The true or Cauchy stress tensor, defined with respect to the deformed metric $\mathbf{G}_i$, in terms of the current area and orientation of a material element, is related to the Kirchhoff stress tensor from

$$\sigma = \left(\frac{g}{G}\right)^{1/2} \tau \tag{3}$$

where $g$ and $G$ represent the determinants of $g_{ij}$ and $G_{ij}$, respectively.

We now assume that an approximate equilibrium state is known at time $t$, satisfying the virtual work principle

$$\int_V q^{ij} \delta u_{j,i} dV = \int_V \tau^{ij} \delta \eta_{ij} dV = \int_{S_F} F^i \delta u_i dS \tag{4}$$

where $S_F$ is part of the surface on which the nominal traction vector is prescribed and the Lagrangian strain tensor components $\eta_{ij}$ are given from

$$\eta_{ij} = \frac{1}{2}(u_{i,j} + u_{j,i} + u^k_{,i} u_{k,j}). \tag{5}$$

Employing a linear incremental approximation for the field quantities, the virtual work principle (4) can be written at time $t + \Delta t$ as follows:

$$\Delta t \int_V \dot{q}^{ij} \delta u_{j,i} dV = \Delta t \int_V (\dot{\tau}^{ij} \delta \eta_{ij} + \tau^{kj} \dot{u}^i_{,k} \delta u_{i,j}) dV$$

$$= \Delta t \int_{S_F} \dot{F}^i \delta u_i dS - \left[ \int_V \tau^{ij} \delta \eta_{ij} dV - \int_{S_F} F^i \delta u_i dS \right] \tag{6}$$

where a superposed dot denotes partial differentiation with respect to time. The bracketed terms on the right-hand side of (6) is an equilibrium correction which vanishes if the solution at time $t$ corresponds to exact equilibrium.

The strain-rate sensitivity for the quasi-static deformations analyzed is modeled using an elastic-viscoplastic von Mises solid. The total strain rate is written as the sum of the elastic and viscoplastic parts

$$\dot{\eta}_{ij} = \dot{\eta}^E_{ij} + \dot{\eta}^P_{ij}. \tag{7}$$

The rate constitutive relationship for the elastic part is taken as

$$\dot{\eta}^E_{ij} = \frac{1}{E} \left[ \frac{1+\nu}{2} (G_{ik}G_{jl} + G_{jk}G_{il}) - \nu G_{ij} G_{kl} \right] \overset{*}{\tau}{}^{kl} \tag{8}$$

where $E$ is Young's modulus, $\nu$ denotes Poisson's ratio and a superposed * denotes the Jaumann rate. The plastic component in (7) is written as in the rate-independent response

$$\dot{\eta}^P_{ij} = \frac{3 \dot{\epsilon}^P_e}{2 \tau_e} S_{ij} \tag{9}$$

where the stress deviator components $s_{ij}$ are obtained from

$$s^{ij} = \tau_{ij} - \frac{1}{3} G^{ij} G_{kl} \tau^{kl}. \tag{10}$$

In (9), $\tau_e$ denotes the effective Kirchhoff stress given as

$$\tau_e^2 = \frac{3}{2} s_{ij} s^{ij}. \tag{11}$$

The viscoplastic behavior is introduced in (9) through the effective plastic strain rate $\dot{\epsilon}^P_e$. As opposed to the rate-independent response where $\dot{\epsilon}^P_e$ is given in terms of the incremental quantities, the strain-rate dependent behavior is modeled assuming $\dot{\epsilon}^P_e$ is determined from the current stress and strain values as

$$\dot{\epsilon}^P_e = H(\epsilon^P_e, \sigma_e). \tag{12}$$

In (12), $\epsilon^P_e$ is the effective viscoplastic strain, obtained from an integration of $\dot{\epsilon}^P_e$ with respect to time and $\sigma_e$ ($= \sqrt{g/G}\, \tau_e$) is the effective true stress. Further, the uniaxial behavior of most metals at room temperature suggests that the strain-rate hardening can be expressed in the following additive form:

$$\sigma_e = \begin{cases} E\epsilon_e & \text{for } \sigma \le \sigma_Y \\ K\left[ (\epsilon^P_e + \epsilon_c)^N + m \ln\left(1 + \dfrac{\dot{\epsilon}^P_e}{\dot{\epsilon}_R}\right) \right] & \text{for } \sigma > \sigma_Y \end{cases} \tag{13}$$

where $N$ is a strain-hardening parameter, $m$ is the strain-rate sensitivity index, $\dot{\epsilon}_R$ is a reference strain rate, and $K$ is a material constant. The subscript $Y$ is employed to denote quantities associated with initial yield and the constant $\epsilon_c$ is determined from the continuity of stress at initial yield. The rate-independent plastic response with power-law strain hardening is resulted from (13) if $m = 0$ or $\dot{\epsilon}^P_e = 0$. The additive form of (13) indicates that for two given $\dot{\epsilon}^P_e$ values, the flow stress differs by the same amount at any level of deformation. Separable forms of uniaxial behavior are also commonly employed, which predict the same ratio of flow stress for two given $\dot{\epsilon}^P_e$ values at any strain level. As will be discussed later, when the stress state becomes nonhomogeneous, the predictions resulting from these alternative forms can differ substantially. At high rates of strain, the strain-softening effect of deformation induced heating in (13) might not be negligible, which is not accounted for in this study.

The finite element analysis developed here is based on the variational principle (6). For this we use the relation between the convected and Jaumann rates to obtain

$$\dot{\tau}^{ij} = \bar{L}^{ijkl} \dot{\eta}_{kl} - L^{ijkl} \dot{\eta}^P_{kl} \tag{14}$$

where $L^{ijkl}$ are the elastic moduli and

$$\bar{L}^{ijkl} = L^{ijkl} - \frac{1}{2}(G^{ik}\tau^{jl} + G^{il}\tau^{jk} + G^{jk}\tau^{il} + G^{jl}\tau^{ik}). \tag{15}$$

When (14) is substituted in (6), since $\dot{\eta}^P_{ij}$ are not dependent on the velocity field due to the viscoplastic representation (12), the terms involving $\dot{\eta}^P_{ij}$ become part of the nodal traction-rate vector.

## 3 Problem Formulation

For our plane-strain formulation we consider a rectangular specimen with length $2L_0$ and average thickness $2h_0$ in its initial undeformed state. In this reference configuration, a Cartesian coordinate system with $x^i \equiv x, y, z$ is chosen. The origin is placed at the center of the specimen and the $x$-$z$ plane is taken as the plane of deformation. The $x$ and $z$-axes are chosen to be in the thickness and length directions, respectively. An initial geometric inhomogeneity is introduced to trigger the neck development. For this, the initital thickness of the specimen is assumed to vary along $z$, given by $(h_0 - \Delta h_0)$, where $\Delta h_0$ is prescribed as

$$\Delta h_0 = \xi h_0 \cos \frac{\pi z}{L_0} \tag{16}$$

with $\xi > 0$. The lateral surfaces $x = (h_0 - \Delta h_0)$ are taken to be traction-free. Symmetry about the mid-planes $x = 0$, $z = 0$ is assumed. The displacement component along $y$-axis is $u_y = 0$. The boundary conditions for the quadrant considered in the numerical computations are

$$\begin{aligned} &\dot{F}^x = 0,\ \dot{u}_z = 0 && \text{at } z = 0 \\ &\dot{F}^z = 0,\ \dot{u}_x = 0 && \text{at } x = 0 \\ &\dot{F}^x = 0,\ \dot{u}_z = \dot{U} = \dot{\epsilon}_a(U + L_0) && \text{at } z = L_0 \end{aligned} \tag{17}$$

where $\dot{\epsilon}_a$ denotes the average axial logarithmic strain rate imposed at $z = L_0$ and the total displacement $U$ of the end section is obtained from $\int \dot{U} dt$.

The finite element analysis performed here is based on constant strain triangles. The grid employs quadrilateral elements made up of four triangular elements formed by the diagonals of the quadrilaterals. The ability of the crossed triangles to handle the nearly isochoric deformations resulting from the incompressibility of the plastic flow is discussed in Nagtegaal et al. (1974). The integrals in (6) are evaluated using a central one-point integration scheme for the constant strain triangular elements employed.

## 4 Results

Since possible implications of the results to the sheet-metal formability analyses will be attempted, we start this section by giving a brief outline of the general features of the forming limit curve studies. Limit strain analysis for various loading combinations in the plane of a sheet metal requires consideration of a range varying from uniaxial tension to equibiaxial tension. In terms of the logarithmic strains, defined along the principal axes of the specimen in the plane, this range corresponds to a variation of these strain ratios between $-0.5$ (uniaxial tension) and 1 (equibiaxial tension). Since bifurcation studies for flow theory analysis proved inadequate in the tensile biaxial range, an alternative approach to finding reasonable critical strains with this theory was presented by Marciniak and Kuczynski (1967), where necking instability was assumed to be triggered by the growth of an initial geometric (or material) nonuniformity in the form of a band. Successful predictions employing different aspects of flow rules, such as yield surface vertices, non-normality of plastic flow, void growth, etc., was later followed by Storen and Rice (1975), Rudnicki and Rice (1975), Hutchinson and Neale (1978a), Needleman and Rice (1978), and Hutchinson and Tvergaard (1981). Limit strain predictions with the classical flow theory of plasticity, however, still remain at an unsatisfactory stage, since studies following Marciniak and Kuczynski (1967) to date have not yet been successful in matching the magnitude of the presumed geometric defects producing agreement with experiments to those measured in real specimens.

The inclusion of the strain-rate effects to the studies of sheet-metal formability were initiated by Marciniak et al. (1973), similar to the rate-independent case, using an approximate method to determine the incremental deformation growth in an initial geometric inhomogeneity in terms of the prescribed uniform section deformations. Like in the rate-independent analysis (Marciniak and Kuczyński, 1967), their analysis for the rate-dependent behavior also predicts an unbounded deformation growth in the groove once the plastic instability sets in. However, unlike the rate-independent case where a definite limit strain can be defined, the uniform section strains for the rate-dependent analysis grow asymptotically to a maximum. This asymptotic value of the uniform section strain is defined as the limit strain with some bounds imposed from fracture considerations of the material in the groove. Similar studies for rate-sensitive behavior were since undertaken among others by Hutchinson and Neale (1978b) and Needleman and Tvergaard (1984) to investigate other related aspects of sheet-metal forming where the same limit strain definition was adopted.

Studies of the forming limit curves covering the whole range of biaxial loading are in general performed, assuming the plane-stress condition, whether in full finite element solutions or in the long-wavelength analyses, in most of the studies cited above. The particular plane-strain analysis performed here is an exact three-dimensional solution which computationally reduces to two dimensions.

A rectangular specimen with an initial length-to-thickness ratio of $(L_0/h_0) = 4$ is considered. The finite element mesh is generated using eight equidistant divisions in the $x$-direction. The quadrilaterals are formed using a total of 44 divisions in

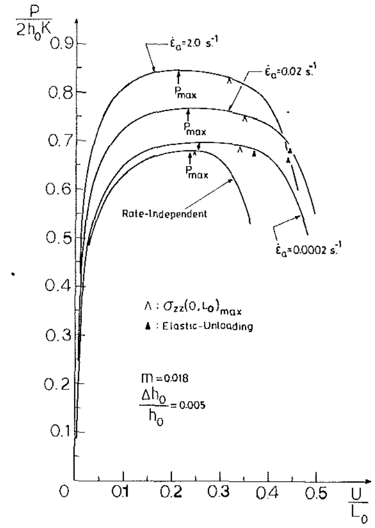


**Fig. 1 Load-elongation curves for rate-independent and rate-dependent responses for the imposed strain rates of $\dot{\epsilon}_a = 2.0, 0.02, 0.0002\ \mathrm{sec}^{-1}$. $((\Delta h_0/h_0) = 0.005)$**

the $z$-direction. Of these, 14 equidistant divisions are chosen to form a finer mesh at the anticipated neck region between $z = 0$ and $0.868h_0$. The remaining part of the specimen is divided into 30 equidistant divisions. The key features of the deformation history reported here are similar to the axisymmetric case reported in Tuğcu (1989).

In (13), the material constants, which were kept the same in all the results presented here, are the strain-hardening parameter $N = 0.22$, the reference strain rate $\dot{\epsilon}_R = 0.000137$, $(E/K) = 50$, $\epsilon_Y = (\sigma_Y/E) = 0.004$. The Poisson's ratio was taken as $\nu = 0.3$. These values together with the range the strain-rate sensitivity index $m$ is varied, and can be considered typical of metals with the exception of the $E/K$ value. The relatively small $E/K$ employed in the analysis provides computational efficiency by allowing larger time increments, as opposed to a more realistic range of 400–500. However, for the parametric study performed here, the particular choice of this material property is not critical to the analysis.

The effect of the imposed strain rate on the load-elongation response is shown in Fig. 1, for a specimen with strain-rate sensitivity parameter $m = 0.018$ and a geometric imperfection corresponding to an initial area defect of $(\Delta h_0/h_0) = 0.005$ at the neck ($z = 0$), given by $\xi = 0.005$ in (16). The rate-independent response is also depicted in the same figure. The three other cases compared correspond to the imposed strain rate values of $\dot{\epsilon}_a = 2.0, 0.02$, and $0.0002\ \mathrm{sec}^{-1}$ from top to bottom, respectively. The arrows are used to indicate the maximum load points which occur at $(U/L_0) = 0.211, 0.230, 0.255, 0.236$ for the rate-dependent cases with $\dot{\epsilon}_a = 2.0, 0.02, 0.0002\ \mathrm{sec}^{-1}$ and the rate-independent response, respectively. The corresponding uniform section strains are $\epsilon_{zz}(0, L_0) = 0.180, 0.196, 0.213$, and 0.190 in the same order as above. It is seen that the attainment of the maximum load occurs at a smaller elongation for a given material when the imposed strain rate is increased. The shift, with respect to the maximum load point of the limiting case of rate-independent response in Fig. 1, is therefore determined from the competition between the strain-rate sensitivity index $m$ and the imposed strain rate $\dot{\epsilon}_a$. Note that the imperfection magnitude also plays a major role in the attainment of the load maximum as will be shown. This and other related aspects are discussed in more detail in Tuğcu (1989).

The onset of plastic instability designated by the circumflexes in Fig. 1 and the rest of the figures is defined as the attainment of the maximum axial ($\sigma_{zz}$) or effective stress ($\sigma_e$) at the uniform

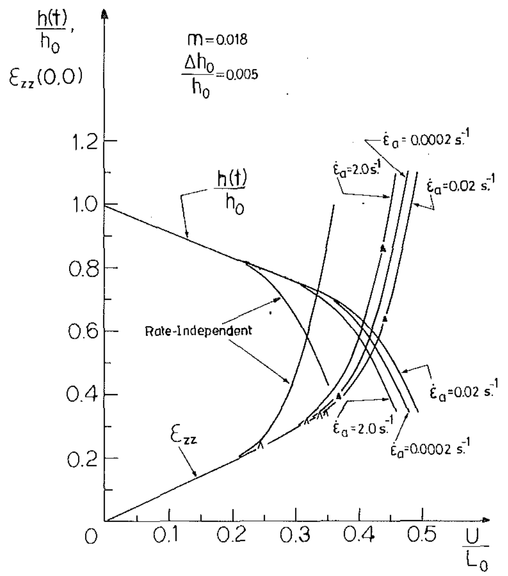


**Fig. 2 The evolution of the normalized neck area and the axial strains at the neck section ($z$ = 0) for the cases depicted in Fig. 1**

end section, $z = L_0$. Note that $\sigma_{ij}$ in this section and in the figures will refer to the physical components of the true stress while $\epsilon_{xx}$ and $\epsilon_{zz}$ denote the logarithmic strain components. For the specimen geometry employed in the analysis ($L_0/h_0 = 4$), the maximum stress states are attained almost simultaneously across the thickness of the end section during the deformation history (differences of the order of a fraction of one percent in engineering strain $U/L_0$ marked the variation in the order of attainment of these maximum stress states along $x$). For consistency, we present our results based on the deformation history of the mid-section $x = 0$. For the rate-independent behavior, this maximum stress state at the end section also marks the onset of elastic unloading. Evidently, in the presence of rate sensitivity effects, a descent from the maximum stress (i.e., relaxation) can happen under continuing viscoplastic straining with decreasing $\dot\epsilon_e^P$ values in (13) until the limiting rate-independent curve corresponding to $\dot\epsilon_e^P = 0$ in (13) is reached. Only then is any further decrease in the stress resulted from elastic unloading. In our figures the point where elastic unloading starts is marked with a solid triangle which designates the maximum strain state at the uniform section $x = 0$, $z = L_0$. This maximum strain state at the uniform section cannot, however, be taken as the limit strain unlike the rate-independent response, as discussed in the next figure.

In Fig. 2 the evolution of the neck section area $h(t)/h_0$ and the axial strain history at the mid-point $x = 0$, $z = 0$ are plotted as a function of the engineering strain $U/L_0$ corresponding to the four cases given in Fig. 1. In this figure, until the maximum stress state at the end section is reached (designated by circumflexes), we observe almost linear changes in the strains and the normalized areas of the neck sections for all the cases shown. Any additional deformation thereof, however, is accompanied with steep changes in the state variables plotted. The maximum strain states associated with the elastic unloading are attained well into the developed stages of neck growth in Fig. 2, especially for the cases with the prescribed strain rates of $\dot\epsilon_a = 2.0$ and $0.02\ \mathrm{sec}^{-1}$. The onset of instability marked with circumflexes occur for the uniform section strains of $\epsilon_{zz}$ (0, $L_0$) = 0.238, 0.260, 0.253, and 0.192 for the rate-dependent cases with $\dot\epsilon_a$ = 2.0, 0.02, 0.0002 $\mathrm{sec}^{-1}$ and the rate-independent response, respectively. The elastic unloading in the same order occurs for $\epsilon_{zz}$ (0, $L_0$) = 0.246, 0.272, 0.258 for viscoplastic behavior, while these two states are identical for the rate-independent case. The uniform section strains given above at the maximum stress and maximum strain states differ little (note that a larger difference will be presented later for $m = 0.045$) despite the significant differences in the elongation levels ($U/L_0$). This is an indicator for the rapid neck growth after the uniform section stress attains a maximum, since the additional end displacement after the onset of instability is taken up mainly by the neck growth. Therefore, on a forming limit curve, little difference would be resulted for the plane-strain case when either maximum stress or maximum strain criteria is employed to define the limit strain. When biaxial strain states in the plane of the sheet are considered, the effect of the choice of the instability criteria is likely to be reflected to a larger degree manifested in the uniform section strain in the $y$-direction accumulated after the attainment of maximum stress in the $z$-direction. Yet, when the plane-stress condition is imposed as is often done in the biaxial strain range, smaller differences in limit strains are expected between the predictions of maximum stress and maximum strain criterion. This is due to the faster neck growth resulting from the plane stress assumption, as opposed to the three-dimensional analysis reported here (Needleman and Tvergaard, 1984). We also note that for a rate-dependent solid, a maximum stress state at the uniform section can only be reached asymptotically (similar to the evolution of the maximum strains), for the type of analysis performed in Marciniak et al. (1973), since the end section strain increases at the prescribed rate of straining.

In Fig. 1 we observe that in the later stages of neck development, the load-elongation curve for the rate-sensitive behavior with $\dot\epsilon_a = 2.0\ \mathrm{sec}^{-1}$ intersects the other rate-dependent responses, indicating a faster neck growth for this case. This is resulted due to the dependence on the imposed rate of straining $\dot\epsilon_a$, introduced through the additive type of uniaxial law (13) adopted. A separable power law, such as that employed in Marciniak et al. (1973), renders the deformation history independent of the imposed strain rate. This in turn means practically identical curves for the variables plotted in Fig. 2 for the separable representation of material strain-rate sensitivity. Experimental evidence to both types of material response, suggesting possible preference for the type of uniaxial law for a particular material, was reported in Tuğcu (1989). With the additive type of uniaxial law employed here, it is seen in Fig. 2 that the attainment of plastic instability during the deformation history is determined from the combined effect of the material strain-rate sensitivity index $m$ and the imposed strain rate $\dot\epsilon_a$. For the particular cases studied here, the onset of necking in increasing order of engineering strains occurs for $\dot\epsilon_a$ = 2.0, 0.0002 and 0.02 $\mathrm{sec}^{-1}$, respectively. Consequently, the subsequent neck development in Fig. 2 is determined by the order the necking instability sets in.

In the biaxial tensile strain range of forming limit curves, the critical instability mode is of diffuse necking type as analyzed here. The final fracture in plane-strain tension, however, often occurs in bands of intense shear which develop in the necking region in the advanced stages of localized deformation (Needleman and Tvergaard, 1984). The formation of shear bands in a specimen with diffuse necking type of initial inhomogeneity, as prescribed in our study, cannot be predicted with the kind of constitutive modeling employed here. Nevertheless, a smaller overall engineering strain at fracture for the case with $\dot\epsilon_a = 2.0\ \mathrm{sec}^{-1}$ can be concluded qualitatively, since shear band initiation is dependent on the gradient of field variables (Becker and Needleman, 1986).

The stress and strain distributions across the thickness of the neck section ($z$ = 0) are depicted in Fig. 3 for the rate-dependent case of Fig. 1 with $\dot\epsilon_a = 0.02\ \mathrm{sec}^{-1}$. The distributions corresponding to the maximum stress and maximum strain state of the uniform end section are displayed in this figure corresponding to the engineering strain values of ($U/L_0$) = 0.348 and 0.443, respectively. Here and subsequently, $\sigma_m = \sigma_{kk}/3$ denotes hydrostatic tension. At the onset of instability

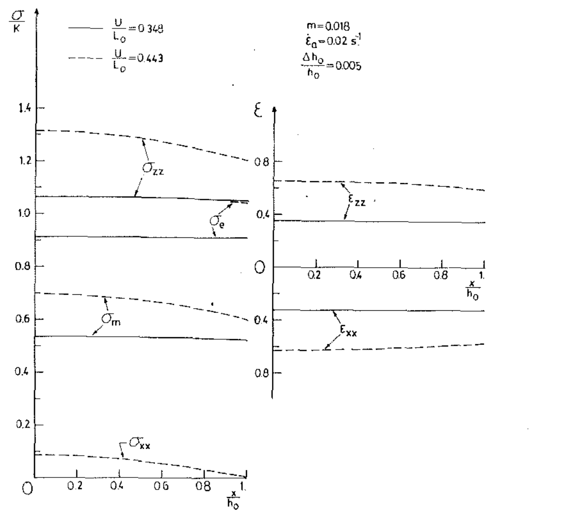


Fig. 3 The stress and strain distributions across the neck section for the rate-dependent response ($m$ = 0.018, $\dot{\epsilon}_a$ = 0.02 sec$^{-1}$.) at maximum stress and maximum strain states (($\Delta h_0/h_0$) = 0.005)

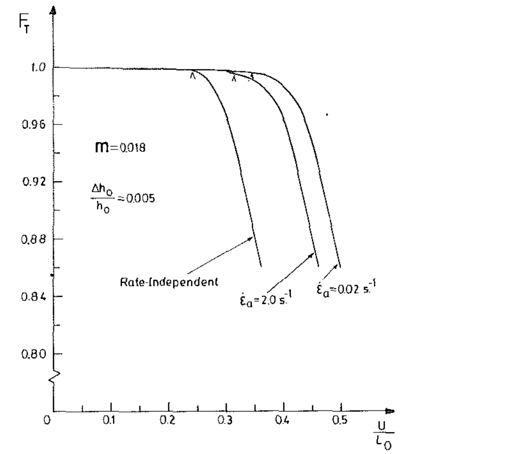


Fig. 5 The evolution of the stress triaxiality factors at the neck ($z$ = 0) for the rate-independent and rate-dependent ($m$ = 0.018) responses for the imposed strain rates of $\dot{\epsilon}$ = 2.0 and 0.02 sec$^{-1}$. (($\Delta h_0/h_0$) = 0.005)

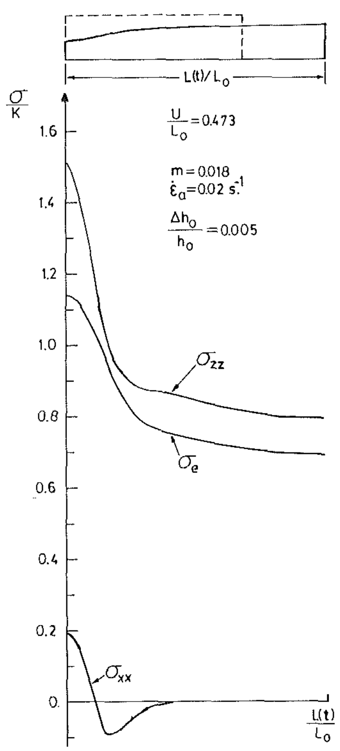

Fig. 4 The stress distributions along the mid-plane ($x$ = 0) and the specimen profile for the rate-dependent response ($m$ = 0.018, $\dot{\epsilon}_a$ = 0.02 sec$^{-1}$.) at the elongation level of ($U/L_0$) = 0.473 (($\Delta h_0/h_0$) = 0.005)

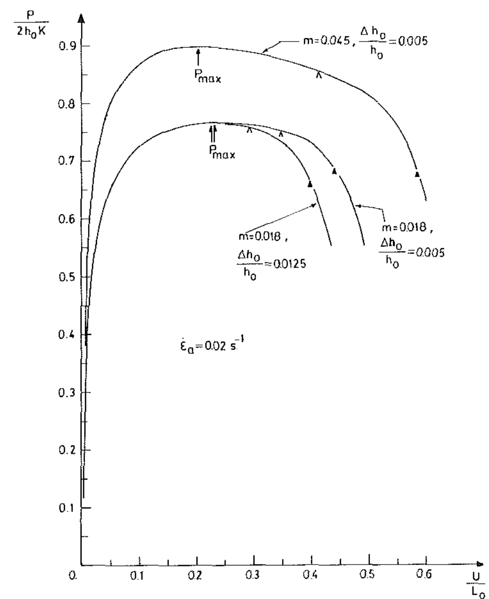


Fig. 6 Load-elongation curves for different strain-rate sensitivity parameters ($m$ = 0.018 and 0.045) and initial thickness inhomogeneities at the neck (($\Delta h_0/h_0$) = 0.005 and 0.0125) for the imposed strain rate of $\dot{\epsilon}_a$ = 0.02 sec$^{-1}$.

given by the maximum stress state, it is seen that the state of stress is uniform and the transverse normal stress is $\sigma_{xx} \approx 0$. The subsequent appearance of the stress $\sigma_{xx}$ is big enough to influence the distribution of the hydrostatic tension $\sigma_m$. The stress distributions along the mid-plane $x = 0$ at $((U/L_0 = 0.473)$ are displayed in Fig. 4 as superimposed on the specimen geometry.

The stress triaxiality factors at the neck ($z = 0$) section are displayed in Fig. 5 corresponding to the rate-independent and rate-dependent cases of Fig. 1 with $\dot{\epsilon}_a = 2.0$ and 0.02 sec$^{-1}$. In plane strain, the triaxiality factor is defined as

$$F_T = \frac{2\bar{\sigma}_e}{\sqrt{3}\bar{\sigma}_{zz}} \tag{18}$$

where the superposed bar denotes the average value across the cross-section. Here too the value of $F_T$, almost equal to unity until the onset of instability, represents the part of the deformation history which is practically uniform and can be predicted with sufficient accuracy employing the plane-stress approximation.

The effects of the material strain-rate sensitivity index and the initial inhomogeneity on the deformation history are demonstrated in Fig. 6. In this figure the rate-dependent case of Fig. 1 with $\dot{\epsilon}_a = 0.02$ sec$^{-1}$ is reproduced. The top curve in Fig. 6 is for a material with $m = 0.045$, while the innermost curve corresponds to an initial area defect of $(\Delta h_0/h_0) = 0.0125$ at $z = 0$ ($\xi = 0.0125$). The rest of the parameters for these curves are identical to that of the mid-curve replotted. From this figure we observe that increasing the initial imperfection 2.5 times within the range considered does not cause significant difference in the load-elongation curve until the attainment of maximum loads. Differences associated with a faster neck development for the larger imperfection case start after load maximum. The onset of necking occurs at the uniform end section strains of $\epsilon_{zz}$ (0, $L_0$) = 0.209 and 0.260 for the large

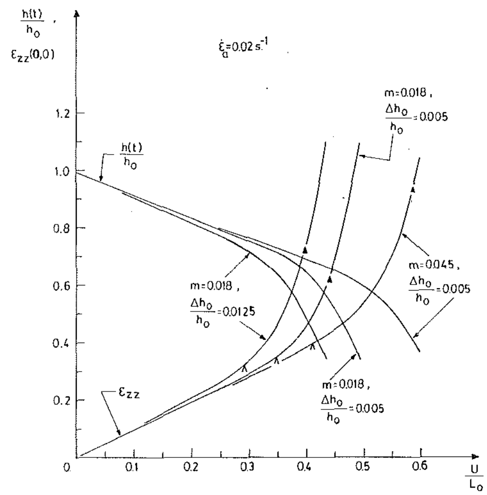


Fig. 7 The evolution of the normalized neck area and the axial strains at the neck section ($z = 0$) for the cases depicted in Fig. 7

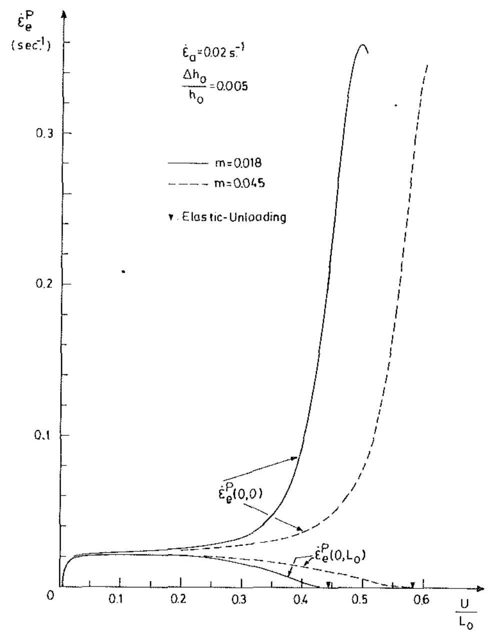


Fig. 8 The evolution of the effective viscoplastic strain rates at the neck ($z = 0$) and the uniform end sections ($z = L_0$) for the rate-dependent responses $m = 0.018$ and $0.045$ ($\dot{\epsilon}_a = 0.02$ sec$^{-1}$., $(\Delta h_0/h_0) = 0.005$)

and small imperfection cases, respectively. The evolutions of the neck area and the axial strain $\epsilon_{zz}$ (0, 0) are displayed in Fig. 7 for all the three cases given in Fig. 6. In Fig. 7 we observe that differences between the two cases with different initial imperfections arise early in the deformation history for $(U/L_0) \leq 0.1$. It can also be concluded that for the right combination of the parameters studied here ($N$, $m$, $\dot{\epsilon}_a$, $\Delta h_0/h_0$), if the condition of plastic instability is met anywhere along the uniform section when the rate-independent stress-strain curve is reached, then additional necks can form in this section as well.

The influence of the strain-rate sensitivity parameter $m$ on necking behavior is seen in Fig. 6, comparing the top ($m = 0.045$) and the mid-curve ($m = 0.18$). The onset of necking for $m = 0.045$ occurs at $(U/L_0) = 0.412$, for the uniform end section strain of $\epsilon_{zz}$ $(0, L_0) = 0.306$. The uniform section strain for this case attains a maximum given by $\epsilon_{zz}$ $(0, L_0) = 0.332$. Therefore, for this value of $m$, a relatively large difference is resulted in the uniform section strains between the maximum stress and maximum strain states. While the elongation span between the maximum load point and the onset of instability is larger for this case, it is also seen that the load levels drop at a faster rate between these two points.

The evolution of the effective viscoplastic strain rate histories for the two cases in Fig. 6, corresponding to $m = 0.018$ and $m = 0.045$, are depicted in Fig. 8 for both the neck and the end section on the mid-plane $x = 0$. From this figure it is seen that the nonuniformity between the viscoplastic strain rate histories of the incipient neck and the end sections appears early in the deformation history. Also to be noted for the case with $m = 0.018$ is that before the numerical computations were arbitrarily terminated, the effective viscoplastic strain rate at the neck section attains a maximum which is followed by a sharp drop with no detectable sign of degeneration in the results. The possibility of numerical deterioration notwithstanding, one likely explanation for this behavior is that, in view of the reductions in the axial load levels, an increase in strain rate can no longer be accomodated, as determined from the interplay between the evolutions of the stress and area of the neck section.

As mentioned previously, the analyses of sheet-metal forming limit curves are traditionally performed by invoking the plane-stress assumption. The validity of this assumption for the whole range of deformation history is certainly a major concern and received due attention (Hutchinson and Neale, 1978c). The evidence presented in Figs. 3 and 5 in particular, indicate that for rate-dependent solids, the maximum stress criteria as the onset of instability, ascertains the validity of this assumption up to the attainment of critical strains. Further, the evolution of the strain-rate history of the uniform end sections depicted in Fig. 8 demonstrates the degree of approximation involved in the approximate long-wavelength analyses, since these solutions are based on the assumption that the uniform sections deform at the constant strain rate imposed. An immediate consequence of this assumption is that while the load-elongation histories shown in Figs. 1 and 6 can be obtained with good accuracy to the end of the plateau regions, the ensuing sharp drops cannot be predicted.

## References


Becker, R., and Needleman, A., 1986, "Effect of Yield Surface Curvature on Necking and Failure in Porous Plastic Solids," ASME Journal of Applied Mechanics, Vol. 53, pp. 491–499.

Hutchinson, J. W., and Neale, K. W., 1978a, "Sheet Necking–II. Time Independent Behaviour," *Mechanics of Sheet Metal Forming*, K. P. Koistinen and N.-M. Wang, eds., Plenum Press, New York, p. 127–153.

Hutchinson, J. W., and Neale, K. W., 1978b, "Sheet Necking–III. Strain-Rate Effects," *Mechanics of Sheet Metal Forming*, K. P. Koistinen and N.-M. Wang, eds., Plenum Press, New York, pp. 269–285.

Hutchinson, J. W., and Neale, K. W., 1978c, "Sheet Necking–I. Validity of Plane Stress Assumptions of the Long Wavelength Approximation," *Mechanics of Sheet Metal Forming*, K. P. Koistinen and N.-M. Wang, eds., Plenum Press, New York, 111–126.

Hutchinson, J. W., and Tvergaard, V., 1981, "Shear Band Formation in Plane Strain," *Int. J. Solids Struct.*, Vol. 17, pp. 451–470.

Marciniak, Z., and Kuczyński, K., 1967, "Limit Strains in the Process of Stretch-Forming Sheet Metal," *Int. J. Mech. Sci.*, Vol. 9, pp. 609–620.

Marciniak, Z., Kuczyński, K., and Pokora, T., 1973, "Influence of the Plastic Properties of a Material on the Forming Limit Diagram for Sheet Metal in Tension," *Int. J. Mech. Sci.*, Vol. 15, pp. 789–805.

Nagtegaal, J. C., Parks, D. M., and Rice, J. R., 1974, "On Numerically Accurate Finite Element Solutions in the Fully Plastic Range," *Comput. Meth. Appl. Mech. Engng.*, Vol. 4, pp. 153–177.

Needleman, A., and Tvergaard, V., 1984, "Limits to Formability in Rate-Sensitive Metal Sheets," *Mechanical Behaviour of Materials—IV*, J. Carlsson and N. G. Ohlson, eds., Pergamon Press, pp. 51–65.

Rudnicki, J. W., and Rice, J. R., 1975, "Conditions for the Localization of Deformation in Pressure-Sensitive Dilatant Materials," *J. Mech. Phys. Solids*, Vol. 23, pp. 371–394.

Stören, S., and Rice, J. R., 1975, "Localized Necking in Thin Sheets," *J. Mech. Phys. Solids*, Vol. 23, pp. 421–441.

Tuğcu, P., 1989, "Tensile Instability in a Round Bar Including the Effect of Material Strain-Rate Sensitivity," *Comput. Meth. Appl. Mech. Engng.*, Vol. 93, pp. 335–341.

# An Analysis of Shear Localization During Bending of a Polycrystalline Sheet

**R. Becker**
Alcoa Technical Center,
Alcoa Center, PA 15069
Assoc. Mem. ASME

*The development of shear localization in a polycrystalline sheet subject to pure bending is analyzed numerically using a slip-based constitutive model. The material response at each finite element integration point is determined by averaging the stiffness matrices from differently oriented FCC crystals. The effects of texture evolution, hardening, and strain-rate sensitivity are incorporated. The model predicts localized plastic deformation at both the tensile and the compressive surfaces of the sheet during bending. Comparison of the numerical results with a section of the bent sheet indicates that strain localization is predicted at the appropriate strain levels and orientations.*

## 1 Introduction

The development of shear bands during plastic deformation may degrade material performance or lead to fracture. The abundance of research dedicated to studying shear bands is an indication of their importance and of the difficulty in understanding shear band formation. Many analytical and numerical models have been employed to study shear band initiation. One of the more difficult aspects of developing these models is in formulating material constitutive relationships which both adequately characterize the behavior of the material and will permit plastic flow localization at realistic strain levels.

A class of constitutive relationships commonly used in shear band studies simulates a yield surface with a vertex (Hill and Hutchinson, 975; Needleman and Rice, 1978; Rudnicki and Rice, 1975; Tvergaard, Needleman and Lo, 1981). The existence of a vertex or a region of sharp curvature at the loading point of the yield surface reduces the stiffness of the material response to abrupt changes in loading path. The motivation for incorporating a yield surface vertex in plasticity models comes from predictions of yield surface vertices from crystal-based plasticity models (Hill, 1967; Hutchinson, 1970; Asaro and Needleman, 1985). In the calculations of Hutchinson (1970) and Asaro and Needleman (1985), these yield surface vertices were found in self-consistent and Taylor-like polycrystal models.

In this study, the Taylor-like polycrystal model developed by Asaro and Needleman (1985) is used to define the constitutive behavior of each element in a finite element model. This is similar to the finite element crystal calculations of Peirce, Asaro, and Needleman (1982, 1983) and of Harren, Dève, and Asaro (1988), except that here the stiffness matrix for each element is determined by the average of the stiffness matrices of eight crystal orientations. Mathur and Dawson (1989) also used a Taylor-like model in a finite element analysis of a rolling process. However, the approach of Mathur and Dawson (1989) is somewhat different in that they used an Eulerian finite element model and the effects of texture evolution were incorporated by an iterative process involving integration of the crystal model along streamlines.

The present analysis is concerned with the development of shear bands in sheet or plate during pure bending. A previous study by Triantafyllidis, Needleman, and Tvergaard (1982) using a plasticity theory with corner effects has demonstrated the ability of finite element models to capture the shear band formation on both the compressive and the tensile surfaces during bending. In their analyses, shear bands initiated at the surfaces and propagated toward the neutral axis. The severity of the shear bands was affected by the wavelength of the initial imperfection and the details of the yield surface vertex characterization. In the present model, the vertex effect enters naturally through use of the Taylor-like polycrystal constitutive model. The behavior of each element is governed by a different set of crystal orientations so that the material is nonhomogeneous. Thus, no geometric imperfection is needed to initiate plastic flow localization.

## 2 Model Description

**2.1 Crystal Constitutive Relations.** The material behavior in the analysis is governed by a rate-dependent slip-based constitutive model. In this model, plastic deformation is assumed to result from slip along crystallographic planes. The formulation of the constitutive relations is identical to the rate-dependent crystal model developed by Peirce et al. (1983). The model accounts for reorientation of the crystal at finite deformation and for the cubic symmetry of the elastic constants. A brief account of the constitutive relations is given below.

Contributed by the Applied Mechanics Division of The American Society of Mechanical Engineers for publication in the ASME Journal of Applied Mechanics.

Discussion on this paper should be addressed to the Technical Editor, Prof. Leon M. Keer, The Technological Institute, Northwestern University, Evanston, IL 60208, and will be accepted until four months after final publication of the paper itself in the Journal of Applied Mechanics.

Manuscript received by the ASME Applied Mechanics Division, Sept. 24, 1990; final revision, Sept. 25, 1991. Associate Technical Editor: R. M. McMeeking.

The deformation of a crystal is by a combination of slip along crystallographic planes and elastic distortion of the crystal lattice. This is represented by a multiplicative decomposition of the deformation gradient

$$\mathbf{F}=\mathbf{F}^{*}\bullet\mathbf{F}^{P}. \tag{1}$$

The elastic distortion of the crystal lattice and rigid rotations are embodied in $\mathbf{F}^*$. The plastic part of the deformation, $\mathbf{F}^P$, includes only the deformation resulting from crystallographic slip without disturbing the crystal lattice. The slip occurs on planes with normals $\mathbf{m}_{(\alpha)}$ along directions denoted by $\mathbf{s}_{(\alpha)}$. Here, the Greek indices represent the 12 slip systems in FCC aluminum alloys. The orthogonal unit vectors $\mathbf{m}_{(\alpha)}$ and $\mathbf{s}_{(\alpha)}$ are defined in the reference orientation of the crystal. Since the crystal lattice is not affected by $\mathbf{F}^P$, the current orientations of the slip plane normals and slip directions are

$$\overset{*}{\mathbf{m}}_{(\alpha)}=\mathbf{m}_{(\alpha)}\bullet\mathbf{F}^{*-1} \quad \text{and} \quad \overset{*}{\mathbf{s}}_{(\alpha)}=\mathbf{F}^{*}\bullet\mathbf{s}_{(\alpha)}. \tag{2}$$

Using Eqs. (1) and (2), the velocity gradient is given by

$$\dot{\mathbf{F}}\bullet\mathbf{F}^{-1}=\dot{\mathbf{F}}^{*}\bullet\mathbf{F}^{*-1}+\sum_{\alpha=1}^{12}\dot{\gamma}^{(\alpha)}\overset{*}{\mathbf{s}}_{(\alpha)}\overset{*}{\mathbf{m}}_{(\alpha)}. \tag{3}$$

The first term incorporates the elastic stretching and the spin of the crystal lattice. The second term is the deformation due to slip with the slip rate along a given slip system being denoted by $\dot{\gamma}^{(\alpha)}$. The plastic part of the velocity gradient is additively decomposed into its symmetric, $\mathbf{D}^P$, and skew-symmetric, $\Omega^P$, parts which can be written as

$$\begin{aligned}\mathbf{D}^{P}&=\sum_{\alpha=1}^{12}\dot{\gamma}^{(\alpha)}\frac{1}{2}(\overset{*}{\mathbf{s}}_{(\alpha)}\overset{*}{\mathbf{m}}_{(\alpha)}+\overset{*}{\mathbf{m}}_{(\alpha)}\overset{*}{\mathbf{s}}_{(\alpha)})=\sum_{\alpha=1}^{12}\dot{\gamma}^{(\alpha)}\mathbf{P}^{(\alpha)}\\ \Omega^{P}&=\sum_{\alpha=1}^{12}\dot{\gamma}^{(\alpha)}\frac{1}{2}(\overset{*}{\mathbf{s}}_{(\alpha)}\overset{*}{\mathbf{m}}_{(\alpha)}-\overset{*}{\mathbf{m}}_{(\alpha)}\overset{*}{\mathbf{s}}_{(\alpha)})=\sum_{\alpha=1}^{12}\dot{\gamma}^{(\alpha)}\mathbf{W}^{(\alpha)}.\end{aligned} \tag{4}$$

Due to the small elastic stretch, $\overset{*}{\mathbf{s}}_{(\alpha)}$ and $\overset{*}{\mathbf{m}}_{(\alpha)}$ are not unit vectors; but they remain orthogonal. Hence, $\mathrm{Tr}(\mathbf{D}^P) = 0$ and the plastic flow is nondilatant.

As suggested by Rice (1971), the resolved shear stress, $\tau^{(\alpha)}$, is chosen such that it is work conjugate to the slip rate, $\dot{\gamma}^{(\alpha)}$. Expressing the plastic work rate in the reference volume,

$$\begin{aligned}\tau:\mathbf{D}^{P}&=\sum_{\alpha=1}^{12}\dot{\gamma}^{(\alpha)}\tau:\mathbf{P}^{(\alpha)}=\sum_{\alpha=1}^{12}\dot{\gamma}^{(\alpha)}(\overset{*}{\mathbf{m}}_{(\alpha)}\bullet\tau\bullet\overset{*}{\mathbf{s}}_{(\alpha)})\\ &=\sum_{\alpha=1}^{12}\dot{\gamma}^{(\alpha)}\tau^{(\alpha)}.\end{aligned} \tag{5}$$

Here, $\tau$ is the symmetric Kirchhoff stress which is related to the Cauchy stress by $\tau = J\sigma$, where $J = \mathrm{Det}(\mathbf{F})$. For most metals the volume change during deformation is small, and little error is introduced by using the Cauchy stress and Kirchhoff stress interchangeably.

The elastic stress-strain response is obtained by assuming that the elastic distortion of the crystal lattice can be obtained from a strain energy function, $\phi$. The elastic properties are determined in terms of the lattice-based second Piola-Kirchhoff stress, $\mathbf{T}^*$, and the Lagrangian strain of the lattice, $\mathbf{E}^* = ½(\mathbf{F}^{*T}\bullet\mathbf{F}^* - \mathbf{I})$. Both of these tensors use the undistorted lattice of the intermediate configuration as a reference configuration. Slip associated with $\mathbf{F}^P$ does not disturb the lattice; hence, formulation of the elasticity relations is independent of $\mathbf{F}^P$.

The stress and stress rate are determined from the strain energy function by

$$\mathbf{T}^{*}=\frac{\partial\phi}{\partial\mathbf{E}^{*}} \quad \text{and} \quad \dot{\mathbf{T}}^{*}=\frac{\partial^{2}\phi}{\partial\mathbf{E}^{*}\partial\mathbf{E}^{*}}:\dot{\mathbf{E}}^{*}=\mathfrak{D}:\dot{\mathbf{E}}^{*}, \tag{6}$$

respectively. Using the relation $\tau = \mathbf{F}^*\bullet\mathbf{T}^*\bullet\mathbf{F}^{*T}$, the rate of change of Kirchhoff stress is

$$\dot{\tau}=\mathbf{F}^{*}\bullet(\mathfrak{D}:\dot{\mathbf{E}}^{*})\bullet\mathbf{F}^{*T}+\dot{\mathbf{F}}^{*}\bullet\mathbf{F}^{*-1}\bullet\tau+\tau\bullet\mathbf{F}^{*-T}\bullet\dot{\mathbf{F}}^{*T}. \tag{7}$$

The elastic part of the velocity gradient can be decomposed into symmetric, $\mathbf{D}^*$, and skew symmetric, $\Omega^*$, parts; $\dot{\mathbf{F}}^*\bullet\mathbf{F}^{*-1} = \mathbf{D}^* + \Omega^*$. Then, by expressing the Lagrangian strain rate of the lattice as $\dot{\mathbf{E}}^* = \mathbf{F}^{*T}\bullet\mathbf{D}^*\bullet\mathbf{F}^*$, the Kirchhoff stress rate is given by

$$\dot{\tau}=\mathfrak{L}:\mathbf{D}^{*}+\Omega^{*}\bullet\tau-\tau\bullet\Omega^{*}. \tag{8}$$

The fourth-order modulus tensor, $\mathfrak{L}$, can be written in Cartesian components on orthonormal base vectors as

$$\mathfrak{L}^{ijkl}=F_{r}^{*i}F_{s}^{*j}F_{t}^{*k}F_{u}^{*l}\mathfrak{D}^{rstu}+\frac{1}{2}(\delta^{ik}\tau^{jl}+\delta^{il}\tau^{jk}+\tau^{il}\delta^{jk}+\tau^{ik}\delta^{jl}), \tag{9}$$

where $\mathfrak{D}^{rstu}$ are the components of the crystal elastic moduli referred to the undistorted, unrotated lattice; and $\delta^{ij}$ is the Kronecker delta. Summation is implied for the repeated Latin indices in Eq. (9). For cubically symmetric crystals with constant elastic moduli, there are three independent elastic constants. If the orthogonal coordinate axes are chosen to coincide with the crystal cube axes, the nonzero components are

$$\begin{aligned}\mathfrak{D}^{kkkk}&=C11\\ \mathfrak{D}^{kkll}&=C12 \quad k\neq l\\ \mathfrak{D}^{lkkl}=\mathfrak{D}^{lklk}&=C44 \quad k\neq l \quad \text{(no summation)}.\end{aligned} \tag{10}$$

Replacing the elastic spin and rate of deformation in Eq. (8) by $\Omega^* = \Omega - \Omega^P$ and $\mathbf{D}^* = \mathbf{D} - \mathbf{D}^P$, and expressing the stress rate in terms of the Jaumann rate, $\hat{\tau}$;

$$\hat{\tau}=\dot{\tau}-\Omega\bullet\tau+\tau\bullet\Omega=\mathfrak{L}:\mathbf{D}-\mathfrak{L}:\mathbf{D}^{P}-\Omega^{P}\bullet\tau+\tau\bullet\Omega^{P}. \tag{11}$$

Writing the stress rate in terms of the slip rate,

$$\hat{\tau}=\mathfrak{L}:\mathbf{D}-\sum_{\alpha=1}^{12}\dot{\gamma}^{(\alpha)}\mathbf{R}^{(\alpha)}, \tag{12}$$

where

$$\mathbf{R}^{(\alpha)}=\mathfrak{L}:\mathbf{P}^{(\alpha)}+\mathbf{W}^{(\alpha)}\bullet\tau-\tau\bullet\mathbf{W}^{(\alpha)}. \tag{13}$$

The description of the rate constitutive equations is completed with a prescription of the slip rate, $\dot{\gamma}^{(\alpha)}$. For the rate-dependent material model considered here, the slip rate is only a function of the resolved shear stress, $\tau^{(\alpha)}$, and resistance of the slip system to slip, $g^{(\alpha)}$. Hence, the terms in the summation in Eq. (12) are completely determined by the current state of the material. For this analysis, the slip rate is taken as

$$\dot{\gamma}^{(\alpha)}=\dot{a}\,\mathrm{sign}(\tau^{(\alpha)})\left|\sinh\frac{\kappa\tau^{(\alpha)}}{g^{(\alpha)}}\right|^{1/m}, \tag{14}$$

where $\kappa = \sinh^{-1}(1)$ and $\dot{a}$ is a reference slip rate characteristic of the slip rate at which the hardening function is determined. For small arguments of the hyperbolic sine, Eq. (14) reduces to a power-law rate relation with exponent $m$. For larger values of the argument, it gives an exponential dependence of the slip rate on the stress.

The slip system hardenss, $g^{(\alpha)}$, changes during deformation due to structure evolution associated with work hardening and recovery processes. The slip system resistance depends on solutes and precipitates in the material. The resistance of a particular system to an imposed strain rate also depends on the dislocation structure of that slip system and on the dislocation structure of the intersecting slip systems. The dislocation structures depend on the deformation history. However, for the heavily worked material considered in this analysis, it will be assumed that all slip systems have the same initial resistance and harden at an equal rate. This rate is determined by the summation of the slip rate on all of the slip systems. The slip system strength is given by

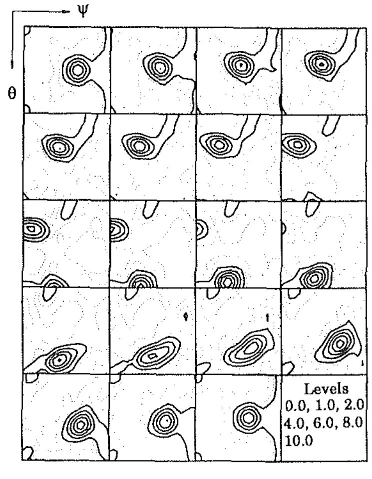


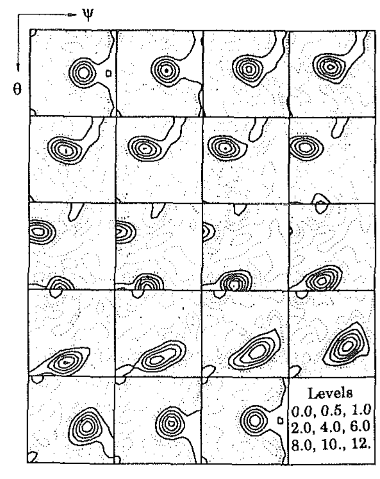


**Fig. 1 Crystal orientation distribution functions for an aluminum sheet: (*a*) from X-ray data, (*b*) reconstructed from discrete orientations**

$$g^{(\alpha)}=\tau_c(\gamma); \quad \gamma=\int_0^t \sum_{\alpha=1}^{12} |\dot{\gamma}^{(\alpha)}|dt, \tag{15}$$

where $\tau_c(\gamma)$ is a function determined experimentally.

The integration of the stress rate from Eq. (12) with the slip rate determined by Eq. (14) requires small time steps for stable numerical integration. The tangent modulus method of Peirce et al. (1983) is used to increase the stable time step size. The reader is referred to Peirce et al. (1983) for details of the method. It is notable that the moduli determined from the tangent modulus procedure are nonsymmetric. Also, except for a few special crystal orientations, the components of the moduli referred to the sample coordinate axes do not possess orthotropic symmetry. Normal stresses applied to a block of material can produce shear strains.

For the finite element analysis, the moduli from eight crystal orientations are averaged to form the material stiffness at each element integration point. The deformation of each of these component crystals is the same. The average stress of the component crystals determines the stress at the integration point. In this way, the constitutive response at an integration point is determined by what is essentially a Taylor-like model which uses the local strain rates determined by the finite element method. The averaging procedure is identical to the averaging procedure used by Asaro and Needleman (1985) in their Taylor-like polycrystal model. The only difference is the small number of grains involved in the present averages. The crystal constitutive model has been implemented as a user subroutine in the commercial finite element code ABAQUS (1988). A description of the implementation is given by Smelser and Becker (1989).

**2.2 Material Properties.** The eight crystal orientations at each integration point were selected at random from a set of 800 orientations which characterize the texture of an aluminum alloy sheet. This gives a different set of crystal orientations for each integration point while maintaining, statistically, the overall texture. These 800 orientations were calculated from the *W* coefficients of the Crystal Orientation Distribution Function (CODF) (see e.g. Bunge, 1982) obtained from analysis of X-ray data taken at the midthickness of the sheet. CODFs representing the X-ray data and CODFs reconstructed from the discrete orientations are given in Figs. 1(*a*) and 1(*b*), respectively.

The slip system hardening relationship, $\tau_c(\gamma)$, was determined based on uniaxial tension tests conducted on sheet specimens. The tensile axis was perpendicular to the rolling direction of the sheet. The hardening response was chosen such that the predicted uniaxial stress-strain curve from a Taylor-like model using the 800 crystal orientations would match the data from the tension tests. The use of the Taylor model accounts for texture evolution effects on the hardening. Because of the texture evolution, obtaining a good fit involves trial and error. After a few iterations, the slip system hardening response was determined to be

$$\tau_c(\gamma)/\sigma_0=0.44(\gamma+0.03)^{0.091}, \tag{16}$$

where $\sigma_0$ is the initial yield strength of the material in uniaxial tension.

The strain-rate sensitivity exponent used in the analysis, $m = 0.005$ in Eq. (14), is within the range of material strain-rate sensitivities determined experimentally. The cubic elastic constants used in Eq. (10) were taken from *Smithells Metals Reference Book* (1983):

$$\begin{aligned} C11/\sigma_0 &= 327.3 \\ C12/\sigma_0 &= 187.88 \\ C44/\sigma_0 &= 85.76 \end{aligned} \tag{17}$$

**2.3 Model Geometry and Boundary Conditions.** The region modeled is a small portion of a sheet with thickness $h$ and length $h/4$, Fig. 2. The sheet is subjected to pure bending around an axis parallel to the rolling direction. The tensile and compressive stresses resulting from the bending are along the transverse direction of the sheet, which is the direction in which the material properties were determined. Equilibrium and compatibility with the material on either side of the model region are maintained by imposing periodic boundary conditions. These boundary conditions require that the surfaces remain straight and free of shear tractions. In addition, the loading is pure bending and no net forces act on the section. These conditions are applied in ABAQUS (1988) through the user multipoint constraint option. Plane-strain conditions are imposed as a constraint on the out-of-plane deformation. The rate of bending was prescribed such that the outer and inner surfaces of the sheet would experience a strain rate approximately equal to $\dot{a}$, Eq. (14). The rate of bending is $\dot{\theta} = 0.5\dot{a}$, where $\theta$ is the angle between the two sides of the model region with normals initially in the $x$-direction.

The finite element mesh used in the analysis is shown in Fig. 3. The discretization consists of 40 quadrilaterals through the thickness of the sheet and 10 elements across the width of the model region. Each of the quadrilaterals is composed of four constant strain triangular elements arranged in a "crossed triangle" configuration. Discontinuities in stress and strain are permitted across the element boundaries. This makes them well suited for capturing shear bands (Peirce et al., 1982; Tvergaard et al., 1981; Needleman and Tvergaard, 1984). Discontinuities in shear strain are possible across the sides of the quadrilaterals as well as across the quadrilateral diagonals. An ideal mesh would be one that is constructed such that the diagonals of the quadrilaterals are along the direction of the shear bands when they form. This mesh design is desirable to capture the shear bands effectively; but, without *a priori* knowledge of the solution, the mesh design is a guess. The mesh design could be improved based on the results from the model, and the calculation rerun. However, only one calculation is run in the present study.

The finite element solution is computationally intensive. The numerical integration of the constitutive equations for eight crystal orientations at each integration point is time consuming.

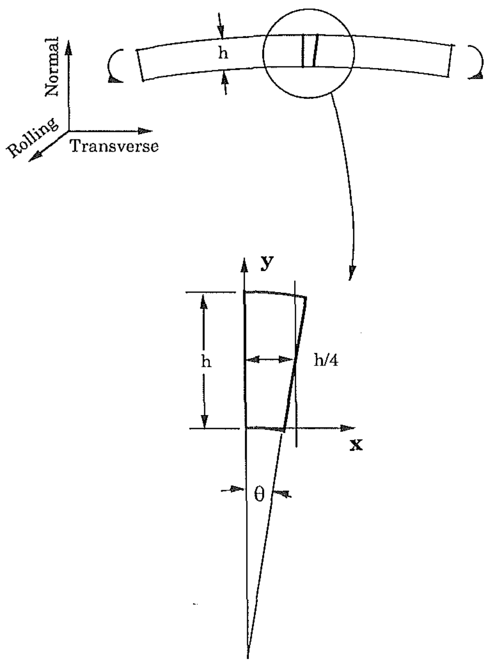


Fig. 2 Orientation of the model region in the sheet

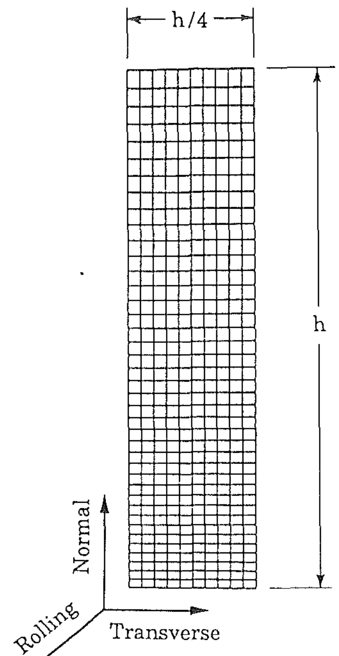


Fig. 3 Finite element discretization

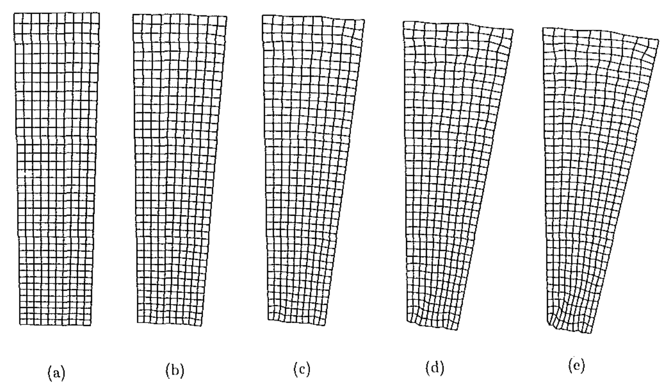


Fig. 4 Deformed finite element meshes. The bend angles in radians are: (*a*) $\theta$ = 0.05; (*b*) $\theta$ = 0.10; (*c*) $\theta$ = 0.15; (*d*) $\theta$ = 0.20; (*e*) $\theta$ = 0.25.

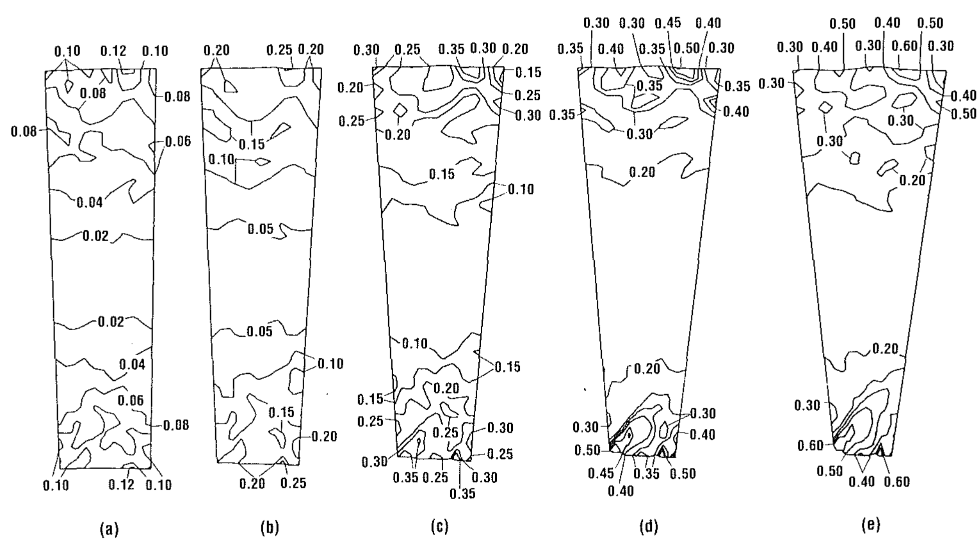


Fig. 5 Contours of maximum principal logarithmic strain. The bend angles in radians are: (*a*) $\theta$ = 0.05; (*b*) $\theta$ = 0.10; (*c*) $\theta$ = 0.15; (*d*) $\theta$ = 0.20; (*e*) $\theta$ = 0.25.

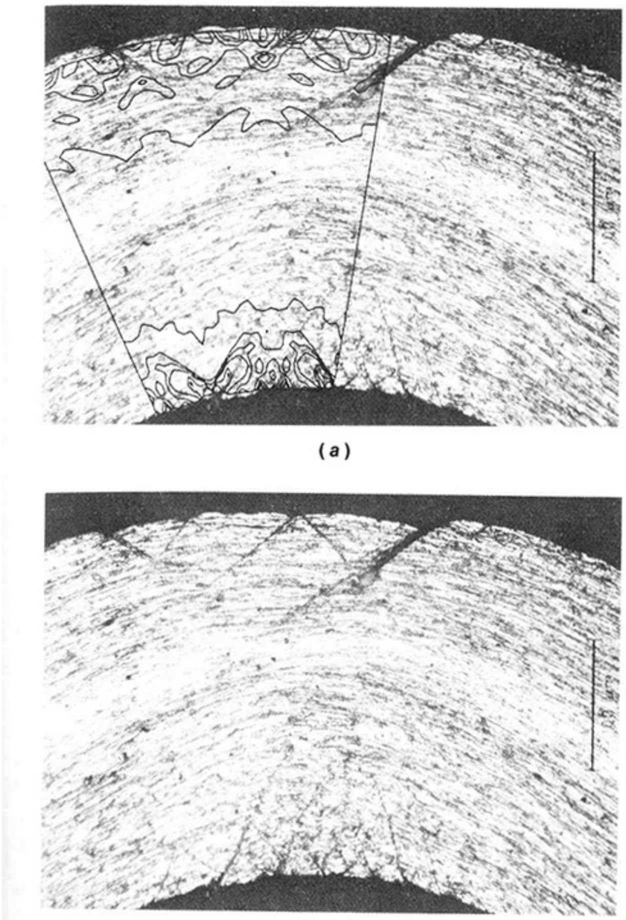

(a)

(b)

Fig. 6 (a) Predicted contours of maximum principal logarithmic strain superposed on a micrograph of a sheet deformed in bending, (b) same micrograph without the contours

In addition, the stiffness matrix resulting from the incremental form of the constitutive relations is nonsymmetric which requires additional computational effort. A large number of time steps are also needed to obtain a solution. The integration of the constitutive relations by the forward gradient method of Peirce et al. (1983) requires small time steps for stable and accurate numerical integration. The calculation was carried out on a CRAY-YMP at the Pittsburgh Supercomputing Center. The solution took approximately 1400 time steps and nine hours of CPU time.

## 3 Results and Discussion

Deformed finite element meshes are shown in Fig. 4 at various bend angles, $\theta$. Corresponding contours of maximum principal logarithmic strain are given in Fig. 5. The material inhomogeneity resulting from different combinations of crystal orientations in the elements causes the deformation to be nonuniform from the outset. The nonuniform deformation near the surface results in surface roughness which introduces geometric imperfections into the model. At $\theta = 0.10$, Fig. 5(*b*), the strain in regions near the upper right and lower left of the model appears to be elevated. By $\theta = 0.15$, Fig. 5(*c*), these regions have developed into bands of enhanced deformation, and the material at the lower left appears to be shearing. The enhanced deformation in these bands persists through $\theta = 0.25$ where the shear in the upper and lower bands is more evident.

In Fig. 6, contours of maximum principal strain at $\theta = 0.20$ are drawn along with the contours for the adjacent sectors of the sheet. The contours in these sectors were determined from the periodic symmetry. This composite contour plot is overlaid on a micrograph of an aluminum sheet deformed in bending. The angles of the regions of enhanced plastic flow indicated by the contour lines closely correspond to the shear band angles on the micrograph. Specific band angles are not determined due to the ambiguity associated with defining angles between the planar bands and the curved surfaces of the bent sheet.

The model also tends to predict a band spacing which is not too different from the shear band spacing in the material. The similarity of the spacing is probably coincidental since the band spacing may be related to the finite element discretization, the size of the region modeled, and the initial distribution of the crystal orientations.

The deformation never totally localizes into bands as it does in true shear bands. The material outside of the bands continues to deform but only at about half of the strain rate as that of material in the bands. One reason for impeded shear localization is the material's resistance to shear. Since the constitutive response of each element is determined by a different set of crystal orientations, each element will exhibit different tendencies for shearing. If the particular set of orientations in an element resists shear, this element will impede the propagation of a shear band and the plastic deformation will be more diffuse. In real materials, other factors such as details of local grain interactions and nonuniform hardening of the grains also affect the propagation of shear bands.

Another reason for the inability of this model to predict true plastic flow localization is a combination of the coarseness of the finite element discretization and the orientation of the bands with respect to the mesh. As was discussed previously, strain discontinuities are possible across the element edges and the quadrilateral diagonals. Comparison of Figs. 4(*e*) and 5(*e*) shows that the bands of enhanced deformation do not follow the element diagonals exactly. As a result, the shear must occur over several elements widths. In this model, several element widths is a significant fraction of the region modeled. A finer mesh which is better oriented to capture strain localization would provide improved spatial resolution for shear band predictions. Presently, however, the cost of calculations with a significantly refined mesh using the crystal constitutive relations is prohibitive.

The distribution of crystal orientations within the model affects the results. Had different sets of eight orientations been chosen at the integration points, the inhomogeneity would be altered and the regions of enhanced plastic flow might be in different locations.

The number of crystal orientations used to determine the properties at the integration points will also affect the homogeneity of the material. For this type of model, one method of choosing the number of orientations to be represented by an element is to determine the number of grains which would be contained within the element volume for three-dimensional calculations or within the element area for two-dimensional analyses. Since the grains in the sheet are elongated in the rolling direction (the out-of-plane direction for the model), it is assumed that the properties in this direction vary slowly and that a two-dimensional model is appropriate here. Based on this criterion and the micrograph of Fig. 6, eight orientations per element is of the correct order of magnitude for this simulation. If the number of orientations is too large, localization behavior will be inhibited. This would result from the requirement that all orientations at an integration point undergo the same deformation. A few unfavorable orientations would impede shear deformation. Also, with a larger number of orientations per element, the property variation from one element to the next would be reduced, decreasing the driving force for the nonuniform deformation.

If the above criterion for selecting the number of orientations per element is assumed to be reasonable, the results shown in Fig. 5(*a*) have interesting implications. The deviation of the 0.02 strain contours from a circular arc (which is their shape for a homogeneous material) is on the same order as the spacing between the 0.02 and 0.04 contours. This implies that perturbations in the strain field due to material inhomogeneities are on the same order as the strain gradients due to the applied deformation. Thus, material inhomogeneity should be considered in the analysis of this sheet in bending; the product of the strain gradient and the microstructural size scale (grain size) is not negligible compared to the strain.

## 4 Conclusions

Predictions of plastic strain localization during bending have been obtained using a slip-based material constitutive model. The moduli from several crystal orientations are averaged in a Taylor-like model to obtain the moduli for use in the finite element analysis. Bands of localized plastic deformation are formed at realistic strain levels and occur at angles which are in agreement with the shear band angles in a bent sheet. True plastic strain localization is impeded by a combination of crystal orientations which resist shearing and the coarseness and orientation of the finite element mesh. A criterion has been suggested which can be used to estimate the number of crystal orientations needed to characterize the behavior of an element. This number could be thought of as a crude measure of size scale which controls the level of material inhomogeneity in the model.

In addition to shear band calculations, this type of constitutive model would also be useful for modeling a variety of processes in which texture evolution (changing anisotropy) is coupled to the deformation. The model can be used to determine the crystallographic texture resulting from forging, rolling and extrusion operations. The model could also be used to include the effects of evolving material anisotropy on formability and earing predictions in sheet forming processes such as drawing and ironing. Although polycrystal constitutive models have many potential applications, cost remains their major drawback.

## Acknowledgments

The author would like to thank D. J. Lege for supplying the micrographs, texture, and hardening behavior for the materials and S. Panchanadeeswaran for determining the discrete orientation distributions. He is also grateful to L. A. Lalli for suggesting the study. Discussions with R. E. Smelser regarding the grain averaging are greatly appreciated.

## References

*ABAQUS User's Manual*, 1988, V-4.7, Hibbitt, Karlsson and Sorensen, Providence, RI.

Asaro, R. J., and Needleman, A., 1985, "Texture Development and Strain Hardening in Rate Dependent Polycrystals," *Acta Metallurgica*, Vol. 33, pp. 923–953.

Bunge, H. J., 1982, *Texture Analysis in Material Science*, Butterworths, London.

Harren, S. V., Dève, H. E., and Asaro, R. J., 1988, "Shear Band Formation in Plane Strain Compression," *Acta Metallurgica*, Vol. 36, pp. 2435–2480.

Hill, R., 1967, "The Essential Structure of Constitutive Laws for Metal Composites and Polycrystals," *Journal of the Mechanics and Physics of Solids*, Vol. 15, pp. 79–95.

Hill, R., and Hutchinson, J. W., 1975, "Bifurcation Phenomena in the Plane Tension Test," *Journal of the Mechanics and Physics of Solids*, Vol. 23, pp. 239–264.

Hutchinson, J. W., 1970, "Elastic-Plastic Behaviour of Polycrystalline Metals and Composites," *Proceedings of the Royal Society of London*, Vol. A319, pp. 247–272.

Mathur, K. A., and Dawson, P. R., 1989, "On Modeling the Development of Crystallographic Texture in Bulk Forming Processes," *International Journal of Plasticity*, Vol. 5, pp. 67–94.

Needleman, A., and Rice, J. R., 1978, "Limits to Ductility Set by Plastic Flow Localization," *Mechanics of Sheet Metal Forming*, D. P. Koistinen and N.-M. Wang, eds., Plenum Press, New York, pp. 237–267.

Needleman, A., and Tvergaard, V., 1984, "Finite Element Analysis of Localization in Plasticity," *Finite Elements—Special Problems in Solid Mechanics*, Vol. 5, T. J. Oden and G. F. Carey, eds., Prentice-Hall, Englewood Cliffs, NJ, pp. 94–267.

Peirce, D., Asaro, R. J., and Needleman, A., 1982, "An Analysis of Nonuniform and Localized Deformation in Ductile Single Crystals," *Acta Metallurgica*, Vol. 30, pp. 1087–1119.

Peirce, D., Asaro, R. J., and Needleman, A., 1983, "Material Rate Dependence and Localized Deformation in Crystalline Solids," *Acta Metallurgica*, Vol. 31, pp. 1951–1976.

Rice, J. R., 1971, "Inelastic Constitutive Relations for Solids: An Internal Variable Theory and its Application to Metal Plasticity," *Journal of the Mechanics and Physics of Solids*, Vol. 19, pp. 433–455.

Rudnicki, J. W., and Rice, J. R., 1975, "Conditions for Localization of Deformation in Pressure-Sensitive Dilatant Materials," *Journal of the Mechanics and Physics of Solids*, Vol. 23, pp. 371–394.

Smelser, R. E., and Becker, R., 1989, "ABAQUS User Subroutines for Material Modeling," *ABAQUS Users' Conference Proceedings*, Stresa, Italy, Hibbitt, Karlsson and Sorensen, Providence, RI, pp. 207–226.

*Smithells Metals Reference Book*, 1983, Sixth Edition, E. A. Brandles, ed., Butterworths, London, p. 15-5.

Triantalyllidis, N., Needleman, A., and Tvergaard, V., 1982, "On the Development of Shear Bands in Pure Bending," *International Journal of Solids and Structures*, Vol. 18, pp. 121–138.

Tvergaard, V., Needleman, A., and Lo, K. K., 1981, "Flow Localization in the Plane Strain Tensile Test," *Journal of the Mechanics and Physics of Solids*, Vol. 29, pp. 115–142.

**H. Cai**[1]
Department of Materials Science and Engineering, The Ohio State University, Columbus, OH 43210

**K. T. Faber**
Department of Materials Science and Engineering, Northwestern University Evanston, IL 60208

# On the Use of Approximation Methods for Microcrack Shielding Problems

*There is experimental evidence that stress-induced microcracking near a macrocrack tip enhances the fracture toughness of brittle materials. In considering the interaction of the macrocrack with multiple microcracks using a discrete model, it is essential to use approximation methods in order to keep the amount of the computation to a tractable level. However, when crack distances are small, the results of the approximation methods can be significantly different from the numerical solution based upon the exact formulation. The results obtained by these approximation methods will be compared with the numerical solution to show the applicability ranges in which the errors are acceptably small. The use of results obtained by the approximation methods outside applicability ranges in literature is shown to lead to incorrect conclusions concerning microcrack shielding.*

## 1 Introduction

There now exists experimental evidence that stress-induced microcracking near a macrocrack tip enhances the fracture toughness of brittle materials (Rühle, et al., 1987; Cai, et al., 1990; Faber, et al., 1990). Experimental studies by Rühle et al. (1987) have provided conclusive evidence of stress-induced microcracking toughening in a zirconia-toughened alumina. Recently, Faber et al. (1990) have shown a relationship between microcrack formation and an increase in toughness in SiC-$TiB_2$ composites with phases of different thermal expansion coefficient. The stress-induced microcracks near the macrocrack tip shield the macrocrack from the applied stress, thereby increasing the fracture toughness.

In addition to experimental studies, microcrack toughening has been also the subject of numerous modeling studies. The two basic approaches are continuum modeling (Evans and Faber, 1981; Clarke, 1984; Evans and Faber, 1984; Evans and Fu, 1985; Charalambides and McMeeking, 1987; Hutchinson, 1987; Ortiz, 1987; Charalambides and McMeeking, 1988; Laws and Brochenbrough, 1988; Ortiz and Giannakopoulos, 1989) and discrete modeling (Hoagland and Embury, 1980; Bowling, et al., 1987; Montagut and Kachanov, 1988). The continuum models are beyond the scope of this paper and will not be discussed further. Discrete models require consideration of the interaction of a macrocrack with microcracks (Kachanov and Montagut, 1986; Rose, 1986b, Rubinstein, 1986; Chudnovsky, et al., 1987a; Chudnovsky, et al., 1987b; Hori and Nemat-Nasser, 1987; Rubinstein and Choi, 1988; Gong and Horii, 1989). For many microcracks necessary to treat the toughening problem, it is essential to use approximation methods to keep the amount of computation to a tractable level. Under certain conditions, the results of these approximation methods are very close to the exact solution. However, when the macrocrack-microcrack and microcrack-microcrack distances are small, the results of the approximation methods can be significantly different from the exact solution. Indiscriminate use of these results could inevitably lead to incorrect conclusions.

The purpose of this work is to evaluate three approximation methods using various microcrack configurations, and to estimate the range within which the approximation methods are applicable. Before doing so, an iterative method to solve the interaction between a macrocrack and an array of microcracks is described. Then, the solution obtained by the iterative method will be checked for the case of a collinear microcrack, for which the exact analytical solution is available.

## 2 The Iterative Method

The present approach is based upon the same principle of superposition and the concept of self-consistency applied to the interaction of cracks. An approximate solution based upon this method is the use of an average traction over each microcrack. An alternative approximation approach is the use of a point representation of microcracks (Hoagland and Embury, 1980; Rose, 1986b; Bowling, et al., 1987). We will present the solution in the context of a stationary macrocrack interacting with microcracks in the absence of residual stresses. The analysis is limited to two dimensions to keep the numerical computation tractable for the problem of a macrocrack interacting with many microcracks.

Consider a single microcrack of length $2c$ and of arbitrary

[1]Present address: National Institute of Standards and Technology, Ceramics Division, Gaithersburg, MD 20899.

Contributed by the Applied Mechanics Division of THE AMERICAN SOCIETY OF MECHANICAL ENGINEERS for publication in the ASME JOURNAL OF APPLIED MECHANICS.

Discussion on this paper should be addressed to the Technical Editor, Prof. Leon M. Keer, The Technological Institute, Northwestern University, Evanston, IL 60208, and will be accepted until four months after final publication of the paper itself in the JOURNAL OF APPLIED MECHANICS.

Manuscript received by the ASME Applied Mechanics Division, Mar. 30, 1990; final revision, Jan. 17, 1991. Associate Technical Editor: C. F. Shih.

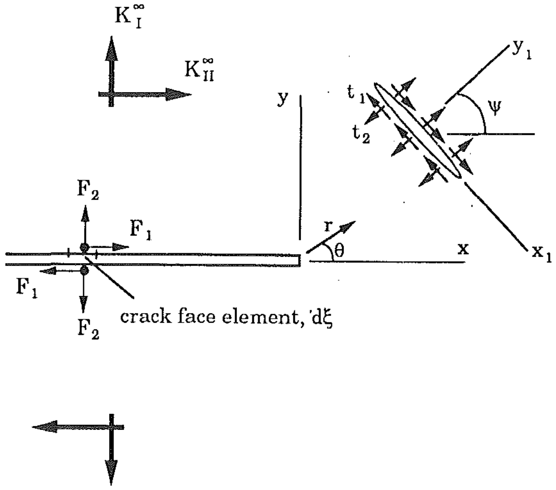


**Fig. 1 Schematic of the main coordinate system and the microcrack coordinate system (adapted from Hoagland and Embury, 1980)**

orientation near the crack tip of a semi-infinite crack with an associated applied stress intensity ($K_I^\infty$ and $K_{II}^\infty$) in two-dimensional space (Fig. 1). The near-tip stress field due to the applied stress without the microcrack is given by the following expression (Kanninen and Popelar, 1985):

$$\boldsymbol{\sigma} = K_I^\infty \boldsymbol{\sigma}_I + K_{II}^\infty \boldsymbol{\sigma}_{II} \tag{1}$$

where $\boldsymbol{\sigma}_I$ and $\boldsymbol{\sigma}_{II}$ are the modes I and II crack-tip stress fields given by

$$\boldsymbol{\sigma}_I = \frac{1}{\sqrt{2\pi r}} \begin{pmatrix} (\cos(\theta/2)[1-\sin(\theta/2)\sin(3\theta/2)] & \cos(\theta/2)\sin(\theta/2)\cos(3\theta/2) \\ \cos(\theta/2)\sin(\theta/2)\cos(3\theta/2) & \cos(\theta/2)[1+\sin(\theta/2)\sin(3\theta/2)] \end{pmatrix} \tag{2a}$$

and

$$\boldsymbol{\sigma}_{II} = \frac{1}{\sqrt{2\pi r}} \begin{pmatrix} -\sin(\theta/2)[2+\cos(\theta/2)\cos(3\theta/3)] & \cos(\theta/2)[1-\sin(\theta/2)\sin(3\theta/2)] \\ \cos(\theta/2)[1-\sin(\theta/2)\sin(3\theta/2)] & \sin(\theta/2)\cos(\theta/2)\cos(3\theta/2) \end{pmatrix}. \tag{2b}$$

The initial traction on the microcrack is given by

$$\mathbf{t} = \mathbf{B} \bullet (\mathbf{n} \bullet \boldsymbol{\sigma}) \tag{3}$$

where $\mathbf{B}$ is the matrix of orthogonal transformation, $\mathbf{n}$ the unit normal of the microcrack, and $\boldsymbol{\sigma}$ the existing stress along the microcrack line without the microcrack. The components of the stress are given in the main coordinate system, unless stated otherwise. The unit normal and the matrix of orthogonal transformation are related to the microcrack orientation angle $\psi$ by the following:

$$\mathbf{n} = (n_1, n_2) = (\cos\psi, \sin\psi), \tag{4}$$

$$\mathbf{B} = \begin{pmatrix} n_2 & -n_1 \\ n_1 & n_2 \end{pmatrix}. \tag{5}$$

The stress field of a microcrack can be computed using Muskhelishvili formalism (Rice, 1968; Muskhelishvili, 1977). The appropriate line integral for the finite crack of length $2c$ has been presented by Rice (1968), and is given as follows:

$$\phi'(z_1) = \frac{1}{2\pi(z_1-c)^{1/2}(z_1+c)^{1/2}} \int_{-c}^{+c} [p_2(s) - ip_1(s)] \frac{(c^2-s^2)^{1/2}}{s-z_1} ds \tag{6}$$

where $i$ is the imaginary unit, $z_1$ is the complex variable in the microcrack coordinate system and $z_1 = x_1 + iy_1$ (refer to Fig. 1), $c$ is the half length of the microcrack, and $p_i = -t_i(s)$. The terms, $t_1(s)$ and $t_2(s)$ are components of $\mathbf{t}$, i.e., $\mathbf{t}(s) = [t_1(s), t_2(s)]$. The stress components in the microcrack coordinate system are:

$$\sigma_{22} - i\sigma_{12} = \phi'(z_1) + \phi'(\bar{z}_1) + (z_1 - \bar{z}_1)\overline{\phi''(z_1)} \tag{7a}$$

$$\sigma_{11} = 4 \text{ Re } [\phi'(z_1)] - \sigma_{22} \tag{7b}$$

where Re indicates the real part of a complex number and a solid line over a complex number indicates its complex conjugate.

The stress field in the presence of a traction-free microcrack is the superposition of the stress field given by the equations listed above and the stress field without the microcrack. In other words, the microcrack stress when added to the exiting stress field produces a traction-free microcrack.

The microcrack stress field introduces tractions along the macrocrack face. To keep the macrocrack traction-free, an image stress field is introduced. The image stress field can be expressed in terms of a Green's function as derived by Hirth et al. (1974). The image stress at $z$ can be expressed in terms of line integrals

$$\sigma_{22} - i\sigma_{12} = \int_{-\infty}^{0} [\varphi'(z) + \varphi'(\bar{z}) + (z-\bar{z})\overline{\varphi''(z)}] d\xi \tag{8a}$$

$$\sigma_{11} + \sigma_{22} = \int_{-\infty}^{0} [4\text{Re}[\varphi'(z)]] d\xi \tag{8b}$$

where

$$\varphi(z) = \frac{1}{2\pi} [\sigma_{12}^M(\xi) + i\sigma_{22}^M(\xi)][\ln(z^{1/2} + i|\xi|^{1/2}) - \ln(z^{1/2} - i|\xi|^{1/2})], \tag{9}$$

and $\sigma_{i2}^M(\xi)$ is the microcrack stress field computed along the macrocrack line. The integrals are evaluated numerically to find the image stress field. The image stress field is then superposed onto the existing stress field. In doing so, new tractions are introduced to the once traction-free microcrack. These additional tractions are removed by applying Eqs. (6) and (7), and additional image stresses are computed using Eq. (8). The process is repeated until the tractions on the microcrack and the macrocrack are lower than a specified small value which varies (from $10^{-4}$ to 2 MPa) depending upon the accuracy required. The self-consistent stress field solution is then obtained.

The change in the stress intensity factor at the macrocrack tip is then computed:

$$\Delta K_I = \sqrt{(2/\pi)} \int_{-\infty}^{0} \frac{\sigma_{22}^M(\xi)}{\sqrt{-\xi}} d\xi \tag{10a}$$

$$\Delta K_{II} = \sqrt{(2/\pi)} \int_{-\infty}^{0} \frac{\sigma_{12}^M(\xi)}{\sqrt{-\xi}} d\xi. \tag{10b}$$

where $\sigma_{ij}^M(\xi)$ is the microcrack stress field evaluated along the macrocrack line. The integrals are evaluated numerically. The mode I stress intensity at the macrocrack tip can be written as

$$K_I = K_I^\infty + \Delta K_I. \tag{11}$$

Generally, this problem cannot be solved analytically, except in the case of collinear microcracks, the solutions of which have been presented by Rubinstein (1985) and Rose (1986a). Therefore, numerical methods are necessary to find the solution for a microcrack of arbitrary location and orientation. The numerical solution above does not represent a problem for the case of one or a few microcracks, but the computation becomes lengthy for multiple microcracks. The approximation methods which follow provide an alternative practical approach to the solution.

The first approximation method involves the use of average tractions on each microcrack, where the traction on a microcrack is averaged over the microcrack length. The stress field of a microcrack subject to a uniform surface traction can be simply expressed in terms of the Westergaard stress function (Westergaard, 1939; Sih, 1966; Eftis and Liebowitz, 1972). The appropriate stress function is

$$Z(z_1)=\frac{1}{\sqrt{1-(c/z_1)^2}}-1 \tag{12}$$

where $z_1$ is the complex variable in the microcrack coordinate system. The microcrack stress field in the microcrack coordinate system can be expressed as

$$\sigma_{11}=t_1[2\mathrm{Im}Z+y_1\mathrm{Re}Z_{,z}]+t_2[\mathrm{Re}Z-y_1\mathrm{Im}Z_{,z}] \tag{13a}$$

$$\sigma_{22}=t_1[-y_1\mathrm{Re}Z_{,z}]+t_2[\mathrm{Re}Z+y_1\mathrm{Im}Z_{,z}] \tag{13b}$$

$$\sigma_{12}=t_1[\mathrm{Re}Z-y_1\mathrm{Im}Z_{,z}]+t_2[-y_1\mathrm{Re}Z_{,z}] \tag{13c}$$

where $t_1$ is the shear component and $t_2$ is the normal component of traction $\mathbf{t}$ on the microcrack surface, $Z_{,z}$ is the first derivative of $Z$ with respect to $z_1$, and Im and Re indicate the imaginary part and the real part of a complex number, respectively.

Further simplification of the average traction method leads to another approximation method involving the use of a point representation of microcracks. In this approach, the traction on a microcrack is simply computed at the microcrack center. This approximation approach has been used in previous discrete modeling of microcrack shielding (Hoagland and Embury, 1980; Rose, 1986b; Bowling, et al., 1987).

## 3 The Approximation Method by Kachanov and Montagut

Kachanov and Montagut (1986) used an approximation method to consider a semi-infinite crack and an array of microcracks. This method is based on the superposition technique and the ideas of self-consistency applied to the average tractions on individual cracks (or microcracks in the case of interaction of a macrocrack with $M$ microcracks). The stress field was represented as a superposition:

$$\boldsymbol{\sigma}(\mathbf{x})=K_I\boldsymbol{\sigma}_I(\mathbf{x})+K_{II}\boldsymbol{\sigma}_{II}(\mathbf{x})+\sum_{i=1}^{M}\boldsymbol{\sigma}_i(\mathbf{x}) \tag{14}$$

where $\boldsymbol{\sigma}_I$ and $\boldsymbol{\sigma}_{II}$ are the modes I and II asymptotic crack-tip fields given in Eq. (2), respectively, and $\boldsymbol{\sigma}_i(\mathbf{x})$ is the stress field of $i$th microcrack loaded by average traction $<\mathbf{t}_i>$. The traction is induced along the microcrack line by other microcracks and the macrocrack stress field, and the average traction is given by

$$\langle \mathbf{t}_i\rangle=K_I\mathbf{n}_i\bullet\langle\boldsymbol{\sigma}_I\rangle_i+K_{II}\mathbf{n}_i\bullet\langle\boldsymbol{\sigma}_{II}\rangle_i+\sum_k \boldsymbol{\Lambda}_{ki}\langle\mathbf{t}_k\rangle \tag{15}$$

where $\mathbf{n}_i$ is the unit normal of $i$th microcrack, $\langle\boldsymbol{\sigma}_I\rangle_i$ and $\langle\boldsymbol{\sigma}_{II}\rangle_i$ are the average near-tip stress fields along the microcrack line, $\langle\mathbf{t}_k\rangle_i$ is the average traction on the microcracks, and $\boldsymbol{\Lambda}_{ki}$ is the transmission factor (the average traction induced on $i$th microcrack by $k$th microcrack subject to unit traction).

There are $M$ vectorial unknowns, $\langle\mathbf{t}_i\rangle$, and two unknown scalars, $K_I$ and $K_{II}$. With two additional conditions characterizing the effects of microcracks on the stress intensity of the macrocrack tip,

$$K_I-K_I^{\infty}=\sqrt{(2/\pi)}\int_{-\infty}^{0}\frac{1}{\sqrt{-\xi}}\sum_{i=1}^{M}\sigma_{(i)22}^{M}(\xi)d\xi \tag{16a}$$

and

$$K_{II}-K_{II}^{\infty}=\sqrt{(2/\pi)}\int_{-\infty}^{0}\frac{1}{\sqrt{-\xi}}\sum_{i=1}^{M}\sigma_{(i)12}^{M}(\xi)d\xi, \tag{16b}$$

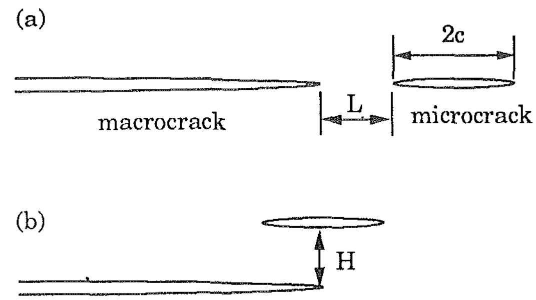


**Fig. 2 Microcrack configurations used to evaluate the approximation methods**

*Table 1 Comparison of the results of the stress intensity by the numerical iterative method and the analytical solution*

| | $(K_I-K_I^\infty)/K_I^\infty$ | | |
|---|---|---|---|
| L/2c | Numerical | Analytical | Error (%) |
| 0.05 | 0.6497 | 0.6539 | 0.65 |
| 0.10 | 0.3859 | 0.3873 | 0.40 |
| 0.15 | 0.2729 | 0.2737 | 0.31 |
| 0.20 | 0.2087 | 0.2092 | 0.26 |
| 0.25 | 0.1671 | 0.1675 | 0.23 |
| 0.30 | 0.1379 | 0.1382 | 0.21 |
| 0.35 | 0.1164 | 0.1166 | 0.20 |
| 0.40 | 0.0999 | 0.1001 | 0.19 |
| 0.45 | 0.0870 | 0.0871 | 0.17 |
| 0.50 | 0.0765 | 0.0766 | 0.17 |

all of the unknowns can be evaluated. In Eq. (16), $K_I$ and $K_{II}$ are the stress intensities at the macrocrack tip; $K_I^\infty$ and $K_{II}^\infty$ are the applied stress intensities, and $\sigma_{(i)ij}^{M}(\xi)$ is the stress of $i$th microcrack evaluated along the macrocrack line.

## 4 Verification of the Numerical Solution

The numerical solution (based upon the exact formulation) obtained by the iterative method for a collinear microcrack of length $2c$ ahead of a macrocrack with an associated applied stress intensity of $K_I^\infty$ (Fig. 2(*a*)) is verified by comparing it to the analytical solution presented by Rubinstein (1985) and Rose (1986a). We consider a range of distances, $L$, between the microcrack tip and the macrocrack tip from 0.05 to 0.5, that is, the macrocrack-microcrack tip distance is 1/20 to 1/2 of the microcrack length. The stress intensity at the macrocrack tip and the stress field at various points were computed. The results of the stress intensity are compared with values computed from the analytical solution in Table 1. The maximum relative error in the range considered is 0.65 percent which is likely due to numerical computation (see Table 1). Better results can be obtained by refinement of the numerical computation.

## 5 Evaluation of Approximation Methods

The approximation methods: the iterative method with average traction (iterative-average), the iterative method with point representation of microcracks (iterative-point) and the approximation method by Kachanov and Montagut (1986) are compared with the numerical solution for certain microcrack orientations. The main emphasis is placed upon the mode I stress intensity, as mode I shielding is of particular interest.

To see the range within which the approximation methods are applicable, the distance between the macrocrack and microcrack is varied and the results obtained are compared. The two configurations considered are a collinear microcrack (Fig. 2(*a*)) and a horizontal microcrack parallel to the macrocrack

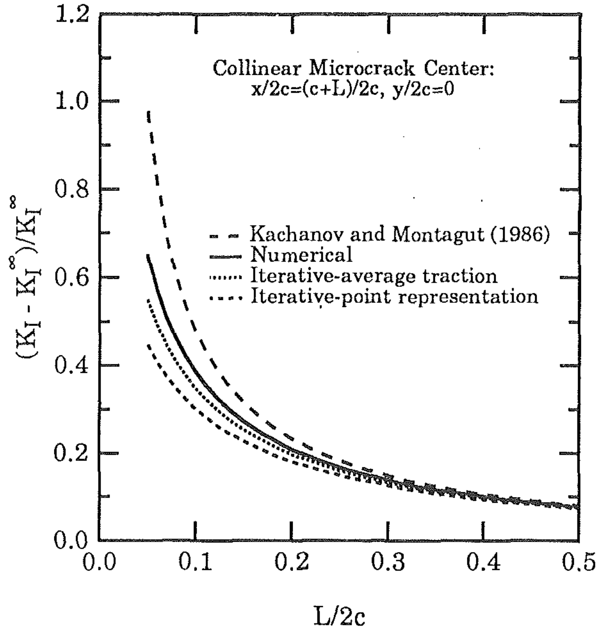


Fig. 3 Comparison of the change in the mode I stress intensity as a function of the normalized macrocrack-microcrack distance computed using the numerical solution, iterative-average traction, iterative-point representation, and the approximation method by Kachanov and Montagut for the collinear microcrack shown in Fig. 2(*a*).

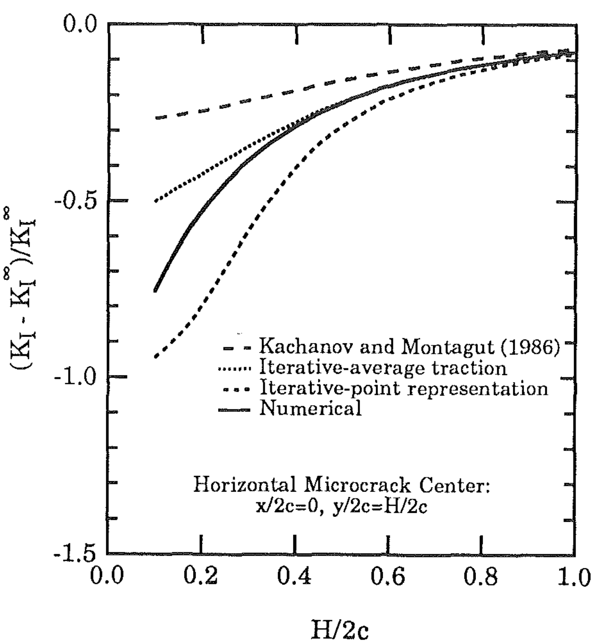


Fig. 4 Comparison of the change in the mode I stress intensity as a function of the normalized macrocrack-microcrack distance computed using the numerical solution, iterative-average traction, iterative-point representation, and the approximation method by Kachanov and Montagut for the horizontal microcrack shown in Fig. 2(*b*)

and centered just above the macrocrack tip (Fig. 2(*b*)). Comparisons of the results are shown in Figs. 3 and 4 for the collinear microcrack and the horizontal microcrack cases, respectively. For the collinear microcrack as shown in Fig. 3, the results obtained by the approximation method by Kachanov and Montagut represent overestimates of antishielding, while those by the iterative-average traction method and the iterative-point representation method represent underestimates of antishielding. For the horizontal microcrack as shown in Fig. 4,

*Table 2 Range of applicability for approximation methods*

| Approximation Method | Applicable Range Collinear microcrack | Horizontal microcrack |
|---|---|---|
| Iterative-average | L/2c > 0.1 | H/2c > 0.3 |
| Iterative-point | L/2c > 0.3 | H/2c > 0.9 |
| Kachanov-Montagut | L/2c > 0.2 | H/2c > 1.0 |

the results obtained by the approximation method by Kachanova and Montagut represent undererstiamtes of shielding, while those by the iterative-point representation method represent overestimates of shielding. In both cases, the results obtained by the iterative-average traction method are closest to the numerical solution based upon the exact formulation. If we use the conventional definition of the relative error for the normalized change in stress intensity $(K_I - K_I^\infty)/K_I^\infty$, and arbitrarily determine that errors of ten percent or less are reasonable for the applicability of the approximation methods, we can compare the range within which the approximation methods are applicable for mode I stress intensities (see Table 2).

## 6 Discussion

In all the cases, the solutions obtained by approximation methods deviate from the exact solution as the distance between the macrocrack and microcrack decreases (Figs. 3 and 4). This is unfortunate because the microcracks nearest to the macrocrack tip have the greatest effects on the stress intensity of the macrocrack tip.

From Table 2, we can see that the iterative-average traction method offers the best accuracy among the three approximation methods discussed. With this method, the defined lowest range is $L/2c = 0.1$ for the collinear microcrack case, and $H/2c = 0.3$ for the horizontal microcrack case.

In the case of a collinear microcrack, the iterative method with point representation of microcracks underestimates the effect of the microcrack on the macrocrack; as a result, it underestimates antishielding (Fig. 3). In the case of a horizontal microcarck, it overestimates shielding (Fig. 4). Therefore, it tends to overestimate shielding.

In the case of the horizontal microcrack, the defined lower limit of applicability for the approximation method by Kachanov and Montagut is unexpectedly high. On the other hand, the defined lower limit of applicability is as low as $L/2c = 0.2$ for the case of collinear microcrack. This favorable configuration of a collinear microcrack was used as the test case for the approximation method by Kachanov and Montagut (1986), and it was concluded that the error remains small for $L/2c$ as small as 0.1 to 0.2. This conclusion does not hold for the case of the horizontal microcrack.

In the approximation method by Kachanov and Montagut, two approximations are involved in solving for the macrocrack-microcrack interaction. The first is the use of the average traction induced on a microcrack. The second approximation is the use of the near-tip stress field in computing the superposed stress field (Eq. (14)). Consider the strong interaction of a macrocrack with a microcrack close to the macrocrack tip. In this case, the superposed stress field obtained by the second approximation is only good for $|\mathbf{x}| << |\mathbf{x}_m|$, where $\mathbf{x}_m$ is the coordinate of the microcrack. Consequently, the use of this approximation in computing the traction on the microcrack is not good because $|\mathbf{x}| \approx |\mathbf{x}_m|$.

In the particular configuration of collinear microcrack in the Kachanov-Montagut treatment, the use of the average traction would results in an underestimate for the change in the stress intensity. On the other hand, the use of the increased stress intensity value at the macrocrack tip ($K_I$) to compute the effect of the macrocrack on the microcrack (refer to Eq. (14)) leads to an overestimate. This overestimate is, in part, compensated by the underestimate due to the use of the average traction. With this compensation, the results obtained by the approximation method by Kachanov and Montagut method turn out to be good for $L/2c$ as low as 0.1 to 0.2, as shown in Fig. 3.

For the horizontal microcrack in the Kachanov-Montagut treatment, the use of the average traction underestimates the change in the stress intensity. At the same time, the use of the reduced stress intensity value at the macrocrack tip ($K_I$) to compute the effect of macrocrack on the microcrack also results in an underestimate. With this compounded underestimate, the results obtained by this method deviate from the exact solution quickly as $H/2c$ becomes small as shown in Fig. 4. We have observed that, in many cases, the approximation method by Kachanov and Montagut results in overestimates of antishielding, and underestimates of shielding, a feature also observed by other researchers (Rubinstein and Choi, 1988). This could explain, in part, why Kachanov and Montagut did not predict appreciable shielding from microcracks (Kachanov and Montagut, 1986; Montagut and Kachanov, 1988).

## 7 Summary

We have compared the results by the approximation methods with the numerical solution based upon the exact formulation for a number of cases. The following summary can be made:

(1) Approximation methods should be applied with caution when the crack distance is small. Outside the applicable range, the results are misleading.

(2) Among the three approximation methods discussed, the iterative method with average tractions generally offers the best results.

(3) In many cases, the approximation method by Kachanov and Montagut overestimates antishielding, and underestimates shielding when the macrocrack-microcrack distance is small.


## Acknowledgment

Support of this work has been provided by the National Science Foundation under Grant No. DMR-8896212.


## References


Bowling, G. D., Faber, K. T., and Hoagland, R. G., 1987, "Computer Simulations of *R*-Curve Behavior in Microcracking Materials," *J. Am. Ceram. Soc.*, Vol. 70, pp. 849–854.

Cai, H., Gu, W.-H., and Faber, K. T., 1990, "Microcrack Toughening in a SiC-TiB$_2$ Composite," *Proceedings of the American Society for Composites, Fifth Technical Conference on Composite Materials in Transition*, Technomic Publishing Co., Lancaster, PA, pp. 892–901.

Charalambides, P. G., and McMeeking, R. M., 1987, "Finite Element Method Simulation of Crack Propagation in a Brittle Microcracking Solid," *Mech. of Mater.*, Vol. 6, pp. 71–87.

Charalambides, P. G., and McMeeking, R. M., 1988, "Near-Tip Mechanics of Stress-Induced Microcracking in Brittle Materials," *J. Am. Ceram. Soc.*, Vol. 71, pp. 465–472.

Chudnovsky, A., Dolgopolsky, A., and Kachanov, M., 1987a, "Elastic Interaction of a Crack with a Microcrack Array—I. Formulation of the Problem and General Form of the Solution," *Int. J. Solids Struct.*, Vol. 23, pp. 1–10.

Chudnovsky, A., Dolgopolsky, A., and Kachanov, M., 1987b, "Elastic Interaction of a Crack with a Microcrack Array—II. Elastic Solution for Two Crack Configurations (Piecewise Constant and Linear Approximations)," *Int. J. Solids Struct.*, Vol. 23, pp. 11–21.

Clarke, D. R., 1984, "A Simple Calculation of Process-Zone Toughening by Microcracking," *J. Am. Ceram. Soc.*, Vol. 67, pp. C15–C16.

Eftis, J., and Liebowitz, H., 1972, "On the Modified Westergaard Equations for Certain Plane Crack Problems," *Int. J. Fract. Mech.*, Vol. 8, pp. 383–392.

Evans, A. G., and Faber, K. T., 1981, "Toughening of Ceramics by Circumferential Microcracking," *J. Am. Ceram. Soc.*, Vol. 64, pp. 394–398.

Evans, A. G., ahd Faber, K. T., 1984, "Crack-Growth Resistance of Microcracking Brittle Materials," *J. Am. Ceram. Soc.*, Vol. 67, pp. 255–260.

Evans, A. G., and Fu, Y., 1985, "Some Effects of Microcracks on the Mechanical Properties of Brittle Solids—II. Microcrack Toughening," *Acta Metall.*, Vol. 33, pp. 1525–1531.

Faber, K. T., Gu, W.-H., Cai, H., Winholtz, R. A., and Magley, D. J., 1991, "Fracture Properties of SiC-Based Particulate Composites," *Proceedings of the NATO Advanced Research Workshop on Toughening Mechanisms in Quasi-Brittle Materials*, Kluwer Academic Publishers, The Netherlands, pp. 3–17.

Gong, S.-X., and Horri, H., 1989, "General Solution to the Problem of Microcracks Near the Tip of a Main Crack," *J. Mech. Phys. Solids*, Vol. 37, pp. 27–46.

Hirth, J. P., Hoagland, R. G., and Gehlen, P. C., 1974, "The Interaction Between Line Force Arrays and Planar Cracks," *Int. J. Solids Struct.*, Vol. 10, pp. 977–984.

Hoagland, R. G., and Embury, J. D., 1980, "A Treatment of Inelastic Deformation Around a Crack Tip due to Microcracking," *J. Am. Ceram. Soc.*, Vol. 63, pp. 404–410.

Hori, M., and Nemat-Nasser, S., 1987, "Interacting Micro-Cracks Near the Tip in the Process Zone of a Macro-Crack," *J. Mech. Phys. Solids*, Vol. 35, pp. 601–629.

Hutchinson, J. W., 1987, "Crack Tip Shielding by Micro-Cracking in Brittle Solids," *Acta Metall.*, Vol. 35, pp. 1605–1619.

Kachanov, M., and Montagut, E., 1986, "Interaction of a Crack with Certain Microcrack Arrays," *Eng. Fract. Mech.*, Vol. 25, pp. 625–636.

Kanninen, M. F., and Popelar, C. H., 1985, *Advanced Fracture Mechanics*, Oxford University Press, New York.

Laws, N., and Brockenbrough, J. R., 1988, "Microcracking in Polycrystalline Solids," *J. Eng. Mater. Technol.*, Vol. 110, pp. 101–104.

Montagut, E., and Kachanov, M., 1988, "On Modelling a Microcracked Zone by "Weakened" Elastic Material and On Statistical Aspects of Crack-Microcrack Interactions," *Int. J. Fract.*, Vol. 37, pp. R55–R62.

Muskhelishvili, N. I., 1977, *Some Basic Problems in the Mathematical Theory of Elasticity*, 2nd English ed., Noordhoff International Publishing, Leyden, The Netherlands.

Ortiz, M., 1987, "A Continuum Theory of Crack Shielding in Ceramics," ASME JOURNAL OF APPLIED MECHANICS, Vol. 54, pp. 54–58.

Ortiz, M., and Giannakopoulos, A. E., 1989, "Maximal Crack Tip Shielding by Microcracking," ASME JOURNAL OF APPLIED MECHANICS, Vol. 56, pp. 279–283.

Rice, J. R., 1968, "Mathematical Analysis in the Mechanics of Fracture," *Fracture*, Vol. II, H. Liebowitz, ed., Academic Press, New York, pp. 191–311.

Rose, L. R. F., 1986a, "Effective Fracture Toughness of Microcracked Materials," *J. Am. Ceram. Soc.*, Vol. 69, pp. 212–214.

Rose, L. R. F., 1986b, "Microcrack Interaction with a Main Crack," *Int. J. Fract.*, Vol. 31, pp. 233–242.

Rubinstein, A. A., 1985, "Macrocrack Interaction with Semi-infinite Microcrack Array," *Int. J. Fract.*, Vol. 27, pp. 113–119.

Rubinstein, A. A., 1986, "Macrocrack-Microdefect Interaction," ASME JOURNAL OF APPLIED MECHANICS, Vol. 53, pp. 505–510.

Rubinstein, A. A., and Choi, H. C., 1988, "Macrocrack Interaction with Transverse Array of Microcracks," *Int. J. Fract.*, Vol. 36, pp. 15–26.

Rühle, M., Evans, A. G., McMeeking, R. M., Charalambides, P. G., and Hutchinson, J. W., 1987, "Microcrack Toughening in Alumina/Zirconia," *Acta Metall.*, Vol. 35, pp. 2701–2710.

Sih, G. C., 1966, "On the Westergaard Method of Crack Analysis," *Int. J. Fract. Mech.*, Vol. 2, pp. 628–631.

Westergaard, H. M., 1939, "Bearing Pressures and Cracks," ASME JOURNAL OF APPLIED MECHANICS, Vol. 61, pp. A49–A53.

# An Interlaminar Shear Stress Continuity Theory for Both Thin and Thick Composite Laminates

**Xianqiang Lu**

**Dahsin Liu**

Department of Metallurgy, Mechanics, and Materials Science,
Michigan State University,
East Lansing, MI 48824

*The interlaminar shear stress plays a very important role in the damage of composite laminates. With higher interlaminar shear stress, delamination can easily occur on the composite interface. In order to calculate the interlaminar shear stress, a laminate theory, which accounts for both the interlaminar shear stress continuity and the transverse shear deformation, was presented in this study. Verification of the theory was performed by comparing the present theory with Pagano's elasticity analysis. It was found that the present theory was able to give excellent results for both stresses and displacements. More importantly, the interlaminar shear stress can be presented directly from the constitutive equations instead of being recovered from the equilibrium equations.*

## Introduction

Fiber-reinforced polymer-matrix composite materials have high in-plane strength and low density. They are excellent materials for high-performance structures. Classical laminate theory has been used in the stress analysis for composite structures. However, it is only accurate for composite laminates with very large aspect ratio, such as those of thin plates. In order to calculate the correct stresses in thick composite plates, transverse shear deformation should be considered. Beside the laminate thickness, there is another reason to account for the shear deformation in the composite analysis. Due to the low shear modulus of polymer matrices, the transverse shear deformation of composite materials is more pronounced than that of conventional metals.

Although the composite materials have high in-plane strength, they are very vulnerable in the thickness direction. Due to the weak bonding between the composite layers, delamination can easily occur on the composite interface. Two types of delamination, namely edge delamination (Pagano and Pipes, 1973) and central delamination (Liu, 1988), have been widely investigated. Both of them can be viewed as a result of interlaminar stress concentration caused by material property mismatch in the thickness direction. It has also been verified by many investigators that delamination has significant effect on the structural integrity. For example, the compressive strength of a composite laminate can be reduced considerably if there is delamination. Consequently, the strength in the thickness direction is as important as that in the in-plane direction. The study of interlaminar stresses has then become an important issue in the composite analysis.

Many techniques have been developed for composite stress analysis. A comprehensive review can be found in an article authored by Kapania and Raciti (1989). Among the different techniques reported, the one receives the most attention in the recent years is the so-called high-order shear deformation theory. Many high-order theories, such as those presented by Yang, Norris, and Stavsky (1966), Nelson and Lorch (1974), Reissner (1975), Lo, Christensen, and Wu (1977), and Reddy (1984) are available for composite analysis. However, because of the nature of two-dimensional approach, the interlaminar stresses from the high-order theories are not single-valued. A post-analysis processing is required to find the correct interlaminar stresses. Lo, Christensen, and Wu (1978) used equilibrium equations in conjunction with in-plane stresses to recover the interlaminar stresses. Although this technique may be able to give accurate results, it is tedious and not suitable for structures with complex configurations.

In order to consider the continuity of the interlaminar stresses across the interface, the composite laminates have to be modeled by individual layers. Ambartsumyan (1970) was among the earliest to present a technique with the transverse shear stress continuity conditions across the composite interface. Based on the parabolic distribution for the transverse shear stresses in a composite layer, he presented a shear deformation theory for the composite analysis. His technique was refined by several other investigators.

Another stress-based technique, which includes the interlaminar stress continuity, was presented by Mau, Tong, and Pian (1972). This technique was named the hybrid-stress finite element method. Spilker (1980) and many other investigators extended this technique for studies with high-order stress assumptions. Pagano (1978) also assumed a stress distribution

Contributed by the Applied Mechanics Division of The American Society of Mechanical Engineers for publication in the ASME Journal of Applied Mechanics.

Discussion on this paper should be addressed to the Technical Editor, Professor Leon M. Keer, The Technological Institute, Northwestern University, Evanston, IL 60208, and will be accepted until four months after final publication of the paper itself in the Journal of Applied Mechanics.

Manuscript received by the ASME Applied Mechanics Division, June 13, 1990; final revision, Dec. 5, 1990. Associate Technical Editor: G. J. Dvorak.

in each layer. He derived the governing equations with the use of a variational approach. The continuity of transverse stresses was satisfied in his formulation.

Instead of assuming the stresses, DiSciuva (1985) presented a displacement field which had piecewise linear continuity through the thickness for in-plane displacements. The out-of-plane displacement, however, was assumed to be constant through the thickness. A variational method was used to formulate the governing equations. Due to the low order of the assumed displacement field, the transverse shear stresses were constant through the thickness. Similar approach was also given by Chou and Carlěone (1973).

A more general theory for composite analysis based on a layer-wise displacement field was presented by Reddy (1987) and Barbero and Reddy (1990). Reddy demonstrated that most of the displacement-based high-order theories could be summed up by a so-called Generalized Laminated Plate Theory (GLPT). Barbero and Reddy (1989) also applied the GLPT to study delamination buckling. Srinivas (1973) and Rehfield and Valisety (1983) introduced a multilayered technique to generalize their plate theory for composite laminates. Hinrichensen and Palazotto (1986) presented a nonlinear finite element analysis for thick composite laminates by using cubic spline functions to model the deformation through the thickness. Since all these studies were focused on the transverse deflection and in-plane stresses and deformation, the interlaminar stress continuity conditions were not considered.

Toledano and Murakami (1987) used a similar displacement field as DiSciuva's in their analysis. The transverse shear strains were constant within each layer. However, they also assumed quadratic transverse shear stress distributions across each individual layer. Reissner's mixed variational principle (Reissner, 1984) was used in their formulation together with the transverse shear stress continuity conditions. They concluded that this technique was valid for improving the in-plane deformation in the composite laminates with transverse shear effect.

In studying the composite delamination, it is important to have an accurate theory for interlaminar stress calculation. In view of the advantages and disadvantages of the techniques reported, it was concluded that a useful theory should satisfy the continuity requirements for both displacements and interlaminar stresses across the composite interface. The interlaminar stresses can then be obtained directly from the constitutive equations instead of from the equilibrium equations. Besides, in deriving the governing equations, the formulation should be variational consistent (Reddy, 1984). It then can be extended for finite element formulation and be used for composite structures with more complex configurations.

Based on the above understanding, an interlaminar shear stress continuity theory with a refined displacement field modified from Reddy's layer-wise theory (Reddy, 1987) is developed. However, both the nodal displacements and rotations are used as independent variables. Being different from Hinrichensen and Palazotto's approach (1986), the nodal rotations are not required to be continuous across the composite interface. The proposed theory can be used for both thin and thick laminate analysis. In addition, the theory can be employed to calculate interlaminar shear stresses directly from the constitutive equations. In order to verify the accuracy of the theory, numerical results from the closed-form solutions are compared with those from Pagano's elasticity analysis (Pagano, 1969).

## Displacement Field

A composite laminate composed of $n$ laminae as shown in Fig. 1 is considered. A Cartesian coordinate system is chosen such that the middle surface of the laminate occupies a domain $\Omega$ in the $x$-$y$ plane while the $z$-axis is normal to this plane. The displacements at a generic point $(x, y, z)$ in the laminate are assumed to be of the form

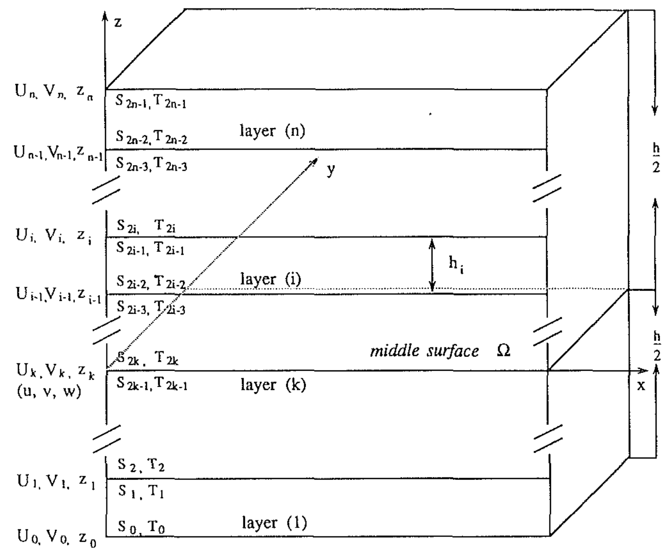


**Fig. 1 Nodal variables and the coordinate system**

$$
\begin{aligned}
u_1(x,y,z) &= u(x,y) + U(x,y,z),\\
u_2(x,y,z) &= v(x,y) + V(x,y,z),\\
u_3(x,y,z) &= w(x,y),
\end{aligned}
\tag{1}
$$

which is the same as the one given by Reddy (1987). $u$, $v$, and $w$ are displacements on the middle surface while $U$ and $V$ are in the individual layer. The assumption of constant $u_3$ through the thickness is justified in view of the relatively small magnitude of transverse normal stress in comparison with other stresses (Ambartsumyan, 1970; Vinson and Sierakowski, 1986). Accordingly, $\sigma_z$ is neglected in this study. However, this argument is questionable under some circumstances (Pagano and Soni, 1989).

In order to include the interlaminar shear stress continuity conditions in the analysis, the in-plane displacements are assumed for layer $(i)$ as follows:

$$
\begin{aligned}
U(x,y,z) &= U_{i-1}(x,y)\phi_1^{(i)}(z) + U_i(x,y)\phi_2^{(i)}(z)\\
&\quad + S_{2i-2}(x,y)\phi_3^{(i)}(z) + S_{2i-1}(x,y)\phi_4^{(i)}(z)\\
V(x,y,z) &= V_{i-1}(x,y)\phi_1^{(i)}(z) + V_i(x,y)\phi_2^{(i)}(z)\\
&\quad + T_{2i-2}(x,y)\phi_3^{(i)}(z) + T_{2i-1}(x,y)\phi_4^{(i)}(z),
\end{aligned}
\tag{2}
$$

where $\phi_j^{(i)}$ are Hermite cubic shape functions which can be expressed as

$$
\begin{cases}
\phi_1^{(i)} = 1 - 3[(z-z_{i-1})/h_i]^2 + 2[(z-z_{i-1})/h_i]^3 \\
\phi_2^{(i)} = 3[(z-z_{i-1})/h_i]^2 - 2[(z-z_{i-1})/h_i]^3 \\
\phi_3^{(i)} = (z-z_{i-1})[1-(z-z_{i-1})/h_i]^2 \\
\phi_4^{(i)} = (z-z_{i-1})^2[(z-z_{i-1})/h_i - 1]/h_i
\end{cases}
\quad z_{i-1} \le z \le z_i,
\tag{3}
$$

$$
\phi_1^{(i)} = \phi_2^{(i)} = \phi_3^{(i)} = \phi_4^{(i)} = 0 \quad z < z_{i-1} \quad \text{or} \quad z > z_i.
$$

The superscript $(i)$ represents for the layer number, i.e., the $i$th layer of the composite laminate, and $h_i$ is the thickness of the layer. As shown in Fig. 1, $U_i$ and $V_i$ are the node values of $U$ and $V$ at the point $(x, y, z_i)$ between layers $(i)$ and $(i + 1)$. $U_i$ and $V_i$ vanish on the middle surface, which is located at the position $z = z_k$. However, $S$'s and $T$'s are the first derivatives of $U$ and $V$ with respect to $z$-axis, respectively. More specifically, $S_{2i}$ and $T_{2i}$ represent the node values of $\partial U/\partial z$ and $\partial V/\partial z$ at the point $(x, y, z_i)$ in layer $(i + 1)$ while $S_{2i-1}$ and $T_{2i-1}$ are at the same point but in layer $(i)$. Figure 1 depicts the variables. It is also noted that although the interlaminar shear stresses are continuous across the interface,

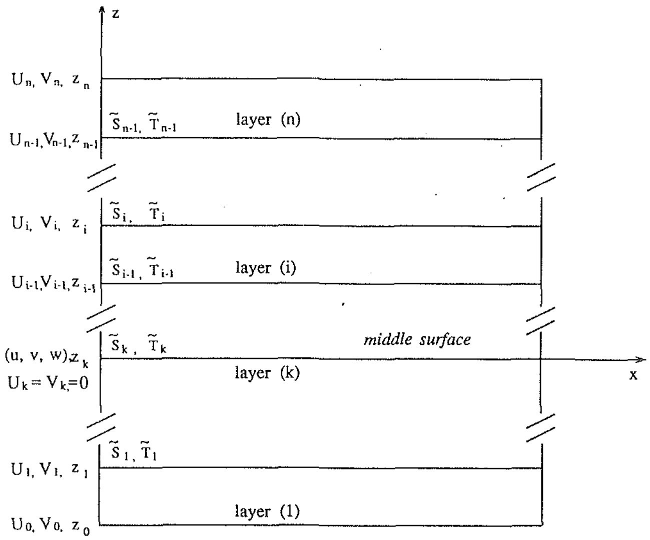


**Fig. 2 Reduced variables**

the interlaminar shear strains are not. Consequently, $S_{2i}$ and $T_{2i}$ are not the same as $S_{2i-1}$ and $T_{2i-1}$. The total number of the assumed variables is then equal to $6n + 3$.

As a summary, the required continuity conditions on the composite interface are displacements and interlaminar shear stresses. The former is satisfied automatically with the use of a global coordinate system while the latter can be expressed as follows:

$$\lim_{z \to z_i} \tau_{xz}^{(i+1)} = \lim_{z \to z_i} \tau_{xz}^{(i)}, \quad \lim_{z \to z_i} \tau_{yz}^{(i+1)} = \lim_{z \to z_i} \tau_{yz}^{(i)}, \quad i = 1, 2, \ldots, n-1. \tag{4}$$

If the composite laminate of interest is of cross-ply sequence, the constitutive equations for the $i$th layer become (Vinson and Sierakowski, 1986)

$$\begin{bmatrix} \sigma_x \\ \sigma_y \\ \sigma_z \\ \tau_{xy} \end{bmatrix}^{(i)} = \begin{bmatrix} Q_{11} & Q_{12} & Q_{13} & 0 \\ Q_{12} & Q_{22} & Q_{23} & 0 \\ Q_{13} & Q_{23} & Q_{33} & 0 \\ 0 & 0 & 0 & 2Q_{66} \end{bmatrix}^{(i)} \begin{bmatrix} \epsilon_x \\ \epsilon_y \\ \epsilon_z \\ \epsilon_{xy} \end{bmatrix},$$

$$\begin{bmatrix} \tau_{yz} \\ \tau_{xz} \end{bmatrix}^{(i)} = \begin{bmatrix} 2Q_{44} & 0 \\ 0 & 2Q_{55} \end{bmatrix}^{(i)} \begin{bmatrix} \epsilon_{yz} \\ \epsilon_{xz} \end{bmatrix}^{(i)}. \tag{5}$$

In addition, for linear strain-displacement relations, the following equations can be employed:

$$\epsilon_x = \frac{\partial u_1}{\partial x}, \quad \epsilon_y = \frac{\partial u_2}{\partial y}, \quad \epsilon_z = \frac{\partial u_3}{\partial z} = 0, \quad \epsilon_{xy} = \frac{1}{2}\left(\frac{\partial u_1}{\partial y} + \frac{\partial u_2}{\partial x}\right),$$

$$\epsilon_{xz} = \frac{1}{2}\left(\frac{\partial u_1}{\partial z} + \frac{\partial u_3}{\partial x}\right), \quad \epsilon_{yz} = \frac{1}{2}\left(\frac{\partial u_2}{\partial z} + \frac{\partial u_3}{\partial y}\right). \tag{6}$$

Substituting Eqs. (1) and (2) into Eqs. (6) and (5), the stresses can be expressed in terms of displacements. With the use of Eq. (4), $S_{2i-1}$ and $T_{2i-1}$ can be verified to be functions of $S_{2i}$ and $T_{2i}$, respectively, i.e.,

$$S_{2i-1} = \frac{Q_{55}^{(i+1)}}{Q_{55}^{(i)}} S_{2i} + \left[\frac{Q_{55}^{(i+1)}}{Q_{55}^{(i)}} - 1\right]\frac{\partial w}{\partial x},$$

$$T_{2i-1} = \frac{Q_{44}^{(i+1)}}{Q_{44}^{(i)}} T_{2i} + \left[\frac{Q_{44}^{(i+1)}}{Q_{44}^{(i)}} - 1\right]\frac{\partial w}{\partial y}, \tag{7}$$

where $i = 1, 2, \ldots, n-1$. In this study, the shear traction-free condition on both top and bottom surfaces is also observed, i.e.,

$$\tau_{xz} = 0,$$

$$\tau_{yz} = 0, \tag{8}$$

at $z = \pm h/2$, where $h$ is the total thickness of the composite laminate. With the same fashion as used in obtaining Eq. (7), the first derivatives at the top and bottom surfaces can also be achieved as follows:

$$S_0 = S_{2n-1} = -\frac{\partial w}{\partial x},$$

$$T_0 = T_{2n-1} = -\frac{\partial w}{\partial y}. \tag{9}$$

Therefore, it is concluded from Eq. (7) and (9) that it only requires four variables, $U_i$, $V_i$, $S_{2i}$, and $T_{2i}$, to express each nodal point. Consequently, the total number of the independent variables is reduced to $4n + 1$. The reduced variables are assigned new notation, i.e., $\tilde{S}_j$ and $\tilde{T}_j$, and are shown in Fig. 2. The displacement field can then be written as follows:

$$u_1(x,y,z) = u(x,y) + \sum_{j=0}^{n} U_j \Phi^j + \sum_{j=1}^{n-1} \tilde{S}_j \Psi_1^j + \left[\sum_{j=1}^{n-1}\left(\frac{Q_{55}^{(j+1)}}{Q_{55}^{(j)}} - 1\right)\Theta_j - \phi_3^{(1)} - \phi_4^{(n)}\right]\frac{\partial w}{\partial x}$$

$$u_2(x,y,z) = v(x,y) + \sum_{j=0}^{n} V_j \Phi^j + \sum_{j=1}^{n-1} \tilde{T}_j \Psi_2^j + \left[\sum_{j=1}^{n-1}\left(\frac{Q_{44}^{(j+1)}}{Q_{44}^{(j)}} - 1\right)\Theta_j - \phi_3^{(1)} - \phi_4^{(n)}\right]\frac{\partial w}{\partial y}$$

$$u_3(x,y,z) = w(x,y). \tag{10}$$

The shape functions in the global coordinate system are given by the following equations:

$$\Phi^j = \begin{cases} \phi_1^{(i)} & j = i-1 \\ \phi_2^{(i)} & j = i \end{cases} \quad \text{layer } (i)$$

$$\Phi^j = 0 \quad \text{others}$$

$$\Psi_1^j = \begin{cases} \phi_3^{(i)} & j = i-1 \\ \dfrac{Q_{55}^{(i+1)}}{Q_{55}^{(i)}}\phi_4^{(i)} & j = i \end{cases} \quad \text{layer } (i)$$

$$\Psi_1^j = 0 \quad \text{others}$$

$$\Psi_2^j = \begin{cases} \phi_3^{(i)} & j = i-1 \\ \dfrac{Q_{44}^{(i+1)}}{Q_{44}^{(i)}}\phi_4^{(i)} & j = i \end{cases} \quad \text{layer } (i)$$

$$\Psi_2^j = 0 \quad \text{others}$$

$$\Theta_j = \begin{cases} \phi_4^{(i)} & j = i \quad \text{layer } (i) \\ 0 & \quad \text{others} \end{cases} \tag{11}$$

## Equilibrium Equations

The principle of virtual displacement is used to derive the equilibrium equations and the corresponding boundary conditions. The principle of virtual displacement can be stated as follows:

$$\int_{-h/2}^{h/2}\int_{\Omega}(\sigma_x\delta\epsilon_x+\sigma_y\delta\epsilon_y+\sigma_z\delta\epsilon_z+2\tau_{xy}\delta\epsilon_{xy}$$

$$+2\tau_{xz}\delta\epsilon_{xz}+2\tau_{yz}\delta\epsilon_{yz})dA\,dz-\int_{\Omega}P_z\delta u_3 dA=0. \quad (12)$$

Substituting Eq. (10) into Eq. (6), the strains can be expressed in terms of displacement variables. Then, combining the strain with Eq. (5), substituting them into Eq. (12), and after integrating by parts and collecting similar terms, the governing equations become as follows:

$$\begin{aligned}
&\delta u: && N_{x,x}+N_{xy,y}=0\\
&\delta v: && N_{xy,x}+N_{y,y}=0\\
&\delta w: && Q_{x,x}+Q_{y,y}-\bar{\lambda}_{x,xx}-\bar{\lambda}_{xy,xy}-\bar{\lambda}_{y,yy}+\bar{\eta}_{x,x}+\bar{\eta}_{y,y}+P_z=0\\
&\delta U_j: && N^j_{x,x}+N^j_{xy,y}-Q^j_x=0 \quad j=0,1,\ldots,n;\ j\neq k\\
&\delta V_j: && N^j_{xy,x}+N^j_{y,y}-Q^j_y=0 \quad j=0,1,\ldots,n;\ j\neq k\\
&\delta \tilde{S}_j: && M^j_{x,x}+M^j_{1xy,y}-R^j_x=0 \quad j=1,2,\ldots,n-1\\
&\delta \tilde{T}_j: && M^j_{2xy,x}+M^j_{y,y}-R^j_y=0 \quad j=1,2,\ldots,n-1.
\end{aligned} \quad (13)$$

The essential and natural boundary conditions can also be obtained. They are listed in the following two columns:

| Essential Boundary Conditions: | Natural Boundary Conditions: |
|---|---|
| $u$ | $N_x n_x+N_{xy}n_y$ |
| $v$ | $N_{xy}n_x+N_y n_y$ |
| $w$ | $\left(Q_x+\bar{\eta}_x-\bar{\lambda}_{x,x}-\frac{1}{2}\bar{\lambda}_{xy,y}\right)n_x+\left(Q_y+\bar{\eta}_y-\bar{\lambda}_{y,y}-\frac{1}{2}\bar{\lambda}_{xy,x}\right)n_y$ |
| $\frac{\partial w}{\partial x}$ | $\bar{\lambda}_x n_x+\frac{1}{2}\bar{\lambda}_{xy}n_y$ |
| $\frac{\partial w}{\partial y}$ | $\frac{1}{2}\bar{\lambda}_{xy}n_x+\bar{\lambda}_y n_y$ |
| $U_j$ | $N^j_x n_x+N^j_{xy}n_y \quad j=0,1,\ldots,n;\ j\neq k$ |
| $V_j$ | $N^j_{xy}n_x+N^j_y n_y \quad j=0,1,\ldots,n;\ j\neq k$ |
| $\tilde{S}_j$ | $M^j_x n_x+M^j_{1xy}n_y \quad j=1,2,\ldots,n-1;$ |
| $\tilde{T}_j$ | $M^j_{2xy}n_x+M^j_y n_y \quad j=1,2,\ldots,n-1. \quad (14)$ |

The resultant forces and moments in Eq. (14) can also be defined as follows:

$$(N_x,N_y,N_{xy})=\int_{-h/2}^{h/2}(\sigma_x,\sigma_y,\tau_{xy})dz$$

$$(Q_x,Q_y)=\int_{-h/2}^{h/2}(\tau_{xz},\tau_{yz})dz$$

$$(N^j_x,N^j_y,N^j_{xy})=\int_{-h/2}^{h/2}(\sigma_x,\sigma_y,\tau_{xy})\Phi^j dz$$

$$(M^j_x,M^j_y,M^j_{1xy},M^j_{2xy})=\int_{-h/2}^{h/2}(\sigma_x\Psi^j_1,\sigma_y\Psi^j_2,\tau_{xy}\Psi^j_1,\tau_{xy}\Psi^j_2)dz$$

$$(\bar{\lambda}_x,\bar{\lambda}_y,\bar{\lambda}_{xy})=\int_{-h/2}^{h/2}(\sigma_x\lambda_1,\sigma_y\lambda_2,\tau_{xy}\lambda_1+\tau_{xy}\lambda_2)dz$$

$$\lambda_1=\left[\sum_{j=1}^{n-1}\left(\frac{Q_{55}^{(j+1)}}{Q_{55}^{(j)}}-1\right)\Theta_j-\phi_3^{(1)}-\phi_4^{(n)}\right]$$

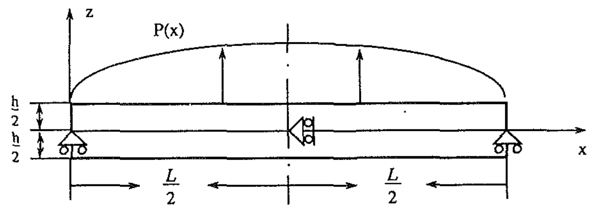


Material properties: $E_1=25\times10^6$ psi, $E_2=10^6$ psi, $G_{12}=.5\times10^6$ psi, $G_{22}=.2\times10^6$ psi, and $\nu_{12}=\nu_{22}=.25$

**Fig. 3 Cylindrical bending of an orthotropic laminate**

$$\lambda_2=\left[\sum_{j=1}^{n-1}\left(\frac{Q_{44}^{(j+1)}}{Q_{44}^{(j)}}-1\right)\Theta_j-\phi_3^{(1)}-\phi_4^{(n)}\right]$$

$$(\bar{\eta}_x,\bar{\eta}_y)=\int_{-h/2}^{h/2}\left(\tau_{xz}\frac{d\lambda_1}{dz},\tau_{yz}\frac{d\lambda_1}{dz}\right)dz$$

$$(Q^j_x,Q^j_y)=\int_{-h/2}^{h/2}\left(\tau_{xz}\frac{d\Phi^j}{dz},\tau_{yz}\frac{d\Phi^j}{dz}\right)dz$$

$$(R^j_x,R^j_y)=\int_{-h/2}^{h/2}\left(\tau_{xz}\frac{d\Psi^j_1}{dz},\tau_{yz}\frac{d\Psi^j_2}{dz}\right)dz. \quad (15)$$

## Solutions for Cross-Ply Laminates

In order to test the accuracy of the present theory, the cylindrical bending of an infinitely long strip examined by Pagano (1969) was studied. The displacement field can be simplified to be functions of $x$ and $z$ only. Figure 3 shows the configuration of the laminate. Therefore, all the derivatives with respect to $y$ in Eqs. (13) and (14) vanish. By combining Eq. (15) with Eq. (13) along with the stresses and strains expressed by the reduced independent variables, the final governing equations can be given in terms of the independent variables, i.e.,

$$A_{11}u_{,xx}+\sum_{\substack{j=0\\ j\neq k}}^{n}B^j_{11}U_{j,xx}+\sum_{m=1}^{n-1}C^m_{11}\tilde{S}_{m,xx}+\gamma_1 w_{,xxx}=0$$

$$(A_{55}+\bar{A}_{55})w_{,xx}+\sum_{\substack{j=0\\ j\neq k}}^{n}(B^j_{55}+\bar{B}^j_{55})U_{j,x}$$

$$+\sum_{m=1}^{n-1}(C^m_{55}+\bar{C}^m_{55})\tilde{S}_{m,x}+(\gamma_2+\bar{\gamma}_2)w_{,xx}$$

$$-(\bar{A}_{11}u_{,xxx}+\sum_{\substack{j=0\\ j\neq k}}^{n}\bar{B}^j_{11}U_{j,xxx}+\sum_{m=1}^{n-1}\bar{C}^m_{11}\tilde{S}_{m,xxx}$$

$$+\bar{\gamma}_1 w_{,xxxx})+P_z=0 \quad (16)$$

$$B^l_{11}u_{,xx}+\sum_{\substack{j=0\\ j\neq k}}^{n}(D^{lj}_{11}U_{j,xx}-D^{lj}_{55}U_j)$$

$$+\sum_{m=1}^{n-1}(E^{lm}_{11}\tilde{S}_{j,xx}-E^{lm}_{55}S_j) \quad l=0,1,\ldots,n$$

$$+\bar{B}^l_{11}w_{,xxx}-(B^l_{55}+\bar{B}^l_{55})w_{,x}=0 \quad l\neq k$$

$$C^{t}_{11}u_{,xx}+\sum_{\substack{j=0\\ j\neq k}}^{n}(E^{jt}_{11}U_{j,xx}-E^{jt}_{55}U_j)$$

$$+\sum_{m=1}^{n-1}(F^{tm}_{11}\tilde{S}_{j,xx}-F^{tm}_{55}\tilde{S}_j)+\overline{C}^{t}_{11}w_{,xxx}-(C^{t}_{55}+\overline{C}^{t}_{55})w_{,x}=0$$

$$t=1,2,\ldots,n-1$$

where the $A_{11}$, $B^{j}_{11}$, $\overline{B}^{j}_{11}$, $C^{m}_{11}$, $\overline{C}^{m}_{11}$, $D^{lj}_{11}$, $E^{lm}_{11}$, $F^{tm}_{11}$, $\gamma_1$, $A_{55}$, $\overline{A}_{55}$, $B^{j}_{55}$, $\overline{B}^{j}_{55}$, $C^{m}_{55}$, $\overline{C}^{m}_{55}$, $D^{lj}_{55}$, $E^{lm}_{55}$, $F^{tm}_{55}$, $\gamma_2$, $\overline{\gamma}_1$, and $\overline{\gamma}_2$ are coefficients of laminate properties. They can be expressed as follows:

$$A_{11}=\sum_{i=1}^{n-1}\int_{z_{i-1}}^{z_i}Q^{(i)}_{11}dz,\quad B^{j}_{11}=\sum_{i=1}^{n-1}\int_{z_{i-1}}^{z_i}Q^{(i)}_{11}\Phi^{j}dz,$$

$$C^{m}_{11}=\sum_{i=1}^{n-1}\int_{z_{i-1}}^{z_i}Q^{(i)}_{11}\Psi^{m}_{1}dz\quad \gamma_1=\sum_{i=1}^{n-1}\int_{z_{i-1}}^{z_i}Q^{(i)}_{11}\lambda_1 dz,$$

$$\gamma_2=\sum_{i=1}^{n-1}\int_{z_{i-1}}^{z_i}Q^{(i)}_{55}\lambda_{1,z}dz\quad A_{55}=\sum_{i=1}^{n-1}\int_{z_{i-1}}^{z_i}Q^{(i)}_{55}dz,$$

$$B^{j}_{55}=\sum_{i=1}^{n-1}\int_{z_{i-1}}^{z_i}Q^{(i)}_{55}\Phi^{j}_{,z}dz,\quad C^{m}_{55}=\sum_{i=1}^{n-1}\int_{z_{i-1}}^{z_i}Q^{(i)}_{55}\Psi^{m}_{1,z}dz$$

$$\overline{A}_{11}=\gamma_1,\quad \overline{B}^{j}_{11}=\sum_{i=1}^{n-1}\int_{z_{i-1}}^{z_i}Q^{(i)}_{11}\Phi^{j}\lambda_1 dz,$$

$$\overline{C}^{m}_{11}=\sum_{i=1}^{n-1}\int_{z_{i-1}}^{z_i}Q^{(i)}_{11}\Psi^{m}_{1}\lambda_1 dz\quad \overline{B}^{j}_{55}=\sum_{i=1}^{n-1}\int_{z_{i-1}}^{z_i}Q^{(i)}_{55}\Phi^{j}_{,z}\lambda_{1,z}dz,$$

$$\overline{C}^{m}_{55}=\sum_{i=1}^{n-1}\int_{z_{i-1}}^{z_i}Q^{(i)}_{55}\Psi^{m}_{1,z}\lambda_{1,z}dz$$

$$\overline{A}_{55}=\gamma_2,\quad \overline{\gamma}_1=\sum_{i=1}^{n-1}\int_{z_{i-1}}^{z_i}Q^{(i)}_{11}\lambda_1^2 dz,\quad \overline{\gamma}_2=\sum_{i=1}^{n-1}\int_{z_{i-1}}^{z_i}Q^{(i)}_{55}\lambda_{1,z}^2 dz$$

$$D^{lj}_{11}=\sum_{i=1}^{n-1}\int_{z_{i-1}}^{z_i}Q^{(i)}_{11}\Phi^{l}\Phi^{j}dz,\quad E^{lm}_{11}=\sum_{i=1}^{n-1}\int_{z_{i-1}}^{z_i}Q^{(i)}_{11}\Phi^{l}\Psi^{m}_{1}dz$$

$$F^{tm}_{11}=\sum_{i=1}^{n-1}\int_{z_{i-1}}^{z_i}Q^{(i)}_{11}\Psi^{t}_{1}\Psi^{m}_{1}dz$$

$$D^{lj}_{55}=\sum_{i=1}^{n-1}\int_{z_{i-1}}^{z_i}Q^{(i)}_{55}\Phi^{l}_{,z}\Phi^{j}_{,z}dz,\quad E^{lm}_{55}=\sum_{i=1}^{n-1}\int_{z_{i-1}}^{z_i}Q^{(i)}_{55}\Phi^{l}_{,z}\Psi^{m}_{1,z}dz$$

$$F^{tm}_{55}=\sum_{i=1}^{n-1}\int_{z_{i-1}}^{z_i}Q^{(i)}_{55}\Psi^{t}_{1,z}\Psi^{m}_{1,z}dz. \quad (17)$$

Since the composite laminate is simply supported at $x=0$ and $x=L$, the boundary conditions are as follows:

$$w(0)=w(L),=0;\quad N_x(0)=N_x(L)=0;\quad \overline{\lambda}_x(0)=\overline{\lambda}_x(L)=0$$
$$N^{m}_{x}(0)=N^{m}_{x}(L)=0;\quad m=0,1,\ldots,n;\ m\neq k$$
$$M^{m}_{x}(0)=M^{m}_{x}(L)=0;\quad m=1,2,\ldots,n-1. \quad (18)$$

The loading $P_z$ is assumed to be a sinusoidal distribution, i.e.,

$$P_z=P_0\sin(\beta x),\quad \beta=\frac{\pi}{L}. \quad (19)$$

In order to satisfy the boundary conditions listed in Eq. (18), the following displacements are assumed:

$$u=\mathbf{u}\cos(\beta x),\quad w=\mathbf{w}\sin(\beta x)$$
$$U_j=\mathbf{U}_j\cos(\beta x)\quad j=0,1,\ldots,n;\ j\neq k$$
$$\tilde{S}_j=\mathbf{S}_j\cos(\beta x)\quad j=1,2,\ldots,n-1 \quad (20)$$

where $\mathbf{u}$, $\mathbf{w}$, $\mathbf{U}_j$ and $\mathbf{S}_j$ are coefficients to be determined. It is obvious that $w$ satisfies the boundary conditions, i.e., $w(0)=w(L)=0$. The satisfaction of the remaining boundary conditions can also be verified by expressing Eq. (15) in terms of displacements. After substituting Eq. (20) into Eq. (15), it can be found that the resultants in Eq. (18) are of sine functions. Therefore, they can satisfy the prescribed boundary conditions. Thus, Eq. (20) can be a set of solution to the governing equations for simply-supported orthotropic laminate under sinusoidal loading. By substituting Eq. (20) into Eq. (16), the coefficients $\mathbf{u}$, $\mathbf{w}$, $\mathbf{U}_j$, and $\mathbf{S}_j$ can be determined and a closed-form solution is obtained.

## Results and Discussions

In order to verify the accuracy of the new theory in the composite stress analysis, Pagano's studies (Pagano, 1969) on the laminates, i.e., [0], [90/0], and [0/90/0], were investigated. The coordinate system of the laminates and the material constants can be found in Fig. 3. The numerical results are sum-

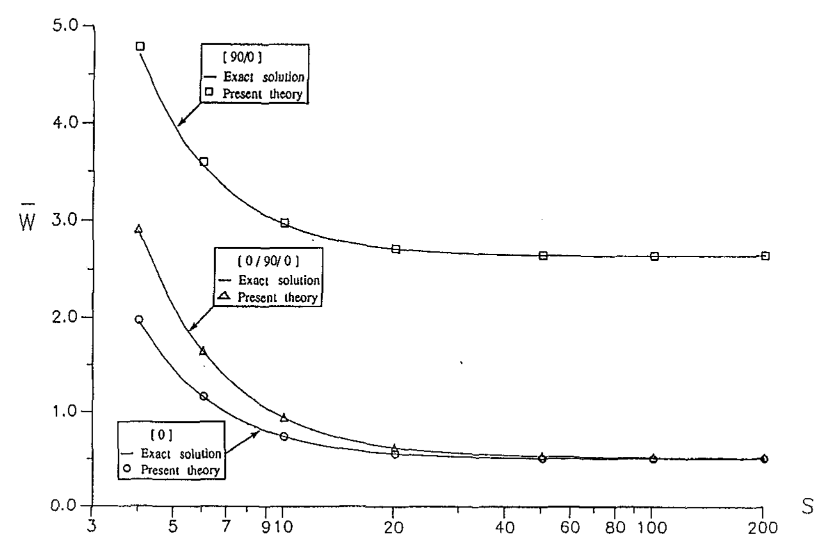


**Fig. 4 Normalized maximum deflection as a function of aspect ratio *S* in logarithmic scale**

marized in the following sections with the same nondimensional terms used by Pagano, i.e.,

$$\bar{\sigma}_x=\frac{\sigma_x\left(\frac{L}{2},z\right)}{P_0},\quad \bar{\tau}_{xz}=\frac{\tau_{xz}(0,z)}{P_0},\quad \bar{u}=\frac{E_T u_1(0,z)}{hP_0},$$

$$\bar{w}=\frac{100h^3E_Tu_3\left(\frac{L}{2}\right)}{P_0L^4},\quad \bar{z}=\frac{z}{h}. \qquad (21)$$

**1 Displacement in the Thickness Direction.** The displacements in the thickness direction, $w$, in the middle of the [0], [90/0], and [0/90/0] laminates as a function of aspect ratio ($S = L/h$) are shown in Fig. 4. Apparently, the results from the present theory agree quite well with those from the exact solution in both large and small aspect ratios. In order to further compare the results from both techniques, the numerical solutions for all three types of cross-ply beam are listed in Table 1. In this study three different values of $S$, i.e., 4, 20, and 100, which represent for thick, intermediate, and thin laminates, were presented. Besides, three different layer numbers were investigated to study the effect of layer number on the accuracy. The results in Table 1 conclude that the present theory gives excellent results of $w$ in all three types of lamination, although the results in the laminates with higher aspect ratio seem to be more accurate. However, the increase in the layer number does not seem to cause any significant effect on the results.

**Table 1 Comparison and numerical results between Pagano's analysis and present theory**

| | S | Pagano's solution | Present theory 2-layer | 4-layer | 6-layer |
|---|---|---|---|---|---|
| [0] | 4 | 1.9490 | 1.9672 | 1.9659 | 1.9659 |
| | 20 | .5519 | .5523 | .5523 | .5523 |
| | 100 | .4940 | .4940 | .4940 | .4940 |
| [0/90] | 4 | 4.6953 | 4.7773 | 4.7812 | 4.7812 |
| | 20 | 2.7027 | 2.7069 | 2.7069 | 2.7069 |
| | 100 | 2.6222 | 2.6230 | 2.6220 | 2.6220 |
| [0/90/0] | 4 | 2.8868 | | | 2.9098 |
| | 20 | .6172 | | | .6176 |
| | 100 | .5140 | | | .5140 |

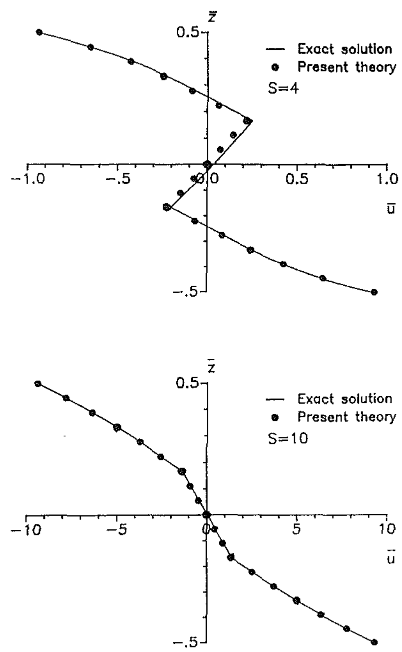


Fig. 5 Comparison of $\bar{u}$ between Pagano's analysis and present theory in the [0/90/0] laminate

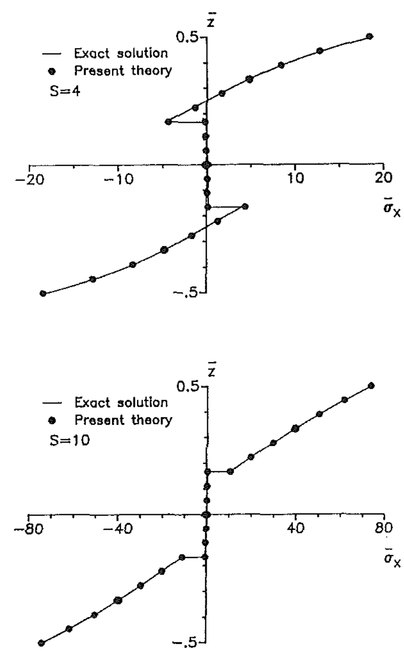


Fig. 6 Comparison of $\bar{\sigma}_x$ between Pagano's analysis and present theory in the [0/90/0] laminate

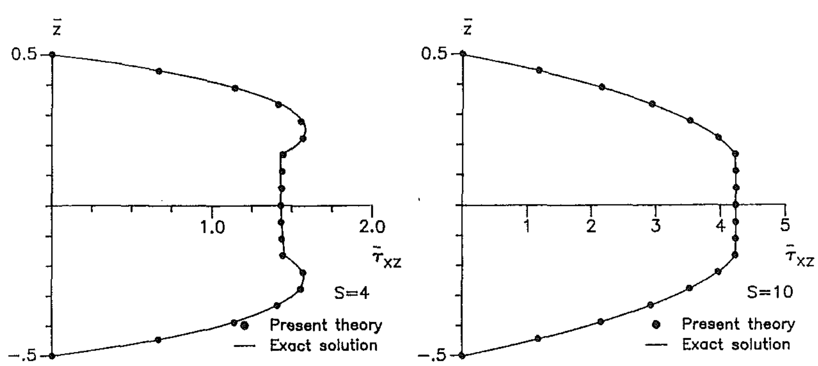


Fig. 7 Comparison of $\bar{\tau}_{xy}$ between Pagano's analysis and present theory in the [0/90/0] laminate

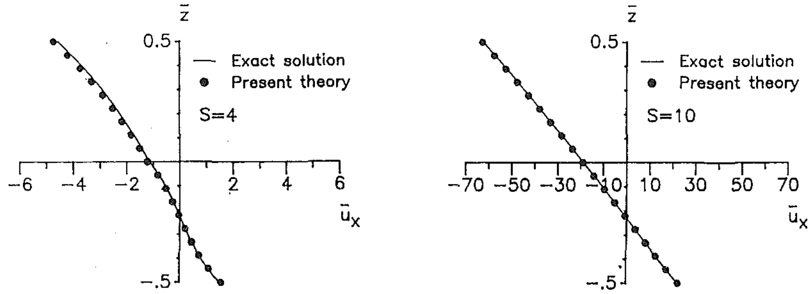


Fig. 8 Comparison of $\bar{u}$ between Pagano's analysis and present theory in the [90/0] laminate

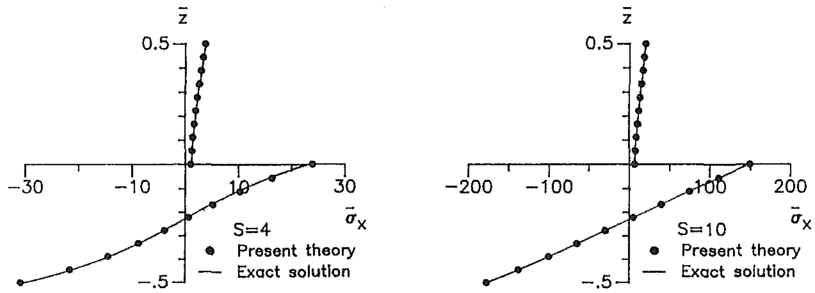


Fig. 9 Comparison of $\bar{\sigma}_x$ between Pagano's analysis and present theory in the [90/0] laminate

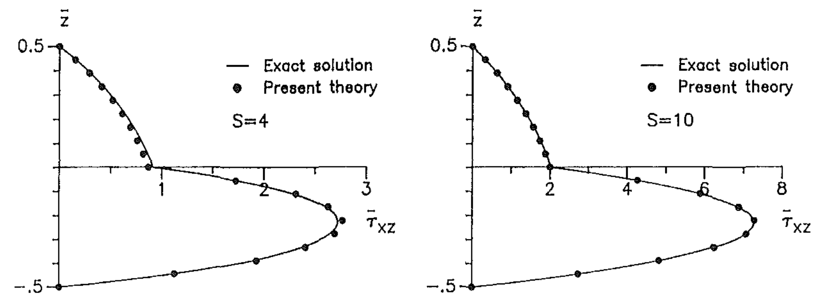


Fig. 10 Comparison of $\bar{\tau}_{xy}$ between Pagano's analysis and present theory in the [90/0] laminate

**2 Symmetric Laminate [0/90/0].** Except the [0] laminate, another symmetric laminate [0/90/0] with $S = 4$ and $S = 10$ were also investigated. The results of in-plane displacement, in-plane stress, and interlaminar shear stress for $S = 4$ and $S = 10$ from 6-layer analysis are shown in Figs. 5, 6, and 7, respectively. Excellent agreements between the present theory and the elasticity analysis can be found from the figures. However, when close to the middle surface, the in-plane displacement of $S = 4$ has a pronounced difference between the two techniques. It is believed that this is due to the assumption of constant $w$ in the present theory. In fact, just because of the constant displacement assumption, both the distributions of in-plane displacement and stress from the present theory are antisymmetric to the middle surface while the interlaminar shear stress symmetric.

**3 Asymmetric Laminate [90/0].** Both $S = 4$ and $S = 10$ for an asymmetric laminate [90/0] were studied. Excellent results were again concluded. The results are shown in Figs. 8, 9, and 10 for in-plane displacement, in-plane stress, and interlaminar shear stress.

## Conclusions

Excellent results were obtained from the present theory. Although the degree-of-freedom in this present study is high, it does not require too many layers in the thickness direction to have accurate solutions. Due to the consideration of interlaminar shear stress continuity, the interlaminar shear stress in the present analysis can be obtained directly from the constitutive equations. No post-analysis processing, which is usually based on the equilibrium equations, is required. Besides, the present theory can be easily extended for finite element formulation (Lee, Liu, and Lu) and can be used in various boundary value problems. However, it should be noted that the transverse normal strain, which is important under some circumstances, is neglected in the present theory.

## References


Ambartsumyan, S. A., 1970, *Theory of Anisotropic Plates*, J. E. Ashton, ed., Technomic Publication Co., Stamford, CT.

Barbero, E. J., and Reddy, J. N., 1990, "An Accurate Determination of Stresses in Thick Laminates Using a Generalized Plate Theory," *International Journal for Numerical Methods in Engineering*, Vol. 29, pp. 1-14.

Barbero, E. J., and Reddy, J. N., 1989, "An Application of the Generalized

Laminate Plate Theory to Delamination Buckling," *Proceedings of the American Society for Composites*, Fourth Technique Conference, pp. 244-251.

Chou, P. C., and Carleone, J., 1973, "Transverse Shear in Laminated Plate Theories," *AIAA Journal*, Vol. 11, pp. 1333-1336.

DiSciuva, M., 1985, "Development of an Anisotropic Multilayered Shear-Deformable Rectangular Plate Element," *Computers and Structures*, Vol. 21, pp. 789-796.

Hinrichensen, R. L., and Palazotto, A. N., 1986, "Nonlinear Finite Element Analysis of Thick Composite Plates Using Cubic Spline Functions," *AIAA Journal*, Vol. 24, pp. 1836-1842.

Kapania, R. K., and Raciti, S., 1989, "Recent Advances in Analysis of Laminated Beams and Plates, Part I: Shear Effects and Buckling," *AIAA Journal*, Vol. 27, pp. 923-934.

Lee, C. Y., Liu, D., and Lu, X., 1992, "Static and Vibration Analysis of Laminated Beams by Using an Interlaminar Shear Stress Continuity Theory," to appear in *International Journal for Numerical Methods in Engineering*.

Liu, D., 1988, "Impact-Induced Delamination: A View of Bending Stiffness Mismatching," *Journal of Composite Materials*, Vol. 22, pp. 674-692.

Lo, K. H., Christensen, R. M., and Wu, E. M., 1977, "A High-Order Theory of Plate Deformation: Part 2—Laminated Plates," ASME JOURNAL OF APPLIED MECHANICS, Vol. 44, pp. 669-676.

Lo, K. H., Christensen, R. M., and Wu, E. M., 1978, "Stress Solution Determination for High Order Plate Theory," *International Journal of Solids and Structures*, Vol. 14, pp. 655-662.

Mau, S. T., Tong, P., and Pian, T. H. H., 1972, "Finite Element Solutions for Laminated Thick Plates," *Journal of Composite Materials*, Vol. 6, pp. 304-311.

Nelson, R. B., and Lorch, D. R., 1974, "A Refined Theory of Laminated Orthotropic Plates," ASME JOURNAL OF APPLIED MECHANICS, Vol. 41, pp. 177-183.

Pagano, N. J., and Pipes, R. B., 1973, "Some Observations on the Interlaminar Strength of Composite Laminates," *International Journal of Mechanical Sciences*, Vol. 15, pp. 679-688.

Pagano, N. J., 1978, "Stress Fields in Composite Laminates," *International Journal of Solids and Structures*, Vol. 14, pp. 385-400.

Pagano, N. J., 1969, "Exact Solutions for Composite Laminates in Cylindrical Bending," *Journal of Composite Materials*, Vol. 3, pp. 398-411.

Pagano, N. J., and Soni, S. R., 1989, *Interlaminar Response of Composite Materials*, N. J. Pagano, ed., Elsevier, pp. 1-68.

Reddy, J. N., 1984, "A Simple Higher-Order Theory for Laminated Composites Plates," ASME JOURNAL OF APPLIED MECHANICS, Vol. 51, pp. 745-752.

Reddy, J. N., 1987, "A Generalization of Two-Dimensional Theories of Laminated Composite Plates," *Communications in Applied Numerical Methods*, Vol. 3, pp. 173-180.

Rehfield, L. W., and Valisetty, R. R., 1983, "A Comprehensive Theory of Planar Bending of Composite Laminates," *Computers and Structures*, Vol. 16, pp. 441-447.

Reissner, E., 1975, "On Transverse Bending of Plate, Including the Effect of Transverse Shear Deformation," *International Journal of Solids and Structures*, Vol. 11, pp. 569-573.

Reissner, E., 1984, "On a Certain Mixed Variational Principle and a Proposed Application," *International Journal for Numerical Methods in Engineering*, Vol. 20, pp. 1366-1368.

Spilker, R. L., 1980, "A Hybrid-Stress Finite-Element Formulation for Thick Multilayer Laminates," *Computers and Structures*, Vol. 26, pp. 507-514.

Srinivas, S., 1973, "A Refined Analysis of Composite Laminates," *Journal of Sound and Vibration*, Vol. 30, pp. 495-507.

Toledano, A., and Murakami, H., 1987, "A Composite Plate Theory for Arbitrary Laminate Configurations," ASME JOURNAL OF APPLIED MECHANICS, Vol. 54, pp. 181-189.

Vinson, J. R., and Sierakowski, R. L., 1986, *The Behavior of Structures Composed of Composite Materials*, Martinus Nijhoff, Dordrecht, The Netherlands.

Yang, P. C., Norris, C. H., and Stavsky, Y., 1966, "Elastic Wave Propagation in Heterogeneous Plates," *International Journal of Solids and Structures*, Vol. 2, pp. 665-684.

# The Influence of Inclusion Shape on the Overall Viscoelastic Behavior of Composites

**Y. M. Wang**
Graduate Student.

**G. J. Weng**
Professor,
Fellow ASME.

Department of Mechanical and
Aerospace Engineering,
Rutgers University,
New Brunswick, NJ 08903

*The Eshelby-Mori-Tanaka method is extended into the Laplace domain to examine the linearly viscoelastic behavior in two types of composite materials: a transversely isotropic one with aligned spheroidal inclusions and an isotropic one with randomly oriented inclusions. Though approximate in nature, the method offers both simplicity and versatility, with explicit results for the sphere, disk, and fiber reinforcements in the transformed domain. The results coincide with some exact solutions for the composite sphere and cylinder assemblage models and, with spherical voids or rigid inclusions, the effective shear property also lies between Christensen's bounds. Consistent with the known elastic behavior, the inverted creep compliances in the time domain indicate that, along the axial direction, aligned needles or fibers provide the most effective improvement for the creep resistance of the aligned composite, but that in the transverse plane the disk reinforcement is far superior. For the isotropic composite disks are always the most effective shape, whereas spheres are the poorest. Comparison with the experimental data for the axial creep strains of a glass/ED-6 resin composite containing 54 percent of aligned fibers indicates that the theory is remarkably accurate in this case.*

## 1 Introduction

Many polymer-matrix composites exhibit a linearly viscoelastic behavior, with an overall response dependent upon the shape, volume fraction, and geometrical arrangement of the inclusions. Directed towards this end, this paper is concerned with the development of a theoretical model which is capable of accounting for these three factors. For simplicity, both phases will be taken to be viscoelastically isotropic, and the shape of inclusions will be represented by a spheroid, with an aspect ratio (length to diameter ratio) $\alpha$. This represents a broad range of inclusion shape, ranging from thin disks, to spheres, and all the way to needles or fibers. Two types of inclusion arrangement will be specifically considered here: one unidirectionally aligned and the other randomly oriented. When the homogeneously dispersed inclusions are perfectly bonded with the matrix, without any void nucleation or growth, these two types of microgeometry will give rise to a transversely isotropic composite and an isotropic one, respectively.

Motivated by the recent success in the application of Mori-Tanaka's (1973) method in composite elasticity, this method will be extended into the viscoelastic domain to address the stated issues. The elastic counterparts of these two problems have been previously investigated by Tandon and Weng (1984, 86), where the aspect-ratio dependence of the five effective moduli of a transversely isotropic composite, and of the effective bulk and shear moduli of an isotropic one have both been established. This method has been proven to be reliable in many selected cases. For instance, for a multiphase composite containing spherical inclusions (Weng, 1984), the isotropic moduli have been shown to coincide with Hashin-Shtrikman's (1963) lower bounds if the matrix is the softest phase, and with their upper bounds if it is the hardest. If the matrix is neither of the two, the predicted moduli will always lie inside the bounds. For an aligned composite, Tandon and Weng's (1984) results have also been proven (Weng, 1990) to coincide with Walpole's (1969) exact solution when $\alpha \rightarrow 0$, and to coincide with Hill (1964) and Hashin's (1965) bounds when $\alpha \rightarrow \infty$ (see Zhao et al. 1989). Tandon and Weng's (1986) study on randomly oriented inclusions also shows that, as the aspect ratio of inclusions changes from 0 to $\infty$, the predicted overall moduli will vary within the bounds with spheres and disks providing the opposite bounds. In a fiber-reinforced composite, if the cross-sectional aspect ratio of the fibers is allowed to change from a circular shape (the conventional fiber) to a thin ribbon, Zhao and Weng (1990) recently have shown that the transversely isotropic moduli of the two-phase composite will vary within the Hill (1964) and Hashin (1965) bounds, again with the circular fibers and thin ribbons (randomly oriented in the transverse plane) taking both ends of the bounds.

It should be recognized, however, that under some special circumstances, such as rigid spheres or cylinders embedded in

Contributed by the Applied Mechanics Division of THE AMERICAN SOCIETY OF MECHANICAL ENGINEERS for publication in the ASME JOURNAL OF APPLIED MECHANICS.

Discussion on this paper should be addressed to the Technical Editor, Prof. Leon M. Keer, The Technological Institute, Northwestern University, Evanston, IL 60208, and will be accepted until four months after publication of the paper itself in the ASME JOURNAL OF APPLIED MECHANICS.

Manuscript received by the ASME Applied Mechanics Division, Sept. 14, 1990; final revision, Mar. 5, 1991. Associate Technical Editor: G. J. Dvorak.

an incompressible matrix (Christensen, 1990), a hybrid composite with two aligned but differently shaped inclusions (Dvorak, 1989; Qiu and Weng, 1990), and an isotropic composite containing randomly oriented anisotropic inclusions (Qiu and Weng, 1990), Mori-Tanaka's theory may be less reliable. Christensen (1990) recently gave a critical examination of Mori-Tanaka's structure and found that their use of Eshelby's (1957) single-inclusion solution in a finite-concentration problem to be questionable. This point was also recognized earlier by Luo and Weng (1987, 89), who sought to calculate Eshelby's type of S-tensor in a three-phase model (the so-called generalized self-consistent geometry) to modify Mori-Tanaka's theory; their findings, however, indicate that the effective bulk modulus of a particle-reinforced composite, and the longitudinal Young's modulus, major Poisson's ratio, plane-strain bulk modulus, and axial shear modulus of a fiber-reinforced composite remain unchanged under this modification. When the matrix is compressible, the effective shear modulus and the transverse shear modulus of these two types of composites, respectively, differ from the original estimates only by a small amount. Christensen's recent assessment appears to support these findings when the matrix is a compressible phase, but, when the inclusions become rigid and the matrix is incompressible, the difference between Mori-Tanaka's prediction and the generalized self-consistent scheme—especially at high concentration—can be substantial. The problem with the application of Mori-Tanaka's method to a hybrid composite arises from the possible asymmetry of the overall moduli tensor; this consequence was first pointed out by Dvorak (1989). Qiu and Weng recently gave a quantitative examination of its severity when one phase is circular fibers and the other is aligned spheroids. It turns out that, when the spheroids are thin disks, the asymmetry is the most pronounced, but it gradually decreases with increasing aspect ratio and disappears when this second phase also becomes circular fibers. With regard to the composite with randomly oriented anisotropic inclusions, Qiu and Weng's (1990) calculations have indicated that the predicted moduli may actually lie outside the Hashin-Shtrikman (1963) type bounds, as established by Walpole (1969).

Thus, with caution, one may conclude that Mori-Tanaka's approach may be applied to some selected problems without ever violating the bounds. This is certainly true for the two types of composite to be considered here. In this connection, Frohlich and Sack (1946) have studied the viscoelastic behavior of a Newtonian fluid with dilute suspension of elastic, spherical inclusions, and Roscoe (1952) has developed a differential scheme to determine the effective viscosity with suspensions of rigid spheres. The first type involving aligned spheroidal inclusions has also been examined by Laws and McLaughlin (1978) using Hill (1965b,c) and Budiansky's (1965) self-consistent approach in elasticity and Stieltjes' convolution integral. The extension of Mori-Tanaka's method to the viscoelastic domain will be accomplished by means of Laplace transform through the correspondence principle (see also Schapery, 1974). Though it is appreciated that this principle will provide the exact viscoelastic property only when the corresponding exact elastic solutions exist (Hashin 1965, 66, 70a,b, Christensen 1969, 79), the original Mori-Tanaka's theory in elasticity is an approximate one and its extension to the viscoelastic problem will remain approximate. The extended method is nonetheless simple and versatile enough to account for the influence of inclusion shape on the overall viscoelastic behavior of a two-phase composite, and the results will coincide with the exact solutions or lie within the bounds when such informations are available.

## 2 Constitutive Equations

In the two-phase composite the inclusions will be referred to as phase 1 and the matrix as phase 0. The elastic bulk and shear moduli of the $r$th phase will be denoted by $\kappa_r$ and $\mu_r$, respectively, and its volume fraction by $c_r$. Both phases may be viscoelastic, and their constitutive equations can be written in either a differential or an integral form. For simplicity, their viscoelastic properties will be taken to be isotropic also, such that, in the differential form, the constitutive equations of the $r$th phase can be decomposed into the hydrostatic and the deviatoric components (see also Hashin, 1965, 1966), respectively,

$$R_r(D)\sigma_{kk}^{(r)} = S_r(D)\epsilon_{kk}^{(r)},$$
$$P_r(D)\sigma_{ij}'^{(r)} = Q_r(D)\epsilon_{ij}'^{(r)}, \tag{1}$$

where $P$, $Q$, $R$, and $S$ are operators and $D$ represents the time differential $D = \frac{d}{dt}$.

The hereditary integral forms can be cast into

$$\sigma_{kk}^{(r)}(t) = 3\int_{-\infty}^{t} K_r(t-\tau)\,\dot{\epsilon}_{kk}^{(r)}(\tau)d\tau,$$

$$\sigma_{ij}'^{(r)}(t) = 2\int_{-\infty}^{t} G_r(t-\tau)\,\dot{\epsilon}_{ij}'^{(r)}(\tau)d\tau, \tag{2}$$

where $K_r$ and $G_r$ are the relaxation moduli of the $r$th phase. Conversely, in terms of the creep functions $I_r$ and $J_r$, one has

$$\epsilon_{kk}^{(r)}(t) = \frac{1}{3}\int_{-\infty}^{t} I_r(t-\tau)\,\dot{\sigma}_{kk}^{(r)}(\tau)d\tau,$$

$$\epsilon_{ij}'^{(r)}(t) = \frac{1}{2}\int_{-\infty}^{t} J_r(t-\tau)\,\dot{\sigma}_{ij}'^{(r)}(\tau)d\tau. \tag{3}$$

The dot on the top, as usual, indicates the differentiation with respect to time.

The Laplace transform (LT) of a function $f(t)$ is written with a hat, as

$$\hat{f}(s) = \int_0^{\infty} f(t)e^{-st}dt. \tag{4}$$

It then follows from the differential form (1) that

$$R_r(s)\hat{\sigma}_{kk}^{(r)}(s) = S_r(s)\hat{\epsilon}_{kk}^{(r)}(s),$$
$$P_r(s)\hat{\sigma}_{ij}'^{(r)}(s) = Q_r(s)\hat{\epsilon}_{ij}'^{(r)}(s). \tag{5}$$

From the integral form (2), one has

$$\hat{\sigma}_{kk}^{(r)}(s) = 3s\hat{K}_r(s)\hat{\epsilon}_{kk}^{(r)}(s),$$
$$\hat{\sigma}_{ij}'^{(r)}(s) = 2s\hat{G}_r(s)\hat{\epsilon}_{ij}'^{(r)}(s), \tag{6}$$

and from (3),

$$\hat{\epsilon}_{kk}^{(r)}(s) = \frac{1}{3}s\hat{I}_r(s)\hat{\sigma}_{kk}^{(r)}(s),$$

$$\hat{\epsilon}_{ij}'^{(r)}(s) = \frac{1}{2}s\hat{J}_r(s)\hat{\sigma}_{ij}'^{(r)}(s). \tag{7}$$

The constitutive Eqs. (5) to (7) in the transformed domain (TD) can be generally written as

$$\hat{\sigma}_{kk}^{(r)}(s) = 3\kappa_r^{TD}(s)\hat{\epsilon}_{kk}^{(r)}(s),$$
$$\hat{\sigma}_{ij}'^{(r)}(s) = 2\mu_r^{TD}(s)\hat{\epsilon}_{ij}'^{(r)}(s), \tag{8}$$

where $\kappa_r^{TD}$ and $\mu_r^{TD}$—as their elastic counterparts—are the bulk and shear moduli of the $r$th phase in the transformed domain. These are given by

$$\kappa_r^{TD} = \frac{1}{3}\frac{S_r(s)}{R_r(s)}, \quad \mu_r^{TD} = \frac{1}{2}\frac{Q_r(s)}{P_r(s)},$$
$$= s\hat{K}_r(s), \qquad = s\hat{G}_r(s),$$
$$= \frac{1}{s\hat{I}_r(s)}, \qquad = \frac{1}{s\hat{J}_r(s)}, \tag{9}$$

following (5), (6), and (7), respectively. In the case of dynamic harmonic loading, the corresponding complex moduli (Hashin 1970a,b, Roscoe 1969, 1972) $\kappa_r^*(iw)$ and $\mu_r^*(iw)$ can be directly used, with $\kappa_r^{TD}(iw) = \kappa_r^*(iw)$ and $\mu_r^{TD}(iw) = \mu_r^*(iw)$.

The moduli and compliances tensors of the $r$th phase in the transformed domain then have the hydrostatic and deviatoric components

$$L_r^{TD} = (3\kappa_r^{TD}, 2\mu_r^{TD}), \quad M_r^{TD} = \left(\frac{1}{3\kappa_r^{TD}}, \frac{1}{2\mu_r^{TD}}\right), \tag{10}$$

in Hill's (1965a) shorthand notation.

## 3 Mori-Tanaka's Theory in the Transformed Domain

The creep and relaxation behavior of the composite can be determined by subjecting it to a constant stress $\bar{\sigma}$ and constant strain $\bar{\epsilon}$, respectively. This is tantamount to the two commonly adopted boundary conditions in the determination of the overall elastic behavior of the heterogeneous material. This can be done by using Weng's (1984) original formulation, but now cast in the transformed domain. For brevity, a second-order tensor will be denoted by a boldfaced Greek letter and a fourth-order one by an ordinary capital letter here.

**3.1 Traction-Prescribed Condition.** Let the composite be subjected to a boundary traction which would give rise to a uniform stress $\hat{\bar{\sigma}}$ in the transformed domain. The strain of the comparison material with $L_0^{TD}$ is now given by

$$\hat{\epsilon}^0 = L_0^{TD^{-1}}\hat{\bar{\sigma}}, \tag{11}$$

under the same traction. Then, following Weng's (1984) analysis in the elastic case, the strain of the composite in the transformed domain can be expressed as

$$\hat{\bar{\epsilon}} = (I + c_1 A^{(\sigma)TD})\hat{\epsilon}^0, \tag{12}$$

where

$$A^{(\sigma)TD} = -[(L_1^{TD} - L_0^{TD})(c_1 I + c_0 S^{TD}) + L_0^{TD}]^{-1}(L_1^{TD} - L_0^{TD}), \tag{13}$$

and the symbol $I$ is the fourth-order symmetric identity tensor, and $S^{TD}$ the Eshelby tensor, but written in terms of the aspect ratio of inclusions $\alpha$ and $L_0^{TD}$ or Poisson's ratio $\nu_0^{TD}$ in the transformed domain. Its components for a spheroidal inclusion can be found, for example, from Mura (1987) with $\nu_0$ replaced by $\nu_0^{TD}$.

The effective moduli tensor of the composite in the transformed domain is defined by $\hat{\bar{\sigma}} = L^{TD}\hat{\bar{\epsilon}}$, and thus from (11) and (12) one finds

$$L^{TD} = L_0^{TD}(I + c_1 A^{(\sigma)TD})^{-1},$$

or

$$M^{TD} = (I + c_1 A^{(\sigma)TD})M_0^{TD}, \tag{14}$$

for the compliances tensor.

These moduli or compliances tensors allow one to determine the overall viscoelastic behavior of the composite. In particular, when the composite is subjected to a constant stress $\bar{\sigma}$ in the real space, the evolution of its creep strain can be found by applying the inverse Laplace transform to $\hat{\bar{\epsilon}}$. Symbolically, it is given by

$$\bar{\epsilon}(t) = \mathcal{L}^{-1}(\hat{\bar{\epsilon}}) = \mathcal{L}^{-1}(M^{TD}\hat{\bar{\sigma}}), \tag{15}$$

where the operator $\mathcal{L}^{-1}$ denotes the said inverse process.

**3.2 Displacement-Prescribed Condition.** A dual formulation can be written for the displacement-prescribed boundary condition which gives rise to a uniform strain $\hat{\bar{\epsilon}}$ in the transformed domain. The equations are entirely analogous, with stress changed to strain, moduli changed to compliances, and Eshelby's S-tensor changed to Hill's (1965) T-tensor. This boundary condition is especially suitable for the determination of the stress relaxation of the composite. The detailed mean stress and mean strain relation for each constituent can be inferred from Weng's (1984) equations but now cast in the transformed domain. This formulation leads to

$$L^{TD} = L_0^{TD}(I - c_1 A^{(\epsilon)TD}), \tag{16}$$

where

$$A^{(\epsilon)TD} = -[c_0(L_1^{TD} - L_0^{TD})S^{TD} + L_0^{TD}]^{-1}(L_1^{TD} - L_0^{TD}), \tag{17}$$

with the superscript $\epsilon$ indicating the strain-controlled process.

Then, if needed, the stress relaxation of the composite under a constant strain $\bar{\epsilon}$ can be evaluated from the Laplace inverse,

$$\bar{\sigma}(t) = \mathcal{L}^{-1}(\hat{\bar{\sigma}}) = \mathcal{L}^{-1}(L^{TD}\hat{\bar{\epsilon}}). \tag{18}$$

As proved by Weng (1984) and Benveniste (1987) in the elastic case, these two formulations are entirely equivalent.

## 4 The Aspect-Ratio Dependence of the Creep Behavior of an Aligned Viscoelastic Composite

We now examine the transversely isotropic creep behavior of the composite as the shape of its aligned inclusions changes from thin disks to spheres, and all the way to continuous fibers.

**4.1 Spherical Inclusions.** In the case of spheres, the composite is isotropic and both (14) and (16) can be decomposed into (see Weng, 1984 for the elastic composite)

$$\kappa^{TD} = \kappa_0^{TD} + \frac{c_1}{1/(\kappa_1^{TD} - \kappa_0^{TD}) + 3c_0/(3\kappa_0^{TD} + 4\mu_0^{TD})},$$

$$\mu^{TD} = \mu_0^{TD} + \frac{c_1}{1/(\mu_1^{TD} - \mu_0^{TD}) + 6c_0(\kappa_0^{TD} + 2\mu_0^{TD})/[5\mu_0^{TD}(3\kappa_0^{TD} + 4\mu_0^{TD})]}. \tag{19}$$

Under a constant stress $\bar{\sigma}_{ij}$, its Laplace transform is $\hat{\bar{\sigma}}_{ij} = \frac{1}{s}\bar{\sigma}_{ij}$. Thus,

$$\hat{\bar{\epsilon}}_{kk} = \frac{1}{3\kappa^{TD}}\frac{1}{s}\bar{\sigma}_{kk}, \quad \hat{\bar{\epsilon}}'_{ij} = \frac{1}{2\mu^{TD}}\frac{1}{s}\bar{\sigma}'_{ij}, \tag{20}$$

and these lead to the creep strain upon the Laplace inversion

$$\bar{\epsilon}_{kk}(t) = \frac{\bar{\sigma}_{kk}}{3}\frac{1}{2\pi i}\int_{\delta - i\infty}^{\delta + i\infty}\frac{1}{s}\frac{1}{\kappa^{TD}}e^{st}ds,$$

$$\bar{\epsilon}'_{ij}(t) = \frac{\bar{\sigma}'_{ij}}{2}\frac{1}{2\pi i}\int_{\delta - i\infty}^{\delta + i\infty}\frac{1}{s}\frac{1}{\mu^{TD}}e^{st}ds, \tag{21}$$

where $\delta$ is a positive number. The coefficients of $\bar{\sigma}_{kk}$ and $\bar{\sigma}'_{ij}$ define the hydrostatic and deviatoric components of the overall creep compliance, respectively, of the composite. The bulk behavior derived here coincides with the exact solution based on Hashin's (1965) composite sphere assemblage. When the inclusions become voids or totally rigid and the Poisson ratio of the matrix remains unchanged in the transformed domain ($\nu_0^{TD} = \nu_0$), the shear behavior derived here also coincides with Christensen's (1969) approximate solution (his Eq. (97)), which has been demonstrated to lie between his bounds for the corresponding complex modulus.

**4.2 Fiber Composites.** When the spheroidal inclusions take the form of circular fibers, both (14) and (16) lead to the following five independent overall moduli in the transformed domain (see Zhao et al. (1989) for the elastic cases)

$$E_{11}^{TD}=c_1E_1^{TD}+c_0E_0^{TD}+\frac{4c_1c_0(\nu_1^{TD}-\nu_0^{TD})^2}{c_1/k_0^{TD}+c_0/k_1^{TD}+1/\mu_0^{TD}},$$

$$\nu_{12}^{TD}=c_1\nu_1^{TD}+c_0\nu_0^{TD}+\frac{c_1c_0(\nu_1^{TD}-\nu_0^{TD})(1/k_0^{TD}-1/k_1^{TD})}{c_1/k_0^{TD}+c_0/k_1^{TD}+1/\mu_0^{TD}},$$

$$\mu_{12}^{TD}=\mu_0^{TD}+\frac{c_1\mu_0^{TD}}{\mu_0^{TD}/(\mu_1^{TD}-\mu_0^{TD})+c_0/2},$$

$$\mu_{23}^{TD}=\mu_0^{TD}+\frac{c_1\mu_0^{TD}}{\mu_0^{TD}/(\mu_1^{TD}-\mu_0^{TD})+c_0(k_0^{TD}+2\mu_0^{TD})/[2(k_0^{TD}+\mu_0^{TD})]},$$

$$\kappa_{23}^{TD}=k_0^{TD}+\frac{c_1}{1/(k_1^{TD}-k_0^{TD})+c_0/(k_0^{TD}+\mu_0^{TD})},\tag{22}$$

respectively, for the longitudinal Young's modulus, major Poisson's ratio, axial shear and transverse shear moduli, and plane-strain bulk modulus in the transformed domain, where $k_r^{TD}$ is the plane-strain bulk modulus of the $r$th phase in the transformed domain. With the exception of $\mu_{23}^{TD}$, the other four moduli coincide with Hashin's (1966) exact solutions for the composite cylinder assemblage model.

If $E_{22}^{TD}$ $(=E_{33}^{TD})$ is needed, it is given by the transversely isotropic relation

$$E_{22}^{TD}=\frac{4\kappa_{23}^{TD}}{\kappa_{23}^{TD}/\mu_{23}^{TD}+1+4\nu_{12}^{TD2}\kappa_{23}^{TD}/E_{11}^{TD}}.\tag{23}$$

In Hill (1965) and Walpole's (1969) shorthand notations, the transversely isotropic moduli tensor $L^{TD}$ can be written as

$$L^{TD}=(2k^{TD},\ l^{TD},\ n^{TD},\ 2m^{TD},\ 2p^{TD}),\tag{24}$$

with

$$k^{TD}=\kappa_{23}^{TD},\quad m^{TD}=\mu_{23}^{TD},\quad p^{TD}=\mu_{12}^{TD},$$
$$E_{11}^{TD}=n^{TD}-l^{TD^2}/k^{TD},\quad \nu_{12}^{TD}=l^{TD}/(2k^{TD}).\tag{25}$$

The compliance tensor $M^{TD}$ then has the components

$$M^{TD}=\left(\frac{n^{TD}}{2k^{TD}E_{11}^{TD}},\ -\frac{\nu_{12}^{TD}}{E_{11}^{TD}},\ \frac{1}{E_{11}^{TD}},\ \frac{1}{2m^{TD}},\ \frac{1}{2p^{TD}}\right).\tag{26}$$

When the composite is subjected to a constant stress $\bar{\sigma}$, we have

$$\hat{\bar{\epsilon}}=M^{TD}\hat{\bar{\sigma}}=M^{TD}\frac{1}{s}\bar{\sigma},\tag{27}$$

and this can be inverted to yield the creep strain tensor

$$\bar{\epsilon}(t)=\frac{1}{2\pi i}\left[\int_{\delta-i\infty}^{\delta+i\infty}\frac{1}{s}M^{TD}e^{st}ds\right]\bar{\sigma}.\tag{28}$$

Equation (27) is of great use in the evaluation of the anisotropic creep behavior for a wide class of fiber-reinforced polymer matrix composites.

**4.3 Aligned Disks.** In this extreme case the microgeometry is identical to the monotonically aligned thin ribbon examined by Zhao and Weng (1990), and the elastic results have been proven to coincide with Walpole's (1969) exact solution for a laminated medium (Weng, 1990). In Walpole's (1969) form for the aligned laminate, the five independent moduli in the transformed domain can be written as

$$k^{TD}=c_1k_1^{TD}+c_0k_0^{TD}+c_1c_0(l_1^{TD}-l_0^{TD})\left(\frac{l_0^{TD}}{n_1^{TD}}-\frac{l_1^{TD}}{n_0^{TD}}\right)\Big/(c_1/n_1^{TD}+c_0/n_0^{TD}),$$

$$l^{TD}=(c_1l_1^{TD}/n_1^{TD}+c_0l_0^{TD}/n_0^{TD})/(c_1/n_1^{TD}+c_0/n_0^{TD}),$$

$$\frac{1}{n^{TD}}=\frac{c_1}{n_1^{TD}}+\frac{c_0}{n_0^{TD}},$$

$$m^{TD}=c_1m_1^{TD}+c_0m_0^{TD},$$

$$\frac{1}{p^{TD}}=\frac{c_1}{p_1^{TD}}+\frac{c_0}{p_0^{TD}},\tag{29}$$

which, by means of the correspondence principle, are exact for this microstructure. The corresponding creep compliances then follow similarly as in the fiber case.

**4.4 General Spheroids.** For the general spheroids with an aspect ratio $\alpha$, Eqs. (14) and (16) can be cast into the following form for the five independent moduli in the transformed domain (see also Tandon and Weng, 1984):

$$\frac{E_{11}^{TD}}{E_0^{TD}}=\frac{1}{1+c_1(A_1+2\nu_0^{TD}A_2)/A},$$

$$\frac{\mu_{12}^{TD}}{\mu_0^{TD}}=1+\frac{c_1}{\mu_0^{TD}/(\mu_1^{TD}-\mu_0^{TD})+2c_0S_{1212}^{TD}},$$

$$\frac{\mu_{23}^{TD}}{\mu_0^{TD}}=1+\frac{c_1}{\mu_0^{TD}/(\mu_1^{TD}-\mu_0^{TD})+2c_0S_{2323}^{TD}},$$

$$\nu_{12}^{TD}=\nu_0^{TD}-c_1\frac{\nu_0^{TD}(A_1+2\nu_0^{TD}A_2)+(A_3-\nu_0^{TD}A_4)}{A+c_1(A_1+2\nu_0^{TD}A_2)},$$

$$\frac{\kappa_{23}^{TD}}{k_0^{TD}}=\frac{(1+\nu_0^{TD})(1-2\nu_0^{TD})A}{(1-\nu_0^{TD})A-c_1[2\nu_0^{TD}A_3-(1-\nu_0^{TD})A_4]-2\nu_{12}^{TD}[\nu_0^{TD}A-c_1(A_3-\nu_0^{TD}A_4)]},\tag{30}$$

or

$$\frac{E_{22}^{TD}}{E_0^{TD}}=\frac{E_{33}^{TD}}{E_0^{TD}}=\frac{1}{1+c_1[-2\nu_0^{TD}A_3+(1-\nu_0^{TD})A_4+(1+\nu_0^{TD})A_5A]/(2A)},$$

where the constants (not tensors) $A_1$, $A_2$, $A_3$, $A_4$, $A_5$, and $A$—in Tandon and Weng's (1984) original notations—depend on the aspect ratio $\alpha$, volume fraction $c_1$ of the inclusions and the moduli $L_r^{TD}$ of the constituents; they are given in Appendix A.

With these relations the overall viscoelastic behavior of the composite can be examined at a given aspect ratio and volume fraction of inclusions. The overall creep under a constant stress, in particular, will follow from the same framework outlined in (24) to (28).

## 5 Composites With Randomly Oriented Spheroidal Inclusions

Mori-Tanaka's basic framework in the transformed domain can be similarly established for this microgeometry following Tandon and Weng's (1986) elastic formulation. This differs from that outlined in Section 3 only in two aspects: First, $\hat{\epsilon}^{pt}$ and $\hat{\epsilon}^*$ are both orientation-dependent and their connection through the $S^{TD}$-tensor should be written in the local, oriented axes, and second, the orientational average, such as $\hat{\bar{\sigma}}=c_0\hat{\bar{\sigma}}^{(0)}+c_1\{\hat{\bar{\sigma}}^{(1)}\}$ for the stress, should be used to evaluate the overall stress and strain in the transformed domain. The procedure is a straightforward one and only the end results will be quoted here.

Before the general results for a given $\alpha$ are provided, the following three special shapes are of particular interest:

**5.1 Spheres.** These results are identical to those given in (19). In the elastic case, this pair of moduli also coincide with

Hashin and Shtrikman's (1963) lower (upper) bounds if the matrix is the softer (harder) phase.

**5.2 Randomly Oriented Circular Disks: $\alpha \to 0$.** In this case, the overall bulk and shear moduli in the transformed domain are

$$\kappa^{TD} = \kappa_1^{TD} + \frac{c_0}{1/(\kappa_0^{TD} - \kappa_1^{TD}) + 3c_1/(3\kappa_1^{TD} + 4\mu_1^{TD})},$$

$$\mu^{TD} = \mu_1^{TD} + \frac{c_0\mu_1^{TD}}{\mu_1^{TD}/(\mu_0^{TD} - \mu_1^{TD}) + 6c_1(\kappa_1^{TD} + 2\mu_1^{TD})/[5(3\kappa_1^{TD} + 4\mu_1^{TD})]}. \tag{31}$$

In direct contrast to (19), this pair of moduli coincide with Hashin and Shtrikman's (1963) upper (lower) bounds in the elastic domain if the matrix is the softer (harder) phase.

**5.3 Randomly Oriented Needles or Slender Rods: $\alpha \to \infty$.** The corresponding overall moduli can be simplified to be

$$\kappa^{TD} = \kappa_1^{TD} + c_0 \Bigg/ \left\{ \frac{1}{\kappa_0^{TD} - \kappa_1^{TD}} + \frac{3c_1}{3\kappa_1^{TD} + \mu_1^{TD} + 3\mu_0^{TD}} \right\},$$

$$\mu^{TD} = \mu_1^{TD} + c_0 \Bigg/ \left\{ \frac{1}{\mu_0^{TD} - \mu_1^{TD}} + \frac{2}{5} c_1 \left[ \frac{1}{\mu_1^{TD} + \mu_0^{TD}} + \frac{1}{\mu_1^{TD} + \mu_0^{TD}/(3 - 4\nu_0^{TD})} + \frac{1}{2} \frac{1}{3\kappa_1^{TD} + \mu_1^{TD} + 3\mu_0^{TD}} \right] \right\}. \tag{32}$$

Comparing the first of (32) to that of (31), it is apparent that, when the matrix is the softer phase ($\mu_1^{TD} > \mu_0^{TD}$), one finds $\kappa_{\text{disk}}^{TD} > \kappa_{\text{needle}}^{TD}$. Though less evident, the same conclusion can be drawn for $\mu^{TD}$ after changing $\nu_0^{TD}$ to $\kappa_0^{TD}$ and $\mu_0^{TD}$.

**5.4 General Spheroids With an Aspect Ratio $\alpha$.** By analogy to Tandon and Weng's (1986) expressions for the elastic case, the overall moduli are

$$\frac{\kappa^{TD}}{\kappa_0^{TD}} = \frac{1}{1 + c_1 p^{TD}}, \quad \frac{\mu^{TD}}{\mu_0^{TD}} = \frac{1}{1 + c_1 q^{TD}}, \tag{33}$$

where

$$p^{TD} = p_2^{TD}/p_1^{TD}, \quad q^{TD} = q_2^{TD}/q_1^{TD},$$

$$p_1^{TD} = 1 + c_1[2(S_{1122}^{TD} + S_{2222}^{TD} + S_{2233}^{TD} - 1)(a_3 + a_4) + (S_{1111}^{TD} + 2S_{2211}^{TD} - 1)(a_1 - 2a_2)]/(3a),$$

$$p_2^{TD} = [a_1 - 2(a_2 - a_3 - a_4)]/(3a),$$

$$\begin{aligned} q_1^{TD} = 1 - c_1 \Bigg\{ & -\frac{1}{15a} [2(a_1 + a_2)(S_{1111}^{TD} - S_{2211}^{TD} - 1) \\ & + (2a_3 - a_4 - a_5 a)(S_{1122}^{TD} - S_{2222}^{TD} + 1) \\ & + (2a_3 - a_4 + a_5 a)(S_{1122}^{TD} - S_{2233}^{TD})] \\ & + \frac{2}{5} \frac{2S_{1212}^{TD} - 1}{2S_{1212}^{TD} + \mu_0^{TD}/(\mu_1^{TD} - \mu_0^{TD})} + \frac{1}{3} \frac{2S_{2323}^{TD} - 1}{2S_{2323}^{TD} + \mu_0^{TD}/(\mu_1^{TD} - \mu_0^{TD})} \Bigg\}, \end{aligned}$$

$$\begin{aligned} q_2^{TD} = & -\frac{2}{5} \frac{1}{2S_{1212}^{TD} + \mu_0^{TD}/(\mu_1^{TD} - \mu_0^{TD})} \\ & -\frac{1}{3} \frac{1}{2S_{2323}^{TD} + \mu_0^{TD}/(\mu_1^{TD} - \mu_0^{TD})} \\ & + \frac{1}{15a} [2(a_1 + a_2 - a_3) + a_4 + a_5 a]. \end{aligned} \tag{34}$$

The constants $a_1$, $a_2$, $a_3$, $a_4$, $a_5$, and $a$ depend on the aspect ratio $\alpha$ and the moduli $L_r^{TD}$ of the constituents; their expressions are listed in Appendix B.

These general expressions reduce to (19), (31), and (32) when $\alpha$ is set equal to 1, 0, and $\infty$, respectively.

With this pair of moduli, the shape dependence of the overall viscoelastic behavior can be found. The evolution of creep strain under a constant stress also follows from (21).

## 6 Numerical Results and Comparison With Experiments

It is now of interest to apply the theory to some practical system. To this end we first note that the preceding results have been given in the transformed domain and that these expressions must be transformed back to the time domain for practical purposes. Now various viscoelastic models can be called for, so that the precise forms of $\kappa_r^{TD}$ and $\mu_r^{TD}$ can be determined.

For instance if the $r$th phase is purely elastic, then simply $\kappa_r^{TD} = \kappa_r$ and $\mu_r^{TD} = \mu_r$. For the three popular viscoelastic models, one has the transformed shear modulus

$$\mu_r^{TD} = \frac{s}{1/\eta_r + s/\mu_r}, \qquad \text{for the Maxwell model,}$$

$$= \mu_r + \eta_r s, \qquad \text{for the Voigt model,}$$

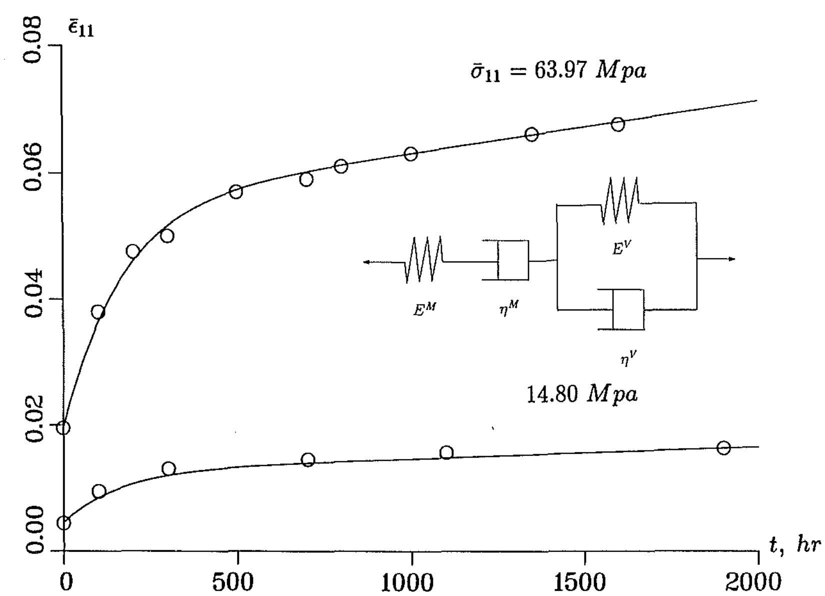


**Fig. 1 Creep behavior of the ED-6 resin by a four-parameter rheological model**

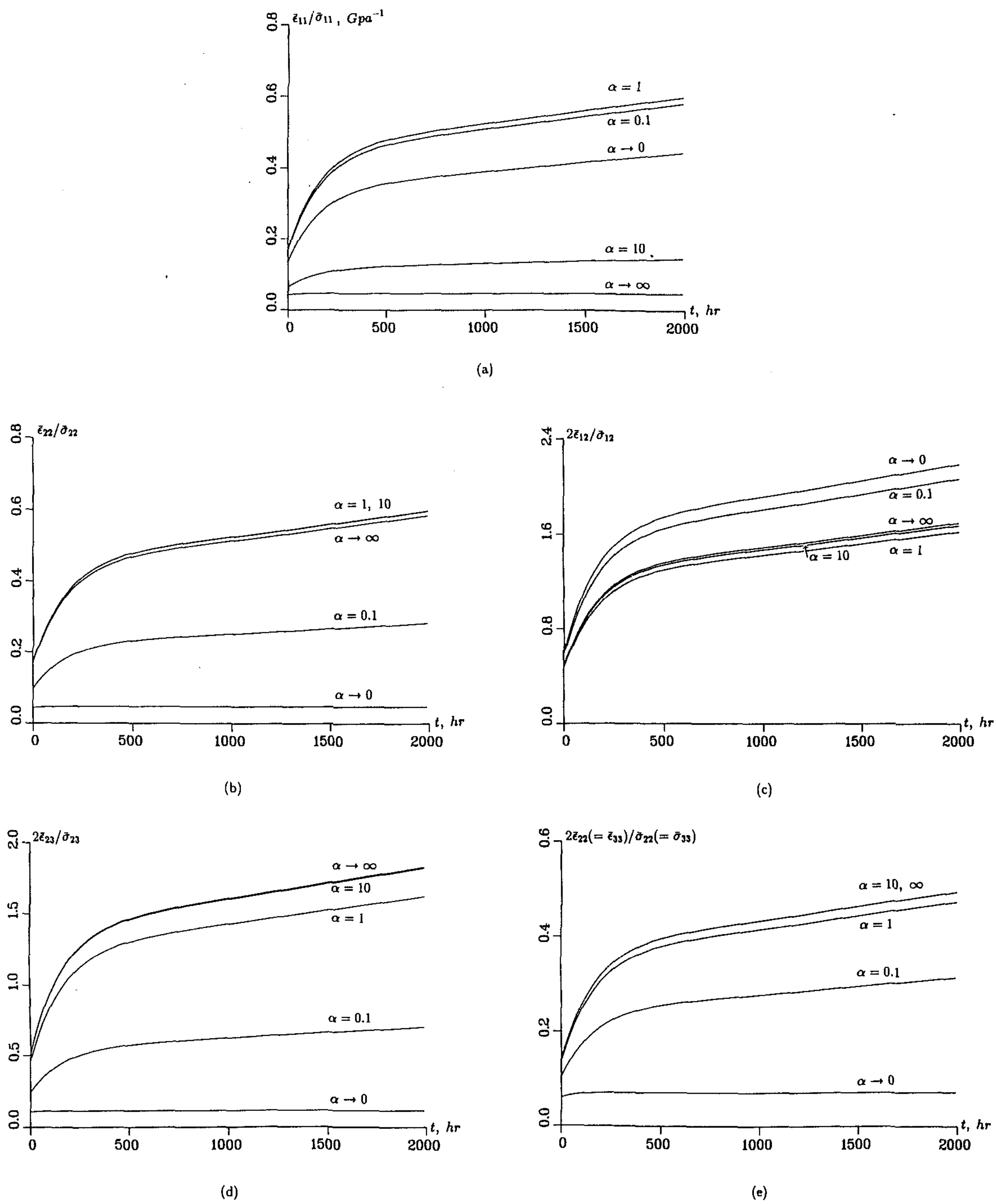


**Fig. 2 The aspect-ratio dependence of the creep compliance under five respective loadings for a transversely isotropic composite with aligned spheroidal inclusions**

$$= \frac{\mu_r s + \mu_r \mu_r' / \eta_r}{s + (\mu_r + \mu_r')/\eta_r}, \quad \text{for a three-parameter standard solid,}$$

$$\text{(no sum over } r) \quad (35)$$

where $\eta_r$ is the shear viscosity and $\mu_r'$ the shear spring constant connected in parallel with the dashpot. A completely parallel set of expressions exist for $\kappa_r^{TD}$. These three models, though useful in their own right are, however, often found inadequate to simulate the observed creep behavior of practical polymeric systems, for they are incapable of showing, respectively, the transient creep, the initial elastic strain, and the long-term steady-state creep.

A more realistic one is the four-parameter model which essentially puts the Maxwell and Voigt models together in series. Since most experiments were carried out under a pure tension, it is more convenient to express these four parameters in tension. As shown in the inset of Fig. 1, these four parameters then can be written as $E^M$, $\eta^M$, and $E^V$, $\eta^V$ with superscripts $M$ and $V$ referring to the Maxwell and the Voigt elements, respectively. The Young's modulus in the transformed domain for this model is found to be

$$E_r^{TD} = \frac{E_r^M \eta_r^M (E_r^V + \eta_r^V s) s}{E_r^M E_r^V + [\eta_r^M E_r^V + E_r^M (\eta_r^M + \eta_r^V)] s + \eta_r^M \eta_r^V s^2}, \quad (36)$$

$$\text{(no sum over } r)$$

for the $r$th phase.

Tensile creep tests for the ED-6 resin were conducted by Skudra and Auzukalns (1973) at 20°C under two constant stress $\bar{\sigma}_{11}$ = 63.97 MPa and 14.80 MPa, and the corresponding creep data are plotted as open circles in Fig. 1. It is well known that the extent of separation between two sets of creep data defines the stress exponent $n$ in a power-law creep $\dot{\epsilon} \sim \sigma^n$ and this pair of data after our simulation confirms that the polymer considered here is indeed linearly viscoelastic ($n \sim 1$). Among the four constants cited above, $E^M$ is also the ordinary Young's modulus $E$ and reflects the initial strain ($t = 0$), $\eta^M$ defines the long-term steady creep rate, and $E^V$ and $\eta^V$ characterize the rate of transition in the nonlinear creep strain versus time curve. Based on this set of data, the material constants for the resin have been found to be

$$E_0^M = 3.27 \text{ GPa} = (E_0), \quad E_0^V = 1.8 \text{ GPa},$$

$$\eta_0^M = 8000 \text{ GPa}\cdot\text{hr}, \quad \eta_0^V = 300 \text{ GPa}\cdot\text{hr}, \tag{37}$$

with a Poisson's ratio $\nu_0$ = 0.38. This set of constants gives rise to the two theoretical curves in Fig. 1 under the same stresses. Here for simplicity the Poisson's ratio has been assumed to remain unchanged in the transformed domain $\nu_0^{TD} = \nu_0$. To verify the validity of such an assumption an additional test under different loading mode, such as pure shear or pure hydrostatic pressure, is required. This unfortunately is not available. The implication of such an assumption is that

$$\mu^{TD}/\mu = E^{TD}/E = \kappa^{TD}/\kappa, \tag{38}$$

for the resin. (On the other hand, one may assume that $\kappa^{TD} = \kappa$; namely creep takes place only under deviatoric stress (as in metals). Then, $E^{TD}/E = (1 - 2\nu^{TD})/(1 - 2\nu)$ and $\mu^{TD}/\mu = (1 - 2\nu^{TD})(1 + \nu)/[(1 - 2\nu)(1 + \nu^{TD})]$. However, since the viscoelastic behavior of most polymers is known to be pressure dependent, $\kappa^{TD} = \kappa$ does not seem to be a good assumption.)

To assess the aspect-ratio dependence of the overall creep behavior, we now consider the inclusions to possess the property of glass fibers, which are elastic at room temperature. Its elastic moduli are

$$\kappa_1^{TD} = \kappa_1 = 39.43 \text{ GPa}, \quad \mu_1^{TD} = \mu_1 = 28.35 \text{ GPa}. \tag{39}$$

The influence of inclusion shape on the creep compliances is now examined.

**6.1 Composite With Aligned Spheroidal Inclusions.** Substituting the transformed moduli $\kappa_r^{TD}$ and $\mu_r^{TD}$ as given by (36) to (39) into (30), the five independent overall moduli in the transformed domain can be obtained for the aligned composite at a given aspect ratio $\alpha$ and volume fraction $c_1$ of the inclusions. The various components of creep compliances can then be evaluated from (28), with the compliances tensor $M^{TD}$ given by (26). Since each component of $M^{TD}$ is rather complicated, the inversion process in (28) was carried out numerically at a given $\alpha$ and $c_1$. The method used employs the Legendre polynomials as suggested by Bellman, Kalaba, and Lockett (1966). The corresponding creep compliances under five respective loadings are plotted in Fig. 2, at $c_1$ = 0.3.

Under a constant tensile stress, the dependence of the axial creep compliance is depicted in Fig. 2($a$). This figure indicates that spherical inclusions ($\alpha$ = 1) at $c_1$ = 0.3 is the most compliant type of reinforcement, whereas the long, continuous fibers ($\alpha \rightarrow \infty$) provide the most superior creep resistance for the composite. Prolate inclusions are in general more superior to the oblate ones ($\alpha$ versus $1/\alpha$) under this loading direction. The initial response at $t$ = 0 represents the elastic compliances, which reduces to the elastic formulation of Tandon and Weng (1984). The stronger creep resistance provided by the thin disks over the spherical particles at this volume fraction is perhaps somewhat unexpected; this, however, has also been observed by Tandon and Weng (1984) in the elastic case and Lee and Mear (1991) in the nonlinear elastoplastic behavior. As the

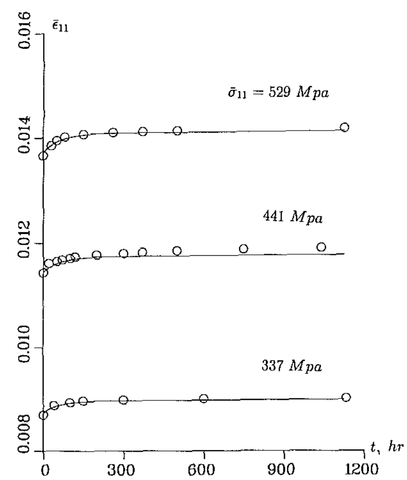


Fig. 3 Comparison between the theoretical predictions and the experimental data for the creep curves of a glass-fiber/ED-6 resin composite at $c_1$ = 0.54

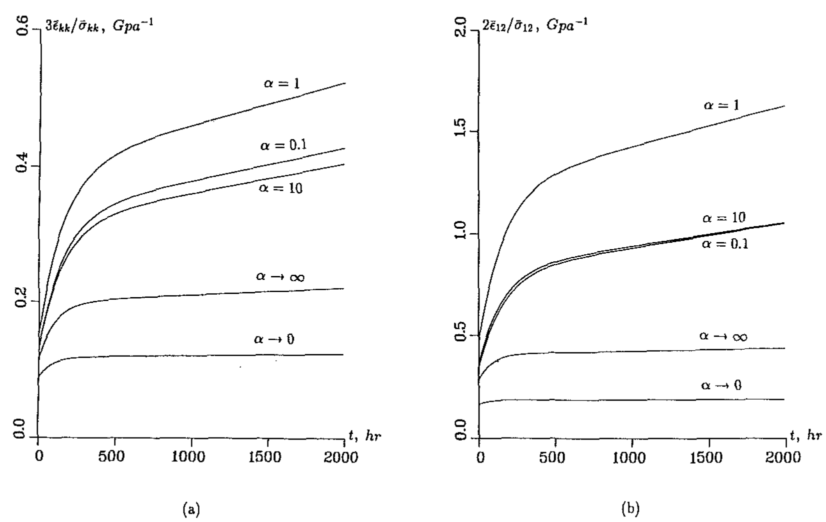


Fig. 4 The aspect-ratio dependence of the creep compliance under hydrostatic and shear loadings for an isotropic composite with randomly oriented spheroidal inclusions

volume concentration of inclusions increases (say beyond 60 percent in an elastic glass/epoxy system; see Fig. 2 of Tandon and Weng, 1984), the spherical inclusions can become more effective than the disks. The three extreme shapes of inclusions $\alpha = 1, \infty$, and 0, also correspond to the explicit results given by (19), (22), and (29), respectively.

The creep compliances under a transverse tension $\bar{\sigma}_{22}$, axial shear $\bar{\sigma}_{12}$, transverse shear $\bar{\sigma}_{23}$, and plane-strain biaxial tension ($\bar{\sigma}_{22} = \bar{\sigma}_{33}$, $\bar{\epsilon}_{11} = 0$), are shown in Fig. 2(*b*), (*c*), (*d*), and (*e*), in turn. It can be observed that under transverse loadings (e.g., $\bar{\sigma}_{22}$, $\bar{\sigma}_{23}$, $\bar{\sigma}_{22} = \bar{\sigma}_{33}$), disks ($\alpha \rightarrow 0$) provide the most effective creep resistance for the composite, with all prolate inclusions $\alpha \geq 1$ offering almost similar amount of influence. The overall axial shear behavior appears to be less sensitive to the inclusion shapes, but here prolate inclusions are somewhat more desirable than the oblate ones.

Although no sufficient experimental data exist to allow for a full assessment of the developed theory, creep tests of a fiber-reinforced composite at three levels of tensile stresses—$\bar{\sigma}_{11}$ = 529 MPa, 441 MPa, and 337 MPa—have been carried out also by Skudra and Auzukalns (1973) at the fiber concentration $c_1 = 0.54$. The corresponding experimental data are reproduced as open circles in Fig. 3. To obtain the theoretical creep curves, we first generate an axial creep compliance curve at this fiber concentration (as the bottom one in Fig. 2(*a*), but at $c_1 = 0.54$), and then multiply it by these three stresses. The theoretical results are also plotted in Fig. 3; the agreement with the experiment is remarkable indeed.

**6.2 Composite With Randomly Oriented Spheroidal Inclusions.** Based on (33) and (34), the aspect-ratio dependence of the hydrostatic and deviatoric components of the overall creep compliance is plotted in Fig. 4(*a*) and (*b*), respectively, at $c_1 = 0.3$. Consistent with the initial elastic behavior, spherical inclusions provide the most compliant composite whereas the circular thin disks give rise to the most effective improvement for the creep resistance of the composite. Below $\alpha = 10$, the prolate and oblate inclusions with the inversed aspect ratios ($\alpha = 1/\alpha$) are almost equally effective. The three special cases $\alpha = 1$, 0, and $\infty$ also correspond to (19), (31), and (32), respectively.

## Acknowledgment

This work was supported by the National Science Foundation Program, under Grants MSS-8918235 and MSS-9114745.

## References

Bellman, R. E., Kalaba, R. E., and Lockett, J. A., 1966, *Numerical Inversion of the Laplace Transform*, Elsevier, New York, p. 32.

Benveniste, Y., 1987, "A New Approach to the Application of Mori-Tanaka's Theory in Composite Materials," *Mechanics of Materials*, Vol. 6, pp. 147–157.

Christensen, R. M., 1969, "Viscoelastic Properties of Heterogeneous Media," *Journal of the Mechanics and Physics of Solids*, Vol. 17, pp. 23–41.

Christensen, R. M., 1979, *Mechanics of Composite Materials*, John Wiley and Sons, New York, p. 288.

Christensen, R. M., 1990, "A Critical Evaluation for a Class of Micromechanics Models," *Journal of the Mechanics and Physics of Solids*, Vol. 38, pp. 379–404.

Dvorak, G. J., 1989, *The Mura Symposium on Micromechanics and Inhomogeneity*, ASME, San Francisco, New York.

Eshelby, J. D., 1957, "The Determination of the Elastic Field of an Ellipsoidal Inclusion and Related Problems," *Proceedings of Royal Society, London*, Vol. A241, pp. 376–396.

Frohlich, H., and Sack, R., 1946, "Theory of the Rheological Properties of Dispersions," *Proceedings of the Royal Society, London*, A185, pp. 415–430.

Hashin, Z., 1965a, "On Elastic Behavior of Fiber Reinforced Materials of Arbitrary Transverse Phase Geometry," *Journal of the Mechanics and Physics of Solids*, Vol. 13, pp. 119–134.

Hashin, Z., 1965b, "Viscoelastic Behavior of the Heterogeneous Media," ASME Journal of Applied Mechanics, Vol. 32, pp. 630–636.

Hashin, Z., 1966, "Viscoelastic Fiber Reinforced Materials," *AIAA Journal*, Vol. 4, pp. 1411–1417.

Hashin, Z., 1970a,b, "Complex Moduli of Viscoelastic Composites—I & II," *International Journal of Solids and Structures*, Vol. 6, pp. 539–552, 797–807.

Hashin, Z., and Shtrikman, S., 1963, "A Variational Approach to the Theory of the Elastic Behavior of Multiphase Materials," *Journal of the Mechanics and Physics of Solids*, Vol. 11, pp. 127–140.

Hill, R., 1964, "Theory of Mechanical Properties of Fiber-Strengthened Materials: I. Elastic Behavior," *Journal of the Mechanics and Physics of Solids*, Vol. 12, pp. 199–212.

Hill, R., 1965a, "Continuum Micro-Mechanics of Elastoplastic Polycrystals," *Journal of the Mechanics and Physics of Solids*, Vol. 13, pp. 89–101.

Hill, R., 1965b, "Theory of Mechanical Properties of Fibre-Strengthened Materials: III. Self-Consistent Model," *Journal of the Mechanics and Physics of Solids*, Vol. 13, pp. 189–198.

Hill, R., 1965c, "A Self-Consistent Mechanics of Composite Materials," *Journal of the Mechanics and Physics of Solids*, Vol. 13, pp. 213–222.

Laws, N., and McLaughlin, R., 1978, "Self-Consistent Estimates for the Viscoelastic Creep Compliances of Composite Materials," *Proceedings of the Royal Society, London*, Vol. A359, pp. 251–273.

Lee, B. J., and Mear, M. E., 1991, "Effect of Inclusion Shape on the Stiffness of Non-Linear Two Phase Composites," *Journal of the Mechanics and Physics of Solids*, Vol. 39, pp. 627–649.

Luo, H. A., and Weng, G. J., 1987, "On Eshelby's Inclusion Problem in a Three-Phase Spherically Concentric Solid, and a Modification of Mori-Tanaka's Method," *Mechanics of Materials*, Vol. 6, pp. 347–361.

Luo, H. A., and Weng, G. J., 1989, "On Eshelby's S-Tensor in a Three-Phase Cylindrically Concentric Solid, and the Elastic Moduli of Fiber-Reinforced Composites," *Mechanics of Materials*, Vol. 8, pp. 77–88.

Mori, T., and Tanaka, K., 1973, "Average Stress in the Matrix and Average Elastic Energy of Materials with Misfitting Inclusions," *Acta Metallurgica*, Vol. 21, pp. 571–574.

Mura, T., 1987, *Micromechanics of Defects in Solids*, 2nd ed., Martinus Nijhoff, Dordrecht, The Netherlands.

Qiu, Y. P., and Weng, G. J., 1990, "On the Application of Mori-Tanaka's Theory Involving Transversely Isotropic Spheroidal Inclusions," *International Journal of Engineering Science*, Vol. 28, pp. 1121–1137.

Roscoe, R., 1952, "The Viscosity of Suspensions of Rigid Spheres," *British Journal of Applied Physics*, Vol. 3, pp. 267–269.

Roscoe, R., 1969, "Bounds for the Real and Imaginary Parts of the Dynamic Moduli of Composite Viscoelastic Systems," *Journal of the Mechanics and Physics of Solids*, Vol. 17, pp. 17–22.

Roscoe, R., 1972, "Improved Bounds for Real and Imaginary Parts of Complex Moduli of Isotropic Viscoelastic Composites," *Journal of the Mechanics and Physics of Solids*, Vol. 20, pp. 91–99.

Schapery, R. A., 1974, "Viscoelastic Behavior and Analysis of Composite Materials," *Composite Materials*, Vol. 2, G. P. Sendeckyj, ed., Academic Press, pp. 85–168.

Skudra, A. M., and Auzukalns, Ya. V., 1973, "Creep and Long-term Strength of Unidirectional Reinforced Plastics in Compression," *Polymer Mechanics*, Vol. 6.5, pp. 718–722.

Tandon, G. P., and Weng, G. J., 1984, "The Effect of Aspect Ratio of Inclusions on the Elastic Properties of Unidirectionally Aligned Composites," *Polymer Composites*, Vol. 5, pp. 327–333.

Tandon, G. P., and Weng, G. J., 1986, "Average Stress in the Matrix and Effective Moduli of Randomly Oriented Composites," *Composites Science and Technology*, Vol. 27, pp. 111–132.

Walpole, L. J., 1969, "On the Overall Elastic Moduli of Composite Materials," *Journal of the Mechanics and Physics of Solids*, Vol. 17, pp. 235–251.

Weng, G. J., 1984, "Some Elastic Properties of Reinforced Solids, with Special Reference to Isotropic Ones Containing Spherical Inclusions," *International Journal of Engineering Science*, Vol. 22, pp. 845–856.

Weng, G. J., 1990, "The Theoretical Connection between Mori-Tanaka's Theory and the Hashin-Shtrikman-Walpole Bounds," *International Journal of Engineering Science*, Vol. 28, pp. 1111–1120.

Zhao, Y. H., Tandon, G. P., and Weng, G. J., 1989, "Elastic Moduli for a Class of Porous Materials," *Acta Mechanica*, Vol. 76, pp. 105–130.

Zhao, Y. H., and Weng, G. J., 1990, "Effective Elastic Moduli of Ribbon-Reinforced Composites," ASME Journal of Applied Mechanics, Vol. 57, pp. 158–167.

# APPENDIX A

## $A_1$, $A_2$, $A_3$, $A_4$, $A_5$, and $A$

Keeping Tandon and Weng's (1984) original notations, these constants (not tensors) are given by

$$A_1 = D_1(B_4 + B_5) - 2B_2,$$

$$A_2 = (1 + D_1)B_2 - (B_4 + B_5),$$

$$A_3 = B_1 - D_1 B_3,$$

$$A_4 = (1 + D_1)B_1 - 2B_3,$$

$$A_5 = (1 - D_1)/(B_4 - B_5),$$

$$A = 2B_2B_3 - B_1(B_4 + B_5), \tag{A1}$$

where, in terms of the Lamé constants $\mu_r^{TD}$ and $\lambda_r^{TD}$ of the $r$th phase,

$$D_1 = 1 + 2(\mu_1^{TD} - \mu_0^{TD})/(\lambda_1^{TD} - \lambda_0^{TD}),$$

$$D_2 = (\lambda_0^{TD} + 2\mu_0^{TD})/(\lambda_1^{TD} - \lambda_0^{TD}),$$

$$D_3 = \lambda_0^{TD}/(\lambda_1^{TD} - \lambda_0^{TD}), \tag{A2}$$

and, with $c_r$ representing the volume fraction,

$$B_1 = c_1D_1 + D_2 + c_0(D_1S_{1111}^{TD} + 2S_{2211}^{TD}),$$

$$B_2 = c_1 + D_3 + c_0(D_1S_{1122}^{TD} + S_{2222}^{TD} + S_{2233}^{TD}),$$

$$B_3 = c_1 + D_3 + c_0[S_{1111}^{TD} + (1 + D_1)S_{2211}^{TD}],$$

$$B_4 = c_1D_1 + D_2 + c_0(S_{1122}^{TD} + D_1S_{2222}^{TD} + S_{2233}^{TD}),$$

$$B_5 = c_1 + D_3 + c_0(S_{1122}^{TD} + S_{2222}^{TD} + D_1S_{2233}^{TD}). \tag{A3}$$

Constants $A_1$, $A_2$, $A_3$, $A_4$, $A_5$, and $A$ are seen to depend on the shape and volume fraction of the inclusions.

## APPENDIX B

### Components of $a_1$, $a_2$, $a_3$, $a_4$, $a_5$, and $a$

These components have been derived by Tandon and Weng (1986), with

$$a_1 = 6(\kappa_1^{TD} - \kappa_0^{TD})(\mu_1^{TD} - \mu_0^{TD})(S_{2222}^{TD} + S_{2233}^{TD} - 1) - 2(\kappa_0^{TD}\mu_1^{TD} - \kappa_1^{TD}\mu_0^{TD}) + 6\kappa_1^{TD}(\mu_1^{TD} - \mu_0^{TD}),$$

$$a_2 = 6(\kappa_1^{TD} - \kappa_0^{TD})(\mu_1^{TD} - \mu_0^{TD})S_{1133}^{TD} + 2(\kappa_0^{TD}\mu_1^{TD} - \kappa_1^{TD}\mu_0^{TD}),$$

$$a_3 = -6(\kappa_1^{TD} - \kappa_0^{TD})(\mu_1^{TD} - \mu_0^{TD})S_{3311}^{TD} - 2(\kappa_0^{TD}\mu_1^{TD} - \kappa_1^{TD}\mu_0^{TD}),$$

$$a_4 = 6(\kappa_1^{TD} - \kappa_0^{TD})(\mu_1^{TD} - \mu_0^{TD})(S_{1111}^{TD} - 1) + 2(\kappa_0^{TD}\mu_1^{TD} - \kappa_1^{TD}\mu_0^{TD}) + 6\mu_1^{TD}(\kappa_1^{TD} - \kappa_0^{TD}),$$

$$a_5 = 1/[S_{3322}^{TD} - S_{3333}^{TD} + 1 - \mu_1^{TD}/(\mu_1^{TD} - \mu_0^{TD})],$$

$$a = 6(\kappa_1^{TD} - \kappa_0^{TD})(\mu_1^{TD} - \mu_0^{TD})[2S_{1133}^{TD}S_{3311}^{TD} - (S_{1111}^{TD} - 1) \times (S_{3322}^{TD} + S_{3333}^{TD} - 1)] + 2(\kappa_0^{TD}\mu_1^{TD} - \kappa_1^{TD}\mu_0^{TD})[2(S_{1133}^{TD} + S_{3311}^{TD}) + (S_{1111}^{TD} - S_{3322}^{TD} - S_{3333}^{TD})] - 6\kappa_1^{TD}(\mu_1^{TD} - \mu_0^{TD})(S_{1111}^{TD} - 1) - 6\mu_1^{TD}(\kappa_1^{TD} - \kappa_0^{TD})(S_{2222}^{TD} + S_{2233}^{TD} - 1) - 6\kappa_1^{TD}\mu_1^{TD}. \tag{B1}$$

# Regular Pyramid Punch Problem

**G. G. Bilodeau**
Department of Mechanical Engineering,
Concordia University,
Montreal, QC H3G 1M8, Canada

*An approximate solution is found for a regular pyramidal punch indenting, without friction, an elastic half-space. The method is based on the reasonable assumption of the stress distribution and of the region of contact. The force-indentation relationship is obtained for a regular pyramidal punch. The results compare well with direct numerical results.*

## Introduction

The closest type of problem, in literature, related to the pyramidal punch problem is that dealing with the conical punch. Numerous papers have dealt with the conical punch of which two are (Love, 1939) and (Galin, 1953). This type of punch problem is axisymmetric and the region of contact is known in advance. In addition, its solution is exact. On the other hand, the pyramid punch problem is nonaxisymmetric with respect to both the stress distribution and the profile of the punch. Furthermore, the stress and the region of contact are not known beforehand, thus approximations must be made. This problem has not been solved before, except in a recent paper (Barber and Billings, 1990) in which, as an example of their approach, a tetrahedral punch is under investigation. Although their solution approximates the direct numerical result of Hartnett's method (Hartnett, 1980) closely, the shape of the contact area is incorrect. The present problem is solved by assuming a reasonable contact area and normal stress, and then determining the area of contact which maximizes the indenting force by the use of an expression for normal displacement found in Fabrikant (1989) and the variational approach (Noble, 1960; Fabrikant, 1989). Several examples of pyramidal punches are solved and compared, where possible, to other solutions.

## Method

**Description of the Problem.** An elastic half-space, $z > 0$, is indented by a rigid pyramidal punch, without friction (the frictionless contact problem is described in Barber and Billings, (1990). The lateral faces of the pyramid are isosceles triangles and the base is an $n$-sided polygon. In the regular pyramid, all the lateral edges are of equal length. The inclination of each triangle face is the angle $\alpha$, which must be close to zero in order to stay within the elastic range. The orientation of the pyramid is such that the apex of the pyramid is indenting the half-space. We use polar coordinates with the origin along the centroidal axis of the polygon. The boundary of contact is

$$\rho = a(\phi). \tag{1}$$

The indentation in polar coordinates is known to be, for this type of problem,

$$\omega(\rho,\phi) = \delta - \rho\tan\alpha\cos(\phi - m\pi/n),\ \frac{(m-1)\pi}{n} < \phi < \frac{(m+1)\pi}{n}, \tag{2}$$

where $m = 2j - 2, j = 1, 2, 3, \ldots, n$. The integer $j$ corresponds to each side starting with $\phi = 0$. For example, for the third side, $j = 3$, $m = 4$, $\omega(\rho, \phi)$ becomes

$$\omega(\rho,\phi) = \delta - \rho\tan\alpha\cos(\phi - 4\pi/n),\ 3\pi/n < \phi < 5\pi/n.$$

In the remainder of the paper, only the interval $-\pi/n < \phi < \pi/n$ will be shown unless clarity is needed. $\delta$ is the indentation of the vertex and $\alpha$ is the inclination of the polyhedral face.

**Assumption of Stress and Contact Boundary.** We must assume both the stress distribution and the contact boundary. The assumption of $\sigma(\rho, \phi)$ is based on the known (Love, 1939) stress distribution for a rigid cone,

$$\sigma(\rho,\phi) = C\cosh^{-1}(a/\rho), \tag{3}$$

where $C$ is a constant and $a$ is the radius of the contact area. In both the cone and the pyramid, the apex ($\rho = 0$) represents a singularity in the stress. Furthermore, the stress goes to zero at the border of the contact area due to a smooth transition to the half-space. The difference between the two punches is that the stress distribution for the pyramid has singularities produced by the lateral edges joining each face of the pyramid. These conditions are restated as:

1 $\sigma(0,\phi) \to \infty$,

2 $\sigma\left(\rho, -\dfrac{\pi}{n}\right) \to \infty,\ \sigma\left(\rho, \dfrac{\pi}{n}\right) \to \infty$,

3 $\sigma(\rho,\phi) = 0$ for $\rho \ge a(\phi)$.

The conditions given above and the stress distribution for the cone allow us to obtain an expression for the stress distribution for a pyramid punch

$$\sigma(\rho,\phi) = Kg(\phi)\cosh^{-1}(a(\phi)/\rho),\ -\pi/n < \phi < \pi/n. \tag{4}$$

Here, $K$ is some constant to be determined later, and $g(\phi)$ is infinite at the lateral edges. The type of singularity and the function represented by $g(\phi)$ will be discussed later. Equation (4) is repeated for the other intervals with appropriate changes

Contributed by the Applied Mechanics Division of THE AMERICAN SOCIETY OF MECHANICAL ENGINEERS for publication in the ASME JOURNAL OF APPLIED MECHANICS.

Discussion on this paper should be addressed to the Technical Editor, Prof. Leon M. Keer, The Technological Institute, Northwestern University, Evanston, IL 60208, and will be accepted until four months after final publication of the paper itself in the ASME JOURNAL OF APPLIED MECHANICS.

Manuscript received by the ASME Applied Mechanics Division, Aug. 15, 1990; final revision, June 17, 1991. Associate Technical Editor: C. Horgan.

for $\phi$. The logarithmic singularity at the apex arises from the stress distribution for the cone. Furthermore, we see that (4) is the stress distribution for a cone multiplied by a function which has a singularity at the lateral edges of the pyramid.

The boundary of the contact area is reasonably assumed to be a polygon of the same type as the base of the pyramid described earlier. Thus, the polygon corresponding to a quadrilateral pyramid is the square. This leads to an expression for $a(\phi)$,

$$a(\phi)=\frac{L}{\cos\phi}, \quad -\pi/n<\phi<\pi/n. \tag{5}$$

Again, (5) is repeated for the other intervals.

**Solving the Problem.** We must determine the constant $K$ in (4). The total force $P$ is found using

$$P=\iint_S \phi(\rho,\phi)dS. \tag{6}$$

Substitution of (4) into (6) gives

$$P=nK\int_{-\pi/n}^{\pi/n}\int_0^{a(\phi)} g(\phi)\cosh^{-1}(a(\phi)/\rho)\rho d\rho d\phi. \tag{7}$$

Multiplication by $n$ in (7) takes into account the other intervals which are identical to the first interval. We now integrate (7) with respect to $\rho$. Substitution of $a(\phi)$ from (5) leads to an expression for $K$,

$$K=\frac{2P}{L^2 I_1}, \tag{8}$$

where

$$I_1=n\int_{-\pi/n}^{\pi/n}\frac{g(\phi)d\phi}{\cos^2\phi}. \tag{9}$$

The integral in (9) is a constant and can be computed numerically for a particular pyramid using a standard computer library such as IMSL.

We now use a well known (Fabrikant, 1989) expression governing the elastic contact problem for a smooth punch which is

$$\omega(\rho,\phi)=H\iint_{S_0}\frac{\sigma(\rho_0,\phi_0)}{R}dS_0, \tag{10}$$

where $R$ is the distance between points ($\rho_0$, $\phi_0$) and ($\rho$, $\phi$). Also, $\omega(\rho, \phi)$ is given in (2) and $H$ (Fabrikant, 1989) is the elastic constant for isotropic solids

$$H=\frac{1-\nu}{2\pi\mu}. \tag{11}$$

Here, $\nu$ and $\mu$ are Poisson's coefficient and the modulus of rigidity, respectively. The integral representation for the reciprocal of the distance given in (Fabrikant, 1989) is

$$\frac{1}{R}=\frac{1}{\sqrt{\rho^2+\rho_0^2-2\rho\rho_0\cos(\phi-\phi_0)}}$$
$$=\frac{2}{\pi}\int_0^{\min(\rho_0,\rho)}\frac{\lambda(x^2/\rho\rho_0,\phi-\phi_0)dx}{[(\rho^2-x^2)(\rho_0^2-x^2)]^{1/2}}, \tag{12}$$

where $\lambda(k,\phi-\phi_0)$ is represented as a sum

$$\lambda(k,\phi-\phi_0)=\sum_{l=-\infty}^{\infty}k^{|l|}e^{il(\phi-\phi_0)}. \tag{13}$$

Substitution of (12) into (10) gives the following expression in terms of the integral $\mathcal{L}$-operator (Fabrikant, 1989),

$$\omega(\rho,\phi)=4H\int_0^{\rho}\frac{dx}{(\rho^2-x^2)^{1/2}}\int_x^{a(\phi)}\frac{\rho_0 d\rho_0}{(\rho_0^2-x^2)^{1/2}}\mathcal{L}\left(\frac{x^2}{\rho\rho_0}\right)\sigma(\rho,\phi). \tag{14}$$

Fabrikant introduces the $\mathcal{L}$-operator, for $k<1$, as

$$\mathcal{L}(k)f(\phi)=\frac{1}{2\pi}\int_0^{2\pi}\lambda(k,\phi-\phi_0)f(\phi_0)d\phi_0. \tag{15}$$

With (15), (14) becomes Eq. (5.4.1) in Fabrikant (1989)

$$\omega(\rho,\phi)=\frac{2}{\pi}H\int_0^{\rho}\frac{dx}{(\rho^2-x^2)^{1/2}}\int_0^{2\pi}d\phi_0 \times\int_x^{a(\phi_0)}\frac{\lambda(x^2/\rho\rho_0,\phi-\phi_0)}{(\rho_0^2-x^2)^{1/2}}\sigma(\rho_0,\phi_0)\rho_0 d\rho_0. \tag{16}$$

Consider the zeroth harmonic, that is $l=0$, to simplify the problem. Substituting (4) into (16), the integrals with respect to $\rho_0$ and $x$ can be evaluated, leading to

$$\omega_0(\rho,\phi)=\frac{2}{\pi}HKn\int_{-\pi/n}^{\pi/n}g(\phi_0)\left[\frac{\pi^2}{4}a(\phi_0)-\frac{\pi}{2}\rho\right]d\phi_0. \tag{17}$$

By using the variational approach (Noble, 1960), we get the following functions (Fabrikant, 1989) which has its maximum value at the exact solution of (10)

$$I(\sigma)=\frac{2}{H}\iint_S\sigma(\rho,\phi)\omega(\rho,\phi)dS - \iint_S\sigma(\rho,\phi)\left[\iint_{S_0}\frac{\sigma(\rho_0,\phi_0)}{R}dS_0\right]dS \tag{18}$$

on letting

$$H\iint_{S_0}\frac{\sigma(\rho_0,\phi_0)}{R}dS_0\approx\omega_0. \tag{19}$$

Substituting (2), (4), and (19) into (18) followed by an integration with respect to $\rho$ leads to

$$I(\sigma)=\frac{n}{H}\int_{-\pi/n}^{\pi/n}g(\phi)\left[\left(K\delta-\frac{\pi}{4}K^2HLF_1\right)a^2(\phi) + \left(\frac{1}{2}K^2HF_2-K\tan\alpha\cos\phi\right)\frac{\pi a^3(\phi)}{6}\right]d\phi, \tag{20}$$

where

$$F_1=n\int_{-\pi/n}^{\pi/n}\frac{g(\phi_0)d\phi_0}{\cos\phi_0}$$
$$F_2=n\int_{-\pi/n}^{\pi/n}g(\phi_0)d\phi_0. \tag{21}$$

After substitution of (5) and (8) into (20), we have

$$I(\sigma)=\frac{2Pn}{HI_1}\left[\delta I_1-\frac{\pi PHF_1}{2L}+\frac{\pi PHF_2I_2}{6I_1L}-\frac{\pi I_1L\tan\alpha}{6}\right] \tag{22}$$

where the integrals $I_1$ (from (9)) and $I_2$ are

$$I_1=n\int_{-\pi/n}^{\pi/n}\frac{g(\phi)d\phi}{\cos^2\phi}$$
$$I_2=n\int_{-\pi/n}^{\pi/n}\frac{g(\phi)d\phi}{\cos^3\phi}. \tag{23}$$

In order to maximize $I(\sigma)$ we use the condition $\partial I(\sigma)/\partial L=0$. The outcome is the following expression relating $P$ and $L$:

$$P=\frac{I_1^2L^2\tan\alpha}{H(3I_1F_1-I_2F_2)}. \tag{24}$$

We set $\rho=0$ in both (2) and (17). Equating the two equations, we obtain a relationship between $\delta$ and $L$

$$L=\frac{\pi PHF_1}{I_1\delta}. \tag{25}$$

Table 1 Force-indentation coefficients

| $n$ | 3 | 4 | 5 | 6 | 8 | 10 | 15 | 20 | 50 |
|---|---|---|---|---|---|---|---|---|---|
| $C_0$ due to $g_1(\phi)$ | 1.777 | 1.491 | 1.398 | 1.355 | 1.316 | 1.300 | 1.285 | 1.280 | 1.274 |
| $C_0$ due to $g_2(\phi)$ | 1.819 | 1.519 | 1.417 | 1.369 | 1.325 | 1.306 | 1.287 | 1.281 | 1.274 |
| $C_0$ due to $g_3(\phi)$ | 1.807 | 1.517 | 1.417 | 1.369 | 1.325 | 1.306 | 1.287 | 1.281 | 1.274 |

Table 2 Area-indentation coefficients

| $n$ | 3 | 4 | 5 | 6 | 8 | 10 | 15 | 20 | 50 |
|---|---|---|---|---|---|---|---|---|---|
| $C_1$ due to $g_1(\phi)$ | 1.895 | 1.579 | 1.458 | 1.398 | 1.341 | 1.316 | 1.292 | 1.284 | 1.275 |
| $C_1$ due to $g_2(\phi)$ | 1.867 | 1.573 | 1.456 | 1.397 | 1.341 | 1.316 | 1.292 | 1.284 | 1.275 |
| $C_1$ due to $g_3(\phi)$ | 1.864 | 1.573 | 1.456 | 1.397 | 1.341 | 1.316 | 1.292 | 1.284 | 1.275 |

Substitution of (25) and (11) in (24) obtains the sought after force-penetration relation for a rectangular pyramid punch

$$P=\frac{3I_1F_1-I_2F_2}{2F_1^2}\left[\frac{4\delta^2\mu}{\pi(1-\nu)\tan\alpha}\right]. \tag{26}$$

Note that (26) is essentially a constant multiplied by the known exact force-penetration relationship for a cone (Galin, 1953). As a matter of fact, when $n$ is sufficiently large, the integrals ($I_1$, $I_2$, $F_1$, $F_2$) will all be closely equal to each other, such that

$$\frac{3I_1F_1-I_2F_2}{2F_1^2}=1, \tag{27}$$

and (26) reduces to the conical solution.

## Results/Examples

We will determine the effect of the singularity type (i.e., $g(\phi)$) at the lateral edges on the results, compare the results to known solutions, and determine how well the approximate stress distribution approximates the punch displacement.

**Comparison of Lateral Edge Singularity Types.** Several punch problems will be considered in which the singularities along the lateral edges will be, for comparison purposes,

1 $g_1(\phi)=\cosh^{-1}\left(\frac{1.5\pi/n}{(\pi/n)^2-\phi^2}\right)$,

2 $g_2(\phi)=(\sqrt{\cos\phi-\cos(\pi/n)})^{-1}$,

3 $g_3(\phi)=\left[\cosh^{-1}\left(\frac{\cos\phi}{\cos(\pi/n)}\right)\right]^{-1}$.

The first and third functions represent logarithmic singularities which are in agreement with the logarithmic singularity observed in the wedge problem. The second function is used to demonstrate that the method is not very sensitive to the type of singularity. Table 1 shows the coefficient relating the force $P$ and the indentation $\delta$ due to the three singularities, such that

$$P=C_0\frac{\mu\delta^2}{(1-\nu)\tan\alpha}. \tag{28}$$

Table 2 compares the relationship between the area of contact and the indentation using the three types of singularities, where

$$A=C_1\frac{\delta^2}{\tan^2\alpha}. \tag{29}$$

From both tables, the results do not change significantly as we change the singularity. Therefore, the method used is not very sensitive to the singularity used along the lateral edges. In addition, this allows some flexibility in choosing the singularity in order to reduce the complexity of the singular function.

**Comparison With Known Results.** For a tetrahedral punch, $n = 3$, $a(\phi)$, and $\sigma(\rho, \phi)$ become

$$a(\phi)=\frac{L}{\cos\phi},\quad -\pi/3<\phi<\pi/3$$

$$\sigma(\rho,\phi)=Kg(\phi)\cosh^{-1}(a(\phi)/\rho),\quad -\pi/3<\phi<\pi/3. \tag{30}$$

Both expressions in (30) are repeated for the other two intervals with appropriate changes in $\phi$. From (26), we have the force indentation relationship due to the logarithmic singularity of $g_1(\phi)$ as

$$P=\frac{1.7773\mu\delta^2}{(1-\nu)\tan\alpha}, \tag{31}$$

and the area of contact in terms of the indentation becomes

$$A=1.895\frac{\delta^2}{\tan^2\alpha}. \tag{32}$$

The numerical solution due to Hartnett's method (Barber and Billings, 1990) is

$$P=\frac{1.7725\mu\delta^2}{(1-\nu)\tan\alpha}, \tag{33}$$

and from a private communication with Barber, the area is

$$A=1.816\frac{\delta^2}{\tan^2\alpha}. \tag{34}$$

Comparison of (31) and (33) leads to a percent deviation of only 0.27 percent. The percent deviation between (32) and (34) is 4.4 percent. This is very good considering that the domain of contact is taken to be a triangle when each side of the triangle should be slightly curved as Hartnett's method suggests (Barber and Billings, 1990). Barber's relationship,

$$P=\frac{1.6960\mu\delta^2}{(1-\nu)\tan\alpha}, \tag{35}$$

compares well with (33), with a percent deviation of 4.3 percent, but the domain of contact is erroneous since there should not be any sharp corners at $\phi = 0$, $2\pi/3$, and $4\pi/3$ as depicted in his expression for $a(\phi)$,

$$a(\phi)=\frac{4\delta(1+\sqrt{1-\cos\phi})}{3\pi\tan\alpha\cos\phi},\quad -\pi/3<\phi<\pi/3. \tag{36}$$

Therefore, the present method approximates very well the shape, size, and area of contact of a tetrahedral punch indenting an elastic half-space.

Similar to what was done with the tetrahedral punch, except that $n = 4$ for the quadrilateral pyramid, we obtain the following expressions for the force and area

$$P=\frac{1.4906\mu\delta^2}{(1-\nu)\tan\alpha},\ A=1.579\frac{\delta^2}{\tan^2\alpha}. \tag{37}$$

In a private communication, Barber calculates the numerical solution for the area as

$$A=1.496\frac{\delta^2}{\tan^2\alpha}. \tag{38}$$

The expression for the area in (37) compares well with that of (38). The percent deviation is 5.5 percent.

For $n \geq 5$, comparisons cannot be made since these problems have not been done before. We can note that the coefficients for the forces should be less than that obtained for the tetrahedral punch and greater than that of the conical punch. Note that the coefficient decreases as the number of faces (that is, $n$) increases. It can be shown that as $n$ becomes very large, we obtain a well-known force displacement relation for the conical punch (Galin, 1953) which is solved exactly as

$$P = \frac{4\mu\delta^2}{\pi(1-\nu)\tan\alpha} \tag{39}$$

and

$$A = \frac{4\delta^2}{\pi\tan^2\alpha}. \tag{40}$$

**Punch Displacement.** We will determine how well the displacement due to the approximate stress distribution matches the prescribed displacement. First of all, the prescribed displacement is given by (2) and repeated here for $-\pi/n < \phi < \pi/n$,

$$\omega(\rho,\phi) = \delta - \tan\alpha\cos\phi. \tag{41}$$

We want $\omega(\rho, \phi)$ in terms of $L$. Using (24) and (25), we obtain a relationship between $L$ and $\delta$ independent of $P$

$$L = \frac{(3I_1F_1 - I_2F_2)\delta}{\pi I_1F_1\tan\alpha}. \tag{42}$$

Now, we have $\omega(\rho, \phi)$ in terms of $L$,

$$\omega(\rho,\phi) = \left[\frac{\pi I_1F_1L}{3I_1F_1 - I_2F_2} - \rho\cos\phi\right]\tan\alpha. \tag{43}$$

Remember that $\delta$ is the indentation from $z = 0$ to the apex and that $\delta/L \neq \tan\alpha$.

In order to obtain the displacement due to the approximate stress distribution we need to integrate numerically Eq. (10), which is

$$\omega(\rho,\phi) = H\iint_{S_0} \frac{\sigma(\rho_0,\phi_0)}{R}\rho_0 d\rho_0\phi_0, \tag{44}$$

where $R$ is given by the first part of (12). Rewriting $\omega(\rho, \phi)$, we get

$$\omega(\rho,\phi) = HK\iint_{S_0} \frac{g(\phi_0)\cosh^{-1}(a(\phi_0)/\rho_0)}{\sqrt{\rho^2+\rho_0^2-2\rho\rho_0\cos(\phi-\phi_0)}}\rho_0 d\rho_0\phi_0. \tag{45}$$

Recall that $g(\phi_0)$ is infinite at $\phi = -\pi/n$ and $\pi/n$. Therefore, we will obtain singularities when $\rho = 0$, $\phi = -\pi/n$ and $\pi/n$, and $(\rho, \phi) = (\rho_0, \phi_0)$. For simplicity we will limit the integration by ignoring the singularities, by considering the tetrahedral problem only, and by letting $L = 1$. The procedure is the same for $n > 3$.

For $n = 3$, we must sum up three integrals, one for each interval. The integrals have been manipulated so that we integrate over the same intervals. The singularities are ignored by integrating close to the point or line of singularity by using $\epsilon = 0.0001$, or

$$\omega(\rho,\phi) = W_1 + W_2 + W_3$$

$$W_1 = HK\int_{-\frac{\pi}{3}+\epsilon}^{\frac{\pi}{3}-\epsilon}\int_{\epsilon}^{a(\phi_0)} \frac{g(\phi_0)\cosh^{-1}(a(\phi_0)/\rho_0)}{\sqrt{\rho^2+\rho_0^2-2\rho\rho_0\cos(\phi-\phi_0)}}\rho_0 d\rho_0 d\phi_0$$

$$W_2 = HK\int_{-\frac{\pi}{3}+\epsilon}^{\frac{\pi}{3}-\epsilon}\int_{\epsilon}^{a(\phi_0)} \times\frac{g(\phi_0)\cosh^{-1}(a(\phi_0)/\rho_0)}{\sqrt{\rho^2+\rho_0^2-2\rho\rho_0\cos(\phi-\phi_0-2\pi/3)}}\rho_0 d\rho_0 d\phi_0 \tag{46}$$

$$W_3 = HK\int_{-\frac{\pi}{3}+\epsilon}^{\frac{\pi}{3}-\epsilon}\int_{\epsilon}^{a(\phi_0)} \times\frac{g(\phi)\cosh^{-1}(a(\phi_0)/\rho_0)}{\sqrt{\rho^2+\rho_0^2-2\rho\rho_0\cos(\phi-\phi_0-4\pi/3)}}\rho_0 d\rho_0 d\phi_0.$$

**Table 3 Approximate and prescribed displacement for $\phi = 0$, $n = 3$, $L = 1.0$**

| $\rho$ | Prescribed $\frac{\omega(\rho,\phi)}{\tan\alpha}$ | Approximate $\frac{\omega(\rho,\phi)}{\tan\alpha}$ | % dev |
|---|---|---|---|
| 0.0 | 1.6562 | 1.6537 | −0.15 |
| 0.1 | 1.5562 | 1.5276 | −1.84 |
| 0.2 | 1.4562 | 1.4211 | −2.41 |
| 0.3 | 1.3562 | 1.3224 | −2.49 |
| 0.4 | 1.2562 | 1.2289 | −2.17 |
| 0.5 | 1.1562 | 1.1303 | −1.46 |
| 0.6 | 1.0562 | 1.0531 | −0.30 |
| 0.7 | 0.9562 | 0.9697 | 1.41 |
| 0.8 | 0.8562 | 0.8888 | 3.81 |
| 0.9 | 0.7562 | 0.8103 | 7.15 |
| 1.0 | 0.6562 | 0.7340 | 11.86 |

**Table 4 Approximate and prescribed displacement for $\phi = \pi/3$, $n = 3$, $L = 1.0$**

| $\rho$ | Prescribed $\frac{\omega(\rho,\phi)}{\tan\alpha}$ | Approximate $\frac{\omega(\rho,\phi)}{\tan\alpha}$ | % dev |
|---|---|---|---|
| 0.0 | 1.6562 | 1.6537 | −0.15 |
| 0.1 | 1.6062 | 1.6792 | 4.54 |
| 0.2 | 1.5562 | 1.6661 | 7.06 |
| 0.3 | 1.5062 | 1.6387 | 8.80 |
| 0.4 | 1.4562 | 1.6018 | 10.00 |
| 0.5 | 1.4062 | 1.5578 | 10.78 |
| 0.6 | 1.3562 | 1.5079 | 11.19 |
| 0.7 | 1.3062 | 1.4530 | 11.24 |
| 0.8 | 1.2562 | 1.3939 | 10.96 |
| 0.9 | 1.2062 | 1.3308 | 10.33 |
| 1.0 | 1.1562 | 1.2640 | 9.35 |
| 1.1 | 1.1062 | 1.1946 | 7.99 |
| 1.2 | 1.0562 | 1.1220 | 6.23 |
| 1.3 | 1.0062 | 1.0470 | 4.05 |
| 1.4 | 0.9562 | 0.9689 | 1.33 |
| 1.5 | 0.9062 | 0.8889 | −1.91 |
| 1.6 | 0.8562 | 0.8070 | −5.75 |
| 1.7 | 0.8062 | 0.7234 | −10.27 |
| 1.8 | 0.7562 | 0.6387 | −15.54 |
| 1.9 | 0.7062 | 0.5537 | −21.60 |
| 2.0 | 0.6562 | 0.4720 | −28.08 |

Obtaining $K$ from (8) and $P/L^2$ from (24), we get $K$ in terms of $\alpha$:

$$K = \frac{I_1^2\tan\alpha}{H(3I_1F_1 - I_2F_2)}. \tag{47}$$

With the logarithmic singularity, $g_1(\phi_0)$, we obtain the results shown in Tables 3 and 4 for $\phi = 0$ and $\phi = \pi/3$, respectively. The largest percent deviation occurs at $\rho = 2.0$ with $\phi = \pi/3$. This is due to the fact that as we move away from the apex, $\phi = \pi/3 - \epsilon$ gets further away from the line singularity at $\phi = \pi/3$. Therefore, the greater deviations far from the apex are expected due to ignoring the singularity at $\phi = \pi/3$. Apart from these deviations the overall results prove to be good, even when ignoring the singularities.

## Conclusions

A general relationship (26) between the force and vertical displacement for a regular pyramidal punch has been obtained in addition to the approximate area and shape of contact for maximum force. The results proved to be excellent. Therefore, by approximating the contact area as a polygon corresponding to the base of the pyramid punch, we obtain an accurate force-displacement relation. It is believed that as $n$ increases, the accuracy should also increase since the intervals of integration ((21) and (23)) become smaller. As a result, a straight line will very closely correspond to the curved boundaries of the contact area. It can also be concluded that the stress for a regular pyramidal punch is approximated by

$$\sigma(\rho,\phi) = Kg(\phi - m\pi/n)\cosh^{-1}[a(\phi - m\pi/n)/\rho],$$
$$\frac{(m-1)\pi}{n} < \phi < \frac{(m+1)\pi}{n}. \quad (48)$$

One may choose from the singularity functions, $g(\phi)$, depending on the accuracy and simplicity required. The above stress distribution approximates the punch displacement quite well. On the whole, the method presented in this paper allows the close approximation to the regular pyramid punch problem. Also, the method may be used to approximate subsurface stresses since the stress distribution in the half space will not depend largely on the distribution at the surface; therefore, error is lower than the error at the surface. Lastly, application of the method presented in this paper to the general pyramid problem may form the basis for future research.


## Acknowledgments

The author would like to thank Prof. J. R. Barber for his preprint and additional data, Dr. V. I. Fabrikant for his guidance and supervision, and the reviewers for their informative suggestions.


## References


Barber, J. R., and Billings, D. A., 1990, "An Approximate Solution for the Contact Area and Elastic Compliance of a Smooth Punch of Arbitrary Shape," *Int. J. Mech. Sci.*, Vol. 32, No. 12, pp. 991-997.

Beyer, W. H., ed., 1981, *CRC Standard Mathematical Tables*, 26th ed., CRC Press, FL.

Fabrikant, V. I., 1989, *Applications of Potential Theory in Mechanics: A Selection of New Results*, Kluwer Academic Publishers.

Galin, L. A., 1961, *Contact Problems in the Theory of Elasticity* (in Russian), Gostekhteorizdat, 1953, translated by H. Moss, Department of Mathematics, North Carolina State College, Raleigh, NC.

Gradshtein, I. S., and Ryzhik, I. M., 1980, *Tables of Integrals, Series and Products* (1963 English translation), Academic Press, New York.

Hartnett, M. J., 1980, "A General Numerical Solution for Elastic Body Contact Problems," *ASME Symposium on Solid Contact and Lubrication*, Chicago, pp. 51-66.

Love, A. E. H., 1939, "Boussinesq's Problem for a Rigid Cone," *Quart. J. Math.* (Oxford Series), Vol. 10, pp. 161-175.

Noble, B., 1960, "The Numerical Solution of the Singular Integral Equation for the Charge Distribution on a Flat Rectangular Lamina," *Sympos. Numerical Treatment of Ordinary Differential Equations, Integral and Integrodifferential Equations*, Proc. Rome Sympos., Sept. 1960, Birkhauser, Berlin-Sturrgart.

# Analysis of a Crack Bridged by a Single Fiber

**G. Meda**

**P. S. Steif**
Assoc. Mem. ASME.

Department of Mechanical Engineering,
Carnegie-Mellon University,
Pittsburgh, PA 15213-3890

*With the goal of assessing the accuracy of a widely used approximate method of analyzing bridged matrix cracks, an idealized problem representing a crack bridged by a single fiber is studied in detail. Our solution technique, which accounts for frictional slip at the fiber-matrix interface explicitly, involves the use of distributions of edge dislocations to represent the opening of the crack faces and the slip at the interface. Through this method, the solution is reduced to a set of three coupled singular integral equations which are solved numerically. The results are compared with those from the approximate method, and some sources of discrepancy between the two results are explored.*

## Introduction

The addition of reinforcing fibers to brittle ceramics sometimes yields a composite that is significantly tougher than the monolithic ceramic. The mechanism by which reinforcing fibers toughen the composite is not completely understood, though there is much evidence that the nature of the fiber-matrix interface plays an important role in the toughening mechanism. In particular, it is believed that a relatively weak interface which can debond prevents matrix cracks from breaking the fibers in their paths as they propagate.

In order to understand how the addition of reinforcing fibers toughens a composite, we need to understand, among other things, how unbroken fibers bridging a matrix crack influence the severity of the stresses near its tip. The influence of bridging fibers on the stresses ahead of a crack tip in ceramics reinforced by unidirectional fibers and loaded parallel to the fiber orientation has been studied by various workers (a partial list is Marshall, Cox, and Evans, 1985; Marshall and Cox, 1987; McCartney, 1987; Mori, Saito, and Mura, 1988; Budiansky and Amazigo, 1989; Thouless, 1989). In most of these studies, the bridging fibers, shown schematically in Fig. 1, are replaced by "equivalent" closing tractions acting on the faces of a crack in a homogeneous body, as shown in Fig. 2. These closing tractions are smeared out and applied as a continuous distribution on the crack faces; the magnitude of the traction at any point is assumed to be a function of the local crack opening displacement, and this function is sometimes determined from a simple shear lag analysis.

Although the approximation associated with replacing bridging fibers by equivalent closing tractions is claimed to be applicable to situations in which cracks are long compared to the fiber spacing (see Marshall, Cox, and Evans, 1985), the validity of this approximation does not appear to have been investigated. While it is plausible that the influence of the bridging fibers far from the crack tip is captured by the closing traction approximation, the validity of this approximation is not obvious for bridging fibers immediately behind the crack tip. Since these nearby bridging fibers are likely to have the greatest effect on the stresses ahead of the tip, it is important to assess the validity of the closing traction approximation for such fibers.

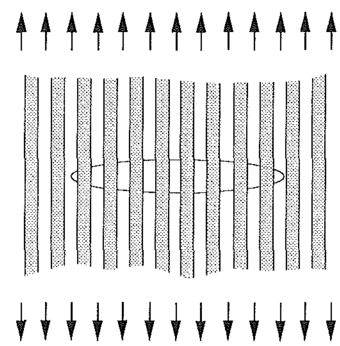

Fig. 1 Matrix crack bridged by intact fibers

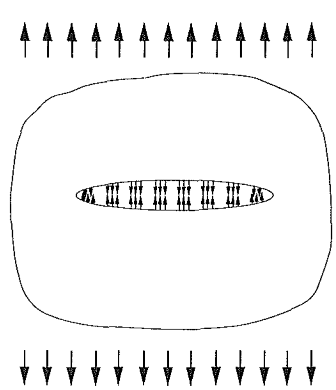

Fig. 2 Bridging fibers replaced by closing tractions on the crack faces

Contributed by the Applied Mechanics Division of The American Society of Mechanical Engineers for publication in the ASME Journal of Applied Mechanics.

Discussion on this paper should be addressed to the Technical Editor, Professor Leon M. Keer, The Technological Institute, Northwestern University, Evanston, IL 60208, and will be accepted until four months after final publication of the paper itself in the Journal of Applied Mechanics.

Manuscript received by the ASME Applied Mechanics Division, Oct. 16, 1990; final revision, Aug. 8, 1991. Associate Technical Editor: D. J. Dvorak.

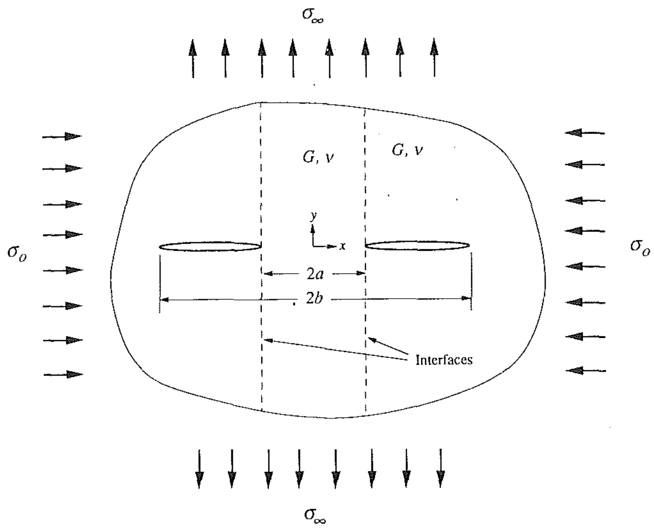


Fig. 3(*a*) Configuration A: Two cracks impinging on interfaces

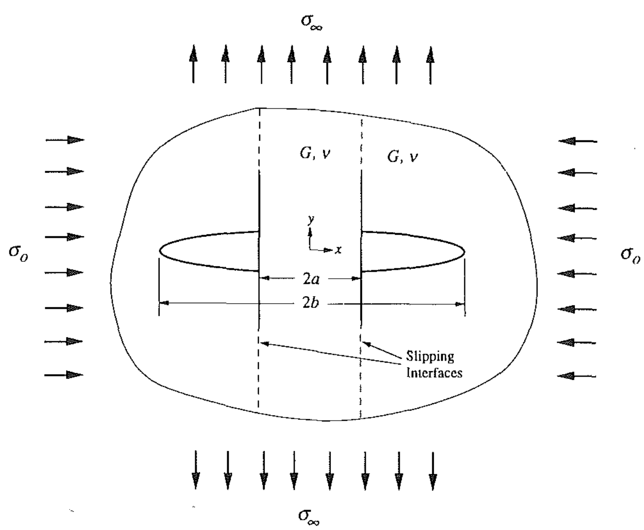


Fig. 3(*b*) Configuration A after slip at the interfaces

The purpose of this paper is to identify and solve a simple mechanics problem that can be used to assess the accuracy of the closing traction model. In particular, we will consider a crack spanned by a single fiber which is allowed to slip with respect to the matrix; of interest will be the degree to which the bridging fiber alters the stress intensity factor at the crack tip. To make the problem tractable, the fibers and the matrix are chosen to have identical moduli, and the fiber and the matrix are taken to be two dimensional. The resulting elasticity problem is one that can be solved both by the closing traction approximation and by a more rigorous dislocation distribution method. Since the latter method is highly accurate, it provides a basis for an assessment of the accuracy of the approximate method.

Clearly, therefore, our purpose is not to provide a detailed quantitative picture of the stresses in the vicinity of bridged matrix cracks; that problem is extremely complex due to the inherent three dimensionality and elastic inhomogeneity. Instead, our goal is to gauge the accuracy of a widely used approximate method in the specific case of a very simple fiber bridging problem. This accuracy might then be indicative of the accuracy of the approximate method when it is applied to more complex problems.

## Problem Statement

The problem under consideration, which we will call configuration $A$, is shown schematically in Fig. 3($a$): An infinite strip occupying $-a<x<a$ is sandwiched between two half-planes, occupying $x<-a$ and $x>a$. The half-plane $x>a$ contains a crack along $a<x<b$, $y=0$; the half-plane $x<-a$ contains a crack along $-b<x<-a$, $y=0$. The half-planes and the strip are homogeneous, isotropic, and linear elastic, having identical moduli $G$ and $\nu$. A tensile stress $\sigma_{yy}=\sigma_\infty$ is applied at infinity.

Thus far, the way in which the strip and the half-planes are connected has been left unspecified. Consider, for example, the strip and the half-planes to be perfectly bonded to one another; then, the problem would be simply that of two collinear cracks in an otherwise homogeneous infinite plane. By contrast, imagine that the strip and the half-planes can slip relative to one another once the interfacial shear stress becomes sufficiently high. Then, under a remote tensile load, the crack tips will open up at $x = \pm a$ (see Fig. 3($b$)) as slip occurs over come portion of the interface. It can be seen, therefore, that the configuration under consideration represents a two-dimensional crack lying along $-b<x<b$ which is spanned, or bridged, by a fiber. The interface conditions we choose to be operative along $x = \pm a$ should reflect the conditions at the fiber-matrix interface.

To model composites with weak interfacial bonding, the interfaces at $x = \pm a$ are taken to permit slip according to a Coulomb friction law, so that at any point on the interface, there is either stick, slip, or opening. Conditions for these states along the interface at $x = a$ can be expressed as follows:

Stick condition:

$$\sigma_{xx}<0,\ |\sigma_{xy}|\le\mu|\sigma_{xx}|,\ \frac{dg}{dt}=0,\ h=0; \tag{1a}$$

Slip condition:

$$\sigma_{xx}<0,\ |\sigma_{xy}|=\mu|\sigma_{xx}|,\ \frac{1}{\sigma_{xy}}\frac{dg}{dt}>0,\ h=0; \tag{1b}$$

Open condition:

$$\sigma_{xx}=\sigma_{xy}=0,\ h\ge 0, \tag{1c}$$

where

$$g=\lim_{\epsilon\to0^+}[v(a+\epsilon,y)-v(a-\epsilon,y)]$$

$$h=\lim_{\epsilon\to0^+}[u(a+\epsilon,y)-u(a-\epsilon,y)].$$

$u$ and $v$ are the $x$ and $y$ components of the displacement, respectively, $\mu$ is the friction coefficient which is assumed to be constant along the interface, and $t$ is a time-like parameter that increases monotonically as loading proceeds. (We ignore the distinction between static and kinetic friction.) The condition $(dg/dt)/\sigma_{xy} > 0$ is the condition of positive energy dissipation during slip.

In applying the Coulomb friction law, the total stresses should be used, including any residual stresses introduced during composite fabrication, such as those due to thermal strain mismatch between the fibers and the matrix. The residual stresses are presumed to be present prior to the application of any loading. To *simulate* such a residual compression at the interface in the present two-dimensional idealization, the plane is subjected to a remote compression $\sigma_{xx} = -\sigma_o$. Consistent with its interpretation as a residual stress, this remote compression is applied first, and then the remote tension $\sigma_{yy}$ is increased monotonically from 0 to $\sigma_\infty$.

This bridged crack problem will be solved accounting explicitly for slip on the interface, and the mode I stress intensity factor at the crack tip at $x = b$, $K_{IA}$, will be computed. This stress intensity factor will then be compared with those obtained using various approximate methods, including a closing-traction model for the bridging strip (described in Appendix A), to get an estimate of the accuracy of those approximate methods.

## Solution Method

The solution method, which is similar to that mentioned by Rice (1968) among others, involves the use of continuously distributed edge dislocations to represent the crack opening and the relative motion at the interfaces. The stress field in configuration $A$ is obtained by superimposing the following two fields: ($i$) the stress field in an infinite plane subjected to remote stress $\sigma_{yy} = \sigma_\infty$, $\sigma_{xx} = -\sigma_o$ and ($ii$) the stress field in an infinite plane containing continuous distributions of edge dislocations on $a < |x| < b$, $y = 0$ and on $|x| = a$. These dislocations are to be distributed in such a way that the final stress field (after superposition) leaves the line segments $a < |x| < b$, $y = 0$ traction-free and satisfies Coulomb friction conditions at each point on $|x| = a$, i.e., one of conditions (1$a$), (1$b$), or (1$c$) at each point on $x = a$ and analogous conditions on $x = -a$. For monotonically increasing tension, conditions (1$a$) and (1$b$) may be simplified to

$$\sigma_{xx}<0,\ \sigma_{xy}\le -\mu\sigma_{xx},\ \frac{dg}{dt}=0,\ h=0 \tag{2a}$$

$$\sigma_{xx}<0,\ \sigma_{xy}= -\mu\sigma_{xx},\ \frac{dg}{dt}>0,\ h=0. \tag{2b}$$

After taking advantage of the symmetry about the $x$- and $y$-axes, the only nonzero dislocation density distributions can be represented by the following Burgers vector densities:

| | |
|---|---|
| $\phi_1(x)\mathbf{j}$ | on $a<x<b,\ y=0$ |
| $-\phi_1(-x)\mathbf{j}$ | on $-b<x<-a,\ y=0$ |
| $\phi_3(y)\mathbf{i}+\phi_2(y)\mathbf{j}$ | on $x=a,\ y>0$ |
| $-\phi_3(-y)\mathbf{i}+\phi_2(-y)\mathbf{j}$ | on $x=a,\ y<0$ |
| $\phi_3(y)\mathbf{i}-\phi_2(y)\mathbf{j}$ | on $x=-a,\ y>0$ |
| $-\phi_3(-y)\mathbf{i}-\phi_2(-y)\mathbf{j}$ | on $x=-a,\ y<0$ |

where $\mathbf{i}$, $\mathbf{j}$ are unit vectors in the $x$ and $y$ directions, respectively. The functions $\phi_1$, $\phi_2$, and $\phi_3$ are defined as

$$\phi_1(x)=\frac{d}{dx}\left[\lim_{\epsilon\to 0^+}[v(x,\ -\epsilon)-v(x,\ +\epsilon)]\right]\quad \text{for } a<x<b$$

$$\phi_2(y)=\frac{d}{dy}\left[\lim_{\epsilon\to 0^+}[v(a+\epsilon,\ y)-v(a-\epsilon,\ y)]\right]\ \text{for } y>0$$

$$\phi_3(y)=\frac{d}{dy}\left[\lim_{\epsilon\to 0^+}\ [u(a+\epsilon,\ y)-u(a-\epsilon,\ y)]\right]\text{for } y>0.$$

Under the monotonically increasing loading considered here, there is a slip length $L_s$, which is a to-be-determined function of $\sigma_\infty$, such that the stick condition holds on the interface for $|y| > L_s$ and the slip or open condition holds at each point on $|y| < L_x$. Therefore, we have

$$\phi_2(y)=\phi_3(y)=0 \qquad \text{for } y>L_s. \tag{3}$$

Let $s_{xx}$, $s_{xy}$, and $s_{yy}$ be the stresses associated with the distributed dislocations; these are given by

$$\frac{2\pi(1-\nu)}{G}s_{yy}(x,\ 0)=\int_a^b \phi_1(t)K_{11}(x,\ t)dt + \int_0^{L_s}\phi_2(t)K_{12}(x,\ t)dt+\int_0^{L_s}\phi_3(t)K_{13}(x,\ t)dt \tag{4}$$

$$\frac{2\pi(1-\nu)}{G}s_{xx}(a,\ y)=\int_a^b \phi_1(t)K_{21}(y,\ t)dt + \int_0^{L_s}\phi_2(t)K_{22}(y,\ t)dt+\int_0^{L_s}\phi_3(t)K_{23}(y,\ t)dt \tag{5}$$

$$\frac{2\pi(1-\nu)}{G}s_{xy}(a,\ y)=\int_a^b \phi_1(t)K_{31}(y,\ t)dt + \int_0^{L_s}\phi_2(t)K_{32}(y,\ t)dt+\int_0^{L_s}\phi_3(t)K_{33}(y,\ t)dt \tag{6}$$

where the kernels $K_{ij}$ are given in Appendix B.

The traction-free condition on the crack faces may now be expressed as

$$s_{yy}(x,\ 0)=-\sigma_\infty \quad (a<x<b). \tag{7}$$

Note that the symmetry conditions on the dislocation density functions ensure that $s_{xy} = 0$ (and hence that $\sigma_{xy} = 0$) on the line $y = 0$, so that Eq. (7) completely specifies the traction-free conditions on the crack faces. The remaining conditions to be imposed are that at each point along $0 < y < L_s$, either the slip condition prevails,

$$s_{xy}(a,\ y)=-\mu[s_{xx}(a,\ y)-\sigma_o],\ s_{xx}(a,\ y) <\sigma_o,\ h(y)=0\ \ (0<y<L_s) \tag{8}$$

or the open condition prevails,

$$s_{xy}(a,\ y)=0,\ s_{xx}(a,\ y)=\sigma_o,\ h(y)>0\ \ (0<y<L_s) \tag{9}$$

where the opening $h$ is given by

$$h(y)=-\int_y^{L_s}\phi_3(t)dt.$$

Equations (7), (8), and (9) are a set of coupled singular integral equations, which can be solved numerically for $\phi_1$, $\phi_2$, and $\phi_3$ in conjunction with the conditions that there be net closure,

$$\int_a^b \phi_1(t)dt+2\int_0^{L_s}\phi_2(t)dt=0$$

and that the corner $(a,\ 0)$ of the quarter plane $x>a$, $y>0$ be stress-free when a Coulomb friction law holds on the interface, as shown by the near-tip analysis of Dollar and Steif (1989),

$$\phi_1(0)-2\phi_3(0)=0.$$

The function $\phi_1$ has an inverse square-root singularity at $x = b$, which is built into it by representing it in the numerical calculations as

$$\phi_1(x)=\hat{\phi}_1(x)\frac{1}{\sqrt{b-x}}$$

where $\hat{\phi}_1$ is nonsingular. Note that $\phi_2(x)$ is *not* singular at $x = a$, where the cracks impinge on frictional interfaces (see, for example, Dollar and Steif, 1989). From $\phi_1$, one can determine $K_{1A}$, the mode I stress intensity factor at the crack tip at $x = b$ in configuration $A$:

$$K_{IA}=\sqrt{\frac{\pi}{2}}\frac{G}{1-\nu}\hat{\phi}_1(b).$$

Since $y = L_s$ is the transition point between stick and slip zones, $\phi_2(y)$ must vanish at $y = L_s$ (Dundurs and Comninou, 1979). This provides a means of determining $L_s$ as a function of $\sigma_\infty$. In practice, however, it is convenient to represent $\phi_2$ as

$$\phi_2(y)=\hat{\phi}_2(y)\frac{1}{\sqrt{L_s-y}}$$

(where $\hat{\phi}_2$ is nonsingular) and adjust $\sigma_\infty$ at a fixed value of $L_s$ until the condition $\hat{\phi}_2(L_s) = 0$ is satisfied.

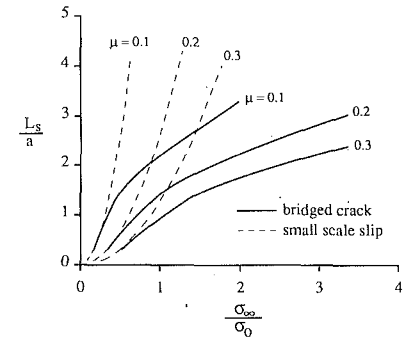


**Fig. 4 Comparison of slip length with small-scale slip approximation**

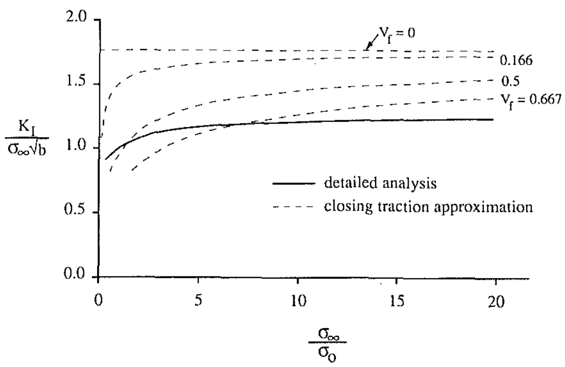


**Fig. 5 Comparison of bridged crack stress intensity factors computed by a detailed analysis and by a closing traction approximation ($b/a$ = 2, $\mu$ = 0.2)**

Some indication of the accuracy of our solution scheme can be gained by considering the limit as $\sigma_\infty/\sigma_o \rightarrow 0$. In this limit, we expect $K_{IA}$ to approach that at the outer tips of two collinear cracks over $a < |x| < b$, $y = 0$ in an infinite plane subjected to a remote tension of $\sigma_\infty$. For $b/a = 2$, the extrapolated value of $K_{IA}$ at $\sigma_\infty/\sigma_o = 0$ is $0.898\sqrt{b}\,\sigma_\infty$, while $K_I$ at the outer tips of two collinear cracks is $0.897\sqrt{b}\,\sigma_\infty$ (Tada, Paris, and Irwin, 1973). Further, when the slip length is small compared to $a$, the $L_s/a$ versus $\sigma_\infty/\sigma_o$ curves approach those of small-scale slipping (Dollar and Steif, 1989), as expected (see Fig. 4).

Additional confidence in our method was gained by applying it to some previously solved problems. The method was used to solve the problem of a single crack impinging on frictional interfaces at both tips, and the results were found to agree well with Dollar and Steif (1989). The method was also used to solve a boundary value problem described in Dollar and Steif (1991) that simulates an infinite crack bridged by fibers. The results from our method were found to agree well with their results.

## Results and Conclusions

As mentioned in the Introduction, the purpose of the analysis of configuration $A$ is to assess the accuracy of closing traction models in analyzing the effect of bridging fibers. To this end, we compare $K_{IB}$, the mode I stress intensity factor computed using a standard closing-traction model (described in Appendix A), which $K_{IA}$, the mode I stress intensity factor in configuration $A$, for $b/a = 2$ and $\mu = 0.2$. In order to apply the closing traction model to our problem, we must select appropriate values for two of the parameters in Eq. (A2): the limiting interfacial shear stress, $\tau$, and the fiber volume fraction, $V_f$. From previous comparisons between the Coulomb friction model and a constant shear stress approximation (Dollar and Steif, 1988, 1989), it is clear that $\tau$ should be set equal to $\mu\sigma_o$. Since the appropriate choice for the fiber volume fraction is

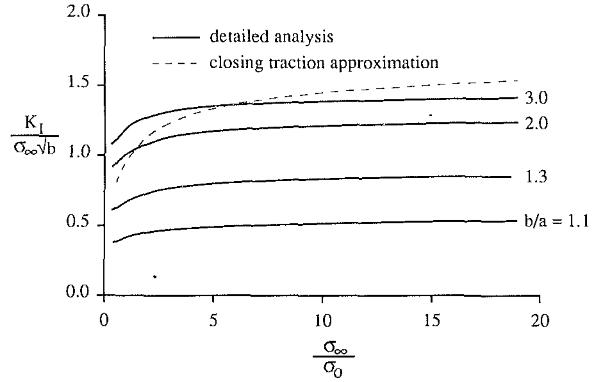


**Fig. 6 Comparison of bridged crack stress intensity factors computed by a detailed analysis and by closing traction approximation ($V_f$ = 0.5, $\mu$ = 0.2)**

less clear, we will compare for the entire range of possible volume fractions, $0 < V_f < 2/(b/a+1)$, the upper limit corresponding to the case where the crack tips at $x = \pm b$ almost impinge upon the adjacent fibers. Figure 5 shows $K_{IB}$ (dashed line) plotted along with $K_{IA}$ (solid line) against $\sigma_\infty/\sigma_o$. It can be seen that there is a significant difference between $K_{IA}$ and $K_{IB}$. As $\sigma_\infty/\sigma_o \rightarrow \infty$, $K_{IB}$ approaches $\sigma_\infty\sqrt{\pi b}$, the mode I stress intensity factor at the tip of a traction-free crack of length $2b$ in an infinite plane subjected to a remote tension of $\sigma_\infty$. Thus, the approximate closing traction analysis predicts the effect of the bridging fibers to die out as the applied stress increases, in contrast to the predictions of the more careful analysis of configuration $A$.

The value of $b/a$ can be thought of as being related to the stage of growth of the bridged matrix crack. A value close to unity corresponds to a short crack, most of which is spanned by the bridging fiber, and larger values corresponding to longer cracks. The maximum possible value of $b/a$ is that at which the crack tips at $x = \pm b$ impinge on the adjacent fibers. In the comparison just made between $K_{IA}$ and $K_{IB}$, $b/a$ was fixed, representing a particular stage of matrix crack growth. $K_{IA}$ was computed for this value of $b/a$, and $K_{IB}$ for comparison was computed for various values of the volume fraction $V_f$ in the possible range $0 < V_f < 2/(b/a+1)$. The comparison between $K_{IA}$ and $K_{IB}$ can also be made from a different perspective: $V_f$ may be fixed, and $K_{IB}$ for this value of $V_f$ can be compared with $K_{IA}$ computed for various values of $b/a$ in the possible range, $1 < b/a < (2-V_f)/V_f$. This would indicate how $K_{IA}$ compares with $K_{IB}$ when configuration $A$ represents various stages of growth of a matrix crack bridged by a single fiber. In Fig. 6, we plot $K_{IB}$ for $V_f = 0.5$, and $K_{IA}$ for several values of $b/a$ in the possible range $1 < b/a < 3$, against $\sigma_\infty/\sigma_o$. From Fig. 6, as well as from Fig. 5, it appears that the closing traction model generally underestimates the closing effect of the bridging fibers.

It is possible to gain some insight into why the closing traction model is in error. To do this, recall that there is a chain of assumptions involved in using the closing-traction model: that bridging fibers can be replaced by closing tractions equal to the tensile stress in the fiber, that these closing tractions can be smeared out over the crack faces, even near the crack tip, and that the stress in the fiber can be related to the crack opening by a shear lag analysis. (Closing traction models used by some workers, e.g., McCartney (1987) and Thoules (1989) do not use the third assumption; they use different methods to relate the closing tractions to the crack opening.) Comparing $K_{IA}$ and $K_{IB}$ gives us an idea of the error introduced by making all three assumptions simultaneously. To separate the errors associated with the various assumptions, we consider the following two problems, where we make the

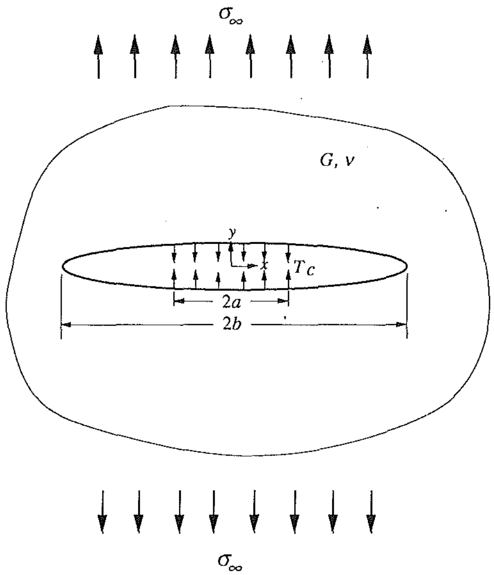


Fig. 7 Bridging fiber replaced by closing tractions

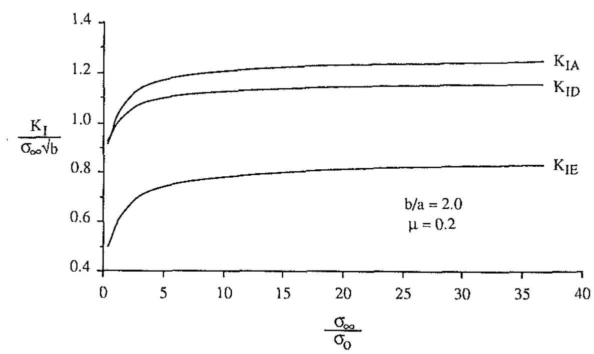


**Fig. 8 Further comparison of bridged crack stress intensity factors computed by different methods. $K_{IA}$: detailed analysis; $K_{ID}$: bridging fiber replaced by correct closing tractions; $K_{IE}$: closing tractions smeared out into a uniform distribution**

first two assumptions one at a time: In the first problem, we compute the stress $\sigma_{yy}$ in the bridging strip at the crack plane in configuration $A$, and apply this distribution as closing tractions on the faces of an uninterrupted crack in an infinite plane as shown in Fig. 7. The resulting mode I stress intensity factor at the crack tip, referred to as $K_{ID}$, is given by

$$K_{ID} = \sigma_\infty \sqrt{\pi b} - 2\sqrt{\frac{b}{\pi}} \int_0^a \frac{T_c(x)}{\sqrt{b^2 - x^2}}\, dx$$

where $T_c(x)$ denotes the fiber stress at the crack plane in configuration $A$:

$$T_c(x) = \sigma_{yy}(x)\,|_{y=0} \qquad \text{for } -a<x<a.$$

A comparison of $K_{ID}$ with $K_{IA}$ will indicate the error introduced by replacing a bridging fiber by closing tractions equal to the stress in the fiber. In the second problem, we smear out the closing tractions used in the first problem, and apply them as a uniform distribution of magnitude

$$\sigma_m = \frac{1}{b} \int_0^a T_c dx$$

on the faces of a crack lying on $-b<x<b$; the resulting mode I stress intensity factor at the crack tip is $K_{IE}$.

A comparison of $K_{IA}$, $K_{ID}$, and $K_{IE}$ (Fig. 8) shows that replacing a bridging strip by closing tractions equal to the tensile stress in the strip overestimates the closing effect slightly, while smearing out these closing tractions overestimates the closing effect significantly. Since, on the other hand, the closing traction model predicts a weaker closing effect, the shear lag approximation must be substantially underestimating the load borne by bridging fibers near the crack tip.

## Summary

A two-dimensional problem that represents a crack spanned by a single fiber has been solved accurately by using continuous distributions of edge dislocations, which leads to a set of simultaneous singular integral equations. This solution provides a means of assessing the accuracy of some approximate models of fiber bridging which involve the replacement of bridging fibers by equivalent closing tractions. In the problem studied here it was found that the standard closing traction model of fiber bridging (described in Appendix A) predicts a substantially weaker bridging effect than that predicted by the more detailed analysis. More specifically, smearing out the effective closing tractions into a continuous distribution on the crack faces artificially increases the bridging effect, while using a simple shear lag analysis to relate the effective closing tractions to the crack opening underestimates the load borne by the bridging fiber. The latter effect clearly predominates.

It must be acknowledged that the standard closing traction model is severely tested when applied to the problem of a crack bridged by a single fiber. However, even for long cracks bridged by many fibers, one suspects that this approximate model will not represent bridging fibers *close* to the crack tip any more accurately than it represents the bridging fiber in the problem studied. Since it is the bridging fibers close to the crack tip that have the most significant effect on the stresses ahead on the tip, it is suggested that the results of such approximate analyses of fiber bridging be utilized with caution.


## Acknowledgments

This research has been supported by the Air Force Office of Scientific Research under grant AFOSR 890548, by the General Electric Engine Business Group, and by the Department of Mechanical Engineering, Carnegie Mellon University.


## References


Budiansky, B., and Amazigo, J. C., 1989, "Toughening by Aligned, Frictionally Constrained Fibers," *J. Mech. Phys. Solids*, Vol. 37, p. 93.

Dundurs, J., and Comninou, M., 1979, "Some Consequences of the Inequality Conditions in Contact and Crack Problems," *Journal of Elasticity*, Vol. 9, p. 71.

Dollar, A., and Steif, P. S., 1988, "Load Transfer in Composites with a Coulomb Friction Interface," *Int. J. Solids Structures*, Vol. 24, p. 789.

Dollar, A., and Steif, P. S., 1989, "A Tension Crack Impinging Upon Frictional Interfaces," ASME Journal of Applied Mechanics, Vol. 56, p. 291.

Dollar, A., and Steif, P. S., 1991, "Stresses in Fibers Spanning an Infinite Matrix Crack," *Int. J. Solids Structures*, Vol. 27, p. 1011.

Marshall, D. B., and Cox, B. N., 1987, "Tensile Fracture of Brittle Matrix Composites: Influence of Fiber Strength," *Acta Metall.*, Vol. 35, p. 2607.

Marshall, D. B., Cox, B. N., and Evans, A. G., 1985, "The Mechanics of Matrix Cracking in Brittle-Matrix Fiber Composites," *Acta Metall.*, Vol. 33, p. 2013.

McCartney, L. N., 1987, "Mechanics of Matrix Cracking in Brittle-Matrix Fiber-Reinforced Composites," *Proc. R. Soc., Lond.*, Vol. A409, p. 329.

Mori, T., Saito, K., and Mura, T., 1988, "An Inclusion Model for Crack Arrest in a Composite Reinforced by Sliding Fibers," *Mechanics of Materials*, Vol. 7, p. 49.

Rice, J. R., 1968, "Mathematical Analysis in the Mechanics of Fracture," *Fracture*, Vol. 2, H. Liebowitz, ed., Academic Press, New York.

Tada, H., Paris, P. C., Irwin, G. R., 1973, *The Stress Analysis of Cracks Handbook*, Del Research Corporation.

Thouless, M. D., 1989, "A Re-examination of the Analysis of Toughening in Brittle-Matrix Composites," *Acta Metall.*, Vol. 37, p. 2297.


## APPENDIX A

In this Appendix, a relatively simple version of the closing-traction model is presented. The fibers bridging a long crack

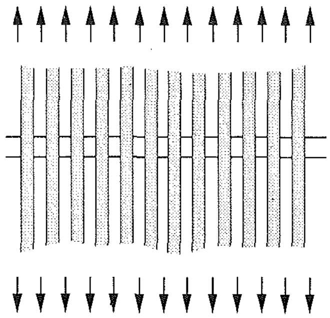

Fig. 9 Schematic of an infinitely long bridged crack

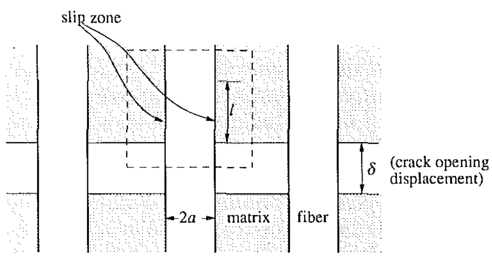


Fig. 10 Geometry for shear lag analysis of crack opening

(see Fig. 1) are replaced by closing tractions, equal to the tensile stresses in the fiber, acting on the faces of an uninterrupted crack in a homogeneous body, as shown in Fig. 2. These closing tractions are then smeared out into a continuous distribution $p$ on the crack faces, which is expressed as a function of the crack opening, $\delta$:

$$p = f(\delta). \qquad \text{(A1)}$$

The spring function $f$ has been determined in many different ways in the literature. We will determine it using a simple shear lag analysis, closely following Marshall, Cox, and Evans (1985).

Consider a long matrix crack bridged by many fibers and subjected to a remote tension of $\sigma_{yy} = \sigma_\infty$ parallel to the fiber orientation, as shown in Fig. 9. The fiber volume fraction is $V_f$, and sliding occurs at the interface when the shear stress exceeds $\tau$, a constant. Let $l$ be the length over which sliding has occurred, as shown in Fig. 10. If $\sigma_f$ is the mean tensile stress in the fiber, we have

$$\sigma_f = \frac{\sigma_\infty}{V_f} - \frac{\tau}{a}\, y \qquad \text{for } y \le l.$$

The mean tensile stress in the matrix, $\sigma_m$, is given by

$$\sigma_m = \frac{\sigma_\infty - \sigma_f V_f}{1 - V_f}$$

$$= \frac{V_f}{1 - V_f}\frac{\tau}{a}\, y \qquad \text{for } y \le l$$

If, consistent with the analysis in this paper, the matrix and fiber are taken to have identical elastic properties, the slip zone ends when $\sigma_m = \sigma_f = \sigma_\infty$, so that

$$l = \frac{\sigma_\infty}{\tau}\frac{1 - V_f}{V_f}\, a$$

The crack opening, $\delta$, is given by

$$\delta = 2\int_0^l (\epsilon_f - \epsilon_m)\, dy$$

$$= \frac{(1-\nu)}{G}\int_0^l (\sigma_f - \sigma_m)\, dy$$

$$= \frac{(1-\nu)}{2G}\frac{l^2}{a}\frac{\tau}{1 - V_f}$$

Hence, the relationship between the mean stress in the fiber at the crack plane, $\sigma_c$, and the crack opening, as determined from a simple shear lag analysis, is

$$\sigma_c = \left[\frac{2G}{(1-\nu)}\frac{\tau}{(1-V_f)a}\right]^{\frac{1}{2}}\sqrt{\delta}.$$

If the closing tractions are to be smeared out, we must reduce the magnitude of $\sigma_c$ by a factor of $1/V_f$, so that the function $f$ in Eq. (A1) is given by

$$f(\delta) = V_f\left[\frac{2G}{1-\nu}\frac{\tau}{(1-V_f)a}\right]^{\frac{1}{2}}\sqrt{\delta}. \qquad \text{(A2)}$$

We are finally left with the problem of a plane under remote tension $\sigma_{yy} = \sigma_\infty$ containing a crack with continuously distributed closing tractions of magnitude $p$ acting on the crack faces. This problem is solved numerically, and the stress intensity factor at the crack tip is determined. The numerical solution method was tested by using it to reproduce some of the results of McCartney (1987).

## APPENDIX B

Expressions for the kernels appearing in Eqs. (4)–(6) are as follows:

$$K_{11}(x,t) = \frac{1}{x-t} - \frac{1}{x+t}$$

$$K_{12}(x,t) = 2\left\{\frac{(x-a)[(x-a)^2+3t^2]}{[(x-a)^2+t^2]^2} - \frac{(x+a)[(x+a)^2+3t^2]}{[(x+a)^2+t^2]^2}\right\}$$

$$K_{13}(x,t) = 2\left\{\frac{t[t^2-(x-a)^2]}{[(x-a)^2+t^2]^2} + \frac{t[t^2-(x+a)^2]}{[(x+a)^2+t^2]^2}\right\}$$

$$K_{21}(y,t) = -\left\{\frac{(a+t)[(a+t)^2-y^2]}{[(a+t)^2+y^2]^2} - \frac{(a-t)[(a-t)^2-y^2]}{[(a-t)^2+y^2]^2}\right\}$$

$$K_{22}(y,t) = -2a\left\{\frac{[4a^2-(y-t)^2]}{[4a^2+(y-t)^2]^2} + \frac{[4a^2-(y+t)^2]}{[4a^2+(y+t)^2]^2}\right\}$$

$$K_{23}(y,t) = \frac{-1}{y-t} + \frac{1}{y+t} - \left\{\frac{(y-t)[(y-t)^2+12a^2]}{[(y-t)^2+4a^2]^2} - \frac{(y+t)[(y+t)^2+12a^2]}{[(y+t)^2+4a^2]^2}\right\}$$

$$K_{31}(y,t) = -\left\{\frac{y[(a+t)^2-y^2]}{[(a+t)^2+y^2]^2} - \frac{y[(a-t)^2-y^2]}{[(a-t)^2+y^2]^2}\right\}$$

$$K_{32}(y,t) = \left\{\frac{(y-t)[(y-t)^2-4a^2]}{[(y-t)^2+4a^2]^2} + \frac{(y+t)[(y+t)^2-4a^2]}{[(y+t)^2+4a^2]^2}\right\} - \frac{1}{y-t} - \frac{1}{y+t}$$

$$K_{33}(y,t) = -2a\left\{\frac{[(y-t)^2-4a^2]}{[(y-t)^2+4a^2]^2} - \frac{[(y+t)^2-4a^2]}{[(y+t)^2+4a^2]^2}\right\}.$$

# On Interface Crack Growth in Composite Plates

**K.-F. Nilsson**

**B. Storåkers**
Mem. ASME.

Department of Solid Mechanics,
Royal Institute of Technology,
S-100 44 Stockholm, Sweden

*Analysis of fracture growth, and in particular at interfaces, is pertinent not only to load-carrying members in composite structures but also as regards, e.g., adhesive joints, thin films, and coatings. Ordinarily linear fracture mechanics then constitutes the common tool to solve two-dimensional problems occasionally based on beam theory. In the present more general effort, an analysis is first carried out for determination of the energy release rate at general loading of multilayered plates with local crack advance either at interfaces or parallel to such. The procedure is accomplished for arbitrary hyperelastic material properties within von Karman plate theory and the results are expressed by aid of an Eshelby energy momentum tensor. By a feasible superposition it is then shown that the original nonlinear plate problem may be reduced to that of an equivalent beam in case of linear material properties. As a consequence of the so-established principle, the magnitude of mode-dependent singular stress amplitude factors is then directly determinable from earlier two-dimensional linear beam solutions for isotropic and anisotropic bimaterials and relevant at determination of cohesive and adhesive fracture. The procedure is illustrated by an analysis of combined buckling and crack growth of a delaminated plate having a nontrivial crack contour.*

## 1 Introduction

In layered composite materials and structures (including surface layers and coatings) crack propagation, or commonly delamination, has become an issue of increasing technological importance. To analyze the matter, however, severe complexities may emerge mainly related to material properties and growth criteria in nonlinear situations. Accordingly, the major concern has so far been restricted to linear material behavior and self-similar crack growth, cf., e.g., Chai et al. (1981), Evans and Hutchinson (1984), and Yin (1985).

The classical criterion for crack growth is associated with that of Griffith and to this end Storåkers and Andersson (1988) have recently established a method to determine energy release rates within von Karman's plate theory in general circumstances. Although the approach may apply to determination of stability of crack growth at perfectly brittle homogeneous materials, it is well known that crack propagation will in general be more involved, and in particular when regarding mode dependence and growth resistance. For homogeneous and isotropic materials cracks usually adapt themselves to propagate in mode I, while at bimaterial interfaces, mixed modes are rather the rule.

When beam-type structures are at issue, usually the energy release rate at growth of straight cracks may, in an asymptotic approximation, be determined by analytical means. At decomposition into stress intensity factors, however, two-dimensional theory must generally be drawn upon. In this spirit split bimaterial beams have recently been analyzed by Suo and Hutchinson (1990) for isotropic materials and additional results pertaining to a variety of geometry and material parameters have been summarized by Hutchinson and Suo (1992).

When it comes to plates or, alternatively, shells, and with the present purpose in mind, it is then definitely advantageous to reduce the problem by one dimension for energy release rates to apply to corresponding beams. It may be shown then, by a feasible superposition procedure, that this may be readily brought about and associated stress intensity factors conveniently determined. In particular, when shearing modes are uncoupled, results will be asymptotically exact. Regarding the remaining in-plane modes arising from opening and sliding, the decompositions by Suo and Hutchinson (1990), may be readily identified and also alternative approaches may be investigated. In case of bimaterials with no unambiguous decomposition singular stress intensity factors may accordingly be determined for plates based on reduced beam results as epitomized by Hutchinson and Suo (1992). Once this issue is resolved, crack growth may be predicted in general circumstances for specific growth criteria.

Contributed by the Applied Mechanics Division of The American Society of Mechanical Engineers for publication in the ASME Journal of Applied Mechanics.

Discussion on this paper should be addressed to the Technical Editor, Professor Leon M. Keer, The Technological Institute, Northwestern University, Evanston, IL 60208, and will be accepted until four months after final publication of the paper itself in the Journal of Applied Mechanics.

Manuscript received and accepted by the ASME Applied Mechanics Division, Nov. 16, 1990. Associate Technical Editor: A. K. Noor.

## 2 Reduction of General Energy Release Rates for Plates to Beams

The present issue concerns deformation and possible crack growth of a multilayer plate composed of an arbitrary number of lamina. For simplicity, though not without loss of gener-

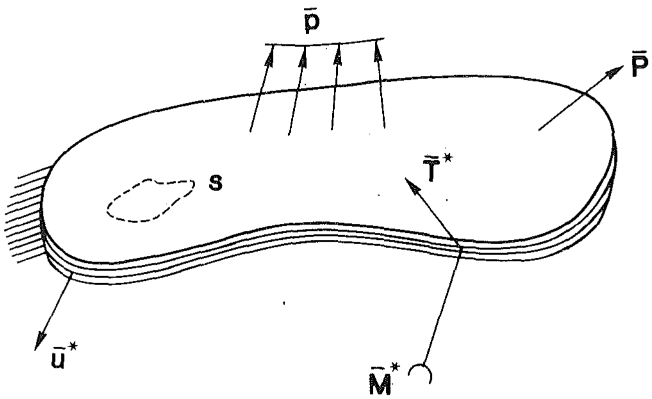


Fig. 1 Multilayered composite plate with a plane crack parallel to an interface

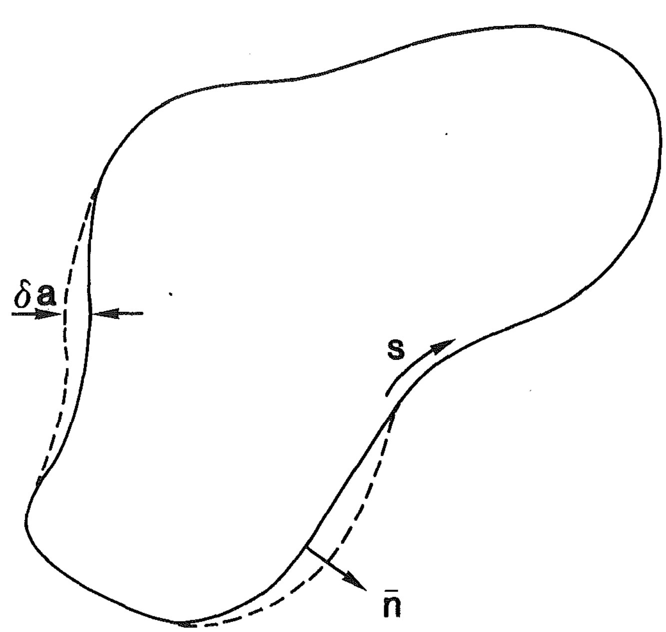


Fig. 2 Smooth delamination growth by an amount $\delta a$ in local normal direction, $\bar{n}$

ality, only a single crack, as shown in Fig. 1, is analyzed. Each lamina is locally homogeneous but otherwise arbitrary. External loading is prescribed either by dynamic or kinematic constraints or mixed ones. The crack as depicted in Fig. 1 must not necessarily be located between two dissimilar lamina, but only be assumed parallel to an interface.

Mainly in order to also accommodate the case of buckling of thin plates, nonlinear kinematics within von Karman's approximation is adopted. Thus, total strains, $e_{\alpha\beta}$, may be composed by a stretching term, $e^m_{\alpha\beta}$, and a curvature term, $e^b_{\alpha\beta}$, such that

$$e_{\alpha\beta}=e^m_{\alpha\beta}+e^b_{\alpha\beta} \tag{1}$$

when expressed in displacements as

$$e^m_{\alpha\beta}=\frac{1}{2}\,(u_{\alpha,\beta}+u_{\beta,\alpha}+u_{3,\alpha}u_{3,\beta}) \tag{2}$$

and

$$e^b_{\alpha\beta}=x_3\kappa_{\alpha\beta},\ \kappa_{\alpha\beta}=-u_{3,\alpha\beta} \tag{3}$$

where, as in ordinary notation, Greek indices run from 1 to 2.

The constitutive behavior is defined by a strain energy function locally for each individual plate member

$$W=W(\epsilon_{\alpha\beta},\ \kappa_{\alpha\beta}), \tag{4}$$

generating membrane forces

$$N_{\alpha\beta}=\frac{\partial W}{\partial\epsilon_{\alpha\beta}}, \tag{5}$$

and bending moments

$$M_{\alpha\beta}=\frac{\partial W}{\partial\kappa_{\alpha\beta}} \tag{6}$$

with the notation simplified to $e^m_{\alpha\beta}=\epsilon_{\alpha\beta}$.

In their approach to determine energy release rates also based on a complementary strain energy function, Storåkers and Andersson (1988) introduced nominal membrane forces defined by

$$s_{\alpha i}=\frac{\partial W}{\partial u_{i,\alpha}}, \tag{7}$$

roman indices running from 1 to 3.

As a consequence of (2) and (5), it then follows that

$$s_{\alpha\beta}=N_{\alpha\beta} \tag{8}$$

and

$$s_{\alpha 3}=N_{\alpha\beta}u_{3,\beta}. \tag{9}$$

When a crack starts to grow smoothly by a local amount $\delta a$ as measured in the normal direction $n_\alpha$ and shown in Fig. 2, the change of the potential energy of the system $\delta U$ reduces to

$$-\delta U=\oint \|P_{\alpha\beta}\|n_\alpha n_\beta\delta a ds \tag{10}$$

where

$$P_{\alpha\beta}=W\delta_{\alpha\beta}-s_{\alpha\gamma}u_{\gamma,\beta}+M_{\alpha\gamma}u_{3,\gamma\beta}-Q_\alpha u_{3,\beta}, \tag{11}$$

Storåkers and Andersson (1988), $Q_\alpha$ denoting the shear force.

In particular, $\|\ \|$ denotes the jump locally at the crack contour and $P_{\alpha\beta}$ corresponds to a plate version of Eshelby's energy momentum tensor satisfying the balance equations

$$P_{\alpha\beta,\alpha}-p_iu_{i,\beta}=0 \tag{12}$$

where $p_i$ is the pressure on plate surfaces as shown in Fig. 1.

In order to determine explicitly the energy released per unit area of local crack growth, it is advantageous to align a coordinate direction $x_1$ normal to the crack front yielding the energy release rate

$$\|P_{11}\|=\|W-s_{1\alpha}u_{\alpha,1}+M_{1\alpha}u_{3,\alpha 1}-Q_1u_{3,1}\|. \tag{13}$$

By the coordinate system so introduced, simple continuity conditions will result at summation of individual lamina. Thus, regarding dynamic variables for in-plane membrane forces

$$s^o_{1\alpha}=\sum_k s^{(k)}_{1\alpha}, \tag{14}$$

and shear forces

$$Q^o_1=\sum_k Q^{(k)}_1, \tag{15}$$

in the notation depicted in Fig. 3, where $k=1,2$.

Likewise, regarding bending moments

$$M^o_{1\alpha}+x^o_3s^o_{1\alpha}=\sum_k\,(M^{(k)}_{1\alpha}+x^{(k)}_3s^{(k)}_{1\alpha}) \tag{16}$$

where $x^o_3$, $x^{(k)}_3$ denotes the distance to the middle surface of the individual plate, members referred to a common surface.

Regarding kinematics, and, in analogy, for compatibility in conformity with the Kirchhoff plate assumption,

$$u^{(k)}_\alpha-x^{(k)}_3u^{(k)}_{3,\alpha}=u^o_\alpha-x^o_3u^o_{3,\alpha},\quad u^{(k)}_3=u^o_3,\quad u^{(k)}_{3,1}=u^o_{3,1}, \tag{17}$$

where $u^o_3$, $u^{(k)}_3$ denotes the displacements at the middle surface of individual plate members and due to continuity, (17) admits

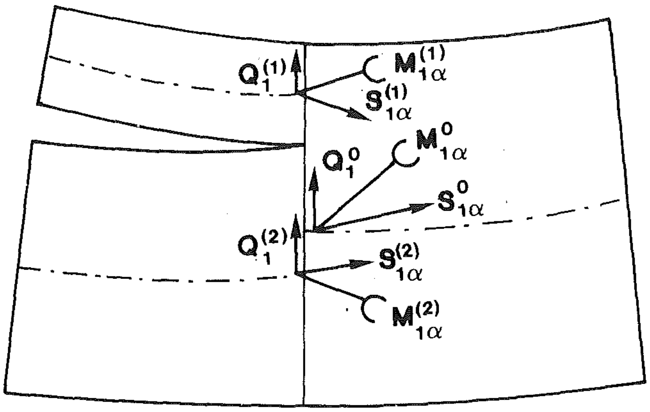


**Fig. 3 Split element with resulting plate variables**

further differentiation with respect to $\partial/\partial x_2$, i.e., along the crack front.

Summing up thus far and making use of the continuity conditions (14) to (17), the specific form of the energy release rate as given by (13) reduces to

$$P = W^o - s^o_{1\alpha}u^o_{\alpha,1} - M^o_{1\alpha}\kappa^o_{\alpha,1} - \sum_k (W^{(k)} - s^{(k)}_{1\alpha}u^{(k)}_{\alpha,1} - M^{(k)}_{1\alpha}\kappa^{(k)}_{\alpha 1}). \quad (18)$$

The general approach for plates and resulting Eq. (18) was sketched earlier (Storåkers, 1989) to apply also to shells, but details are still open for exploration. In case of imperfect plates, the matter may be formally dealt with within the Marguerre theory.

From several points of view it now proves advantageous for the so-posed plate problem to formally reduce the expression for the energy release rate by a superposition resulting in an equivalent split beam. Thus, a local homogeneous superposition at the crack front with

$$\bar{u}^o_i = -u^o_i, \quad (19)$$

together with associated derivatives, will render the deformation to vanish locally at the uncracked plate, as proposed in an ad hoc manner in particular situations by earlier writers, but more decisively and generally by Gudmundson (1989).

The associated superposed strains and curvatures then become

$$\bar{\epsilon}^o_{\alpha\beta} = -\epsilon^o_{\alpha\beta}, \quad \bar{\kappa}^o_{\alpha\beta} = -\kappa^o_{\alpha\beta}, \quad (20)$$

respectively, with dynamic variables accordingly.

By expressing the so-introduced locally homogeneous superposition by aid of variables associated with the cracked part of the plate, the resulting strains and curvatures become

$$\bar{\epsilon}^{(k)}_{\alpha 3} - x^{(k)}_3\bar{\kappa}^{(k)}_{\alpha\beta} = -\epsilon^o_{\alpha\beta} + x^o_3\kappa^o_{\alpha\beta}, \quad \bar{\kappa}^{(k)}_{\alpha\beta} = -\kappa^o_{\alpha\beta} \quad (21)$$

where $k = 1,2$.

Then, from a purely formal point of view, the energy release rate as given by (18) may be rearranged as

$$P = -\sum_k (W^{(k)} + \overline{W}^{(k)} - s^{(k)}_{1\alpha}u^{(k)}_{\alpha,1} - \bar{s}^{(k)}_{1\alpha}\bar{u}^{(k)}_{\alpha,1} - M^{(k)}_{1\alpha}\kappa^{(k)}_{\alpha 1} - \overline{M}^{(k)}_{1\alpha}\bar{\kappa}^{(k)}_{\alpha 1}). \quad (22)$$

So far the strain energy function $W$, (4), has been left unspecified, but towards a resulting true superposition principle, it is obvious that material linearity is required. Involving the restriction that $W$ is a quadratic though still otherwise arbitrary function of $\epsilon_{\alpha\beta}$, $\kappa_{\alpha\beta}$, then

$$2W = s_{\alpha\beta}\epsilon_{\alpha\beta} + M_{\alpha\beta}\kappa_{\alpha\beta}, \quad (23)$$

with an obvious associated reciprocity relation

$$s^{(1)}_{\alpha\beta}\epsilon^{(2)}_{\alpha\beta} + M^{(1)}_{\alpha\beta}\kappa^{(2)}_{\alpha\beta} = s^{(2)}_{\alpha\beta}\epsilon^{(1)}_{\alpha\beta} + M^{(2)}_{\alpha\beta}\kappa^{(1)}_{\alpha\beta}. \quad (24)$$

Thus, based on the introduced kinematic superposition (19), (20) with resulting continuity conditions (14), (16), (17) and the prescribed constitutive linearity (24), then (22) reduces to

$$P = -\sum_k \Big\{ \frac{1}{2} [(s^{(k)}_{\alpha\beta} + \bar{s}^{(k)}_{\alpha\beta})(\epsilon^{(k)}_{\alpha\beta} + \bar{\epsilon}^{(k)}_{\alpha\beta}) + (M^{(k)}_{\alpha\beta} + \overline{M}^{(k)}_{\alpha\beta})(\kappa^{(k)}_{\alpha\beta} + \bar{\kappa}^{(k)}_{\alpha\beta})] - (s^{(k)}_{1\alpha} + \bar{s}^{(k)}_{1\alpha})(u^{(k)}_{\alpha,1} + \bar{u}^{k}_{\alpha,1}) - (M^{(k)}_{1\alpha} + \overline{M}^{(k)}_{1\alpha})(\kappa^{(k)}_{\alpha 1} + \bar{\kappa}^{(k)}_{\alpha 1}) \Big\} \quad (25)$$

remembering also the kinematic continuity at the crack front, i.e.,

$$\bar{u}^{(k)}_{\alpha,2} + u^{(k)}_{\alpha,2} = 0, \quad \bar{u}^{(k)}_{3,\alpha} + u^{(k)}_{3,\alpha} = 0, \quad \bar{u}^{(k)}_{3,\alpha 2} + u^{(k)}_{3,\alpha 2} = 0 \quad (26)$$

by (17).

Through the Föppl strain definition, (2), finally the strain energy release rate simplifies to

$$P = \frac{1}{2}\sum_k [(s^{(k)}_{1\alpha} + \bar{s}^{(k)}_{1\alpha})(\epsilon^{(k)}_{1\alpha} + \bar{\epsilon}^{(k)}_{1\alpha}) + (M^{(k)}_{11} + \overline{M}^{(k)}_{11})(\kappa^{(k)}_{11} + \bar{\kappa}^{(k)}_{11})]. \quad (27)$$

As a consequence the energy release rate, as originally expressed for a nonlinear cracked plate, now follows simply for an equivalent split beam, although all three modes of opening, sliding, and shearing are involved. This technical result might possess some intrinsic virtues as regards energy release rates, but the main objective is continued partitioning of fracture modes from beams modeled in one or two dimensions.

## 3 Mode Partitioning of the Energy Release Rate

Already at homogeneous material behavior it is well known that the prediction of crack growth may not ordinarily result in a very high accuracy in mixed-mode situations when based on a simple energy balance criterion. Instead, it is customary, in Irwin's spirit, to decompose fracture parameters into the three fundamental crack modes by stress intensity factors. A crack growth criterion then has to be defined in a form

$$f(K_I, K_{II}, K_{III}) = 0 \quad (28)$$

to be given for a specific material.

In particular, when related to the energy release rate,

$$G = \frac{1-\nu^2}{E}(K_I^2 + K_{II}^2) + \frac{1}{2\mu}K_{III}^2 \quad (29)$$

for an isotropic material in ordinary notation, (28) may apply to one particular form when $G = G_c$ within Griffith's approach.

It is evident by (29) that in case of homogeneity, and at least cubic isotropy, the stress intensity factors are uncoupled and readily identified by the expression for the energy release rate. This is also so in more general situations and as regards the present plate theory when shearing modes are uncoupled from in-plane loading, resulting in opening $K_I$ and sliding $K_{II}$, the stress intensity factor $K_{III}$ may be immediately identified by (27) and (29) to read

$$K_{III}^2 = \sum_k \mu^{(k)}(s^{(k)}_{12})(\epsilon^{(k)}_{12} + \bar{\epsilon}^{(k)}_{12}) \quad (30)$$

when in-plane properties may be arbitrarily anisotropic.

The remaining modes are due to extension and bending given explicitly only by a coupled effective value. To attempt a further decomposition it is worthwhile, for simplicity, to first retain the assumptions of in-plane homogeneity and isotropy. Further, to make contact with engineering notation, new variables are introduced according to Fig. 4 such that by (27) and (29), an effective value becomes

$$K_I^2 + K_{II}^2 = \frac{E}{2(1-\nu^2)}[-(N\epsilon_1 + M\kappa_1) + N\epsilon_2 + M^*\kappa_2], \quad (31)$$

where, due to equilibrium,

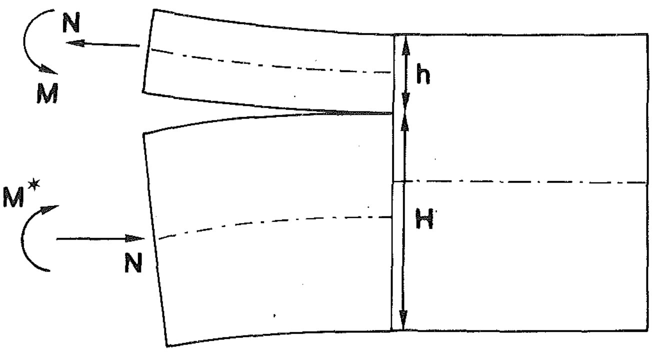


**Fig. 4 Split element with resulting beam variables after superposition**

$$M^* = M + N(h+H)/2. \tag{32}$$

To determine the stress intensity factors individually in a nonapproximate manner is only possible in truly symmetric and antisymmetric situations. Thus, in case of symmetry-induced geometry, $h = H$, and loading, $N = 0$, then at pure bending, $\kappa_1 = -\kappa_2$ with

$$K_I^2 = -\frac{E}{(1-\nu^2)} M\kappa_1, \quad K_{II} = 0 \tag{33}$$

exactly.

Likewise, in purely antisymmetric situations such that $h = H$ and $N = -2M/h$, then at antisymmetric bending $\kappa_1 = \kappa_2$ and

$$K_I = 0, \quad K_{II}^2 = -\frac{3E}{8(1-\nu^2)} M\kappa_1. \tag{34}$$

These results may also be combined and are asymptotically exact when $t \ll a$ (characteristic thickness to crack length) in the sense that it is tacitly assumed inherent in the present plate model. Thus, at combinations of loadings resulting in (33) and (34), mixed-mode fracture toughness results are viable for determination. Some particular cases for pure and mixed-mode split beams, also in case of orthotropy, have been illustrated by Hutchinson and Suo (1992). Although in an exact asymptotic sense cracks are required to be of infinite length, these writers have concluded that characteristic lengths of approximately $a > 3t$ will suffice at reasonable accuracy.

Explicitly, (33) and (34) may also be recovered from earlier direct beam results as given, e.g., by Tada et al. (1985). In the case of pure bending, these writers have also proposed a more general approach, and with nonsymmetric properties implying $\kappa_1 \neq -\kappa_2$. Such an attempt is, however, deemed to be approximate.

When based on (31), (32), it should be remembered that in (33) and (34) two solutions exist for $K_I$ and $K_{II}$, respectively, and they must be properly identified. If $K_I < 0$, the solution is physically inadmissible, as crack lips will be overlapping in the present situation. For $K_{II}$, the proper sign of sliding must be in conformity with the external loading.

Starting from a different assumption, Williams (1988) has argued that for two beams having equal curvatures, pure mode II will result and admit decoupling in general situations. Again, this proposal will simply predict mode I at pure bending, although it is known from two-dimensional analysis in this situation that the ratio $K_{II}/K_I$ is generally nonzero, except in case of full symmetry. In particular, when the thickness of one member is vanishing, the mode ratio will take on a maximum value $K_{II}/K_I$ of 0.786 as determined by a boundary collocation method (Cotterell et al., 1985) and 0.777 by an integral equation method (Thouless et al., 1987).

Additional two-dimensional results for a split beam subjected to stretching and bending are given by Suo and Hutchinson (1990) for isotropic bimaterials. For the particular case of homogeneous beam properties at pure bending, the mode results for the thickness ratio are reproduced in Fig. 5. It may be seen in particular that a mode II component may be substantial, although the external loading is due only to symmetric bending moments.

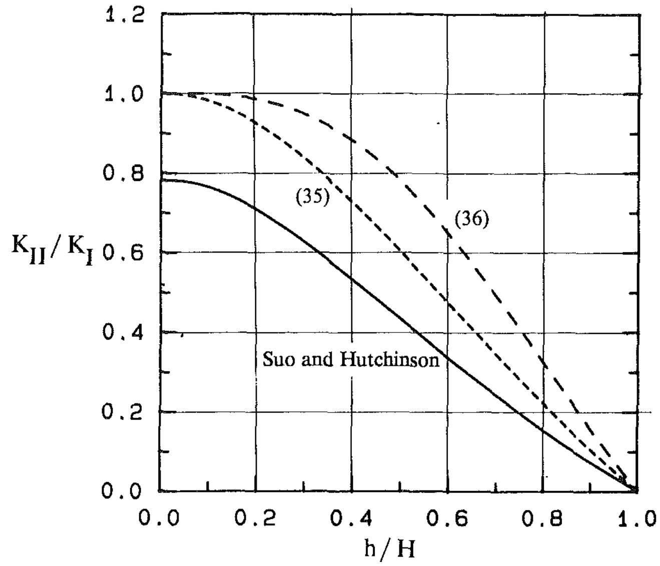


**Fig. 5 Ratio of stress intensity factors, $K_{II}/K_I$, as function of thickness ratio, $h/H$, for pure bending of a split beam according to Suo and Hutchinson (1990), (35) and (36), respectively**

Although similar findings are available from two-dimensional analysis, also in more general situations it might be tempting in the spirit of Williams (1988) to attempt a decomposition of stress intensity factors from kinematic symmetry and antisymmetry arguments based on the Euler-Bernoulli beam theory (Storåker's (1989)).

Possible candidates may be based on maximum strains at the crack tip resulting in

$$\frac{K_{II}}{K_I} = \frac{h\kappa_1 + H\kappa_2}{h\kappa_1 - H\kappa_2} \tag{35}$$

or deflections such that

$$\frac{K_{II}}{K_I} = \frac{\kappa_1 + \kappa_2}{\kappa_1 - \kappa_2} \tag{36}$$

as related to Fig. 4.

Based on (27), (35), and (36), it is readily found that in both cases the energy release rate decouples. The resulting ratios $K_{II}/K_I$ are also given in Fig. 5 as a comparison to exact ones by Suo and Hutchinson (1990). It is evident though that the accuracy is at most moderate, although symmetry assumptions based on strains, (35), are favorable as compared to deflections, (36). Whatever measures are adopted though, when the thickness of one beam member is vanishing, i.e., $\kappa_2 \to 0$, it is inevitable that $K_{II}/K_I \to 1$, $(\kappa_2/\kappa_1 < 0)$, which is in substantial contrast to the exact value 0.777 as indicated above.

An alternative to determine energy release rates in reduced form (and applicable also to plates) was recently proposed by Schapery and Davidson (1990). In particular, their approach is based on resulting internal forces and moments acting at crack-tip boundaries. For decomposition into stress intensity factors, Schapery and Davidson (1990) rely on finite element solutions as demonstrated by way of particular illustrations. These writers also recognize the advantage of possibly avoiding numerical two-dimensional solutions, and by conjecture, essentially assume $K_I$-values to be independent of in-plane forces.

Following this approach, in the discriminating case of pure bending as analyzed previously, the conjecture does indeed lead to nonvanishing $K_{II}$-values, although in the extreme case of vanishing thickness, $K_{II}/K_I$ turns out to be $\sqrt{3}$ in contrast to the exact value 0.777 in case of homogeneity and isotropy. Thus, to arrive at a general but reasonable approximation for beams of stress intensity factors, it is not to be anticipated remembering also the severe kinematical constraints introduced by the Euler-Bernoulli theory in two-dimensional situations.

Recapitulating then members discussed so far (such as laminates, sandwich plates, and thin films) may manifest themselves through nonlinear plates as outlined above, and again by the superposition principle, the resulting energy release rate will reduce locally to that of crack growth in an equivalent linear beam. Toward prediction of mode-dependent fracture, however, it is notoriously well known that for interface cracks in bimaterials, stress intensity factors may not be unambiguously defined. Thus, separability of modes at interface cracks of anisotropic bimaterials is much restricted. For one thing, necessary and sufficient conditions have only recently been detailed by Qu and Bassani (1988) for purely two-dimensional situations or when in-plane and antiplane deformations decouple. The resulting standard square-root singularity has then been explicitly illustrated for a finite Griffith crack by Bassani and Qu (1989).

At the interface of a plane isotropic bimaterial case, singular stresses may be expressed by aid of complex variables in the notation by Rice (1988) as

$$\sigma_{22}+i\sigma_{12}=\frac{Kr^{i\epsilon}}{\sqrt{2\pi r}} \tag{37}$$

where

$$K=K_1+iK_2, \quad \epsilon=\frac{1}{2\pi}\ln\frac{1-\beta}{1+\beta} \tag{38}$$

with $\beta$ given by the Dundurs parameter,

$$2\beta=\frac{\mu_1(1-2\nu_2)-\mu_2(1-2\nu_1)}{\mu_1(1-\nu_2)+\mu_2(1-\nu_1)}, \tag{39}$$

for Hookean materials.

For a bimaterial, when stress amplitudes are given in a complex fashion, their dimension also becomes awkward. At first instance, however, this does not affect the original problem posed to reduce results for nonlinear plates to that of nonlinear beams, as at any event, the energy release rate will be a real-valued quantity (Malyshev and Salganik, 1965), and in particular, for isotropic solids (Hutchinson et al., 1987),

$$G=\left(\frac{1-\nu_1}{\mu_1}+\frac{1-\nu_2}{\mu_2}\right)\frac{K\overline{K}}{4\cosh^2\pi\epsilon}+\left(\frac{1}{\mu_1}+\frac{1}{\mu_2}\right)\frac{K_{III}^2}{4}. \tag{40}$$

Thus, once the energy release rate has been identified in equivalent beam variables, the composition of singular stresses may be immediately read off from the two-dimensional results given for individually isotropic bimaterials (Suo and Hutchinson (1990) and also orthotropic ones, Suo (1990)).

Only when $\beta=0$ in (39) do the stress amplitudes in (38) reduce to the conventional stress intensity factors. The energy release rate may then be decomposed into

$$G=\frac{1}{2}\left(\frac{1-\nu_1^2}{E_1}+\frac{1-\nu_2^2}{E_2}\right)(K_I^2+K_{II}^2)+\frac{1}{4}\left(\frac{1}{\mu_1}+\frac{1}{\mu_2}\right)K_{III}^2 \tag{41}$$

(Hutchinson, 1990), with all three modes unambiguously present at uncoupled shearing.

Toward identifying fracture parameters, for representative materials, $\epsilon$ is usually expected to be small by a few percent (Suga et al., 1988). A pragmatic view used to obtain stress intensity factors, as advocated in particular by Hutchinson (1990), is to suppress the oscillatory material behavior and adopt $\beta=0$. In this approximation, the ratio of stress intensity factors will reduce to an ordinary value while the energy release rate may be left unaffected. The matter will not be elaborated upon further at this time.

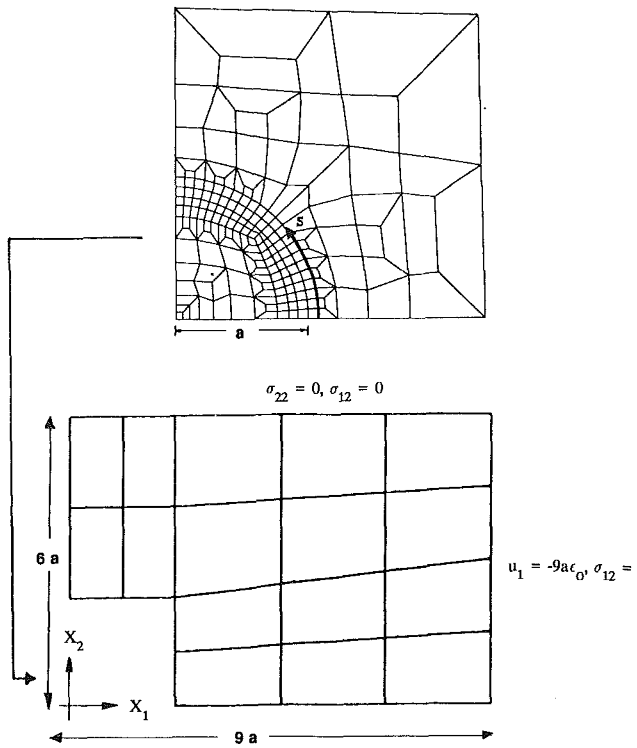


**Fig. 6 FEM mesh for a circular delamination under uniaxial nominal compression**

## 4 Buckling and Growth of a Circular Delamination Under Uniaxial Compression

The efforts so far have been focused on an efficient method to determine energy release rates eventually and ensuing identification of stress intensities at nonlinear kinematics. What remains to elaborate on is a procedure to predict and analyze interfacial fracture initiation and possible growth. To deal with the latter problem (which is, essentially, to determine a moving boundary), a recent method proposed by Nilsson and Giannakopoulos (1990a, 1990b) will be drawn upon.

Crack growth for delaminated plate members had been dealt with earlier, to a large extent, for rectilinear and circular crack contours; (e.g., Chai et al., 1981; Evans and Hutchinson, 1984; and Yin, 1985) and by commonly implying material homogeneity and isotropy. On the other hand, for nontrivial contours, cracks seem to have been analyzed only for initiation. To that end and in order to also accommodate combined buckling and crack growth, the necessary details will be briefly outlined.

The problem in formulating von Karman equations for bifurcation buckling and post-buckling is a standard one and has essentially been posed previously, save for the equilibrium equations

$$s_{\alpha\beta,\alpha}+p_\beta=0 \tag{42}$$

and

$$M_{\alpha\beta,\alpha\beta}+s_{\alpha3,\alpha}+p_3=0 \tag{43}$$

in the previous notation, and obvious boundary conditions consonant with Fig. 1.

A particular member to be analyzed was chosen as a single embedded circular delamination on a thick substrate subjected to uniaxial nominal compression. To deal with delamination growth a finite element mesh, combined with an automatic mesh generator, was designed as shown in Fig. 6. Due to

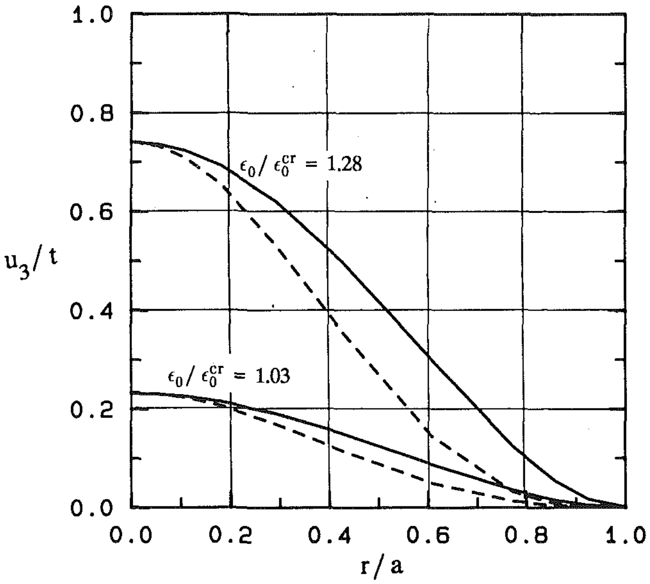


Fig. 7 Transverse displacement distribution for buckled plate, $u_3/t$, along $x_1=0$, (—), and $x_2=0$, (----), for $\epsilon_0/\epsilon_0^{cr}=1.03$ and 1.28, respectively

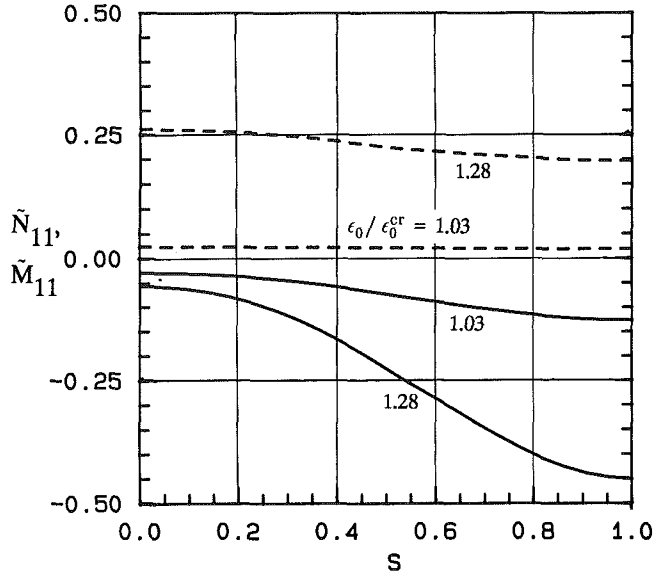


Fig. 8 Nondimensional beam variables $\tilde{N}_{11}(s)$, (----), and $\tilde{M}_{11}(s)$, (—), along the circular delamination front for $\epsilon_1/\epsilon_0^{cr}=1.03$ and 1.28, respectively

symmetry of the stated problem, only one quarter was modeled. Thus, the global plate illustrated was rectangular with side lengths $18a$ and $12a$—the circular delamination having the radius $a$.

When the prospective crack front moves, the associated mesh must be updated. Then the front is adopted as an internal boundary and is displaced. The associated change of element angles was minimized (in a weak sense) resulting in a new effective mesh in a way as detailed by Nilsson and Giannakopoulos (1990a, 1990b).

The finite element method itself was based on the plate theory using four-noded shell elements (Bathe, 1982) and implemented in a finite element code Solvia. The program utilizes large deformations in the sense of full Green-Lagrange finite strains and Mindlin's plate theory. For computational convenience, these features were presently adopted. With small strains and transverse deflections being of the same order of laminate thickness, however, the actual difference from the moderate rotation von Karman theory was found to be negligible.

The illustrated procedure was chosen partly for technical reasons and, for simplicity, the homogeneous isotropic linear elastic material behavior, $E,\nu$, was adopted. Further, the substrate was assumed to be substantially thicker than the plate lamina, $t$.

As a consequence, the kinematical constraints

$$u_3=0, \quad u_{3,\alpha}=0 \tag{44}$$

were enforced for the thick plate including the internal boundary.

For nominal uniaxial compression, the conjugate boundary conditions for the global plate reduce to

$$u_1=-9a\epsilon_0, \quad \sigma_{12}=0 \tag{45}$$

for $x_1=9a$ and

$$\sigma_{2\alpha}=0 \tag{46}$$

for $x_2=6a$ in conformity with Fig. 6. For explicitness, $t/a=0.05$ and $\nu=0.3$ were chosen.

Once the boundary value problem had been formulated in the manner outlined, the bifurcation buckling problem was solved first. It was found then that buckling initiated at $\epsilon_o^{cr}=2.52\ (t/a)^2$, the critical value of nominal strain as prescribed in (45). The associated buckling mode was then drawn upon to carry out a post-buckling analysis.

The results for transverse displacements $u_3/t$ of the delaminated plate are shown in Fig. 7 for two loadings $\epsilon_o=1.03\ \epsilon^{cr}$ and $1.28\ \epsilon_o^{cr}$, respectively. It is evident then that the relative change in shape is not substantial when normalized displacements are still less than unity. What is more noteworthy, however, and to be further elaborated upon below, is that contact will occur at $x_1=a$, $x_2=0$ at higher loading.

The resulting forces $N_{1\alpha}$ and moment $M_{11}$ aligned locally at the crack front (and necessary to determine energy release rates) are readily found from the nonlinear plate analysis, and subsequently also the associated beam variables from the superposition principle. In order to reproduce the superposed beam variables as in (27), it proved practical to introduce nondimensional forms according to

$$\tilde{N}_{1\alpha}=\frac{1-\nu^2}{Et}\left(\frac{a}{t}\right)^2(s_{1\alpha}+\bar{s}_{1\alpha}),$$

$$\tilde{M}_{11}=\frac{1-\nu^2}{Et^2}\left(\frac{a}{t}\right)^2(M_{11}+\overline{M}_{11}) \tag{47}$$

and also similarly for energy release rates

$$\tilde{G}=\frac{1-\nu^2}{Et}\left(\frac{a}{t}\right)^4 G \tag{48}$$

and stress intensity factors

$$\tilde{K}_{I,II}=\frac{1-\nu^2}{Et^{1/2}}\left(\frac{a}{t}\right)^2 K_I,\ K_{II} \tag{49}$$

where accordingly,

$$\tilde{G}=\tilde{K}_I^2+\tilde{K}_{II}^2 \tag{50}$$

at vanishing $K_{III}$.

Shear forces $\tilde{N}_{12}$ were found to be of the order of one percent as related to compressive forces $\tilde{N}_{11}$, and accordingly, the magnitude of the stress intensity factor $K_{III}$ proved to be negligible and will not be discussed further. A similar feature in resembling circumstances has been reported by Whitcomb (1988) based on three-dimensional finite element results and by Chai (1990) for a Rayleigh-Ritz procedure.

The values of the remaining local beam variables are reproduced by a coordinate $s$ scaled along the current crack contour as was shown earlier in Fig. 2 (generally) and in Fig. 6. In Fig. 8 the results for $\tilde{N}_{11}$, $\tilde{M}_{11}$ are shown for two cases of the external loading where the smaller one corresponds approximately to

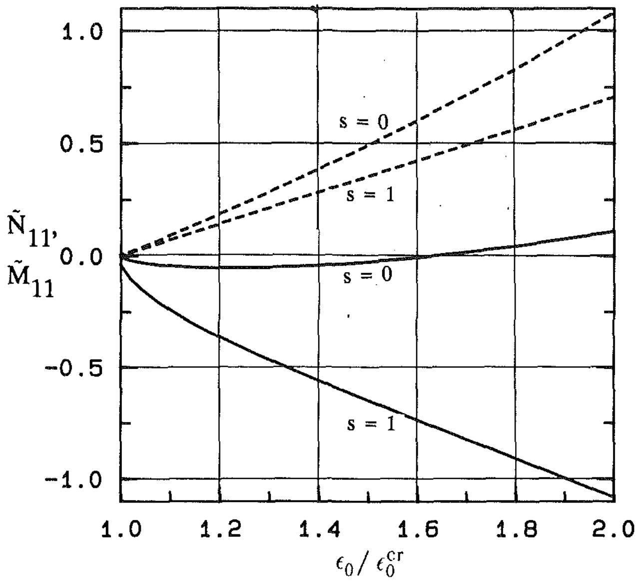


Fig. 9 Nondimensional beam variables, $\tilde{N}_{11}$, (····), and $\tilde{M}_{11}$, (—) normal, $s=0$, and transverse, $s=1$, to the loading direction as function of the compressive loading, $\epsilon_0/\epsilon_0^{cr}$

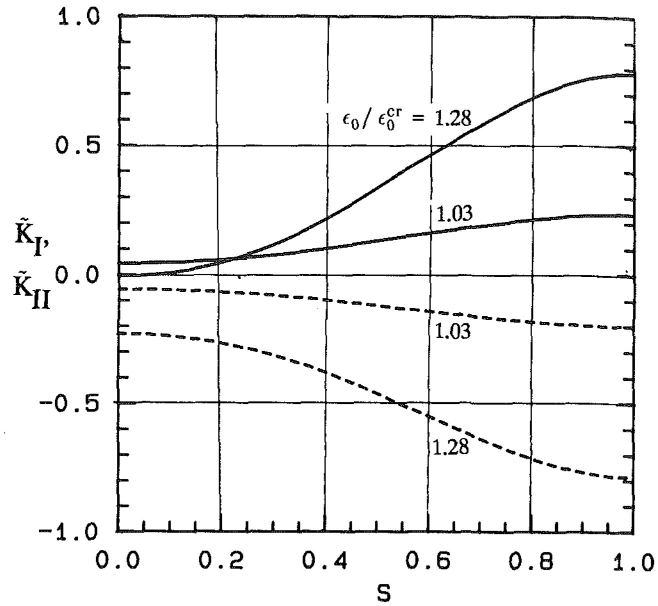


Fig. 10 Nondimensional stress intensity factors, $\tilde{K}_I$, (—), and $\tilde{K}_{II}$, (····), along the circular delamination front for $\epsilon_0/\epsilon_0^{cr}=1.03$ and 1.28, respectively

initiation of buckling and the larger one to an increase of 25 percent. As may be seen, the reduced compressive force $\tilde{N}_{11}$ ($s$) is fairly evenly distributed along the crack contour in both cases, although their magnitudes differ by a factor of ten. The bending moment $\tilde{M}_{11}$ ($s$) increases along the crack front at initial buckling and substantially so at higher loading.

Extreme values for the beam variables appear in the loading direction and its transverse. In Fig. 9, pertinent results are shown as a function of nominal strain up to twice the value for initial buckling. The compressive force increases monotonically at the crack front, whereas the bending moment locally reaches a maximum at about 20 percent above the nominal buckling strain and eventually changes sign at 65 percent indicating approaching crack-lip overlapping.

Once the reduced beam variables have been determined, the corresponding stress intensity factors may be readily read off from the two-dimensional results by Suo and Hutchinson (1990). In particular, for identical isotropic materials and a lamina of vanishing thickness, the stress intensity factors reduce to

$$\tilde{K}_I=\frac{1}{\sqrt{2}}\,(-\tilde{N}_{11}\cos\omega-2\sqrt{3}\tilde{M}_{11}\sin\omega) \tag{51}$$

$$\tilde{K}_{II}=\frac{1}{\sqrt{2}}\,(-\tilde{N}_{11}\sin\omega-2\sqrt{3}\tilde{M}_{11}\cos\omega) \tag{52}$$

where $\omega=52,1^o$.

It should be observed first that when $\tilde{N}_{11}>-2\sqrt{3}\tilde{M}_{11}\tan\omega$, $K_I$ becomes negative and crack lips will be expected to overlap. Presently, for the case studied, this will occur at $s=0$ for $\epsilon_o=1.28\,\epsilon_o^{cr}$. Thus at still higher loading, when physically acceptable results are to apply, contact has to be considered when two-dimensional theory is observed. In contrast, from Fig. 9 it may be seen that at $\epsilon_o=1.28\cdot\epsilon_o^{cr}$ the bending moment (implying positive curvature) is still negative everywhere, and based on plate theory contact will not be expected until $\epsilon_o=1.65\,\epsilon_o^{cr}$. In retrospect then, the venture of extracting stress intensity factors from pure beam theory appears even less appealing.

Accordingly, the difference between results based on resulting forces and moments on one hand and local stress amplitudes on the other should be clearly emphasized when crack closure is at issue. The matter has recently been analyzed by Chai (1990) at buckling of embedded elliptical delaminations based on a Rayleigh-Ritz procedure. In particular, for the circular case, Chai found no closure to occur at uniform compression whether at the crack front or elsewhere. At uniaxial compression, however, Chai found that closure will always occur and initiate at crack tips. In the present case, overlapping is expected at $\epsilon_o=1.25\,\epsilon_o^{cr}$ in good agreement with the value 1.28 above. The influence of contact on delamination buckling is otherwise little known, but the matter has recently been approached in the present circumstances also by Whitcomb (1989a, 1990). In the case of uniform compression and multiple delaminations based on plate theory Larsson (1991) has found that the influence on energy release rates might be substantial.

In Fig. 10 the stress intensity factors $\tilde{K}_I(s)$ and $\tilde{K}_{II}(s)$ are given for the two load levels. Both factors increase monotonically along the crack front at both loadings yielding maxima transversely to the applied nominal uniaxial compression. It should be observed, however, that at increased loading $K_I$ decreases for $s<0.2$, approximately, again remembering that contact may be imminent.

In Fig. 11, stress intensity factors at the extreme points at the crack contour are given as a function of the compressive loading. At the maximum values and transversely to the loading, both factors increase monotonically and are of fairly equal magnitude. At the loading direction $K_{II}$ also increases monotonically, but considerably less so. As has already been premised, $K_I$ reaches a maximum, approximately at ten percent above the buckling load, and at higher loading, 28 percent, $K_I$ is expected to change its sign.

In order to predict fracture initiation and growth of delaminated members, a growth criterion is of necessity. It is a common experience in fracture mechanics that, in general, critical values for sliding modes ($K_{II}$) are higher than those of opening ($K_I$). Several criteria for composites have been proposed and formulated based on particular material-dependent parameters, some of them summarized by Storåkers (1989), and in general circumstances discussed as to consequences by Hutchinson and Suo (1992). Presently, and once a criterion has been established for a particular material expressed by aid of stress intensity factors, the automatic mesh generator worked out to simulate the evolution of the crack front may be directly applied. It goes without saying, though, that at anisotropic material behavior and nontrivial crack contours, determination

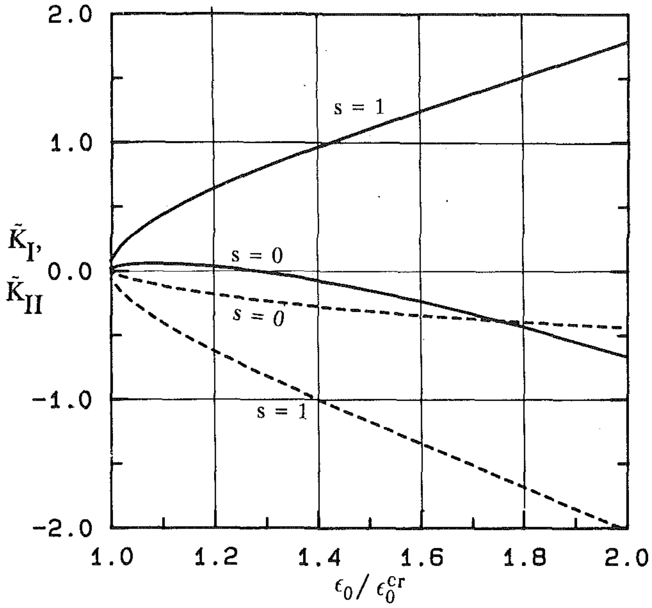


Fig. 11 Nondimensional stress intensity factors, $\tilde{K}_I$, (—), and $\tilde{K}_{II}$, (····), normal, $s=0$, and transverse, $s=1$, to the loading direction as function of the compressive loading, $\epsilon_0/\epsilon_0^{cr}$

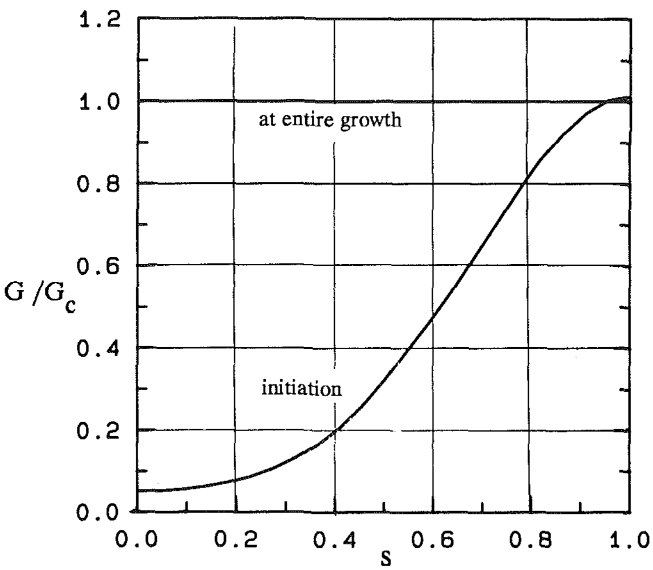


Fig. 12 Normalized energy release rate, $G/G_c$, along delamination contour at initiation of growth and at entire front propagation

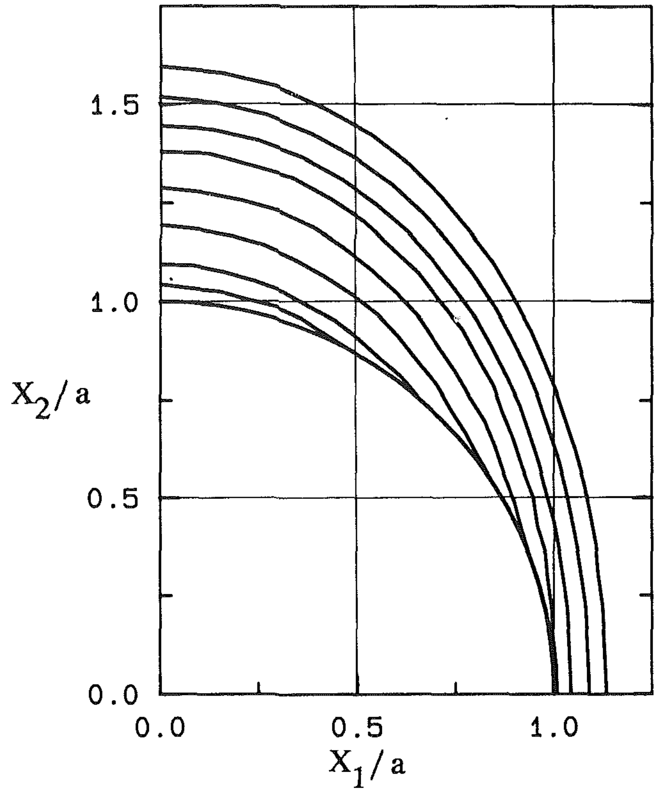


Fig. 13 Loci of delamination front at consecutive stages of growth

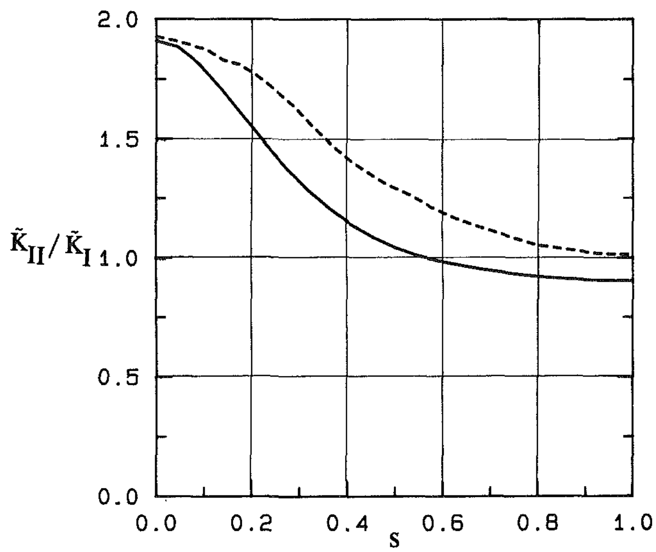


Fig. 14 Ratio of stress intensity factors, $\tilde{K}_{II}(s)/\tilde{K}_I(s)$, at initiation, (—) and after 38 percent of crack length growth of delamination front, (····)

of growth might be technically quite intricate. To complete the present intention and illustrate the method for growth prediction, the simple Griffith criterion

$$G = G_c \tag{53}$$

will be presently retained. From a recent review by Sela and Isai (1989) of fracture properties of different composite material systems, in case of graphite/PEEK (polyetheretherketone), data may be well accommodated by Eq. (53) while, for instance, graphite/epoxy seems to exhibit pronounced mode dependence.

In practical situations a typical value of $\tilde{G}_c$, (48), is of order unity and presently $\tilde{G}_c = 0.281$ was chosen to analyze the evolution of the crack front.

In Fig. 12, the normalized distribution of the energy release rate, $\tilde{G}(s)/\tilde{G}_c$, is given for the initially circular crack front and shows a substantial variation. Evidently, the growth criterion is first fulfilled at $s=1$, and accordingly growth will first be initiated transversely to the loading.

In Fig. 13, the determined evolution of the crack front is shown for different values of the external loading based directly on computer results with the lacking smoothness at kinks indicating the accuracy. Growth is initiated at $\epsilon_o = 1.08\ \epsilon_o^{cr}$ and the whole front is finally moving at $\epsilon_o = 0.79\ \epsilon_o^{cr}$. Thus, the external load required to sustain crack growth is steadily decreasing, and at the last front shown in Fig. 13, it corresponds to $\epsilon_o = 0.68\ \epsilon_o^{cr}$. In this sense the system must be termed unstable.

As emphasized, however, this result is sensitive to the particular fracture criterion used. In Fig. 14, the ratio $K_{II}(s)/K_I(s)$

is shown at local initiation of growth and at full crack length. Thus, although the moving front is almost of elliptical shape in the advanced stages of growth, as shown in Fig. 13, this feature might be closely related to the simple quadratic fracture criterion employed in (50) and (53). The predicted transverse delamination growth at buckling under uniaxial compression has, however, been observed experimentally for different materials by several investigators recently, for instance, by Whitcomb (1989b) for a toughened graphite/epoxy.

## 5 Concluding Remarks

It was shown that the energy release rate, due to smooth local crack growth along a delamination front for plate members at moderate rotations, proved to be equivalent to that of associated linear beams by an appropriate superposition procedure. When constitutive coupling is not at hand, however, stress intensity factors $K_{III}$ at shearing could be extracted exactly by beam analysis. A further general decomposition into in-plane mode-dependent variables proved to be of inadequate accuracy in general when based on beam theory and simple symmetry arguments. Instead, to determine the remaining stress intensity factors and to detect imminent contact, it proved powerful, by the introduced reduction of plate theory, to draw upon earlier asymptotic numerical analyses of split bimaterial beams. An effective method was devised earlier by finite elements and an automatic mesh generator was employed to determine propagation of delamination fronts. Accordingly, the procedure proposed offers a unified analysis of the fracture process in fairly general circumstances.

## References


Bathe, K. J., 1982, *Finite Element Procedures in Engineering Analysis*, Prentice-Hall, Englewood Cliffs, N.J.

Bassani, J. L., and Qu, J., 1989, "Finite Crack on Bimaterial and Bicrystal Interfaces." *Journal of the Mechanics and Physics of Solids*, Vol. 37, pp. 435–453.

Chai, H., Babcock, C. D., and Knauss, W. G., 1981, "One Dimensional Modeling of Failure in Laminated Plates by Delamination Buckling," *International Journal of Solids and Structures*, Vol. 17, pp. 1069–1083.

Chai, H., 1990, "Three-Dimensional Fracture Analysis of Thin-Film Debonding," *International Journal of Fracture*, Vol. 46, pp. 237–256.

Cotterell, B., Kamminga, J., and Dickson, F. P., 1985, "The Essential Mechanics of Conchoidal Flaking," *International Journal of Fracture*, Vol. 29, pp. 101–119.

Evans, A. G., and Hutchinson, J. W., 1984, "On The Mechanics of Delamination and Spalling in Compressed Films," *International Journal of Solids and Structures*, Vol. 20, pp. 455–466.

Gudmundson, P., 1989, personal communication, Department of Solid Mechanics, Royal Institute of Technology, Stockholm, Sweden.

Hutchinson, J. W., Mear, M. E., and Rice, J. R., 1987, "Crack Paralleling an Interface Between Dissimilar Materials," ASME Journal of Applied Mechanics, Vol. 54, pp. 828–832.

Hutchinson, J. W., 1990, "Mixed Mode Fracture Mechanics of Interfaces," *Acta-Scripta Metallurgica Proceedings Series*, Vol. 4, pp. 295–306.

Hutchinson, J. W., and Suo, Z., 1992, "Mixed Mode Cracking in Layered Materials," *Advances in Applied Mechanics*, Vol. 29, J. W. Hutchinson and T. H. Wu, eds., Academic Press, New York, pp. 63–191.

Larsson P.-L., 1991, "On Multiple Delamination Buckling and Growth in Composite Plates," *International Journal of Solids and Structures*, Vol. 27, pp. 1623–1637.

Malyshev, B. M., and Salganik, R. L., 1965, "The Strength of Adhesive Joints using the Theory of Cracks," *International Journal of Fracture*, Vol. 1, pp. 114–128.

Nilsson, K.-F., and Giannakopoulos, A. G., 1990a, "Finite Element Simulation of Delamination Growth," *Proceedings of the first International Conference on Computer-Aided Assessment and Control of Localized Damage*, M. H. Aliabadi, C. A. Brebbia, and D. J. Cartwright, eds., pp. 299–313.

Nilsson, K.-F., and Giannakopoulos, A. G., 1990b, "Finite Element Simulation of Delamination Growth," Report-125, Department of Solid Mechanics, Royal Institute of Technology, Stockholm, Sweden.

Qu, J., and Bassani, J. L., 1989, "Cracks on Bimaterial and Bicrystal Interfaces," *Journal of the Mechanics and Physics of Solids*, Vol. 37, pp. 417–433.

Rice, J. R., 1988, "Elastic Fracture Mechanics Concepts for Interfacial Cracks," ASME Journal of Applied Mechanics, Vol. 55, pp. 98–103.

Sela, N., and Isai, D., 1989, "Interlaminar Fracture Toughness and Toughening of Laminated Composite Materials: A Review," *Composites*, Vol. 20, pp. 423–435.

Schapery, R. A., and Davidson, B. D., 1990, "Prediction of Energy Release Rate for Mixed-Mode Delamination Using Classical Plate Theory," Texas A&M University, Report No. MM. 9045-90-3.

SOLVIA, Licensed by Solvia Engineering AB, Västerås, Sweden.

Suga, T., Elssner, G., and Schmauder, S., 1988, "Composite Parameters and Mechanical Compatibility of Material Joints," *Journal of Composite Materials*, Vol. 22, pp. 917–934.

Storåkers, B., and Andersson B., 1988, "Nonlinear Plate Theory Applied to Delamination in Composites," *Journal of the Mechanics and Physics of Solids*, Vol. 36, pp. 689–718.

Storåkers, B., 1989, "Nonlinear Aspects of Delamination in Structural Members," *Proceedings of the 17th International Congress of Theoretical and Applied Mechanics*, P. Germain, M. Piau, and D. Caillerie, eds., Elsevier, New York, pp. 315–336.

Suo, Z., 1990, "Delamination Specimens for Orthotropic Materials," ASME Journal of Applied Mechanics, Vol. 57, pp. 627–634.

Suo, Z., and Hutchinson, J. W., 1990, "Interface Crack Between Two Elastic Layers," *International Journal of Fracture*, Vol. 43, pp. 1–18.

Tada, H., Paris, P. C., and Irwin, G. R., 1985, *The Stress Analysis of Cracks Handbook*, Del Research, St. Louis, MO.

Thouless, M. D., Evans, A. G., Ashby, M. F., and Hutchinson, J. W., 1987, "The Edge Cracking and Spalling of Brittle Plates," *Acta Metallurgica*, Vol. 35, pp. 1333–1341.

Whitcomb, J. D., 1988, "Mechanics of Instability-Related Delamination Growth," NASA TM-100622.

Whitcomb, J. D., 1989a, "Three-Dimensional Analysis of a Postbuckled Embedded Delamination," *Journal of Composite Materials*, Vol. 23, pp. 862–889.

Whitcomb, J. D., 1989b, "Predicted and Observed Effects of Stacking Sequence and Delamination Size on Instability Related Delamination Growth," *Journal of Composites Technology and Research*, Vol. 11, pp. 94–98.

Whitcomb, J. D., 1990, "Analysis of a Laminate with a Postbuckled Embedded Delamination, Including Contact Effects," Texas A&M University Report No. CMC 0000-90-2.

Williams, J. G., 1988, "On the Calculation of Energy Release Rates for Cracked Laminates," *International Journal of Fracture*, Vol. 36, pp. 101–119.

Yin, W. L., 1985, "Axisymmetric Buckling and Growth of a Circular Delamination in a Compressed Laminate," *International Journal of Solids and Structures*, Vol. 21, pp. 503–514.

**Tungyang Chen**[1]

**George J. Dvorak**
Fellow ASME.

Department of Civil Engineering,
Rensselaer Polytechnic Institute,
Troy, NY 12180-3590

**Yakov Benveniste**

Department of Solid Mechanics,
Materials and Structures,
Tel-Aviv University,
Tel-Aviv, Israel

# Mori-Tanaka Estimates of the Overall Elastic Moduli of Certain Composite Materials

*Simple, explicit formulae are derived for estimates of the effective elastic moduli of several multiphase composite materials with the Mori-Tanaka method. Specific results are given for composites reinforced by aligned or randomly oriented, transversely isotropic fibers or platelets, and for fibrous systems reinforced by aligned, cylindrically orthotropic fibers.*

## 1 Introduction

Estimates of overall elastic moduli of composite materials, in terms of phase geometry and moduli, can be obtained by several well-known methods. For example, the Hashin-Shtrikman bounds which bracket the actual magnitudes of the moduli are available for many two-phase and multiphase systems (Hashin and Shtrikman 1963, Walpole 1969, 1981, 1984). Also, self-consistent estimates have been available for many years for such systems as aligned fiber composites (Hill 1965a), two-phase media reinforced by spherical particles (Budiansky 1965), or by randomly orientated inclusions of various shapes (Walpole 1969), and for multiphase aggregates with fibrous and penny-shaped (platelet) inclusions (Laws, 1974). Other such estimates were found by Christensen and Waals (1972), Boucher (1974), Berryman (1980), Cleary, Chen, and Lee (1980), and Willis (1981). The conditions which guarantee that the self-consistent estimates lie within the bounds were established by Hill (1965b) and Walpole (1969, 1981).

In its recent reformulation by Benveniste (1987), the Mori-Tanaka (1973) method offers another alternative to finding estimates of elastic moduli and local fields in composite materials. Recent applications include the work of Weng (1984) who found the effective bulk and shear moduli of two and three-phase composites with spherical isotropic inclusions in an isotropic matrix. Benveniste, Dvorak, and Chen (1989) applied this method to coated fiber composites. Zhao, Tandon, and Weng (1989) derived the effective moduli for a class of porous materials with various distributions. Norris (1989) examined many aspects of the method and its relation to the Hashin-Shtrikman bounds.

The present paper is concerned with evaluation of estimates of overall elastic moduli of certain composite materials by the Mori-Tanaka method. In particular, we consider multiphase composites reinforced either by aligned fibers or platelets, and similar systems with randomly oriented reinforcement. In either case, the reinforcement may be isotropic or transversely isotropic. Moreover, we examine fibrous composites reinforced by cylindrically orthotropic fibers. As Benveniste, Dvorak, and Chen (1991a) have shown, both the Mori-Tanaka and the self-consistent methods deliver diagonally symmetric estimates of overall stiffness in the selected systems. However, such symmetry does not obtain in estimates of overall stiffness for multiphase systems with inclusions of different shapes or orientation.

We start with a summary of most of the present results. This is followed by an outline of the method and its application to the selected systems. For the most part, the derivation is relatively straightforward. However, the cylindrically orthotropic fibers call for a special treatment. Some of the moduli are found by replacement of the actual fiber by an equivalent transversely isotropic fiber, but this approach does not extend to the shear modulus in the transverse plane. That particular result can be extracted only from a numerical evaluation of the overall stiffness tensor.

## 2 Phase and Overall Properties

Fibers and platelets used as composite reinforcements are often transversely isotropic. The same is true for composite aggregates reinforced by aligned fibers or platelets. If the axis of symmetry is chosen as parallel to the $x_1$-axis of a Cartesian coordinate system, then the elastic response of a transversely isotropic solid may be described in the form:

$$\begin{bmatrix} s \\ \sigma \end{bmatrix} = \begin{bmatrix} k & l \\ l & n \end{bmatrix} \begin{bmatrix} e \\ \epsilon \end{bmatrix} \qquad (1)$$

$$\tau_{23} = 2m\epsilon_{23},\ \tau_{12} = 2p\epsilon_{12},\ \tau_{13} = 2p\epsilon_{13}$$

where

$$s = \frac{1}{2}(\sigma_{22} + \sigma_{33}),\ \sigma = \sigma_{11},\ e = \epsilon_{22} + \epsilon_{33},\ \epsilon = \epsilon_{11}, \qquad (2)$$

and $k$, $l$, $m$, $n$, and $p$ are Hill's elastic moduli (1964). In particular, $k$ is the plane-strain bulk modulus for lateral dil-

Contributed by the Applied Mechanics Division of THE AMERICAN SOCIETY OF MECHANICAL ENGINEERS for publication in the ASME JOURNAL OF APPLIED MECHANICS.

Discussion on this paper should be addressed to the Technical Editor, Professor Leon M. Keer, The Technological Institute, Northwestern University, Evanston, IL 60208, and will be accepted until four months after final publication of the paper itself in the JOURNAL OF APPLIED MECHANICS.

Manuscript received by the ASME Applied Mechanics Division, Nov. 28, 1990; final revision, Aug. 1, 1991. Associate Technical Editor: L. M. Keer.

atation without longitudinal extension, $n$ is the modulus for longitudinal uniaxial straining, $l$ is the associated cross modulus, $m$ is the shear modulus in any transverse direction, and $p$ is the shear modulus for longitudinal shearing.

For an isotropic material, these moduli are related to the bulk and shear moduli $K$ and $G$ as:

$$k=K+\frac{1}{3}G,\ l=K-\frac{2}{3}G,\ n=K+\frac{4}{3}G,\ m=p=G. \tag{3}$$

In what follows, the above notation will be used both for the phase and overall moduli. The phase properties will have a subscript $r = 1, 2, \ldots N$, while the overall quantities will appear without a subscript.

Some fibers, particularly carbon fibers, are cylindrically orthotropic. Their elastic moduli in the tangential, radial, and axial directions are distinct. Nine stiffness coefficients describe this kind of anisotropy. In a cylindrical coordinate system, the stress-strain relation of a cylindrically orthotropic solid is usually written as:

$$\begin{Bmatrix}\sigma_r\\ \sigma_\phi\\ \sigma_z\\ \sigma_{r\phi}\\ \sigma_{z\phi}\\ \sigma_{rz}\end{Bmatrix}=\begin{bmatrix}C_{rr} & C_{r\phi} & C_{rz} & 0 & 0 & 0\\ C_{\phi r} & C_{\phi\phi} & C_{\phi z} & 0 & 0 & 0\\ C_{zr} & C_{z\phi} & C_{zz} & 0 & 0 & 0\\ 0 & 0 & 0 & G_{r\phi} & 0 & 0\\ 0 & 0 & 0 & 0 & G_{z\phi} & 0\\ 0 & 0 & 0 & 0 & 0 & G_{rz}\end{bmatrix}\begin{Bmatrix}\epsilon_r\\ \epsilon_\phi\\ \epsilon_z\\ 2\epsilon_{r\phi}\\ 2\epsilon_{z\phi}\\ 2\epsilon_{rz}\end{Bmatrix} \tag{4}$$

where $z$ is the axis of rotational symmetry, and $C_{ij}$, $G_{r\phi}$, $G_{z\phi}$, and $G_{rz}$ are stiffness coefficients.

## 3 Summary of Present Results

For convenience, we first summarize the main results for several systems of practical interest: composites reinforced by aligned, transversely isotropic fibers or platelets, systems with randomly oriented, transversely isotropic fiber or platelet reinforcement, and unidirectionally reinforced materials with cylindrically orthotropic fibers. Derivation of the results appear in Sections 5, 6, and 7.

**3.1 Unidirectional Fibrous Composites.** We consider a system reinforced by aligned, transversely isotropic fibers ($r = 2, 3, \ldots N$) in a transversely isotropic matrix ($r = 1$). Many different fiber materials may be admitted at the same time. The overall elastic moduli of such a fiber system are:

$$p=\frac{\sum_{r=1}^{N}\frac{c_r p_r}{p_1+p_r}}{\sum_{r=1}^{N}\frac{c_r}{p_1+p_r}},\ m=\frac{\sum_{r=1}^{N}\frac{c_r m_r}{m_r+\gamma_1}}{\sum_{r=1}^{N}\frac{c_r}{m_r+\gamma_1}},\ \gamma_1=\left(\frac{1}{m_1}+\frac{2}{k_1}\right)^{-1} \tag{5}$$

$$k=\frac{\sum_{r=1}^{N}\frac{c_r k_r}{k_r+m_1}}{\sum_{r=1}^{N}\frac{c_r}{k_r+m_1}},\ l=\frac{\sum_{r=1}^{N}\frac{c_r l_r}{k_r+m_1}}{\sum_{r=1}^{N}\frac{c_r}{k_r+m_1}}, \tag{6}$$

$$n=\sum_{r=1}^{N}c_r n_r-\sum_{r=1}^{N}c_r\frac{(l_r-l_1)^2}{k_r+m_1}+\frac{\left[\sum_{r=1}^{N}\frac{c_r(l_r-l_1)}{k_r+m_1}\right]^2}{\sum_{r=1}^{N}\frac{c_r}{k_r+m_1}}. \tag{7}$$

We now list the results for two-phase systems of technological interest; the subscripts $f$ and $m$ represent the fiber and matrix, respectively:

$$p=\frac{2c_f p_m p_f+c_m(p_m p_f+p_m^2)}{2c_f p_m+c_m(p_f+p_m)} \tag{8}$$

$$m=\frac{m_m m_f(k_m+2m_m)+k_m m_m(c_f m_f+c_m m_m)}{k_m m_m+(k_m+2m_m)(c_f m_m+c_m m_f)} \tag{9}$$

$$k=\frac{c_f k_f(k_m+m_m)+c_m k_m(k_f+m_m)}{c_f(k_m+m_m)+c_m(k_f+m_m)} \tag{10}$$

$$l=\frac{c_f l_f(k_m+m_m)+c_m l_m(k_f+m_m)}{c_f(k_m+m_m)+c_m(k_f+m_m)} \tag{11}$$

$$n=c_m n_m+c_f n_f+(l-c_f l_f-c_m l_m)\frac{l_f-l_m}{k_f-k_m}. \tag{12}$$

It should be mentioned that the effective plane-strain bulk modulus $k$ and cross modulus $l$ in (10) and (11), predicted by the Mori-Tanaka method, coincide with those derived by Hill (1964, Eq. (3.6)) for the cylindrical composite element. In two-phase fibrous media, the effective modulus $n$ obeys the universal connections, hence all the moduli $k$, $l$, $n$ have the same values as those derived by Hill (1964). Therefore, for axisymmetric loading situations, the Mori-Tanaka predictions coincide with those suggested by the composite cylinder model.

Furthermore, Norris (1989) has shown that the Mori-Tanaka approximation for multiphase composites, where all particles have the same shape and alignment, satisfies the appropriate Hashin-Shtrikman or Hill-Hashin bounds.

**3.2 Unidirectional Platelet-Reinforced Composites.** As above, we denote the matrix as $r = 1$, and the platelets as $r = 2, 3, \ldots N$. Transverse isotropy or isotropy via (3) is assumed in all phases, together with alignment of the phase symmetry axes with $x_1$. The overall elastic moduli of such composite are

$$p^{-1}=\sum_{r=1}^{N}c_r p_r^{-1},\ m=\sum_{r=1}^{N}c_r m_r,\ n^{-1}=\sum_{r=1}^{N}c_r n_r^{-1},$$
$$\frac{l}{n}=\sum_{r=1}^{N}c_r\frac{l_r}{n_r},\ k=\sum_{r=1}^{N}c_r k_r+\frac{l^2}{n}-\sum_{r=1}^{N}c_r\frac{l_r^2}{n_r}. \tag{13}$$

Surprisingly, the effective Mori-Tanaka moduli $k$, $l$, $m$, $n$, $p$ of composites with aligned platelet reinforcement are identical with those derived from the self-consistent model by Laws (1974, Eqs. (42)–(46)). Moreover, we note that they also coincide with the effective moduli of a laminated plate (Postma, 1955).

**3.3 Composites With Randomly Oriented Fibers or Platelets.** We assume that both the matrix ($r = 1$) and the composite are isotropic and characterized by the bulk and shear moduli $K_1$, $K$, and $G_1$, $G$. The elastic moduli of the reinforcing phases $r = 2, 3, \ldots N$ are defined in the local coordinates of each phase $r$, and in those coordinates each phase may be transversely isotropic or isotropic. The overall moduli of composites with such random reinforcements are

$$K=K_1+\frac{1}{3}\sum_{r=2}^{N}c_r\frac{(\delta_r-3K_1\alpha_r)}{\left[c_1+\sum_{r=2}^{N}c_r\alpha_r\right]},$$

$$G=G_1+\frac{1}{2}\sum_{r=2}^{N}c_r\frac{(\eta_r-2G_1\beta_r)}{\left[c_1+\sum_{r=2}^{N}c_r\beta_r\right]}, \tag{14}$$

where the parameters $\alpha_r$, $\beta_r$, $\delta_r$, $\eta_r$ depend on the moduli and geometry of the phases.

For fibrous systems, these parameters are given as in terms of phase moduli of the phases as

$$\alpha_r=\frac{3K_1+3G_1+k_r-l_r}{3G_1+3k_r} \tag{15}$$

$$\beta_r=\frac{1}{5}\left[\frac{4G_1+(2k_r+l_r)}{3G_1+3k_r}+\frac{4G_1}{p_r+G_1}+\frac{2(\gamma_1+G_1)}{\gamma_1+m_r}\right] \tag{16}$$

$$\delta_r=\frac{1}{3}\left[n_r+2l_r+\frac{(2k_r+l_r)(3K_1+2G_1-l_r)}{k_r+G_1}\right] \tag{17}$$

$$\eta_r=\frac{1}{5}\left[\frac{2}{3}(n_r-l_r)+\frac{8m_rG_1(3K_1+4G_1)}{m_r(3K_1+4G_1)+G_1(3K_1+3m_r+G_1)}\right.$$
$$\left.+\frac{8p_rG_1}{p_r+G_1}+\frac{4k_rG_1-4l_rG_1-2l_r^2+2k_rl_r}{3k_r+3G_1}\right] \tag{18}$$

where in this case (isotropic matrix) $\gamma_1$ in (5) reduces to

$$\gamma_1=\frac{3G_1K_1+G_1^2}{3K_1+7G_1}. \tag{19}$$

For penny-shaped, randomly oriented inclusions, the above parameters assume the values

$$\alpha_r=\frac{K_1}{n_r}+\frac{2}{3}\frac{n_r-l_r}{n_r},\ \beta_r=\frac{1}{5}\left[\frac{7n_r+2l_r+4G_1}{3n_r}+\frac{2G_1}{p_r}\right]$$
$$\delta_r=K_1+2K_1\frac{l_r}{n_r}+\frac{4}{3}\left[k_r-\frac{l_r^2}{n_r}\right],$$
$$\eta_r=\frac{1}{5}\left[4m_r+\frac{2}{3}\left(k_r-\frac{l_r^2}{n_r}\right)+\frac{16}{3}G_1-\frac{4}{3}G_1\frac{l_r}{n_r}\right]. \tag{20}$$

If the fibers or penny-shaped inclusions are *isotropic*, then one can verify that

$$\delta_r=3K_r\alpha_r,\ \eta_r=2G_r\beta_r, \tag{21}$$

and for composites with reinforcements of these two kinds, the bulk and shear moduli in (14) can be simplified as

$$K=K_1+\sum_{r=2}^{N}c_r(K_r-K_1)\frac{\alpha_r}{\left[c_1+\sum_{r=2}^{N}c_r\alpha_r\right]}$$
$$G=G_1+\sum_{r=2}^{N}c_r(G_r-G_1)\frac{\beta_r}{\left[c_1+\sum_{r=2}^{N}c_r\beta_r\right]}. \tag{22}$$

For such isotropic fibers or needle-shaped inclusions, (15) and (16) reduce to

$$\alpha_r=\frac{3K_1+3G_1+G_r}{3K_r+3G_1+G_r} \tag{23}$$

$$\beta_r=\frac{1}{5}\left[\frac{4G_1+3K_r}{3K_r+3G_1+G_r}+\frac{4G_1}{G_1+G_r}+\frac{2(\gamma_1+G_1)}{\gamma_1+G_r}\right]. \tag{24}$$

Therefore, for two-phase media with randomly oriented fibrous reinforcements, the effective bulk modulus $K$ and shear modulus $G$ become

$$K=K_2-c_1(K_2-K_1)\left[1-c_2\frac{3K_2-3K_1}{3K_2+G_2+3G_1}\right]^{-1} \tag{25}$$

$$G=G_2-c_1(G_2-G_1)\left[1-\frac{1}{5}\frac{G_2-G_1}{3K_2+3G_1+G_2}\right.$$
$$\left.-\frac{2}{5}c_2\frac{G_2-G_1}{G_2+\gamma_1}-\frac{2}{5}c_2\frac{G_2-G_1}{G_2+G_1}\right]^{-1}. \tag{26}$$

Equations (25) and (26) can be compared with similar but not identical results found from the self-consistent method by Walpole (1969, Eq. (60)).

For randomly oriented, isotropic, penny-shaped inclusions, ($20_1$) reduces to

$$\alpha_r=\frac{3K_1+4G_r}{3K_r+4G_r},\ \beta_r=\frac{2}{5}\frac{G_1}{G_r}+\frac{1}{5}\frac{9K_r+8G_r+4G_1}{3K_r+4G_r} \tag{27}$$

and the overall bulk and shear moduli of two-phase media can be obtained as

$$K=K_2-c_1(K_2-K_1)\left[1-c_2\frac{3(K_2-K_1)}{3K_2+4G_2}\right]^{-1} \tag{28}$$

$$G=G_2-c_1(G_2-G_1)\left[1-\frac{4}{5}c_2\frac{G_2-G_1}{3K_2+4G_2}-\frac{2}{5}c_2\frac{G_2-G_1}{G_2}\right]^{-1}. \tag{29}$$

It is interesting to note that (28) and (29) are exactly the same expressions as those derived with the self-consistent method by Walpole (1969, Eq. (61)).

Also, it should be mentioned that Benveniste (1987) has recently proved that the bulk and shear moduli predicted by the Mori-Tanaka method for a two-phase composite with randomly oriented ellipsoidal particles will lie within the Hashin-Shtrikman bounds.

**3.4 Composites Reinforced by Cylindrically Orthotropic Fibers.** The constitutive Eq. (4) suggests that cylindrically orthotropic fibers have constant moduli in the cylindrical coordinate system. However, most overall moduli must be evaluated in a Cartesian system, where the fiber properties are no longer constant. The effective moduli of unidirectional composites of this kind are still those of a transversely isotropic solid, and can be obtained from the Mori-Tanaka procedure, but at least one of the overall moduli, the transverse shear modulus $m$, may not be found in closed form. Except for $m$, evaluation of the moduli is best accomplished by introduction of a *replacement fiber* which, under certain overall stress states has the same effective properties as the cylindrically orthotropic fiber described by (4). In particular, in their recent study of thermomechanical behavior of composite systems reinforced by coated cylindrically orthotropic fibers, Chen, Dvorak, and Benveniste (1990) and Hashin (1990) observed that *in axisymmetric loading situations* the cylindrically orthotropic fiber can be replaced by an equivalent *transversely isotropic* fiber without changing the fields of outer phases and the overall behavior of the composite. Moreover, we show in Section 7 that a replacement fiber with an effective modulus $p_f$ can also be found for the longitudinal shear loading case. No such replacement seems possible for transverse normal or shear loading.

The effective moduli of the replacement fiber are recorded here as

$$k_f=(C_{rr}\eta+C_{r\phi})/2,\ l_f=\frac{C_{rz}\eta+C_{\phi z}}{\eta+1},\ p_f=\sqrt{G_{\phi z}G_{rz}}$$
$$n_f=\frac{l^2}{k}+[(C_{rz}H_1+C_{\phi z}H_1+C_{zz})$$
$$-\frac{2}{1+\eta}\frac{C_{rz}\eta+C_{\phi z}}{C_{rr}\eta+C_{r\phi}}(C_{rr}H_1+C_{r\phi}H_1+C_{rz})], \tag{30}$$

where the $C_{ij}$ were defined in (4), $p_f$ is derived in Section 7, and

$$\eta=(C_{\phi\phi}/C_{rr})^{\frac{1}{2}},\ H_1=\frac{C_{\phi z}-C_{rz}}{C_{rr}-C_{\phi\phi}}. \tag{31}$$

These effective fiber moduli can be employed in (8), and (10) to (12), to find the corresponding overall moduli of the unidirectional composite reinforced by the cylindrically orthotropic fibers. The overall transverse shear modulus $m$ must be extracted from the overall stiffness derived in Section 7.

## 4 The Mori-Tanaka Method

To introduce the derivation of the above results we summarize here the essence of this method, in the form which was recently suggested by Benveniste (1987). A representative volume element $V$ of the composite is chosen such that under homogeneous boundary conditions it represents the macroscopic response of the composite. The volume is filled with a certain number of homogeneous phases which are perfectly bonded to a common matrix. The phase volume fractions $c_r$ satisfy $\Sigma\, c_r = 1$; $r = 1, 2, .. N$. In the sequel, $r = 1$ denotes the *matrix* phase. The volume $V$ is subjected to uniform displacement or traction boundary conditions

$$\mathbf{u}(S) = \epsilon^0 \mathbf{x}, \quad \mathbf{t}(S) = \sigma^0 \mathbf{n} \tag{32}$$

where $\mathbf{u}$ and $\mathbf{t}$ denote the applied displacement and traction; $\epsilon^0$, $\sigma^0$ are constant strain and stress tensors, and $\mathbf{n}$ is the outside normal to $S$.

The objective is to evaluate the overall elastic stiffness $\mathbf{L}$ and its inverse, the compliance $\mathbf{M}$, of the composite aggregate, defined by

$$\bar{\sigma} = \mathbf{L}\epsilon^0, \ \bar{\epsilon} = \mathbf{M}\sigma^0, \tag{33}$$

where $\bar{\sigma}$ and $\bar{\epsilon}$ denote the volume average stresses and strains in $V$. An intermediate step is evaluation of the elastic fields in the phases. Those are found in terms of phase volume averages (Hill 1963)

$$\epsilon_r = \mathbf{A}_r \epsilon^0, \quad \sigma_r = \mathbf{B}_r \sigma^0, \tag{34}$$

where $\mathbf{A}_r$ and $\mathbf{B}_r$ are referred to as mechanical concentration factors. Under the boundary conditions ($32_1$) and ($32_2$), the local and overall field averages in $V$ are respectively related by

$$\epsilon^0 = \sum_{r=1}^{N} c_r \epsilon_r, \quad \sigma^0 = \sum_{r=1}^{N} c_r \sigma_r. \tag{35}$$

Then, the overall elastic moduli $\mathbf{L}$ and compliance $\mathbf{M}$ follow as

$$\mathbf{L} = \sum_{r=1}^{N} c_r \mathbf{L}_r \mathbf{A}_r, \quad \mathbf{M} = \sum_{r=1}^{N} c_r \mathbf{M}_r \mathbf{B}_r. \tag{36}$$

In the evaluation of the concentration factors by the Mori-Tanaka method, each inclusion is regarded as a solitary inhomogeneity embedded in an infinite matrix material under a remotely applied strain or stress equal to the matrix average $\epsilon_1$ or $\sigma_1$. For ellipsoidal inclusions, the local fields in such solitary inhomogeneities are uniform, and can be evaluated in terms of partial concentration factors $\mathbf{T}_r$, $\mathbf{W}_r$:

$$\epsilon_r = \mathbf{T}_r \epsilon_1, \quad \sigma_r = \mathbf{W}_r \sigma_1. \tag{37}$$

Once the $\mathbf{T}_r$ and $\mathbf{W}_r$ are known, one can utilize (35) to establish that

$$\epsilon_1 = \left[\sum_{r=1}^{N} c_r \mathbf{T}_r\right]^{-1} \epsilon^0, \quad \sigma_1 = \left[\sum_{r=1}^{N} c_r \mathbf{W}_r\right]^{-1} \sigma^0, \tag{38}$$

and derive the mechanical concentration factors in (34) as

$$\mathbf{A}_r = \mathbf{T}_r \left[\sum_r c_r \mathbf{T}_r\right]^{-1}, \quad \mathbf{B}_r = \mathbf{W}_r \left[\sum_r c_r \mathbf{W}_r\right]^{-1}. \tag{39}$$

The effective stiffness and compliance tensors $\mathbf{L}$ and $\mathbf{M}$ then follow from (36) and (39):

$$\mathbf{L} = \left[\Sigma\, c_r \mathbf{L}_r \mathbf{T}_r\right]\left[\Sigma\, c_r \mathbf{T}_r\right]^{-1}, \quad \mathbf{M} = \left[\Sigma\, c_r \mathbf{M}_r \mathbf{W}_r\right]\left[\Sigma\, c_r \mathbf{W}_r\right]^{-1}. \tag{40}$$

The partial concentration factors in (37) are conveniently expressed in the form

$$\mathbf{T}_r = [\mathbf{I} + \mathbf{P}(\mathbf{L}_r - \mathbf{L}_1)]^{-1}, \ \mathbf{W}_r = [\mathbf{I} + \mathbf{Q}(\mathbf{M}_r - \mathbf{M}_1)]^{-1} \tag{41}$$

where the tensors of $\mathbf{P}$ and $\mathbf{Q}$ depend only on the shape of the inclusion, and on the elastic moduli of the surrounding matrix. For example, for an inclusion in the shape of a circular cylinder in a transversely isotropic matrix, the nonvanishing terms of $\mathbf{P}$, written in a ($6 \times 6$) array are (Walpole, 1969),

$$P_{22} = P_{33} = \frac{k_1 + 4m_1}{8m_1(k_1 + m_1)}, \quad P_{23} = P_{32} = \frac{-k_1}{8m_1(k_1 + m_1)},$$
$$P_{55} = P_{66} = \frac{1}{2p_1}, \quad P_{44} = \frac{k_1 + 2m_1}{2m_1(k_1 + m_1)} \tag{42}$$

in terms of the elastic moduli (1) or (3) of the matrix ($r = 1$). Similarly, for a circular disk in a plane normal to the direction of $x_1$,

$$P_{11} = \frac{1}{n_1}, \quad P_{55} = P_{66} = \frac{1}{p_1}. \tag{43}$$

Alternatively, (41) can be written in terms of the overall constraint tensors $\mathbf{L}_1^*$, $\mathbf{M}_1^*$ (Hill, 1965b) which relate the uniform fields in the inclusion $r$ to the uniform applied fields $\sigma^0$ and $\epsilon^0$ as

$$\sigma_r - \sigma^0 = \mathbf{L}_1^*(\epsilon^0 - \epsilon_r), \quad \epsilon_r - \epsilon^0 = \mathbf{M}_1^*(\sigma^0 - \sigma_r). \tag{44}$$

Those are connected to the partial concentration factors by

$$\mathbf{T}_r = (\mathbf{L}_1^* + \mathbf{L}_r)^{-1}(\mathbf{L}_1^* + \mathbf{L}_1), \ \mathbf{W}_r = (\mathbf{M}_1^* + \mathbf{M}_r)^{-1}(\mathbf{M}_1^* + \mathbf{M}_1). \tag{45}$$

The determination of $\mathbf{L}^*$ and $\mathbf{M}^*$ relies on solutions of boundary value problems for a uniformly stressed or strained cavity in the infinite matrix medium. For example, the nonvanishing terms of the overall constraint compliance $\mathbf{M}_1^*$ of a circular cylindrical cavity are (Walpole, 1969; Laws, 1974):

$$(M_1^*)_{22} = (M_1^*)_{33} = \frac{1}{2}\left(\frac{1}{m_1} + \frac{1}{k_1}\right), \quad (M_1^*)_{23} = (M_1^*)_{32} = -\frac{1}{2k_1}$$
$$(M_1^*)_{55} = (M_1^*)_{66} = \frac{1}{p_1}, \quad (M_1^*)_{44} = \frac{1}{m_1} + \frac{2}{k_1}. \tag{46}$$

## 5 Composites Reinforced by Aligned Inclusions

**5.1 Aligned Fiber or Needle-Shaped Inclusions.** We now proceed to derive the results which were summarized in Section 3.1. First, consider a single fiber in an infinite matrix ($r = 1$) subjected to a longitudinal shear strain $2\epsilon_1$ on its outside boundary. In this dilute configuration, $2\epsilon_1$ is equal to the average matrix strain, and the overall stress is a pure shear $\tau_1 = 2p_1\epsilon_1$. This is an antiplane problem, hence the stress and strain in the fiber $r$ have only the longitudinal shear components $\tau_r = 2p_r\epsilon_r$. These local and overall quantities are related, according to ($44_1$) and ($46_3$), as

$$\tau_r - \tau_1 = 2p_1(\epsilon_1 - \epsilon_r). \tag{47}$$

From the phase constitutive relations and (47), one finds that $\tau_r/\tau_1 = 2p_r/(p_r + p_1)$, and the average matrix longitudinal shear stress follows from ($35_2$) as

$$\tau_1=\left[\sum_{r=1}^{N} c_r \frac{2p_r}{p_r+p_1}\right]^{-1}\tau^0, \tag{48}$$

where $\tau^0$ is the overall longitudinal shear stress that is actually applied to the composite. The average phase strains in $(35_1)$ can be written here as

$$\sum_{r=1}^{N} c_r \frac{\tau_r}{p_r}=\frac{\tau^0}{p}. \tag{49}$$

Finally, a substitution of (47) and (48) in (49) leads to the expression for the effective longitudinal shear modulus $p$ in $(5_1)$.

A similar procedure can be extended to the transverse shear loading case. The constraint tensor in $(46_4)$, $(44_1)$ reduces to $\gamma_1 = (1/m_1 + 2/k_1)^{-1}$, hence $\tau_r - \tau_1 = 2\gamma_1(\epsilon_1 - \epsilon_r)$, where $\tau_r$ and $\epsilon_r$ represent the corresponding transverse shear stress and shear strain in the phase $r$, respectively. As in the derivation of the longitudinal shear loading case, the average stress in the matrix is

$$\tau_1=\left[\sum_{r=1}^{N} c_r \frac{m_r(m_1+\gamma_1)}{m_1(m_r+\gamma_1)}\right]^{-1}\tau^0, \tag{50}$$

and the effective transverse shear modulus $m$ can then be derived in the form given by $(5_2)$.

Next, a pure lateral dilatation is applied without longitudinal straining; i.e., $e^0 \neq 0$, $\epsilon^0 = 0$ in (1). The local stress and strain relation is thus reduced to $s_r = k_r e_r$, and from $(46_1)$ and $(46_2)$ the corresponding equation for the constraint modulus is $(s_r - s_1) = m_1(e_1 - e_r)$. This and $(35_2)$ imply that

$$\frac{s_r}{s_1}=\frac{k_r(k_1+m_1)}{k_1(k_r+m_1)},\quad s_1=\left[\sum_{r=1}^{N} c_r \frac{k_r(k_1+m_1)}{k_1(k_r+m_1)}\right]^{-1}s^0. \tag{51}$$

Then, the effective plane-strain bulk modulus $k$ given by $(6_1)$ can be derived from $(35_1)$.

In the same loading situation as above, $\epsilon^0 = 0$ suggests that

$$\bar{s} = ke^0,\ \bar{\sigma}=le^0. \tag{52}$$

From $(35_2)$ and (52), one can write the average longitudinal stress as

$$\sum_{r=1}^{N} c_r \frac{l_r}{k_r} s_r=\frac{l}{k} s^0. \tag{53}$$

Then, (51), and $(6_1)$ lead to the expression for the effective cross modulus $l$ in $(6_2)$.

For evaluation of the modulus $n$, consider overall uniaxial straining without lateral contraction, i.e., $\epsilon^0 \neq 0$, $e^0 = 0$ in (1). The phase averages in the transverse plane and in the longitudinal direction are

$$\Sigma c_r e_r=0,\ \Sigma c_r s_r=l\epsilon^0,\ \Sigma c_r\sigma_r=n\epsilon^0,\ \epsilon_r=\epsilon^0,\qquad r=1,2..,N. \tag{54}$$

Using $(54_1)$, Eqs. $(54_2)$ and $(54_3)$ can be recast as:

$$\sum_{r=1}^{N} c_r(k_r-k_1)e_r=\left[l-\sum_{r=1}^{N} c_r l_r\right]\epsilon^0,$$
$$\sum_{r=1}^{N} c_r(l_r-l_1)e_r=\left(n-\sum_{r=1}^{N} c_r n_r\right)\epsilon^0. \tag{55}$$

In two-phase media, $n$ follows from (55) and from the universal connections for two-phase fibrous media with transversely isotropic constituents (Hill 1964):

$$\frac{n-c_1n_1-c_2n_2}{l-c_1l_1-c_2l_2}=\frac{l_1-l_2}{k_1-k_2}. \tag{56}$$

In multiphase systems, one additional condition is needed for evaluation of $n$, namely the magnitude of $e_r/\epsilon^0$. In the Mori-Tanaka method, one can use $(41_1)$ and $(39_1)$, with the **P** tensor given in (42) to obtain the necessary components:

$$\frac{e_r}{\epsilon}=\frac{l_1-l_r}{k_r+m_1}-\frac{\dfrac{1}{k_r+m_1}\displaystyle\sum_{r=1}^{N}\frac{c_r(l_r-l_1)}{k_r+m_1}}{\displaystyle\sum_{r=1}^{N}\frac{c_r}{k_r+m_1}}. \tag{57}$$

Then, the effective modulus $n$ in (7) for longitudinal uniaxial straining can be obtained from $(55_2)$ and (57).

**5.2 Aligned Penny-Shaped Inclusions.** Consider penny-shaped or disk-shaped reinforcement with the normal to the plane face of the platelet in the $x_1$-direction. Due to the simple form of the **P** tensor in (43), the partial strain concentration factor can be derived from $(41_1)$. The nonvanishing components are:

$$T^r_{11}=\frac{n_1}{n_r},\ T^r_{12}=T^r_{13}=\frac{l_1-l_r}{n_r},$$
$$T^r_{22}=T^r_{33}=T^r_{44}=1,\ T^r_{55}=T^r_{66}=\frac{p_1}{p_r}. \tag{58}$$

The effective moduli can be derived as in Section 5.1 or by applying (58) directly in (40). In either case, the results obtained appear in (13).

## 6 Randomly Oriented Inclusions

In this section, the matrix is assumed to be isotropic and the inclusions at most transversely isotropic in their respective local coordinate systems. The effective properties predicted by the Mori-Tanaka method follow from a modification of $(40_1)$ and have the form (Benveniste 1987),

$$\mathbf{L}=\mathbf{L}_1+\sum_{r=2}^{N} c_r\{(\mathbf{L}_r-\mathbf{L}_1)\mathbf{T}_r\}\left[\sum_{r=1}^{N} c_r\{\mathbf{T}_r\}\right]^{-1}. \tag{59}$$

Curly brackets $\{\boldsymbol{\Delta}\}$ denote the average of $\boldsymbol{\Delta}$ over all possible orientations. Note that all such averaged quantities in (59) are isotropic fourth-order tensors, even though the underlying tensor quantities, such as $\mathbf{T}_r$, need not be isotropic. Hill (1965c) and Walpole (1981) pointed out that any general isotropic tensor $\boldsymbol{\Lambda}$ is subject to the spectral decomposition

$$\boldsymbol{\Lambda}=a\mathbf{J}+b\mathbf{K} \tag{60}$$

where $a$ and $b$ are certain scalars, and

$$J_{ijkl}=\frac{1}{3}\delta_{ij}\delta_{kl},\ K_{ijkl}=\frac{1}{2}(\delta_{ik}\delta_{jl}+\delta_{il}\delta_{jk}-\frac{2}{3}\delta_{ij}\delta_{kl})$$
$$\mathbf{JJ}=\mathbf{J},\ \mathbf{KK}=\mathbf{K},\ \mathbf{JK}=\mathbf{KJ}=\mathbf{0}. \tag{61}$$

This invites the notation $\boldsymbol{\Lambda} = (a, b)$, $\boldsymbol{\Lambda}^{-1} = (1/a, 1/b)$ in lieu of that in (60).

To evaluate the overall elastic moduli (59), we recall the following result of Kröner (1958). For any fourth-order tensor $\Delta_{ijkl}$, the orientation averaged quantity $\{\boldsymbol{\Delta}\}$ can be expressed as

$$\{\boldsymbol{\Delta}\}=(\alpha,\beta),\quad \{\boldsymbol{\Delta}\}^{-1}=\left(\frac{1}{\alpha},\frac{1}{\beta}\right) \tag{62}$$

where the scalars $\alpha$, $\beta$ are given as

$$\alpha=\frac{1}{3}\Delta_{iijj},\ \beta=\frac{1}{5}\Delta_{ijij}-\frac{1}{15}\Delta_{iijj}. \tag{63}$$

To apply this result to the $\mathbf{L}_r$ and $\mathbf{T}_r$ tensors we write

$$\{\mathbf{T}_r\} = (\alpha_r, \beta_r), \quad \{\mathbf{L}_r\mathbf{T}_r\} = (\delta_r, \eta_r) \tag{64}$$

and utilize it in (59) to arrive at the expressions for the effective bulk and shear moduli that appear in (14).

Certain simplifications are possible for two-phase media with isotropic constituents, where one can rewrite (59) as

$$\mathbf{L} = \mathbf{L}_2 + c_1\{\mathbf{L}_1 - \mathbf{L}_2\}[c_1\mathbf{I} + c_2\{\mathbf{T}_2\}]^{-1}. \tag{65}$$

Since both phases are isotropic then the first orientation average term in (65) becomes

$$\{\mathbf{L}_1 - \mathbf{L}_2\} = (3K_1 - 3K_2, \; 2G_1 - 2G_2) \tag{66}$$

where $K_1$, $G_1$ are matrix moduli.

## 7 Cylindrically Orthotropic Fibers

**7.1 Replacement Fiber.** With reference to the discussion in Section 3.4, we present the derivation of the effective longitudinal shear modulus $p_f$ of a replacement fiber. Under remotely applied stress $\sigma^0_{yz}$, the admissible displacement field selected in the fiber, and the nonvanishing components of stress are (Chen, Dvorak, and Benveniste, 1990):

$$u^f_z = A^f r^q \sin\phi, \; \sigma^f_{rz} = G_{rz} A^f q r^{q-1} \sin\phi, \; \sigma^f_{\phi z} = G_{\phi z} A^f r^{q-1} \cos\phi, \tag{67}$$

where $q = \sqrt{G_{\phi z}/G_{rz}}$ for the original fiber, and $q = 1$ for the transversely isotropic replacement fiber. To insure that the local field in the outer phase does not change after replacement of the fiber, the interfacial quantities, $u^f_z$ and $\sigma^f_{rz}$, must both be identical in the replacement fiber and in the original, cylindrically orthotropic fiber. Evaluation of this requirement leads to the equivalent longitudinal shear modulus of transversely isotropic fiber in the form listed in ($30_3$).

Moreover, the average stress $\bar{\sigma}^f_{yz}$ must have the same magnitude in both fibers. Evaluation of this condition provides the following expression for the effective longitudinal shear modulus of the replacement fiber:

$$p_f = \frac{G_{rz} q + G_{\phi z}}{q+1}. \tag{68}$$

It can be shown that ($30_3$) and (68) are identical, hence either represents the unique longitudinal shear modulus of the replacement fiber.

**7.2 Evaluation of the Overall Transverse Shear Modulus $m$.** In a homogeneous elastic medium subjected to a uniform field of simple shear deformation in the transverse $xy$-plane, the displacement components are defined by:

$$u_x = cx, \; u_y = -cy, \; u_z = 0, \tag{69}$$

where $c$ is a constant. In cylindrical coordinates this becomes

$$u_r = cr\cos 2\phi, \; u_\phi = -cr\sin 2\phi, \; u_z = 0. \tag{70}$$

In analogy with (70), we assume that the displacement field in a cylindrically orthotropic medium under transverse shear has the general form:

$$u_r = U_r(r)\cos 2\phi, \; u_\phi = U_\phi(r)\sin 2\phi, \; u_z = 0, \tag{71}$$

where $U_r(r)$, $U_\phi(r)$ are unknown functions of $r$, which need to be determined from the equations of equilibrium in cylindrical coordinates. The requisite substitution provides the following equations for evaluation of $U_r(r)$, $U_\phi(r)$:

$$C_{rr}\frac{d^2U_r}{dr^2} + \frac{C_{rr}}{r}\frac{dU_r}{dr} - \left(\frac{4}{r^2}G_{r\phi} + \frac{1}{r^2}C_{\phi\phi}\right)U_r + \frac{2(C_{r\phi}+G_{r\phi})}{r}\frac{dU_\phi}{dr} - \frac{2}{r^2}(G_{r\phi}+C_{\phi\phi})U_\phi = 0 \tag{72}$$

$$-\frac{2(G_{r\phi}+C_{r\phi})}{r}\frac{dU_r}{dr} - \frac{2(G_{r\phi}+C_{\phi\phi})}{r^2}U_r + G_{r\phi}\frac{d^2U_\phi}{dr^2} + \frac{G_{r\phi}}{r}\frac{dU_\phi}{dr} - \frac{G_{r\phi}+4C_{\phi\phi}}{r^2}U_\phi = 0. \tag{73}$$

These can be solved analytically, the result is:

$$\begin{aligned} U_r(r) = {} & 2[(G_{r\phi}+C_{\phi\phi}) - \eta_1(C_{r\phi}+G_{r\phi})]Ar^{\eta_1} + 2[(G_{r\phi}+C_{\phi\phi}) + \eta_1(C_{r\phi}+G_{r\phi})]Br^{\eta_1} \\ & + 2[(G_{r\phi}+C_{\phi\phi}) - \eta_2(C_{r\phi}+G_{r\phi})]Cr^{\eta_2} + 2[(G_{r\phi}+C_{\phi\phi}) + \eta_2(C_{r\phi}+G_{r\phi})]Dr^{-\eta_2} \end{aligned} \tag{74}$$

$$\begin{aligned} U_\phi(r) = {} & [C_{rr}\eta_1^2 - (4G_{r\phi}+C_{\phi\phi})]Ar^{\eta_1} + [C_{rr}\eta_1^2 - (4G_{r\phi}+C_{\phi\phi})]Br^{-\eta_1} + [C_{rr}\eta_2^2 - (4G_{r\phi}+C_{\phi\phi})]Cr^{\eta_2} \\ & + [C_{rr}\eta_2^2 - (4G_{r\phi}+C_{\phi\phi})]Dr^{-\eta_2} \end{aligned} \tag{75}$$

where $\eta_1^2$ and $\eta_2^2$ are the roots of

$$C_{rr}G_{r\phi}\eta^4 + [4C_{r\phi}^2 + 8C_{r\phi}G_{r\phi} - 4C_{rr}C_{\phi\phi} - G_{r\phi}(C_{rr}+C_{\phi\phi})]\eta^2 + 9G_{r\phi}C_{\phi\phi} = 0,$$

and A, B, C, and D are certain constants.

In the Mori-Tanaka procedure, one must first solve an auxiliary problem for a single fiber in an infinite matrix volume. The displacements (71), (74), and (75) are admitted in the fiber domain, while the displacements in the matrix are special forms of (74) and (75) for a transversely isotropic or isotropic medium. In any event, to assure boundedness of the displacements at the origin, the terms which contain the negative powers of $\eta_1$ and $\eta_2$ must be excluded. The resulting admissible displacement field are best written in terms of the transverse normal stress $\sigma^0$ as

$$u^f_r = \frac{b\sigma^0}{4G_{r\phi}}\left\{2[(G_{r\phi}+C_{\phi\phi}) - \eta_1(C_{r\phi}+G_{r\phi})]a_1\left(\frac{r}{b}\right)^{\eta_1} + 2[(G_{r\phi}+C_{\phi\phi}) - \eta_2(C_{r\phi}+G_{r\phi})]c_1\left(\frac{r}{b}\right)^{\eta_2}\right\}\cos 2\phi \tag{76}$$

$$u^f_\phi = \frac{b\sigma^0}{4G_{r\phi}}\left\{[C_{rr}\eta_1^2 - (4G_{r\phi}+C_{\phi\phi})]a_1\left(\frac{r}{b}\right)^{\eta_1} + [C_{rr}\eta_2^2 - (4G_{r\phi}+C_{\phi\phi})]c_1\left(\frac{r}{b}\right)^{\eta_2}\right\}\sin 2\phi$$

$$u^f_z = 0$$

$$u^m_r = \frac{b\sigma^0}{4m^m}\left[\frac{2}{b}r + (\xi_m+1)\frac{b}{r}a_2 + \left(\frac{b}{r}\right)^3 c_2\right]\cos 2\phi$$

$$u^m_\phi = \frac{b\sigma^0}{4m^m}\left[-\frac{2}{b}r - (\xi_m-1)\frac{b}{r}a_2 + \left(\frac{b}{r}\right)^3 c_2\right]\sin 2\phi \tag{77}$$

$$u^m_z = 0,$$

where

$$\xi_m = (2m^m + k^m)/k^m,$$

and $\sigma^0$ is the normal transverse stress applied at infinity. As yet unknown constants $a_1$, $a_2$, $c_1$, and $c_2$ have been introduced to replace the A, B, C, D constants in (74) and (75). Since the matrix is regarded as transversely isotropic, we have used the connections between elastic constants to introduce the Hill's moduli $k^m$ and $m^m$.

To complete the solution of the auxiliary problem, the four unknown constants must be evaluated from the usual continuity requirements for the stresses $\sigma_{rr}$, $\sigma_{r\phi}$ and the displacements $u_r$, $u_\phi$ at the interface $r = a$. However, the resulting equations are coupled, and are best solved numerically. Once the constants are known, the phase stress fields under overall transverse shear loading can be derived from the displacement fields (76) to (77), and the appropriate constitutive relations (1) or (4).

This completes the solution of the auxiliary problem, and opens the way to evaluation of the Mori-Tanaka estimate of the overall stiffness which contains the unknown transverse shear modulus $m$. Of course, the above solution delivers the auxiliary stress and strain fields in the phases in the cylindrical coordinate system, and both the fields and the phase moduli must be first transformed into the Cartesian system. As in Chen et al. (1990, Section 3), we denote the cylindrical system by the vector $\xi$, the fields themselves by primed letters $\sigma'$ ($\xi$) and $\epsilon'$ ($\xi$), and the phase properties in the $\xi$ system by $\mathbf{L}'$, $\mathbf{M}'$. Note that the factor 2 must appear in the shear terms of the $6 \times 1$ strain vector. In the Cartesian coordinates, these quantities are denoted by similar but unprimed letters.

At any point in a given phase $r$, the transformation of the stress and strain fields between the current, cylindrical, and the Cartesian components is written as

$$\sigma_r(\mathbf{x}) = \mathbf{R}\sigma_r'(\epsilon), \qquad \epsilon_r(\mathbf{x}) = \mathbf{S}\epsilon_r'(\xi), \tag{78}$$

where, the transformation matrices $\mathbf{R}$ and $\mathbf{S}$ are related by $\mathbf{R}^T = \mathbf{S}^{-1}$. Of course, in a transformation between the cylindrical and Cartesian systems, $\mathbf{R}$ and $\mathbf{S}$ are functions of the angle $\phi$. Next, write the phase constitutive relations, such as (4), in the symbolic form:

$$\sigma_r'(\xi) = \mathbf{L}_r'(\xi)\epsilon_r'(\xi),\ \epsilon_r'(\xi) = \mathbf{M}_r'(\xi)\sigma_r'(\xi). \tag{79}$$

Equations (78) and (79) provide the relations

$$\sigma_r(\mathbf{x}) = \mathbf{R}\mathbf{L}_r'\mathbf{S}^{-1}\epsilon_r(\mathbf{x}),\ \epsilon_r(\mathbf{x}) = \mathbf{S}\mathbf{M}_r'\mathbf{R}^{-1}\sigma_r(\mathbf{x}) \tag{80}$$

at each point $\mathbf{x}$. Note that $\mathbf{S}$, $\mathbf{R}$, $\mathbf{L}_r'$, $\mathbf{M}_r'$ may now be functions of $\mathbf{x}$, but for brevity in notation the argument will be omitted in the sequel.

The local fields in (80) are related to the uniform, remotely applied fields $\epsilon^0$ and $\sigma^0$ through certain influence functions $\mathbf{A}_r(\mathbf{x})$, $\mathbf{B}_r(\mathbf{x})$; their volume averages, the mechanical concentration factors, appear in (34). Thus, under overall applied strain, ($32_1$), the local strain field in ($80_2$) may be replaced by the term $\mathbf{A}_r(\mathbf{x})\ \epsilon^0$, and the result substituted into the formal phase constitutive relation $\sigma_r = \mathbf{L}_r\epsilon_r$. When solved for $r$, the relation yields the result

$$\mathbf{L}_r = \left[ \frac{1}{V_r} \int_{V_r} \mathbf{R}\mathbf{L}_r'\mathbf{S}^{-1}\mathbf{A}_r(\mathbf{x})dV_r \right] \mathbf{A}_r^{-1}. \tag{81}$$

A similar operation on the local stress field in ($80_1$), but under boundary conditions ($32_2$), leads to

$$\mathbf{M}_r = \left[ \frac{1}{V_r} \int_{V_r} \mathbf{S}\mathbf{M}_r'\mathbf{R}^{-1}\mathbf{B}_r(\mathbf{x})dV_r \right] \mathbf{B}_r^{-1}. \tag{83}$$

The above transformation relations are valid for any actual composite material or its model. Of course, in the Mori-Tanaka model one can employ the expressions (39) for $\mathbf{A}_r$ and $\mathbf{B}_r$ to find

$$\mathbf{L}_r = \left[ \frac{1}{V_r} \int_{V_r} \mathbf{R}\mathbf{L}_r'\mathbf{S}^{-1}\mathbf{T}_r(\mathbf{x})dV_r \right] \mathbf{T}_r^{-1},$$

$$\mathbf{M}_r = \left[ \frac{1}{V_r} \int_{V_r} \mathbf{S}\mathbf{M}_r'\mathbf{R}^{-1}\mathbf{W}_r(\mathbf{x})dV_r \right] \mathbf{W}_r^{-1}. \tag{83}$$

Recall that the partial concentration factors and the underlying influence functions follow from the solution (77) of the auxiliary problem, and the transformation relations (78). When substituted into (83), they provide the necessary phase stiffnesses and concentration factors for evaluation of the overall stiffness and compliance in (40). Of course, the procedure yields all components of $\mathbf{L}$ and $\mathbf{M}$. However, the magnitudes of the moduli $k$, $l$, $n$, and $p$ for the present system are already known from (30) and (8), (10), (11), and (12), and only the magnitude of $m$ represents new information.

We note in passing that in a transversely isotropic solid with the $x_1$-axis of symmetry, the Hill's elastic moduli and the stiffness coefficients are related as follows:

$$L_{11} = n,\ L_{12} = L_{13} = l,\ L_{22} = L_{33} = k + m, \tag{84}$$
$$L_{23} = k - m,\ L_{44} = m,\ L_{55} = L_{66} = p.$$

## 8 Closure

The formulation of the Mori-Tanaka method does not guarantee diagonal symmetry of the estimated overall stiffness tensor. Indeed, it is easy to construct systems for which the predicted stiffness is not diagonally symmetric. However, Benveniste, Dvorak, and Chen (1991a,b) prove that the Mori-Tanaka estimates are symmetric in all two-phase systems of any geometry, and in those multiphase systems where all inclusions have the same shape and orientation, or the $P$ tensor. Such proof was also constructed for the unidirectional composite reinforced by coated, cylindrically orthotropic fibers. This suggests that the present estimates of overall stiffness for all systems with aligned fibers or inclusions are diagonally symmetric. An analogous conclusion for the randomly orientated reinforcement is indicated by (65).

Both the Mori-Tanaka and the self-consistent methods provide approximations which are admissible only if they are bracketed by available Hashin-Shtrikman bounds. For the Mori-Tanaka method, this question was recently explored by Norris (1989), who shows that the effective moduli estimated by the Mori-Tanaka approximation for two-phase composites always satisfy the Hashin-Shtrikman and Hill-Hashin bounds. However, this property does not generalize to general multiphase composites. The status of the estimates for aligned platelet reinforced systems, and for multiphase random reinforcement, remains to be established.

## Acknowledgment

This work has been supported by the ONR/DARPA-Hi-TASC program at Rensselaer.

**Note:** For more discussion of the Mori-Tanaka method, the reader is referred to the recent papers by Weng (1990) and Ferrari (1991).

## References

Benveniste, Y., 1987, "A New Approach to the Application of Mori-Tanaka's Theory in Composite Materials," *Mech. Mat.*, Vol. 6, pp. 147–157.

Benveniste, Y., Dvorak, G. J., and Chen, T., 1989, "Stress Fields in Composites with Coated Inclusions," *Mech. Mat.*, Vol. 7, pp. 305–317.

Benveniste, Y., Dvorak, G. J., and Chen, T., 1991a, "On Diagonal and

Elastic Symmetry of the Approximate Effective Stiffness Tensor of Heterogeneous Media," *J. Mech. Phys. Solids*, Vol. 39, pp. 927-946.

Benveniste, Y., Dvorak, G. J., and Chen, T., 1991b, "On Effective Properties of Composites with Coated Cylindrically Orthotropic Fibers," *Mech. Mat.*, Vol. 12, pp. 289-297.

Berryman, J. G., 1980, "Long-Wavelength Propagation in Composite Elastic Media, II. Ellipsoidal Inclusions," *J. Acoust. Soc. Amer.*, Vol. 68, pp. 1820-1831.

Boucher, S., 1974, "On the Effective Moduli of Isotropic Two-Phase Elastic Composites," *J. Comp. Mat.*, Vol. 8, pp. 82-89.

Budiansky, B., 1965, "On the Elastic Moduli of Some Heterogeneous Materials," *J. Mech. Phys. Solids*, Vol. 13, pp. 223-227.

Chen, T., Dvorak, G. J., and Benveniste, Y., 1990, "Stress Fields in Composites Reinforced by Coated Cylindrically Orthotropic Fibers," *Mech. Mat.*, Vol. 9, pp. 17-32.

Christensen, R. M., and Waals, F. M., 1972, "Effective Stiffness of Randomly Oriented Fiber Composites," *J. Comp. Mat.*, Vol. 6, pp. 518-532.

Cleary, M. P., Chen, I. W., and Lee, S. M., 1980, "Self-Consistent Techniques for Heterogeneous Solids," *J. Engng. Mech.*, Vol. 106, pp. 861-887.

Eshelby, J. D., 1957, "The Determination of the Elastic Field of an Ellipsoidal Inclusion and Related Problems," *Proc. Roy. Soc. London*, Vol. A241, pp. 376-396.

Ferrair, M., 1991, "Asymmetry of the High Concentration Limit of the Mori-Tanaka Effective Medium Theory," *Mech. Mat.*, Vol. 11, pp. 251-256.

Hashin, Z., and Shtrikman, S., 1963, "A Variational Approach to the Theory of the Behavior of Multiphase Materials," *J. Mech. Phys. Solids*, Vol. 11, pp. 127-140.

Hashin, Z., 1990, "Thermoelastic Properties and Conductivity of Carbon/Carbon Fiber Composites," *Mech. Mat.*, Vol. 8, pp. 293-308.

Hill, R., 1963, "Elastic Properties of Reinforced Solids: Some Theoretical Principles," *J. Mech. Phys. Solids*, Vol. 11, pp. 357-372.

Hill, R., 1964, "Theory of Mechanical Properties of Fiber-Strengthened Materials: I. Elastic Behavior," *J. Mech. Phys. Solids*, Vol. 12, pp. 199-212.

Hill, R., 1965a, "Theory of Mechanical Properties of the Fibre-Strengthened Materials—III Self-Consistent Model," *J. Mech. Phys. Solids*, Vol. 13, pp. 189-198.

Hill, R., 1965b, "A Self-Consistent Mechanics of Composite Materials," *J. Mech. Phys. Solids*, Vol. 12, pp. 213-222.

Hill, R., 1965c, "Continuum Micro-Mechanics of Elastoplastic Polycrystals," *J. Mech. Phys. Solids*, Vol. 13, pp. 89-101.

Kröner, E., 1958, "Berechnung der elastischen Konstanten des Vielkristalls aus Konstanten des Einkristalls," *Z. Phys.*, Vol. 136, pp. 504-518.

Laws, N., 1974, "The Overall Thermoelastic Moduli of Transversely Isotropic Composites According to the Self-Consistent Method," *Int. J. Engng. Sci.*, Vol. 12, pp. 79-87.

Mori, T., and Tanaka, K., 1973, "Average Stress in Matrix and Average Elastic Energy of Materials with Misfitting Inclusions," *Acta Metal.* Vol. 21, pp. 571-574.

Norris, A. N., 1989, "An Examination of the Mori-Tanaka Effective Medium Approximation for Multiphase Composites," ASME JOURNAL OF APPLIED MECHANICS, Vol. 56, pp. 83-88.

Postma, G. W., 1955, "Wave Propagation in a Stratified Medium," *Geophysics*, Vol. 20, pp. 780-806.

Walpole, L. J., 1969, "On the Overall Elastic Moduli of Composite Materials," *J. Mech. Phys. Solids*, Vol. 17, pp. 235-251.

Walpole, L. J., 1981, "Elastic Behavior of Composite Material: Theoretical Foundations," *Advances in Applied Mechanics*, Vol. 21, C. S. Yih, ed., Academic Press, New York, pp. 170-242.

Walpole, L. J., 1984, "The Analysis of the Overall Elastic Properties of Composite Materials," *Fundamentals of Deformation and Fracture*, B. A. Bilby, K. J. Miller and J. R. Willis, eds., pp. 91-107.

Weng, G. J., 1984, "Some Elastic Properties of Reinforced Solids, with Special Reference to Isotropic Ones Containing Spherical Inclusions," *Int. J. Engng. Sci.*, Vol. 22, pp. 845-856.

Weng, G. J., 1990, "The Theoretical Connection Between Mori-Tanaka's Theory and the Hashin-Shtrikman-Walpole Bounds," *Int. J. Eng. Sci.*, Vol. 28, pp. 1111-1120.

Willis, J. R., 1981, "Variational and Related Methods for the Overall Properties of Composites," *Advances in Applied Mechanics*, Vol. 21, C. S. Yih, ed., Academic Press, New York, pp. 1-78.

Zhao, Y. H., Tandon, G. P., and Weng, G. J., 1989, "Elastic Moduli for a Class of Porous Materials," *Acta Mechanica*, Vol. 76, pp. 105-130.

Hong Teng

A. Agah-Tehrani[1]

Department of Theoretical and Applied Mechanics,
University of Illinois at Urbana-Champaign,
Urbana, IL 61801

# Interfacial Slippage of a Unidirectional Fiber Composite Under Longitudinal Shearing

*Interfacial slippage of a unidirectional fiber composite under longitudinal shearing is analyzed. The finite concentration of fibers has been taken into account by utilizing the composite cylinder model in the formulation of the problem. The resulting mixed boundary value problem leads to a system of dual series equations, which is then reduced to a Fredholm integral equation of the first kind with a logarithmic singularity. The extent of slip region, which depends on the level of applied load along with the distribution of shear tractions at the fiber-matrix interface, is determined by solving the integral equation numerically.*

## Introduction

When a fiber composite material is subjected to longitudinal shearing, slip may occur at the fiber-matrix interface if the applied shear stress exceeds some critical value. In a recent paper, Steif and Dollar (1988) treated the problem of fiber-matrix slippage for a dilute fiber composite. By considering a single fiber in an infinite matrix under a remote shear stress, they were able to solve for the extent of slip zone under a given load level of loading. The solution of a screw dislocation located at the interface of a single fiber and an infinite matrix was first obtained and then used to derive a singular integral equation governing the problem which has a Cauch-type kernel.

The volume content of fibers is an important parameter in determining properties of a fiber-reinforced composite material and significantly affects its overall strength. Therefore it is of particular interest to include the influence of fiber volume fraction in the analysis of initiation and progression of slippage at the fiber-matrix interface. The purpose of the present investigation is to study such effect when the applied loading is longitudinal shearing.

The composite cylinder model for unidirectional fiber composites is employed in order to take into account the fiber volume fraction in the formulation of the problem. This model was first introduced by Hashin and Rosen (1964) and has been used in contexts that differ from the present one (Smith and Spencer, 1970; Zweben and Rosen, 1970; Budiansky and Hutchinson, 1986). The resulting mixed boundary value problem for the fiber-matrix interfacial slippage leads to a system of dual series equations. The dual series equations can be reduced to a Fredholm integral equation of the first kind with a logarithmically singular kernel, with the unknown function being the distribution of shear traction along the portion of the interface that remains intact. Although great difficulty is generally to be expected in numerically solving Fredholm equations of the first kind with a smooth kernel, the presence of the logarithmic singularity makes the integral equation amenable to numerical solution. The extent of slip region as a function of the level of applied load is then determined by imposing the condition that throughout the entire fiber-matrix interface the shear stress should not exceed the critical value.

Problems related to fiber-reinforced composites under longitudinal shearing have been studied by a number of authors (for example, Smith, 1969; Budiansky and Carrier, 1984). Problems on fiber-matrix interfacial slippage have also been studied previously (Budianksy and Hutchinson, 1986; Piggott, 1987; Steif and Dollar, 1988). The dual series approach (Sneddon, 1966; Erdogan, 1978) adopted in this paper has been used by many authors in solving various mixed boundary value problems such as the separation of an inclusion from an infinite matrix (Noble and Hussain, 1966; Keer, Dundurs, and Kiattikomol, 1973), and the bending of cracked plates (Keer and Sve, 1970).

## Formulation of the Problem

Consider a unidirectional fiber composite subjected to a remote longitudinal shear stress $\tau_0$ as illustrated in Fig. 1. Both the fibers and the matrix are taken to be homogeneous, isotropic and linearly elastic, with shear moduli of $G_f$ and $G_m$, respectively. It is assumed that the interface between the fibers and the matrix can only support shear traction up to a maximum value, say, $\tau_s$, beyond which slip can occur along parts of the interface. As in Steif and Dollar (1988), we assume that the shear stress over the slipped portion of the interface is maintained at this maximum value.

Utilizing the aforementioned composite cylinder model, we

[1]Current address: Department of Mechanical Engineering, San Diego State University, San Diego, CA 92182.

Contributed by the Applied Mechanics Division of The American Society of Mechanical Engineers for publication in the ASME Journal of Applied Mechanics.

Discussion on this paper should be addressed to the Technical Editor, Professor Leon M. Keer, The Technological Institute, Northwestern University, Evanston, IL 60208, and will be accepted until four months after final publication of the paper itself in the Journal of Applied Mechanics.

Manuscript received by the ASME Applied Mechanics Division, Nov. 15, 1990; final revision, Apr. 30, 1991. Associate Technical Editor: S. K. Datta.

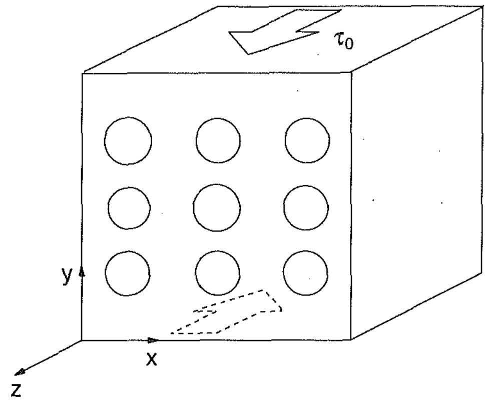


Fig. 1 Longitudinal shearing of a unidirectional fiber composite

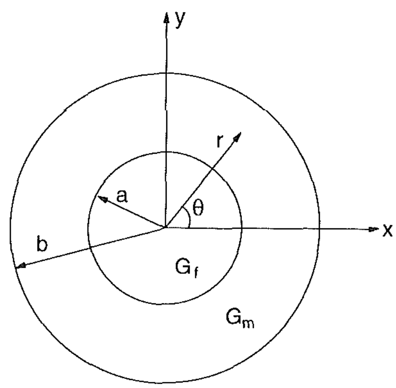


Fig. 2 Coordinate system for the composite cylinder model

can confine our analysis of the current problem to a representative volume element consisting of a circular cylinder of fiber material and a surrounding concentric cylindrical shell of matrix material with their axis in the fiber direction as shown in Fig. 2. The radius of the inner cylinder $a$ is that of the fiber and the outer radius of the matrix shell $b$ is chosen so that the volume fraction of the fiber in the composite cylinder is the same as the overall fiber volume fraction $V_f$ of the gross composite material, i.e., $a^2/b^2 = V_f$.

The problem is that of the antiplane strain deformation. The only nonvanishing displacement is the longitudinal component $w$, which can be represented by a harmonic function. The extent of the unslipped segments of the fiber-matrix interface is specified by the angle $\alpha$ shown in Fig. 3. The magnitude of $\alpha$ depends on the fiber-matrix shear modulus ratio $G_f/G_m$, fiber volume fraction $V_f$ as well as the applied load $\tau_0$. It can be seen that by virtue of symmetry of the problem, there exist two slip zones, one defined by $\alpha < \theta < \pi - \alpha$ and the other by $\pi + \alpha < \theta < 2\pi - \alpha$. The traction must be continuous over the entire interface, while the displacement may be discontinuous across the slip region.

The displacement function $w(r, \theta)$ satisfies Laplace's equation

$$\nabla^2 w = 0 \tag{1}$$

with corresponding stress components given by

$$\tau_{rz} = G\frac{\partial w}{\partial r}, \quad \tau_{\theta z} = G\frac{1}{r}\frac{\partial w}{\partial \theta} \tag{2}$$

where $G$ denotes the shear modulus.

The foregoing expressions are valid for both the fiber and the matrix, provided that the proper shear modulus is used. In order for one to be able to consider the composite cylinder shown in Fig. 2 as a representative volume element of the overall material under the remote longitudinal shear stress $\tau_0$, the boundary condition on the external surface of the matrix shell becomes

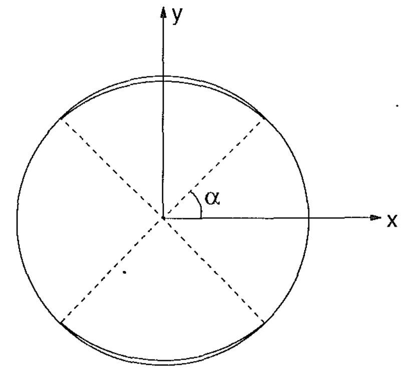


Fig. 3 The region of slippage at the fiber-matrix interface

$$\tau_{rz} = \tau_0 \sin\theta, \quad r = b, \quad 0 \le \theta \le 2\pi. \tag{3}$$

The symmetries contained in the problem imply that the analysis can be limited, without loss of generality, to the first quadrant. The solutions to Laplace's Eq. (1) in the two regions of $0 < r < a$ and $a < r < b$, denoted by $\overline{w}$ and $w$, respectively, can be represented by the following series:

$$\overline{w} = \sum_{n=1,3,\ldots}^{\infty} \overline{A}_n r^n \sin n\theta, \quad 0<r<a, \quad 0 \le \theta \le \pi/2 \tag{4}$$

$$w = \sum_{n=1,3,\ldots}^{\infty} \left(A_n r^n + \frac{B_n}{r^n}\right) \sin n\theta, \ a<r<b, \quad 0 \le \theta \le \pi/2. \tag{5}$$

Using (2), the radial shear stress components can be expressed as

$$\overline{\tau}_{rz} = G_f \sum_{n=1,3,\ldots}^{\infty} n\overline{A}_n r^{n-1} \sin n\theta, \quad 0<r<a, \quad 0 \le \theta \le \pi/2 \tag{6}$$

$$\tau_{rz} = G_m \sum_{n=1,3,\ldots}^{\infty} n\left(A_n r^{n-1} - \frac{B_n}{r^{n+1}}\right) \sin n\theta, \quad a<r<b, \quad 0 \le \theta \le \pi/2. \tag{7}$$

Similar expressions may be written for the tangential shear stress components $\overline{\tau}_{\theta z}$ and $\tau_{\theta z}$.

The solutions are required to satisfy the boundary conditions at $r = a$

$$\overline{\tau}_{rz}(a, \theta) = \tau_{rz}(a, \theta) \le \tau_s, \quad 0 \le \theta \le \alpha \tag{8}$$

$$\overline{\tau}_{rz}(a, \theta) = \tau_{rz}(a, \theta) = \tau_s, \quad \alpha \le \theta \le \pi/2 \tag{9}$$

$$\overline{w}(a, \theta) = w(a, \theta), \quad 0 \le \theta \le \alpha \tag{10}$$

and the boundary condition at $r = b$

$$\tau_{rz}(b, \theta) = \tau_0 \sin\theta, \quad 0 \le \theta \le \pi/2. \tag{11}$$

The boundary conditions are mixed, and it can be easily shown that they lead to the following dual series equations:

$$G_f \sum_{n=1,3,\ldots}^{\infty} n a^{n-1} \overline{A}_n \sin n\theta = \tau_s, \quad \alpha \le \theta \le \pi/2 \tag{12}$$

$$\sum_{n=1,3,\ldots}^{\infty} (1+\beta_n) a^n \overline{A}_n \sin n\theta = F(\theta), \quad 0 \le \theta \le \alpha \tag{13}$$

where

$$\lambda = \frac{G_f}{G_m} \tag{14}$$

$$\beta_n = \lambda \frac{1+V_f^n}{1-V_f^n} \tag{15}$$

$$F(\theta) = \frac{2}{1-V_f}\frac{\tau_0}{G_m} a \sin\theta. \tag{16}$$

It is noted that the angle $\alpha$ which specifies the unslipped portion of the fiber-matrix interface is unknown as a priori and is to be determined as a part of the solution of the foregoing dual series equations. Before discussing the method of solving the mixed boundary value problem now formulated via a system of dual series relations, we first derive the load conditions for initiation of slippage at the interface.

Obviously, the aforementioned critical stress level $\tau_s$ up to which the fiber-matrix interface can sustain shear traction without slip depends on the bond strength of the interface. It is conceivable that under sufficiently small load and proper fiber-matrix interfacial strength, no slippage will occur. In this case, we have $\alpha = \pi/2$ and the boundary condition (9) no longer applies, thus the problem reduces to that of the perfect bond. The shear stress at the interface in this instance can be easily found to be

$$\tau(\theta)=\frac{2\lambda}{\lambda+1+(\lambda-1)V_f}\tau_0\sin\theta,\quad 0\leq\theta\leq\pi/2. \tag{17}$$

Clearly, the perfect bond solution is valid if and only if the following inequality is satisfied:

$$\frac{2\lambda}{\lambda+1+(\lambda-1)V_f}\tau_0\sin\theta<\tau_s,\quad 0\leq\theta\leq\pi/2. \tag{18}$$

Hence, we obtain the nonslip condition

$$\frac{2\lambda}{1+\lambda+(\lambda-1)V_f}\tau_0<\tau_s. \tag{19}$$

In other words, slip will occur for values of the remote longitudinal shear load $\tau_0$ that satisfy

$$\frac{\tau_0}{\tau_s}>\frac{1+\lambda+(\lambda-1)V_f}{2\lambda}. \tag{20}$$

For the special case when $V_f = 0$, this condition reduces to the one given by Steif and Dollar (1988), i.e., a single fiber in an infinite matrix.

## Solution of the Dual Series Equations

We now proceed to construct the solution for the mixed boundary value problem formulated through a pair of dual series equations given by (12) and (13), assuming that slip has occurred at the fiber-matrix interface, i.e., the value of $\tau_0/\tau_s$ is greater than $(1+\lambda+(\lambda-1)V_f)/2\lambda$. For this purpose, let $H(\theta)$ denote the shear traction along the unslipped portion of the interface. From (6) and (9) we have

$$G_f\sum_{n=1,3,\ldots}^{\infty} na^{n-1}\,\overline{A}_n\sin n\theta=\begin{cases}H(\theta), & 0\leq\theta<\alpha\\ \tau_s, & \alpha<\theta\leq\pi/2\end{cases}. \tag{21}$$

The Fourier coefficients $\overline{A}_n$ are then given by

$$\overline{A}_n=\frac{4}{\pi G_f n a^{n-1}}\int_0^{\alpha}H(\phi)\,\sin n\phi d\phi+\frac{4}{\pi G_f n^2 a^{n-1}}\tau_s\cos n\alpha \tag{22}$$
$$n=1,3,\ldots\,.$$

Substituting (22) into the second of the dual series Eq. (13) and changing the order of integration and summation, we arrive at a Fredholm integral equation of the first kind

$$\int_0^{\alpha}H(\phi)K(\theta,\,\phi)d\phi=f(\theta),\quad 0\leq\theta\leq\alpha \tag{23}$$

where

$$K(\theta,\,\phi)=\sum_{n=1,3,\ldots}^{\infty}(1+\beta_n)\frac{1}{n}\sin n\theta\,\sin n\,\phi \tag{24}$$

$$f(\theta)=\frac{\pi\lambda}{2(1-V_f)}\tau_0\sin\theta-\tau_s\sum_{n=1,3,\ldots}^{\infty}(1+\beta_n)\frac{1}{n^2}\cos n\alpha\sin n\theta. \tag{25}$$

The kernel of the integral Eq. (23) contains a logarithmic singularity. To see this, let (24) be rewritten in the form

$$K(\theta,\,\phi)=(1+\lambda)\sum_{n=1,3,\ldots}^{\infty}\frac{1}{n}\sin n\theta\,\sin n\phi$$
$$+2\lambda\sum_{n=1,3,\ldots}^{\infty}\frac{V_f^n}{1-V_f^n}\frac{1}{n}\sin n\theta\sin n\phi. \tag{26}$$

Since $V_f < 1$, the second series in (26) is always bounded while the first one can be summed exactly to yield

$$\sum_{n=1,3,\ldots}^{\infty}\frac{1}{n}\sin n\theta\sin n\phi=\frac{1}{4}\log\left|\tan\frac{\theta+\phi}{2}\right|$$
$$-\frac{1}{4}\log\left|\tan\frac{\theta-\phi}{2}\right|. \tag{27}$$

Hence, the kernel function becomes unbounded at $\theta = \phi$.

Due to the presence of the logarithmic singularity, for an arbitrary value of $\alpha$, the solution of the integral Eq. (23) will exhibit a square-root singularity at $\theta = \alpha$. Since no such singularity may be allowed, and the shear stress throughout the entire interface is bounded by $\tau_s$ and must be less than $\tau_s$ over the unslipped region, the extent of slip as specified by the angle $\alpha$ is determined by imposing the following end condition

$$H(\alpha)=\tau_s. \tag{28}$$

Note that the function $f(\theta)$ on the right-hand side of (23) is not well behaved at $\theta = \alpha$, since at this point its derivative becomes unbounded as can be verified without difficulty by differentiating the expression (25). Hence, in view of the results given in Tuck (1980), it appears that the integral Eq. (23), which possesses a logarithmically singular kernel, has a unique solution that satisfies the end condition (28). The numerical solution carried out confirms this conclusion.

## Numerical Solution and Results

It is well known that in general a Fredholm integral equation of the first kind with a nonsingular kernel can be very difficult to solve numerically. Indeed, this fact might partly account for the past preference for reducing dual series equations to an integral equation of the second kind (Westmann and Yang, 1967; Keer and Sve, 1970; Keer, Dundurs, and Kiattikomol, 1973). However, the logarithmic singularity present in the current problem makes the integral Eq. (23) suitable for a numerical solution by an effective technique discussed in Jaswon and Symm (1977), and Tuck (1980), which approximates the unknown function as a piecewise-constant step function.

Thus, by discretizing the integral Eq. (23), a system of simultaneous linear algebraic equations is readily derived (see Appendix). In solving the integral Eq. (23) numerically, the value of $\alpha$ that satisfies the end condition (28) under a given level of load $\tau_0$ has to be solved by an iterative procedure. The bisection method was found to be quite effective to this end. The infinite series involved in the numerical evaluations converge rather slowly and in order to accelerate the convergence an appropriate integral formula was found to replace these series. In subsequent computations, 40 simultaneous equations were found to be adequate for achieving sufficient accuracy.

The calculations were carried out for two different fiber-matrix shear modulus ratios of $\lambda = 5.0$ and $\lambda = 0.2$. The first one corresponds to the case when the material of fibers is stiffer than that of matrix and the second one corresponds to stiffer matrix material.

In both cases, the extent of slip region at the fiber-matrix interface, defined by $\alpha_s = \pi/2-\alpha$, as a function of the nondimensionalized load level $\tau_0/\tau_s$ was computed for various fiber volume fractions. For simplicity, the distribution of shear tractions along the interface was presented here only for the value of fiber volume fraction equal to 0.4. These results are plotted accordingly. The extent of slippage given in this paper for the special case of zero fiber volume fraction, i.e., $V_f = 0$, agrees well with the results calculated by Steif and Dollar (1988).

The results presented in Figs. 4 and 5 indicate that for finite concentration of fibers, that is, $V_f \neq 0$, composite materials with stiffer fibers behave rather differently from those with softer fibers. Clearly, this phenomenon will not be observed for the case when $V_f = 0$, since then the extent of slippage at

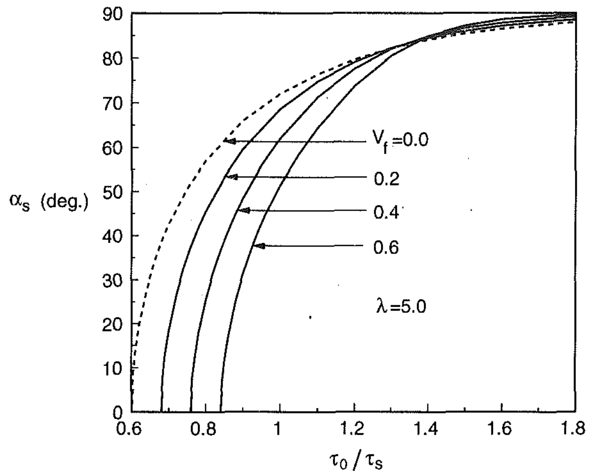


**Fig. 4 Extent of slippage as a function of nondimensionalized load level for λ = 5.0**

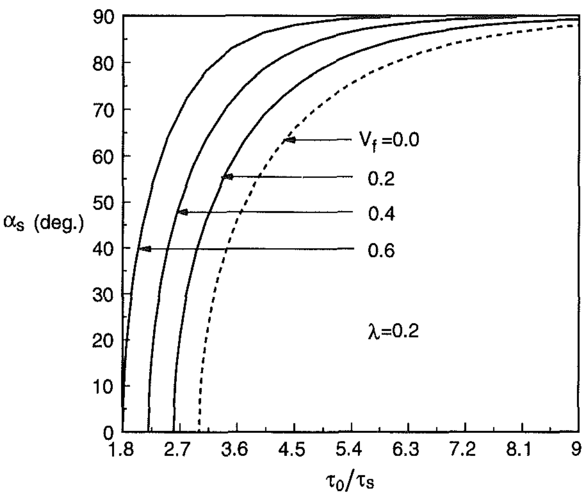


**Fig. 5 Extent of slippage as a function of nondimensionalized load level for λ = 0.2**

the fiber-matrix interface only depends on a single parameter $2\lambda\tau_0/(1+\lambda)\tau_s$.

Figure 4 indicates that for $\lambda > 1$, the level of loading required to initiate slip increases as fiber volume fraction increases, and up to a point, which is in fact very close to the complete debonding of the fiber-matrix interface, the extent of slip region under the same applied stress level is always smaller for a composite having larger fiber volume fraction. The minimum stress needed to cause slippage at the interface varies with different values of fiber volume fraction, and the complete slippage takes place only as the applied shear stress goes to infinity. Similarly, observations can also be made regarding the case when $\lambda < 1$ as shown in Fig. 5. By examining the results presented in Figs. 4 and 5, one can conclude that for composite materials with stiffer fibers, increase in fiber volume content tends to increase the resistance to interfacial slippage in longitudinal shear, while for composite materials having softer fibers, increasing fiber volume fraction, on the other hand, results in decreasing such resistance.

For a typical case when $\lambda = 5.0$, $V_f = 0.4$, and $\tau_0/\tau_s = 1.0$, comparison of the distributions of shear traction $\tau$ along the fiber-matrix interface for perfect bonding and slipping displays the nature of the redistribution of the interfacial shear tractions due to partial debonding (see Fig. 8). The same qualitative trend of redistribution of $\tau$ can also be seen for other values of $\lambda$, $V_f$, and $\tau_0/\tau_s$. The results presented in Figs. 6 and 7 show that as the slip zone progresses, the stress level $\tau$ over the unslipped portion of the fiber-matrix interface intensifies and rapidly reaches the critical value $\tau_s$.

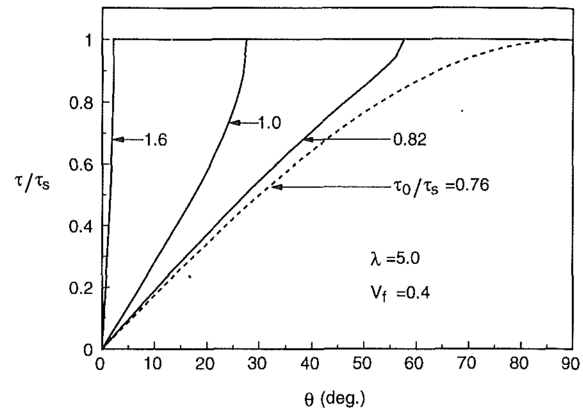


**Fig. 6 Distribution of shear traction along the fiber-matrix interface for λ = 5.0 and $V_f$ = 0.4**

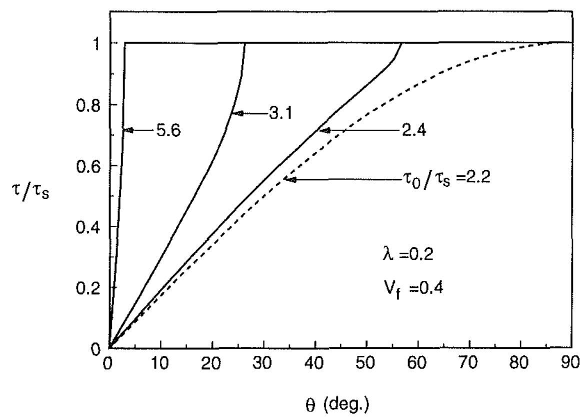


**Fig. 7 Distribution of shear traction along the fiber-matrix interface for λ = 0.2 and $V_f$ = 0.4**

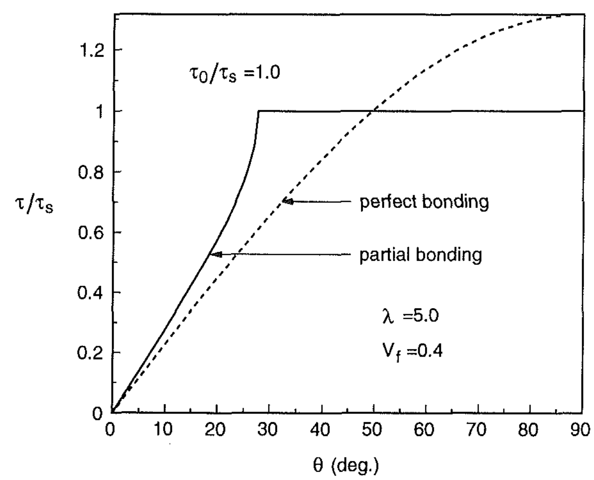


**Fig. 8 Comparison of shear tractions along the fiber-matrix interface with and without slip for the case λ = 5.0, $V_f$ = 0.4 and $\tau_0/\tau_s$ = 1.0**

Finally, it should be mentioned that by utilizing the composite cylinder model, the interaction between fibers has been taken into account only approximately. The accuracy of the results obtained by using the composite cylinder model is expected to be quite satisfactory up to certain fiber volume fractions. At large fiber volume fractions, however, the results may not reflect the true behavior of the composite material under consideration.

## Acknowledgment


This work was partially supported by the National Center for Composite Materials Research, the University of Illinois at Urbana-Champaign.

## References

Budiansky, B., and Carrier, G. F., 1984, "High Shear Stresses in Stiff-fiber Composites," ASME JOURNAL OF APPLIED MECHANICS, Vol. 51, pp. 733–735.

Budiansky, B., and Hutchinson, J. W., 1986, "Matrix Fracture in Fiber-reinforced Ceramics," *J. Mech. Phys. Solids*, Vol. 34, pp. 167–189.

Erdogan, F., 1978, "Mixed Boundary-Value Problems in Mechanics," *Mechanics Today*, S. Nemat-Nasser, ed., Vol. 4, pp. 1–86.

Hashin, Z., and Rosen, B. W., 1964, "The Elastic Moduli of Fiber-reinforced Materials," ASME JOURNAL OF APPLIED MECHANICS, Vol. 31, pp. 223–232.

Jaswon, M. A., and Symm, G. T., 1977, *Integral Equation Methods in Potential Theory and Elastostatics*, Academic Press, New York.

Keer, L. M., and Sve, C., 1970, "On the Bending of Cracked Plates," *Int. J. Solids and Structures*, Vol. 6, pp. 1545–1559.

Keer, L. M., Dundurs, J., and Kiattikomol, K., 1973, "Separation of a Smooth Circular Inclusion from a Matrix," *Int. J. Engng. Sci.*, Vol. 11, pp. 1221–1233.

Noble, B., and Hussain, M. A., 1969, "Exact Solution of Certain Dual Series for Indentation and Inclusion Problems," *Int. J. Engng. Sci.*, Vol. 7, pp. 1149–1161.

Piggott, M. R., 1987, "Debonding and Friction at Fiber-polymer Interfaces. I: Criteria for Failure and Sliding," *Composites Sci. and Tech.*, Vol. 30, pp. 295–306.

Smith, E., 1969, "The Extension of Circular-arc Cracks in Antiplane Strain Deformation," *Int. J. Engng. Sci.*, Vol. 7, pp. 973–991.

Smith, G. E., and Spencer, A. J. M., 1970, "Interfacial Tractions in a Fiber-reinforced Elastic Composite Material," *J. Mech. Phys. Solids*, Vol. 18, pp. 81–100.

Sneddon, I. N., 1966, *Mixed Boundary Value Problems in Potential Theory*, North-Holland, Amsterdam.

Steif, P. S., and Dollar, A., 1988, "Longitudinal Shearing of a Weakly Bonded Fiber Composite," ASME JOURNAL OF APPLIED MECHANICS, Vol. 55, pp. 618–623.

Steif, P. S., and Dollar, A., 1988, "Load Transfer in Composites with a Coulomb Friction Interface," *Int. J. Solids and Structures*, Vol. 24, pp. 789–803.

Tuck, O. E., 1980, "Application and Solution of Cauchy Singular Integral Equations," *The Application and Numerical Solution of Integral Equations*, R. S. Anderssen, et al., eds., Sijthoff and Noordhoff, Alphen ann Rijn, The Netherlands, pp. 21–49.

Westmann, R. A., and Yang, W. H., 1967, "Stress Analysis of Cracked Rectangular Beams," ASME JOURNAL OF APPLIED MECHANICS, Vol. 34, pp. 693–701.

Zweben, C., and Rosen, B. W., 1970, "A Statistical Theory of Material Strength with Application to Composite Materials," *J. Mech. Phys. Solids*, Vol. 18, pp. 189–206.


## APPENDIX

A brief description of the numerical scheme for solving the integral Eq. (23) is given here.

By dissecting the interval $[0, \alpha]$ into $N$ subintervals $[\phi_{j-1}, \phi_j]$, $j = 1, 2, \ldots N$, we can write (23) in the form

$$\sum_{j=1}^{N} \int_{\phi_{j-1}}^{\phi_j} \overline{H}(\phi) K(\theta, \phi) d\phi = \bar{f}(\theta) \tag{A1}$$

where $\overline{H}(\phi) = H(\phi)/\tau_s$ and $\bar{f}(\theta) = f(\theta)/\tau_s$. Note that no approximation is involved in this step.

Then we approximate $\overline{H}(\theta)$ by a step function, i.e., replace it within the $j$th subinterval $[\phi_{j-1}, \phi_j]$ by a constant $\overline{H}_j$, giving

$$\sum_{j=1}^{N} \overline{H}_j \int_{\phi_{j-1}}^{\phi_j} K(\theta, \phi) d\phi \approx \bar{f}(\theta). \tag{A2}$$

If we now evaluate the integrals at the midpoint of each subinterval, we arrive at a set of linear equations

$$\sum_{j=1}^{N} K_{ij} \overline{H}_j = \bar{f}_i, \quad i = 1,2,\ldots N \tag{A3}$$

where

$$K_{ij} = \int_{\phi_{j-1}}^{\phi_j} K(\theta_i, \phi) d\phi \tag{A4}$$

$$\bar{f}_i = \bar{f}(\theta_i) \tag{A5}$$

$$\theta_i = \frac{1}{2}(\phi_{i-1} + \phi_i). \tag{A6}$$

For computational convenience we let the subintervals be of equal length so that

$$\theta_i = \left(i - \frac{1}{2}\right)\frac{\alpha}{N}, \quad \phi_j = j\frac{\alpha}{N} \tag{A7}$$

$$i = 1,2,\ldots N \quad j = 0,1,2,\ldots N.$$

The $K_{ij}$ can be evaluated to yield

$$K_{ij} = (1+\lambda) \sum_{n=1,3\ldots}^{\infty} \frac{1}{n^2} \sin n\theta_i (\cos n\phi_{j-1} - \cos n\phi_j)$$
$$+ 2\lambda \sum_{n=1,3\ldots}^{\infty} \frac{V_f^n}{1-V_f^n} \frac{1}{n^2} \sin n\theta_i (\cos n\phi_{j-1} - \cos n\phi_j) \tag{A8}$$
$$i,j = 1,2,\ldots N$$

The $\bar{f}_i$ can be expressed as

$$\bar{f}_i = \frac{\pi\lambda}{2(1-V_f)} \frac{\tau_0}{\tau_s} - (1+\lambda) \sum_{n=1,3\ldots}^{\infty} \frac{1}{n^2} \cos n\alpha \sin n\theta_i$$
$$- 2\lambda \sum_{n=1,3,\ldots}^{\infty} \frac{V_f^n}{1-V_j^n} \frac{1}{n^2} \cos n\alpha \sin n\theta_i \tag{A9}$$
$$i = 1,2,\ldots N.$$

In both (A8) and (A9), the second infinite sums are fast convergent whereas the first series converge very slowly. However, by using the formula

$$\sum_{n=1,3,\ldots}^{\infty} \frac{1}{n} \cos nz = -\frac{1}{2} \log \left|\tan\frac{z}{2}\right|, \quad 0 < z < \pi, \tag{A10}$$

the slowly convergent series can be calculated in the following manner:

$$4 \sum_{n=1,3,\ldots}^{\infty} \frac{1}{n^2} \sin n\theta_i (\cos n\phi_{j-1} - \cos n\phi_j)$$
$$= \int_{\theta_i+\phi_{j-1}}^{\theta_i+\phi_j} \log\left|\tan\frac{z}{2}\right| dz + \int_{\theta_i-\phi_{j-1}}^{\theta_i-\phi_j} \log\left|\tan\frac{z}{2}\right| dz \tag{A11}$$
$$\sum_{n=1,3,\ldots}^{\infty} \frac{1}{n^2} \cos n\alpha \sin n\theta_i = -\frac{1}{4} \int_{\alpha-\theta_i}^{\alpha+\theta_i} \log\left|\tan\frac{z}{2}\right| dz \tag{A12}$$
$$i, j = 1,2,\ldots N.$$

Using (A7), one can show that the series in (A11) are symmetric with respect to $i$ and $j$ so that only the case when $i \geq j$ needs to be considered in the computations. Since the integrand in (A11) and (A12) is not well behaved near $z = 0$ and $z = \pi$, the integrals are evaluated via the following procedure:

$$\int_{z_1}^{z_2} \log\left|\tan\frac{z}{2}\right| dz = z_2 \log\left|\tan\frac{z_2}{2}\right| - z_1 \log\left|\tan\frac{z_1}{2}\right|$$
$$- \pi \log\left|\cos\frac{z_1}{2}\right| + \pi \log\left|\cos\frac{z_2}{2}\right|$$
$$+ \frac{1}{2} \int_{z_1}^{z_2} \left(\pi - z/\sin^2\frac{z}{2}\right) \tan\frac{z}{2}\, dz. \tag{A13}$$

The resulting integral in (A13) can be calculated by any numerical method, for instance, Simpson's rule is found to be very effective.

The system of Eqs. (A3) is then solved for $\overline{H}_i$ by adjusting $\alpha$ so as to satisfy the end condition

$$\overline{H}_N = 1 \tag{A14}$$

providing the desired numerical solution to the present problem.

S. A. Dunn[1]
Department of Mechanical and Manufacturing Engineering,
University of Melbourne,
Parkville, Australia

# Analysis of Thermal Conduction Effects on Thermoelastic Temperature Measurements for Composite Materials

*Measurement of the temperature changes which occur as a body undergoes a change in stress is becoming a widely used technique for the analysis of surface stress fields. In this paper, an investigation into the effects of thermal conduction on surface thermoelastic temperature changes for composite materials is reported. A mathematical model which shows the effects of thermal conduction is developed, and the results from this model are compared with experimental data. The mathematical model is then extended to solve for heat transfer between two thermally dissimilar materials. It is shown how this model can be used to account for the effects of a surface epoxy layer on the observed thermoelastic temperature changes.*

## 1 Introduction

There are many examples in the literature of the application of thermoelastic temperature measurement to composite materials; for example, see Kageyama et al. (1988), Heller et al. (1989), and Zhang and Sandor (1990). It was first reported in Dunn et al. (1989) that the quantitative determination of surface stresses from measured surface temperature changes can be extremely difficult for certain laminate configurations. It was shown how this difficulty arises due to the nonadiabatic effects which can be present due to the different thermoelastic heat generated in different plies of a composite material. The adiabatic thermoelastic equation describing the reversible change in temperature generated in a two-dimensional anisotropic material due to applied stresses in the elastic regime can be written as

$$-\rho c\,\frac{\Delta T}{T}=\alpha_1\Delta\sigma_1+\alpha_2\Delta\sigma_2 \tag{1}$$

in which $\rho$ is the density, $c$ is the specific heat, $\Delta T$ is the change in temperature, $T$ is the absolute temperature, $\alpha$ is the coefficient of linear thermal expansion, $\Delta\sigma$ is the change in stress, and the subscripts 1 and 2 denote the longitudinal and transverse to fiber directions, respectively. The mechanics of composite materials show that the stresses in different plies may vary greatly depending on the fiber orientations. As a consequence, the temperatures generated in each ply, as described by Eq. (1), will be very different. These temperature discontinuities give rise to very high temperature gradients leading to significant thermal conduction. This, coupled with the fact that the thickness of a typical ply in a graphite/epoxy laminate is from $120 \times 10^{-6}$m to $150 \times 10^{-6}$m, means that such thermal conduction can greatly affect the observed temperatures on the surface of the laminate.

Experimental results presented here show how thermal conduction can affect the observed surface temperature changes for a commonly used laminate configuration. A mathematical model is developed which describes this effect. An important feature of this model is that it has the capability to take into account the effects of the surface layer of epoxy which will exist on every composite material unless removed by abrading.

## 2 Specimens and Equipment

In this paper the results for two composite lay-ups will be presented; a $[(\pm 45\text{ deg})]_6]_s$ graphite/epoxy and $[(0\text{ deg}, \pm 45\text{ deg})_4]_s$ graphite/epoxy. The specimens were 30 mm wide and 145 mm long with bonded aluminum end tabs. The graphite/epoxy material used was AS4/3501-6. The loading was applied via bolts which passed through holes in the end tabs and composite material. These bolts were tightened, clamping bushes on either side of the end fittings such that the stress concentration effects of the holes were minimized.

Loads were applied to the specimens with a 50kN MTS servohydraulic testing machine. The temperature changes on the surface of the specimens were measured using the infrared detector of a SPATE 8000 system and the data from the infrared detector and load cell of the MTS testing machine were

[1]Permanent Address: Aircraft Structures Division, Aeronautical Research Laboratory, 506 Lorimer Street, Fishermen's Bend, Australia.

Contributed by the Applied Mechanics Division of THE AMERICAN SOCIETY OF MECHANICAL ENGINEERS for publication in the ASME JOURNAL OF APPLIED MECHANICS.

Discussion on this paper should be addressed to the Technical Editor, Professor Leon M. Keer, The Technological Institute, Northwestern University, Evanston, IL 60208, and will be accepted until four months after final publication of the paper itself in the JOURNAL OF APPLIED MECHANICS.

Manuscript received by the ASME Applied Mechanics Division, Nov. 15, 1990; final revision, Feb. 1, 1991. Associate Technical Editor: A. K. Noor.

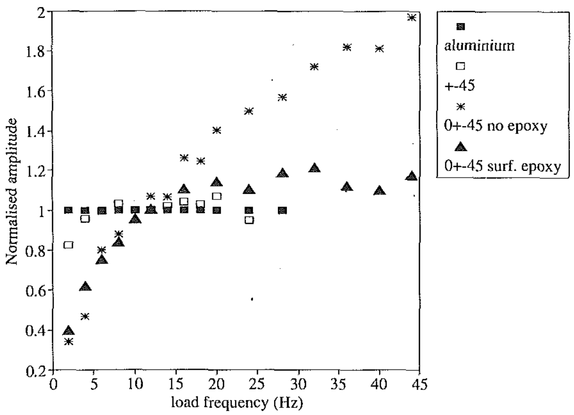


**Fig. 1 Normalized amplitude of infrared detector response versus frequency of loading for aluminium, $[(\pm 45\ \mathrm{deg})_6]_s$ and $[(0\ \mathrm{deg}, \pm 45\ \mathrm{deg})_4]_s$ laminates with and without a surface layer of epoxy. (Note: the aluminium, $[(\pm 45\ \mathrm{deg})_6]_s$ and $[(0\ \mathrm{deg}, \pm 45\ \mathrm{deg})_4]_s$ specimen without surface epoxy are normalized against their respective amplitudes at 10 Hz. The amplitude of the $[(0\ \mathrm{deg}, \pm 45\ \mathrm{deg})_4]_s$ specimen with a surface layer of epoxy is normalized against the amplitude of the $[(0\ \mathrm{deg}, \pm 45\ \mathrm{deg})_4]_s$ specimen without a surface layer of epoxy at 10 Hz.)**

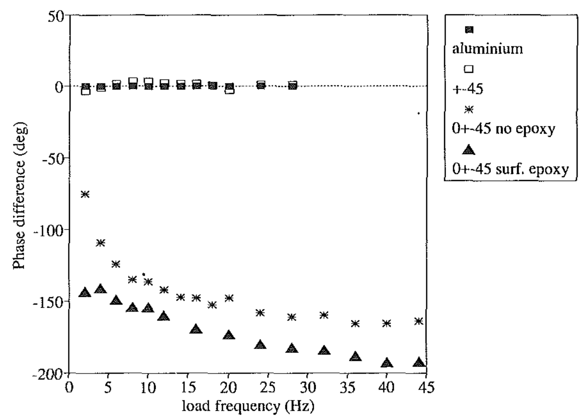


**Fig. 2 Phase difference between load input and infrared detector response versus frequency of loading for aluminium, $[(\pm 45\ \mathrm{deg})_6]_s$ and $[(0\ \mathrm{deg}, \pm 45\ \mathrm{deg})_4]_s$ laminates with and without a surface layer of epoxy**

analyzed using a Wavetek 804A Multi-Channel Signal Processor.

## 3 Frequency Effects

**3.1 Experimental Evidence.** The following experiments investigate the effects of loading frequency, while maintaining a constant load amplitude, on the amplitude and phase of the thermoelastic temperature response for $[(\pm 45\ \mathrm{deg})_6]_s$ and $[(0\ \mathrm{deg}, \pm 45\ \mathrm{deg})_4]_s$ graphite/epoxy specimens. The $[(0\ \mathrm{deg}, \pm 45\ \mathrm{deg})]_{4}]_s$ specimen was tested in two configurations: *i.* in the as cured condition, and *ii.* with the surface epoxy abraded away. The results are compared with those for an aluminium specimen.

The results for the magnitude of the detector response divided by the cyclic load amplitude and normalized by the response at 10 Hz for an aluminium alloy specimen, a $[(\pm 45\ \mathrm{deg})_6]_s$ and a $[(0\ \mathrm{deg}, \pm 45\ \mathrm{deg})_4]_s$ specimen in conditions *i.* and *ii.* (as described above) are presented in Fig. 1. The corresponding phase difference between the measured load and infrared responses at the loading frequency are shown in Fig. 2. (Note: The polarity of the infrared detector is such that a reduction in temperature leads to an increase in output voltage and that the experimental data was corrected for system electronic effects at low frequencies as in Wong (1990).)

The results presented in Figs. 1 and 2 show that the aluminium and $[(\pm 45\ \mathrm{deg})_6]_s$ specimens behave in a similar manner with loading frequency. The $[(0\ \mathrm{deg}, \pm 45\ \mathrm{deg})]_{4s}$ specimen, however, responds in a very different manner with adiabatic conditions apparently not being achieved at a frequency of 45 Hz. (Note: Similar results were first presented in Dunn et al. (1989); it has since been found that the emissivity enhancing paint layer used for those results had a significant effect on the observed phase response for the $[(0\ \mathrm{deg}, \pm 45\ \mathrm{deg})_4]_s$ specimen. As a consequence, the tests were repeated without any paint on the specimen. Such a surface coating of paint is not required for composite materials because of their relatively high infrared emissivity of 0.92 (Griffs et al., 1981). The reason for the significant effect on the phase response for this specimen will become obvious in the section dealing with the mathematical modeling of the surface epoxy layer on such specimens.) The following analysis examines the thermoelastic heat generated in a $[(0\ \mathrm{deg}, \pm 45\ \mathrm{deg})_4]_s$ specimen and shows why thermal conduction makes it behave differently from the aluminium and $[(\pm 45\ \mathrm{deg})_6]_s$ specimens. The effects of a surface epoxy layer on a $[(0\ \mathrm{deg}, \pm 45\ \mathrm{deg})_4]_s$ specimen are then examined.

**3.2 Analysis of the Thermoelastic Heat Generated in a Composite Material.** To determine the heat generated in the composite material, it is necessary to investigate the contribution from each of the two constituents, the fibers and matrix material, for each ply. To do this, it is necessary to determine the stiffnesses and Poisson's ratios for the laminate as a whole such that the strains may be determined. Given these strains, the average stresses in the matrix material and the fibers in each ply may be approximated. Equation (1) may then be used to determine the heat generation in each material. Wong (1990) has shown that the heat transfer between fiber and matrix is very rapid. This means that, given the heat generated in each of the constituents, the only information required to determine the overall heat generated in the ply is the fiber/matrix volume ratio $V_f/V_m$ and the respective densities and specific heats.

Given an orthotropic material, the relationship between the stresses and strains with respect to the laminate orthotropic $(x, y)$ axes, may be written as

$$\begin{Bmatrix} \epsilon_x \\ \epsilon_y \\ \gamma_{xy} \end{Bmatrix} = \begin{bmatrix} 1/E_x & -\nu_{yx}/E_y & 0 \\ -\nu_{xy}/E_x & 1/E_y & 0 \\ 0 & 0 & 1/G_{xy} \end{bmatrix} \begin{Bmatrix} \sigma_x \\ \sigma_y \\ \tau_{xy} \end{Bmatrix}. \tag{2}$$

In order to approximate the average stresses in the fibers, the strains with respect to the ply orthotropic (1, 2) axes must be determined. The relationship between the strains in the two axes systems is given as

$$\begin{Bmatrix} \epsilon_1 \\ \epsilon_2 \\ \gamma_{12} \end{Bmatrix} = \begin{bmatrix} m^2 & n^2 & mn \\ n^2 & m^2 & -mn \\ -2mn & 2mn & m^2-n^2 \end{bmatrix} \begin{Bmatrix} \epsilon_x \\ \epsilon_y \\ \gamma_{xy} \end{Bmatrix}. \tag{3}$$

where $m = \cos\theta$ and $n = \sin\theta$ ($\theta$ is the angle between the 1, 2-axes and the $x$, $y$-axes). Given that the thermoelastic heat generation (Eq. (1)) is dependent only upon the principle stresses, an average of these stresses in the fibers may be approximated using

$$\begin{Bmatrix} \sigma_1 \\ \sigma_2 \end{Bmatrix} = \frac{1}{1-\nu_{12}\nu_{21}} \begin{bmatrix} E_1 & \nu_{12}E_2 \\ \nu_{21}E_1 & E_2 \end{bmatrix} \begin{Bmatrix} \epsilon_1 \\ \epsilon_2 \end{Bmatrix} \tag{4}$$

and substituting in the fiber material properties. It is important to note here that these equations are not adequate to determine the maximum stresses or stress distribution which occur in

Table 1 Material properties for AS graphite fibers and high modulus matrix material (Chamis, 1984)

| | | |
|---|---|---|
| fibre longitudinal modulus | $E_{f1}$ | 214 GPa |
| fibre transverse modulus | $E_{f2}$ | 13.8 GPa |
| fibre longitudinal Poisson's ratio | $\nu_{f12}$ | 0.20 |
| fibre transverse Poisson's ratio | $\nu_{f21}$ | 0.013 |
| fibre long. thermal exp. coeff. | $\alpha_{f1}$ | $-1.0 \times 10^{-6}$/K |
| fibre trans. thermal exp. coeff. | $\alpha_{f2}$ | $10 \times 10^{-6}$/K |
| fibre density | $\rho_f$ | 1744 kg/m$^3$ |
| fibre specific heat | $c_f$ | 837 J/kgK |
| matrix modulus | $E_m$ | 5.2 GPa |
| matrix Poisson's ratio | $\nu_m$ | 0.35 |
| matrix thermal exp. coeff. | $\alpha_m$ | $72 \times 10^{-6}/K$ |
| matrix density | $\rho_m$ | 1246 kg/m$^3$ |
| matrix specific heat | $c_m$ | 1047 J/kgK |

Table 2 Laminate properties for [(0 deg, ±45 deg)$_4$]$_s$ laminate

| | | |
|---|---|---|
| longitudinal modulus | $E_x$ | 57.4 GPa |
| transverse modulus | $E_y$ | 24.2 GPa |
| longitudinal Poisson's ratio | $\nu_{xy}$ | 0.68 |
| transverse Poisson's ratio | $\nu_{yx}$ | 0.29 |
| fibre/matrix volume ratio | $V_f/V_m$ | 0.6/0.4 |

either the fiber or matrix materials. To do this, micromechanical effects must be investigated. Nevertheless, these equations give an approximation to the average stresses in these materials. Equation (1), which is used to calculate the heat generated in the materials, is a linear equation, and the heat diffusion between fiber and matrix is very rapid; given this, such average stresses, rather than a micromechanical stress distribution, are all that is required for these purposes.

The fiber stresses from Eq. (4) may be substituted into Eq. (1) to determine the thermoelastic heat generated in the fibers of a particular ply. The same process may be carried out to determine the thermoelastic heats that would be generated in the matrix material (Note: Because the matrix material is isotropic, and strains are assumed to be constant throughout the laminate, the heat generated in the matrix is the same throughout the laminate.)

When investigating the thermoelastic heat generated in composite materials, other researchers have found significant irreversible heating due to viscoelastic effects (Bakis and Reifsnider, 1988). The material used here was tested for nonlinearities arising due to irreversible heating. Such effects were found to be significant only at much higher strain amplitudes than those applied here for the frequency range used in these tests.

The mechanical and thermal properties of these materials used in this analysis are given in Table 1.

The laminate properties for a [(0 deg, ±45 deg)$_4$]$_s$ lay-up in terms of the orthotropic axes of the laminate are presented in Table 2.

For a [(0 deg, ±45 deg)$_4$]$_s$ laminate with no shear stress applied, the laminate properties from Table 2 may be substituted into Eq. (2) to give $\epsilon_x$ and $\epsilon_y$ in terms of $\sigma_x$ and $\sigma_y$. For the case studied here in which the laminate is subjected to uniaxial loading in the $x$-direction, the parameters are determined in terms of $\epsilon_x$ giving $\epsilon_y = -\nu_{xy}\epsilon_x$. These strains are then substituted into Eq. (3) to give the strains with respect to the ply axes in terms of $\epsilon_x$. Given $\epsilon_1$ and $\epsilon_2$, Eq. (3), with the material properties given in Table 1, may then be used to approximate the average stresses in the components of the composite material. Equation (1) may then be used to determine the normalized thermoelastic change in temperature in terms of $\epsilon_x$.

Carrying out these substitutions give

$$\left.\frac{\Delta T}{\epsilon_x T}\right|_{0 \text{ deg fibers}} = \frac{-2.8\times 10^5}{\rho_f c_f}$$
$$\left.\frac{\Delta T}{\epsilon_x T}\right|_{45 \text{ deg fibers}} = \frac{-0.08\times 10^5}{\rho_f c_f} \tag{5}$$
$$\left.\frac{\Delta T}{\epsilon_x T}\right|_{\text{matrix}} = \frac{1.8\times 10^5}{\rho_m c_m}.$$

A useful assumption is that the heat generated in the matrix and fiber materials rapidly diffuses to give the same temperature rise in both materials; this is shown in Wong (1990) to be a valid assumption for all but very high frequencies (> 1000 Hz). Using this assumption, an equation describing the energy in each ply may be written as

$$\rho_{\text{ply}} c_{\text{ply}} \Delta T_{\text{ply}} = V_f \rho_f c_f \Delta T_f + V_m \rho_m c_m \Delta T_m \tag{6}$$

and using

$$\rho_{\text{ply}} c_{\text{ply}} = V_f \rho_f c_f + V_m \rho_m c_m \tag{7}$$

gives

$$\Delta T_{\text{ply}} = \frac{V_f \rho_f c_f \Delta T_f + V_m \rho_m c_m \Delta T_m}{V_f \rho_f c_f + V_m \rho_m c_m}. \tag{8}$$

The results given in Eq. (5) and the fiber/matrix volume ratio, $V_f/V_m$, may then be substituted into Eq. (8) to give the normalized adiabatic temperature generated in each ply. For a [(0 deg, ±45 deg)$_4$]$_s$ laminate subjected to uniaxial load in the $x$-direction, the normalized thermoelastic temperature changes ($\Delta T/\epsilon_x T$) generated in the plies is found to be $-0.07$ for the 0 deg ply and 0.05 for the 45 deg ply.

Additional work is in progress which involves a means of determining the ratios of the heating in the different plies of a composite material from experimental data. The results from this work show very good correlation between the ratios determined from the experimental data and those found using the previous analysis for both a [(0 deg, ±45 deg)$_4$]$_s$ laminate and a [(90 deg, ±45 deg)$_4$]$_s$ laminate.

An interesting aside to this analysis is to look at the heat generated in a unidirectional laminate loaded in the fiber direction. An experiment carried out by Wong (1990) found that the thermoelastic heat generated in a unidirectional laminate was such that it suggested that the $\alpha_x$ of the laminate was positive whereas most published values of $\alpha_x$ for such a laminate are negative. Carrying out an analysis of the expected thermoelastic heat generated in a unidirectional specimen following the previous method and using a laminate longitudinal Poisson's ratio of 0.26 gives the normalized heat generated in the fibers as $-2.2\times 10^5/\rho_f c_f$ and that in the matrix as $4.22 \times 10^5/\rho_m c_m$. Using the same fiber matrix volume ratio as previously, the total normalized temperature change in the laminate is 0.03. This positive result is in accord with the experimental results presented in Wong (1990).

**3.3 Mathematical Modeling of Frequency Effects.** The frequency effects can be demonstrated by modeling the thermal conduction within the laminate. Wong (1990) has modeled the frequency effects for a similar laminate using a finite difference technique; an analytical solution for the same problem will be developed here.

To examine the temperature distribution $T(x, t)$ through the thickness of a laminate, the laminate will be modeled as an infinite slab allowing the use of the one-dimensional heat equation.

$$K\frac{\partial^2 T}{\partial x^2} + w(x, t) = \rho c \frac{\partial T}{\partial t} \tag{9}$$

in which $K$ is the thermal conductivity and $w(x, t)$ is the time-varying heat generated through the thickness.

Using a Fourier cosine transformation, Luikov (1968) solves Eq. (9) for an infinite slab of thickness $2R$ with the initial temperature taken to be

$$T(x, 0) = f(x) \tag{10}$$

and the boundary condition is taken as

$$-\kappa \frac{\partial T(R, t)}{\partial x}+q(t)=0 \tag{11}$$

in which $\kappa$ is the thermal diffusivity ($\kappa = K/\rho c$) and $q(t)$ is the heat flux absorbed at the surface of the slab. The solution given by Luikov (1968) is

$$\begin{aligned}T(x, t)=&\frac{1}{R}\left\{\int_0^R f(x)dx+\frac{\kappa}{K}\int_0^t q(\tau)d\tau + \frac{1}{c\rho}\int_0^t\int_0^R w(x, \tau)\, dx d\tau\right\}\\ &+\frac{2}{R}\sum_{n=1}^{\infty} \cos\frac{n\pi x}{R}\exp\left(-\frac{\kappa n^2\pi^2 t}{R^2}\right)\int_0^R f(x)\cos\frac{n\pi x}{R}dx\\ &+\frac{2\kappa}{KR}\sum_{n=1}^{\infty}(-1)^n\cos\frac{n\pi x}{R}\int_0^t q(\tau)\exp\left[-\frac{\kappa n^2\pi^2}{R^2}(t-\tau)\right]d\tau\\ &+\frac{2}{Rc\rho}\sum_{n=1}^{\infty}\cos\frac{n\pi x}{R}\int_0^t\int_0^R w(x, t)\exp\left[-\frac{\kappa n^2\pi^2}{R^2}(t-\tau)\right]\cos\frac{n\pi x}{R}dxd\tau.\end{aligned} \tag{12}$$

To study the effects of thermoelastic heating on a composite material, the heat absorbed at the surface, $q(t)$, can be set to zero defining the boundary condition given in Eq. (11) as an adiabatic boundary. This is shown by finite difference analysis in Wong (1990) to be an acceptable boundary condition. The initial temperature distribution, $f(x)$ may also be set to zero. Equation (12) then reduces to

$$\begin{aligned}T(x, t)=\frac{1}{Rc\rho}\Bigg(&\int_0^t\int_0^R w(x, \tau)dx\, d\tau\\ &+2\sum_{n=1}^{\infty}\cos\frac{n\pi x}{R}\int_0^t\int_0^R w(x, t)\exp\left[-\frac{\kappa n^2\pi^2}{R^2}(t-\tau)\right]\cos\frac{n\pi x}{R}dx\, d\tau\Bigg).\end{aligned} \tag{13}$$

This model may then be used to solve for the temperature distribution in a laminated slab of $m$ plies with cyclic heat generation throughout its thickness of the form

$$w(x, t)=\begin{cases} v_1\cos\omega t & \text{if } 0 < x < \chi_1 R;\\ v_2\cos\omega t & \text{if } \chi_1 R < x < \chi_2 R;\\ \cdot & \cdot\\ \cdot & \cdot\\ v_m\cos\omega t & \text{if } \chi_{m-1} R < x < R\end{cases} \tag{14}$$

where $v_j$ is the maximum rate of heat generated per unit volume in the $j$th ply. $v_j$ may be written as

$$v_j=\frac{1}{2}\omega\rho c a_j \tag{15}$$

where $a_j$ is the peak-to-peak temperature generated within the $j$th ply under adiabatic conditions.

Substituting the input described by Eqs. (14) and (15) into Eq. (13) and carrying out the integrations yields

$$\begin{aligned}T(x, t)=&\frac{1}{2}\sin\omega t\left[\left\{\sum_{j=1}^{m-1}\chi_j(a_j-a_{j+1})\right\}+a_m\right]\\ &+\frac{1}{\pi}\left[\sum_{n=1}^{\infty}\frac{1}{n}\cos\frac{n\pi x}{R}\left(\frac{\sin\omega t+\eta\cos\omega t-\eta e^{-\gamma t}}{(1+\eta^2)}\right)\right.\\ &\left.\times\left\{\sum_{j=1}^{m-1}(\alpha_j-a_{j+1})\sin\chi_j n\pi\right\}\right]\end{aligned} \tag{16}$$

where $\gamma = \kappa n^2\pi^2/R^2$ and $\eta=\gamma/\omega$. Observing the temperatures at the surface, $(x=R)$, as $t\rightarrow\infty$, Eq. (16) becomes

$$\begin{aligned}T(R, t)|_{t\rightarrow\infty}=&\frac{1}{2}\sin\omega t\left[\left\{\sum_{j=1}^{m-1}\chi_j(a_j-a_{j+1})\right\}+a_m\right]\\ &+\frac{1}{\pi}\left[\sum_{n=1}^{\infty}\frac{(-1)^n}{n}\frac{\sin\omega t+\eta\cos\omega t}{(1+\eta^2)}\left\{\sum_{j=1}^{m-1}(a_j-a_{j+1})\sin\chi_j\eta\pi\right\}\right].\end{aligned} \tag{17}$$

A check that can be carried out on this model is to investigate its behavior as $\omega\rightarrow\infty$. As $\omega\rightarrow\infty$, it would be expected that the surface temperature amplitude would be unaffected by conduction giving $T(R, t)|_{t\rightarrow\infty,\omega\rightarrow\infty}$ to be $a_m/2$. As $\omega\rightarrow\infty$, $\eta\rightarrow 0$, giving

$$\begin{aligned}T(R,t)|_{t\rightarrow\infty,\omega\rightarrow\infty}=&\frac{1}{2}\sin\omega t\left[\left\{\sum_{j=1}^{m-1}\chi_j(a_j-a_{j+1})\right\}+a_m\right]\\ &+\frac{1}{\pi}\sin\omega t\left[\sum_{n=1}^{\infty}\frac{(-1)^n}{n}\left\{\sum_{j=1}^{m-1}(a_j-a_{j+1})\sin\chi_j n\pi\right\}\right].\end{aligned} \tag{18}$$

Given that (Gradshteyn and Ryzhik, 1980)

$$\sum_{n=1}^{\infty}\frac{(-1)^n}{n}\sin pn\pi=-\frac{\pi p}{2}, \tag{19}$$

it can be seen from Eq. (18) that

$$T(R,t)|_{t\rightarrow\infty,\omega\rightarrow\infty}=\frac{a_m}{2}\sin\omega t, \tag{20}$$

as is expected.

This is the analytic solution to the problem solved in Wong (1990) by finite difference techniques. For the $[(0\text{ deg}, \pm 45\text{ deg})_4]_s$ laminate used here, the ply thicknesses were $140 \times 10^{-6}$ m. Using these ply thicknesses, heating in each ply as found in Section 3.2 and a thermal diffusivity of $7\times10^{-7}$ m$^2$/s (Chen et al., 1985), Eq. (17) was solved and the results were plotted with the experimental data for the $[(0\text{ deg}, \pm 45\text{ deg})_4]_s$ specimen in Figs. 3 and 4. The results from Eq. (17) agree quite well with those found experimentally for the specimen with no surface layer of epoxy (although there is some divergence in the amplitude at higher frequencies). Similar agreement was found between the experimental results and numerical modeling presented in Wong (1990) where the surface layer of epoxy was removed prior to testing (Wong, 1991). As can be seen in Figs. 3 and 4, there is a significant difference between the case with the surface epoxy layer removed and that for the surface in the "as-cured" condition. An understanding of the effects of the surface epoxy layer is essential to the understanding of results for most composite specimens which will have such a layer of epoxy. It will also have the advantage of leading to a fuller understanding of the effects of the surface layer of paint which is commonly applied to metallic specimens to increase their infrared emissivity for the purposes of thermoelastic stress measurement.

**3.4 Effects of a Surface Layer of Epoxy.** To include the effects of a surface epoxy layer on the observed temperature changes, a "composite" problem, in the heat conduction sense, must be solved. The reason for this is that the thermal diffusivity for the epoxy layer is significantly different from that for the rest of the laminate. This problem can be solved by looking at two simultaneous equations of the form of Eq. (12); one for the surface epoxy layer and another for the laminate. For these equations, the terms involving the heat flux, $q(t)$, must be left in to allow for heat transfer between the two materials. The equations take the form

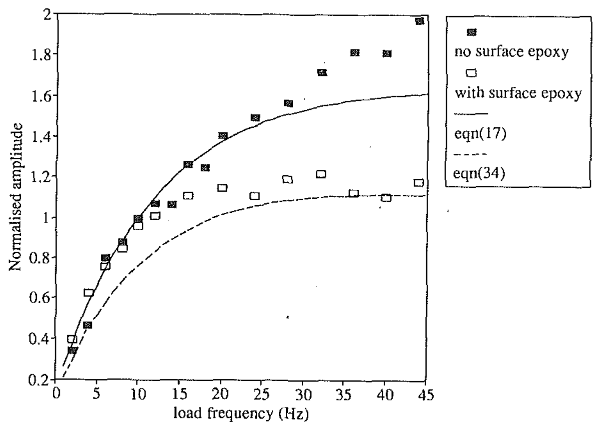


Fig. 3 Normalized amplitude of infrared detector response versus frequency of loading for the [(0 deg, ±45 deg)$_4$]$_s$ specimen with and without a surface layer of epoxy compared with the results from Eqs. (17) and (34). (Note: the experimental results are normalized against the amplitude for the specimen without a surface layer of epoxy at 10 Hz; the analytic results are normalized against the amplitude of the surface temperature changes at 10 Hz from Eq. (17))

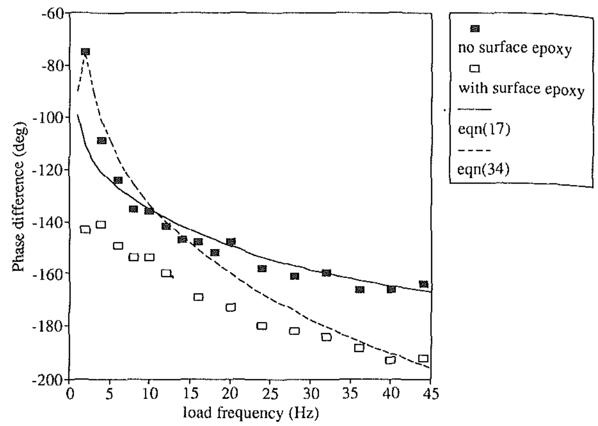


Fig. 4 Phase difference between load input and infrared detector response versus frequency of loading for [(0 deg, ±45 deg)$_4$]$_s$ laminates both with and without a surface layer of epoxy compared with the phase difference between the input and the surface temperature changes found from Eqs. (17) and (34)

$$T_p(x,t)=\frac{1}{R_p\rho_pC_p}\left(\int_0^t q(\tau)d\tau+\int_0^t\int_0^{R_p} w_p(x,\tau)dxd\tau + 2\sum_{n=1}^{\infty}(-1)^n\cos\frac{n\pi x}{R_p}\int_0^t q(\tau)\exp\left[-\frac{\kappa_pn^2\pi^2}{R_p^2}(t-\tau)\right]d\tau + 2\sum_{n=1}^{\infty}\cos\frac{n\pi x}{R_p}\int_0^t\int_0^{R_p} w_p(x,t)\exp\left[-\frac{\kappa_pn^2\pi^2}{R_p^2}(t-\tau)\right]\cos\frac{n\pi x}{R_p}dxd\tau\right) \quad (21)$$

for the substratum of plies (subscript $p$), and

$$T_e(x,t)=\frac{1}{R_e\rho_eC_e}\left(\int_0^t q(\tau)d\tau+\int_0^t\int_0^{R_e} w_e(x,\tau)dxd\tau + 2\sum_{n=1}^{\infty}(-1)^n\cos\frac{n\pi x}{R_e}\int_0^t q(\tau)\exp\left[-\frac{\kappa_en^2\pi^2}{R_e^2}(t-\tau)\right]d\tau + 2\sum_{n=1}^{\infty}\cos\frac{n\pi x}{R_e}\int_0^t\int_0^{R_e} w_e(x,t)\exp\left[-\frac{\kappa_en^2\pi^2}{R_e^2}(t-\tau)\right]\cos\frac{n\pi x}{R_e}dxd\tau\right) \quad (22)$$

for the surface epoxy layer (subscript $e$).

The interface conditions applying to Eqs. (21) and (22) are

$$T_e(R_e,t)=T_p(R_p,t) \quad (23)$$

and

$$q_e(t)=-q_p(t). \quad (24)$$

The heating $w_p(x,t)$ is as given in Eq. (14). The heating for the surface epoxy layer is

$$w_e(x,t)=\frac{1}{2}\,\omega\rho_ec_ea_e\cos\omega t. \quad (25)$$

Substituting the interface conditions given in Eqs. (23) and (24), the surface epoxy heating of Eq. (25) and the ply heating of Eq. (14) into (21) and (22) gives the integral equation

$$\frac{\xi_p-a_e}{2}\sin\omega t + \frac{1}{\pi}\left\{\sum_{n=1}^{\infty}\frac{1}{n}\cos n\pi\left[\frac{\sin\omega t+\eta_p\cos\omega t-\eta_pe^{-\gamma_p(t-\tau)}}{(1+\eta_p^2)}\right]\Xi_{pn}\right\}$$

$$=\int q(\tau)\left\{(b_e+b_p)+2b_e\sum_{n=1}^{\infty}e^{-\gamma_e(t-\tau)}+2b_p\sum_{n=1}^{\infty}e^{-\gamma_p(t-\tau)}\right\}d\tau \quad (26)$$

in which

$$\xi_p=\left\{\sum_{j=1}^{m-1}\chi_j(a_j-a_{j+1})\right\}+a_m, \quad (27)$$

$$\Xi_{pn}=\sum_{j=1}^{m-1}(a_j-a_{j+1})\sin\chi_jn\pi \quad (28)$$

and

$$b_p=1/R_p\rho_pc_p$$

$$b_e=1/R_e\rho_ec_e. \quad (29)$$

Equation (26) is a Volterra integral equation of the first kind with a difference kernel and is most easily solved by taking Laplace transforms and making use of the convolution theorem, giving

$$\left(\frac{\xi_p-a_e}{2}\right)\frac{\omega}{s^2+\omega^2} + \frac{1}{\pi}\left\{\sum_{n=1}^{\infty}\frac{1}{n}\cos n\pi\frac{\Xi_{pn}}{1+\eta_p^2}\left[\frac{\omega}{s^2+\omega^2}+\frac{\eta_ps}{s^2+\omega^2}-\frac{\eta_p}{s+\gamma_p}\right]\right\}$$

$$=\mathcal{Q}(s)\left\{\frac{b_e+b_p}{s}+2b_e\sum_{n=1}^{\infty}\frac{1}{s+\gamma_e}+2b_p\sum_{n=1}^{\infty}\frac{1}{s+\gamma_p}\right\} \quad (30)$$

in which $s$ is the Laplace operator and $\mathcal{Q}(s)$ is the Laplace transform of $q(t)$. Given that the only interest here lies in the particular solution and not in any transients that may occur, Eq. (30) may be condensed to give

$$\mathcal{Q}(s)=\left[\left(\frac{\xi_p-a_e}{2}\right)\omega+\sum_{n=1}^{\infty}\frac{\cos n\pi}{n\pi}\frac{\Xi_{pn}}{1+\eta_p^2}(\omega+\eta_ps)\right]\Bigg/$$

$$\left[(s^2+\omega^2)\left(\frac{b_p+b_e}{s}+2b_e\sum_{n=1}^{\infty}\frac{1}{s+\gamma_e}+2b_p\sum_{n=1}^{\infty}\frac{1}{s+\gamma_p}\right)\right] \quad (31)$$

Equation (31) may be inverted using the inversion theory for Laplace transformations

$$\mathcal{L}^{-1}\left(\frac{\phi(s)}{\psi(s)}\right)=\sum_{j=1}^{J}\frac{\phi(s_j)}{\psi'(s_j)}e^{s_jt} \quad (32)$$

in which there are $J$ roots, $s_j$, of $\psi(s)$. To solve for the steady-state cyclic response, the only roots required are $\pm i\omega$.

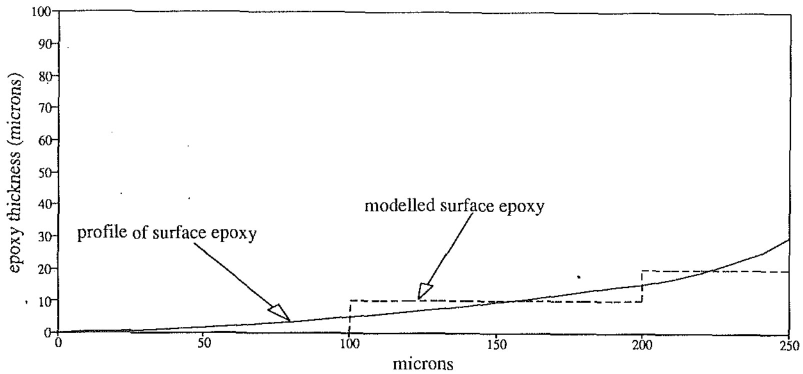


**Fig. 5 Diagram showing a typical half-wavelength of the variation in cross-section of the profile of the surface layer of epoxy for a $[(0\ \mathrm{deg}, \pm 45\ \mathrm{deg})_4]_s$ specimen (solid line) and the surface epoxy layer as used in the mathematical model (dashed line)**

The result of this inversion will be $q(t)$ of the form

$$q(t)|_{t\to\infty} = \zeta_s \sin\omega t + \zeta_c \cos\omega t. \tag{33}$$

Inverting the Laplace transform and looking at the temperatures of the surface layer of epoxy, $T_e(0,t)$, gives

$$T_e(0,t)|_{t\to\infty} = b_e\left\{\frac{\zeta_s}{\omega}\cos\omega t + \frac{\zeta_c}{\omega}\sin\omega t + \frac{a_e}{2b_e}\sin\omega t\right\}$$
$$+2b_e\left\{\sum_{n=1}^{\infty}\frac{(-1)^n}{\omega(1+\eta_e^2)}\left[\zeta_s(-\cos\omega t+\eta_e\sin\omega t)\right.\right.$$
$$\left.\left.+\zeta_c(\sin\omega t+\eta_e\cos\omega t)\right]\right\}. \tag{34}$$

Using Eq. (31), the heat transfer across the interface of the two materials can now be determined, and given this, Eq. (34) gives the temperature changes which would be observed on the surface.

Before these equations can be used, the nature of the surface epoxy layer must be determined. For the specimens used here, a relatively coarse fiberglass bleed cloth was used in the curing process. Examination of the surface epoxy layer under a microscope shows that the cross-section of the surface epoxy is as shown in Fig. 5. This epoxy layer was modeled as shown by the dashed lines in Fig. 5 giving the observed flux as an average of the three layers, weighted with respect to their surface areas. Using this surface model, the model used for the substratum of plies in the previous section, the heat generated in the epoxy as for the matrix in Section 3.2 and taking the thermal diffusivity for the epoxy to be $1\times10^{-7}\mathrm{m}^2/\mathrm{s}$ (Chamis, 1984), Eq. (34) gives results for the frequency variation of the surface temperature as shown in Figs. 3 and 4. As can be seen, these analytical results compare favorably with those found experimentally and certainly exhibit the correct trend in the differences shown between the case for no surface epoxy layer and that with the surface epoxy layer.

## 4 Discussion

Two analytic solutions for the temperature distributions through a laminate subjected to different amounts of thermoelastic heat generation throughout its thickness have been developed. The first case considered involved treating the material as being homogeneous. Similar analytic models have been developed by Belgen (1968) and McKelvie (1987) in order to investigate the nonadiabatic effects experienced by a metallic plate in bending. The solutions presented by these authors (based on a solution to the problem given in Carslaw and Jaeger (1959)) can be extended to the case for a composite material. The model presented here, however, is more general in that it allows heat transfer across the boundary thereby greatly facilitating the extension of the model to a "composite" model in the heat transfer sense (i.e., modeling materials with different thermal properties).

The next model investigated the temperature distribution through the thickness of a laminate with a surface layer of epoxy. The model developed is general and can be used to solve for the temperature distribution through two materials irrespective of the thickness and thermal properties. The effects of paint coatings on plates in bending were investigated by Belgen (1968), McKelvie (1987), and Mackenzie (1989). These studies neglected the "thermal load" that the coating places on the substrate material but it was considered that this effect would be small for a thin paint layer generating small amounts of thermoelastic heat with respect to an aluminium substrate. For the case of the laminate studied here, with a surface layer of epoxy, the above assumption is not necessarily valid. This is because the thickness of the epoxy layer can be much thicker than that for an emissivity enhancing paint layer and the thermoelastic heat generated in the epoxy layer is very significant with respect to that of the substratum of plies. The model presented here can be used to examine the effects of a surface layer of paint on a specimen and the effects due to imperfect thermal contact between the coating and substrate discussed in Mackenzie (1989) can be easily included.

There appears to be quite good correlation between the experimental results and those determined using the mathematical models. It is thought that in the cases where there is some divergence between the experimental and analytical results, that this is primarily due to the inexact knowledge of the mechanical and thermal properties of the material used.

## 5 Conclusion

In this paper, the thermoelastic heat developed in each ply of a graphite/epoxy laminate has been analytically determined from the mechanical and thermal properties of the fiber and matrix materials. A mathematical model was then developed to show how thermal conduction affects the thermoelastically generated temperature distribution through the thickness of the laminate. A further mathematical model was then developed to solve for the "composite" problem (in the heat conduction sense) such that the effects of a surface layer of epoxy on the laminate could be investigated. The results of the two mathematical models were found to compare well with experimental results for a $[(0\ \mathrm{deg}, \pm 45\ \mathrm{deg})_4]_s$ specimen, with and without a surface layer of epoxy.

## Acknowledgments

The author gratefully acknowledges the advice and assistance given by Dr. I. H. Grundy of the Department of

Mathematics, RMIT, Victorian University of Technology, and Drs. J. G. Sparrow, A. K. Wong, and T. G. Ryall of Aircraft Structures Division, Aeronautical Research Laboratory.

## References

Bakis, C. E., and Reifsnider, K. L., 1988, "Nondestructive Evaluation of Fiber Composite Laminates by Thermoelastic Emission," *Review of Progress in Quantitative Nondestructive Evaluation*, Vol. 7B, pp. 1109–1116.

Belgen, M. H., 1968, "Infrared Radiometric Stress Instrumentation Application Range Study," NASA Report CR-1067.

Carslaw, H. S., and Jaeger, J. C., 1959, *Conduction of Heat in Solids*, 2nd ed., Oxford University Press, Oxford, U.K.

Chamis, C. C., 1984, "Simplified Composite Micromechanics Equations for Strength, Fracture Toughness and Environmental Effects," *39th Annual Conference, Reinforced Plastics/Composites Institute, The Society of the Plastics Industry, Inc.*, Session 11-D, pp. 1–16.

Chen, J. K., Sun, C. T., and Chang, C. I., 1985, "Failure Analysis of a Graphite/Epoxy Laminate Subjected to Combined Thermal and Mechanical Loading," *J. Comp. Materials*, Vol. 19, pp. 408–423.

Dunn, S. A., Lombardo, D., and Sparrow, J. G., 1989, "The Mean Stress Effect in Metallic Alloys and Composites," *Stress and Vibration: Recent Developments in Industrial Measurement and Analysis*, Peter Stanley, ed., SPIE-Vol. 1084, pp. 129–142.

Gradshteyn, I. S., and Ryzhik, I. M., 1980, *Tables of Integrals, Series, and Products*, Alan Jaffrey, ed., Academic Press.

Griffis, C. A., Masumura, R. A., and Chang, C. I., 1981, "Thermal Response of Graphite/Epoxy Composite Subjected to Rapid Heating," *J. Comp. Materials*, Vol. 15, pp. 427–442.

Heller, M., Williams, J. F., Dunn, S. A., and Jones, R., 1989, "Thermoelastic Analysis of Composite Specimens," *Composite Structures*, Vol. 11, pp. 309–324.

Kageyama, K., Ueki, K., and Kikuchi, M., 1988, "Thermoelastic Technique Applied to Stress Analysis of Carbon Fiber Reinforced Composite Materials," *Proceedings of the VI International Congress on Experimental Mechanics*, pp. 931–936.

Luikov, A. V., 1968, *Analytical Heat Diffusion Theory*, J. P. Hartnett, ed., Academic Press.

Mackenzie, A. K., 1989, "Effects of Surface Coatings on Infra-Red Measurements of Thermoelastic Responses," *Stress and Vibration: Recent Developments in Industrial Measurement and Analysis*, Peter Stanley, ed., SPIE-Vol. 1084, pp. 59–71.

McKelvie, J., 1987, "Consideration of the Surface Temperature Response to Cyclic Thermoelastic Heat Generation," *Stress Analysis by Thermoelastic Techniques*, B. C. Gasper, ed., SPIE-VOl. 731, pp. 44–53.

Wong, A. K., 1990, "A Non-Adiabatic Thermoelastic Theory and the Use of SPATE on Composite Laminates," *Proceedings of the 9th International Conference on Experimental Mechanics*, Copenhagen, Vol. 2, pp. 793–802.

Wong, A. K., 1991, private communication.

Zhang, D., and Sandor, B. I., 1990, "A Thermoelasticity Theory for Damage in Anisotropic Materials," *Fatigue Fract. Engng. Mater. Struct.*, Vol. 13, No. 5, pp. 497–509

# Influence of Porosity on Plane Strain Tensile Crack-Tip Stress Fields in Elastic-Plastic Materials: Part I

**W. J. Drugan**
Professor,
Mem. ASME.

**Y. Miao**
Graduate Research Assistant.

Department of Engineering Mechanics,
University of Wisconsin-Madison,
Madison, WI 53706

*We perform an analytical first study of the influence of a uniform porosity distribution, for the entire range of porosity level, on the stress field near a plane strain tensile crack tip in ductile material. Such uniform porosity distributions (approximately) arise in incompletely sintered or previously deformed (e.g., during processing) ductile metals and alloys. The elastic-plastic Gurson-Tvergaard constitutive formulation is employed. This model has a sound micromechanical basis, and has been shown to agree well with detailed numerical finite element solutions of, and with experiments on, voided materials. To facilitate closed-form analytical results to the extent possible, we treat nonhardening material with constant, uniform porosity. We show that the assumption of singular plastic strain in the limit as the crack tip is approached renders the governing equations statically determinate with two permissible types of near-tip angular sector: one with constant Cartesian components of stress ("constant stress"); and one with radial stress characteristics ("generalized centered fan"). The former admits an exact asymptotic closed-form stress field representation, and although we prove the latter does not, we derive a highly accurate closed-form approximate representation. We show that complete near-tip solutions can be constructed from these two sector types for the entire range of porosity. These solutions are comprised of three asymptotic sector configurations: (i) "generalized Prandtl field" for low porosities ($0 \le f \le .02979$), similar to the plane strain Prandtl field of fully dense materials, with a fully continuous stress field but sector extents that vary with porosity; (ii) "plane-stress-like field" for intermediate porosities ($.02979 < f < .12029$), resembling the plane stress solution for fully dense materials, with a ray of radial normal stress discontinuity but sector extents that vary with porosity; (iii) two constant stress sectors for the remaining high porosity range, with a ray of radial normal stress discontinuity and fixed sector extents. Among several interesting features, the solutions show that increasing porosity causes significant modification of the angular variation of stress components, particularly for a range of angles ahead of the crack tip, while also causing a drastic reduction in maximum hydrostatic stress level.*

## 1 Introduction

Several classes of ductile alloys exhibit porosity. Examples include alloys produced by powder metallurgical techniques, and other alloys in which prior deformation has caused void nucleation and growth by fracture of second-phase particles and/or by particle-matrix debonding. To achieve a fundamental understanding of and accurate predictive capabilities for fracture in such materials, it is necessary to generalize the near-crack-tip stress and deformation field solutions for fully dense materials, upon which current nonlinear fracture mechanics is based, to encompass constitutive models that account for porosity.

Continuum-mechanical constitutive models have been developed that incorporate porosity, and hence relax the classical plasticity assumptions that yield is unaffected by hydrostatic stress and that plastic strain is incompressible. Perhaps the best known of such models that have a sound micromechanical basis is that of Gurson (1977). This model considers a characteristic volume element that is an aggregate of spherical or cylindrical voids in a ductile matrix, with the matrix material idealized as being rigid-plastic and obeying the Huber-Mises yield criterion. By employing averaging techniques similar to those of Bishop and Hill (1951), Gurson (1977) used approximate upper-bound solutions on the microlevel to derive a

Contributed by the Applied Mechanics Division of THE AMERICAN SOCIETY OF MECHANICAL ENGINEERS for publication in the ASME JOURNAL OF APPLIED MECHANICS.

Discussion on this paper should be addressed to the Technical Editor, Professor Leon M. Keer, The Technological Institute, Northwestern University, Evanston, IL 60208, and will be accepted until four months after final publication of the paper itself in the JOURNAL OF APPLIED MECHANICS.

Manuscript received by the ASME Applied Mechanics Division, Nov. 5, 1990; final revision, Apr. 2, 1991. Associate Technical Editor: R. M. Bowen.

macroscopic yield condition for porous material. This yield criterion was subsequently modified by Tvergaard (1981, 1982) by introducing additional constants, which were demonstrated to bring its predictions into much better agreement with two-dimensional numerical finite element analyses of material containing periodic distributions of cylindrical or spherical voids. Recently, Hom and McMeeking (1989) have carried out three-dimensional finite strain, finite element computations that model deformations of materials idealized as containing initially spherical voids in periodic cubic arrays. They found that although it cannot precisely describe this material's behavior under all deformation conditions, the Gurson model with Tvergaard's modifications does reasonably well overall. This model has also been shown by several researchers to agree well with experimental data from specimens of known porosity produced by powder metallurgy, as reviewed by Tvergaard (1990).

Our objective in this paper is to employ this reasonably realistic Gurson-Tvergaard model of porous metals and alloys to explore the influence of the entire range of porosity level on plane strain tensile crack-tip fields. To facilitate closed-form analytical solutions to the degree possible, and to permit visualization-assisting representations in terms of stress characteristics, we model the material as being ideally plastic, and we treat the porosity as being uniform.

To our knowledge, previous studies of the effect of porosity on crack fields in ductile metals and alloys have been numerical finite element analyses. Of these, we mention the works of Aravas and McMeeking (1985), Aoki et al. (1987), Needleman and Tvergaard (1987), and Jagota et al. (1987).

Recently, Pan and co-workers (Li and Pan (1990), Dong and Pan (1991)) have analyzed near-tip crack fields in elastic-plastic materials in which the effects of porosity are modeled by a simple Drucker-Prager type yield condition (which consists of a linear combination of the effective stress and the hydrostatic stress) and an associated flow rule. They obtained closed-form asymptotic stress fields for perfectly plastic material, while for power-law hardening materials the angular-dependent functions in the asymptotic stress and strain solutions are not closed-form. They employed this constitutive model to characterize polymers and ceramics, as opposed to metals as considered here; comparisons between our results reveal similarities as well as significant differences, as will be discussed.

## 2 Governing Equations

We employ a small-displacement-gradient formulation to analyze a plane strain Mode I stationary crack in macroscopically homogeneous, isotropic, elastic-ideally plastic, spherically voided Gurson-Tvergaard material. Crack surfaces are taken to be traction-free.

With reference to Fig. 1, let Cartesian axes $x_1$, $x_2$, and $x_3$ be chosen so that $x_3$ and $x_1$ are parallel to the (straight) crack front and the crack surfaces, respectively. Throughout the paper, components of tensors with respect to this Cartesian system will be denoted by Latin indices $i, j, k, l$ with range 1, 2, 3 or by Greek indices $\alpha$, $\beta$, $\gamma$ with range 1, 2 only; the summation convention for repeated subscripts applies to both types. Let $r$, $\theta$ be polar coordinates in the $x_1$-$x_2$ plane and

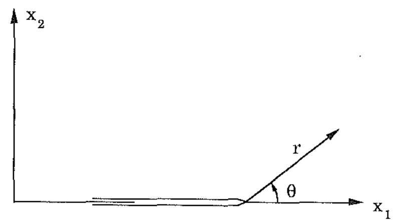


**Fig. 1 The Cartesian coordinate system, with $x_3$ being directed out of the paper; polar coordinates $r$, $\theta$ are centered at the crack tip**

centered at the crack tip with $\theta = 0$ coinciding with the positive $x_1$-axis.

**2.1 Equilibrium.** Plane equilibrium when no body forces act requires the stress tensor to be symmetric, $\sigma_{\alpha\beta} = \sigma_{\beta\alpha}$, and to satisfy

$$\partial\sigma_{\alpha\beta}/\partial x_\alpha = 0 \tag{1}$$

or in polar coordinates

$$r\partial\sigma_{rr}/\partial r + \partial\sigma_{r\theta}/\partial\theta + \sigma_{rr} - \sigma_{\theta\theta} = 0, \quad r\partial\sigma_{r\theta}/\partial r + \partial\sigma_{\theta\theta}/\partial\theta + 2\sigma_{r\theta} = 0. \tag{2}$$

**2.2 Yield Condition and Stress-Strain Equations.** Tvergaard's (1981, 1982) modification of Gurson's (1977) yield condition is

$$\Phi(\sigma) = \frac{3}{2}\, s_{ij}s_{ij} + 2q_1 f \cosh\left[\frac{q_2\sigma_{kk}}{2}\right] - 1 - q_1^2 f^2 = 0, \tag{3}$$

where the void volume fraction $f$ of the material is here assumed uniform everywhere and constant during deformation; s is the deviatoric stress tensor; and here and throughout the paper, stresses are nondimensionalized by the uniaxial yield strength $\sigma_y$. The parameters $q_1$ and $q_2$ are unity for the original Gurson model, but Tvergaard (1981, 1982) and Hom and McMeeking (1989) have shown that with $q_1 = 1.5$ and $q_2 = 1$, the Gurson model agrees more closely with numerical analyses of periodic void arrays; and Tvergaard (1990) has reviewed comparisons of (3) with experiments on porous metals that show good agreement when $q_1$ and $q_2$ take these or similar values. Thus, $q_1$ and $q_2$ are positive and finite, and later in specific calculations we take $q_2 = 1$.

We assume an additive decomposition of total strain increments into elastic and plastic parts, and following Gurson (1977), that plastic strain increments can be derived from (3) via the associated flow rule, $d\epsilon_{ij}^p = d\lambda\partial\Phi(\sigma)/\partial\sigma_{ij}$; thus

$$d\epsilon_{ij} = d\epsilon_{ij}^e + d\epsilon_{ij}^p = \frac{1+\nu}{E^*}\, d\sigma_{ij} - \frac{\nu}{E^*}\, d\sigma_{kk}\delta_{ij} + d\lambda\left\{3s_{ij} + q_1 q_2 f \sinh\left[\frac{q_2\sigma_{kk}}{2}\right]\delta_{ij}\right\}, \tag{4}$$

where $E^*$ is Young's modulus nondimensionalized by $\sigma_y$, $\nu$ is Poisson's ratio, $\delta_{ij}$ is the Kronecker delta, and $d\lambda \geq 0$ is an undetermined parameter.

**2.3 Asymptotic Forms of the Governing Equations in Singular Plastic Sectors.** The governing equations just summarized adopt simplified forms as $r \to 0$ because of two assumptions we make: (i) that the material is nonhardening; (ii) that at least one component of the plastic strain increment tensor is singular as the crack tip is approached. The nonhardening assumption, coupled with the yield condition (3), requires that all stress components be bounded. This is evident since the term $(-1 - q_1^2 f^2)$ is always negative and finite, and both $3/2 s_{ij}s_{ij}$ and $2q_1 f \cosh[q_2\sigma_{kk}/2]$ are positive for all $f > 0$ and hence (3) demands that each of these be finite. These latter restrictions show, respectively, that all deviatoric stresses $s_{ij}$ must be finite and that $\sigma_{kk}$ must be finite for nonzero $f$. Therefore, $\sigma_{ij} = s_{ij} + \sigma_{kk}\delta_{ij}/3$ must be finite for nonzero $f$. Stresses are also bounded near a traction-free crack tip for $f = 0$, as proved by Drugan (1985).

Drugan (1985) also proved Rice's (1982) statement that boundedness of all components of the stress tensor requires $r\partial\sigma_{ij}/\partial r \to 0$ as $r \to 0$, so that the equilibrium equations (2) reduce to, for $r \to 0$:

$$\sigma_{rr} - \sigma_{\theta\theta} + \sigma_{r\theta}' = 0, \quad \sigma_{\theta\theta}' + 2\sigma_{r\theta} = 0 \tag{5a,b}$$

or, in terms of Cartesian stress components

$$\sigma_{11}' \sin\theta = \sigma_{12}' \cos\theta, \quad \sigma_{22}' \cos\theta = \sigma_{12}' \sin\theta, \tag{6}$$

where $\sigma' \equiv \lim_{r\to 0} \partial\sigma(r, \theta)/\partial\theta$ (in particular, $\sigma'_{r\theta} \equiv \lim_{r\to 0} \partial\sigma_{r\theta}/\partial\theta$, etc.).

Stress boundedness requires that elastic strains be finite, as must the quantity $[3s_{ij} + q_1q_2f \sinh(q_2\sigma_{kk}/2)\delta_{ij}]$ also. When these facts are coupled with our assumption that at least one in-plane component of plastic strain increment is singular for $r \to 0$, it is clear from (4) that $d\lambda \to +\infty$ as $r \to 0$. Applying this fact together with the plane strain requirement $d\epsilon_{33} = 0$ to (4), we obtain the following asymptotic ($r \to 0$) restriction on stresses in singular plastic strain regions:

$$3s_{33} + q_1q_2f \sinh\left[\frac{q_2\sigma_{kk}}{2}\right] = 0. \qquad (7)$$

Therefore, the plane strain condition (7) and the yield condition (3) together with the two equilibrium equations ($5a,b$) or (6) render stresses statically determinate in singular plastic near-tip angular sectors.

Instead of using the yield condition in the form (3), a differential form proves more convenient for asymptotic analysis. Differentiating (3) with respect to $\theta$, taking the limit as $r \to 0$ and simplifying via (6) and (7) results in

$$[\sigma'_{rr} + \sigma'_{\theta\theta}]\left\{3s_{rr} + q_1q_2f \sinh\left[\frac{q_2\sigma_{kk}}{2}\right]\right\} = 0. \qquad (8)$$

Thus, our asymptotic governing equation system is now ($5a$, $b$), (7) and (8) for the four stress components in singular plastically deforming near-tip sectors.

## 3 Stress Distributions in Singular Plastic Near-Tip Sectors

We shall now analyze the statically determinate asymptotic governing equation set for stresses in singular plastic sectors; since we derived this set from an incremental plasticity formulation, the results in this section are valid for both stationary and quasi-statically growing cracks. (Following Rice (1982), for quasi-statically growing cracks, where singular (in $r$) strain increments can integrate to finite strains, singular plastic sectors are defined as those in which $d\epsilon^p_{33}/d\epsilon^p_{\alpha\beta} \to 0$ as $r \to 0$ for at least one $\alpha$, $\beta$ pair; this also leads to (7).)

There are evidently two possible solutions to (8):

$$\sigma'_{rr} + \sigma'_{\theta\theta} = 0 \quad \text{or} \quad 3s_{rr} + q_1q_2f \sinh\left[\frac{q_2\sigma_{kk}}{2}\right] = 0. \qquad (9a,b)$$

**3.1 Constant Stress Plastic Sector.** It is easily shown (e.g., Rice, 1982) that ($9a$) with (6) require

$$\sigma_{11} = \text{constant}, \quad \sigma_{22} = \text{constant}, \quad \sigma_{12} = \text{constant}. \qquad (10)$$

To determine $\sigma_{33}$, we differentiate (7) with respect to $\theta$ and apply (10) to obtain

$$\sigma'_{33}\left\{4 + q_1q_2^2f \cosh\left[\frac{q_2\sigma_{kk}}{2}\right]\right\} = 0 \quad \Rightarrow \sigma_{33} = \text{constant} \qquad (11)$$

since the braced term in (11) is positive for any $f \geq 0$. Therefore, in an angular sector where ($9a$) holds, all Cartesian components of stress are asymptotically constant; we term this a *"constant stress" plastic sector.*

In such a constant stress sector, stress components can be represented in polar coordinates as

$$\sigma_{rr} = c_1 + c_2 \cos 2\theta + c_4 \sin 2\theta, \quad \sigma_{33} = c_3 \qquad (13a)$$

$$\sigma_{\theta\theta} = c_1 - c_2 \cos 2\theta - c_4 \sin 2\theta, \quad \sigma_{r\theta} = -c_2 \sin 2\theta + c_4 \cos 2\theta \qquad (13b)$$

where constants $c_1$, $c_2$, $c_3$, and $c_4$ must satisfy the plane strain condition (7) and the yield condition (3) written in terms of the $c_n$'s:

$$c_3 - c_1 + \frac{1}{2}\, q_1q_2f \sinh\left\{q_2\left[c_1 + \frac{c_3}{2}\right]\right\} = 0 \qquad (14a)$$

$$3(c_2^2 + c_4^2) + (c_1 - c_3)^2 + 2q_1f \cosh\left\{q_2\left[c_1 + \frac{c_3}{2}\right]\right\} - 1 - q_1^2f^2 = 0. \qquad (14b)$$

**3.2 Generalized Centered Fan Plastic Sector.** Equation ($9b$) when combined with (7) and ($5a,b$) can be manipulated to show that the governing equation system for this second sector type is

$$\sigma''_{\theta\theta} + 2q_1q_2f \sinh\left[\frac{q_2}{2}\,(3\sigma_{\theta\theta} + \sigma''_{\theta\theta})\right] = 0 \qquad (15a)$$

$$\sigma_{rr} = \sigma_{\theta\theta} + \frac{\sigma''_{\theta\theta}}{2}, \quad \sigma_{r\theta} = -\frac{\sigma'_{\theta\theta}}{2}, \quad \sigma_{33} = \sigma_{rr}. \qquad (15b,c,d)$$

It is evident that the system (15) is solved by first solving the transcendental ordinary differential equation ($15a$) then directly calculating the other stress components from the remaining equations.

To attempt an analytical solution of ($15a$), we make the change of variable

$$\sigma(\theta) \equiv \frac{q_2}{2}\,(3\sigma_{\theta\theta} + \sigma''_{\theta\theta}) = \frac{3q_2}{2}\left(\frac{\sigma_{kk}}{3}\right); \qquad (16)$$

thus, $\sigma(\theta)$ is simply a multiple of the hydrostatic stress. Combining (16) with ($15a$) permits determination of $\sigma_{\theta\theta}$ in terms of $\sigma$:

$$\sigma_{\theta\theta} = \frac{2}{3q_2}\,[\sigma + q_1q_2^2f \sinh(\sigma)]. \qquad (17)$$

Substituting this into ($15a$) gives the transformed equation

$$\sigma''[1 + q_1q_2^2f \cosh(\sigma)] + [\sigma'^2 + 3]q_1q_2^2f \sinh(\sigma) = 0, \qquad (18)$$

which, when multiplied by $d\sigma$, rearranged and integrated becomes

$$\frac{[1 + q_1q_2^2f \cosh(\sigma)]d\sigma}{\{C - 3[1 + q_1q_2^2f \cosh(\sigma)]^2\}^{1/2}} = \pm d\theta. \qquad (19)$$

Here, $C$ is an integration constant. Unfortunately, (19) appears to admit no closed-form integration for any $f \neq 0$. Thus, we must resort to numerical or approximate analytical solutions for the stresses in such a sector. We term this a "generalized centered fan" plastic sector since, as illustrated shortly, one family of characteristics consists of radial lines emanating from the crack tip; also, in the limit $f \to 0$, ($9b$) implies $s_{rr} \to 0$, which defines a centered fan sector in fully dense material (see, e.g., Rice, 1982).

After attempting several approximate solution schemes for (19), including a perturbation expansion in $f$ and Picard's iterative method, we found that the approximate approach giving the best accuracy for the full range of $f$ and $\theta$ appears to be a truncated series expansion in $\theta$, with retention of up to cubic terms providing the best compromise between accuracy and simplicity:

$$\sigma(\theta) \cong \xi_0 + \xi_1(\theta - \theta_1) + \xi_2(\theta - \theta_1)^2 + \xi_3(\theta - \theta_1)^3 \qquad (20)$$

where $\theta_1$ and $\theta_2$ ($\theta_1 < \theta < \theta_2$) define the asymptotic boundary locations of a generalized centered fan sector. Observe that this approximate representation contains four undetermined constants for a given $\theta_1$. We have found that the closest agreement between this representation and accurate numerical solutions of (18) is obtained by enforcing continuity of hydrostatic stress (which is required, as proved in the Appendix) across both generalized centered fan boundaries, i.e.,

$$\sigma(\theta_1^+) = \frac{q_2}{2}\,\sigma_{kk}(\theta_1^-), \quad \sigma(\theta_2^-) = \frac{q_2}{2}\,\sigma_{kk}(\theta_2^+) \qquad (21)$$

and continuity of $\sigma_{r\theta}$ across the leading fan boundary, i.e.,

$$\sigma'(\theta_1^+) = -\frac{3q_2\sigma_{r\theta}(\theta_1^-)}{1 + q_1q_2^2f \cosh[q_2\sigma_{kk}(\theta_1^-)/2]}. \qquad (22)$$

A fourth condition on the four unknowns in (20) is obtained by substituting (20) into (18) and requiring the $O(1)$ term to vanish (i.e., requiring (18) to be exactly satisfied at $\theta = \theta_1$). Together, these four conditions require

$$\xi_0 = q_2\sigma_{kk}(\theta_1^-)/2, \quad \xi_1 = -\frac{3q_2\sigma_{r\theta}(\theta_1^-)}{1+q_1q_2^2 f\cosh(\xi_0)}$$

$$\xi_2 = -\frac{(\xi_1^2+3)q_1q_2^2 f\sinh(\xi_0)}{2[1+q_1q_2^2 f\cosh(\xi_0)]},$$

$$\xi_3 = \frac{q_2\sigma_{kk}(\theta_2^+)/2-\xi_0}{(\theta_2-\theta_1)^3} - \frac{\xi_1}{(\theta_2-\theta_1)^2} - \frac{\xi_2}{\theta_2-\theta_1}. \quad (23)$$

It is easily shown that the approximate solution (20) with (23) reduces to the exact solution for fully dense material as $f \to 0$.

Thus, our approximate analytical representations for stresses in a generalized centered fan sector are (17) and

$$\sigma_{rr} = \sigma_{33} = \frac{1}{3q_2}[2\sigma - q_1q_2^2 f\sinh(\sigma)],$$

$$\sigma_{r\theta} = -\frac{\sigma'}{3q_2}[1+q_1q_2^2 f\cosh(\sigma)] \quad (24)$$

with $\sigma$ given by (20) with (23). As will be discussed, this approximation shows excellent agreement with accurate numerical results.

To obtain accurate numerical solutions for the stresses in a generalized centered fan plastic sector, we employ a fourth-order Runge-Kutta integration scheme. This is accomplished by changing (15) to a first-order O.D.E. system:

$$\sigma_{rr}' = \sigma_{r\theta}\frac{q_1q_2^2 f\cosh\left[q_2\left(\sigma_{rr}+\frac{1}{2}\sigma_{\theta\theta}\right)\right]-2}{q_1q_2^2 f\cosh\left[q_2\left(\sigma_{rr}+\frac{1}{2}\sigma_{\theta\theta}\right)\right]+1},$$

$$\sigma_{r\theta}' = \sigma_{\theta\theta}-\sigma_{rr}, \quad \sigma_{\theta\theta}' = -2\sigma_{r\theta}. \quad (25a,b,c)$$

Here, (25$a$) is obtained by applying (15$d$) to (9$b$), differentiating with respect to $\theta$, then applying (5$b$); (25$b$,$c$) are rearrangements of (5$a$,$b$), and $\sigma_{33}$ is given by (15$d$).

## 4 Complete Near-Tip Stress Field for Low Porosities: Generalized Prandtl Field

As just shown, constant stress and generalized centered fan plastic sectors are the only two possible types of stress distribution satisfying the asymptotic governing equations under the assumptions that for $r \to 0$, yield is attained and at least one component of plastic strain is singular. We now seek a complete near-tip stress field that satisfies these assumptions at all angles about the crack tip, while also satisfying the traction-free crack face boundary conditions, traction continuity between sectors, and stress symmetry requirements along the $\theta = 0$ line. We observed earlier that as $f \to 0$, the governing equations reduce to those for a plane strain Mode I stationary crack in Huber-Mises material. It is well known that for a stationary crack in this latter material, the near-tip stress field is not unique, but the Prandtl stress distribution, illustrated in Figs. 2($a$) and 3($a$), is the only one possible if the stress component $\sigma_{rr}$ is assumed fully continuous, $s_{33} = 0$, and the material is at yield for all angles $\theta$ about the tip of a Mode I tensile crack. Although this Prandtl field applies for incompressible elastic-plastic materials, we expect a stress field quite similar to it for porous materials when porosity is small; in the present section we show this to be the case, calling the result the "generalized Prandtl field."

Similar to the Prandtl field, the generalized Prandtl field consists of three sectors, as illustrated in Fig. 2($b$): a constant stress sector C adjacent to the crack surface; another constant stress sector A ahead of the crack tip; and a generalized centered fan sector B joining sectors A and C. The border between sectors A and B is defined as $\theta_1$, and that between sectors B and C as $\theta_2$.

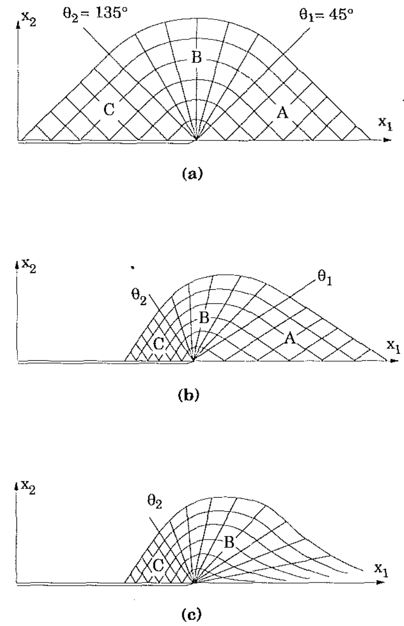


**Fig. 2 The generalized Prandtl field solution configuration in terms of stress characteristics: ($a$) $f = 0$; ($b$) $0 < f < 0.04468/q_1$, and angles $\theta_1$ and $\theta_2$ vary with $f$; ($c$) $f = 0.04468/q_1$, and $\theta_1 = 0$, $\theta_2 \approx 133.9$ deg**

**4.1 Determination of Stresses in Constant Stress Sector C ($\theta_2 < \theta < \pi$).** With reference to (13$b$), the traction-free condition on $\theta = \pi$ requires

$$c_1 = c_2, \quad c_4 = 0. \quad (26)$$

Therefore, $c_1$ and $c_3$, and hence the stresses in Sector C, are completely determined by (14) for each fixed $f$. These equations are solved numerically. We make a change of variable by calling $x \equiv c_1 + c_3/2$, which, via (14$a$) implies

$$c_1 = \frac{2}{3}\left[x + \frac{1}{4}q_1q_2 f\sinh(q_2x)\right],$$

$$c_3 = \frac{2}{3}\left[x - \frac{1}{2}q_1q_2 f\sinh(q_2x)\right]. \quad (27)$$

Then, using (26) and (27), (14$b$) becomes

$$\frac{4}{3}x^2 + \frac{2}{3}xq_1q_2 f\sinh(q_2x) + \frac{1}{3}q_1^2q_2^2f^2\sinh^2(q_2x)$$

$$+2q_1 f\cosh(q_2x) - 1 - q_1^2f^2 = 0. \quad (28)$$

We have proved that (28) has two and only two equal and opposite roots for each $0 \le f < 1/q_1$. To obtain the Prandtl field in the $f \to 0$ limit, the positive root, hence the positive $c_1$ and $c_3$ values, are chosen; the alternate solution leads to $\sigma_{\theta\theta}(r, \theta = 0) < 0$ which is physically inappropriate since it does not correspond to tensile loading of the crack.

**4.2 Stresses in Generalized Centered Fan Sector B ($\theta_1 < \theta < \theta_2$).** To calculate the stresses in the generalized centered fan sector numerically, the boundary values of $\sigma_{\alpha\beta}$ at $\theta = \theta_2$, $\sigma_{\alpha\beta}(\theta_2^-)$, are necessary, as is the boundary location $\theta_2$. We prove in the Appendix that *all* components of stress must be continuous across a boundary between a constant stress plastic sector and a generalized centered fan plastic sector. Thus, from (13) and (26),

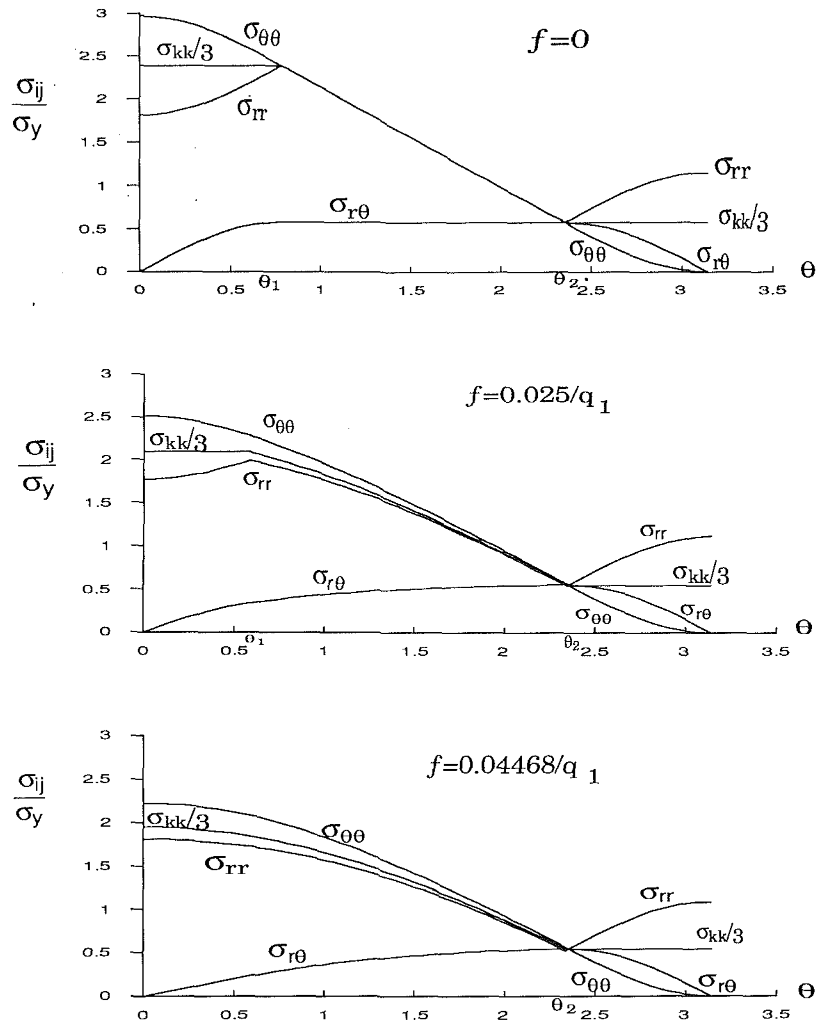


**Fig. 3 Polar components of stress as functions of angle $\theta$ for selected values of $f$ that span the range of applicability of the generalized Prandtl field**

$$\sigma_{rr}(\theta_2^-) = c_1(1+\cos 2\theta_2), \quad \sigma_{r\theta}(\theta_2^-) = -c_1 \sin 2\theta_2$$
$$\sigma_{\theta\theta}(\theta_2^-) = c_1(1-\cos 2\theta_2), \quad \sigma_{33}(\theta_2^-) = c_3, \quad (29)$$

where $c_1$ and $c_3$ are given by (27) after solving (28). The boundary location $\theta_2$ is determined by applying the generalized centered fan condition (15$d$) to (29)

$$\theta_2 = \pi - \frac{1}{2} \arccos\left[\frac{c_3}{c_1} - 1\right] \quad (30)$$

which is so chosen that it becomes the same as that of the Prandtl field when the void volume fraction $f \to 0$. Thus, $\sigma_{ij}(\theta)$ in the generalized centered fan are calculated numerically for a given $f$ by first solving (28) and (27), then determining $\theta_2$ from (30), and finally applying (29) as boundary values to begin integrating (25).

**4.3 Stresses in Constant Stress Sector A ($0 < \theta < \theta_1$).** The Mode I stress symmetry condition requires $\sigma_{12}(\theta = 0) = 0$; hence, via (10),

$$\sigma_{12}(r,\theta) = 0 \quad \text{throughout Sector A.} \quad (31)$$

Again invoking the result proved in the Appendix, all stress components must be continuous across the border between Sectors B and A. Thus, (31) demands $\sigma_{12}(\theta_1^+) = 0$; application of this condition to the numerical integration of (25) in the generalized centered fan sector shows where that sector ends (i.e., determines $\theta_1$). The other (constant) Cartesian components of stress in Sector A are then immediately determined by enforcing full stress continuity across $\theta_1$.

Enforcing the obvious restriction $0 \le \theta_1 \le \theta_2 \le \pi$, the numerical analysis just described reveals that the generalized Prandtl field exists for all

$$0 < f \le f_1 \approx .04468/q_1 \quad (= .02979 \text{ for } q_1 = 1.5), \quad (32)$$

with $f_1$ being the porosity $f$ at which the generalized centered fan sector B extends to $\theta = 0$, and hence constant stress sector A vanishes. This limiting case is illustrated in Fig. 2($c$). Table 1 summarizes values for parameters of the generalized Prandtl field throughout its admissible $f$ range, (32). In this table, $c_n$ are the values of the parameters appearing in (13) for Sector C (recall (26)), while $a_n$ are the values of those same parameters for Sector A (where $a_4 = 0$ via (31)). Thus, (13) with these parameter values give analytical expressions for the stresses in Sectors C and A. We also provide values for $\xi_n$, which facilitate approximate analytical representations of the generalized centered fan stress components via (20) with (17) and (24); these are accurate to within a few percent throughout Sector B for the entire $f$-range (32), except that $\sigma_{r\theta}$ is slightly less accurate (within ten percent) when both $f$ is near $f_1$ and $\theta$ is near $\theta_2$.

The near-tip stress distributions for three values of $f$ spanning the range (32) are displayed in Fig. 3. Observe that increasing porosity causes significant modification of the $\theta$-variation of stress components, particularly for a range of angles ahead of the tip; it also causes a drastic reduction in maximum hydrostatic stress level. For example, maximum hydrostatic stress decreases by about 21 percent when porosity increases from zero to about 3 percent (having taken $q_1$ = 1.5)!

**4.4 Characteristics for the Generalized Prandtl Field.** As noted above, the stress field associated with the generalized Prandtl field is entirely continuous and asymptotically satisfies equilibrium (1), the Gurson-Tvergaard yield criterion (3), and the plane strain restriction (7). We apply Hill's (1950) approach to find the characteristic curves of this system. It is straightforward to show that at any point on a characteristic curve, stresses must satisfy

$$3s_{tt}+q_1q_2f\sinh\left[\frac{1}{2}q_2\sigma_{kk}\right]=0, \tag{33}$$

and $\partial\sigma_{tt}/\partial n$ cannot be uniquely determined, where $n$ and $t$ denote, respectively, the directions along the outward normal and the tangent of the characteristic curve. Equations (33) and (7) together show that on a characteristic curve

$$\sigma_{33}=\sigma_{tt}. \tag{34}$$

By applying this condition and the full stress continuity of the generalized Prandtl field, we have proved that for such an asymptotic stress field there exist two characteristic curves at every material point, and their slopes are continuous everywhere. It is these characteristic curves that we illustrate in Fig. 2 (and will illustrate later in Fig. 4). In addition, similar to the results of Li and Pan (1990) for the Drucker-Prager model, for any $0 < f \le f_1$ the two families of characteristic curves are no longer orthogonal—their intersection angle increases from $\pi/2$ as $f$ increases from 0; at the limit $f \to f_1$ the intersection angle at $\theta = 0$ becomes $\pi$. That is, the equations change type to parabolic on the crack line at this particular value of $f$. However, the angular span of the generalized centered fan sector is greater than $\pi/2$ for $f > 0$ and increases with increasing $f$ in our solutions (see Table 1), while it remains $\pi/2$ for any pressure sensitivity in the Li and Pan (1990) solutions.

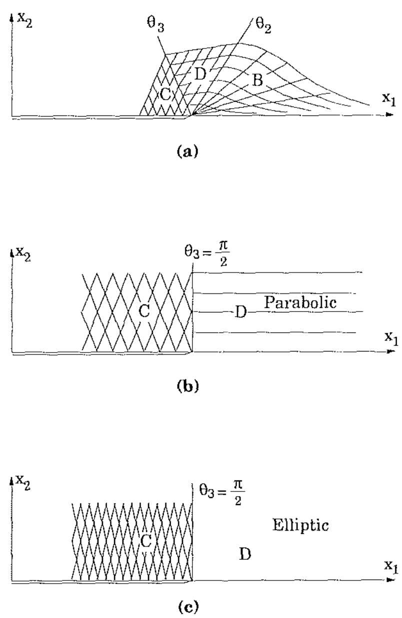


**Fig. 4** (*a*) The plane-stress-like solution configuration in terms of stress characteristics, which applies for $0.04468/q_1 < f < 0.18043/q_1$, with $\theta_2$ and $\theta_3$ varying with $f$; (*b*) solution configuration for $f = 0.18043/q_1$; (*c*) solution configuration for $0.18043/q_1 < f < 1/q_1$

## 5 Near-Tip Stress Fields for Intermediate Porosities: Plane-Stress-Like Distributions

The preceding analysis shows that the generalized Prandtl field is the unique continuous near-tip stress field for plane strain Mode I Gurson-Tvergaard porous material under the assumption of singular plastic strain at all angles about the crack tip as $r \to 0$. The corresponding numerical calculations show that in the special case $q_2 = 1$ (the value for $q_2$ suggested by Tvergaard's (1981, 1982) and Hom and McMeeking's (1989) numerical analyses), the generalized Prandtl field exists only for the $f$-range given in (32), with the generalized centered fan sector extending to the crack symmetry line (i.e., $\theta_1 = 0$) at $f = f_1$, while for $f > f_1$, $\theta_1 < 0$, which is physically inappropriate since it implies a violation of Mode I symmetry. However, an interesting fact is that the generalized Prandtl field for $f = f_1$ (Fig. 2(*c*)) is reminiscent of the Hutchinson (1968) solution for the stress field near a plane *stress* Mode I stationary crack in (fully dense) Huber-Mises material, which consists of a centered fan sector beginning at $\theta = 0$ followed by *two* constant stress sectors with a stress jump across their mutual border. The difference is that the Hutchinson solution has one additional constant stress sector. Thus, we attempted for $f > f_1$ to find a solution configuration similar to that of Hutchinson (1968), as illustrated in Fig. 4(*a*).

**5.1 Stresses in Generalized Centered Fan Sector B ($0 \le \theta < \theta_2$).** To determine the stresses in Sector B of Fig. 4(*a*), we must first determine boundary conditions for all stress components at $\theta = 0$. Mode I symmetry requires

$$\sigma_{r\theta}(\theta=0)=0. \tag{35a}$$

In addition, stresses at $\theta = 0$ must satisfy the restrictions for a generalized centered fan sector (15*d*), (9*b*), and (3) (which together embody the plane strain, equilibrium, and yield conditions). Solving these subject to the tensile crack loading requirement ($\sigma_{\theta\theta}(0) > 0$) gives

$$\sigma_{\theta\theta}(0)=\frac{2}{3}\left[Q+\frac{1}{q_2}\ln\left\{[(1+q_2^2)(q_2^{-2}+q_1^2f^2)]^{1/2}-q_2^{-1}+Q\right\}\right.$$
$$\left.-\frac{1}{q_2}\ln(q_1q_2f)\right] \tag{35b}$$

$$\sigma_{33}(0)=\sigma_{rr}(0)=\sigma_{\theta\theta}(0)-Q, \tag{35c}$$

**Table 1** Parameter values for the generalized Prandtl field ($0 \le f \le 0.04468/q_1$)

| $q_1f$ | $c_1$ | $c_3$ | $\theta_1$ | $\theta_2$ | $a_1$ | $a_2$ | $a_3$ | $\xi_0$ | $\xi_1$ | $\xi_2$ | $\xi_3$ |
|---|---|---|---|---|---|---|---|---|---|---|---|
| 0.000000 | 0.5774 | 0.5774 | 45.0° | 135.0° | 2.391 | -0.5774 | 2.391 | 3.587 | -1.732 | 0.0000 | 0.0000 |
| 0.008937 | 0.5702 | 0.5659 | 41.1° | 134.8° | 2.290 | -0.4923 | 2.223 | 3.402 | -1.289 | -.2752 | .06769 |
| 0.02682 | 0.5560 | 0.5436 | 32.4° | 134.4° | 2.124 | -0.3537 | 1.974 | 3.111 | -.7381 | -.4088 | .05753 |
| 0.03575 | 0.5491 | 0.5328 | 26.1° | 134.1° | 2.056 | -0.2904 | 1.878 | 2.995 | -.5064 | -.4273 | .04409 |
| 0.04468 | 0.5422 | 0.5222 | 0.00° | 133.9° | 2.016 | -0.2066 | 1.809 | 2.920 | 0.000 | -.4378 | .02159 |

Table 2 Parameter values for the plane-stress-like field ($0.04468/q_1 \leq f \leq 0.18043/q_1$)

| $q_1 f$ | $c_1$ | $c_3$ | $\theta_2$ | $\theta_3$ | $d_1$ | $d_2$ | $d_3$ | $d_4$ | $\xi_0$ | $\xi_1$ | $\xi_2$ | $\xi_3$ |
|---|---|---|---|---|---|---|---|---|---|---|---|---|
| .04468 | 0.5422 | 0.5222 | 133.9° | 133.9° | .5433 | 0.5421 | 0.5233 | -.0001 | 2.920 | 0.000 | -.4378 | .02159 |
| .06968 | 0.5232 | 0.4936 | 62.4° | 101.3° | 1.354 | -.2435 | 1.231 | -.3191 | 2.477 | 0.000 | -.4357 | .00695 |
| .09468 | 0.5047 | 0.4665 | 45.4° | 95.7° | 1.319 | -.2938 | 1.164 | -.1614 | 2.171 | 0.000 | -.4327 | .00483 |
| 0.1197 | 0.4867 | 0.4407 | 33.5° | 92.8° | 1.253 | -.2763 | 1.078 | -.0073 | 1.938 | 0.000 | -.4287 | .00367 |
| 0.1447 | 0.4690 | 0.4162 | 23.3° | 91.0° | 1.183 | -.2443 | 0.9953 | -.0026 | 1.750 | 0.000 | -.4239 | .00273 |
| 0.1697 | 0.4517 | 0.3928 | 11.7° | 90.1° | 1.116 | -.2121 | 0.9193 | -.0003 | 1.592 | 0.000 | -.4182 | .00149 |
| 0.1804 | 0.4444 | 0.3831 | 0.00° | 90.0° | 1.088 | -.1990 | 0.8888 | 0.0 | | | | |

Table 3 Parameter values for the two constant stress sectors field ($0.18043/q_1 \leq f \leq 1/q_1$)

| $q_1 f$ | $c_1$ | $c_3$ | $d_1$ | $d_2$ | $d_3$ |
|---|---|---|---|---|---|
| 0.18043 | 0.444401 | 0.383084 | 1.087837 | -0.199034 | 0.888804 |
| 0.25 | 0.398474 | 0.324642 | 0.924238 | -0.127291 | 0.716252 |
| 0.40 | 0.306625 | 0.220783 | 0.642506 | -0.0292563 | 0.446850 |
| 0.55 | 0.222381 | 0.140722 | 0.425368 | 0.01939447 | 0.264027 |
| 0.70 | 0.143944 | 0.0793210 | 0.252823 | 0.03506573 | 0.106025 |
| 0.80 | 0.09426576 | 0.0470420 | 0.156806 | 0.03172561 | 0.07798514 |
| 1.00 | 0.0 | 0.0 | 0.0 | 0.0 | 0.0 |

where

$$Q \equiv \{1 + 2q_2^{-2} + q_1^2 f^2 - 2q_2^{-1}[(1+q_2^2)(q_2^{-2} + q_1^2 f^2)]^{1/2}\}^{1/2}. \tag{35d}$$

With the boundary conditions given by (35), stresses can be calculated in the generalized centered fan by numerically integrating the previously derived (25).

**5.2 Stresses in Constant Stress Sectors D ($\theta_2 < \theta < \theta_3$) and C ($\theta_3 < \theta < \pi$).** The general solution for stresses in a constant stress sector in polar components is as given previously by (13) and (14). Stresses in Sector C of Fig. 4(*a*) are exactly the same as those given in Section 4.1, and are thus known for any given $f$. Therefore, we have six unknown constants: $c_1, \ldots, c_4$ of Sector D, which we shall call $d_1, \ldots, d_4$, and $\theta_2$ and $\theta_3$; these can be determined by enforcing full stress continuity across $\theta = \theta_2$ (again, see the Appendix) and traction continuity across $\theta = \theta_3$. The results are

$$d_1 = [\sigma_{\theta\theta}(\theta_2^-) + \sigma_{rr}(\theta_2^-)]/2, \quad d_2 = c_1 + (d_1 - c_1)\cos 2\theta_3$$

$$d_3 = \sigma_{rr}(\theta_2^-), \quad d_4 = (d_1 - c_1)\sin 2\theta_3; \tag{36}$$

$$c_1 \sin 2\theta_2 + (d_1 - c_1)\sin 2(\theta_3 - \theta_2) = \sigma_{r\theta}(\theta_2^-), \tag{37a}$$

$$d_1 - c_1 \cos 2\theta_2 - (d_1 - c_1)\cos 2(\theta_3 - \theta_2) = \sigma_{\theta\theta}(\theta_2^-), \tag{37b}$$

where $d_1$ is a function of $\theta_2$ only, as shown in (36); thus, (37*a*, *b*) can be used to determine both $\theta_2$ and $\theta_3$.

Numerical calculations show that for $q_2 = 1$ and each given $f$ in the range

$$0.04468/q_1 < f \leq f_2 \approx 0.18043/q_1 \quad (=0.12029 \text{ for } q_1 = 1.5), \tag{38}$$

there is a unique solution for $\theta_2$ and $\theta_3$ satisfying $0 \leq \theta_2 < \theta_3 \leq \pi$, and stresses are continuous across $\theta = \theta_2$ *while stresses $\sigma_{rr}$ and $\sigma_{33}$ jump across the $\theta = \theta_3$ ray*. Hence, this type of solution is very similar to the Hutchinson (1968) solution for a plane stress Mode I stationary crack in fully dense Huber-Mises material, and we call it the "plane-stress-like" stress field. Values of parameters corresponding to this near-tip sector assembly, i.e., to the range of $f$ delimited by (38), are presented in Table 2. It is found that $\theta_2 \to \theta_3 \approx 133.9$ deg as $f \to f_1 \approx .04468/q_1$; from this point of view, the generalized Prandtl field evolves directly into the plane-stress-like field. The numerical calculations also show that both $\theta_2$ and $\theta_3$ decrease as $f$ increases; specifically, as $f \to 0.18043/q_1$, $\theta_2 \to 0$ and $\theta_3 \to 90$ deg. That is, in this limit the generalized centered fan sector vanishes, and the resulting stress field consists of only two constant stress sectors with stress jumps across the ray $\theta = \theta_3 \approx 90$ deg. The corresponding field of characteristics for solutions in the range (38) is also established; as illustrated in Fig. 4(*a*) and noted previously, it is similar to that for a Mode I plane stress stationary crack in a Huber-Mises material. In each stress sector, the slopes of characteristics are continuous functions of stress components; therefore, they are continuous everywhere except across the $\theta = \theta_3$ ray, because a stress jump does exist there. In the $f \to 0.18043/q_1$ limit, Fig. 4(*b*), the characteristic lines at each material point in Sector D coincide with one another and are parallel to the $x_1$-axis, indicating that the equations have become parabolic there. Figure 5(*a*, *b*) displays the near-tip angular variation of stress components for selected $f$ values within the range of applicability (38) of this plane-stress-like construction.

## 6 Near-Tip Stress Field at High Porosities: Two Constant Stress Sectors.

We now investigate whether the near-tip configuration for $f = f_2$ can apply for larger void volume fractions also. That is, we assume that the stress field contains only two constant stress plastic sectors C and D, with initially unknown mutual border location $\theta = \theta_3$. Thus, the stresses in Sector C are completely determined as in Section 4.1, and general representations of the stress components in Sector D are still given by (13) with (14), where again for Sector D we rename the constants $c_n$ as $d_n$ in these equations. The only unknowns are thus $d_1$, $d_2$, $d_3$, and $\theta_3$, since Mode I symmetry requires $d_4 = 0$.

Enforcing traction continuity across $\theta = \theta_3$, we have

$$-d_2 \sin 2\theta_3 = -c_1 \sin 2\theta_3 \tag{39a}$$

$$d_1 - d_2 \cos 2\theta_3 = c_1(1 - \cos 2\theta_3). \tag{39b}$$

Equation (39*a*) has solutions:

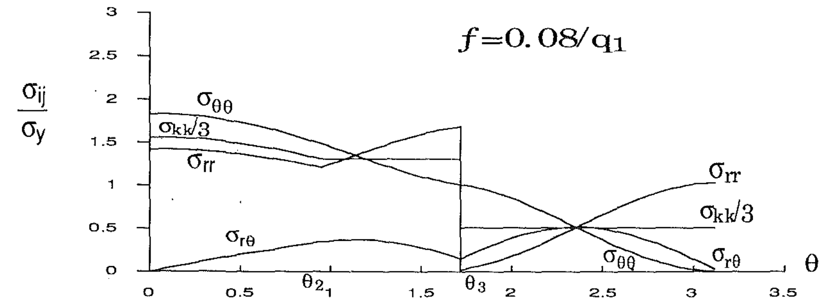


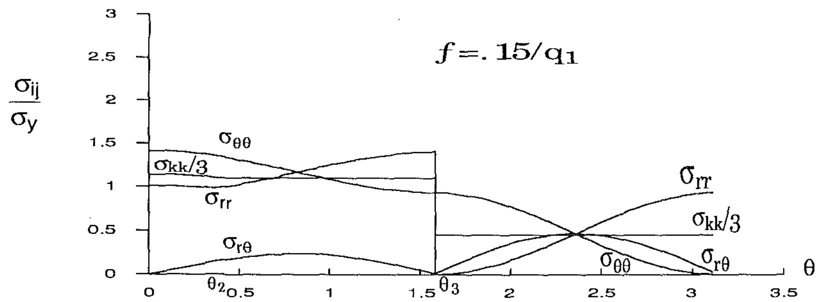


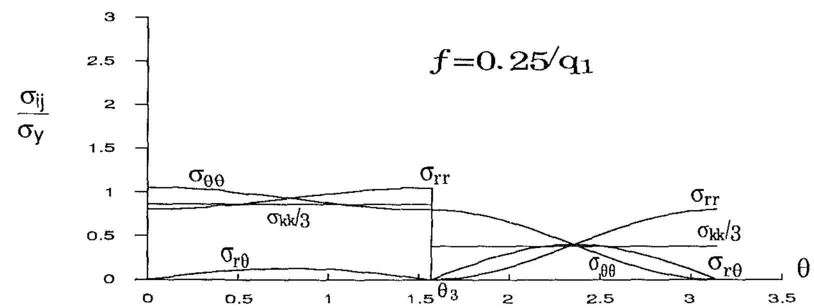


**Fig. 5 Polar components of stress as functions of angle $\theta$ for selected values of $f$ in the plane-stress-like solution configuration [$f = 0.08/q_1$ and $f = 0.15/q_1$] and in the two-constant-stress-sector solution configuration [$f = 0.25/q_1$]**

$$c_1 = d_2 \quad \text{or} \quad \sin 2\theta_3 = 0 \quad \left(\Rightarrow \theta_3 = 0, \frac{\pi}{2}, \pi\right). \qquad (40a,b)$$

Solution (40*a*) can be shown to have $\sigma_{\theta\theta}(\theta = 0) = 0$, which does not meet our requirement of tensile crack loading. For a similar reason, $\theta_3 = 0$ and $\theta_3 = \pi$ in (40*b*), which give continuous constant stress fields, are not appropriate either.

Thus, $\theta_3 = \pi/2$ is the only appropriate solution for $f > 0.18043/q_1$. The constants $d_n$ are determined by numerically solving (39*b*) and (14) (in terms of $d_n$'s) for each given $f$; specific results are reported in Table 3. This stress field has jumps in $\sigma_{rr}$ and $\sigma_{33}$ across the $\theta = \pi/2$ line. Also, there are no real characteristics for stresses in Sector D: The equations have become elliptic there. This solution configuration is illustrated in Fig. 4(*c*), and a representative stress plot is given in Fig. 5(*c*).

Finally, Figure 6 combines results from all three near-tip solution configurations obtained in this paper to show how the maximum hydrostatic stress level, which occurs directly ahead of the crack tip ($r \to 0$, $\theta = 0$), decreases with increasing porosity for the entire porosity range. As noted earlier, the maximum hydrostatic stress level can be seen to decrease

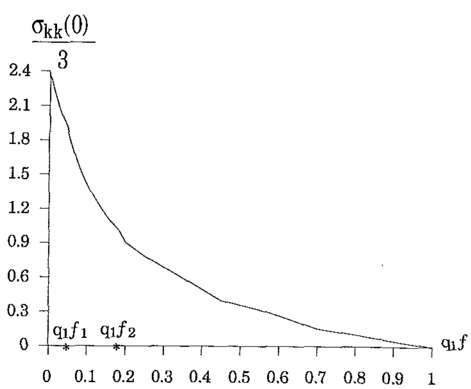


**Fig. 6 Hydrostatic stress level (normalized by the matrix material's uniaxial yield stress) directly ahead of the crack tip versus Tvergaard-adjusted void volume fraction. Transition porosity levels between the different near-tip solution configurations are indicated.**

strongly with increasingly porosity, especially at lower porosity levels.

## 7 Discussion

The results derived herein are expected to be physically meaningful in an *annular* region surrounding a crack tip, as is also true of previous "small strain" asymptotic solutions for crack-tip fields in fully dense materials (see, e.g., the lucid review paper of Hutchinson (1983)). The outer radius of this annular region is sufficiently small compared to, e.g., the maximum plastic zone radius that the asymptotic forms employed here are valid, while its inner radius is on the order of two or three times the crack-tip opening displacement, since at distances from the crack tip greater than this, the effects of large geometry changes and high void growth rates can be ignored. The large-deformation numerical finite element results of Aoki et al. (1987) and Jagota et al. (1987) support this conclusion.

One of the simplifying assumptions made in the present analysis is that the material experiences plastic response at all angles about the crack tip. As demonstrated, solutions exhibiting this feature do exist for the entire range of porosity. For $f > .04468/q_1$ ($= .02979$ for $q_1 = 1.5$), we showed these solutions to involve stress discontinuities. Although these are correct solutions, we are suspicious that another set of solutions may exist for this porosity range, possessing a sector of purely elastic response and exhibiting fully continuous stress fields. We are currently investigating this possibility.

## Acknowledgments

Support of this work by the Mechanics Division of the Office of Naval Research under Grant N00014-89-J-1206 and by the National Science Foundation under Grant MSS-8552486 is gratefully acknowledged. We thank the anonymous reviewers of this paper for helpful comments.

## References

Aoki, S., Kishimoto, K., Yoshida, T., and Sakata, M., 1987, "A Finite Element Study of the Near Crack Tip Deformation of a Ductile Material Under Mixed Mode Loading," *Journal of the Mechanics and Physics of Solids*, Vol. 35, pp. 431-455.

Aravas, N., and McMeeking, R. M., 1985, "Microvoid Growth and Failure in the Ligament Between a Hole and a Blunt Crack Tip," *International Journal of Fracture*, Vol. 29, pp. 21-38.

Bishop, J. F. W., and Hill, R., 1951, "A Theory of the Plastic Distortion of a Polycrystalline Aggregate under Combined Stresses," *Philosophical Magazine*, Vol. 42, pp. 414-427.

Dong, P., and Pan, J., 1991, "Elastic-Plastic Analysis of Cracks in Pressure-Sensitive Materials," *International Journal of Solids and Structures*, Vol. 28, pp. 1113-1127.

Drugan, W. J., 1985, "On the Asymptotic Continuum Analysis of Quasi-Static Elastic-Plastic Crack Growth and Related Problems," ASME JOURNAL OF APPLIED MECHANICS, Vol. 52, pp. 601-605.

Gurson, A. L., 1977, "Continuum Theory of Ductile Rupture by Void Nucleation and Growth: Part I—Yield Criteria and Flow Rules for Porous Ductile Media," *Journal of Engineering Materials and Technology*, Vol. 99, pp.2-15.

Hill, R., 1950, *The Mathematical Theory of Plasticity*, Clarendon Press, Oxford, U.K.

Hom, C. L., and McMeeking, R. M., 1989, "Void Growth in Elastic-Plastic Materials," ASME JOURNAL OF APPLIED MECHANICS, Vol. 56, pp. 309-317.

Hutchinson, J. W., 1968, "Plastic Stress and Strain Fields at a Crack Tip," *Journal of the Mechanics and Physics of Solids*, Vol. 16, pp. 337-347.

Hutchinson, J. W., 1983, "Fundamentals of the Phenomenological Theory of Nonlinear Fracture Mechanics," ASME JOURNAL OF APPLIED MECHANICS, Vol. 50, pp.1042-1051.

Jagota, A., Hui, C.-Y., and Dawson, P. R., 1987, "The Determination of Fracture Toughness for a Porous Elastic-Plastic Solid," *International Journal of Fracture*, Vol. 33, pp. 111-124.

Li, F. Z., and Pan, J., 1990, "Plane-Strain Crack-Tip Fields for Pressure-Sensitive Dilatant Materials," ASME JOURNAL OF APPLIED MECHANICS, Vol. 57, pp. 40-49.

Needleman, A., and Tvergaard, V., 1987, "An Analysis of Ductile Rupture Modes at a Crack Tip," *Journal of the Mechanics and Physics of Solids*, Vol. 35, pp. 151-183.

Rice, J. R., 1982, "Elastic-Plastic Crack Growth," *Mechanics of Solids: The R. Hill 60th Anniversary Volume*, H. G. Hopkins and M. J. Sewell, eds., Pergamon Press, Oxford, U.K., pp. 539-562.

Tvergaard, V., 1981, "Influence of Voids on Shear Band Instabilities Under Plane Strain Conditions," *International Journal of Fracture*, Vol. 17, pp. 389-407.

Tvergaard, V., 1982, "On Localization in Ductile Materials Containing Spherical Voids," *International Journal of Fracture*, Vol. 18, pp. 237-252.

Tvergaard, V., 1990, "Material Failure by Void Growth to Coalescence," *Advances in Applied Mechanics*, Vol. 27, pp. 83-151.

## APPENDIX

Here we prove that all stresses must be continuous across the mutual border between a generalized centered fan plastic sector and a constant stress plastic sector located, respectively, on the "−" and "+" sides of the $\theta = \Theta$ ray, without loss. Traction continuity requires

$$[\![\sigma_{\theta\theta}]\!]=0, \quad [\![\sigma_{r\theta}]\!]=0 \qquad (\mathrm{A}1a,b)$$

where $[\![\sigma_{ij}]\!] \equiv \sigma_{ij}(\Theta^+) - \sigma_{ij}(\Theta^-)$, with $\sigma_{ij}(\Theta^-)$ satisfying (9$b$), (15$d$), and (3), while $\sigma_{ij}(\Theta^+)$ satisfy (7) and (3). Applying these conditions to (A1), the resulting equations can be combined and rearranged to show

$$G(u,v) \equiv \frac{16}{3}u^2 + \frac{4}{3}(q_1q_2f)^2 \sinh^2(q_2u)\cosh^2(q_2v) + \frac{8}{3}q_1q_2fu\sinh(q_2u)\cosh(q_2v) - 4q_1f\sinh(q_2u)\sinh(q_2v) + 4q_1q_2fu\sinh[q_2(u+v)] = 0, \qquad (\mathrm{A}2)$$

where we have defined

$$u \equiv \frac{1}{4}[\sigma_{kk}(\Theta^-) - \sigma_{kk}(\Theta^+)], \quad v \equiv \frac{1}{4}[\sigma_{kk}(\Theta^-) + \sigma_{kk}(\Theta^+)]. \qquad (\mathrm{A}3)$$

For arbitrary $v$, it is easy to demonstrate via (A2) that $G(u, v)$ has the properties

$$G(0,v)=0, \quad \frac{\partial G}{\partial u}(u,v)<0\ (u<0), \quad \frac{\partial G}{\partial u}(u,v)=0\ (u=0), \quad \frac{\partial G}{\partial u}(u,v)>0\ (u>0). \qquad (\mathrm{A}4)$$

This shows that the only solution of (A2) is $u = 0$ (i.e., $[\![\sigma_{kk}]\!] = 0$), which together with (A3), (7) holding in both sectors, and (A1$a$) gives

$$[\![\sigma_{rr}+\sigma_{33}]\!]=0, \quad [\![2\sigma_{33}-\sigma_{rr}]\!]=0 \qquad (\mathrm{A}5)$$

$$\rightarrow [\![\sigma_{33}]\!]=0=[\![\sigma_{rr}]\!]. \qquad (\mathrm{A}6)$$

**Gerald Wempner**
Professor of Mechanics,
Engineering Science and Mechanics
Program,
School of Civil Engineering,
Georgia Institute of Technology,
Atlanta, GA 30332-0355
Fellow ASME

# The Complementary Potentials of Elasticity, Extremal Properties, and Associated Functionals

## Introduction

The powerful principles of virtual work and minimum potential were set forth in the 18th century. Brief historical accounts are given by Lanczos (1949) and Langhaar (1962). The former principle applies to any mechanical system; the latter applies to any conservative system. The complementary theorem of Castigliano (1879) applies only to infinitesimal displacements. Quite recently, a complementary theorem for finite deformations was given by Fraeijs de Veubeke (1972) and by Koiter (1973a). Other work on the complementary theorem and applications were presented by Zubov (1970), Koiter (1973b), Christoffersen (1973), Ogden (1975, 1977) and Nemat-Nasser (1977). Earlier developments of "energetical principles" are recounted by Oravas and McLean (1966).

The complementary functional of Faeijs de Veubeke has an extremal property which admits a criterion for stability, akin to the criterion of Trefftz (1933). That criterion has been employed by Popelar (1974) and by Masur and Popelar (1976) and presented in generality by Koiter (1976).

In a previous article (1980), the author set the complementary principles in the context of a general functional which served to show the complementarity and the extremal properties of the potentials. The foregoing developments utilized the Jaumann (1918) components of stress and the rotation of the principal lines of strain. Indeed, dependence on the rotation is a feature of the complementary functional. Here the complementary functional is defined in a general form which bears a striking resemblance to the definition of the complementary-energy density. The potential, the complementary functional, the related functionals of Hu-Washizu (1955) and Hellinger-Reissner (1914, 1950) are all presented in terms of the alternative measures of strain and stress: engineering strain with Jaumann stress and Cauchy-Green (1841) strain with Piola-Kirchhoff-Trefftz (1833, 1852, 1933)[1] stress. All are valid for finite deformations.

[1]The components, $S^{ij}$ in Eq. (7), are variously called the second Piola-Kirchhoff components and the Kirchhoff-Trefftz components. The work of Trefftz (1933) gives a graphic description.

Contributed by the Applied Mechanics Division of THE AMERICAN SOCIETY OF MECHANICAL ENGINEERS for publication in the JOURNAL OF APPLIED MECHANICS.

Discussion on this paper should be addressed to the Technical Editor, Professor Leon M. Keer, and will accepted until four month after final publication of the paper itself in the JOURNAL OF APPLIED MECHANICS.

Manuscript received by the ASME Applied Mechanics Division, Apr. 10, 1990; final revision, Mar. 11, 1991. Associate Technical Editor: J. H. Simmonds.

## Kinematics

The notations follow the author's previous work (1980) in accordance with the notations of Green and Adkins (1960). Basic quantities follow:

$\mathbf{r}, \mathbf{R}$ = position vector of initial, current states, (undeformed, deformed)
$\mathbf{V} = \mathbf{R} - \mathbf{r}$
$\theta^i$ = arbitrary coordinate $(i=1, 2, 3)$
$\mathbf{g}_i; \mathbf{G}_i = \partial\mathbf{r}/\partial\theta^i; \partial\mathbf{R}/\partial\theta^i = \mathbf{r}_{,i}; \mathbf{R}_{,i}$
$\mathbf{g}^i\bullet\mathbf{g}_j = \mathbf{G}^i\bullet\mathbf{G}_j = \delta^i_j$ = Kronnecker delta
$g_{ij}, G_{ij} = \mathbf{g}_i\bullet\mathbf{g}_j, \mathbf{G}_i\bullet\mathbf{G}_j$
$\sqrt{g} = \mathbf{g}_1\bullet(\mathbf{g}_2\times\mathbf{g}_3)$ = metric of initial volume
$\epsilon_{ijk} = \mathbf{g}_i\bullet(\mathbf{g}_j\times\mathbf{g}_k)$ = permutation tensor
$s_i, S_i$ = length along the $\theta^i$ line in the initial, current state
$\hat{\mathbf{n}}_\alpha, \hat{\mathbf{N}}_\alpha$ = unit vector tangent to the initial, current line of principal strain $(\alpha = 1,2,3)$
$r_{\beta\alpha} = \hat{\mathbf{n}}_\beta\bullet\hat{\mathbf{N}}_\alpha$, cosine of the angle between an initial and rotated principal line

Two measures of strain are useful. First, the component of the Cauchy-Green tensor is

$$\gamma_{ij} = \frac{1}{2}\,(G_{ij} - g_{ij}). \tag{1}$$

Physical components (Green and Zerna, 1954) are

$$\epsilon_{ij} = \frac{\gamma_{ij}}{\sqrt{g_{\underline{ii}}g_{\underline{jj}}}}.$$

The underscoring of repeated indices negates the summation, otherwise implied by the convention. Stretching of a line is given by the ratio:

$$\frac{dS_i}{ds_i} = \sqrt{1 + 2\epsilon_{\underline{ii}}}.$$

Fraeijs de Veubeke (1972) employed components of engineering strain such that principal lines (signified by Greek indices) experience extensional strains $\epsilon_{\underline{\alpha}} = dS_{\underline{\alpha}}/ds_{\underline{\alpha}} - 1$ $(\alpha = 1, 2, 3)$. Then the tensor of engineering strain is given by the transformation to arbitrary coordinates $(\theta^i)$:

$$h_{ij} = \epsilon_{\underline{\alpha}}\,\frac{\partial s_\alpha}{\partial\theta^i}\,\frac{\partial s_\alpha}{\partial\theta^j} - g_{ij}. \tag{2}$$

The engineering strain $(h_{ij})$ was introduced by Alumae (1949), and again by Simmonds and Danielson (1970), both in nonlinear theories of shells.

A rigid rotation carries the unit vector $\hat{\mathbf{n}}_\alpha$ (tangent to the initial principal line) to the unit vector $\hat{\mathbf{N}}_\alpha$ (tangent to the current principal line:

$$\hat{\mathbf{N}}_\alpha = r^{\beta}_{\cdot\alpha}\hat{\mathbf{n}}_\beta.$$

In the arbitrary system of coordinates $(\theta^i)$, the triad $(\mathbf{g}^i)$ is rigidly rotated to a similar triad

$$\mathbf{g}_i' = r^{j}_{\cdot i}\mathbf{g}_j \quad \left(r^{j}_{\cdot i} = r^{\beta}_{\cdot\alpha}\frac{\partial\theta^j}{\partial s_\beta}\frac{\partial s_\alpha}{\partial\theta^i}\right). \tag{3}$$

Note that *only* the principal lines are rotated to their final positions; the rotation of every other line differs by virtue of shear strain. The exception is simple dilatation, wherein every line experiences the same rotation. The current tangent vector $(\mathbf{G}_i)$ results from the rigid rotation and subsequent "stretch":

$$\mathbf{G}_i = (h_i^j + \delta_i^j)r^{k}_{\cdot j}\mathbf{g}_k. \tag{4}$$

It is noteworthy that

$$h_{ij} = h_{ji} = \mathbf{g}_i' \cdot \mathbf{R}_{,j} - g_{ij} \tag{5}$$

or, stated otherwise,

$$\mathbf{g}_i' \cdot \mathbf{R}_{,j} = \mathbf{g}_j' \cdot \mathbf{R}_{,i}.$$

## Virtual Work of Stress

The virtual work of stresses (per unit *initial* volume) is $\mathbf{T}^i \cdot \mathbf{R}_{,i}$, wherein $\mathbf{T}^i$ is the stress vector upon the $\theta^i$ surface; it is related to the physical stress $\mathbf{s}^i$ (force per unit *initial* area):

$$\mathbf{s}^i = \mathbf{T}^i/\sqrt{g^{\underline{ii}}} \tag{6}$$

The stress may be referred to the triad $\mathbf{g}_i'$ or $\mathbf{G}_i$. The former rotates with the material, just as the principal lines of strain; the latter remains tangent to the convected line. Accordingly, the work during virtual displacement $\delta\mathbf{R}$ has the alternative forms:

$$\mathbf{T}^i \cdot \delta\mathbf{R}_{,i} = T^{ij}\mathbf{g}_j' \cdot \delta\mathbf{R}_{,i} = S^{ij}\mathbf{G}_j \cdot \delta\mathbf{R}_{,i}. \tag{7a}$$

In accordance with (5) and (1), respectively,

$$\mathbf{T}^i \cdot \delta\mathbf{R}_{,i} = \mathbf{T}^{ij}\delta h_{ij} = S^{ij}\delta\gamma_{ij}. \tag{7b}$$

The Jaumann components $T^{ij}$ and the Kirchhoff-Trefftz components $S^{ij}$ are conjugate to the engineering strain $h_{ij}$ and Cauchy-Green strain $\gamma_{ij}$, respectively. The former are referred to the triad $\mathbf{g}_i'$, the latter to $\mathbf{G}_i$; in accordance with $(7a)$:

$$T^{ij} = \mathbf{g}'^j \cdot \mathbf{T}^i,\ S^{ij} = \mathbf{G}^j \cdot \mathbf{T}^i.$$

Two subtle, but relevant, features are noteworthy. First, in view of the symmetry of both strains, only the symmetrical parts of the stress tensors play a role in the work (7). Secondly, the form $\mathbf{T}^i = S^{ij}\mathbf{G}_j$ expresses the stress in terms of the "stretched" vectors $\mathbf{G}_i$ and in $(7b)$ that "stretch" is incorporated in the strain $\gamma_{ij}$. Specifically, a variation of stress $\delta\mathbf{T}^i$ embodies a rotation of the reference triads ($\mathbf{g}_i'$ or $\mathbf{G}_i$), but stretch of $\mathbf{G}_i$ is incorporated in the variation of $\gamma_{ij}$. Finally, physical components (force per unit *initial* area) of each stress follow:

$$\sigma'^{ij} = \sqrt{\frac{g^{\underline{ii}}}{g_{\underline{jj}}}}\,T^{ij},\ \sigma^{ij} = \sqrt{\frac{g^{\underline{ii}}}{G_{\underline{jj}}}}\,S^{\underline{ij}}.$$

It is noteworthy that the former contains only the initial metric $(g_{\underline{jj}})$ whereas the latter involves the deformed $(G_{\underline{jj}})$.

## Internal Energy and Complementary Energy

If the deformation is adiabatic, then the internal energy (per unit *initial* volume) of the elastic material has the alternative forms:

$$\overline{W}(h_{ij}) \text{ or } W^*(\gamma_{ij})$$

In accordance with $(7b)$, the symmetrical parts of the respective stresses are

$$T^{(ij)} = \frac{\partial\overline{W}}{\partial h_{ij}}, \qquad S^{(ij)} = \frac{\partial W^*}{\partial\gamma_{ij}}. \tag{8a, b}$$

In the usual manner, complementary energies, $\overline{W}_c$ and $W_c'$, are defined by the Legendre transformation:

$$\overline{W} + \overline{W}_c = T^{ij}h_{ij}, \qquad W^* + W_c^* = S^{ij}\gamma_{ij} \tag{9a, b}$$

Under the conditions for the inversion of $(8a, b)$ in a neighborhood of the current state, the complementary functions, $\overline{W}_c$ and $W_c^*$ are functions of the respective symmetric stresses and the strain-stress equations follow:

$$h_{ij} = \frac{\partial\overline{W}_c}{\partial T^{(ij)}}, \qquad \gamma_{ij} = \frac{\partial W_c^*}{\partial S^{(ij)}}. \tag{10a, b}$$

## General Functional and Complementary Parts

A primitive functional $P$ was used previously (1978) by the author:

$$P = \int_v [\mathbf{T}^i \cdot \mathbf{R}_{,i} - \mathbf{f} \cdot \mathbf{R}]dv - \int_a [\mathbf{t} \cdot \mathbf{R}]da - \int_{a_v} [(\mathbf{R} - \tilde{\mathbf{R}}) \cdot \mathbf{t}]da. \tag{11}$$

Here, $\mathbf{f}$ denotes the body force (per unit initial volume), $v$ the initial volume, $t$ the surface traction (per unit initial area), $a$ and $a_v$ denote the entire surface and the part on which position is prescribed, $\mathbf{R} = \tilde{\mathbf{R}}$, the prescribed position. If the stress satisfies the conditions of equilibrium $((\mathbf{T}^i\sqrt{g})_{,i} + \sqrt{g}\,\mathbf{f} = 0$ in $v$, $\mathbf{T}^i n_i = \mathbf{t}$ on $a$) and the displacement is compatible ($\mathbf{R}$ and $\mathbf{R}_{,i}$ continuous in $v$, $\mathbf{R} = \tilde{\mathbf{R}}$ on $a$), then $P = 0$. Stated otherwise, $P$ is stationary among all statically and kinematically admissible variations of $\mathbf{T}^i$ and $\mathbf{R}$, respectively. The last may be construed as a statement of the principles of "virtual force" and "virtual displacement."

Now, the initial term on the right side of (11), and the equations $(9a, b)$, provide alternative integrals:

$$\int_v \mathbf{T}^i \cdot \mathbf{R}_{,i}dv = \int_v (\overline{W} + \overline{W}_c + T_i^i)dv \tag{12a}$$

$$= \int_v \left(W^* + W_c^* + \frac{1}{2}S_i^i + \frac{1}{2}\mathbf{T}^i \cdot \mathbf{R}_{,i}\right)dv. \tag{12b}$$

Substitution of $(12a)$ or $(12b)$ into the general functional (11) gives

$$P = \overline{P}_w + \overline{P}_c = P_w^* + P_c^* \tag{13a, b}$$

wherein $\overline{P}_w = P_w^*$ is the potential, expressed in terms of alternative internal energies, $\overline{W}(h_{ij}) = W(\gamma_{ij})$; $\overline{P}_c$ and $\overline{P}_c^*$ are the complementary functionals

$$\overline{P}_c = \int_v (\overline{W}_c + T^{ij}g_{ij})dv - \int_{a_v} [\mathbf{t} \cdot \mathbf{R}]da - \int_{a_v} [\mathbf{t} \cdot (\mathbf{R} - \tilde{\mathbf{R}})]da \tag{14a}$$

$$P_c^* = \int_{a_v} \left(W_c^* + \frac{1}{2}S_i^i + \frac{1}{2}\mathbf{T}^i \cdot \mathbf{G}_i\right)dv - \int_{a_v} [\mathbf{t} \cdot \mathbf{R}]da - \int_{a_v} [\mathbf{t} \cdot (\mathbf{R} - \tilde{\mathbf{R}})]da. \tag{14b}$$

Here, the potential of body forces and surface tractions are for dead loadings (constant loads). Again, the resemblance between (13) and (9) is striking. More important are the extremal properties: If the body is in a state of stable equilibrium, then (presumably) the potential ($\overline{P}_w$ and $P_w^*$) is a relative minimum. For all admissible (equilibrated) states $P = 0$ or, stated otherwise, the complementary functional is a relative maximum ($\Delta\overline{P}_c = -\Delta\overline{P}_w$, $\Delta P_w^* = -\Delta P_w^*$).

The functional $\overline{P}_c$ is that given in the earlier work (Wempner, 1978). The functional $(14b)$ deserves further exposition. Since only equilibrated variations of stress are admissible, $\delta\mathbf{T}^i n_i = \delta\mathbf{t}$ on the surface $a_v$, $\delta\mathbf{t} = 0$ on $a_t$, and $(\delta\mathbf{T}^i\sqrt{g})_{,i} = 0$ in the interior, the application of the Gauss theorem gives

$$\delta P_c^* = \int_v \left[ \frac{\partial W_c^*}{\partial S_{ij}} \delta S_{ij} + \frac{1}{2} \delta S^{ij} g_{ij} - \frac{1}{2} \delta \mathbf{T}^i \cdot \mathbf{R}_{,i} \right] dv - \int_{a_v} [\delta\mathbf{t} \cdot (\mathbf{R} - \tilde{\mathbf{R}})] da.$$

As noted before, the variation of stress implies a variation (rotation) of the basis $(\mathbf{G}_i)$, so that

$$\delta\mathbf{T}^i = \delta S^{ij}\mathbf{G}_j + S^{ij}\delta\Omega \times \mathbf{G}_j = \delta S^{ij}\mathbf{G}_j + S^{ij}\delta\Omega^k \epsilon_{kjs}\mathbf{G}^s$$

Accordingly, the variation $\delta P_c^*$ takes the form

$$\delta P_c^* = \int_v \left[ \left( \frac{\partial W_c^*}{\partial S^{ij}} + \frac{1}{2} g_{ij} - \frac{1}{2} G_{ij} \right) \delta S_{ij} + S_{ij}\epsilon_{kji}\delta\Omega^k \right] dv - \int_{a_v} [\delta\mathbf{t} \cdot (\mathbf{R} - \tilde{\mathbf{R}})] da$$

The stationary conditions follow:

$$\frac{1}{2}(G_{ij} - g_{ij}) = \frac{\partial W_c^*}{\partial S^{ij}}, \qquad S^{ij} = S^{ji}$$

$$\mathbf{R} = \tilde{\mathbf{R}} \text{ (on } a_v).$$

## Functionals and Stationary Theorem of Hu-Washizu

The functional and stationary theorem of Hu-Washizu is commonly expressed in terms of the strain and stress tensors, $\gamma_{ij}$ and $S^{ij}$. Less common is the expression in terms of the tensors $h_{ij}$ and $T^{ij}$. The functional is obtained by augmenting the potential $\overline{P}_w$ with the kinematical constraints, viz.,

$$T^{ij}(h_{ij} - \mathbf{g}_j \cdot \mathbf{R}_{,i} + g_{ij}) \text{ in } v$$

$$\mathbf{t} \cdot (\mathbf{R} - \tilde{\mathbf{R}}) \text{ on } a_v.$$

The result follows:

$$H_w = \int_v [\overline{W}_w - T^{ij}g_{ij} - T^{ij}(h_{ij} - \mathbf{g}_j' \cdot \mathbf{R}_{,i}) - - \mathbf{f} \cdot \mathbf{R}] dV - \int_{a_t} [\mathbf{t} \cdot \mathbf{R}] da - \int_{a_v} [\mathbf{t} \cdot (\mathbf{R} - \tilde{\mathbf{R}})] da \quad (15)$$

Now, $\overline{H}_w = \overline{H}_w(h_{ij}, r_{ij}, T^{ij}, \mathbf{R})$, a functional of strain, rotation (of $\mathbf{g}_i'$), stress, and displacement. Continuity is the only condition for admissibility of the fields. $\delta H_w = 0$, if and only if all kinematical, statical, and constitutive conditions are satisfied. For arbitrary variation of the rotation $(r_{ij})$, one obtains the condition of vanishing moment

$$T^{ij}(h_i^k + \delta_i^k) = T^{ik}(h_i^j + \delta_i^j). \quad (16)$$

## Functionals and Stationary Theorem of Hellinger-Reissner

The functional of Hellinger-Reissner has alternative forms, as a functional of stress and displacement, $T^{ij}$ and $\mathbf{R}$, or $S^{ij}$ and $\mathbf{R}$. These follow immediately from (14*a*) or (14*b*). It is only necessary to apply the Gauss theorem to the first integral on surface $a_v$:

$$\int_{a_v} [\mathbf{t} \cdot \mathbf{R}] da = \int_v \left[ \frac{1}{\sqrt{g}} (\mathbf{T}^i\sqrt{g})_{,i} \cdot \mathbf{R} + \mathbf{T}^i \cdot \mathbf{R}_{,i} \right] dv - \int_{a_t} [\mathbf{t} \cdot \mathbf{R}] da.$$

Here, the tractions are in equilibrium, $\mathbf{t} = \mathbf{T}^i n_i$ on $a$, and the stress satisfies equilibrium, $(\mathbf{T}^i\sqrt{g})_{,i} = -\sqrt{g}\mathbf{f}$ in $v$. The functionals $\overline{P}_c$ and $P_c^*$ take the forms:

$$\overline{P}_c = \int_v [\overline{W}_c - \mathbf{T}^i \cdot (\mathbf{R}_{,i} - \mathbf{g}_i') + \mathbf{f} \cdot \mathbf{R}] dv - \int_{a_t} [\mathbf{t} \cdot \mathbf{R}] da - \int_{a_v} [\mathbf{t} \cdot (\mathbf{R} - \tilde{\mathbf{R}})] da \quad (17a)$$

$$P_c^* = \int_v \left[ W_c^* - \frac{1}{2} S^{ij}(\mathbf{R}_{,i} \cdot \mathbf{R}_{,j} - g_{ij}) + \mathbf{f} \cdot \mathbf{R} \right] dv - \int_{a_t} [\mathbf{t} \cdot \mathbf{R}] da - \int_{a_v} [\mathbf{t} \cdot (\mathbf{R} - \tilde{\mathbf{R}})] da \quad (17b)$$

Now, one considers $\overline{P}_c(T^{ij}, \mathbf{R})$ and $P_c^*(S^{ij}, \mathbf{R})$. The theorem asserts that the functionals are stationary with respect to arbitrary variations of the stress and displacement. The latter leads to the equilibrium condition $(\mathbf{T}^i\sqrt{g})_{,i} + \sqrt{g}\,\mathbf{f} = 0$. One could accept a priori the condition $h_{ij} = h_{ji}$ or, equivalently, $\mathbf{g}_i' \cdot \mathbf{R}_{,j} = \mathbf{g}_j' \cdot \mathbf{R}_{,i}$; otherwise, the variation $\delta\mathbf{g}_i' = \delta\Omega \times \mathbf{g}_i'$ leads to the equilibrium requirement (16).

## Conclusion

The foregoing presentation of the functionals gives a definition (13*a*, *b*) of the complementary functionals, analogous to the complementary functions (9*a*, *b*). The sum in either case is the primitive functional $P$ which vanishes for all equilibrium states. The extremal properties of the potential (form $\overline{P}_w$ or $P_w^*$) and its complement (form $\overline{P}_c$ or $P_c^*$) is established.

Any of the functionals and the associated extremal, or stationary, properties might be employed for the approximation of the deformed equilibrium states. Of course, the complementary functionals admit only stresses which satisfy equilibrium, a difficult prerequisite. The minimum potential requires only the requisite continuity of the displacement. The functional of Hu-Washizu is a modification of the potential which admits approximation of strain and stress; moreover, the function ($\overline{H}_w = \overline{P}_w$, or $H_w^* = P_w^*$) *is* the potential, *if* the strains are fully compatible with the displacement. Because the functionals of Hu-Washizu and Hellinger-Reissner admit also approximations of strain and stress, they are useful tools in the formulation of finite elements. Specific advantages in the approximation of shells are described in the author's review (1989). The forms given are all valid for finite deformations of any elastic body.

## Acknowledgment

The author appreciates the support provided by the National Science Foundation under auspices of the Structures Program and the direction of Dr. Ken Chong.

## References

Alumae, N. A., 1949, "Differential Equations of Equilibrium for Thin Elastic Shells in the Post-Buckling State," *Prik. Mat. Mek.*, Vol. 13, pp. 95–106.

Castigliano, C. A. P., 1879, *The Theory of Equilibrium of Elastic Systems and Its Application* (transl. by E. S. Andrews, French ed., Dover, New York (1966).

Cauchy, A. L., 1841, "Memoire sur les dilatations, les condensations et les rotations produits par un changement de forme dans un systeme de points materials," *Ex. d'an Phys. Math.*, Vol. 2.

Christoffersen, J., 1973, "On Zubov's Principle of Stationary Complementary Energy and a Related Principle," Report 44, Danish Center Appl. Math. Mech.

Fraeijs de Veubeke, B,. 1972, "A New Variational Principle For Finite Elastic Displacements," *International Journal of Engineering Science*, Vol. 10, pp. 745–763.

Green, A. E., and Zerna, W., 1954, *Theoretical Elasticity*, Oxford University Press.

Green, A. E., and Adkins, J. E., 1960, *Large Elastic Deformations*, Oxford Univ. Press, p. 5.

Green, G., 1841, "On the Propagation of Light in Crystallized Media," *Phil. Soc.*, Vol. 7, pp. 295–296.

Hellinger, E., 1914, "Die Algemeinen Ansätze der Mechanik der Continua," *Encyklopädie der mathematischen Wissenschaften*, Vol. 4, No. 4.

Hu, H. C., 1955, "On Some Variational Principles in the Theory of Elasticity and Plasticity," *Scientia Sinica*, Vol. 4.

Jaumann, G., 1918, "Physik der kontinuierlichen Medien," *Denkschr. Akad. Wiss, Wein*, Vol. 95, pp. 461–562.

Kirchhoff, G., 1852, "Über die Gleichungen des Gleichgewichts eines Elastischen Körpers bei nicht unendlich kleinen Verschiebungen seiner Teile," *Sitzungsberichte Akad. Wiss.*, Wein, Vol. 9, pp. 762–773.

Koiter, W. T., 1973a, "On the Principle of Stationary Complementary Energy in the Nonlinear Theory of Elasticity," *SIAM Journal of Applied Mathematics*, Vol. 25, pp. 424–434.

Koiter, W. T., 1973b, "On the Complementary Energy Theorem in Nonlinear Elasticity Theory," Report WTHD 43 (1973); Report WTHD 72, Technical University, Delft (1975).

Koiter, W. T., 1976, "Complementary Energy, Neutral Equilibrium and Buckling," *Koninkl. Nederl. Akad. Wetenschappen*, Series B, Vol. 79, No. 3, pp. 183–200.

Lanczos, C., 1949, *The Variational Principles of Mechanics*, 1st ed, University of Toronto Press.

Langhaar, H. L., 1962, *Energy Methods in Applied Mechanics*, 1st ed., John Wiley and Sons, New York.

Masur, E. F., and Popelar, C. H., 1976, "On the Use of the Complementary Energy in the Solution of Buckling Problems," *International Journal of Solids and Structures*, Vol. 12, pp. 203–216.

Nemat-Nasser, S., 1977, "A Note on Complementary Energy and Reissner's Principle in Non-Linear Elasticity," *Iranian Journal of Science and Technology*, Vol. 6, pp. 95–101.

Ogden, R. W., 1975, "A Note on Variational Theorems in Non-Linear Elastostatics, *Math. Proc. Cambridge Phil. Soc.*, Vol. 77, pp. 609–615.

Ogden, R. W., 1977, "Inequalities Associated with the Inversion of Elastic Stress-Deformation Relations and Their Implications," *Math. Proc. Cambridge Phil. Soc.*, Vol. 81, pp. 313–324.

Oravas, G. AE., and McLean, L., 1966, "Historical Development of Energetical Principles in Elastomechanics," *Applied Mechanics Reviews*, Vol. 19, Part I, pp. 647–658; Part II, pp. 919–933.

Piola, G., 1833, "La meccanica de' corpi naturelmente estesi trattata col calcolo delle variazioni," *Opusc. mat. fis di diversi autori*, Vol. 1, Milano.

Popelar, C. H,. 1974, "Assured Upper Bounds Via Complementary Energy," *ASCE Journal of Engineering Mechanics Division*, Vol. 100, No. EM4, pp. 623–633.

Reissner, E., 1950, "On a Variational Theorem in Elasticity," *Journal of Mathematics and Physics*, Vol. 25.

Simmonds, J. G., and Danielson, D. A., 1970, "Nonlinear Shell Theory with a Finite Rotation Vector," *Koninkl. Nederl. Akad. van Wetenschappen*, Vol. 73, pp. 460–478.

Toupin, R. A., 1956, "The Elastic Dielectric," *Journal of Rational Mechanics and Analysis*, Vol. 15, pp. 849–914.

Trefftz, E., 1933, "Zur Theorie der Stabilität des elastichen Gleichgewichts," *Zeit. angew. Math. Mech.*, Vol. 13, p. 160.

Washizu, K., 1955, "On the Variational Principles of Elasticity and Plasticity," Technical Report No. 25-18, M.I.T., Cambridge, Mass.

Wempner, G., 1978, *Complementary Theorems of Solids Mechanics*, S. Nemat-Nasser, ed., Pergamon Press, New York.

Wempner, G., 1989, "Mechanics and Finite Elements of Shells," *Applied Mechanics Reviews*, Vol. 42.

Zubov, L. M., 1970, "The Stationary Principle of Complementary Work in Nonlinear Theory of Elasticity," *Prik. Mat. Mekh.*, Vol. 34, pp. 241–245.

# Equilibrium Configurations of Cantilever Beams Subjected to Inclined End Loads

**S. Navaee**
Visiting Assistant Professor.

**R. E. Elling**
Professor.

Department of Civil Engineering,
Clemson University,
Clemson, SC 29634-0911

*In this study, equilibrium configurations of a cantilever beam subjected to an end load with constant angle of inclination is investigated. It is shown analytically that if the beam is sufficiently flexible, there are multiple equilibrium solutions for a specific beam and loading condition. A method is also presented for the determination of these deflected configurations. The cantilever beam studied in this research is considered to be initially straight and prismatic in addition to being homogeneous, elastic, and isotropic. The procedure outlined in this paper is utilized to show that for each combination of load and beam parameters, there are certain number of equilibrium configurations for a cantilever beam. The ranges of these combinations, along with some examples of the deflected shapes of the beams, are provided for several load inclination angles.*

## Introduction

The problem of large deflections of cantilever beams subjected to concentrated end loads has been investigated by many researchers. Deflection of a straight prismatic cantilever beam subjected to an end transverse load was discussed by Barten (1944, 1945). The same problem was investigated later by Bisshopp and Drucker (1945). Conway (1956) obtained the solution to the nonlinear bending of a circular cantilever beam subjected to an end transverse, and end axial load (loads not simultaneously applied). A numerical procedure was also proposed by Wang (1968) to obtain the deflection of a beam with a transverse concentrated end load.

The problem of bending of a straight, or circular arc cantilever beam under the simultaneous action of a transverse and axial end load was solved by Mitchell (1959). Also, two other approaches to the analysis of a cantilever beam subjected to an inclined end load were introduced by Frisch-Fay (1961).

In all the studies mentioned above and other similar studies, only one equilibrium shape was obtained for a beam with a prescribed end loading. In the work presented by Love (1944), Timoshenko and Gere (1961), and Frisch-Fay (1962), several equilibrium configurations of a beam with end axial loads were shown, but it should be mentioned that these equilibrium configurations were not caused by the same value of the load. In a study done by Reid (1984), using a numerical procedure it was shown that alternate equilibrium positions are possible for a cantilever beam under the action of an end transverse load perpendicular to the undeformed axis of the beam. The numerical technique used in Reid's work has several shortcomings, i.e., it may not guarantee all possible solutions, or it may require tremendous computational effort.

In the paper presented here, a comprehensive study is done on the deflected configurations of a cantilever beam subjected to a specified inclined end load, and a method is presented for the complete determination of all possible deflected shapes of the beam with minimum computational effort. It is through the application of the procedures outlined in this paper that the authors have established that for each particular combination of load and beam parameters, there are certain number of equilibrium configurations for a cantilever beam. Determination of the ranges of these combinations and the specific numbers of equilibrium configurations of the beams in each of these ranges are also demonstrated in this paper. It should be mentioned that no published study could be cited by the authors that show these results.

The cantilever beam studied in this research is considered to be initially straight and prismatic in addition to being homogeneous, elastic, and isotropic. The formulation of this problem is based on the Bernoulli-Euler theorem for beams which states that the curvature is proportional to the bending moment. When applying this theorem, the moment curvature relationship is written in a general form, so that large as well as small deflections can be computed. In the work presented here, apart from the assumptions inherent in the use of the Bernoulli-Euler equation, it is also assumed that the beam is inextensible.

The computer program developed in this research is capable of analyzing cantilever beams subjected to loads with any angle of inclination. However, in this paper the results are presented for cases in which the forces are applied at angles of inclination of 45, 90, 135, and 180 degrees measured with respect to the original undeformed axis of the beams. The software written in this work employs the Fortran programming language as

Contributed by the Applied Mechanics Division of THE AMERICAN SOCIETY OF MECHANICAL ENGINEERS for publication in the ASME JOURNAL OF APPLIED MECHANICS.

Discussion on this paper should be addressed to the Technical Editor Professor Leon M. Keer, The Technological Institute, Northwestern University, Evanston, IL 60208 and will be accepted until four months after final publication of the paper itself in the ASME JOURNAL OF APPLIED MECHANICS.

Manuscript received by the ASME Applied Mechanics Division, Aug. 15, 1990; final revision, Apr. 22, 1991. Associate Technical Editor: R. L. Huston.

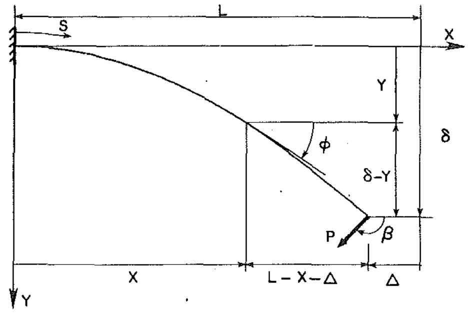


**Fig. 1 Deflected shape of a cantilever beam subjected to an inclined end load**

implemented in NAS/XL-60, a mainframe computer system at Clemson University.

In this paper, the formulation of the problem is presented for the case when the angle of inclination of the load measured with respect to the undeformed axis of the beam is between 0 deg and +180 deg. Obviously, the equilibrium configurations of the beam subjected to loads with angles of inclination in the range between 0 deg and −180 deg are merely the mirror images of the equilibrium configurations obtained for the positive range of angles of inclination.

## Theoretical Formulation

As shown in Fig. 1, the cantilever beam is subjected to an inclined load $P$ at the free end. The origin is placed at the supported end of the beam and downward deflection is considered positive.

Upon substituting for the moment in the Bernoulli-Euler equation and taking the derivatives of both sides of this equation with respect to $S$,

$$EI\,\frac{d^2\phi}{dS^2} = P(\cos\beta\sin\phi - \sin\beta\cos\phi), \tag{1}$$

where $E$, $I$, $\phi$, and $S$ are, respectively, the modulus of elasticity, moment of inertia of the cross-section, slope, and arc length. Note that $\beta$ is the angle of inclination of the load measured with respect to the undeformed axis of the beam as shown in Fig. 1.

The nonlinear differential equation of the beam given in (1) can be integrated numerically to yield the solutions for the deflected shapes of the beam. However, since not all the required boundary conditions are known at either end of the beam, the numerical integration process is an iterative one. The approach introduced by Frisch-Fay (1961) circumvents many of the problems involved in the straightforward integration of (1). Using this approach and introducing a dimensionless parameter $\alpha$ defined as

$$\alpha = +\sqrt{\frac{PL^2}{EI}}, \tag{2}$$

where $L$ is the undeformed length of the beam, the expression for the curvature of the beam is obtained as

$$\frac{d\phi}{dS} = \pm\frac{\sqrt{2}\alpha}{L}\sqrt{\cos(\beta-\gamma) - \cos(\beta-\phi)}. \tag{3}$$

In (3), $\gamma$ is the slope at the free end of the beam. Introducing a new variable $\theta$ defined as

$$\theta = \beta - \phi, \tag{4}$$

and assuming that the beam is inextensible, (3) can be used to yield

$$\alpha = \mp\frac{1}{\sqrt{2}}\int_{\beta}^{\theta_L}\frac{d\theta}{\sqrt{\cos\theta_L - \cos\theta}}, \tag{5}$$

where

$$\theta_L = \beta - \gamma. \tag{6}$$

Although a complete solution for the end slope of a cantilever beam corresponding to a particular value of $\alpha$ appears possible through the direct use of (5), this equation has several shortcomings. First, the sign on the right side of (5) is not clearly established. The sign in this equation is determined by the sign of the beam's curvature given in (3). If the curvature along a deflected length of the beam changes sign, the signs of (3), and (5) also change (i.e., for this deflected shape of the beam the sign in (5) is sometimes positive and sometimes negative). Since the locations and number of points at which the curvature changes sign along the length of the beam is not known at the outset, (5) cannot be used without modification to obtain the end slopes for beams along which the curvature changes sign. Thus, further transformation of (5) is necessary.

The second shortcoming of (5) is that the integrand shown in this equation has a singularity at its upper limit of integration when $\theta = \theta_L$. The problem associated with this singularity in the numerical integration process are also removed through a further transformation of (5). To remedy the shortcomings of (5), two new variables, $\psi$ and $k$, are introduced as:

$$\sin^2\psi = \frac{1+\cos\theta}{2k^2} \tag{7}$$

and

$$k^2 = \frac{1+\cos\theta_L}{2}, \tag{8a}$$

or

$$k = \pm\cos\left(\frac{\theta_L}{2}\right). \tag{8b}$$

Using (7), (8$a$), (4), and (6), Eq. (3) can be written as

$$\frac{d\psi}{dS} = \pm\frac{\alpha}{L}\sqrt{1-k^2\sin^2\psi}. \tag{9}$$

Upon rearranging (9),

$$\int_0^S dS = \pm\frac{L}{\alpha}\int_{\psi_0}^{\psi_S}\frac{d\psi}{\sqrt{1-k^2\sin^2\psi}}, \tag{10}$$

where $\psi_0$ and $\psi_S$ are, respectively, the value of $\psi$ at the origin and at the end of arc length $S$ measured from the fixed end of the beam. Utilizing (4) and (7),

$$\psi_0 = \sin^{-1}\left[\frac{\cos\left(\frac{\beta}{2}\right)}{k}\right] \tag{11}$$

$$\psi_S = \sin^{-1}\left[\frac{\cos\left(\frac{\beta-\phi_S}{2}\right)}{k}\right]. \tag{12}$$

Using (10) and noting that the beam was assumed inextensible, the expression for $\alpha$ in terms of $\psi$ can be written as

$$\alpha = \pm\int_{\psi_0}^{\psi_L}\frac{d\psi}{\sqrt{1-k^2\sin^2\psi}} = \pm[F(k,\psi_L) - F(k,\psi_0)], \tag{13}$$

where $\psi_L$ is the value of $\psi$ at the free end of the beam defined by

$$\psi_L = \sin^{-1}(\pm 1). \tag{14}$$

Also note that in (3), $F(k, \psi_L)$ and $F(k, \psi_0)$ are elliptic integrals of the first kind.

Now the authors proceed to show how the shortcomings of (5) have been remedied through the introduction of variables $\psi$ and $k$ and conversion of (5) to (13). Note that $d\psi/dS$ in (9)

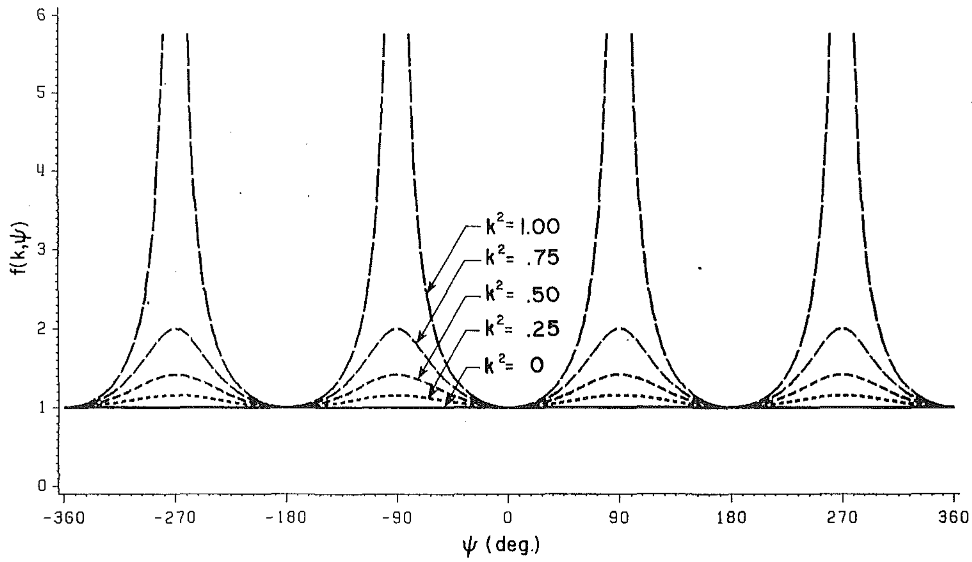


**Fig. 2 Distributions of the integrand in Eq. (13) versus $\psi$ plotted for several values of $k^2$**

can never be zero for finite values of $\alpha$. The value of $d\psi/dS$ can only be zero when $k^2 = 1$; in this case the term $F(k, \psi_L)$, and consequently $\alpha$ in (13) become infinitely large. Therefore, it is concluded that the value of $d\psi/dS$ along the length of the beam can never change sign for finite values of $\alpha$ (i.e., even if the curvature changes sign). Using this argument, it can be seen that the sign in (9), and (13) no longer originates from the sign of the curvature, as was the case in (5). The sign can be chosen as either plus or minus as will be discussed later in this paper. Therefore, the sign problem associated with (5) has been removed as a result of the transformation of this equation to (13). It is no longer necessary to change the sign in (13) every time the curvature changes sign along the length of the beam. Furthermore, the integrand in (13) does not have a singularity for finite values of $\alpha$.

The derivation of (13) follows the procedure introduced by Frisch-Fay (1961) to analyze the deflection of thin cantilever beams. In the work presented by Frisch-Fay (1961), a single equilibrium solution was obtained for a cantilever beam having a specific end load and a specific set of beam parameters. However, as can be seen from (11), (14), and the discussion that follows, the upper and lower limits of the integral given in (13) can have multiple values. Thus the possibility exists that, for a given set of beam parameters and end loading, there may be multiple solutions satisfying (13). The work which follows develops these alternate beam solutions.

Examining (11) and keeping in mind that in this equation the value of $k$ can be positive or negative, it is noticed that when $|\psi_0|$ is in the range $0 < |\psi_0| < 2\pi$, eight different values for $\psi_0$ are possible. Upon introducing a new variable $\omega$ defined as

$$\omega = \sin^{-1}\left|\frac{\cos\left(\frac{\beta}{2}\right)}{k}\right|, \tag{15}$$

where

$$0 \leq \omega \leq \frac{\pi}{2},$$

these eight solutions for $\psi_0$ can be identified as $\omega$, $(-2\pi + \omega)$, $(+\pi - \omega)$, $(-\pi - \omega)$, $-\omega$, $(+2\pi - \omega)$, $(-\pi + \omega)$, and $(+\pi + \omega)$. Similarly, examining (14), it is observed that when $|\psi_L|$ is in the range $0 < |\psi_L| < 2\pi$, four different values for $\psi_L$ are possible. These four solutions for $\psi_L$ are $+\pi/2$, $-3\pi/2$, $-\pi/2$, and $+3\pi/2$. The eight possible values for $\psi_0$ (when $0 < |\psi_0| < 2\pi$), and four possible values of $\psi_L$ (when $0 < |\psi_L| < 2\pi$) can be used in 32 different combinations in (13).

The functional relationship between the integrand shown in (13) and $\psi$ is plotted for several values of $k^2$ in Fig. 2. Studying the 32 combinations of the upper and lower limits of the integral in (13) and Fig. 2, it can be noted that half of the 32 integrals have positive values and the rest have negative values. Since the value of the parameter $\alpha$ in (2) is defined as positive, by narrowing the choices of $\psi_0$ and $\psi_L$ combinations to the ones for which the integral in (13) is positive, (13) can be rewritten as

$$\alpha = \int_{\psi_0}^{\psi_L} \frac{d\psi}{\sqrt{1 - k^2\sin^2\psi}} = F(k,\psi_L) - F(k,\psi_0). \tag{16}$$

Since the integrand in (16) is both an even function (the value of the integrand is the same when evaluated at the same positive and negative value of $\psi$), and also periodic, some of the 16 possible combinations for $\psi_0$ and $\psi_L$ in (16) yield identical integrals. It has been determined in this research that a complete set of solutions for the deflected equilibrium configurations of cantilever beams can be obtained by considering only 7 of these 16 possible combinations. These seven combinations are listed in (17) through (23) as:

Integral 1:

$$\alpha = \int_{\omega}^{\frac{\pi}{2}} f(k,\psi) d\psi. \tag{17}$$

Integral 2:

$$\alpha = \int_{-\pi-\omega}^{\frac{\pi}{2}} f(k,\psi) d\psi. \tag{18}$$

Integral 3:

$$\alpha = \int_{-2\pi+\omega}^{\frac{\pi}{2}} f(k,\psi) d\psi. \tag{19}$$

Integral 4:

$$\alpha = \int_{-\omega}^{\frac{\pi}{2}} f(k,\psi)d\psi. \tag{20}$$

Integral 5:

$$\alpha = \int_{-\pi+\omega}^{\frac{\pi}{2}} f(k,\psi)d\psi. \tag{21}$$

Integral 6:

$$\alpha = \int_{-\pi-\omega}^{\frac{3\pi}{2}} f(k,\psi)d\psi. \tag{22}$$

Integral 7:

$$\alpha = \int_{-2\pi+\omega}^{\frac{3\pi}{2}} f(k,\psi)d\psi, \tag{23}$$

where in (17) through (23),

$$f(k,\psi) = \frac{1}{\sqrt{1-k^2\sin^2\psi}}. \tag{24}$$

It should be stated that the seven possible independent combinations of $\psi_0$ and $\psi_L$ shown in (17) through (23) are for the case when $0 < |\psi_0| < 2\pi$ and $0 < |\psi_L| < 2\pi$. There are other combinations if we consider all possible values of $\psi_0$ and $\psi_L$. These combinations can be obtained by adding and subtracting multiples of $2\pi$ to the upper and lower limits of the integrals listed in (17) through (23). However, the combinations obtained in this manner result in larger values of $\alpha$ and are not included in the present discussion.

## Number of Possible Equilibrium Configurations

Plotting the variance of $\alpha$ with the end slope using the expressions of $\alpha$ given in (17) through (23), it is established in this research that multiple solutions for $\gamma$ are possible corresponding to a specific value of $\alpha$. This indicates that multiple equilibrium configurations are possible for a beam and loading condition.

This variance of $\alpha$ with end slope is plotted in Fig. 3, corresponding to the case when the angle of inclination of the load is 135 deg with respect to the original undeformed axis of the beam. In this figure, the number next to each distribution indicates which integral produced that particular distribution.

The number of equilibrium configurations of a cantilever beam, for any particular value of the parameter $\alpha$, can be determined by drawing a horizontal line at that value of $\alpha$ on the $\alpha$ versus end slope plot, and counting the number of times this line intersects the plotted curves. For example, in Fig. 3, when $\beta = 135$ deg, only one equilibrium configuration exists for $\alpha = 1$, while seven equilibrium positions are possible for $\alpha = 12$. The values, or the ranges of values of $\alpha$ and the corresponding number of equilibrium positions of cantilever beams, are summarized in Tables 1 through 4, for the cases when $\beta = 45$ deg, 90 deg, 135 deg, and 180 deg, respectively.

From an inspection of Tables 1 through 3, it is seen that when a beam is subjected to an inclined end load (other than an axial end load), the beam can have from one to seven different equilibrium configurations. It is also noted that the beam can possess an even number of equilibrium positions for certain specific values of $\alpha$ and an odd number of equilibrium positions for specific ranges of $\alpha$ values. The even number of solutions correspond to an "$\alpha$ = constant" line which is just tangent to the relative minimum points of the $\alpha$ versus end slope curves. For example, in Fig. 3, when $\beta = 135$ deg, a horizontal line corresponding to the equation $\alpha = 2.438$ is just tangent to the $\alpha$ versus end slope curve for integral 4, and intersects the $\alpha$ versus end slope curve for integral 1.

Note that the $\alpha$ values of $\pi/2$, $3\pi/2$, $5\pi/2$, $7\pi/2$, and $9\pi/2$ given in Table 4 correspond, respectively, to the first five buckling loads for a cantilever beam. When subjected to an axial load ($\beta = 180$ deg), the beam can have one, three, five, seven, or nine different deflected shapes. Note that for this case (the axial load case) the straight undeformed position of the beam is counted as one possible equilibrium configuration of the beam.

## Computation of the End Slope

Although the use of (16) permits a determination of $\alpha$ if the end slope $\gamma$ of a beam is known, an analyst is generally faced with the inverse problem, i.e., having to determine the end slope of a beam when the value of $\alpha$ is specified. Note that in (16), both $k$ and $\psi_0$ are functions of the end slope.

For a specific value of $\alpha$, $\alpha = \alpha^*$, the intersection of the line $\alpha = \alpha^*$ with the curve $\alpha = \alpha(\gamma)$ produces the value or values for the end slope of the beam corresponding to $\alpha^*$. Many numerical techniques exist which establish the solution

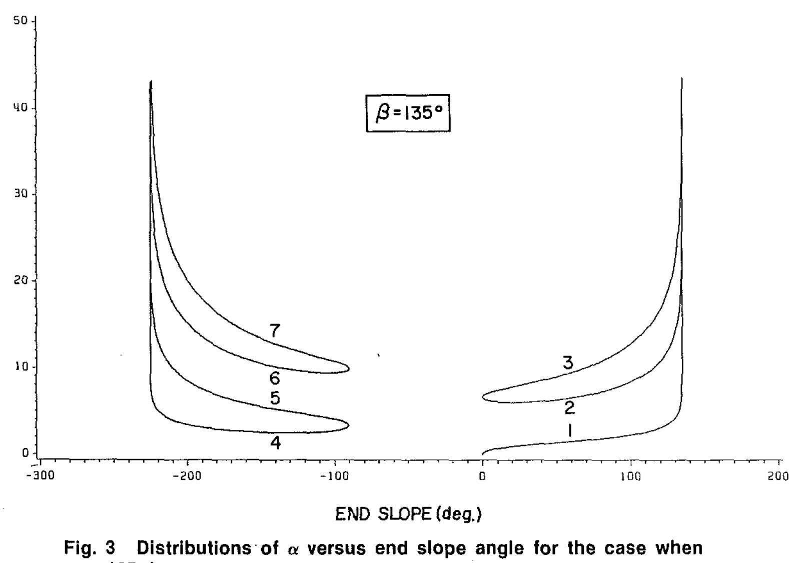


**Fig. 3 Distributions of $\alpha$ versus end slope angle for the case when $\beta$ = 135 deg**

**Table 1 The ranges or values of $\alpha$ and the corresponding numbers of equilibrium configurations of cantilever beams subjected to end loads with angle of inclination of 45 deg**

| $\alpha$ Ranges/Values | Equilibrium Configurations |
|---|---|
| $0 < \alpha < 4.479$ | 1 |
| $\alpha = 4.479$ | 2 |
| $4.479 < \alpha < 9.442$ | 3 |
| $\alpha = 9.442$ | 4 |
| $9.442 < \alpha < 14.295$ | 5 |
| $\alpha = 14.295$ | 6 |
| $14.295 < \alpha < 19.200$ | 7 |

In Table 1, the limiting values of $\alpha$ are rounded off to three decimal digits. Also note that the $\alpha$ values of 4.479, 9.442, 14.295, and 19.200 correspond to the relative minimum points of the $\alpha$ vs. end slope distributions for this case.

**Table 2 The ranges or values of $\alpha$ and the corresponding numbers of equilibrium configurations of cantilever beams subjected to end loads with angle of inclination of 90 deg**

| $\alpha$ Ranges/Values | Equilibrium Configurations |
|---|---|
| $0 < \alpha < 3.214$ | 1 |
| $\alpha = 3.214$ | 2 |
| $3.214 < \alpha < 7.142$ | 3 |
| $\alpha = 7.142$ | 4 |
| $7.142 < \alpha < 10.935$ | 5 |
| $\alpha = 10.935$ | 6 |
| $10.935 < \alpha < 14.832$ | 7 |

In Table 2, the limiting values of $\alpha$ are rounded off to three decimal digits. Also note that the $\alpha$ values of 3.214, 7.142, 10.935, and 14.832 correspond to the relative minimum points of the $\alpha$ vs. end slope distributions for this case.

**Table 3 The ranges or values of $\alpha$ and the corresponding numbers of equilibrium configurations of cantilever beams subjected to end loads with angle of inclination of 135 deg**

| $\alpha$ Ranges/Values | Equilibrium Configurations |
|---|---|
| $0 < \alpha < 2.438$ | 1 |
| $\alpha = 2.438$ | 2 |
| $2.438 < \alpha < 5.938$ | 3 |
| $\alpha = 5.938$ | 4 |
| $5.938 < \alpha < 9.325$ | 5 |
| $\alpha = 9.325$ | 6 |
| $9.325 < \alpha < 13.068$ | 7 |

In Table 3, the limiting values of $\alpha$ are rounded off to three decimal digits. Also note that the $\alpha$ values of 2.438, 5.938, and 9.325 correspond to the relative minimum points of the distributions shown in Fig. 3. The value of $\alpha = 13.068$, although not shown in Fig. 3, corresponds to the relative minimum value of the integral obtained by adding $4\pi$ to the upper limit of integral 1.

**Table 4 The ranges of $\alpha$ and the corresponding numbers of equilibrium configurations of cantilever beams subjected to end loads with angle of inclination of 180 deg**

| $\alpha$ Ranges | Equilibrium Configurations |
|---|---|
| $0 < \alpha < \pi/2$ | 1 |
| $\pi/2 < \alpha < 3\pi/2$ | 3 |
| $3\pi/2 < \alpha < 5\pi/2$ | 5 |
| $5\pi/2 < \alpha < 7\pi/2$ | 7 |
| $7\pi/2 < \alpha < 9\pi/2$ | 9 |

The $\alpha$ values of $\pi/2$, $3\pi/2$, $5\pi/2$, $7\pi/2$, and $9\pi/2$ correspond to the minimum points of the $\alpha$ vs. end slope distributions for this case. Also note that these five values of $\alpha$ correspond respectively to the first five buckling loads for a cantilever beam.

for $\alpha(\gamma) = \alpha^*$. One such technique used in this study is the False-Position Method, a relatively simple scheme well adapted for use with a computer. This method has been discussed in many textbooks (e.g., Chapra and Canale, 1985).

## Solution Procedure for Obtaining the Equilibrium Configurations

In this section of the paper, the focus will be on determination of the deflected equilibrium configurations of the beams once the end slopes have been computed. If the slope at the end of any particular equilibrium configuration of a beam is known, several techniques can be employed to obtain the coordinates of points along the length of the beam. In the following discussion, a technique similar to the one proposed by Frisch-Fay (1961) has been utilized to obtain all the possible solutions. This technique involves the computation of slopes and $x$ and $y$-coordinates along the deflected length of beam in terms of the elliptic integrals.

Since in our discussion we have limited the choices of $\psi_0$ and $\psi_L$ to the ones listed in (17) through (23), (10) can be written as

$$S = \frac{L}{\alpha} [F(k,\psi_S) - F(k,\psi_0)], \tag{25}$$

where $F(k, \psi_S)$ and $F(k, \psi_0)$ are elliptic integrals of the first kind. To obtain the value of $\psi_S$ corresponding to a particular value of $S$ in (25), again a numerical procedure such as the False-Position Method can be applied. After calculating the correct value of $\psi_S$ (at any arc length $S$), the slope angle $\phi_S$ at that location can be determined utilizing (12)

$$\phi_S = \beta - 2 \cos^{-1}(k \sin \psi_S). \tag{26}$$

The $x$ and $y$-coordinates at the end of any arc length $S$ for a particular equilibrium configuration can be obtained by utilizing the equations:

$$X_S = \int_0^S \cos(\beta - \theta) dS, \tag{27}$$

and

$$Y_S = \int_0^S \sin(\beta - \theta) dS. \tag{28}$$

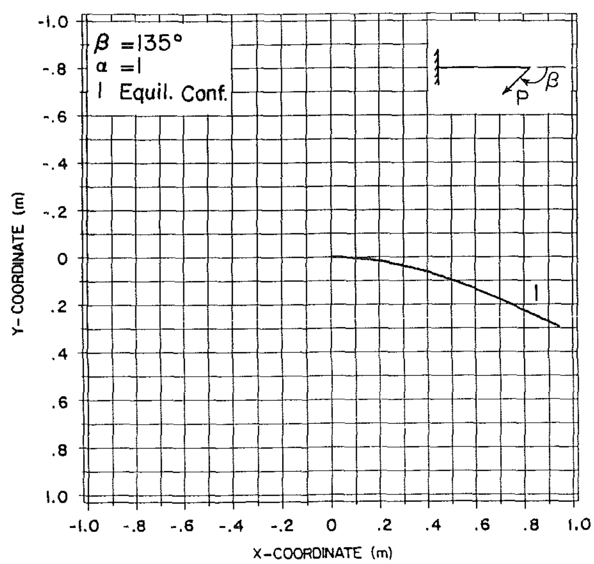


Fig. 4(*a*)

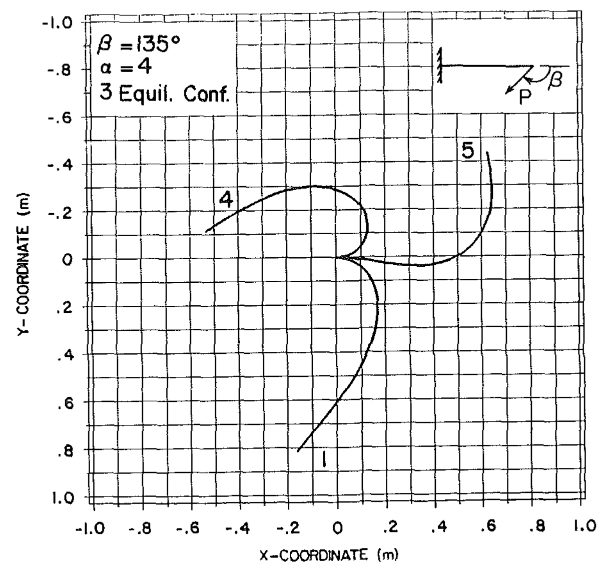


Fig. 4(*c*)

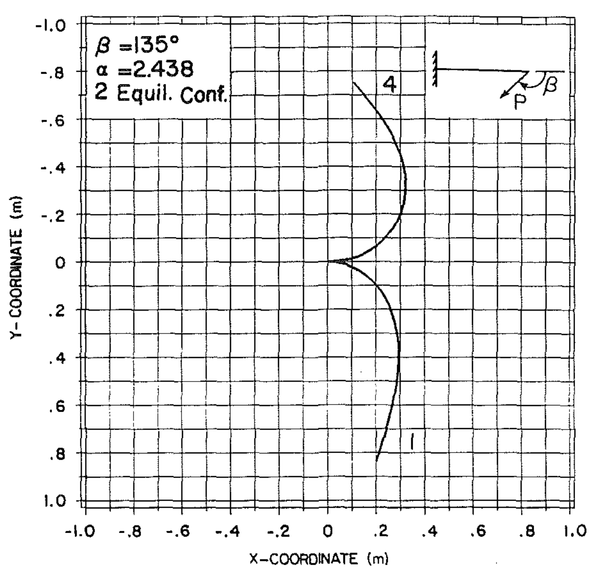


Fig. 4(*b*)

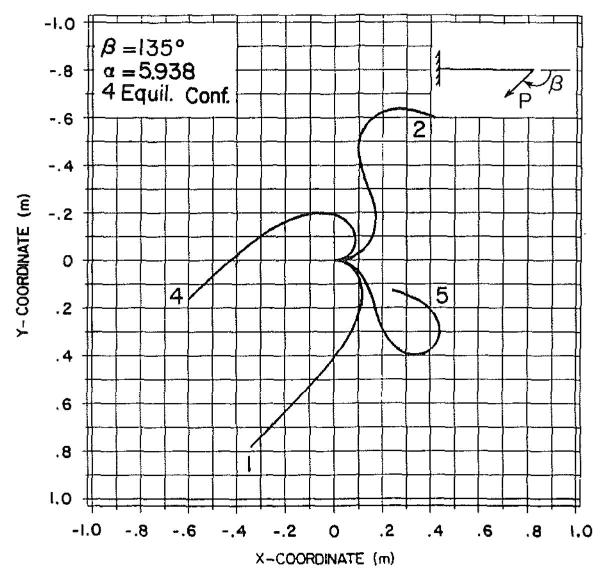


Fig. 4(*d*)

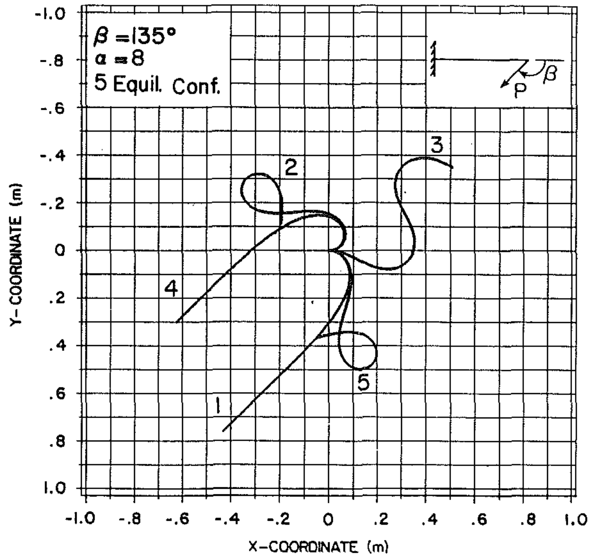


Fig. 4(*e*)

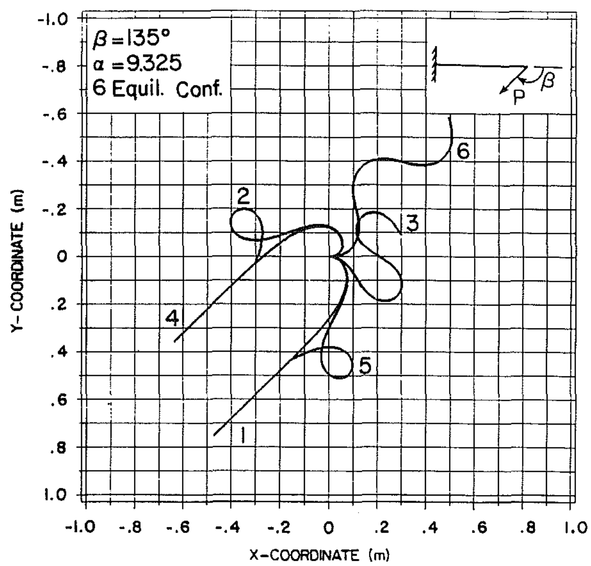


Fig. 4(*f*)

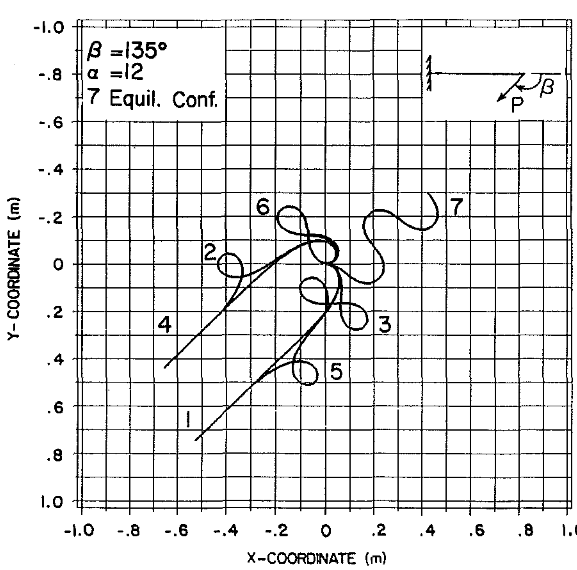


Fig. 4(*g*)

**Fig. 4 Equilibrium configurations of a cantilever beam for the case when $\beta$ = 135 deg**

When the expressions for cos $\theta$ from (7), sin $\theta$, and $dS$ from (10), are substituted in (27) and (28), the results are:

$$X_S = \frac{L}{\alpha}\{\cos\beta[-2E(k,\psi_S)+F(k,\psi_S)+2E(k,\psi_0)-F(k,\psi_0)] + 2k\sin\beta[-\cos\psi_S+\cos\psi_0]\}, \quad (29)$$

and

$$Y_S = \frac{L}{\alpha}\{\sin\beta[-2E(k,\psi_S)+F(k,\psi_S)+2E(k,\psi_0)-F(k,\psi_0)] - 2k\cos\beta[-\cos\psi_S+\cos\psi_0]\}. \quad (30)$$

In (29) and (30), $E(k, \psi_S)$ and $E(k, \psi_0)$ are elliptic integrals of the second kind, while $F(k, \psi_S)$, $F(k, \psi_0)$ are elliptic integrals of the first kind.

Examples of the possible deflected equilibrium configurations of cantilever beams in each one of the ranges of $\alpha$ given in Tables 3 and 4 are plotted in Figs. 4 and 5. These plots are for cases when $\beta$ = 135 deg, and 180 deg. In all the examples shown in these figures, the beam parameters are kept constant and values of $\alpha$ are varied by increasing or decreasing the applied load. The specific parameters of the beam used in this study are:

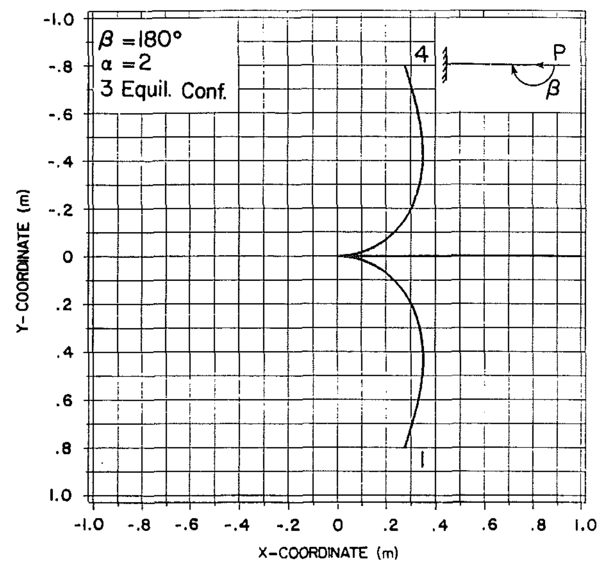


Fig. 5(*a*)

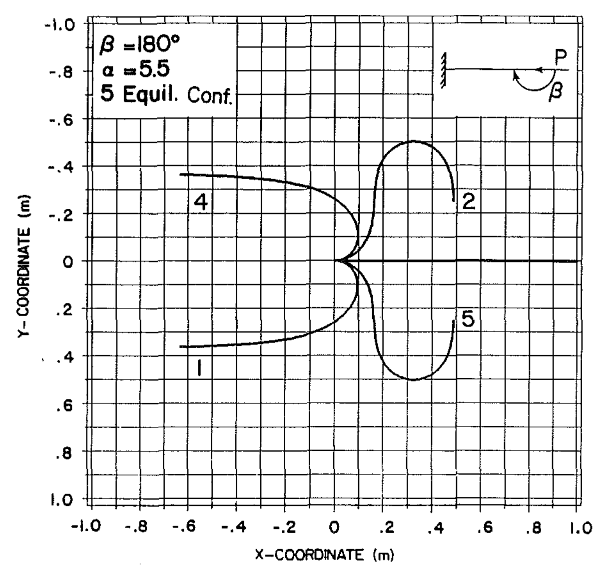


Fig. 5(*b*)

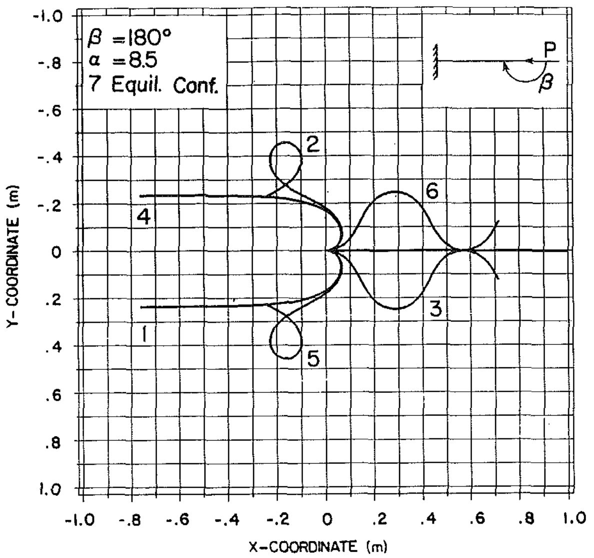


Fig. 5(*c*)

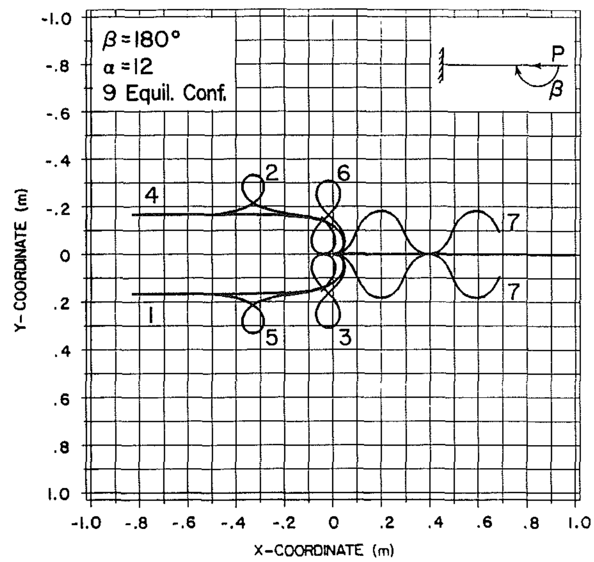


Fig. 5(*d*)

**Fig. 5 Equilibrium configurations of a cantilever beam for the case when $\beta$ = 180 deg**

$$L = 1 \text{ m } (39.37 \text{ in.})$$
$$E = 207 \text{ GPa } (30 \times 10^6 \text{ psi})$$
$$I = 150 \times 10^{-14} \text{ m}^4 \ (3.60 \times 10^{-6} \text{ in.}^4).$$

In Figs. 4 and 5, the numbers next to each equilibrium configuration indicates which integral was used to obtain that particular equilibrium position.

It should be mentioned that in this study all numerical integrations were performed utilizing the Ten Point Gauss-Legendre Formula. The weighting factors and function arguments in this formula were obtained from Lowan et al. (1942).

## Summary and Comments

It is demonstrated in this paper that the number of possible deflected shapes of a cantilever beam subjected to an end load is dependent on a dimensionless parameter $\alpha$. This parameter is a function of the applied load and also a function of the length, moment of inertia, and modulus of elasticity of the beam. It has been determined that as $\alpha$ increases, the number of deflected configurations of the beam also increases. Determination of the ranges of $\alpha$ and the numbers of specific equilibrium configurations of the beams in each one of these ranges are also discussed in this paper.

Studying the deflected shapes of the beams similar to the ones shown in Figs. 4 and 5, it is noted that alternate equilibrium configurations for cantilever beams subjected to end loads are possible only for values of $\alpha$ which produce very large deflections of the beams. This indicates that only one equilibrium shape is possible for all the cases in which small displacement theory can be used with only small error as a basis for the analysis.

## References

Barten, H. J., 1944, "On the Deflection of a Cantilever Beam," *Quarterly of Applied Mathematics*, Vol. 2, pp. 168–171.

Barten, H. J., 1945, "On the Deflection of a Cantilever Beam," *Quarterly of Applied Mathematics*, Vol. 3, pp. 275–276.

Bisshopp, K. E., and Drucker, D. C., 1945, "Large Deflection of Cantilever Beams," *Quarterly of Applied Mathematics*, Vol. 3, pp. 272–275.

Chapra, S. C., and Canale, R. P., 1985, *Numerical Methods for Engineers*, McGraw-Hill, New York.

Conway, H. D., 1956, "The Nonlinear Bending of Thin Circular Rods," ASME Journal of Applied Mechanics, Vol. 23, pp. 7–10.

Frisch-Fay, R., 1961, "A New Approach to the Analysis of the Deflection of Thin Cantilevers," ASME Journal of Applied Mechanics, Vol. 28, pp. 87–90.

Frisch-Fay, R., 1962, *Flexible Bars*, Butterworths, London, pp. 1–32.

Love, A. E. H., 1944, *A Treatise on the Mathematical Theory of Elasticity*, 4th ed., Dover, New York, pp. 399–426.

Lowan, A. N., Davids, N., and Levenson, A., 1942, "Tables of the Zeros of the Legendre Polynomials of Order 1–16 and the Weight Coefficients for Gauss Mechanical Quadrature Formula," *Bulletin of the American Mathematical Society*, Vol. 48, pp. 739–743.

Mitchell, T. P., 1959, "The Nonlinear Bending of Thin Rods," ASME Journal of Applied Mechanics, Vol. 26, pp. 40–43.

Navaee, S., 1989, "Alternate Equilibrium Configurations of Flexible Cantilever Beams," Ph.D. Dissertation, Clemson University, Clemson, SC.

Reid, M. D., 1984, "Stress Analysis of a Lift Pole," M.S. Thesis, Clemson University, Clemson, SC.

Timoshenko, S. P., and Gere, J. M., 1961, *Theory of Elastic Stability*, 2nd ed., McGraw-Hill, New York, pp. 76–82.

Wang, T. M., 1968, "Nonlinear Bending of Beams with Concentrated Loads," *Journal of the Franklin Institute*, Vol. 285, pp. 386–390.

**E. J. Sapountzakis**
Graduate Student.

**J. T. Katsikadelis**
Professor of Structural Analysis.

Department of Civil Engineering,
National Technical University of Athens,
Zografou Campus,
GR 157 73, Greece

# Unilaterally Supported Plates on Elastic Foundations by the Boundary Element Method

*A boundary element solution is developed for the unilateral contact problem of a thin elastic plate resting on elastic homogeneous or nonhomogeneous subgrade. The reaction of the subgrade may depend linearly, or nonlinearly, on the deflection of the plate. The contact between the plate and the subgrade is unbonded. The subgrade surface is not necessarily plane, and miscontact between plate and subgrade due to initial gaps is also encountered. The solution procedure is based on the integral representation of the deflection for the biharmonic equation in which the unknown subgrade reaction is treated as loading term. The effectiveness of the proposed method is illustrated by several examples.*

## 1 Introduction

In most investigations concerning plates supported on elastic foundation it is assumed that the bodies in contact (plate and subgrade) are bonded to each other and, consequently, compressive as well as tensile reactions are considered to be admissible. In this case the contact region is a priori known and the main effort is directed towards the evaluation of the deflection surface and the contact pressure.

However, for many foundation materials, the admission of tensile stresses across the interface separating the plate from the foundation is not realistic. When there is no bonding between plate and subgrade, regions of no contact develop beneath the plate under certain loading conditions and separation between the two bodies takes place at contours where the compressive pressure vanishes. Consequently, the contact region is unknown and the vanishing of the compressive stress provides the condition for the determination of the contact region.

Enormous work has been done for plates resting on elastic foundation with bonded contact between plate and subgrade. Since no attempt is made here to summarize the various researches in this area, we mention only the books of Selvadurai (1979) and Vlasov and Leontiev (1966) where extended literature on this subject is presented. On the other hand, relatively little work has been done for plates unilaterally supported on elastic foundation (Selvadurai, 1979). To the authors' knowledge, with regard to the unbonded plate contact, the majority of the presented methods are limited to axisymmetric problems (Weitsman, 1969; Pu and Hussain, 1970; Gladwell and Iyer, 1974). Problems involving a receding contact between an elastic layer and a half-space are analyzed by Keer et al. (1972) and Tsai et al. (1974) leading to the Fredholm integral equations related to the contact tractions. Solution for an infinite plate with unbonded contact on a Winkler foundation is given by Weitsman (1969), and for a circular plate by Weitsman (1970) and Hofmann (1938). An incremental numerical technique for the simulation of structural elements in receding/advancing contact (Mahmoud et al., 1986), the boundary integral equation method for the unilateral buckling of thin elastic plates (Bezine et al., 1985), variational methods (Kartvelishvili, 1976), and an attempt towards mixed finite elements (Panagiotopoulos and Talaslidis, 1980) have also been used.

In this paper, a boundary element solution is presented for the unilateral contact problem of a thin elastic plate resting on elastic homogeneous or nonhomogeneous foundation. The plate may have arbitrary shape and be subjected to any loading and boundary conditions. The subgrade model consists of closely spaced independent springs. The subgrade reaction may depend linearly (Winkler) or nonlinearly on the deflection. The subgrade surface is not necessarily plane, thus, miss contact between plate and subgrade due to initial gaps is also encountered. The solution procedure is based on the integral representation of the deflection which is established using the fundamental solution of the linear part of the governing operator, whereas the unknown subgrade reaction is included in the loading term. Application of the boundary element technique and Gauss integration for the domain integrals involving the unknown domain quantities yields a system of nonlinear algebraic equations from which the deflection surface is computed by an iterative process.

Actually the proposed method is not a pure boundary element method, since it requires discretization within the domain to determine the unknown field quantities. However, the number of the linear equations is still defined by the boundary discretization, thereby retaining most of the advantages over a possible pure domain discretization method. The domain discretization, in this work, is performed using Gauss inte-

Contributed by the Applied Mechanics Division of The American Society of Mechanical Engineers for publication in the ASME Journal of Applied Mechanics.

Discussion on this paper should be addressed to the Technical Editor, Prof. Leon M. Keer, The Technological Institute, Northwestern University, Evanston, IL 60208, and will be accepted until four months after final publication of the paper itself in the Journal of Applied Mechanics.

Manuscript received by the ASME Applied Mechanics Division, Sept. 29, 1990; final revision, Jan. 20, 1991. Associate Technical Editor: A. K. Noor.

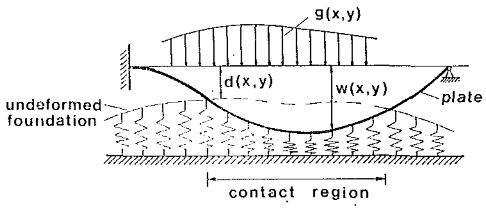


Fig. 1 Cross-section of deflected plate and foundation model

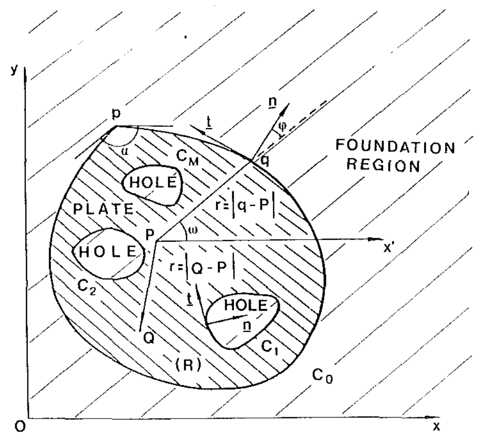


Fig. 2 Two-dimensional region occupied by the plate

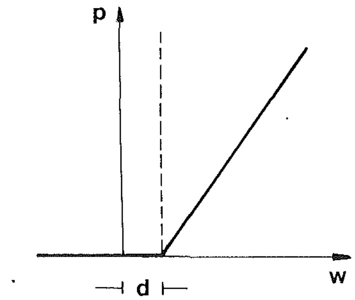


Fig. 3(*a*)

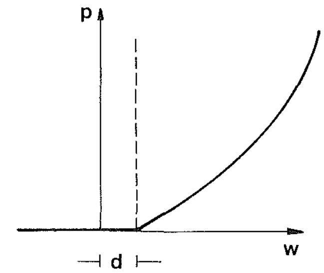


Fig. 3(*b*)

Fig. 3 Unilateral contact law $p=f(w-d)U(w-d)$ for a linear (*a*) and a nonlinear (*b*) Winkler-type spring

gration over regions of arbitrary shape (Katsikadelis and Sapountzakis, 1987; Katsikadelis, 1990) which renders the method very effective.

Several numerical examples are worked out to illustrate the effectiveness of the proposed method.

## 2 Governing Equations

Consider a thin elastic plate of thickness $h$ occupying the two-dimensional multiply connected region $R$ of the $xy$-plane, bounded by the $K+1$ curves $C_0, C_1, C_2, \ldots, C_K$ and resting, in general, on a nonlinear Winkler-type elastic foundation (Figs. 1 and 2). The curves $C_i$ $(i=0, 1, 2, \ldots, K)$ may be piecewise smooth, i.e., the boundary may have a finite number of corners. For unbonded contact between plate and subgrade, the interaction pressure at the interface is compressive and can be represented by the following relation:

$$p=f(w-d)U(w-d) \tag{1}$$

in which $f(w-d)$ is in general a nonlinear function of its argument $w-d$; $w=w(x, y)$ is the deflection of the plate; $d=d(x, y)$ is a function representing the initial gap between plate and subgrade (Fig. 1); and $U(w-d)$ is the unit step function defined as

$$U(w-d)=\begin{vmatrix} 0 & \text{if } w-d<0 \\ 1 & \text{if } w-d\geq 0 \end{vmatrix} \quad d\geq 0. \tag{2}$$

The particular case $f(w-d)=k(w-d)$, $k$ being a constant denoting the subgrade reaction modulus, describes the conventional Winkler model (Fig. 3).

Assuming that there are no friction forces at the interface the deflection $w(P)$ at any point $P$: $(x, y)\epsilon R$ satisfies the following differential equation

$$D\nabla^4 w+f(w-d)U(w-d)=g \tag{3}$$

where $\nabla^4=(\nabla^2)=(\partial^2/\partial x^2+\partial^2/\partial y^2)^2$ is the biharmonic operator; $g=g(x, y)$ is the transverse loading; $D=\mathrm{Eh}^3/12(1-\nu^2)$ is the flexural rigidity, $E$ and $\nu$ being the elastic constants of the material of the plate.

Moreover, the deflection $w$ must satisfy the following boundary conditions on the boundary $C=U_{i=0}^{i=K}C_i$ of the plate

$$\alpha_1 w+\alpha_2 Vw=\alpha_3 \tag{4a}$$

$$\beta_1\frac{\partial w}{\partial n}+\beta_2 Mw=\beta_3 \tag{4b}$$

where $\alpha_i=\alpha_i(p)$, $\beta_i=\beta_i(p)$, $p\epsilon C$ $(i=1, 2, 3)$ are given functions specified on the boundary $C$ and $M$, $V$ are differential operators defined in intrinsic coordinates as (Katsikadelis, 1982)

$$M=-D\left[\nabla^2+(\nu-1)\left(\frac{\partial^2}{\partial s^2}+\kappa\frac{\partial}{\partial n}\right)\right] \tag{5a}$$

$$V=-D\left[\frac{\partial}{\partial n}\nabla^2-(\nu-1)\frac{\partial}{\partial s}\left(\frac{\partial^2}{\partial s\partial n}-\kappa\frac{\partial}{\partial s}\right)\right] \tag{5b}$$

in which $\kappa=\kappa(s)$ is the curvature of the boundary; $\partial/\partial s$ and $\partial/\partial n$ denote differentiation with respect to the arc length $s$ and the outward normal $n$ to the boundary, respectively. The quantities $Mw$ and $Vw$ represent the bending moment and the effective shearing force along the boundary. The boundary conditions (4$a$,$b$) are the most general linear boundary conditions for the plate problem. It is apparent that all kinds of conventional boundary conditions (clamped, simply supported, free or guided edge) can be derived from these equations by specifying appropriately the functions $\alpha_i(s)$ and $\beta_i(s)$ (e.g., for the clamped egde it is $\alpha_1=\beta_1=1$, $\alpha_2=\alpha_3=\beta_2=\beta_3=0$, for the simply supported edge it is $\alpha_1=\beta_2=1$, $\alpha_2=\alpha_3=\beta_1=\beta_3=0$).

In case of free or transversely elastically restrained edges, the boundary conditions (4$a$,$b$) must be supplemented by the corner condition

$$c_{1k}w+c_{2k}[\![Tw]\!]_k=c_{3k},\ c_{2k}\neq 0 \tag{6}$$

where $c_{ik}$ $(i=1, 2, 3)$ are specified functions at the corner point $p_k$ and $T$ is the operator (Katsikadelis, 1982)

$$T=D(1-\nu)\left(\frac{\partial^2}{\partial s\partial n}-\kappa\frac{\partial}{\partial s}\right). \tag{7}$$

Therefore, $Tw$ is the twisting moment along the boundary and $[\![Tw]\!]_k$ is its jump of discontinuity at the corner point $p_k$.

## 3 Solution Procedure

For any pair of functions $w$ and $v$ which are four times continuously differentiable inside $R$ and three times continuously differentiable on the boundary $C$, the following reciprocal identity, known also as Rayleigh-Green identity, is valid (Duff and Naylor, 1966):

$$\iint_R (v\nabla^4 w - w\nabla^4 v)d\sigma$$
$$= \int_C \left( v\frac{\partial}{\partial n}\nabla^2 w - w\frac{\partial}{\partial n}\nabla^2 v - \frac{\partial v}{\partial n}\nabla^2 w + \frac{\partial w}{\partial n}\nabla^2 v \right) ds, \quad (8)$$

application of relation (8) for the function $w$ satisfying Eq. (3) and the function

$$v = \frac{1}{8\pi D} r^2 lnr,\ r = |P-Q| \quad (9)$$

which is a particular singular solution of the equation

$$D\nabla^4 v = \delta(P-Q)\ P{:}(x,y),\ Q{:}(\xi,\eta)\epsilon R. \quad (10)$$

The following integral representation for the deflection $w$ is obtained

$$w(P) = -\frac{1}{2\pi D}\iint_R \Lambda_4(r) f(w-d) U(w-d) d\sigma$$
$$+ \frac{1}{2\pi D}\iint_R \Lambda_4(r) g d\sigma$$
$$-\frac{1}{2\pi}\int_C [\Lambda_1(r)\Omega + \Lambda_2(r)X + \Lambda_3(r)\Phi + \Lambda_4(r)\Psi] ds \quad (11)$$

where the kernels $\Lambda_i(r)$, $(i = 1, 2, 3, 4)$ are given as

$$\Lambda_1(r) = -\frac{\cos\varphi}{r} \qquad \Lambda_2(r) = lnr + 1 \quad (12a,b)$$

$$\Lambda_3(r) = -\frac{1}{4}(2rlnr + r)\cos\varphi \quad \Lambda_4(r) = \frac{1}{4} r^2 lnr \quad (12c,d)$$

and the following notation has been used

$$\Omega = w,\ X = \frac{\partial w}{\partial n},\ \Phi = \nabla^2 w,\ \Psi = \frac{\partial}{\partial n}\nabla^2 w. \quad (13)$$

Notice that for the line integral it is $r = |P-q|$, whereas for the domain integrals, it is $r = |P-Q|$, $P$, $Q\epsilon R$, $q\epsilon C$; $\varphi = \widehat{\mathbf{r},\mathbf{n}}$ is the angle between the direction of $\mathbf{r}$ and the normal $\mathbf{n}$ to the boundary at point $q$.

Application of the operator $\nabla^2 = \partial^2/\partial x^2 + \partial^2/\partial y^2$ to Eq. (11) results in the integral representation of the Laplacian as

$$\nabla^2 w(P) = -\frac{1}{2\pi D}\iint_R \Lambda_2(r) f(w-d) U(w-d) d\sigma$$
$$+ \frac{1}{2\pi D}\iint_R \Lambda_2(r) g d\sigma - \frac{1}{2\pi}\int_C [\Lambda_1(r)\Phi + \Lambda_2(r)\Psi] ds. \quad (14)$$

Equation (11) involves five unknown quantities, i.e., the deflection $w$ inside the domain $R$ and the boundary quantities $\Omega = \Omega(s)$, $X = X(s)$, $\Phi = \Phi(s)$, $\Psi = \Psi(s)$. Four additional equations are established using the boundary equation method (Katsikadelis and Armenakas, 1989). According to this method the boundary conditions ($4a,b$) by virtue of Eqs. ($5a,b$) and notation (13) can be written as

$$\alpha_1\Omega - D\alpha_2\left[\Psi - (\nu-1)\frac{\partial}{\partial s}\left(\frac{\partial X}{\partial s} - \kappa\frac{\partial \Omega}{\partial s}\right)\right] = \alpha_3 \quad (15)$$

$$\beta_1 X - D\beta_2\left[\Phi + (\nu-1)\left(\frac{\partial^2\Omega}{\partial s^2} + \kappa X\right)\right] = \beta_3. \quad (16)$$

Moreover, letting point $P \to p\epsilon C$ in Eqs. (11) and (14), the following two boundary integral equations are derived

$$\alpha\Omega = -\frac{1}{D}\iint_R \Lambda_4 f(w-d) U(w-d) d\sigma + \frac{1}{D}\iint_R \Lambda_4 g d\sigma$$
$$-\int_C (\Lambda_1\Omega + \Lambda_2 X + \Lambda_3\Phi + \Lambda_4\Psi) ds \quad (17)$$

$$\alpha\Phi = -\frac{1}{D}\iint_R \Lambda_2 f(w-d) U(w-d) d\sigma$$
$$+ \frac{1}{D}\iint_R \Lambda_2 g d\sigma - \int_C (\Lambda_1\Phi + \Lambda_2\Psi) ds \quad (18)$$

where $\alpha$ is the angle between the tangents at point $p$ (see Fig. 2). Relations (11), (15), (16), (17), and (18) constitute a set of five simultaneous equations which can be solved to yield the deflection $w$ of the plate.

The stress resultants at a point $P$ inside $R$ are obtained by direct differentiation of Eq. (11) using the relations

$$M_x = -D\left(\frac{\partial^2 w}{\partial x^2} + \nu\frac{\partial^2 w}{\partial y^2}\right)$$
$$M_y = -D\left(\frac{\partial^2 w}{\partial y^2} + \nu\frac{\partial^2 w}{\partial x^2}\right) \quad M_{xy} = D(1-\nu)\frac{\partial^2 w}{\partial x \partial y}$$
$$Q_x = -D\frac{\partial \nabla^2 w}{\partial x} \quad Q_y = -D\frac{\partial \nabla^2 w}{\partial y} \quad (19)$$

while the stress resultants $M_n$, $M_t$, $M_{nt}$, $V_n$ along the boundary are obtained from relations

$$M_n = -D\left[\Phi + (\nu-1)\left(\frac{\partial^2\Omega}{\partial s^2} + \kappa X\right)\right]$$
$$M_t = -D\left[\nu\Phi - (\nu-1)\left(\frac{\partial^2\Omega}{\partial s^2} + \kappa X\right)\right]$$
$$M_{nt} = D(1-\nu)\left(\frac{\partial X}{\partial s} + \kappa\frac{\partial\Omega}{\partial s}\right)$$
$$V_n = -D\left[\Psi - (\nu-1)\left(\frac{\partial^2 X}{\partial s^2} - \frac{\partial\kappa}{\partial s}\frac{\partial\Omega}{\partial s} - \kappa\frac{\partial^2\Omega}{\partial s^2}\right)\right]. \quad (20)$$

The indicated derivatives in Eqs. (19) are given by Eqs. (A1) of the Appendix.

## 4 Numerical Solution

An analytic solution of the system of simultaneous equations, which form relations (11), (15), (16), (17), and (18), is out of the question. However, a numerical solution is feasible. The differential equations are treated using the finite difference method, the boundary integrals using the boundary element method, and the domain integrals using the finite sector method (Katsikadelis, 1990). Thus, using constant boundary elements to approximate the unknown boundary quantitites, unevenly spaced finite difference to approximate the derivatives, and a collocation technique, the following system of simultaneous algebraic equations is established:

$$\begin{bmatrix} \mathbf{A}_{11} & \mathbf{A}_{12} & \mathbf{0} & \mathbf{A}_{14} \\ \mathbf{A}_{21} & \mathbf{A}_{22} & \mathbf{A}_{23} & \mathbf{0} \\ \mathbf{A}_{31} & \mathbf{A}_{32} & \mathbf{A}_{33} & \mathbf{A}_{34} \\ \mathbf{0} & \mathbf{0} & \mathbf{A}_{43} & \mathbf{A}_{44} \end{bmatrix} \begin{bmatrix} \mathbf{\Omega} \\ \mathbf{X} \\ \mathbf{\Phi} \\ \mathbf{\Psi} \end{bmatrix} = \begin{bmatrix} \mathbf{B}_1 \\ \mathbf{B}_2 \\ \mathbf{B}_3 \\ \mathbf{B}_4 \end{bmatrix} + \begin{bmatrix} \mathbf{0} \\ \mathbf{0} \\ \mathbf{C}_3 \\ \mathbf{C}_4 \end{bmatrix}^{[p]} \quad (21a)$$

$$\mathbf{w} = \mathbf{B}_5 + \mathbf{C}_5\mathbf{p} + [\mathbf{A}_{51}\ \ \mathbf{A}_{52}\ \ \mathbf{A}_{53}\ \ \mathbf{A}_{54}][\mathbf{\Omega}\ \ \mathbf{X}\ \ \mathbf{\Phi}\ \ \mathbf{\Psi}]^T \quad (21b)$$

where

$$\mathbf{\Omega} = [\Omega_1\ \Omega_2\ \cdots\ \Omega_N]^T \quad \mathbf{X} = [X_1\ X_2\ \cdots\ X_N]^T$$
$$\mathbf{\Phi} = [\Phi_1\ \Phi_1\ \cdots\ \Phi_N]^T \quad \mathbf{\Psi} = [\Psi_1\ \Psi_2\ \cdots\ \Psi_N]^T \quad (22)$$

are the values of the unknown boundary quantities at the nodal points of the $N$ boundary elements

$$\mathbf{w} = [w_1 \; w_2 \; \cdots \; w_M]^T$$

and

$$\mathbf{p} = [p_1 \; p_2 \; \cdots \; p_M]^T \tag{23}$$

are the values of the deflection $w$ and the subgrade reaction $p = f(w-d)U(w-d)$ at the $M$ Gauss integration points inside the domain $R$.

The elements of the constant matrices $\mathbf{A}_{kl}$ ($k=1, 2, 3, 4, 5$, $l=1, 2, 3, 4$), $\mathbf{B}_m$ ($m=1, 2, 3, 4, 5$), $\mathbf{C}_m$ ($m=3, 4, 5$) are given by Eqs. (A3) in the Appendix.

The integrals in the expressions for the coefficients $(A_{31})_{ij}$ and $(A_{32})_{ij}$ have been obtained using the relation $\cos\varphi ds = r d\omega$ (Katsikadelis and Armenakas, 1984).

Equations (21*a*,*b*) are linear with respect to the boundary quantities $\mathbf{\Omega}$, $\mathbf{X}$, $\mathbf{\Phi}$, $\mathbf{\Psi}$ which can be readily eliminated from Eqs. (21*b*). Thus, solving Eq. (21*a*) for $\mathbf{\Omega}$, $\mathbf{X}$, $\mathbf{\Phi}$, $\mathbf{\Psi}$ and substituting them into Eqs. (21*b*), we obtain the following equations:

$$\mathbf{w} = \mathbf{H}\mathbf{p} + \mathbf{G} \tag{24}$$

where

$$\mathbf{H} = \mathbf{C}_5 + [\mathbf{A}_{51} \; \mathbf{A}_{52} \; \mathbf{A}_{53} \; \mathbf{A}_{54}] \begin{bmatrix} \mathbf{A}_{11} & \mathbf{A}_{12} & \mathbf{0} & \mathbf{A}_{14} \\ \mathbf{A}_{21} & \mathbf{A}_{22} & \mathbf{A}_{23} & \mathbf{0} \\ \mathbf{A}_{31} & \mathbf{A}_{32} & \mathbf{A}_{33} & \mathbf{A}_{34} \\ \mathbf{0} & \mathbf{0} & \mathbf{A}_{43} & \mathbf{A}_{44} \end{bmatrix}^{-1} \begin{bmatrix} \mathbf{0} \\ \mathbf{0} \\ \mathbf{C}_3 \\ \mathbf{C}_4 \end{bmatrix} \tag{25a}$$

$$\mathbf{G} = \mathbf{B}_5 + [\mathbf{A}_{51} \; \mathbf{A}_{52} \; \mathbf{A}_{53} \; \mathbf{A}_{54}] \begin{bmatrix} \mathbf{A}_{11} & \mathbf{A}_{12} & \mathbf{0} & \mathbf{A}_{14} \\ \mathbf{A}_{21} & \mathbf{A}_{22} & \mathbf{A}_{23} & \mathbf{0} \\ \mathbf{A}_{31} & \mathbf{A}_{32} & \mathbf{A}_{33} & \mathbf{A}_{34} \\ \mathbf{0} & \mathbf{0} & \mathbf{A}_{43} & \mathbf{A}_{44} \end{bmatrix}^{-1} \begin{bmatrix} \mathbf{B}_1 \\ \mathbf{B}_2 \\ \mathbf{B}_3 \\ \mathbf{B}_4 \end{bmatrix}. \tag{25b}$$

Equations (24) constitute a system of nonlinear algebraic equations which can be solved numerically to yield the values of the deflection at the internal Gauss points. Back substitution into Eqs. (21*a*) gives the values of the boundary quantities $\Omega$, $X$, $\Phi$, $\Psi$ at the nodal points. Subsequently, using the discretized form of Eq. (11), the deflection at any point $P$ within the plate is computed. That is,

$$w(P) = \frac{1}{2\pi D} \sum_{k=1}^{M} (C_5)_{Pk} f(w_k - d_k) U(w_k - d_k) + (B_5)_P + \sum_{j=1}^{N} [(A_{51})_{Pj}\Omega_j (A_{52})_{Pj} X_j + (A_{53})_{Pj}\Phi_j + (A_{54})_{Pj}\Psi_j]. \tag{26}$$

The solution of Eq. (24) for the numerical examples presented in the next section has been accomplished iteratively by employing the two-term acceleration method (Isaacson and Keller, 1966).

An initial vector, say $\mathbf{w}^{(o)} = \mathbf{0}$, is assumed. Using this vector and Eq. (1), the values of the subgrade reaction $\mathbf{p}^{(o)}$ at the $M$ Gauss points inside the domain $R$ are obtained. Introducing the vector $\mathbf{p}^{(o)}$ into Eq. (24), a vector $\mathbf{w}^{(1)}$ is computed. Subsequently, the vector $\mathbf{w}^{(k)}$, $k > 2$ is obtained from Eq. (24) as

$$\mathbf{w}^{(k)} = \mathbf{H}\mathbf{p}^{(k-1)} + \mathbf{G} \tag{27}$$

where

$$p_i^{(k-1)} = p(\alpha w_i^{(k-1)} + \beta w_i^{(k-2)}), \; \alpha + \beta = 1, \; i = 1, 2, \ldots, M. \tag{28}$$

The procedure converges to the solution vector $\mathbf{w}$ by choosing appropriately the weight factors $\alpha$ and $\beta$. For an example problem, the region of the permissible values of the parameters

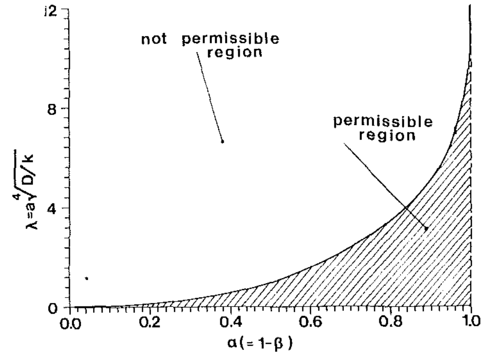


**Fig. 4 Permissible values of the weight factors $\alpha$ and $\beta$ for the convergence of the two-term acceleration method for a clamped or a simply supported rectangular plate with ratio $b/a = 1.2$**

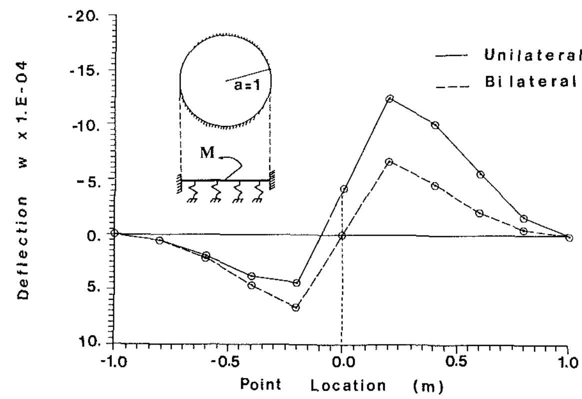


**Fig. 5 Deflections along the diameter of a clamped circular plate ($D = 192.3077$)**

$\alpha$ and $\beta$ was investigated (Fig. 4). The convergence depends on the mechanical and geometrical properties of the plate and the subgrade. Moreover, the optimum values were observed on the line separating the permissible and not permissible regions.

It should be mentioned that the kernels

$$\frac{\partial^2 \Lambda_4(r)}{\partial x^2}, \; \frac{\partial^2 \Lambda_4(r)}{\partial y^2}, \; \frac{\partial^2 \Lambda_4(r)}{\partial x \partial y}, \; \frac{\partial \Lambda_2(r)}{\partial x}, \; \frac{\partial \Lambda_2(r)}{\partial y}$$

$r = |P-Q|$, $P$, $Q \epsilon R$ involved in the domain integrals (Eqs. (A1) of the Appendix) exhibit a singularity at $P = Q$ and special care must be taken for their evaluation. This singularity is extracted before employing the Gauss integration using the following technique.

In general, these kernels can be written in the form

$$F(P,Q) = R(P,Q) + S(P,Q) \tag{29}$$

where $R(P,Q)$ and $S(P,Q)$ are the regular and singular parts of the function $F(P,Q)$, respectively. Thus, the domain integrals can be written as

$$\iint_R F(P,Q) h(Q) d\sigma_Q = \iint_R R(P,Q) h(Q) d\sigma_Q + \iint_R [h(Q) - h(P)] S(P,Q) d\sigma_Q + h(P) \iint_R S(P,Q) d\sigma_Q. \tag{30}$$

With the assumption that $\partial h / \partial r$ is bounded, it is

$$\lim_{P \to Q} [h(Q) - h(P)] S(P,Q) = 0.$$

Consequently, the first two-domain integrals in the right-hand

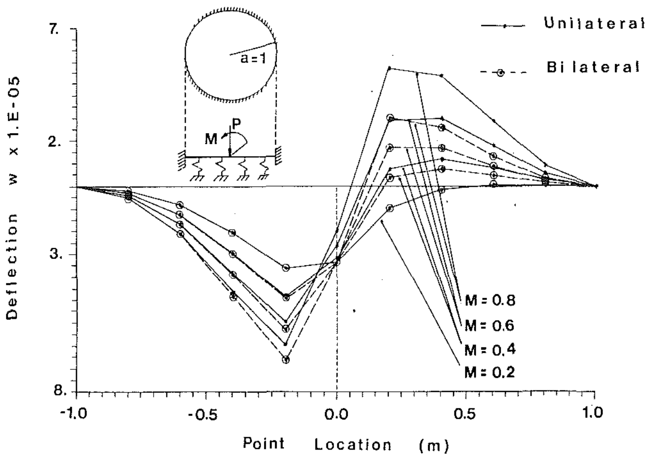


Fig. 6 Deflections along the diameter of a clamped circular plate ($D = 192.3077$)

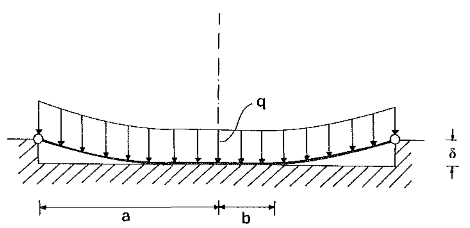


Fig. 7 Simply supported circular plate resting on an absolutely rigid foundation with initial gap ($a = 2.5$, $D = 175$, $\delta = 0.00037$)

side of Eq. (30) are regular. Finally, the third domain integral involving the singular part $S(P,Q)$ can be converted into a line integral on the boundary $C$ of the plate (Nerantzaki and Katsikadelis, 1988).

## 5 Numerical Examples

On the basis of the analytical and numerical procedures presented in the previous sections, a computer program has been written and representative examples have been studied to demonstrate the range of applications of the developed method.

In all the examples treated, the numerical results have been obtained using 60 constant boundary elements with parabolic approximation of their geometry and 100 Gauss nodal points by dividing the interior of the plate into 4 sectors on each of which a 25 point Gauss-Radau integration is performed.

The worked-out examples are:

1 a clamped circular plate with unit radius loaded by a unit concentrated moment $M = 1$ at its center and resting on a tensionless foundation with $\lambda = a/\sqrt[4]{D/k} = 3$. In Fig. 5 the deflections of the plate along its diameter are compared with the corresponding values of the deflection surface of the plate resting on a bilateral Winkler foundation with the same subgrade reaction modulus. Moreover, in Fig. 6 the deflections along the diameter of the plate loaded by a unit concentrated load and a concentrated moment at its center and resting on a tensionless foundation with $\lambda = a/\sqrt[4]{D/k} = 11$ are compared with the corresponding values of the deflection surface of the plate resting on a bilateral Winkler foundation having the same subgrade reaction modulus.

2 a uniformly loaded circular plate, as shown in Fig. 7, simply supported along the edge and resting on an absolutely rigid foundation with initial gap $\delta$. The radius $b$ of the contact area of the aforementioned plate obtained by this method, $b = 0.78$, is in very good agreement with the corresponding value obtained from an analytical solution, $b = 0.76$ (Hofmann, 1938).

3 a clamped and a simply supported rectangular plate with sides $a = 5.0$ and $b = 6.0$, loaded by a concentrated load $P = 1$ at its center and resting on a tensionless linear foundation. In Table 1 the deflections of the plate along the center line parallel to the $x$-axis are presented as compared with the corresponding values of the plate resting on a Winkler foundation having the same subgrade reaction modulus. Moreover, in Fig. 8 the deflection contours of the clamped rectangular plate for various values of the parameter $\lambda$ are presented.

4 a simply supported rectangular plate with sides $a = 5.0$ and $b = 6.0$ loaded by a concentrated load $P = 1$ at its center and unilaterally supported on a nonhomogeneous or a nonlinear foundation. In Table 2 the deflections of the plate along the center line parallel to the $x$-axis are presented as compared, wherever possible, with the corresponding values of the plate bilaterally supported.

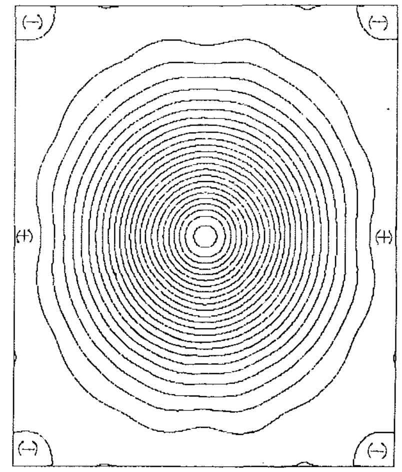


Fig. 8(a)

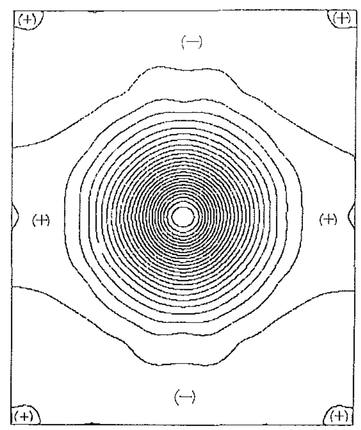


Fig. 8(b)

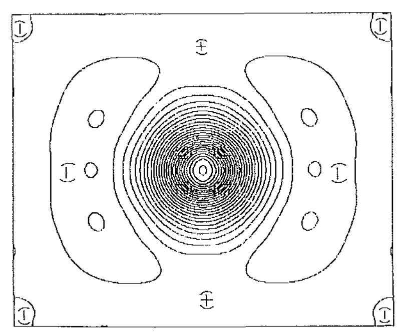

Fig. 8(c)

Fig. 8 Deflection contours of a clamped rectangular plate ($D = 192.3077$) resting on a tensionless linear foundation with subgrade reaction modulus (a) $\lambda = a/\sqrt[4]{D/k} = 3$ ($\Delta w = 0.000033$), (b) $\lambda = a/\sqrt[4]{D/k} = 5$ ($\Delta w = 0.000033$), (c) $\lambda = a/\sqrt[4]{D/k} = 7$ ($\Delta w = 0.0000027$).

Table 1 Deflections of $\overline{w}=w/(Pa^2/D)$ of a rectangular plate resting on a Winkler foundation

| $y/b$ | $x/a$ | Clamped $\lambda=a/\sqrt[4]{D/k}=7$ Unilateral | Clamped $\lambda=a/\sqrt[4]{D/k}=7$ Bilateral Katsikadelis (1982) | Simply supported $\lambda=a/\sqrt[4]{D/k}=11$ Unilateral | Simply supported $\lambda=a/\sqrt[4]{D/k}=11$ Bilateral Katsikadelis (1982) |
|---|---|---|---|---|---|
| | 0.0 | 0.2561E-02 | 0.2551E-02 | 0.1041E-02 | 0.1033E-02 |
| | 0.2 | 0.1201E-02 | 0.1174E-02 | 0.2181E-03 | 0.2123E-03 |
| 0.0 | 0.4 | 0.2091E-03 | 0.2325E-03 | −0.8269E-04 | −0.1161E-04 |
| | 0.6 | −0.5934E-04 | −0.1732E-04 | −0.1332E-03 | −0.5615E-05 |
| | 0.8 | −0.4633E-04 | −0.2083E-04 | −0.8593E-04 | 0.3589E-06 |

Table 2 Deflections $\overline{w}=w/(Pa^2/D)$ of a simply supported rectangular plate resting on nonhomogeneous and on nonlinear foundations

| $y/b$ | $x/a$ | Nonhomogeneous $f=16DEw\exp 0.1(x^2+y^2)$ Unilateral | Nonhomogeneous Bilateral Katsikadelis and Sapountzakis (1987) | Nonlinear $f=w^{1/3}$ Unilateral | Nonlinear $f=10w^{1/3}$ Unilateral |
|---|---|---|---|---|---|
| | 0.0 | 0.4912E-02 | 0.4900E-02 | 0.1972E-01 | 0.3314E-02 |
| | 0.2 | 0.3074E-02 | 0.3066E-02 | 0.1670E-01 | 0.1624E-02 |
| 0.0 | 0.4 | 0.1204E-02 | 0.1205E-02 | 0.1188E-01 | 0.1761E-03 |
| | 0.6 | 0.2668E-03 | 0.2745E-03 | 0.7234E-02 | −0.2678E-03 |
| | 0.8 | −0.2718E-05 | 0.5091E-05 | 0.3318E-02 | −0.2312E-03 |

## 6 Concluding Remarks

A boundary element solution is developed for the unilateral contact problem of a thin elastic plate resting on elastic foundation. The main conclusions drawn from this investigation are the following:

1 Plates of arbitrary shape subjected to any type of boundary conditions and loading can be analyzed.

2 The subgrade reaction may depend linearly or nonlinearly on the deflection of the plate.

3 Miscontact between plate and subgrade due to initial gaps is also encountered.

4 The method is well suited for computer-aided analysis.

5 The iterative method converges. The convergence is slow for high values of the parameter $\lambda$.

6 The difference between the deflections of unilaterally and bilaterally supported plates increases with the eccentricity of the load, with the parameter $\lambda$ and decreases with the distance from the boundary.

7 The use of the fundamental solution of the linear part of the governing operator alleviates the method from the computational difficulties arising from the use of special functions (Kelvin, Hankel).

8 The method retains most of the advantages of a BEM solution over a pure domain discretization method.

## References


Bezine, G., Cimetiere, A., and Gelbert, P., 1985, "Unilateral Buckling of Thin Elastic Plates by the Boundary Integral Equation Method," *Int. J. Num. Meth. Eng.*, Vol. 21, pp. 2189–2199.

Duff, G., and Naylor, D., 1966, *Differential Equations of Applied Mathematics*, John Wiley and Sons, New York.

Gladwell, G. M. L., and Iyer, K. R. P., 1974, "On Foundations that React in Compression Only," ASME JOURNAL OF APPLIED MECHANICS, Vol. 37, pp. 1019–1030.

Hofmann, R., 1938, "Über ein Nichtlineares Problem der Plattenstatik," *Z. Angew. Math Mech.*, Vol. 18, pp. 226–232.

Isaacson, E., and Keller, H. B., 1966, *Analysis of Numerical Methods*, John Wiley and Sons, New York.

Kartvelishvili, V. M., 1976, "Numerical Solutions of Two Contact Problems for Elastic Plates," *Izv. ANSSSR Mekhanika Tverdogo Tela*, Vol. 11, No. 6, pp. 68–72.

Katsikadelis, J. T., 1982, "The Analysis of Plates on Elastic Foundation by the Boundary Integral Equation Method," Ph.D. Thesis presented to the Polytechnic Institute of New York, in partial fulfillment of the requirements.

Katsikadelis, J. T., 1990, "A Gaussian Quadrature Technique for Two-Dimensional Domains of Arbitrary Shape," to be published.

Katsikadelis, J. T., and Armenàkas, A. E., 1984, "Analysis of Clamped Plates on Elastic Foundation by the Boundary Integral Equation Method," ASME JOURNAL OF APPLIED MECHANICS, Vol. 51, pp. 574–580.

Katsikadelis, J. T., and Armenàkas, A. E., 1989, "A New Boundary Equation Solution to the Plate Problem," ASME JOURNAL OF APPLIED MECHANICS, Vol. 56, pp. 364–374.

Katsikadelis, J. T., and Sapountzakis, E. J., 1987, "Numerical Evaluation of the Green Function for the Biharmonic Equation Using BEM with Application to Static and Dynamic Analysis of Plates," *Proceedings of 9th International Conference on Boundary Element Methods in Engineering*, Stuttgart, Germany, Springer-Verlag, New York.

Keer, L. M., Dundurs, J., and Tsai, K. C., 1972, "Problems Involving a Receding Contact Between a Layer and a Half Space," ASME JOURNAL OF APPLIED MECHANICS, Vol. 39, pp. 1115–1120.

Mahmoud, F. F., Salamon, N. J., and Pawlak, T. P., 1986, "Simulation of Structural Elements in Receding/Advancing Contact," *Computers and Structures*, Vol. 22, No. 4, pp. 629–635.

Nerantzaki, M. S., and Katsikadelis, J. T., 1988, "A Green's Function Method for Non-Linear Analysis of Plates," *Acta Mechanica*, Vol. 75, pp. 211–225.

Panagiotopoulos, P. D., and Talaslidis, D., 1980, "A Linear Analysis Approach to the Solution of Certain Classes of Variational Inequality Problems in Structural Analysis," *Int. J. Solids and Structures*, Vol. 16, pp. 991–1005.

Pu, S. L., and Hussain, M. A., 1970, "Note on the Unbonded Contact Between Plates and an Elastic Halfspace," ASME JOURNAL OF APPLIED MECHANICS, Vol. 37, pp. 859–861.

Selvadurai, A. P. S., 1979, *Elastic Analysis of Soil-Foundation Interaction*, Elsevier, New York.

Timoshenko, S. P., and Woinowsky-Krieger, S., 1959, *Theory of Plates and Shells*, McGraw-Hill, New York.

Tsai, K. C., Dundurs, J., and Keer, L. M., 1974, "Elastic Layer Pressed Against a Half Space," ASME JOURNAL OF APPLIED MECHANICS, Vol. 41, pp. 703–707.

Tsai, N. C., and Westmann, R. E., 1967, "Beams on Tensionless Foundation," *J. Eng. Mech. Div. Proc. ASCE*, Vol. 93, No. EM5, pp. 1–12.

Vlasov, V. Z., and Leontiev, N. M., 1966, "Beams, Plates, Shells on Elastic Foundations," (translated from Russian), Israel Program for Scientific Translation, Jerusalem.

Weitsman, Y., 1969, "On the Unbonded Contact Between Plates and an Elastic Halfspace," ASME JOURNAL OF APPLIED MECHANICS, Vol. 36, pp. 198–202.

Weitsman, Y., 1970, "On Foundations that React in Compression Only," ASME JOURNAL OF APPLIED MECHANICS, Vol. 37, pp. 1019–1030.


# APPENDIX

## Derivatives of the Integral Representation for the Deflection of the Plate

$$\frac{\partial^2 w(P)}{\partial x^2}=-\frac{1}{2\pi D}\int\int_R \frac{\partial^2 \Lambda_4(r)}{\partial x^2} f(w-d)U(w-d)d\sigma + \frac{1}{2\pi D}\int\int_R \frac{\partial^2 \Lambda_4(r)}{\partial x^2} g d\sigma - \frac{1}{2\pi}\int_C \left[\frac{\partial^2 \Lambda_1(r)}{\partial x^2}\Omega + \frac{\partial^2 \Lambda_2(r)}{\partial x^2}X + \frac{\partial^2 \Lambda_3(r)}{\partial x^2}\Phi + \frac{\partial^2 \Lambda_4(r)}{\partial x^2}\Psi\right]ds \quad (A1a)$$

$$\frac{\partial^2 w(P)}{\partial y^2}=-\frac{1}{2\pi D}\int\int_R \frac{\partial^2 \Lambda_4(r)}{\partial y^2} f(w-d)U(w-d)d\sigma + \frac{1}{2D}\int\int_R \frac{\partial^2 \Lambda_4(r)}{\partial y^2} g d\sigma - \frac{1}{2\pi}\int_C \left[\frac{\partial^2 \Lambda_1(r)}{\partial y^2}\Omega + \frac{\partial^2 \Lambda_2(r)}{\partial y^2}X + \frac{\partial^2 \Lambda_3(r)}{\partial y^2}\Phi + \frac{\partial^2 \Lambda_4(r)}{\partial y^2}\Psi\right]ds \quad (A1b)$$

$$\frac{\partial^2 w(P)}{\partial x\partial y}=-\frac{1}{2\pi D}\int\int_R \frac{\partial^2 \Lambda_4(r)}{\partial x\partial y} f(w-d)U(w-d)d\sigma + \frac{1}{2\pi D}\int\int_R \frac{\partial^2 \Lambda_4(r)}{\partial x\partial y} g d\sigma - \frac{1}{2\pi}\int_C \left[\frac{\partial^2 \Lambda_1(r)}{\partial x\partial y}\Omega + \frac{\partial^2 \Lambda_2(r)}{\partial x\partial y}X + \frac{\partial^2 \Lambda_3(r)}{\partial x\partial y}\Phi + \frac{\partial^2 \Lambda_4(r)}{\partial x\partial y}\Psi\right]ds \quad (A1c)$$

$$\frac{\partial \nabla^2 w(P)}{\partial x} = -\frac{1}{2\pi D}\int\int_R \frac{\partial \Lambda_2(r)}{\partial x} f(w-d)U(w-d)d\sigma + \frac{1}{2\pi D}\int\int_R \frac{\partial \Lambda_2(r)}{\partial x} g d\sigma - \frac{1}{2\pi}\int_C \left[\frac{\partial \Lambda_1(r)}{\partial x}\Phi + \frac{\partial \Lambda_2(r)}{\partial x}\Psi\right] ds \quad (A1d)$$

$$\frac{\partial \nabla^2 w(P)}{\partial y} = -\frac{1}{2\pi D}\int\int_R \frac{\partial \Lambda_2(r)}{\partial y} f(w-d)U(w-d)d\sigma + \frac{1}{2\pi D}\int\int_R \frac{\partial \Lambda_2(r)}{\partial y} g d\sigma - \frac{1}{2\pi}\int_C \left[\frac{\partial \Lambda_1(r)}{\partial y}\Phi + \frac{\partial \Lambda_2(r)}{\partial y}\Psi\right] ds \quad (A1e)$$

where

$$\frac{\partial^2 \Lambda_1}{\partial x^2} = -\frac{2}{r^3}\cos(2\omega-\varphi) \quad (A2a)$$

$$\frac{\partial^2 \Lambda_1}{\partial y^2} = \frac{2}{r^3}\cos(2\omega-\varphi) \quad (A2b)$$

$$\frac{\partial^2 \Lambda_1}{\partial x \partial y} = -\frac{2}{r^3}\sin(2\omega-\varphi) \quad (A2c)$$

$$\frac{\partial^2 \Lambda_2}{\partial x^2} = \frac{1}{r^2}(\sin^2\omega - \cos^2\omega) \quad (A2d)$$

$$\frac{\partial^2 \Lambda_2}{\partial y^2} = \frac{1}{r^2}(\cos^2\omega - \sin^2\omega) \quad (A2e)$$

$$\frac{\partial^2 \Lambda_2}{\partial x \partial y} = -\frac{\sin^2\omega}{r^2} \quad (A2f)$$

$$\frac{\partial^2 \Lambda_3}{\partial x^2} = \frac{\sin\varphi\cos\omega\sin\omega}{r} - \frac{\cos\varphi}{2r} \quad (A2g)$$

$$\frac{\partial^2 \Lambda_3}{\partial y^2} = -\frac{\sin\varphi\cos\omega\sin\omega}{r} - \frac{\cos\varphi}{2r} \quad (A2h)$$

$$\frac{\partial^2 \Lambda_3}{\partial x \partial y} = -\frac{\sin\varphi\cos 2\omega}{2r} \quad (A2i)$$

$$\frac{\partial^2 \Lambda_4}{\partial x^2} = \frac{1}{2}lnr + \frac{1}{4} + \frac{1}{2}\cos^2\omega \quad (A2j)$$

$$\frac{\partial^2 \Lambda_4}{\partial y^2} = \frac{1}{2}lnr + \frac{1}{4} + \frac{1}{2}\sin^2\omega \quad (A2k)$$

$$\frac{\partial^2 \Lambda_4}{\partial x \partial y} = \frac{1}{4}\sin 2\omega \quad (A2l)$$

$$\frac{\partial \Lambda_1}{\partial x} = -\frac{\cos(\omega-\varphi)}{r^2} \quad \frac{\partial \Lambda_1}{\partial y} = -\frac{\sin(\omega-\varphi)}{r^2} \quad (A2m,n)$$

$$\frac{\partial \Lambda_2}{\partial x} = -\frac{\cos\omega}{r} \quad \frac{\partial \Lambda_2}{\partial y} = -\frac{\sin\omega}{r} \quad (A2o,p)$$

in which $\omega = \mathbf{x}\hat{,}\mathbf{r}$ is the angle between the $x$-axis and the vector $\mathbf{r}$ and $\varphi = \mathbf{r}\hat{,}\mathbf{n}$ is the angle between the vector $\mathbf{r}$ and the outward normal $\mathbf{n}$ (see Fig. 2).

## Elements of the Matrices A, B, C

$$(A_{11})_{i,i-1} = -(\alpha_2)_i s_i\left(-\frac{\partial \kappa_i}{\partial s}s_i + 2\kappa_i\right) \quad (A3a)$$

$$(A_{11})_{ii} = (\alpha_1)_i/[(\nu-1)De_i] + (\alpha_1)_i(s_{i-1}+s_i)\left[(s_{i-1}-s_i)\frac{\partial \kappa_i}{\partial s} + 2\kappa_i\right] \quad (A3b)$$

$$(A_{11})_{i,i+1} = -(\alpha_2)_i s_{i-1}\left(\frac{\partial \kappa_i}{\partial s}s_{i-1} + 2\kappa_i\right) \quad (A3c)$$

$$(A_{12})_{i,i-1} = 2(\alpha_2)_i s_i \quad (A3d)$$

$$(A_{12})_{ii} = -2(\alpha_2)_i(s_{i-1}+s_i) \quad (A3e)$$

$$(A_{12})_{i,i+1} = 2(\alpha_2)_i s_{i-1} \quad (A3f)$$

$$(A_{14})_{ii} = -(\alpha_2)_i/[(\nu-1)De_i] \quad (A3g)$$

$$(A_{21})_{i,i-1} = -2(\beta_2)_i s_i \quad (A3h)$$

$$(A_{21})_{ii} = 2(\beta_2)_i(s_{i-1}+s_i) \quad (A3i)$$

$$(A_{21})_{i,i+1} = -2(\beta_2)_i s_{i-1} \quad (A3j)$$

$$(A_{22})_{ii} = (\beta_1)_i/[(\nu-1)De_i] - (\beta_2)_i\kappa_i/e_i \quad (A3k)$$

$$(A_{23})_{ii} = -(\beta_2)_i/[(\nu-1)e_i] \quad (A3l)$$

$$(A_{31})_{ij} = -\int_j d\omega_{iq} + \alpha\delta_{ij} \quad (A3m)$$

$$(A_{32})_{ij} = \int_j (lnr_{iq}+1)ds_q \quad (A3n)$$

$$(A_{33})_{ij} = -\frac{1}{4}\int_j r_{iq}^2(2lnr_{iq}+1)d\omega_{iq} \quad (A3o)$$

$$(A_{34})_{ij} = \frac{1}{4}\int_j r_{iq}^2 lnr_{iq} ds_q \quad (A3p)$$

$$(A_{43})_{ij} = (A_{31})_{ij} \quad (A3q)$$

$$(A_{44})_{ij} = (A_{32})_{ij} \quad (A3r)$$

$$(A_{51})_{lj} = \frac{1}{2\pi}\int_j d\omega_{lq} + \alpha\delta_{lj} \quad (A3s)$$

$$(A_{52})_{lj} = -\frac{1}{2\pi}\int_j (lnr_{lq}+1)ds_q \quad (A3t)$$

$$(A_{53})_{lj} = \frac{1}{8\pi}\int_j r_{lq}^2(2lnr_{lq}+1)d\omega_{lq} \quad (A3u)$$

$$(A_{54})_{lj} = -\frac{1}{8\pi}\int_j r_{lq}^2 lnr_{lq} ds_q \quad (A3v)$$

$$(B_1)_i = \alpha_3(s_i)/[De_i(\nu-1)] \quad (A4a)$$

$$(B_2)_i = \beta_3(s_i)/[De_i(\nu-1)] \quad (A4b)$$

$$(B_3)_i = \frac{1}{4D}\int\int_R r_{iQ}^2 lnr_{iQ} g_Q d\sigma_Q \quad (A4c)$$

$$(B_4)_i = \frac{1}{D}\int\int_R (lnr_{iQ}+1) g_Q d\sigma_Q \quad (A4d)$$

$$(B_5)_l = \frac{1}{8\pi D}\int\int_R r_{lQ}^2 lnr_{lQ} g_Q d\sigma_Q \quad (A4e)$$

$$(C_3)_i = \frac{1}{4D}C_m r_{im}^2 lnr_{im} \quad (A4f)$$

$$(C_4)_i = \frac{1}{D}C_m(lnr_{im}+1) \quad (A4g)$$

$$(C_5)_l = -\frac{1}{8\pi D}C_m r_{lm}^2 lnr_{lm} \quad (A4h)$$

where $i = 1, 2, \ldots, N$, $j = 1, 2, \ldots, N$, $l$, $m = 1, 2, \ldots, M$; $s_{i-1}$, $s_i$ are the arc lengths between the nodal points $i-1$, $i$, and $i$, $i+1$, respectively; $e_i = 1/[s_{i-1}s_i(s_{i-1}+s_i)]$; $r_{iP} = |p_i - P|$; $P \in R$; $r_{iq} = |p_i - q|$, $q \in j$-element; $\omega_{iq}$ = is the angle between the $x$-axis and the line $r_{ij}$ (see Fig. 2); $(\alpha_n)_i$ and $(\beta_n)_i$ ($n = 1, 2, 3$) are the values of the functions $\alpha_n(s)$ and $\beta_n(s)$, respectively, at the nodal point $i$; the symbol $\int_j$ indicates integration over the $j$-element; $C_m$ are the modified weight factors of the Gauss integration on the domain $R$ (Katsikadelis, 1990).

Charles R. Steele
Professor,
Fellow ASME.

Yoon Young Kim[1]
Research Associate,
Assoc. Mem. ASME.

Division of Applied Mechanics,
Stanford University,
Stanford, CA 94305

# Modified Mixed Variational Principle and the State-Vector Equation for Elastic Bodies and Shells of Revolution

*A modified mixed variational principle is established for a class of problems with one spatial variable as the independent variable. The specific applications are on the three-dimensional deformation of elastic bodies and the nonsymmetric deformation of shells of revolution. The possibly novel feature is the elimination in the variational formulation of the stress components which cannot be prescribed on the boundaries. The result is a form exactly analogous to classical mechanics of a dynamic system, with the equations of state exactly in the form of the canonical equations of Hamilton. With the present approach, the correct scale factors of the field variables to make the system self-adjoint are readily identified, and anisotropic materials including composites can be handled effectively. The analysis for shells of revolution is given with and without the transverse shear deformation considered.*

## 1 Introduction

The objective of the present paper is to show that the state-vector equations can be derived from a modified mixed variational principle. By the state vector, we mean a vector whose components can be prescribed on the boundary of the one-dimensional problem. The present analysis is applied to three-dimensional deformation of elastic bodies and nonsymmetric deformation of shells of revolution. The vector equations are usually derived from the field equations. It appears that a direct variational approach offers less manipulation than the conventional method and correct scale factors of the field variables to make the system self-adjoint. Furthermore, once a variational principle is established for a set of variables, then the equations for other sets of variables are easily obtained. In what follows, we briefly review the papers related to the state-vector formulation.

In the area of elasticity problems, many investigators have used the state-vector formalism. Particularly, problems in anisotropic materials have been treated with this formalism. One advantage of the state-vector formulation is that three stresses and three displacements, which are of immediate interest, are treated simultaneously as the components of the six-dimensional state vector. Stroh (1962) and Ingebrigtsen and Tonning (1969) utilize the state-vector formalism to study surface waves propagating in anisotropic crystals. Recently, Braga and Herrmann (1988) also make use of the state-vector form of equations to investigate plane waves in anisotropic layered composites. In these works, the state-vector equations are derived from the field equations.

The state-vector formulation has also been used in the analysis of shells of revolution. Cohen (1964, 1974, 1979) derives the eighth and tenth-order differential equations from the field equations which are solved by the field method, a stable numerical solution technique. Steele and Skogh (1970) adopt the formulation to develop asymptotic solutions. Wunderlich, et al. (1989) also utilize the state-vector equation for nonsymmetric deformation of shells of revolution in conjunction with the finite element calculation. To derive the state-vector equation, Steele and Balch (1989) employ a modified variational principle similar to what will be presented here. Balch and Steele (1988) also demonstrate that the vector equation is very useful for asymptotic-numeric analysis of nonsymmetric deformation of general shells of revolution that the state-vector equation would be the best form for an efficient asymptotic-numeric solution procedure.

In other fields such as optimal control, the state-vector formalism has also been used (see, e.g., DeRusso, Roy, and Close, 1965). Unlike in the control theory, however, the derivation of the state-vector equation from the usual field equations is not a simple task in some areas of solid mechanics such as shells. Since the usual field equations in shells involve variables that cannot be prescribed on the boundary, the elimination of these variables is mandatory to obtain the state-vector equation.

[1]Currently Assistant Professor, Department of Mechanical Design and Production Engineering, Seoul National University, Seoul, Korea.

Contributed by the Applied Mechanics Division of The American Society of Mechanical Engineers for publication in the ASME Journal of Applied Mechanics.

Discussion on this paper should be addressed to the Technical Editor, Professor Leon M. Keer, The Technological Institute, Northwestern University, Evanston, IL 60208, and will be accepted until four months after final publication of the paper itself in the Journal of Applied Mechanics.

Manuscript received by the ASME Applied Mechanics Division, Mar. 20, 1990; final revision, Oct. 18, 1990. Associate Technical Editor: J. G. Simmonds.

The present variational formulation is developed for the three-dimensional elastic bodies first and then for the shells of revolution. In each part, a modified mixed variational principle is established from the Hellinger-Reissner mixed variational principle, and the derivation of the state-vector equations follows. The crucial step in the analysis is the elimination of the stress components which cannot be prescribed on the boundaries. The results are given in complex form for elastic bodies and in real form for shells of revolution.

For the elastic bodies, the results are obtained with an assumption that the Fourier transformed solutions are possible in two spatial coordinates. The field variables in the state-vector equation consist of three displacement and three traction quantities. Due to the assumption, there exists a potential and the corresponding differential equations are self-adjoint. However, it is observed that the derived equations also hold even when a potential function is not possible. The state-vector equations are presented in both the Cartesian and cylindrical coordinate systems.

For the shells of revolution, nonsymmetric deformation is expressed in a Fourier series in the circumferential direction. The variables associated with the transverse shear deformation are included in the ten field variables. The Sanders stress resultants and strains are employed to obtain consistent results. As a special case, the eighth-order state-vector equation based on the Love-Kirchhoff kinematic assumption is also worked out.

The present analysis is carried out within the framework of the linear theory. Varying material and geometric properties along the independent spatial variable are allowed, and anisotropic layered materials can be handled.

We remark that the state-vector equations which are the Euler-Lagrange equations of the present variational problems have exactly the analogous form to the canonical equations of Hamilton for a dynamic system. The difference is that the independent variable of the present problems is the space variable instead of time. Consequently, the problems considered in the paper including vibration problems in the frequency domain are all two-point boundary value problems. Thin shells, in particular, are stiff systems which require very fine mesh when the finite element method is used. The only successful forward integration technique appears to be the field method (see, e.g., Cohen, 1964). The asymptotic method is a powerful tool to handle efficiently this kind of problems (see, e.g., Steele 1965; Steele and Skogh, 1970).

## 2 Three-Dimensional Elastic Bodies

The Hellinger-Reissner mixed variational principle for three-dimensional elastic bodies can be stated as (Hellinger, 1914; Reissner, 1950)

$$\delta\Pi=\delta\left\{\int\int\int_V L_R dV+\int\int_S R dS\right\}=0 \tag{1}$$

where $V$ is the volume of the body and $S$ is the surface surrounding the body. The potential of the surface traction is denoted by $R$, and Reissner's energy density $L_R$ is

$$L_R=\mathbf{F}_1^T\mathbf{D}_1+\mathbf{F}_2^T\mathbf{D}_2-\int\mathbf{D}_1^T d\mathbf{F}_1-\int\mathbf{D}_2^T d\mathbf{F}_2-\mathbf{D}^T\mathbf{P} \tag{2}$$

where $-\mathbf{D}^T\mathbf{P}$ represents the potential due to the external load. The superscript $T$ in Eq. (2) denotes transposition. For bodies in which the Cartesian coordinate system is appropriate, we define

$$\mathbf{F}_1=\begin{Bmatrix}\sigma_{xx}\\ \sigma_{xy}\\ \sigma_{xz}\end{Bmatrix};\ \mathbf{D}_1=\begin{Bmatrix}\epsilon_{xx}\\ 2\epsilon_{xy}\\ 2\epsilon_{xz}\end{Bmatrix} \tag{3a,b}$$

$$\mathbf{F}_2=\begin{Bmatrix}\sigma_{yy}\\ \sigma_{zz}\\ \sigma_{yz}\end{Bmatrix};\ \mathbf{D}_2=\begin{Bmatrix}\epsilon_{yy}\\ 2\epsilon_{zz}\\ 2\epsilon_{yz}\end{Bmatrix} \tag{4a,b}$$

and

$$\mathbf{P}=\begin{Bmatrix}p_x\\ p_y\\ p_z\end{Bmatrix};\ \mathbf{D}=\begin{Bmatrix}u_x\\ u_y\\ u_z\end{Bmatrix}, \tag{5}$$

where stress and strain are denoted by $\sigma$ and $\epsilon$, and the displacement and body force are designated by $u$ and $p$, respectively. The subscripts in (3)–(5) follow the usual definition (Timoshenko and Goodier, 1970).

For later use, we also define a vector $\mathbf{F}$ that can be prescribed at the $x$ = constant surface:

$$\mathbf{F}=\begin{Bmatrix}\sigma_{xx}\\ \sigma_{xy}\\ \sigma_{xz}\end{Bmatrix}. \tag{6}$$

In the Cartesian coordinate system, $\mathbf{F}=\mathbf{F}_1$.

The vector form of the constitutive relations for linear elastic anisotropic behavior can be given in terms of the symmetric matrix $\mathbf{\Gamma}$:

$$\begin{Bmatrix}\mathbf{F}_1\\ \mathbf{F}_2\end{Bmatrix}=\begin{bmatrix}\mathbf{\Gamma}_{11} & \mathbf{\Gamma}_{12}\\ \mathbf{\Gamma}_{21} & \mathbf{\Gamma}_{22}\end{bmatrix}\begin{Bmatrix}\mathbf{D}_1\\ \mathbf{D}_2\end{Bmatrix}, \tag{7}$$

where

$$\mathbf{\Gamma}_{11}=\mathbf{\Gamma}_{11}^T;\ \mathbf{\Gamma}_{12}=\mathbf{\Gamma}_{21}^T;\ \mathbf{\Gamma}_{22}=\mathbf{\Gamma}_{22}^T.$$

The partial inversion of the relation (7) leads to

$$\begin{Bmatrix}\mathbf{D}_1\\ \mathbf{F}_2\end{Bmatrix}=\begin{bmatrix}\mathbf{\Phi}_{11} & \mathbf{\Phi}_{12}\\ \mathbf{\Phi}_{21} & \mathbf{\Phi}_{22}\end{bmatrix}\begin{Bmatrix}\mathbf{F}_1\\ \mathbf{D}_2\end{Bmatrix} \tag{8}$$

where

$$\mathbf{\Phi}_{11}=\mathbf{\Phi}_{11}^T=\mathbf{\Gamma}_{11}^{-1} \tag{9a}$$

$$\mathbf{\Phi}_{12}=-\mathbf{\Phi}_{21}^T=-\mathbf{\Gamma}_{11}^{-1}\mathbf{\Gamma}_{12} \tag{9b}$$

$$\mathbf{\Phi}_{22}=\mathbf{\Phi}_{22}^T=\mathbf{\Gamma}_{22}-\mathbf{\Gamma}_{21}\mathbf{\Gamma}_{11}^{-1}\mathbf{\Gamma}_{12}. \tag{9c}$$

The matrices $\mathbf{\Gamma}$ and $\mathbf{\Phi}$ are given in Appendix A for isotropic materials.

First, we express $L_R$ explicitly only in terms of $\mathbf{D}_1$, $\mathbf{D}_2$, and $\mathbf{F}_1$ through the modified constitutive relations (8). Performing the integration in (2) then yields

$$L_R=\mathbf{F}_1^T(\mathbf{D}_1+\mathbf{\Phi}_{21}^T\mathbf{D}_2)+\frac{1}{2}\mathbf{D}_2^T\mathbf{\Phi}_{22}\mathbf{D}_2-\frac{1}{2}\mathbf{F}_1^T\mathbf{\Phi}_{11}\mathbf{F}_1-\mathbf{D}^T\mathbf{P}. \tag{10}$$

For the purpose of deriving a modified mixed variational principle that will lead to the state-vector equation, we consider the deformation that can be expressed as

$$\mathbf{H}(x,y,z)=\mathrm{Re}\{\overline{\mathbf{H}}(x)\exp[i(k_y y+k_z z)]\} \tag{11}$$

where $\mathbf{H}$ stands for any vector defined in (3)–(6). In Eq. (11), $\overline{\mathbf{H}}(x)$ may be regarded as the Fourier transformed variables or the Fourier series coefficients of $\mathbf{H}(x, y, z)$, and $k_y$ and $k_z$ are assumed to be real valued. Using Eq. (11) and integrating over $y$ and $z$, Eqs. (1)–(2) can be recast into the following form

$$\delta\overline{\Pi}_R=\delta\left\{\mathrm{Re}\int_{x_1}^{x_2}(\overline{L}_R+\overline{S})dx\right\}=0$$

where

$$\overline{L}_R=\mathbf{F}_1^{*T}(\mathbf{D}_1+\mathbf{\Phi}_{21}^T\mathbf{D}_2)+\frac{1}{2}\mathbf{D}_2^{*T}\mathbf{\Phi}_{22}\mathbf{D}_2-\frac{1}{2}\mathbf{F}_1^{*T}\mathbf{\Phi}_{11}\mathbf{F}_1-\mathbf{D}^{*T}\mathbf{P}, \tag{12}$$

and $\overline{S}$ is the potential of the edge traction. In Eq. (12), $(\cdot)^*$ represents the complex conjugate of $(\cdot)$.

To relate $[\overline{\mathbf{D}}_1(x), \overline{\mathbf{D}}_2(x)]$ and $\overline{\mathbf{D}}(x)$, we use the kinematic relation. (Timoshenko and Goodier, 1970):

$$\overline{\mathbf{D}}_1 = \frac{d\overline{\mathbf{D}}}{dx} + \overline{\mathbf{G}}_2\overline{\mathbf{D}} \tag{13a}$$

$$\overline{\mathbf{D}}_2 = \overline{\mathbf{G}}_3\overline{\mathbf{D}}. \tag{13b}$$

The elements of the matrices $\overline{\mathbf{G}}_2$, and $\overline{\mathbf{G}}_3$ are

$$\overline{\mathbf{G}}_2 = \begin{bmatrix} 0 & 0 & 0 \\ ik_y & 0 & 0 \\ ik_z & 0 & 0 \end{bmatrix}$$

$$\overline{\mathbf{G}}_3 = \begin{bmatrix} 0 & ik_y & 0 \\ 0 & 0 & ik_z \\ 0 & ik_z & ik_y \end{bmatrix}.$$

The relation between $\overline{\mathbf{F}}_1(x)$ and $\overline{\mathbf{F}}(x)$ is simply

$$\overline{\mathbf{F}}_1(x) = \overline{\mathbf{F}}(x). \tag{14}$$

By substituting (13) and (14), we finally obtain the following modified form of the mixed variational principle:

$$\delta\overline{\Pi}_M = \delta\left\{\mathrm{Re}\int_{x_1}^{x_2}(\overline{L}_{MR} + \overline{S})\,dx\right\}$$

$$= \frac{1}{2}\,\delta\int_{x_1}^{x_2}(\overline{L}_{MR} + \overline{L}^*_{MR} + \overline{S} + \overline{S}^*)\,dx = 0. \tag{15}$$

The modified energy density $\overline{L}_{MR}$ in (15) can be written in a compact form

$$\overline{L}_{MR} = \overline{\mathbf{F}}^{*T}\frac{d\overline{\mathbf{D}}}{dx} + \overline{\mathbf{D}}^{*T}\overline{\mathbf{E}\mathbf{F}} - \frac{1}{2}\,\overline{\mathbf{F}}^{*T}\mathbf{C}\overline{\mathbf{F}} + \frac{1}{2}\,\overline{\mathbf{D}}^{*T}\overline{\mathbf{K}\mathbf{D}} - \overline{\mathbf{D}}^{*T}\overline{\mathbf{P}}$$

in which

$$\overline{\mathbf{E}}^{*T} = \overline{\mathbf{G}}_2 + \mathbf{\Phi}_{21}^T\overline{\mathbf{G}}_3 \tag{16a}$$

$$\mathbf{C} \;= \mathbf{C}^T = \mathbf{\Phi}_{11} \tag{16b}$$

$$\overline{\mathbf{K}} \;= \overline{\mathbf{K}}^{*T} = \overline{\mathbf{G}}_3^{*T}\mathbf{\Phi}_{22}\overline{\mathbf{G}}_3 \tag{16c}$$

$$\overline{\mathbf{B}} \;= \overline{\mathbf{P}}. \tag{16d}$$

Note that $\mathbf{C}$ is a real symmetric matrix and that $\overline{\mathbf{K}}$ is a Hermitian matrix. The matrices $\mathbf{C}$, $\overline{\mathbf{E}}$, and $\overline{\mathbf{K}}$ for isotropic materials are explicitly given in Appendix A.

Considering the variations of the force vector $\overline{\mathbf{F}}^*$ and the displacement vector $\overline{\mathbf{D}}^*$, the Euler-Lagrange equations of the variational problem are obtained:

$$\frac{\partial(\overline{L}_{MR} + \overline{L}^*_{MR})}{\partial\overline{\mathbf{F}}^*} = \frac{d\overline{\mathbf{D}}}{dx} + \overline{\mathbf{E}}^{*T}\overline{\mathbf{D}} - \mathbf{C}\overline{\mathbf{F}} = 0$$

$$-\frac{d}{dx}\left(\frac{\partial(\overline{L}_{MR} + \overline{L}^*_{MR})}{\partial\left(\dfrac{d\overline{\mathbf{D}}^*}{dx}\right)}\right) + \frac{\partial(\overline{L}_{MR} + \overline{L}^*_{MR})}{\partial\overline{\mathbf{D}}^*} =$$

$$-\frac{d\overline{\mathbf{F}}}{dx} + \overline{\mathbf{E}\mathbf{F}} + \overline{\mathbf{K}\mathbf{D}} - \overline{\mathbf{B}} = 0.$$

The two equations can be put together as

$$-\frac{d}{dx}\begin{Bmatrix} \overline{\mathbf{F}} \\ \overline{\mathbf{D}} \end{Bmatrix} + \begin{bmatrix} \overline{\mathbf{E}} & \overline{\mathbf{K}} \\ \mathbf{C} & \overline{\mathbf{M}} \end{bmatrix}\begin{Bmatrix} \overline{\mathbf{F}} \\ \overline{\mathbf{D}} \end{Bmatrix} = \begin{Bmatrix} \overline{\mathbf{B}} \\ \mathbf{0} \end{Bmatrix} \tag{17}$$

where

$$\overline{\mathbf{M}} = -\overline{\mathbf{E}}^{*T}.$$

The present result (17) agrees with that derived by Braga and Herrmann (1988). It is noted that the coefficient matrix is associated wtih the fundamental elasticity tensor (Chadwick and Smith, 1977).

Thus far, the modified mixed variational principle and the state-vector equation are derived in the Cartesian coordinate system. In the subsequent derivation, we apply the same procedure used for the Cartesian coordinate system to bodies for which the cylindrical coordinates are suitable. In this case, we define

$$\mathbf{F}_1 = \begin{Bmatrix} \sigma_{rr} \\ \sigma_{r\theta} \\ \sigma_{rz} \end{Bmatrix};\; \mathbf{D}_1 = \begin{Bmatrix} \epsilon_{rr} \\ 2\epsilon_{r\theta} \\ 2\epsilon_{rz} \end{Bmatrix} \tag{18a,b}$$

$$\mathbf{F}_2 = \begin{Bmatrix} \sigma_{\theta\theta} \\ \sigma_{zz} \\ \sigma_{\theta z} \end{Bmatrix};\; \mathbf{D}_2 = \begin{Bmatrix} \epsilon_{\theta\theta} \\ \epsilon_{zz} \\ 2\epsilon_{\theta z} \end{Bmatrix} \tag{19a,b}$$

and

$$\mathbf{P} = \begin{Bmatrix} p_r \\ p_\theta \\ p_z \end{Bmatrix};\; \mathbf{D} = \begin{Bmatrix} u_r \\ u_\theta \\ u_z \end{Bmatrix}. \tag{20}$$

The definition of $\mathbf{F}$ is

$$\mathbf{F} = r\mathbf{F}_1. \tag{21}$$

As in the Cartesian coordinate system, we consider the deformation that can be expressed as

$$\mathbf{H}(r,\theta,z) = \mathrm{Re}\{\mathbf{H}(r)\exp[i(\kappa_\theta\theta + k_z z)]\} \tag{22}$$

where $\mathbf{H}$ stands for any vector defined in (18)–(21). Following the same procedure for the Cartesian coordinate system, we obtain the same form of the state-vector Eq. (17) with $x$ replaced by $r$. The definition of the matrices in Eq. (17) must be replaced with

$$\mathbf{E}^{*T} = \overline{\mathbf{G}}_2 + \mathbf{\Phi}_{21}^T\overline{\mathbf{G}}_3 \tag{23a}$$

$$\mathbf{C} \;= \mathbf{C}^T = \frac{1}{r}\,\mathbf{\Phi}_{11} \tag{23b}$$

$$\overline{\mathbf{K}} \;= \overline{\mathbf{K}}^{*T} = r\overline{\mathbf{G}}_3^{*T}\mathbf{\Phi}_{22}\overline{\mathbf{G}}_3 \tag{23c}$$

$$\overline{\mathbf{B}} \;= r\overline{\mathbf{P}}, \tag{23d}$$

where $\overline{\mathbf{G}}_2$ and $\overline{\mathbf{G}}_3$ are given by (Timoshenko and Goodier, 1970)

$$\overline{\mathbf{G}}_2 = \begin{bmatrix} 0 & 0 & 0 \\ \dfrac{i\kappa_\theta}{r} & -\dfrac{1}{r} & 0 \\ ik_z & 0 & 0 \end{bmatrix}$$

$$\overline{\mathbf{G}}_3 = \begin{bmatrix} \dfrac{1}{r} & \dfrac{i\kappa_\theta}{r} & 0 \\ 0 & 0 & ik_z \\ 0 & ik_z & \dfrac{i\kappa_\theta}{r} \end{bmatrix}.$$

The matrices $\mathbf{C}$, $\overline{\mathbf{E}}$, and $\overline{\mathbf{K}}$ for isotropic materials are explicitly given in Appendix A.

## 3 Shells of Revolution

Figure 1 shows the coordinate system in an element of a shell of revolution. The meridional, circumferential, and normal displacements are denoted by $u_s$, $u_\theta$, and $u_n$, and the meridional and circumferential rotation angles of the normal to the middle surface are denoted by $\chi_s$, and $\chi_\theta$. The angle $\varphi$ between the normal to the meridian and the $z$-axis is given by

$$\varphi = \tan^{-1}\frac{dz}{dr}.$$

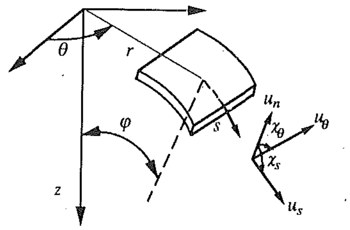


**Fig. 1 The element of a shell of revolution and the coordinate system. The meridional, circumferential, and normal displacements, $u_s$, $u_\theta$, $u_n$ and the meridional and circumferential rotation angles, $\chi_s$, $\chi_\theta$ are also shown.**

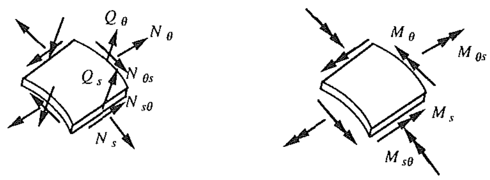


**Fig. 2 Force and moment resultants acting on a shell element**

The force and moment resultants and their directions of positive action are shown in Fig. 2. It is sometimes convenient to use the variables based on the $r$, $\theta$, and $z$-coordinate system. The relations between $(u_r, u_z, N_r, N_z)$ and $(u_s, u_n, N_s, Q_s)$ are provided by

$$u_r = u_s\cos\varphi + u_s\sin\varphi$$
$$u_z = u_s\sin\varphi - u_n\cos\varphi$$
$$N_r = N_s\cos\varphi + Q_s\sin\varphi$$
$$N_z = N_s\sin\varphi - Q_s\cos\varphi.$$

The mixed variational principle for shells of revolution can be stated as

$$\delta\Pi = \delta\left\{\int_0^{2\pi}\left[\int_{s_1}^{s_2} L_R ds + R\right] r d\theta\right\} = 0$$

where $R$ is the potential of the edge load. The energy density $L_R$ is expressed as

$$L_R = \mathbf{F}_1^T\mathbf{D}_1 + \mathbf{F}_2^T\mathbf{D}_2 - \int \mathbf{D}_1^T d\mathbf{F}_1 - \int \mathbf{D}_2^T d\mathbf{F}_2 - \mathbf{D}^T\mathbf{P} + \frac{1}{2}\mathbf{D}^T\mathcal{K}\mathbf{D} \quad (24)$$

with

$$\mathbf{F}_1 = \begin{Bmatrix} M_s \\ \hat{M}_{s\theta} \\ Q_s \\ N_s \\ \tilde{N}_{s\theta} \end{Bmatrix};\ \mathbf{D}_1 = \begin{Bmatrix} \kappa_s \\ 2\tilde{\kappa}_{s\theta} \\ \chi_s - \beta_s \\ \epsilon_s \\ 2\hat{\epsilon}_{s\theta} \end{Bmatrix} \quad (25a,b)$$

$$\mathbf{F}_2 = \begin{Bmatrix} M_\theta \\ Q_\theta \\ N_\theta \end{Bmatrix};\ \mathbf{D}_2 = \begin{Bmatrix} \kappa_\theta \\ \chi_\theta - \beta_\theta \\ \epsilon_\theta \end{Bmatrix} \quad (26a,b)$$

and

$$\mathbf{P} = \begin{Bmatrix} 0 \\ 0 \\ p_r \\ p_z \\ p_\theta \end{Bmatrix};\ \mathbf{D} = \begin{Bmatrix} \chi_s \\ \chi_\theta \\ u_r \\ u_z \\ u_\theta. \end{Bmatrix} \quad (27)$$

In (25), we defined $\hat{A}_{\alpha\beta} = (A_{\alpha\beta} + A_{\beta\alpha})/2$, and it is assumed that $M_{s\theta} = M_{\theta s}$. The modified curvature term $\tilde{\kappa}_{s\theta}$ and the shear stress resultant $\tilde{N}_{s\theta}$ introduced by Sanders (1959) (see also Koiter, 1960; Budiansky and Sanders, 1963; Naghdi, 1972) are defined as

$$\tilde{\kappa}_{s\theta} = \frac{1}{2}[(\kappa_{s\theta} + \kappa_{\theta s}) - \zeta(\epsilon_{s\theta} - \epsilon_{\theta s})]$$

$$\tilde{N}_{s\theta} = \frac{1}{2}[(N_{s\theta} + N_{\theta s}) + \zeta(M_{s\theta} - M_{\theta s})]$$
$$= \frac{1}{2}(N_{s\theta} + N_{\theta s})$$

with

$$\zeta = \frac{1}{2}\left(\frac{1}{r_1} - \frac{1}{r_2}\right)$$

in which the principal radii of curvature, $r_1$ and $r_2$, are $r_1 = ds/d\varphi$, and $r_2 = r/\sin\varphi$, respectively. The terms $\mathbf{D}^T\mathcal{K}\mathbf{D}$ and $-\mathbf{D}^T\mathbf{P}$ in (24) represent the potentials due to the elastic foundation stiffness $\mathcal{K}$, and the external load, respectively.

As for the three-dimensional bodies, $L_R$ for shells of revolution can be written only in terms of $\mathbf{D}_1$, $\mathbf{D}_2$, and $\mathbf{F}_1$. The result is[2]

$$L_R = \mathbf{F}_1^T(\mathbf{D}_1 + \mathbf{\Phi}_{21}^T\mathbf{D}_2) + \frac{1}{2}\mathbf{D}_2^T\mathbf{\Phi}_{22}\mathbf{D}_2 - \frac{1}{2}\mathbf{F}_1^T\mathbf{\Phi}_{11}\mathbf{F}_1.$$
$$- \mathbf{D}^T\mathbf{P} + \frac{1}{2}\mathbf{D}^T\mathcal{K}\mathbf{D}. \quad (28)$$

The task is now to write the energy density $L_R$ only in terms of the quantities that can be prescribed at the edges, namely the displacement vector $\mathbf{D}$ and the force vector $\mathbf{F}$ that is defined as

$$\mathbf{F} = \begin{Bmatrix} rM_s \\ rM_{s\theta} \\ rN_r \\ rN_z \\ rN_{s\theta} \end{Bmatrix}.$$

To find the relations between $\mathbf{F}_1$ and $\mathbf{F}$ and between $\mathbf{D}_1$, $\mathbf{D}_2$ and $\mathbf{D}$, consider a deformation with the following explicit circumferential dependence:

$$\mathbf{F}_1 = \begin{Bmatrix} M_s^{(n)}\cos n\theta \\ \hat{M}_{s\theta}^{(n)}\sin n\theta \\ Q_s^{(n)}\cos n\theta \\ N_s^{(n)}\cos n\theta \\ \tilde{N}_{s\theta}^{(n)}\sin n\theta \end{Bmatrix};\ \mathbf{D}_1 = \begin{Bmatrix} \kappa_s^{(n)}\cos n\theta \\ 2\tilde{\kappa}_{s\theta}^{(n)}\sin n\theta \\ (\chi_s^{(n)} - \beta_s^{(n)})\cos n\theta \\ \epsilon_s^{(n)}\cos n\theta \\ 2\hat{\epsilon}_{s\theta}^{(n)}\sin n\theta \end{Bmatrix} \quad (29a,b)$$

$$\mathbf{F}_2 = \begin{Bmatrix} M_\theta^{(n)}\cos n\theta \\ Q_\theta^{(n)}\sin n\theta \\ N_\theta^{(n)}\cos n\theta \end{Bmatrix};\ \mathbf{D}_2 = \begin{Bmatrix} \kappa_\theta^{(n)}\cos n\theta \\ (\chi_\theta^{(n)} - \beta_\theta^{(n)})\sin n\theta \\ \epsilon_\theta^{(n)}\cos n\theta \end{Bmatrix} \quad (30a,b)$$

and

$$\mathbf{F} = \begin{Bmatrix} rM_s^{(n)}\cos n\theta \\ rM_{s\theta}^{(n)}\sin n\theta \\ rN_r^{(n)}\cos n\theta \\ rN_z^{(n)}\cos n\theta \\ rN_{s\theta}^{(n)}\sin n\theta \end{Bmatrix};\ \mathbf{P} = \begin{Bmatrix} 0 \\ 0 \\ p_r^{(n)}\cos n\theta \\ p_z^{(n)}\cos n\theta \\ p_\theta^{(n)}\sin n\theta \end{Bmatrix};\ \mathbf{D} = \begin{Bmatrix} \chi_s^{(n)}\cos n\theta \\ \chi_\theta^{(n)}\sin n\theta \\ u_r^{(n)}\cos n\theta \\ u_z^{(n)}\cos n\theta \\ u_\theta^{(n)}\sin n\theta \end{Bmatrix} \quad (31)$$

in which the superscripted quantities with $(n)$ are the Fourier coefficients of the $n$th circumferential harmonic.

[2]The constitutive equations for shells of revolution are of the same form as (7) and (8), although the definition of $\mathbf{D}_1$, etc., is different. For shells made of homogeneous materials, $\mathbf{\Pi}$ and $\mathbf{\Phi}$ are listed in Appendix B.

The Sanders kinematic relations, which yield zero strains for rigid body motions (Sanders, 1959), are employed to express $\mathbf{D}_1$ and $\mathbf{D}_2$ in terms of $\mathbf{D}$ (see, e.g., Steele, 1971; Naghdi, 1972):

$$\mathbf{D}_1^{(n)} = \mathbf{G}_1 \frac{d\mathbf{D}^{(n)}}{ds} + \mathbf{G}_2^{(n)}\mathbf{D}^{(n)} \tag{32a}$$

$$\mathbf{D}_2^{(n)} = \mathbf{G}_3^{(n)}\mathbf{D}^{(n)} \tag{32b}$$

where $\mathbf{D}_1^{(n)}$, $\mathbf{D}_2^{(n)}$ and $\mathbf{D}^{(n)}$ are the Fourier coefficients in Eqs. (29*b*), (30*b*), and (31*c*). The elements of the matrices $\mathbf{G}_1$, $\mathbf{G}_2^{(n)}$, and $\mathbf{G}_3^{(n)}$ are

$$\mathbf{G}_1 = \begin{bmatrix} 1 & 0 & 0 & 0 & 0 \\ 0 & 1 & 0 & 0 & -\zeta \\ 0 & 0 & s_\varphi & -c_\varphi & 0 \\ 0 & 0 & c_\varphi & s_\varphi & 0 \\ 0 & 0 & 0 & 0 & 1 \end{bmatrix} \tag{33a}$$

$$\mathbf{G}_2^{(n)} = \begin{bmatrix} 0 & 0 & 0 & 0 & 0 \\ \mp\frac{n}{r} & -\frac{c_\varphi}{r} & \mp\frac{\zeta n c_\varphi}{r} & \mp\frac{\zeta n s_\varphi}{r} & -\frac{\zeta c_\varphi}{r} \\ 1 & 0 & 0 & 0 & 0 \\ 0 & 0 & 0 & 0 & 0 \\ 0 & 0 & \mp\frac{n c_\varphi}{r} & \mp\frac{n s_\varphi}{r} & -\frac{c_\varphi}{r} \end{bmatrix} \tag{33b}$$

$$\mathbf{G}_3^{(n)} = \begin{bmatrix} \frac{c_\varphi}{r} & \pm\frac{n}{r} & 0 & 0 & 0 \\ 0 & 1 & \mp\frac{n s_\varphi}{r} & \pm\frac{n c_\varphi}{r} & -\frac{s_\varphi}{r} \\ 0 & 0 & \frac{1}{r} & 0 & \pm\frac{n}{r} \end{bmatrix} \tag{33c}$$

with

$$s_\varphi = \sin\varphi;\ c_\varphi = \cos\varphi.$$

The upper sign of $\{\pm, \mp\}$ in (33) corresponds to the deformation of (29)–(31) whereas the lower sign corresponds to the deformation of (29)–(31) with cosines and sines interchanged. The relation between $\mathbf{F}_1$ and $\mathbf{F}$ is

$$r\mathbf{F}_1^{(n)} = (\mathbf{G}_1^T)^{-1}\mathbf{F}^{(n)}. \tag{34}$$

Note that $\mathbf{G}_1^{-1}$ can be obtained just by changing the sign of the off-diagonal elements of $\mathbf{G}_1$.

By substituting (32) and (34) into (28) and integrating over $\theta$, we obtain the following modified form of the mixed variational principle:

$$\delta\Pi^{(n)} = \delta\left\{\int_{s_1}^{s_2} L_{MR}^{(n)} ds + R^{(n)}\right\} = 0 \tag{35}$$

where $R^{(n)}$ is the potential of the edge load for the $n$th circumferential harmonic. The modified energy density $L_{MR}^{(n)}$ in (35), which is expressed only in terms of $\mathbf{F}^{(n)}$ and $\mathbf{D}^{(n)}$, can be written in a compact form

$$L_{MR}^{(n)} = \mathbf{F}^{(n)T}\frac{d\mathbf{D}^{(n)}}{ds} + \mathbf{D}^{(n)T}\mathbf{E}^{(n)}\mathbf{F}^{(n)} - \frac{1}{2}\mathbf{F}^{(n)T}\mathbf{C}\mathbf{F}^{(n)} + \frac{1}{2}\mathbf{D}^{(n)T}\mathbf{K}^{(n)}\mathbf{D}^{(n)} - \mathbf{D}^{(n)T}\mathbf{B}^{(n)} \tag{36}$$

in which

$$\mathbf{E}^{(n)T} = \mathbf{G}_1^{-1}[\mathbf{G}_2^{(n)} + \mathbf{\Phi}_{21}^T\mathbf{G}_3^{(n)}] \tag{37a}$$

$$\mathbf{C} = \mathbf{C}^T = \frac{1}{r}\mathbf{G}_1^{-1}\mathbf{\Phi}_{11}(\mathbf{G}_1^{-1})^T \tag{37b}$$

$$\mathbf{K}^{(n)} = \mathbf{K}^{(n)T} = r[\mathbf{G}_3^{(n)T}\mathbf{\Phi}_{22}\mathbf{G}_3^{(n)} + \mathcal{K}] \tag{37c}$$

$$\mathbf{B}^{(n)} = r\mathbf{P}^{(n)}. \tag{37d}$$

The symmetric matrices $\mathbf{C}$ and $\mathbf{K}^{(n)}$ have dimensions of "compliance" and "stiffness," respectively.

Considering the variations of the force vector $\mathbf{F}^{(n)}$ and the displacement vector $\mathbf{D}^{(n)}$, the Euler-Lagrange equations of the variational problem are obtained:

$$\frac{\partial L_{MR}^{(n)}}{\partial \mathbf{F}^{(n)}} = \frac{d\mathbf{D}^{(n)}}{ds} + \mathbf{E}^{(n)T}\mathbf{D}^{(n)} - \mathbf{C}\mathbf{F}^{(n)} = 0 \tag{38}$$

$$-\frac{d}{ds}\left(\frac{\partial L_{MR}^{(n)}}{\partial\left(\frac{d\mathbf{D}^{(n)}}{ds}\right)}\right) + \frac{\partial L_{MB}^{(n)}}{\partial \mathbf{D}^{(n)}} = -\frac{d\mathbf{F}^{(n)}}{ds} + \mathbf{E}^{(n)}\mathbf{F}^{(n)} + \mathbf{K}^{(n)}\mathbf{D}^{(n)} - \mathbf{B}^{(n)} = 0. \tag{39}$$

The two equations can be put together as

$$-\frac{d}{ds}\begin{Bmatrix} \mathbf{F}^{(n)} \\ \mathbf{D}^{(n)} \end{Bmatrix} + \begin{bmatrix} \mathbf{E}^{(n)} & \mathbf{K}^{(n)} \\ \mathbf{C} & -\mathbf{E}^{(n)T} \end{bmatrix}\begin{Bmatrix} \mathbf{F}^{(n)} \\ \mathbf{D}^{(n)} \end{Bmatrix} = \begin{Bmatrix} \mathbf{B}^{(n)} \\ \mathbf{0} \end{Bmatrix}. \tag{40}$$

The matrices $\mathbf{C}$, $\mathbf{E}^{(n)}$, and $\mathbf{K}^{(n)}$ for isotropic materials are explicitly given in Appendix B.

For the axisymmetric deformation ($n = 0$), Eq. (40) produces two sets of equations, one for torsionless axisymmetric deformation, and the other for torsional deformation. The matrices $\mathbf{E}^{(0)}$, $\mathbf{K}^{(0)}$, and $\mathbf{C}$ for the torsionless axisymmetric deformation, which are the same matrices obtained by Steele and Balch (1989), have the form for a shell with isotropic behavior:

$$\mathbf{E}^{(0)} = \frac{1}{r}\begin{bmatrix} \nu c_\varphi & r s_\varphi \\ 0 & \nu c_\varphi \end{bmatrix} \tag{41a}$$

$$\mathbf{K}^{(0)} = \frac{Et}{r}\begin{bmatrix} \frac{t^2 c_\varphi^2}{12} & 0 \\ 0 & 1 \end{bmatrix} \tag{41b}$$

$$\mathbf{C} = \frac{1}{Etr}\begin{bmatrix} \frac{1}{c^2} & 0 \\ 0 & \mu s_\varphi^2 + (1-\nu^2)c_\varphi^2 \end{bmatrix} \tag{41c}$$

with the definition

$$\mathbf{F}^{(0)} = \begin{Bmatrix} rM_s^{(0)} \\ rN_r^{(0)} \end{Bmatrix};\ \mathbf{D}^{(0)} = \begin{Bmatrix} \chi_s^{(0)} \\ u_r^{(0)} \end{Bmatrix}.$$

The vector representing the applied load in (40) must be replaced as

$$\begin{Bmatrix} \mathbf{B}^{(0)} \\ \mathbf{0} \end{Bmatrix} \Rightarrow \begin{Bmatrix} \mathbf{B}^{(0)} \\ \mathbf{G}^{(0)} \end{Bmatrix}$$

where

$$\mathbf{B}^{(0)} = \begin{Bmatrix} rN_z^{(0)}c_\varphi \\ rp_r^{(0)} - \nu N_z^{(0)}s_\varphi \end{Bmatrix};\ \mathbf{G}^{(0)} = \begin{Bmatrix} 0 \\ -\frac{1-\nu^2-\mu}{Et}N_z^{(0)}c_\varphi s_\varphi \end{Bmatrix}.$$

The equation for $N_z^{(0)}$, which corresponds to the vertical equilibrium, is

$$-\frac{d(rN_z^{(0)})}{ds} = rp_z^{(0)}.$$

The vertical displacement $u_z^{(0)}$ can be found from

$$\frac{du_z^{(0)}}{ds} = \frac{1-\nu^2-\mu}{Et}N_z^{(0)}c_\varphi s_\varphi + \frac{\mu c_\varphi^2 + (1-\nu^2)s_\varphi^2}{Et}N_z^{(0)} + c_\varphi\chi_s^{(0)} - \frac{\nu s_\varphi}{r}u_r^{(0)}.$$

The vector equation for the torsional motion of an isotropic shell is of the form (40) with $n = 0$ in which $\mathbf{F}^{(0)}$ and $\mathbf{D}^{(0)}$ are defined as

$$\mathbf{F}^{(0)}=\begin{Bmatrix} rM_{s\theta}^{(0)} \\ rN_{s\theta}^{(0)} \end{Bmatrix} \; ; \; \mathbf{D}^{(0)}=\begin{Bmatrix} \chi_\theta^{(0)} \\ u_\theta^{(0)} \end{Bmatrix}.$$

The corresponding matrices are

$$\mathbf{E}^{(0)}=\frac{1}{r}\begin{bmatrix} -c_\varphi & 0 \\ -2\zeta c_\varphi & -c_\varphi \end{bmatrix} \tag{42a}$$

$$\mathbf{K}^{(0)}=\frac{Et}{\mu r}\begin{bmatrix} r^2 & -rs_\varphi \\ -rs_\varphi & s_\varphi^2 \end{bmatrix} \tag{42b}$$

$$\mathbf{C}=\frac{2(1+\nu)}{Etr}\begin{bmatrix} \frac{12}{t^2}+\zeta^2 & \zeta \\ \zeta & 1 \end{bmatrix}. \tag{42c}$$

The load vector $\mathbf{B}^{(0)}$ is simply

$$\mathbf{B}^{(0)}=\begin{Bmatrix} 0 \\ rp_\theta^{(0)} \end{Bmatrix}.$$

The uncoupling between the membrane and bending behavior for axisymmetric deformations of a plate ($\zeta \to 0$, $\varphi \to 0$) can be easily observed from Eqs. (40)–(42).

## 4 Love-Kirchoff Theory in Shells of Revolution

When the Love-Kirchhoff kinematics is imposed such that

$$\chi_s=\beta_s;\; \chi_\theta=\beta_\theta,$$

some modifications become necessary due to the reduced number of independent variables. In this case, the edge work $\delta W$ at $s =$ constant can be written as

$$\delta W=\mathbf{F}^T\delta\mathbf{D}$$

where the column vectors $\mathbf{F}$ and $\mathbf{D}$ are redefined as

$$\mathbf{F}=\begin{Bmatrix} rM_s \\ r(N_{s\theta}+M_{s\theta}/r_2) \\ rN_r \\ rN_z \end{Bmatrix} \; ; \; \mathbf{D}=\begin{Bmatrix} \chi_s \\ u_\theta \\ u_r \\ u_z \end{Bmatrix}.$$

We note the relation

$$N_{s\theta}+M_{s\theta}/r_2=\tilde{N}_{s\theta}+\rho\hat{M}_{s\theta}$$

with

$$\rho=\frac{1}{2}\left(\frac{3}{r_2}-\frac{1}{r_2}\right).$$

We also redefine the energy density $L_R$ as

$$L_R=\overline{\mathbf{F}}_1^T\overline{\mathbf{D}}_1+\overline{\mathbf{F}}_2^T\overline{\mathbf{D}}_2-\int\overline{\mathbf{D}}_1^T d\overline{\mathbf{F}}_1-\int\overline{\mathbf{D}}_2^T\overline{\mathbf{F}}_2$$
$$-\mathbf{D}^T\mathbf{P}+\frac{1}{2}\mathbf{D}^T\mathcal{K}\mathbf{D}+\overline{Q}_s(\chi_s-\beta_s), \tag{43}$$

with the definition

$$\overline{\mathbf{F}}_1=\begin{Bmatrix} M_s \\ \tilde{N}_{s\theta}+\rho\hat{M}_{s\theta} \\ N_s \end{Bmatrix} \; ; \; \overline{\mathbf{D}}_1=\begin{Bmatrix} \kappa_s \\ \hat{\epsilon}_{s\theta}+\tilde{\kappa}_{s\theta}/\rho \\ \epsilon_s \end{Bmatrix}$$

$$\overline{\mathbf{F}}_2=\begin{Bmatrix} M_\theta \\ \hat{M}_{s\theta}-\tilde{N}_{s\theta}/\rho \\ N_\theta \end{Bmatrix} \; ; \; \overline{\mathbf{D}}_2=\begin{Bmatrix} \kappa_\theta \\ \tilde{\kappa}_{s\theta}-\rho\hat{\epsilon}_{s\theta} \\ \epsilon_\theta \end{Bmatrix}.$$

The effective shear resultant $\overline{Q}_s$, which can be interpreted as the Lagrange multiplier in (43), is defined as

$$\overline{\mathbf{Q}}_s=Q_s+\frac{1}{r}\frac{\partial M_{s\theta}}{\partial\theta},$$

Using the constitutive equation

$$\begin{Bmatrix} M_s \\ \hat{M}_{s\theta} \\ N_s \\ \tilde{N}_{s\theta} \\ M_\theta \\ N_\theta \end{Bmatrix}=\begin{bmatrix} \boldsymbol{\Gamma} \\ 6\times 6 \end{bmatrix}\begin{Bmatrix} \kappa_s \\ 2\tilde{\kappa}_{s\theta} \\ \epsilon_s \\ 2\hat{\epsilon}_{s\theta} \\ \kappa_\theta \\ \epsilon_\theta \end{Bmatrix},$$

and the relations

$$\begin{Bmatrix} \overline{\mathbf{F}}_1 \\ \overline{\mathbf{F}}_2 \end{Bmatrix}=[\mathbf{T}]\begin{Bmatrix} M_s \\ \hat{M}_{s\theta} \\ N_s \\ \tilde{N}_{s\theta} \\ M_\theta \\ N_\theta \end{Bmatrix} \; ; \; \begin{Bmatrix} \overline{\mathbf{D}}_1 \\ \overline{\mathbf{D}}_2 \end{Bmatrix}=[(\mathbf{T}^{-1})^T]\begin{Bmatrix} \kappa_s \\ 2\tilde{\kappa}_{s\theta} \\ \epsilon_s \\ 2\hat{\epsilon}_{s\theta} \\ \kappa_\theta \\ \epsilon_\theta \end{Bmatrix}$$

where

$$\mathbf{T}=\begin{bmatrix} 1 & 0 & 0 & 0 & 0 & 0 \\ 0 & \rho & 0 & 1 & 0 & 0 \\ 0 & 0 & 1 & 0 & 0 & 0 \\ 0 & 0 & 0 & 0 & 1 & 0 \\ 0 & 1 & 0 & -1/\rho & 0 & 0 \\ 0 & 0 & 0 & 0 & 0 & 1 \end{bmatrix}$$

we can relate $(\overline{\mathbf{F}}_1, \overline{\mathbf{F}}_2)$ and $(\overline{\mathbf{D}}_1, \overline{\mathbf{D}}_2)$:

$$\begin{Bmatrix} \overline{\mathbf{F}}_1 \\ \overline{\mathbf{F}}_2 \end{Bmatrix}=[\mathbf{T}\boldsymbol{\Gamma}\mathbf{T}^T]\begin{Bmatrix} \overline{\mathbf{D}}_1 \\ \overline{\mathbf{D}}_2 \end{Bmatrix}$$
$$\equiv\begin{bmatrix} \overline{\boldsymbol{\Gamma}}_{11} & \overline{\boldsymbol{\Gamma}}_{12} \\ \overline{\boldsymbol{\Gamma}}_{21} & \overline{\boldsymbol{\Gamma}}_{22} \end{bmatrix}\begin{Bmatrix} \overline{\mathbf{D}}_1 \\ \overline{\mathbf{D}}_2 \end{Bmatrix}. \tag{44}$$

The partial inversion of (44) results in the same form as (8) and (9) with all the quantities barred.

Adopting the same procedure used for (10), we obtain

$$L_R=\overline{\mathbf{F}}_1^T(\overline{\mathbf{D}}_1+\overline{\boldsymbol{\Phi}}_{21}^T\overline{D}_2)+\frac{1}{2}\overline{\mathbf{D}}_2^T\overline{\boldsymbol{\Phi}}_{22}\overline{\mathbf{D}}_2-\frac{1}{2}\overline{\mathbf{F}}_1^T\overline{\boldsymbol{\Phi}}_{11}\overline{\mathbf{F}}_1$$
$$-\mathbf{D}^T\mathbf{P}+\overline{Q}_s(\chi_s-\beta_s). \tag{45}$$

If we redefine some variables as

$$\mathbf{F}_1=\begin{Bmatrix} \overline{\mathbf{F}}_1 \\ Q_s \end{Bmatrix} \; ; \; \mathbf{D}_1=\begin{Bmatrix} \overline{\mathbf{D}}_1 \\ \chi_s-\beta_s \end{Bmatrix}$$

$$\mathbf{F}_2=\overline{\mathbf{F}}_2 \; ; \; \mathbf{D}=\overline{\mathbf{D}}_2$$

$$\boldsymbol{\Phi}_{11}=\begin{bmatrix} & & & 0 \\ & \overline{\boldsymbol{\Phi}}_{11} & & 0 \\ & & & 0 \\ 0 & 0 & 0 & 0 \end{bmatrix} \; ; \; \boldsymbol{\Phi}_{21}=-\boldsymbol{\Phi}_{12}^T=\begin{bmatrix} & 0 \\ \overline{\boldsymbol{\Phi}}_{21} & 0 \\ & 0 \end{bmatrix} \; ; \; \boldsymbol{\Phi}_{22}=\overline{\boldsymbol{\Phi}}_{22},$$

the energy density $L_R$ in (45) can be cast into exactly the same form as (10).

To relate $\mathbf{D}_1$ and $\mathbf{D}_2$ to $\mathbf{D}$, we use one of the kinematic assumption, $\chi_\theta = \beta_\theta$ in the strain-displacement relation. The results are[3] written as (32) with

[3]Similar circumferential dependences to (29)–(31) are assumed.

$$\mathbf{G}_1 = \begin{bmatrix} 1 & 0 & 0 & 0 \\ 0 & 1 & 0 & 0 \\ 0 & 0 & c_\varphi & s_\varphi \\ 0 & 0 & s_\varphi & -c_\varphi \end{bmatrix}$$

$$\mathbf{G}_2^{(n)} = \begin{bmatrix} 0 & 0 & 0 & 0 \\ -\dfrac{n}{r\rho} & -\dfrac{c_\varphi}{r} & -\dfrac{nc_\varphi}{r} & -n\left(\dfrac{s_\varphi}{r} - \dfrac{1}{\rho r^2}\right) \\ 0 & 0 & 0 & 0 \\ 1 & 0 & 0 & 0 \end{bmatrix}$$

$$\mathbf{G}_3^{(n)} = \begin{bmatrix} \dfrac{c_\varphi}{r} & \dfrac{n^2 s_\varphi}{r^2} & \dfrac{n^2 s_\varphi}{r^2} & -\dfrac{n^2 c_\varphi}{n^2} \\ -\dfrac{n}{r} & 0 & 0 & \dfrac{n}{r^2} \\ 0 & \dfrac{n}{r} & \dfrac{1}{r} & 0 \end{bmatrix}.$$

Furthermore, the relation between $\mathbf{F}_1$ and $\mathbf{F}$ can be shown to be

$$r\mathbf{F}_1^{(n)} = (\mathbf{G}_1^{-1})^T \mathbf{F}^{(n)}.$$

Following the same procedure used in the previous section, we obtain exactly the same form of equations as before—Eq. (36) through Eq. (40).

## 5 Observations

First, we note that due to the relation between $\overline{\mathbf{M}}$ and $\overline{\mathbf{E}}$, and the Hermitian property of $\mathbf{C}$ and $\mathbf{K}$, the differential operator $\mathfrak{L}$ defined below is self-adjoint:

$$\mathfrak{L}[\eta] = \mathbf{J}\left(-\frac{d\eta}{dx} + \mathbf{A}\eta\right) \tag{46}$$

where $\mathbf{A}$ is the coefficient matrix of Eq. (17). In (46), we introduced $\mathbf{J}$ and $\eta$ such that

$$\mathbf{J} = \begin{bmatrix} \mathbf{0} & \mathbf{1} \\ -\mathbf{1} & \mathbf{0} \end{bmatrix} \; ; \; \eta = \begin{Bmatrix} \overline{\mathbf{F}} \\ \overline{\mathbf{D}} \end{Bmatrix}.$$

To prove the self-adjointness of $\mathfrak{L}[\eta]$, it should suffice to show that (see, e.g., Ince, 1956)

$$\eta_b^{*T}\mathfrak{L}[\eta_a] = (\eta_a^{*T}\mathfrak{L}[\eta_b])^{*T} - \frac{d}{dx}\,[\overline{\mathbf{F}}_b^{*T}\overline{\mathbf{D}}_a - \overline{\mathbf{D}}_b^{*T}\overline{\mathbf{F}}_a] \tag{47}$$

where $\eta_a$ and $\eta_b$ are the solutions of $\mathfrak{L}[\eta] = 0$. From Eq. (47) (and with $\mathfrak{L}[\eta_a] = \mathfrak{L}[\eta_b] = 0$), the reciprocal theorem (see, e.g., Love, 1927) immediately comes out:

$$\frac{d}{dx}\,[\overline{\mathbf{F}}_b^{*T}\overline{\mathbf{D}}_a - \overline{\mathbf{D}}_b^{*T}\overline{\mathbf{F}}_a] = 0$$

or

$$[\overline{\mathbf{F}}_b^{*T}\overline{\mathbf{D}}_a - \overline{\mathbf{F}}_b^{*T}\overline{\mathbf{F}}_a]_{x_1}^{x_2} = 0.$$

The same form applies to shells of revolution.

For the three-dimensional deformation of elastic bodies, the variational principle was derived by restricting $k_y$, $k_z$, and $\kappa_\theta$ in (11) and (22) to be real valued. If we had assumed that $k_y$, $k_z$, and $\kappa_\theta$ are complex valued, however, no modified variational principle like (15) would have been possible; the mechanical systems have no potential. Nevertheless, $k_y$, $k_z$, and $\kappa_\theta$ can be generalized to be complex-valued in $\overline{\mathbf{E}}$, $\overline{\mathbf{K}}$, and $\overline{\mathbf{M}}$ of the final form of the state-vector Eq. (17). With this generalization, $\overline{\mathbf{M}} \neq -\overline{\mathbf{E}}^{*T}$, and $\overline{\mathbf{K}}$ is no longer a Hermitian matrix.

Interestingly enough, the present result is exactly analogous to the Hamiltonian mechanics for a dynamic system. To see the analogy, we reconsider the case for shells of revolution. The Hamiltonian $H^{(n)}$ corresponding the functional $\Pi^{(n)}$ can be found as (see, e.g., Goldstein, 1980 or Gelfand and Fomin, 1963)

$$\begin{aligned} H^{(n)}(s,\mathbf{D}^{(n)},\mathbf{F}^{(n)}) &= -L_{MR}^{(n)}(s,\mathbf{D}^{(n)},d\mathbf{D}^{(n)}/ds) + \mathbf{F}^{(n)T}\frac{d\mathbf{D}^{(n)}}{ds} \\ &= -\mathbf{D}^{(n)T}\mathbf{E}^{(n)}\mathbf{F}^{(n)} + \frac{1}{2}\mathbf{F}^{(n)T}\mathbf{C}\mathbf{F}^{(n)} \\ &\quad -\frac{1}{2}\mathbf{D}^{(n)T}\mathbf{K}^{(n)}\mathbf{D}^{(n)} + \mathbf{D}^{(n)T}\mathbf{B}^{(n)}. \end{aligned} \tag{48}$$

In Eq. (48), the components of the force vector $\mathbf{F}^{(n)}$ are interpreted as the conjugate momenta:

$$\mathbf{F}^{(n)} = \frac{\partial L_{MR}^{(n)}(s,\mathbf{D}^{(n)},d\mathbf{D}^{(n)}/ds)}{\partial\left(\dfrac{d\mathbf{D}^{(n)}}{ds}\right)}.$$

It is now apparent that the system (40) represents the canonical equations of Hamilton, which are

$$\frac{d\mathbf{D}^{(n)}}{ds} = \frac{\partial H^{(n)}}{\partial \mathbf{F}^{(n)}}$$

$$\frac{d\mathbf{F}^{(n)}}{ds} = -\frac{\partial H^{(n)}}{\partial \mathbf{D}^{(n)}}.$$

The arc-length variable $s$, the displacement $\mathbf{D}^{(n)}$, and the force $\mathbf{F}^{(n)}$ are analogous to the time, the generalized coordinates and momenta of a dynamic system. It is well known that $H^{(n)}$ is a first integral of the Euler-Lagrange equations if $H^{(n)}$ does not depend on $s$ explicitly. In the present shell problem, this is true if a cylindrical shell with a constant thickness made of a homogeneous material is subjected to pressure or edge loading. A similar result can be obtained for the three-dimensional bodies.

It is remarked that the proper scale factor of the field variables is crucial for $\mathfrak{L}$ to be self-adjoint. In the present problem, $\mathbf{D}$ and $\mathbf{F}$ satisfy a criterion that $\mathbf{F}^T\delta\mathbf{D}$ has the dimension of work. As long as this criterion is satisfied, the resulting $\mathfrak{L}$ is always self-adjoint.

To generalize the choice of the field variables, suppose that we wish to use new variables $\mathbf{D}_g$ and $\mathbf{F}_g$ defined as

$$F_g = \mathbf{RF} \; ; \; \mathbf{D}_g = \mathbf{R}^{-1^T}\mathbf{D},$$

where $\mathbf{R}$ is any real nonsingular square matrix. Note the relation

$$\mathbf{F}^T\delta\mathbf{D} = \mathbf{F}_g^T\delta\mathbf{D}_g.$$

By substitution, we can easily show that the state-vector equation becomes for the three-dimensional bodies

$$-\frac{d}{dx}\begin{Bmatrix} \overline{\mathbf{F}}_g \\ \overline{\mathbf{D}}_g \end{Bmatrix} + \begin{bmatrix} \mathbf{R}\overline{\mathbf{E}}\mathbf{R}^{-1} + \dfrac{d\mathbf{R}}{dx}\mathbf{R} & \mathbf{R}\overline{\mathbf{K}}\mathbf{R}^T \\ \mathbf{R}^{-1^T}\mathbf{C}\mathbf{R}^{-1} & -\left(\mathbf{R}\overline{\mathbf{E}}\mathbf{R}^{-1} + \dfrac{d\mathbf{R}}{dx}\mathbf{R}\right)^{*T} \end{bmatrix} \times \begin{Bmatrix} \overline{\mathbf{F}}_g \\ \overline{\mathbf{D}}_g \end{Bmatrix} = \begin{Bmatrix} \mathbf{R}\overline{\mathbf{B}} \\ 0 \end{Bmatrix}. \tag{49}$$

Exactly the same form applies to the shell of revolution.

For wave propagation or steady-state vibration of the elastic bodies where the deformation has the form (in the Cartesian coordinate system)

$$\mathbf{H}(x,y,z,t) = \mathrm{Re}\{\overline{\mathbf{H}}(x)\exp[i(k_y y + k_z z - \omega t)]\}, \tag{50}$$

we replace $\overline{\mathbf{K}}$ of (16c) as

$$\overline{\mathbf{K}} \Leftarrow \overline{\mathbf{K}} - \rho\omega^2\mathbf{1}. \tag{51}$$

In Eqs. (50 and (51), $t$ and $\omega$ are time and frequency and $\rho$ is the density of the body. When the cylindrical system is used, replace $\overline{\mathbf{K}}$ of (23$c$) as

$$\overline{\mathbf{K}} \Leftarrow \overline{\mathbf{K}} - r\rho\omega^2\mathbf{1},$$

with $\mathbf{H}$ similar to (50). The extension to dynamic problems is also valid for the shells of revolution. In addition, we note that the present variational principle (not just the final state-vector equations) can be extended to include linear viscoelastic theory as long as we use real form solutions such as (29)–(31) (not the complex form such as (11, 22)).

As pointed out in the Introduction, the state-vector differential equations have been and may be useful for asymptotic-numeric treatment. As far as the direct use of the principle is concerned, a finite element formulation may be pursued directly from the present variational principle. A hybrid perturbation-Galerkin method (Gear and Anderson, 1989) may also be applied to the present variational problem to seek for asymptotic-numeric solutions.

## References


Balch, C. D., and Steele, C. R., 1988, "Non-Axisymmetric Deformation of Thin Paraboloidal Shells with Initial Prestress," SHELLTECH Report 88-2.

Braga, A. M. B., and Herrmann, G., 1988, "Plane Waves in Anisotropic Layered Composites," *Wave Propagation in Structural Composite*, A. K. Mal and T. C. Ting, eds.) ASME-AMD Vol. 90, pp. 81–98.

Budiansky, B., and Sanders, J. L., 1963, "On the Best First-Order Linear Shell Theory," *Progress in Applied Mechanics, The Prager Anniversary Volume*, MacMillan, New York, pp. 129–140.

Cohen, G. A., 1964, "Computer Analysis of Asymmetrical Deformation of Orthotropic Shells of Revolution," *AIAA*, Vol. 2, pp. 932–934.

Cohen, G. A., 1974, "Numerical Integration of Shell Equations Using the Field Method," ASME JOURNAL OF APPLIED MECHANICS, Vol. 41, pp. 261–266.

Cohen, G. A., 1979, "FASOR—A Second Generation Shell of Revolution Code," *Computers and Structures*, Vol. 10, pp. 301–309.

DeRusso, P. M., Roy, R. J., and Close, C. M., 1965, *State Variables for Engineers*, John Wiley and Sons, New York.

Geer, J. F., and Anderson, C. M., 1989, "A Hybrid Perturbation-Galerkin Method for Differential Equations Containing a Parameter," *ASME Applied Mechanics Reviews*, Vol. 42, pp. S69–S77.

Gelfand, I. M., and Fomin, S. V., 1963, *Calculus of Variations*, Prentice-Hall, Englewood Cliffs, N.J.

Goldstein, H., 1980, *Classical Mechanics*, 2nd ed., Addison-Wesley, Reading, PA.

Hellinger, E., 1914, "Die allgemeinen Ansätze der Mechanik der Kontinua," *Encyklopädie der Mathematischen Wissenshaften*, Vol. 4, No. 4, pp. 654–655.

Ince, E. L., 1956, *Ordinary Differential Equations*, Dover, New York.

Ingebrigsten, K. A., and Tonning, A., 1969, "Elastic Surface Waves in Crystals," *Phys. Rev.*, Vol. 184, pp. 942–951.

Koiter, W. T., 1960, "A Consistent First Approximation in the General Theory of Elastic Shells," *Theory of Elastic Shells* (Proceedings of 1st IUTAM Symposium), W. T. Koiter, ed., North-Holland Pub. Co., Amsterdam, pp. 12–33.

Love, A. E. H., 1927, *A Treatise on the Mathematical Theory of Elasticity*, 4th ed., Dover, New York.

Mindlin, R. D., 1951, "Influence of Rotary Inertia and Shear on Flexural Motions of Isotropic, Elastic Plate," ASME JOURNAL OF APPLIED MECHANICS, Vol. 12, pp. 31–38.

Naghdi, P. M., 1972, *The Theory of Shells and Plates*, in *Handbuch der Physik* VIa/2), Springer, Berlin.

Reissner, E., 1945, "The Effect of Transverse Shear Deformation on the Bending of Elastic Plates," ASME JOURNAL OF APPLIED MECHANICS, Vol. 12, pp. A69–A77.

Reissner, E., 1950, "On a Variational Theorem in Elasticity," *J. Math. Phys.*, Vol. 29, pp. 90–95.

Sanders, J. L., 1959, "An Improved First-Approximation Theory for Thin Shells," NASA Technical Report R-24.

Steele, C. R., 1965, "Shells with Edge Loads of Rapid Variation: Part II, ASME JOURNAL OF APPLIED MECHANICS, Vol. 32, pp. 87–98.

Steele, C. R., 1971, "A Geometric Optics Solution for the Thin Shell Equation," *Int. J. Eng. Sci.*, Vol. 9, pp. 681–704.

Steele, C. R., and Skogh, J., "Slope Discontinuities in Pressure Vessels," ASME JOURNAL OF APPLIED MECHANICS, Vol. 37, pp. 587–595.

Steele, C. R., and Balch, C. D., 1989, *Theory of Thin Shells*, (Stanford University Lecture Notes).

Stroh, A. N., 1962, "Steady State Problems in Anisotropic Elasticity," *J. Math. Phys.*, Vol. 41, pp. 77–103.

Timoshenko, S. P., and Goodier, J. N., 1970, *Theory of Elasticity*, 3rd ed., McGraw-Hill, New York.

Wunderlich, W., Obrecht, H., Springer, H., and Lu, Z., 1989, "A Semi-Analytic Approach to the Nonlinear Analysis of Shells of Revolution," *Analytical and Computational Models of Shells*, A. K. Noor, T. Belytschko, and J. C. Simo, eds., ASME, New York.


## APPENDIX A

In the Cartesian coordinates, the matrices $\mathbf{C}$, $\overline{\mathbf{E}}$, and $\overline{\mathbf{K}}$ for isotropic behavior have the following forms:

$$\mathbf{C} = \begin{bmatrix} \dfrac{1}{\lambda+2G} & 0 & 0 \\ 0 & \dfrac{1}{G} & 0 \\ 0 & 0 & \dfrac{1}{G} \end{bmatrix} \tag{A1}$$

$$\overline{\mathbf{E}}^{*T} = \begin{bmatrix} 0 & \dfrac{\lambda}{\lambda+2G} ik_y & \dfrac{\lambda}{\lambda+2G} ik_z \\ ik_y & 0 & 0 \\ ik_z & 0 & 0 \end{bmatrix} \tag{A2}$$

and

$$\overline{\mathbf{K}} = \begin{bmatrix} 0 & 0 & 0 \\ 0 & \left(\lambda+2G-\dfrac{\lambda^2}{\lambda+2G}\right)k_y^2 + Gk_z^2 & \left(\lambda+G-\dfrac{\lambda^2}{\lambda+2G}\right)k_yk_z \\ 0 & \left(\lambda+G-\dfrac{\lambda^2}{\lambda+2G}\right)k_yk_z & \left(\lambda+2G-\dfrac{\lambda^2}{\lambda+2G}\right)k_z^2 + Gk_y^2 \end{bmatrix} \tag{A3}$$

where $\lambda$ and $G$ are the Lamé constant and shear modulus, respectively.

In the cylindrical coordinate system,

$$\mathbf{C} = \frac{1}{r}\begin{bmatrix} \dfrac{1}{\lambda+2G} & 0 & 0 \\ 0 & \dfrac{1}{G} & 0 \\ 0 & 0 & \dfrac{1}{G} \end{bmatrix} \tag{A4}$$

$$\overline{\mathbf{E}}^{*T} = \begin{bmatrix} \dfrac{\lambda}{\lambda+2G}\dfrac{1}{r} & \dfrac{\lambda}{\lambda+2G}\dfrac{i\kappa_\theta}{r} & \dfrac{\lambda}{\lambda+2G}\dfrac{ik_z}{r} \\ \dfrac{i\kappa_\theta}{r} & -\dfrac{1}{r} & 0 \\ ik_z & 0 & 0 \end{bmatrix} \tag{A5}$$

and

$$
\overline{\mathbf{K}}=\begin{bmatrix}
\left(\lambda+2G-\frac{\lambda^2}{\lambda+2G}\right)\frac{1}{r^2} & \left(\lambda+2G-\frac{\lambda^2}{\lambda+2G}\right)\frac{i\kappa_\theta}{r^2} & \left(\lambda-\frac{\lambda^2}{\lambda+2G}\right)\frac{ik_z}{r} \\
-\left(\lambda+2G-\frac{\lambda^2}{\lambda+2G}\right)\frac{i\kappa_\theta}{r^2} & \left(\lambda+2G-\frac{\lambda^2}{\lambda+2G}\right)\frac{\kappa_\theta^2}{r^2}+Gk_z^2 & \left(\lambda+G-\frac{\lambda^2}{\lambda+2G}\right)\frac{\kappa_\theta k_z}{r} \\
-\left(\lambda-\frac{\lambda^2}{\lambda+2G}\right)\frac{ik_z}{r} & \left(\lambda+G-\frac{\lambda^2}{\lambda+2G}\right)\frac{\kappa_\theta\kappa_\theta}{r} & \left(\lambda+2G-\frac{\lambda^2}{\lambda+2G}\right)k_z^2+G\frac{\kappa_\theta^2}{r^2}
\end{bmatrix}. \qquad \text{(A6)}
$$

## APPENDIX B

For isotropic materials, the constitutive matrix $\mathbf{\Gamma}$ is given by

$$
\mathbf{\Gamma}_{11}=Et\begin{bmatrix}
c^2 & 0 & 0 & 0 & 0 \\
0 & \frac{c^2(1-\nu)}{2} & 0 & 0 & 0 \\
0 & 0 & \frac{1}{\mu} & 0 & 0 \\
0 & 0 & 0 & \frac{1}{1-\nu^2} & 0 \\
0 & 0 & 0 & 0 & \frac{1}{2(1+\nu)}
\end{bmatrix} \qquad \text{(B1)}
$$

$$
\mathbf{\Gamma}_{21}=\mathbf{\Gamma}_{12}^T=Et\begin{bmatrix}
\nu c^2 & 0 & 0 & 0 & 0 \\
0 & 0 & 0 & 0 & 0 \\
0 & 0 & 0 & \frac{\nu}{1-\nu^2} & 0
\end{bmatrix}
$$

$$
\mathbf{\Gamma}_{22}=Et\begin{bmatrix}
c^2 & 0 & 0 \\
0 & \frac{1}{\mu} & 0 \\
0 & 0 & \frac{1}{1-\nu^2}
\end{bmatrix} \qquad \text{(B3)}
$$

where $E$ is Young's modulus, $\nu$ is Poisson's ratio, $t$ is the thickness of the shell, and the "reduced thickness" $c$ is defined as

$$
c^2=\frac{t^2}{12(1-\nu^2)}.
$$

The shear flexibility factor $\mu$ is given by (Reissner, 1945)

$$
\mu=\frac{12(1+\nu)}{5}.
$$

Mindlin (1951) also derived a shear flexibility factor close to Reissner's.

The explicit forms of the matrices $\mathbf{E}^{(n)}$, $\mathbf{C}$, and $\mathbf{K}^{(n)}$ for isotropic materials are

$$
\mathbf{E}^{(n)}=\frac{1}{r}\begin{bmatrix}
\nu c_\varphi & \mp n & rs_\varphi & -rc_\varphi & 0 \\
\pm\nu n & -c_\varphi & 0 & 0 & 0 \\
0 & \mp 2\zeta nc_\varphi & \nu c_\varphi & \nu s_\varphi & \mp nc_\varphi \\
0 & \mp 2\zeta ns_\varphi & 0 & 0 & \mp ns_\varphi \\
0 & -2\zeta c_\varphi & \pm\nu nc_\varphi & \pm\nu ns_\varphi & -c_\varphi
\end{bmatrix} \qquad \text{(B4)}
$$

$$
\mathbf{C}=\frac{1}{Etr}\begin{bmatrix}
\frac{1}{c^2} & 0 & 0 & 0 & 0 \\
0 & \frac{2}{c^2(1-\nu)}+2\zeta^2(1+\nu) & 0 & 0 & 2\zeta(1+\nu) \\
0 & 0 & \mu s_\varphi^2+(1-\nu^2)c_\varphi^2 & (1-\nu^2-\mu)c_\varphi s_\varphi & 0 \\
0 & 0 & (1-\nu^2-\mu)c_\varphi s_\varphi & \mu c_\varphi^2+(1-\nu^2)s_\varphi^2 & 0 \\
0 & 2\zeta(1+\nu) & 0 & 0 & 2(1+\nu)
\end{bmatrix} \qquad \text{(B5)}
$$

and

$$
\mathbf{K}^{(n)}=\frac{Et}{r}\begin{bmatrix}
\frac{t^2c_\varphi^2}{12} & \pm\frac{nt^2c_\varphi}{12} & 0 & 0 & 0 \\
\pm\frac{nt^2c_\varphi}{12} & \frac{n^2t^2}{12}+\frac{r^2}{\mu} & \mp\frac{nrs_\varphi}{\mu} & \mp\frac{nrc_\varphi}{\mu} & \frac{-rs_\varphi}{\mu} \\
0 & \mp\frac{nrs_\varphi}{\mu} & \frac{n^2s_\varphi^2}{\mu}+1 & -\frac{n^2c_\varphi s_\varphi}{\mu} & \pm n\left(\frac{s_\varphi^2}{\mu}+1\right) \\
0 & \pm\frac{nrc_\varphi}{\mu} & -\frac{n^2c_\varphi s_\varphi}{\mu} & \frac{n^2c_\varphi^2}{\mu} & \mp\frac{nc_\varphi s_\varphi}{\mu} \\
0 & -\frac{rs_\varphi}{\mu} & \pm n\left(\frac{s_\varphi^2}{\mu}+1\right) & \mp\frac{nc_\varphi s_\varphi}{\mu} & \frac{s_\varphi^2}{\mu}+n^2
\end{bmatrix} \qquad \text{(B6)}
$$

where the upper sign of $\{\pm, \mp\}$ in (B4)–(B6) corresponds to the deformation of (29)–(31) whereas the lower sign corresponds to the deformation of (29)–(31) with cosines and sines interchanged.

**S. K. Datta**
Fellow ASME.

**T. H. Ju**
Department of Mechanical Engineering,
Center for Space Construction,
University of Colorado,
Boulder, CO 80309-0427

**A. H. Shah**
Department of Civil Engineering,
University of Manitoba,
Winnipeg, Canada R3T 2N2, Canada

# Scattering of an Impact Wave by a Crack in a Composite Plate

*The surface responses due to impact load on an infinite uniaxial graphite/epoxy plate containing a horizontal crack is investigated both in time and frequency domain by using a hybrid method combining the finite element discretization of the near-field with boundary integral representation of the field outside a contour completely enclosing the crack. This combined method leads to a set of linear unsymmetric complex matrix equations, which are solved to obtain the response in the frequency domain by biconjugate gradient method. The time-domain response is then obtained by using an FFT. In order to capture the time-domain characteristics accurately, high-order finite elements have been used. Also, both the six-node singular elements and eight-node transition elements are used around the crack tips to model the crack-tip singularity. From the numerical results for surface responses it seems possible to clearly identify both the depth and length of this crack.*

## Introduction

Ultrasonic waves provide an efficient means of characterizing defects in structures. For this purpose it is necessary to analyze scattering by such defects. However, scattering by crack-like defects in a plate-like structure is a complicated phenomenon and the problem is made more difficult if it is a composite plate. In recent years, considerable progress has been made toward understanding wave propagation in anisotropic composite plates (Datta, et al., 1988a,b; Mal, 1988; Nayfeh and Chimenti, 1989; Rokhlin et al., 1986). But not much work has been done on the scattering by cracks in a composite plate. Recently, Karim and Kundu (1988) and Karim et al. (1989) studied scattering of elastic waves in a layered half-space and in layered fiber-reinforced composite plates by interface cracks using a boundary integral formulation. They considered antiplane motions, and the method used by these authors is limited to planar defects. Recently, both Sánchez-Sesma (1987) and Bond (1990) reviewed various applicable numerical techniques for a wave scattering problem. Both authors recommended that the family of boundary methods are well suited for scattering by various defects. This is not only because the investigated regions that can be studied by these methods include both near and far fields and arbitrarily shaped scatterers, but they also are good for mid-frequency ranges (when the flaw size is of the same order as the wavelength).

In this study we have used a hybrid method from the family of boundary methods that have been used in recent years for time-domain calculations of elastic waves scattered by a horizontal crack in a transversely isotropic plate. In the past, this method has been successfully applied to homogeneous or layered isotropic half-space for frequency domain calculations (e.g., Shah et al., 1982; Franssens and Lagasse, 1984; Khair et al., 1989; Bouden et al., 1990; Liu et al., 1989). This numerical technique allows one to limit the size of the finite element mesh roughly to that of the cross-section of the scatterer. There is another advantage of this hybrid method over various boundary element methods. It is that this method couples the boundary integral over a surface independent of the scatterer surfaces. Thus, one can use the same Green's functions for different scatterer geometries and multiple scatterers by proper modifications of the interior finite element mesh. Since the evaluation of the Green's functions is the most time-consuming part in the boundary methods, this uncoupling of the boundary integral representation from the scatterer boundary is a major advantage. In this paper we have also made use of an efficient quadrature scheme (Xu and Mal, 1985, 1987) for the Green's function computations.

The hybrid method leads to a complex matrix equation, where the matrix is sparse and unsymmetric. The unsymmetric complex part arises from the coupling with the Green's function boundary integral representation. The choice of an economic method to solve these equations involves minimization of some function of both computation time and required storage. Direct methods usually lead to a lot of fill-ins which destroy the sparsity of the matrix and increase the storage needs. In general, one has to reorder the rows and columns of the matrix to reduce fill-ins. At present, there exists no simple and practical algorithms which produce minimum fill-ins. Here, we use a compacted data structure (Nour-Omid and Taylor, 1984) to store only nonzero terms of the sparse matrix in a column list scheme. This reduces the storage needs a great deal and can be used directly for iterative solution techniques. In general, the conjugate gradient method is an effective solution technique for large and sparse systems when the matrix is Hermitian and positive definite. However, the case when the matrix is unsymmetric is substantially more difficult to

Contributed by the Applied Mechanics Division of THE AMERICAN SOCIETY OF MECHANICAL ENGINEERS for publication in the ASME JOURNAL OF APPLIED MECHANICS.

Discussion on this paper should be addressed to the Technical Editor, Professor Leon M. Keer, The Technological Institute, Northwestern University, Evanston, IL 60208, and will be accepted until four months after final publication of the paper itself in the JOURNAL OF APPLIED MECHANICS.

Manuscript received by the Applied Mechanics Division, July 11, 1990; final revision, July 3, 1991. Associate Technical Editor: L. M. Keer.

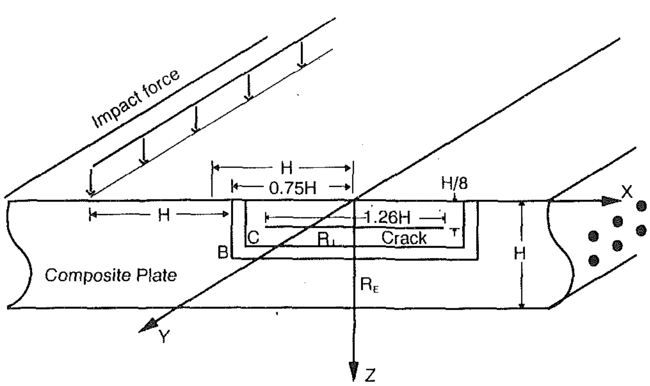


**Fig. 1 Configuration of a composite plate**

solve efficiently by means of iterative methods. This difficulty has led to the development of a wide variety of generalized conjugate gradient methods with varying degrees of success (e.g., Saad and Schultz, 1985; Ashby et al., 1988; Joubert and Manteuffel, 1990). Recently, the biconjugate gradient or Lanczos method (Lanczos, 1950; Fletcher, 1976; Saad, 1982), which is one of the most effective methods so far (Langtangen and Tveito, 1988), has been used to solve large unsymmetric equations.

For the scattering problems considered here it has been found that by taking advantage of the sparsity of the matrix, the biconjugate gradient method provides satisfactory solutions for large unsymmetric complex matrix equations.

## Formulation of the Problem

Figure 1 shows the geometry of a horizontal crack in a composite plate. As shown, this defect lies inside a fictitious contour (rectangular) C. We define the interior region $R_I$ to be bounded outside by the imaginary boundary B. Note that B encloses C. The exterior region $R_E$ is bounded inside by the contour C. The area between the contour C and boundary B is shared by both regions. The interior region $R_I$ is discretized with finite elements and an integral representation over C for the displacements on the boundary B is introduced to solve for the scattered field.

Considering the plane-strain case, let $u_i$ be the displacement component in the $i$th direction in the Cartesian frame and $\sigma_{ij}$ the second-order Cauchy stress tensor ($i$, $j$ = 1, 3) having time-harmonic behavior of the form $e^{-i\omega t}$, where $\omega$ is the circular frequency. In each region, $u_i$ and $\sigma_{ij}$ satisfy the equation of motion

$$\sigma_{ij,j}+\rho\omega^2 u_i=-f_i \qquad (i,j=1,3) \tag{1}$$

where $\rho$ is the mass density, $f_i$ the force per unit volume, and the factor $e^{-i\omega t}$ has been dropped. The continuity of traction and displacement at the interfaces must be satisfied.

**Exterior Region $R_E$: Boundary Integral Representation.** In this region the displacement $u_i$ is composed of two parts:

$$u_i=u_i^{(f)}+u_i^{(s)} \tag{2}$$

where $u_i^{(f)}$ is the free-field displacement (including the incident waves and their reflections) and $u_i^{(s)}$ the scattered field. The scattered displacement field is represented by a surface integral as will be discussed.

In order to derive the boundary integral representation on B, we start from Betti's reciprocity theorem. A pair of solutions to Eq. (1) satisfies

$$\int\int_A (\mathbf{f}\cdot\mathbf{v}-\mathbf{g}\cdot\mathbf{u})dA=\oint_C(\mathbf{u}\cdot\mathbf{s}-\mathbf{v}\cdot\mathbf{t})dC. \tag{3}$$

Here, $\mathbf{u}$, $\mathbf{t}$ represent the displacement and surface traction caused by body force $\mathbf{f}$, while $\mathbf{v}$, $\mathbf{s}$ are the displacement and surface traction due to body force $\mathbf{g}$ in region $R_E$. The scattered field is taken to be the first field. The second field is the Green's solution. The scattered field has no sources inside $R_E$, hence $\mathbf{f}=0$. For the Green's displacement field, the source is represented by

$$\mathbf{g}=\delta(x-x')\delta(z-z')e^{-i\omega t}\mathbf{e}_i$$

where $\mathbf{e}_i$ is the unit vector in the $i$th direction. This represents a line source at $(x', z')$ varying in time with circular frequency $\omega$. Therefore, the Green's function and the scattered fields are the solutions of the following equations:

$$\Sigma_{ijk,k}+\rho\omega^2 G_{ij}=-\delta_{ij}\delta(x-x')\delta(z-z') \tag{4}$$

and

$$\sigma_{jk,k}^{(s)}+\rho\omega^2 u_j^{(s)}=0, \tag{5}$$

respectively. In the above equations, $j$ stands for the displacement direction and $i$ stands for the force direction. $G_{ij}$ and $\Sigma_{ijk}$ are the Green's displacement tensor and the corresponding stresses. Omitting some of the details, it is easily shown that

$$u_i(x',z')=\oint_C(u_j\Sigma_{ijk}-G_{ij}\sigma_{jk})n_k dC+u_i^{(f)}(x',z'). \tag{6}$$

Equation (6) is the integral representation of the total field at any point in the exterior region $R_E$.

**Interior Region $R_I$: Finite Element Technique.** This region encloses all the inhomogeneities. In order to get the solution in region $R_I$, we use the finite element technique. In this approach, the area of interest $R_I$ is discretized into N elements. In each element the displacement is written in the usual way in terms of the shape functions and the nodal displacements in the matrix form as the following:

$$\mathbf{u}_e=\begin{Bmatrix}u\\ w\end{Bmatrix}$$

$$=\begin{bmatrix}\phi_1 & 0 & \dots & \phi_n & 0\\ 0 & \phi_1 & \dots & 0 & \phi_n\end{bmatrix}\begin{Bmatrix}u_1\\ w_1\\ \vdots\\ u_n\\ w_n\end{Bmatrix} \tag{7}$$

$$=\mathbf{\Phi}\mathbf{d}_e$$

in which $n$ is the number of nodes per element and subscript ($e$) is the element identifier. The strain within an element related to the nodal displacement $\mathbf{d}_e$ is given by

$$\begin{aligned}\mathbf{e}&=\mathbf{D}\mathbf{u}_e\\ &=\mathbf{D}\mathbf{\Phi}\mathbf{d}_e\\ &=\mathbf{B}\mathbf{d}_e\end{aligned} \tag{8}$$

where $\mathbf{D}$ is an operator matrix

$$\mathbf{D}=\begin{bmatrix}\dfrac{\partial}{\partial x} & 0\\ 0 & \dfrac{\partial}{\partial z}\\ \dfrac{\partial}{\partial z} & \dfrac{\partial}{\partial x}\end{bmatrix}. \tag{9}$$

In order to determine the elemental impedance matrix, let us consider the energy function $E_e$ in frequency domain

$$\begin{aligned}E_e&=U_e+K_e-W_e\\ &=\frac{1}{2}\int\int(\sigma^{*T}\epsilon-\rho\omega^2\mathbf{u}^{*T}\mathbf{u})dxdz\\ &\qquad-\frac{1}{2}\int(\mathbf{u}_B^{*T}\mathbf{t}_B+\mathbf{t}_B^{*T}\mathbf{u}_B)dc\end{aligned} \tag{10}$$

where $U_e$ and $K_e$ are the corresponding strain and kinetic energies, $W_e$ is the surface traction work potential and $\mathbf{t}_B$, $\mathbf{u}_B$ represent, respectively, the traction force and the displacement at the boundary $B$, and '*' represents complex conjugate. $\sigma$ and $\epsilon$ are stress and strain column vectors, respectively, defined as

$$\sigma = [\sigma_{xx}\sigma_{zz}\sigma_{zx}]^T \tag{11a}$$

$$\epsilon = [\epsilon_{xx}\epsilon_{zz}\epsilon_{zx}]^T. \tag{11b}$$

The stress $\sigma$ is related to the strain $\epsilon$

$$\sigma = \mathbf{C}\epsilon \tag{12}$$

where $\mathbf{C}$ is a $3 \times 3$ symmetric matrix of the element material elastic constants. Substituting Eqs. (7), (8), and (12) into Eq. (10) and taking the variation with respect to $\mathbf{u}^*$ leads to the equation of motion for region $R_I$, which can be written as

$$\begin{bmatrix} \mathbf{S}_{BB} & \mathbf{S}_{BI} \\ \mathbf{S}_{IB} & \mathbf{S}_{II} \end{bmatrix} \begin{Bmatrix} \mathbf{d}_B \\ \mathbf{d}_I \end{Bmatrix} = \begin{Bmatrix} \mathbf{y}_B \\ \mathbf{y}_I \end{Bmatrix} \tag{13}$$

where the elemental impedance matrices $\mathbf{S}_{ij}$ are represented by

$$\mathbf{S}_e = \int\int_{Ae} (\mathbf{B}_e^T\mathbf{C}\mathbf{B}_e - \rho\omega^2\mathbf{\Phi}_e^T\mathbf{\Phi}_e)\,dxdz. \tag{14}$$

It is clear from Eq. (14) that $\mathbf{S}_e$ is a symmetric matrix. In Eq. (13), $\mathbf{d}_I$ and $\mathbf{d}_B$ represent the interior and boundary nodal displacements, respectively. $\mathbf{y}_B$ represents the interaction forces between regions $R_E$ and $R_I$ at the boundary nodes. Since there are no forces on the interior nodes, $\mathbf{y}_I = 0$, and Eq. (13) becomes

$$\begin{bmatrix} \mathbf{S}_{BB} & \mathbf{S}_{BI} \\ \mathbf{S}_{IB} & \mathbf{S}_{II} \end{bmatrix} \begin{Bmatrix} \mathbf{d}_B \\ \mathbf{d}_I \end{Bmatrix} = \begin{Bmatrix} \mathbf{y}_B \\ \mathbf{0} \end{Bmatrix}. \tag{15}$$

Using the constitutive relation to express $\sigma_{jk}$ and Eq. (7) to represent the displacement, and evaluating the integrals at all the nodes $N_B$ on the boundary B, Eq. (6) becomes

$$\mathbf{d}_B = \mathbf{d}_B^{(f)} + \left[\oint_C (\mathbf{\Phi}_I^T\mathbf{\Sigma} - \mathbf{G}\mathbf{C}\mathbf{B}_I)\mathbf{n}dC\right]\mathbf{d}_I + \left[\oint_C (\mathbf{\Phi}_B^T\mathbf{\Sigma} - \mathbf{G}\mathbf{C}\mathbf{B}_B)\mathbf{n}dC\right]\mathbf{d}_B \tag{16}$$

where $\mathbf{B}_I = \mathbf{D}\mathbf{\Phi}_I$, $\mathbf{B}_B = \mathbf{D}\mathbf{\Phi}_B$. Equation (16) can be written as

$$\mathbf{d}_B = \mathbf{d}_B^{(f)} + \mathbf{A}_{BI}\mathbf{d}_I + \mathbf{A}_{BB}\mathbf{d}_B \tag{17}$$

where $\mathbf{A}_{BI}$ is $2N_B \times 2N_I$ and $\mathbf{A}_{BB}$ is $2N_B \times 2N_B$ complex matrices. Combining Eq. (17) and the second of Eq. (15), we obtain

$$\begin{bmatrix} \mathbf{I} - \mathbf{A}_{BB} & -\mathbf{A}_{BI} \\ \mathbf{S}_{IB} & \mathbf{S}_{II} \end{bmatrix} \begin{Bmatrix} \mathbf{d}_B \\ \mathbf{d}_I \end{Bmatrix} = \begin{Bmatrix} \mathbf{d}_B^{(f)} \\ \mathbf{0} \end{Bmatrix}. \tag{18}$$

The total field solutions at a certain frequency can be obtained by solving Eq. (18). Note that the square matrix on the left-hand side of Eq. (18) is usually quite large, sparse, and unsymmetric.

## Numerical Solution Scheme

**Evaluation of Green's Functions.** The Green's functions for a given medium in frequency domain can be expressed in the form of an infinite integral with respect to the horizontal wave number $(k)$

$$I = \int_0^\infty F(k,z,z')e^{ik(x-x')}dk. \tag{19}$$

The computational effort required to accomplish this to a high degree of accuracy is usually quite large. In order to reduce the time of computation of the Green's functions, we adopt an efficient quadrature scheme (Xu and Mal, 1985, 1987) in which the kernels $F(k, z, z')$ of the wave number integrals are represented by means of Chebyshev polynomials in finite and semi-infinite panels, and resulting oscillatory integrals are evaluated analytically. To do this, Eq. (19) is written as

$$I = \int_0^{k_c} F(x,z,z')e^{ik(x-x')}dk + \int_{k_c}^\infty F(x,z,z')e^{ik(x-x')}dk \tag{20}$$

where $k_c$ is chosen such that the curve fitting of the semi-infinite panel is convergent within required accuracy. One advantage of this integration scheme is that for given sources or receivers having the same depth we have to do the fitting (most time-consuming part) of the complex kernel with Chebyshev polynomials only once. This reduces the computation time considerably when a large number of sources or receivers have the same depth.

**Biconjugate Gradient Method.** The biconjugate gradient method was first introduced by Lanczos (1950, 1952) for obtaining the eigenvalues of unsymmetric real matrices. The method was later extended by Fletcher (1976) to treat real indefinite systems of equations. The method was then extended by Wong (1978) and Jacobs (1980) to treat complex nonsymmetric matrix equations.

The algorithm of biconjugate gradient method is listed as follows:

$$\mathbf{r}_0 = \mathbf{b} - \mathbf{A}\mathbf{x}_0 = \mathbf{p}_0 \tag{21}$$

$$\mathbf{w}_0 = \mathbf{q}_0 = \bar{\mathbf{r}}_0 \tag{22}$$

where the overbar denotes the conjugate of a complex number. Then we evaluate

$$a_k = \frac{\langle \mathbf{r}_k;\mathbf{q}_k \rangle}{\langle \mathbf{A}\mathbf{p}_k;\mathbf{w}_k \rangle} \tag{23}$$

$$\mathbf{x}_{x+1} = \mathbf{x}_k + a_k\mathbf{p}_k \tag{24}$$

$$\mathbf{r}_{k+1} = \mathbf{r}_k + a_k\mathbf{A}\mathbf{p}_k \tag{25}$$

$$\mathbf{q}_{k+1} = \mathbf{q}_k - \bar{a}_k\mathbf{A}^*\mathbf{w}_k \tag{26}$$

$$c_k = \frac{\langle \mathbf{r}_{k+1};\mathbf{q}_{k+1} \rangle}{\langle \mathbf{r}_k;\mathbf{q}_k \rangle} \tag{27}$$

$$\mathbf{p}_{k+1} = \mathbf{r}_{k+1} + c_k\mathbf{p}_k \tag{28}$$

$$\mathbf{w}_{k+1} = \mathbf{q}_{k+1} + \bar{c}_k\mathbf{w}_k. \tag{29}$$

The biconjugate gradient method was never very popular because, (a) it did not minimize any functional and, (b) it was not known a priori when the method would break down. Hence, neither the residuals nor the errors in the solution would decrease monotonically at each iteration. However, the advantage of the biconjugate gradient method is that it does not square the condition number of the original equations. In many cases, the biconjugate gradient method gives some of the fastest solution times among all generalized conjugate gradient methods (Langtangen and Tveito, 1988). Today it is considered as one of the most efficient iterative methods for nonsymmetric systems, and it is used in a variety of application areas (Sarkar, 1981, 1987; Sarkar et al., 1988).

For the scattering problem considered here we have used the biconjugate gradient method to solve the system of equations as shown in Eq. (18). The iteration was terminated when the following error criterion was satisfied

$$\frac{\|\mathbf{A}\mathbf{x}_k - \mathbf{b}\|}{\|\mathbf{b}\|} \le 10^{-6}. \tag{30}$$

**Storage Scheme of Matrix.** Equation (18) is solved by the biconjugate gradient method in which only the multiplication of matrix and vector is involved. This does not destroy the sparsity pattern of the matrix at any iterative step. Hence, a compacted data structure (Nour-Omid and Taylor, 1984) which stores only the nonzero terms of the stiffness matrix is a suitable storage scheme has been used. More details have been given by S. W. Liu and S. K. Datta (1990).

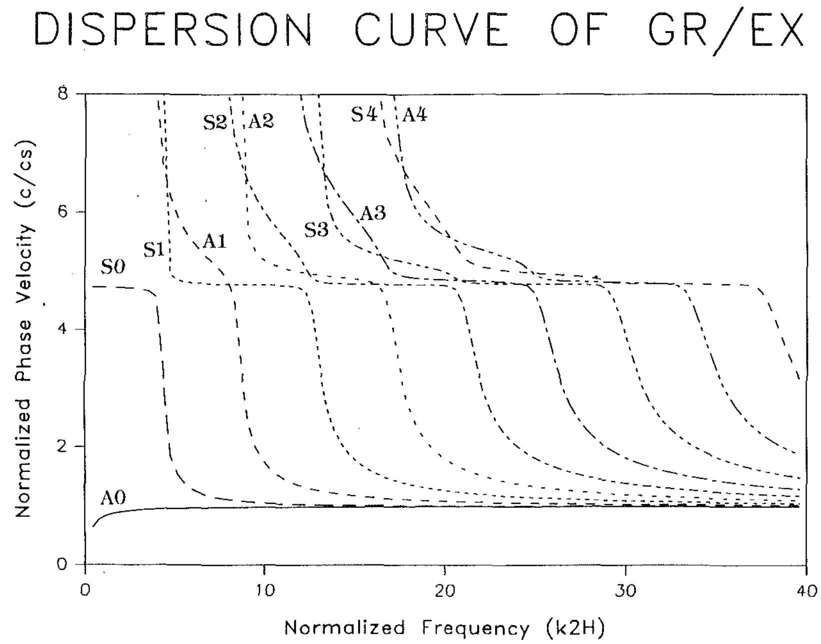


**Fig. 2 Normalized dispersion curves for graphite/epoxy plate**

It may be noted that the required storage for this compacted structure varies linearly with the number of equations. Therefore, the saving is more for larger problems and the storage requirement of the compacted assembly is not affected by the node ordering. This is important for our method because we can number the nodes in any convenient order without increasing the storage.

## Results and Discussions

The method discussed in previous section has been implemented in a FORTRAN program. As an example, we present here results for the surface displacements of an infinite plate with a horizontal crack. It may be noted from the procedure described previously that the method is easily implemented for any other defect geometry or for multiple defects. We consider the plate to be transversely isotropic with symmetry axis lying parallel to the $x$-axis. The plate specimen for which numerical results are given is made of graphite/epoxy with elastic constants $C_{11} = 160.7$ GPa, $C_{33} = 13.96$ GPa, $C_{55} = 7.07$ GPa and $C_{13} = 6.44$ GPa. The density is 1.8 g/cm$^3$. Thus, the longitudinal and shear wave speed along the fibers are 9.45 mm/$\mu$s and 1.98 mm/$\mu$s, respectively. The geometry of the problem is shown in Fig. 1. The fibers are aligned along $x$-direction, plate thickness is 5.08 mm, the crack with length 6.4 mm is located horizontally at a depth of 0.635 mm from one of the free surfaces (later, we'll call this surface as top surface). The line load is applied in $z$-direction at top surface 5.68 mm horizontal distance away from the left crack tip.

**Numerical Accuracy and Convergence Rate.** The hybrid method used in this study has been tested for its accuracy for different finite element meshes by performing the zero-scatterer test. This is done by giving the crack the same material properties as those of the surrounding medium. The relative error of the calculated total displacement and the incident displacement field is kept within five percent by adjusting the number of finite elements. Generally, ten elements per wavelength is enough to accomplish the accuracy desired.

In order to obtain the time-domain responses, we calculated the frequency-domain responses for frequencies ranging from zero to 1 MHz. The size of the finite element mesh has been chosen according to the numerical accuracy desired at the highest frequency.

The finite element part of current problem is composed of 400 elements and 1274 nodes, the nodes on boundary B being 49. The total degree-of-freedom is 2548, and the iteration numbers vary from 1717 to 2558 as the frequencies vary from the lowest to the highest of the frequency range under investigation.

**Incident Signal.** The incident wave signal is taken to be a Ricker wavelet defined as (Ricker, 1977)

$$u(\tau) = (2\pi^2 f_c^2 \tau^2 - 1)e^{-\pi^2 f_c^2 \tau^2} \tag{31a}$$

where $f_c$ is the characteristic frequency (normalized) of a wavelet. The time of peak amplitude (= 1.0) is at $\tau = 0$, where $\tau$ is nondimensional time defined as $\tau = tc_s/H$, $c_s$ being the shear wave velocity along fiber direction and $t$ is the time.

The Fourier transform of the Ricker wavelet is

$$u(k_2H) = \int_{-\infty}^{+\infty} u(\tau) e^{ik_2H\tau} d\tau$$

$$= -\frac{(k_2H)^2}{2\pi^{5/2} f_c^3} e^{\frac{-(k_2H)^2}{4\pi^2 f_c^2}} \tag{31b}$$

which has the peak amplitude $(2/\sqrt{\pi} f_c e)$ at $\epsilon_o = 2\pi f_c$. The amplitudes approach zero rapidly after $k_2H > 3\epsilon_o$; therefore, the high frequency responses are filtered out. $k_2$ is shear wave number along fiber direction. The precise values for $\epsilon_o$ in current study can be found in the next subsection.

**Numerical Results.** For the propagation of waves in the homogeneous plate of transversely isotropic material, the dispersion equation separates into two, one for the symmetric motion and the other for the antisymmetric case. Figure 2 shows the normalized dispersion curves for the graphite/epoxy plate considered here. These curves are seen to reach a pronounced plateau at normalized phase velocity $(c/c_s)$ equal to 4.7, which is the ratio of longitudinal wave velocity to shear wave velocity along the fiber direction. The Rayleigh wave velocity in this plate is 0.988 of shear wave velocity. The cut-off frequencies of the various branches play an important role in the frequency response as discussed in the following. These are marked on Figs. 3($a$) and 6.

Figure 3($a$) shows the vertical surface response spectra at points on the top surface without the crack due to a vertical

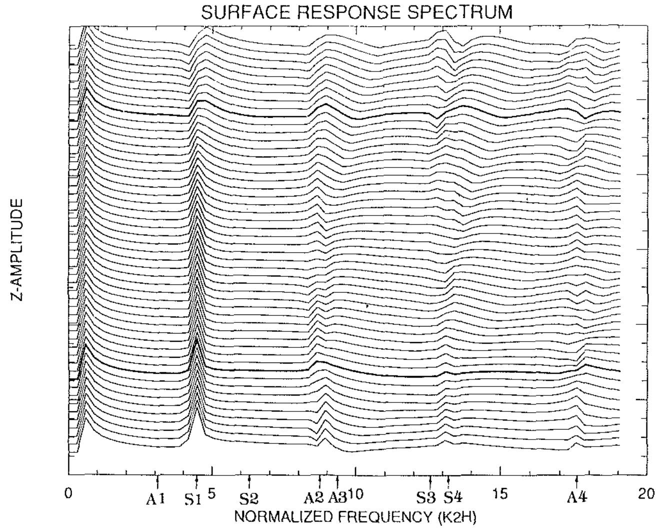


**Fig. 3(*a*) Surface response spectrum of a graphite/epoxy plate without crack due to an impulsive load. The observation points are between $x = -5.0$ mm and $x = 5.0$ mm on the top surface.**

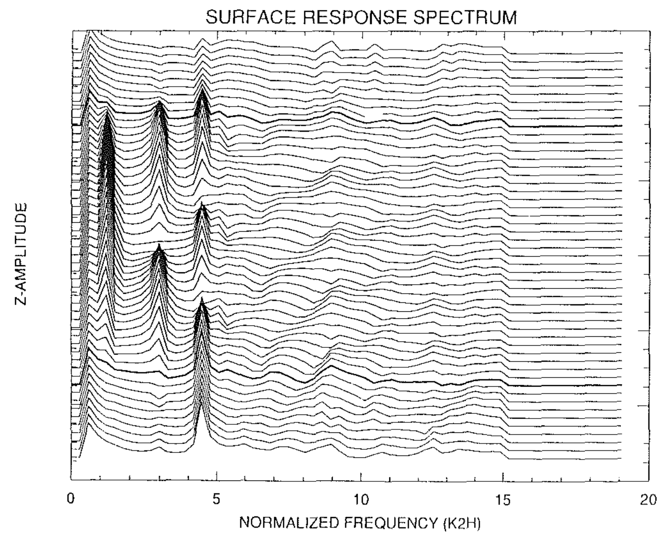


**Fig. 3(*b*) Surface response spectrum of a graphite/epoxy plate with crack due to an impulsive load. The observation points are the same as those in Fig. 3(*a*).**

impulsive (delta function) load. Referring to Fig. 1, these points lie equally between $x = -5.0$ mm to $x = 5.0$ mm. For plotting convenience, we have replaced amplitudes at the first two frequencies at each point to zero. This causes the fictitious peaks at $k_2H$ equal to 0.425. The cut-off frequencies for the first four symmetric and antisymmetric modes have been marked as S1 through S4 and A1 through A4 in this figure. The maxima at $k_2H$ equal to $1.4\pi$(S1), $2.8\pi$(A2), $4.2\pi$(S4), and $5.6\pi$(A4) are seen in this figure and they are related to the cut-off frequencies of the symmetric and antisymmetric longitudinal modes ($\sqrt{\beta}(2n-1)\pi$, $\sqrt{\beta}2n\pi$), respectively. Here, $\beta = C_{33}/C_{55}$. There are two thick curves in this figure which show the spectra at stations right above the two crack tips on the top surface. Figure 3(*b*) is the vertical surface response spectra of this graphite/epoxy plate in the presence of the crack due to the same impulsive load. Note that the extent of this region falls outside that of the FE region (Fig. 1). Thus, the response presented in this figure is a composite of the data obtained from the FE and integral representation computations. Comparing with Fig. 3(*a*), not only those aforementioned peaks, but also more peaks can be found in Fig. 3(*b*). The maxima at $k_2H$ equal to $\pi$(A1), $2\pi$(S2), $3\pi$(A3) and $4\pi$(S3) are identified as cut-off frequencies of antisymmetric and symmetric shear

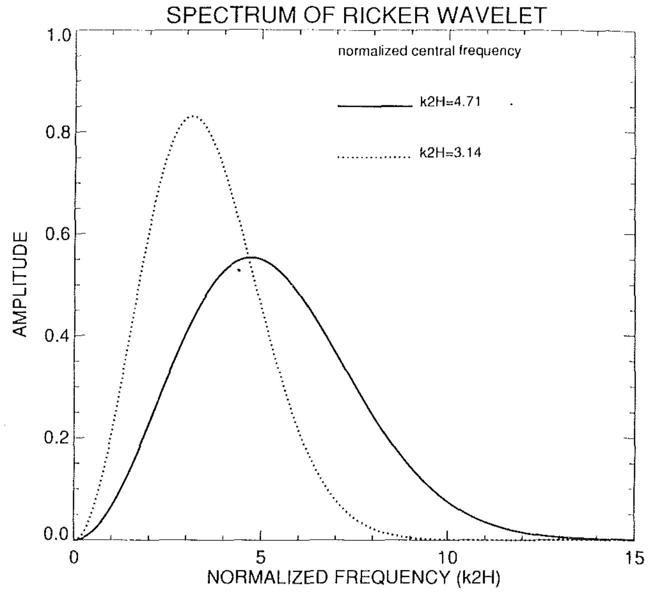


**Fig. 4 Spectra of Ricker wavelet at normalized central frequencies 4.71 (292 kHz) and 3.14 (195 kHz)**

modes, respectively. These shear modes have been excited due to the presence of the crack. The peaks at $k_2H$ equal to 5.14 is related to the depth of the crack. Because the ratio of crack length to crack depth is large ($\approx 10$), we can model this problem locally as two separate plates with thicknesses H/8 and 7/8H. The cut-off frequencies for the thinner plate are eight times those for the original plate with thickness equal to H and they are far beyond the frequency range we are investigating. However, the cut-off frequencies for 7/8H plate are expected to be found in Fig. 3(*b*). The aforementioned value 5.14 is exactly the cut-off frequency for the first symmetric mode of the 7/8H plate. Thus, this determines the depth of the crack. Another group of peaks at $k_2H$ equal to 1.2 is due to the resonance of the finite plate above the horizontal crack. L. M. Keer et al. (1984) and P. Cawley and C. Theodorakopoulos (1989) have studied this effect in their papers. They proposed that the resonance frequency for a defect may be predicted by using plate theory with length equal to crack length and thickness equal to crack depth. The natural frequency of this plate is 1.13 ($k_2H$) for simply supported ends and 2.56 ($k_2H$) for clamped ends which provide lower and upper bounds of the frequency of this peak. This result is consistent with those models that have been suggested by these authors.

Figures 5(*a*) and 5(*b*) show the time-domain response. The incident signals have the time dependence given by Eq. (31*a*) (Ricker pulse) and spectra with normalized central frequencies $\epsilon_o$ equal to 4.71 (292 kHz) and 3.14 (195 kHz) as shown in Fig. 4. In Fig. 5(*a*) the arrival of the Rayleigh wave at receivers from $x = -5.0$ mm to $x = 5.0$ mm is marked by the dotted line. Since the source is at $x = -8.88$ mm, the wavespeed is 1.7 mm/$\mu$s. From Fig. 2, we can identify the Rayleigh wave speed at normalized central frequency ($k_2H$) 4.71 to be 1.8 mm/$\mu$s. The error of our prediction is 5.5 percent. This is followed by diffracted Rayleigh waves propagating back and forth between the crack tips. In fact, the time of one round trip by these waves can be used also to estimate the length of the crack and this complements the estimate obtained from the resonance frequency. Figure 5(*b*) shows the same feature except that the arrival of the first Rayleigh wave is not as pronounced as in Fig. 4. This is because the frequency of the pulse is fairly low. However, the back and forth propagating Rayleigh wave is still easily discernible. It is thus seen that the crack can be characterized even with a low-frequency pulse. This seems promising, since the composite materials under

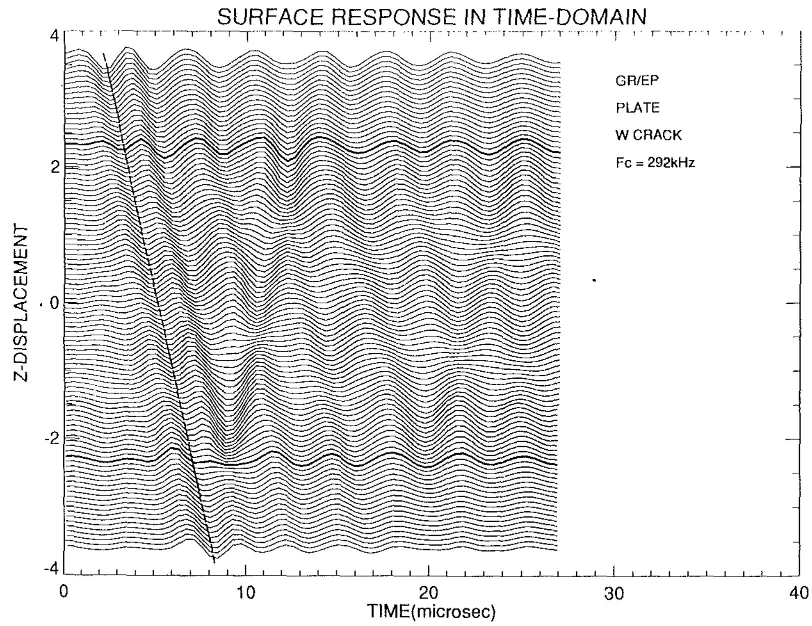


**Fig. 5(*a*) Time-domain surface displacements of Fig. 3(*b*) with Ricker wavelet as incident signal. The normalized central frequency is 4.71.**

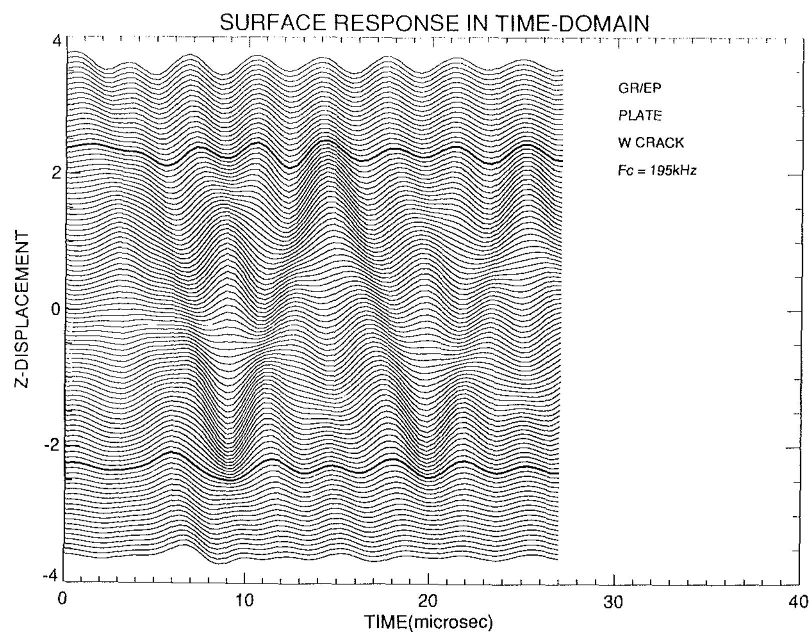


**Fig. 5(*b*) Time-domain surface displacements of Fig. 3(*b*) with Ricker wavelet as incident signal. The normalized central frequency is 3.14.**

consideration are usually very attenuative (in this study attenuation has been neglected).

Figures 6–8 show the frequency dependence of the vertical displacement amplitudes at the origin (point 1, the point right above the crack center), at a point 6.5 H from the source (point 2), and at the epicentral point on the bottom surface (point 3), respectively, in the absence and presence of the crack. The source has impulsive time dependence. The resonance peak at $k_2H = 1.2$ is dominant in Fig. 6, barely visible in Fig. 8 and is absent in Fig. 7. The sharp peaks at the cut-off frequency $k_2H = 1.4\pi$ are quite pronounced in all these figures. It is noted that they are sharper on the topside of plate than at the epicenter. This is perhaps because points 1 and 2 lie along the fiber direction, whereas point 3 is transverse to it, relative to the source. Other features are: The peak at $k_2H = 5.14$ is visible in Fig. 6, but not in the other two; the peak at $k_2H = 1.4\pi$ at point 2 is larger in the absence of the crack than when the crack is present; the peak at $k_2H = \pi$ is visible in Figs. 7 and 8 but absent in Fig. 6. Thus, it may be necessary to make measurements at more than one location in order to capture the defect features.

## Conclusion

In this paper, a hybrid method combining the boundary integral representation and finite element technique has been used to investigate the time-domain response due to waves scattered by a horizontal crack in a transversely isotropic plate. From computed results, we can quantitatively characterize this crack. Thus, the data presented can aid in ultrasonic nondestructive evaluation. In addition, we verify that the plate theory with simply supported ends is a good model in explaining resonance effects of a crack near a free surface if the crack length-to-depth ratio is large.

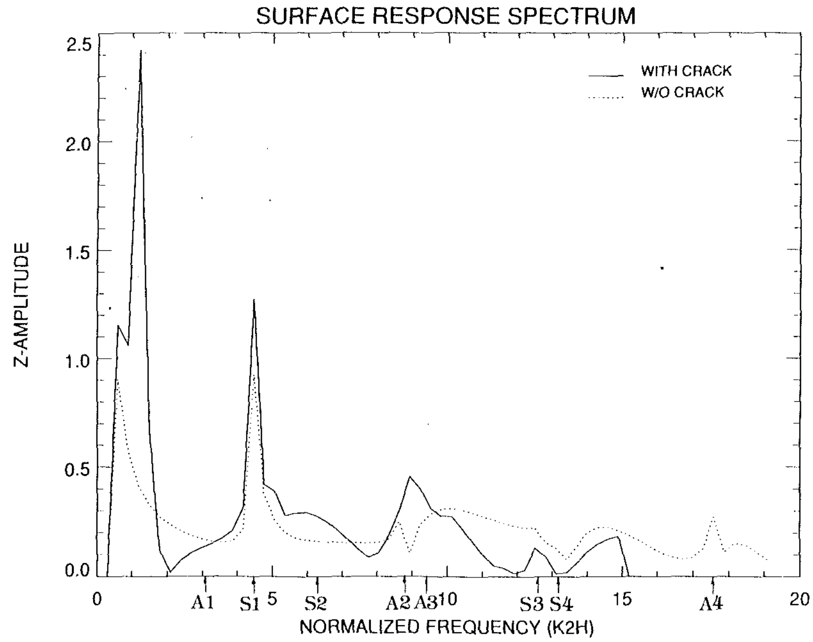


**Fig. 6 Spectrum of surface displacements of a graphite/epoxy plate with and without crack due to an impulsive load. Receiver is at the origin.**

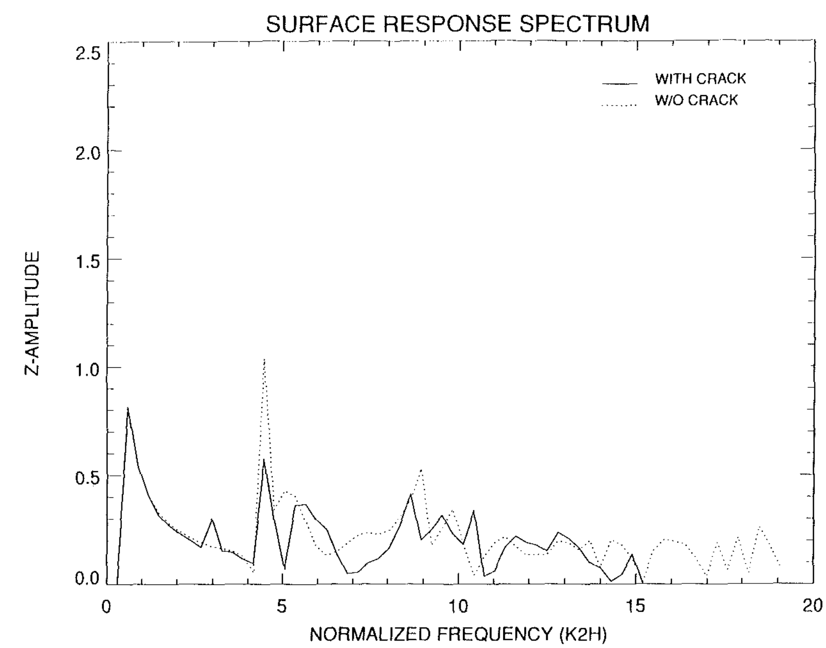


**Fig. 7 Spectrum of surface displacements of a graphite/epoxy plate with and without crack due to an impulsive load. Receiver is at 6.5 H from source on the top surface.**

Since we use singular elements at crack tips, from the crack-opening displacements the stress intensity factors can be calculated. Studies of SIF will be presented in a separate paper.

## Acknowledgments

The work reported here was supported in part by grants from the Office of Naval Research (#N00014-86-K-0280) and NASA (#NAGW-1388).

## References

Ashby, S. F. Manteuffel, T. A., and Saylor, P. E., 1988, "A Taxonomy for Conjugate Gradient Methods," Lawrence Livermore National Laboratory Report UCRL-98508.

Bond, L. J., 1990, "Numerical Techniques and Their Use to Study Wave Propagation and Scattering—A Review," *Proceedings of the IUTAM Symposium on Elastic Wave Propagation and Ultrasonic Evaluation*, pp. 17-27.

Bouden, M., Khair, K. R., and Datta, S. K., 1990, "Ground Motion Amplification by Cylindrical Valleys Embedded in Layered Medium," *Intl. J. Earthquake Eng. Struct. Dyn.*, Vol. 19, pp. 497-512.

Cawley, P., and Theodorakopoulos, C., 1989, "The Membrane Resonance Method of Nondestructive Testing," *Journal of Sound and Vibration*, Vol. 130, No. 2, pp. 299-311.

Datta, S. K., Ledbetter, H. M., Shindo, Y., and Shah, A. H., 1988a, "Phase Velocity and Attenuation of Plane Elastic Waves in a Particle-Reinforced Composite Medium," *Wave Motion*, Vol. 10, No. 2, pp. 171-182.

Datta, S. K., Shah, A. H., Bratton, R. L., and Chakraborty, T., 1988b, "Wave Propagation in Laminated Composite Plates," *Journal of Acoustical Society of America*, Vol. 83, No. 6, pp. 2020-2026.

Fletcher, R., 1976, "Conjugate Gradient Methods for Indefinite Systems,"

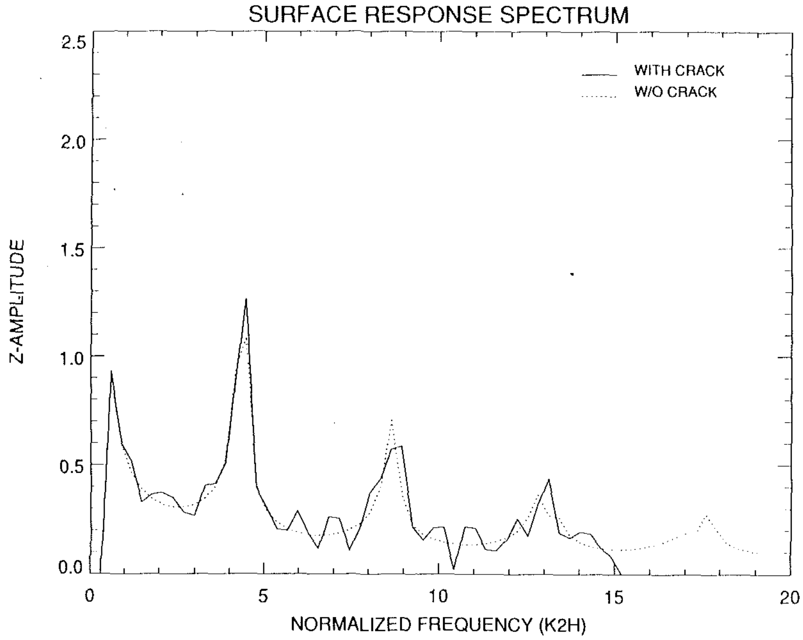


**Fig. 8 Spectrum of surface displacements of a graphite/epoxy plate with and without crack due to an impulsive load. Receiver is located on the bottom surface right below the source position.**


*Numerical Analysis Dundee 1975* (Lecture Notes in Mathematics, No. 506), G. A. Watson, ed., Springer, New York, pp. 73–89.

Franssens, G. R., and Lagasse, P. E., 1984, "Scattering of Elastic Waves by a Cylindrical Obstacle Embedded in a Multilayered Medium," *J. Acoust. Soc. Am.*, Vol. 76, pp. 1535–1542.

Jacobs, D. A., 1980, "Generalizations of the Conjugate Gradient Method for Solving Nonsymmetric and Complex Systems of Algebraic Equations," Tech. Rept., Central Electricity Research Labs., Leatherhead, Surrey, U.K.

Joubert, W. D., and Manteuffel, T. A., 1990, *Iterative Method for Nonsymmetric Linear Systems, in Iterative Methods for Large Linear Systems*, D. R. Kincaid and L. J. Hayes, eds., Academic Press, Boston, pp. 149–171.

Karim, M. R., and Kundu, T., 1988, "Transient Surface Response of Layered Isotropic and Anisotropic Half-Spaces with Interface Cracks: SH Case," *International Journal of Fracture*, Vol. 37, pp. 245–262.

Karim, M. R., Kundu, T., and Desai, C. S., 1989, "Detection of Delamination Cracks in Layered Fiber-Reinforced Composite Plates," *Journal of Pressure Vessel Technology*, Vol. 111, pp. 165–171.

Keer, L. M., Lin, W., and Achenbach, J. D., 1984, "Resonance Effects for a Crack Near a Free Surface," ASME JOURNAL OF APPLIED MECHANICS, Vol. 51, pp. 65–70.

Khair, K. R., Datta, S. K., and Shah, A. H., 1989, "Amplification of Obliquely Incident Seismic Waves by Cylindrical Alluvial Valleys of Arbitrary Cross-Sectional Shape. Part I. Incident P and SV Waves," *Bull. Seism. Soc. Am.*, Vol. 79, pp. 610–630.

Langtangen, H. P., and Tveito, A., 1988, "A Numerical Comparison of Conjugate Gradient-Like Methods," *Communications in Applied Numerical Methods*, Vol. 4, pp. 793–798.

Lanczos, C., 1950, "An Iteration Method for the Solution of the Eigenvalue Problem of Linear Differential and Integral Equations," *J. Res. Nat. Bureau Standards*, Vol. 45, pp. 255–282.

Lanczos, C., 1952, "Solutions of Systems of Linear Equations by Minimized Iterations," *J. Res. Nat. Bureau Standards*, Vol. 49, pp. 33–35.

Liu, S. W., Datta, S. K., Khair, K. R., and Shah, A. H., 1989, "Three-Dimensional Dynamics of Pipelines Buried in Backfilled Trenches due to Oblique Incidence of Body Waves," *Soil Dyn. and Earthquake Eng.*, to be published.

Liu, S. W., and Datta, S. K., 1991, "Time-Domain Response of Ground Surface due to Incident SH Waves," *Computational Mechanics*, Vol. 8, pp. 99–109.

Mal, A. K., 1988, "Wave Propagation in Layered Composite Laminates Under Periodic Surface Loads," *Wave Motion*, Vol. 10, pp. 257–266.

Nayfeh, A. H., and Chimenti, D. E., 1989, "Free Wave Propagation in Plates of General Anisotropic Media," ASME JOURNAL OF APPLIED MECHANICS, Vol. 56, pp. 881–886.

Nour-Omid, B., and Taylor, R. L., 1984, "An Algorithm for Assembly of the Stiffness Matrices into a Compacted Data Structure," *Eng. Comput.*, Vol. 1, pp. 312–316.

Ricker, N. H., 1977, *Transient Waves in Visco-Elastic Media*, Elsevier, Amsterdam.

Rokhlin, S. I., Bolland, T. K., and Adler, L., 1986, "Reflection and Refraction of Elastic Waves on a Plane Interface Between Two Generally Anisotropic Media," *Journal of Acoustical Society of America*, Vol. 79, pp. 906–918.

Saad, Y., 1982, "The Lanczos Biorthogonalization Algorithm and Other Oblique Projection Methods for Solving Large Unsymmetric Systems," *SIAM J. Numer. Anal.*, Vol. 19, pp. 485–506.

Saad, Y., and Schultz, M. H., 1985, "Conjugate Gradient-Like Algorithms for Solving Nonsymmetric Linear Systems," *Mathematics of Computation*, Vol. 44, pp. 417–424.

Sánchez-Sesma, F. J., 1987, "Site Effects on Strong Ground Motion," *Soil Dyn. and Earthquake Eng.*, Vol. 6, pp. 124–132.

Sarkar, T. K., Siarkiewicz, K., and Stratton, R., 1981, "Survey of Numerical Methods for Solution of Large Systems of Linear Equations for Electromagnetic Field Problems," *IEEE Trans. Antennas Propagat.*, Vol. 29, pp. 847–856.

Sarkar, T. K., 1987, "On the Application of the Generalized Biconjugate Gradient Method," *J. Electromagn. Waves and Appls.*, Vol. 1, pp. 223–242.

Sarkar, T. K., Yang, X., and Arvas, E., 1988, "A Limited Survey of Various Conjugate Gradient Methods for Solving Complex Matrix Equations Arising in Electromagnetic Wave Interactions," *Wave Motion*, Vol. 10, pp. 527–546.

Shah, A. H., Wong, K. C., and Datta, S. K., 1982, "Diffraction of Plane SH Waves in a Half-Space," *Intl. J. Earthquake Eng. Struct. Dyn.*, Vol. 10, pp. 519–528.

Wong, Y. S., 1978, *Iterative Methods for Problems in Numerical Analysis*, Ph.D. Dissertation, Oxford University.

Xu, P.-C., and Mal, A. K., 1985, "An Adaptive Integration Scheme for Irregularly Oscillatory Functions," *Wave Motion*, Vol. 7, pp. 235–243.

Xu, P.-C., and Mal, A. K., 1987, "Calculation of the Inplane Green's Functions for a Layered Viscoelastic Solid," *Bull. Seism. Soc. Am.*, Vol. 77, pp. 1823–1837.

**M. Guiggiani**
Researcher,
Dipartimento di Costruzioni
Meccaniche e Nucleari,
Universita di Pisa,
56126 Pisa, Italy

**G. Krishnasamy**[1]
Graduate Student.

**T. J. Rudolphi**
Assoc. Professor.

Department of Aerospace Engineering
and Engineering Mechanics,
Iowa State University,
Ames, IA 50011

**F. J. Rizzo**[2]
Professor and Chairman,
Department of Theoretical
and Applied Mechanics,
University of Illinois
at Urbana-Champaign,
Urbana, IL 61801
Mem. ASME

# A General Algorithm for the Numerical Solution of Hypersingular Boundary Integral Equations

*The limiting process that leads to the formulation of hypersingular boundary integral equations is first discussed in detail. It is shown that boundary integral equations with hypersingular kernels are perfectly meaningful even at non-smooth boundary points, and that special interpretations of the integrals involved are not necessary. Careful analysis of the limiting process has also strong relevance for the development of an appropriate numerical algorithm. In the second part, a new general method for the evaluation of hypersingular surface integrals in the boundary element method (BEM) is presented. The proposed method can be systematically applied in any BEM analysis, either with open or closed surfaces, and with* curved *boundary elements of any kind and order (of course, provided the density function meets necessary regularity requirements at each collocation point). The algorithm operates in the parameter plane of intrinsic coordinates and allows any hypersingular integral in the BEM to be* directly *transformed into a sum of a double and a one-dimensional regular integrals. Since all singular integrations are performed analytically, standard quadrature formulae can be used. For the first time, numerical results are presented for hypersingular integrals on curved (distorted) elements for three-dimensional problems.*

## 1 Introduction

Boundary integral equations with *hypersingular* kernels arise whenever the gradient (or, e.g., the normal derivative) of a classical boundary integral equation is taken. In fact, such equations involve the derivatives of already strongly singular kernels.

So far, the typical field of application of hypersingular equations has been the study of the scattering of waves by thin screens or cracks. In static and dynamic elastic crack analysis, they are sometimes referred to as traction boundary integral equations. However, in many other fields, the reliable application of hypersingular boundary integral equations (HBIE's) would be desirable and useful. To mention but a few, symmetric BIE formulations, design sensitivity analyses, resolution of fictitious eigenfrequencies, plate bending, are all fields that would benefit from, if not require, application of hypersingular boundary integral equations. Moreover, hypersingular BIE's would also allow stresses in elastic (or elastoplastic) problems to be computed directly on the boundary. However, for the most part, HBIE's seem to have been avoided, whenever not actually required in a given problem.

In those cases where the use of such HBIE's appeared unavoidable (e.g., crack problems), several schemes have been devised to lower the order of kernel singularity before numerical treatment.

The integration-by-parts approach has been the most largely pursued (e.g., Sládek and Sládek (1984), Bonnet (1986, 1989), Polch et al. (1987), Nishimura and Kobayashi (1989)). To avoid the hypersingular kernels, some derivatives are shifted from these kernels onto the boundary layers (e.g., crack opening displacement), thus obtaining a formulation in terms of strongly singular kernels. The same final formulae are obtained through other approaches (Zhang and Achenbach, 1989). Bonnet (1986, 1989) also obtained a further regularization for curved three-dimensional cracks by employing a version of Stokes' theorem. However, numerical results are so far available only for flat cracks.

Recently, Krishnasamy et al. (1990) presented another general approach to the numerical treatment of HBIE's. It is essentially based on the conversion of all integrals with hypersingular kernels into a sum of line integrals, surface integrals

[1]Presently, Research Engineer, PDA Engineering, Costa Mesa, CA 92626.
[2]Presently, Professor, Department of Aerospace Engineering and Engineering Mechanics and Center for NDE, Iowa State University, Ames, IA 50011.

Contributed by the Applied Mechanics Division of THE AMERICAN SOCIETY OF MECHANICAL ENGINEERS for publication in the JOURNAL OF APPLIED MECHANICS.

Discussion on this paper should be addressed to the Technical Editor, Prof. Leon M. Keer, The Technological Institute, Northwestern University, Evanston, IL 60208, and will be accepted until four months after final publication of the paper itself in the JOURNAL OF APPLIED MECHANICS.

Manuscript received by the ASME Applied Mechanics Division, Apr. 27, 1990; final revision, Feb. 11, 1991. Associate Technical Editor: A. K. Noor.

with a less singular integrand, and a solid angle. The conversion is achieved through Stokes' theorem, and it is performed before any discretization. Since no integration by parts is performed, the problem is still formulated in terms of the original variables. Numerical results are presented for flat cracks.

In Budreck and Achenbach (1988) the regularization is achieved through divergence theorem, but it is carried out after discretization of the traction integral equation. However, this method is applicable only on flat cracks and allows only one collocation point per element (usually, constant approximation).

Another regularization of HBIE's can be achieved by the use of known elementary solutions of the governing equation, as suggested by Rudolphi (1990, 1991). Basically, this approach can be regarded as the extension of the well-known rigid-body motion approach for standard BIE's. While very attractive in some cases, this method fails when dealing with open surfaces as it is the case in crack analysis.

In the present paper a different idea is pursued. It is demonstrated that all hypersingular integrals arising in the boundary element method (BEM) can be *directly* transformed into ordinary (regular) integrals in the parameter plane of intrinsic coordinates through simple (although rigorous) manipulations.

The method is absolutely general and has proved to be very effective. All singular integrations are performed *analytically*, and standard quadrature formulae are used only for regular integrals. For the first time, numerical results are presented for hypersingular integrals on *curved* elements.

The proposed method can be regarded as the extension to hypersingular integrals of the method developed by Guiggiani and Gigante (1990) for integrals with a strong singularity, also typical in the BEM.

First, however, a novel (careful) analysis of the limiting process involved in any singular boundary integral equation is presented. It provides some important theoretical insights, and has strong relevance for the development of the numerical method mentioned previously.

## 2 Derivation of Hypersingular Boundary Integral Equations

In this section the limiting process to obtain HBIE's at (in general) nonsmooth boundary point is described in an attempt to clarify some still possibly obscure points. It is also a necessary preamble to the derivation of the numerical method that forms the subject of the next section.

For the sake of brevity and clarity, analysis is hereafter restricted to three-dimensional potential problems (Laplace operator). However, all results are applicable to any other scalar or vector elliptic problem since only the order of singularity is relevant. When appropriate, the corresponding equations for vector problems (such as static or time-harmonic elasticity) will be also provided.

Let us first consider the well-known standard boundary integral equation for the harmonic function $u(\mathbf{x})$ on a three-dimensional domain $\Omega$, bounded by the regular surface $S$ (Kellog, 1929) with unit outward normal $\boldsymbol{n}(\mathbf{x}) = \{n_i\}$ (Fig. 1)

$$\lim_{\epsilon \to 0^+} \left\{ \int\!\!\int_{(S-e_\epsilon)+s_\epsilon} [T(\mathbf{y}, \mathbf{x})u(\mathbf{x}) - U(\mathbf{y}, \mathbf{x})q(\mathbf{x})] dS_x \right\} = 0, \quad (1)$$

where $q = \partial u / \partial n = u_{,i} n_i$ denotes the normal derivative of the potential. The kernel functions $U$ and $T$ represent the fundamental solution and its normal derivative, respectively.

If $r = [(x_i - y_i)(x_i - y_i)]^{1/2}$ denotes the distance between the source point $\mathbf{y}$ and integration point $\mathbf{x}$, the fundamental solution $U$ has a weak singularity of order $r^{-1}$, when $r \to 0$, while the other kernel function $T = \partial U / \partial n(\mathbf{x})$ has a strong singularity of order $r^{-2}$.

Since in Eq. (1) both the source point $\mathbf{y} = \{y_i\}$ and the integration point $\mathbf{x} = \{x_i\}$ lie on the surface $S$, a limiting process is necessary. Actually, since Eq. (1) stems from Green's second identity, it may be only formulated on a domain not including the singular point $\mathbf{y}$. The situation is exemplified in Fig. 1, where a (vanishing) neighborhood $v_\epsilon$ of $\mathbf{y}$ has been removed from the original domain $\Omega$. The integration is thus performed on the boundary $S_\epsilon = (S - e_\epsilon) + s_\epsilon$ of the new domain $\Omega_\epsilon = \Omega - v_\epsilon$ (Fig. 1). Of course, the integration must be done before taking the limit. Since Eq. (1) already states that the value of the overall limit is zero, we may expect that all divergent parts (if any) will be cancelled out in the end.

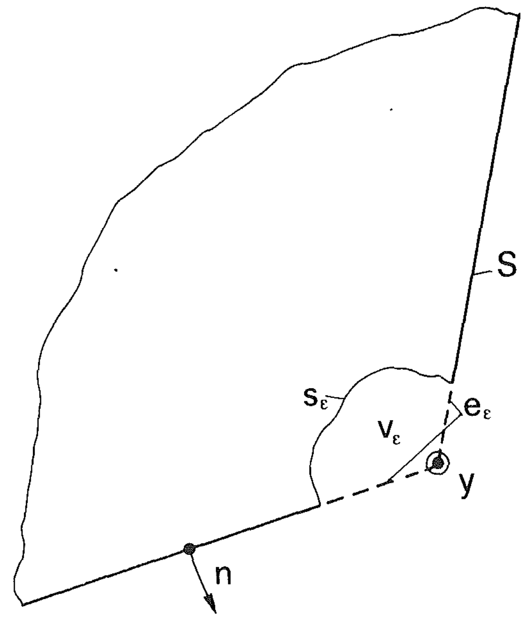

Fig. 1 General vanishing neighborhood around the source point

Notice that it is not necessary to restrict the shape of $v_\epsilon$. It may have any shape, provided $\mathbf{y}$ is an exterior point for $\Omega_\epsilon$ and $S_\epsilon$ is a regular surface in the sense of Kellog (1929). Equation (1) is the Green's second identity for the two harmonic functions $u$ and $U$ on $\Omega_\epsilon$.

Therefore, it is *not necessary* to take a sphere (a circle in two dimensions) to exclude the point $\mathbf{y}$. A sphere is merely the most convenient shape because it simplifies the analytical manipulations, but its selection does not affect the final result, that is the value of the limit (see also, Rudolphi et al. (1988) and Brockett et al. (1989)). This is to say that the choice of a sphere is not at all mandatory, and, accordingly, a priori "interpretations" (e.g., in the principal value sense) are not actually necessary when dealing with singular BIE's.

However, once the shape of the vanishing neighborhood $v_\epsilon$ has been selected, both $e_\epsilon$ and $s_\epsilon$ are uniquely determined (Fig. 1), and their shapes must be preserved while $\epsilon \to 0^+$ (we assume that the maximum chord of $v_\epsilon$ approaches 0 when $\epsilon \to 0$). More importantly, the shape of $e_\epsilon$ must be *consistent* with the shape of $s_\epsilon$ throughout the process. Any violation (for example, due to the discretization process) would lead to erroneous results, as pointed out in Guiggiani and Gigante (1990).

Since all functions of $\mathbf{y}$ in Eq. (1) are regular ($U$, $T \in C^\infty$, on $\Omega - v_\epsilon$), we can differentiate it with respect to any coordinate $y_i$ of the source point, thus obtaining

$$\lim_{\epsilon \to 0^+} \left\{ \int\!\!\int_{(S-e_\epsilon)+s_\epsilon} [V_i(\mathbf{y}, \mathbf{x})u(\mathbf{x}) - W_i(\mathbf{y}, \mathbf{x})q(\mathbf{x})] dS_x \right\} = 0, \quad (2)$$

where

$$W_i = \frac{\partial U}{\partial y_i},$$

$$V_i = \frac{\partial T}{\partial y_i} = \frac{\partial U}{\partial x_k \partial y_i} n_k(\mathbf{x}). \quad (3)$$

For instance, for three-dimensional potential problems, we have

$$W_i(\mathbf{y}, \mathbf{x}) = \frac{1}{4\pi r^2} r_{,i},$$

$$V_i(\mathbf{y}, \mathbf{x}) = -\frac{1}{4\pi r^3}\left[3r_{,i}\frac{\partial r}{\partial n} - n_i\right], \quad (4)$$

where $r_{,i} = \partial r/\partial x_i = -\partial r/\partial y_i$. As expected, the kernel $W_i$ shows a *strong* singularity of order $r^{-2}$ while the kernel $V_i$ is *hypersingular* of order $r^{-3}$, as $r \to 0$.

Now, we assume that the potential $u \in C^{1,\alpha}$, at $\mathbf{y}$, that is, $u$ is differentiable at $\mathbf{y}$, with its first derivatives satisfying a Hölder condition. Accordingly, the potential $u(\mathbf{x})$ and its normal derivative $q(\mathbf{x})$ can be represented by the following expansions:

$$u(\mathbf{x}) = u(\mathbf{y}) + u_{,k}(\mathbf{y})(x_k - y_k) + O(r^{1+\alpha}),$$

$$q(\mathbf{x}) = u_{,k}(\mathbf{x}) n_k(\mathbf{x}) = u_{,k}(\mathbf{y}) n_k(\mathbf{x}) + O(r^\alpha), \quad (5)$$

where $\alpha$ is a positive constant (usually, $\alpha = 1$). This fact has also relevance in the selection of the discretization scheme, as it has to satisfy the same regularity requirements ($u \in C^{1,\alpha}$, and $q \in C^{0,\alpha}$) at each collocation point (see next). As also stated, e.g., in Martin and Rizzo (1989) and Krishnasamy et al. (1990), these continuity requirements are demanded by the nature of the hypersingularity, no matter what method is used.

By adding and subtracting in (2) the relevant terms of expansions (5), a more convenient form of the HBIE (2) is obtained as

$$\lim_{\epsilon \to 0^+} \left\{ \int_{(S-e_\epsilon)} [V_i(\mathbf{y}, \mathbf{x}) u(\mathbf{x}) - W_i(\mathbf{y}, \mathbf{x}) q(\mathbf{x})] dS_x \right.$$

$$+ \int_{s_\epsilon} (V_i[u(\mathbf{x}) - u(\mathbf{y}) - u_{,k}(\mathbf{y})(x_k - y_k)]$$

$$- W_i[q(\mathbf{x}) - u_{,k}(\mathbf{y}) n_k(\mathbf{x})]) dS_x + u(\mathbf{y}) \int_{s_\epsilon} V_i dS_x$$

$$\left. + u_{,k}(\mathbf{y}) \int_{s_\epsilon} [V_i(x_k - y_k) - W_i n_k(\mathbf{x})] dS_x \right\} = 0. \quad (6)$$

Since we have to manipulate Eq. (6), we select the most convenient shape for $s_\epsilon$, that is a sphere centered at $\mathbf{y}$ and of radius $\epsilon$. The selected shape of $s_\epsilon$ also enforces the shape of $e_\epsilon$, which becomes a symmetric neighborhood on $S$ around the singular point $\mathbf{y}$ (Fig. 1). Although the value of the limit taken as a whole in either Eqs. (2) or (6) is completely independent on the selected shape of $v_\epsilon$, the value of each term in (6), taken separately, does actually depend upon the shape of either $e_\epsilon$ or $s_\epsilon$.

Since $s_\epsilon$ is a sphere, the limits of all integrals on $s_\epsilon$ in (6) can be evaluated explicitly. Because of the expansions (5) and since $dS_x = O(\epsilon^2)$ on $s_\epsilon$, it follows that

$$\lim_{\epsilon \to 0^+} \int_{s_\epsilon} (V_i[u(\mathbf{x}) - u(\mathbf{y}) - u_{,k}(\mathbf{y})(x_k - y_k)]$$

$$- W_i[q(\mathbf{x}) - u_{,k}(\mathbf{y}) n_k(\mathbf{x})]) dS_x = 0, \quad (7)$$

so that we only have to consider the limit of the other integrals on $s_\epsilon$. They are given by (see Appendix A for a detailed derivation when $\mathbf{y}$ is at a corner point)

$$\lim_{\epsilon \to 0^+} \int_{s_\epsilon} [V_i(x_k - y_k) - W_i n_k(\mathbf{x})] dS_x = c_{ik}(\mathbf{y}), \quad (8)$$

and

$$\lim_{\epsilon \to 0^+} \int_{s_\epsilon} V_i dS_x = \lim_{\epsilon \to 0} \frac{b_i(\mathbf{y})}{\epsilon}, \quad (9)$$

where $c_{ik}$ and $b_i$ are (bounded) coefficients that only depend upon the local geometry of $S$ at $\mathbf{y}$. A few comments are in order here.

The coefficients $c_{ik}(\mathbf{y})$ are the *free-term coefficients* of the hypersingular boundary integral equation for the potential derivatives. Indeed, they are multiplied by $u_{,k}(\mathbf{y})$ in Eq. (6). Notice that, in general, both kernels $W_i$ and $V_i$ in (8) contribute to them (see Appendix A). At smooth boundary points, the free-term coefficients simply become $c_{ik} = 0.5\,\delta_{ik}$.

On the other hand, Eq. (9) states that the limit on $s_\epsilon$ of the integral of $V_i$ is either zero or unbounded, depending on the value of $b_i(\mathbf{y})$. It is shown in Appendix A that $b_i = 0$ if $\mathbf{y}$ is an internal point for $\Omega$. If $\mathbf{y}$ is a boundary point, then $b_i \neq 0$ (in general), and the limit in (9) is unbounded of order $\epsilon^{-1}$. However, this problem is only apparent and it causes no trouble. As a matter of fact, the apparent inconsistency arose only because we artificially separated the integrals on $s_\epsilon$ from the integral on $(S - e_\epsilon)$. If they are considered *together* as they are in the original Eq. (6), no unbounded quantities arise at all, as will be shown below. The separation into integrals on $s_\epsilon$ and on the remaining surface $(S - e_\epsilon)$ is allowed only when each single term remains bounded by itself, which is not always the case in HBIE's.

According to the analysis above, the hypersingular boundary integral equation for scalar problems can be written in the following form:

$$c_{ik}(\mathbf{y}) u_{,k}(\mathbf{y}) + \lim_{\epsilon \to 0^+} \left\{ \int_{(S-e_\epsilon)} [V_i(\mathbf{y}, \mathbf{x}) u(\mathbf{x}) \right.$$

$$\left. - W_i(\mathbf{y}, \mathbf{x}) q(\mathbf{x})] dS_x + u(\mathbf{y}) \frac{b_i(\mathbf{y})}{\epsilon} \right\} = 0. \quad (10)$$

A similar HBIE may be obtained for vector problems, such as elasticity (either two-dimensional, three-dimensional, or axisymmetric)

$$c_{ikjh}(\mathbf{y}) u_{j,h}(\mathbf{y}) + \lim_{\epsilon \to 0^+} \left\{ \int_{(S-e_\epsilon)} [V_{ikj}(\mathbf{y}, \mathbf{x}) u_j(\mathbf{x}) \right.$$

$$\left. - W_{ikj}(\mathbf{y}, \mathbf{x}) t_j(\mathbf{x})] dS_x + u_j(\mathbf{y}) \frac{b_{ikj}(\mathbf{y})}{\epsilon} \right\} = 0, \quad (11)$$

where $u_j$ and $t_j$ are the displacement and traction components, respectively. Once again, if $\mathbf{y}$ is a smooth boundary point (and $s_\epsilon$ had a spherical shape), the free term in (11) simply reduces to $0.5\,\delta_{ij}\delta_{kh} u_{j,h}(\mathbf{y}) = 0.5 u_{i,k}(\mathbf{y})$. The kernels in (11) are obtained by differentiating with respect to $y_k$ the corresponding kernels in the standard BIE: $W_{ikj} = \partial U_{ij}(\mathbf{y}, \mathbf{x})/\partial y_k$, and $V_{ikj} = \partial T_{ij}(\mathbf{y}, \mathbf{x})/\partial y_k$. Their expressions for elastic problems are given in Appendix B. Equations like (11) can be used to compute all displacement derivatives $u_{i,j}(\mathbf{y})$ at any boundary point, which allows for the evaluation of the whole stress tensor $\sigma_{ij}(\mathbf{y})$ *directly on the boundary*. Additional information on HBIE's for vector problems are provided in Guiggiani et al. (1991).

In Eqs. (10) and (11) the limiting process is still indicated explicitly. This differs from common practice wherein the notation and names Cauchy principal value and Hadamard finite part are introduced, as could be easily done here as well. We choose not to do so here, however, since the explicit expressions in (10) and (11) may perhaps have clearer meaning. We also show thereby that such names and notation, however useful to some, are not necessary in the derivation of (10) and (11).

The numerical treatment proceeds *directly* from equations

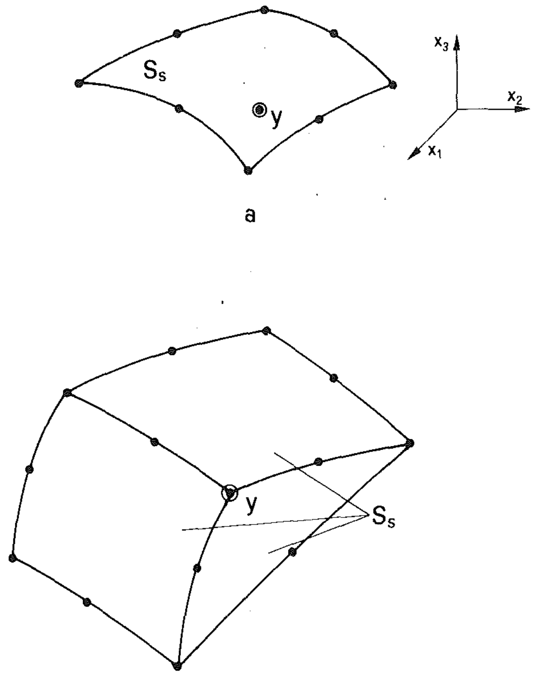


Fig. 2 (*a*) Source point on one element; (*b*) adjacent elements connected to the source point

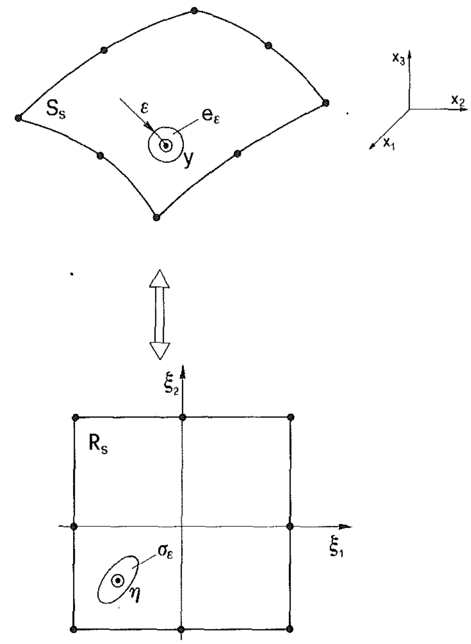


Fig. 3 Image in the parameter plane of the boundary element and of the vanishing neighborhood

in the form of (10) or (11). Care will be exercised to preserve the features of the limiting process when the discretization of the geometry is introduced.

## 3 Numerical Evaluation of Hypersingular Integrals

As mentioned previously, our goal is the evaluation of the bounded quantity

$$\lim_{\epsilon \to 0^+} \left\{ \int_{(S-e_\epsilon)} [V_i(\mathbf{y}, \mathbf{x}) u(\mathbf{x}) - W_i(\mathbf{y}, \mathbf{x}) q(\mathbf{x})] dS_x + u(\mathbf{y}) \frac{b_i(\mathbf{y})}{\epsilon} \right\}, \quad (12)$$

where $W_i = O(r^{-2})$ and $V_i = O(r^{-3})$, and, consistently with the already obtained $c_{ik}(\mathbf{y})$ and $b_i(\mathbf{y})$, the neighborhood $e_\epsilon$ around $\mathbf{y}$ on $S$ is given by

$$e_\epsilon = \{\mathbf{x} \in S \mid |\mathbf{x} - \mathbf{y}| \le \epsilon\}. \quad (13)$$

Our goal can be splitted into the evaluation of

$$\lim_{\epsilon \to 0^+} \left\{ -\int_{(S-e_\epsilon)} W_i(\mathbf{y}, \mathbf{x}) q(\mathbf{x}) dS_x \right\}, \quad (14)$$

and

$$\lim_{\epsilon \to 0^+} \left\{ \int_{(S-e_\epsilon)} V_i(\mathbf{y}, \mathbf{x}) u(\mathbf{x}) dS_x + u(\mathbf{y}) \frac{b_i(\mathbf{y})}{\epsilon} \right\}. \quad (15)$$

Since $W_i$ is only strongly singular, the evaluation of (14) can be achieved by the direct method proposed by Guiggiani and Gigante (1990) (see also Guiggiani, 1992a). On the other hand, due to the hypersingularity of $V_i$, a new method is needed for the evaluation of expression (15).

We denote that portion of $S$ containing the singular point $\mathbf{y}$ by $S_s$. If discontinuous elements with collocation at element interiors are used, then $S_s$ consists of just one element (Fig. 2(*a*)); whereas if $C^{1,\alpha}$-continuous element are used to represent $u$, $S_s$ consists of all adjacent elements connected to the singular point $\mathbf{y}$ (Fig. 2(*b*)). At present, the development of general $C^{1,\alpha}$-continuous elements for three-dimensional problems seems problematic. Therefore, we restrict ourselves to cases in which $\mathbf{y}$ belongs to just one boundary element. However, our analysis is equally applicable to the other case and the final formula will be given for both cases.

As usual, on each boundary element, the potential is represented by shape functions $N^c(\xi_1, \xi_2)$ of local intrinsic coordinates $\xi = (\xi_1, \xi_2)$, so that $u(\mathbf{x}) = \Sigma_c N^c[\xi(\mathbf{x})]u^c$. Therefore, from a computational standpoint, the subgoal (15) actually results into the evaluation of the integral $I$ defined on the element(s) $S_s$

$$I = \lim_{\epsilon \to 0^+} \left\{ \int_{(S_s-e_\epsilon)} V_i(\mathbf{y}, \mathbf{x}) N^a(\xi(\mathbf{x})) dS_x + N^a(\eta) \frac{b_i(\mathbf{y})}{\epsilon} \right\}, \quad (16)$$

where $N^a$ represents those shape functions (usually just one) that are not zero at $\eta$, the image in the parameter plane of the collocation point $\mathbf{y}$ (quite often, $N^a(\eta) = 1$, although with hierarchical elements this might not be necessarily the case).

By means of the usual representation for the geometry in terms of shape functions and nodal coordinates

$$x_k(\xi) = \sum_c M^c(\xi) x_k^c, \quad k = 1, 2, 3, \quad (17)$$

the boundary element $S_s$ is mapped onto a region $R_s$ of standard shape in the parameter plane (usually, a square, or a right triangle). Accordingly, the neighborhood $e_\epsilon$ of $\mathbf{y}$ in the three-dimensional space is mapped onto a neighborhood $\sigma_\epsilon$ of $\eta$ in the parameter plane (Fig. 3). It is important to note that, in general, $\sigma_\epsilon$ is not necessarily a circle. In the parameter plane of intrinsic coordinates, expression (16) becomes

$$I = \lim_{\epsilon \to 0^+} \left\{ \int_{R_s - \sigma_\epsilon} V_i(\mathbf{y}, \mathbf{x}(\xi)) N^a(\xi) J(\xi) d\xi_1 d\xi_2 + N^a(\eta) \frac{b_i(\mathbf{y})}{\epsilon} \right\}, \quad (18)$$

where $dS_x = J(\xi) d\xi_1 d\xi_2$. It is worth noting that, provided the $N^a[\xi(\mathbf{x})]$ for $u$ are $C^{1,\alpha}$-continuous at $\mathbf{y}$, the boundary elements can be of any kind and order.

Following a common practice in the BEM, polar coordinates $(\rho, \theta)$ centered at $\eta$ (the image of $\mathbf{y}$) are defined in the parameter plane (Fig. 4)

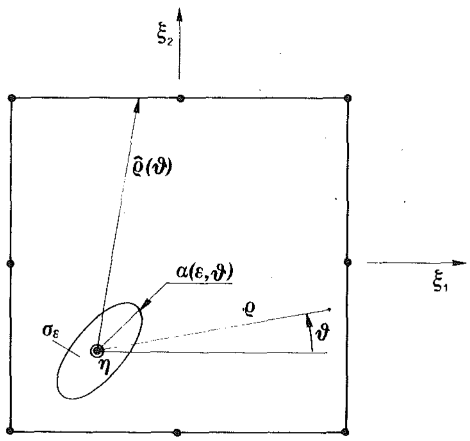


**Fig. 4 Polar coordinates in the parameter plane**

$$\begin{cases} \xi_1 = \eta_1 + \rho \cos\theta \\ \xi_2 = \eta_2 + \rho \sin\theta \end{cases} \tag{19}$$

so that $d\xi_1 d\xi_2 = \rho d\rho d\theta$. Hence, from (18) and (19) we obtain

$$I = \lim_{\epsilon \to 0^+} \left\{ \int_0^{2\pi} \int_{\alpha(\epsilon,\theta)}^{\hat{\rho}(\theta)} F(\rho, \theta) d\rho d\theta + N^a(\eta) \frac{b_i(\mathbf{y})}{\epsilon} \right\}, \tag{20}$$

where $F(\rho, \theta) = V_i N^\alpha J \rho = O(\rho^{-2})$ is the hypersingular integrand, $\rho = \alpha(\epsilon, \theta)$ is the equation in polar coordinates of $\sigma_\epsilon$ (Fig. 4), and $\rho = \hat{\rho}(\theta)$ is the equation in polar coordinates of the external contour of the parameter domain $R_s$ (Fig. 4).

Now, let us analyze the singular function $F(\rho, \theta)$. Since it is singular of order $\rho^{-2}$, we have a (Laurent) series expansion with respect to $\rho$ in the form

$$F(\rho, \theta) = \frac{F_{-2}(\theta)}{\rho^2} + \frac{F_{-1}(\theta)}{\rho} + O(1). \tag{21}$$

Notice that both $F_{-2}$ and $F_{-1}$ are just real functions of $\theta$ (even when $F(\rho, \theta)$ is complex valued, as in time-harmonic problems). The dependence on $\theta$ is crucial for expansion (21) to actually represent the asymptotic behavior of $F(\rho, \theta)$, when $\rho \to 0$. Expansion (21) is one of the key ingredients of the present analysis.

Also of basic relevance is the Taylor series expansion for $\alpha(\epsilon, \theta)$, with respect to $\epsilon$

$$\rho = \alpha(\epsilon, \theta) = \epsilon\beta(\theta) + \epsilon^2\gamma(\theta) + O(\epsilon^3). \tag{22}$$

Note that, in general, $\rho = \epsilon\beta(\theta)$ is the equation of an ellipse (Fig. 4).

A systematic way of obtaining the explicit expressions of $F_{-2}(\theta)$, $F_{-1}(\theta)$, $\beta(\theta)$ and $\gamma(\theta)$ is presented in Appendix C. Although, at first, it may seem quite a difficult task, it is shown that they can be easily and systematically obtained for any kernel function and for any kind of boundary element.

Adding and subtracting the first two terms of the series expansion (21) in expression (20), we obtain

$$\begin{aligned} I = \lim_{\epsilon \to 0^+} \Bigg\{ & \int_0^{2\pi} \int_{\alpha(\epsilon,\theta)}^{\hat{\rho}(\theta)} \left[ F(\rho, \theta) - \left( \frac{F_{-2}(\theta)}{\rho^2} + \frac{F_{-1}(\theta)}{\rho} \right) \right] d\rho d\theta \\ & + \int_0^{2\pi} \int_{\alpha(\epsilon,\theta)}^{\hat{\rho}(\theta)} \frac{F_{-1}(\theta)}{\rho} d\rho d\theta \\ & + \int_0^{2\pi} \int_{\alpha(\epsilon,\theta)}^{\hat{\rho}(\theta)} \frac{F_{-2}(\theta)}{\rho^2} d\rho d\theta + N^a(\eta) \frac{b_i(\mathbf{y})}{\epsilon} \Bigg\} = \\ & = I_0 + I_{-1} + I_{-2}. \end{aligned} \tag{23}$$

Each term $I_0$, $I_{-1}$, and $I_{-2}$ in (23) is now analyzed separately.

According to Eq. (21), in $I_0$ the integrand is *regular*. Therefore, the limit is straightforward and simply becomes

$$I_0 = \int_0^{2\pi} \int_0^{\hat{\rho}(\theta)} \left[ F(\rho, \theta) - \left( \frac{F_{-2}(\theta)}{\rho^2} + \frac{F_{-1}(\theta)}{\rho} \right) \right] d\rho d\theta. \tag{24}$$

This double integral can be evaluated by standard quadrature rules.

Now, let us consider $I_{-1}$ and integrate to get

$$\begin{aligned} I_{-1} &= \lim_{\epsilon \to 0^+} \int_0^{2\pi} \int_{\alpha(\epsilon,\theta)}^{\hat{\rho}(\theta)} \frac{F_{-1}(\theta)}{\rho} d\rho d\theta \\ &= \lim_{\epsilon \to 0^+} \int_0^{2\pi} F_{-1}(\dot{\theta}) [\ln|\hat{\rho}(\theta)| - \ln|\alpha(\epsilon, \theta)|] d\theta \\ &= \int_0^{2\pi} F_{-1}(\theta) \ln|\hat{\rho}(\theta)| d\theta - \lim_{\epsilon \to 0^+} \int_0^{2\pi} F_{-1}(\theta) \ln|\epsilon\beta(\theta)| d\theta \\ &= \int_0^{2\pi} F_{-1}(\theta) \ln\left|\frac{\hat{\rho}(\theta)}{\beta(\theta)}\right| d\theta - \lim_{\epsilon \to 0^+} \left\{ \ln\epsilon \int_0^{2\pi} F_{-1}(\theta) d\theta \right\} \\ &= \int_0^{2\pi} F^{-1}(\theta) \ln\left|\frac{\hat{\rho}(\theta)}{\beta(\theta)}\right| d\theta. \end{aligned} \tag{25}$$

Equation (25) shows that $I_{-1}$ is equivalent to a simple *regular* one-dimensional integral. In the derivation of this equation, first we integrated *analytically* with respect to $\rho$ (i.e., the singular part), then we made use of expansion (22) for $\alpha(\epsilon, \theta)$, and, finally, we considered the property $\int_0^{2\pi} F_{-1}(\theta) d\theta = 0$. This property obviously follows from inspection of $F_{-1}(\theta)$, since $F_{-1}(\theta) = -F_{-1}(\theta + \pi)$, as shown in Appendix C. However, the fact that the above integral must vanish need not be shown explicitly for each case. Indeed, if the integral from 0 to $2\pi$ of $F_{-1}(\theta)$ were not zero, the last limit in (25) would be unbounded, which leads to a contradiction since $I$ has been shown to be bounded (it follows from the validity of the second Green identity on $\Omega_\epsilon$, on which everything here is based). A similar statement can also be found in Guiggiani and Gigante (1990).

A similar treatment applies to $I_{-2}$ such that

$$\begin{aligned} I_{-2} &= \lim_{\epsilon \to 0^+} \left\{ \int_0^{2\pi} \int_{\alpha(\epsilon,\theta)}^{\hat{\rho}(\theta)} \frac{F_{-2}(\theta)}{\rho^2} d\rho d\theta + N^a(\eta) \frac{b_i(\mathbf{y})}{\epsilon} \right\} \\ &= \lim_{\epsilon \to 0^+} \left\{ \int_0^{2\pi} F_{-2}(\theta) \left[ -\frac{1}{\hat{\rho}(\theta)} + \frac{1}{\alpha(\epsilon,\theta)} \right] d\theta + N^a(\eta) \frac{b_i(\mathbf{y})}{\epsilon} \right\} \\ &= \lim_{\epsilon \to 0^+} \left\{ \int_0^{2\pi} \frac{F_{-2}(\theta)}{\epsilon\beta(\theta)} \left( 1 - \epsilon \frac{\gamma(\theta)}{\beta(\theta)} \right) d\theta + N^a(\eta) \frac{b_i(\mathbf{y})}{\epsilon} \right\} \\ &\qquad - \int_0^{2\pi} \frac{F_{-2}(\theta)}{\hat{\rho}(\theta)} d\theta \\ &= \lim_{\epsilon \to 0^+} \left( \frac{1}{\epsilon} \right) \left\{ \int_0^{2\pi} \frac{F_{-2}(\theta)}{\beta(\theta)} d\theta + N^a(\eta) b_i(\mathbf{y}) \right\} \\ &\qquad - \int_0^{2\pi} F_{-2}(\theta) \left[ \frac{\gamma(\theta)}{\beta^2(\theta)} + \frac{1}{\hat{\rho}(\theta)} \right] d\theta \\ &= -\int_0^{2\pi} F_{-2}(\theta) \left[ \frac{\gamma(\theta)}{\beta^2(\theta)} + \frac{1}{\hat{\rho}(\theta)} \right] d\theta. \end{aligned} \tag{26}$$

Therefore, $I_{-2}$ is also equivalent to just a one-dimensional *regular* integral. Owing to the higher order of singularity of the integrand (cf. (25)), in this case both terms $\epsilon\beta(\theta)$ and $\epsilon^2\gamma(\theta)$ in the expansion (22) for $\alpha(\epsilon, \theta)$ were relevant. As a general rule, the higher the order of singularity, the larger is the number of terms that have relevance.

Interestingly enough, the singularity cancellation we have been speaking about is made explicit in (26). The unbounded term $N^a b_i/\epsilon$ due to an integral on $s_\epsilon$ (see (9)) is cancelled out by a corresponding unbounded term arising from the integral

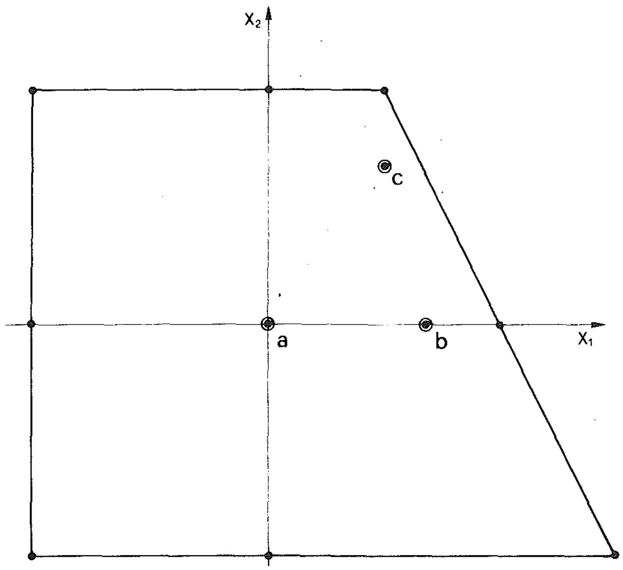


Fig. 5 Plane distorted element and collocation points

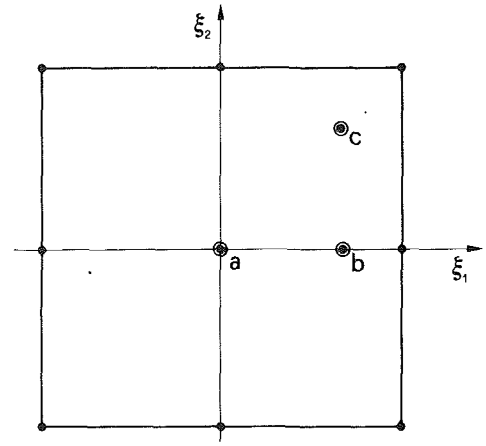


Fig. 6 Image in the parameter plane

on $(S_s - e_\epsilon)$, so that the final result is perfectly bounded and meaningful. This cancellation is strictly related to the nature of the kernels involved, in the sense that the kernels must be obtained from the fundamental solution of the problem under consideration through application of the proper differential operators. For instance, in potential problems (Laplace equation) it only occurs if both terms within square brackets in the hypersingular kernel function (4) are considered together.

It is worth noting that in (25) and (26) the use of the expansion for $F(\rho, \theta)$ allowed all singular integrations to be carried out *analytically*. Furthermore, the expansion for $\alpha(\epsilon, \theta)$ allowed all limiting processes to be performed *exactly*.

**3.1 Final Formula for Hypersingular Surface Integrals.** By collecting the previous results, the following final formula for the evaluation of hypersingular integrals in three-dimensional BEM analyses can be given

$$I = \int_0^{2\pi} \int_0^{\hat{\rho}(\theta)} \left\{ F(\rho, \theta) - \left[ \frac{F_{-2}(\theta)}{\rho^2} + \frac{F_{-1}(\theta)}{\rho} \right] \right\} d\rho d\theta$$
$$+ \int_0^{2\pi} \left\{ F_{-1}(\theta) \ln \left| \frac{\hat{\rho}(\theta)}{\beta(\theta)} \right| - F_{-2}(\theta) \left[ \frac{\gamma(\theta)}{\beta^2(\theta)} + \frac{1}{\hat{\rho}(\theta)} \right] \right\} d\theta. \quad (27)$$

Expression (27) is the fundamental result of the present paper. It proves that the quantity $I$, originally given by a limiting process involving a hypersingular integral plus an unbounded term (see (16), and also (18), (20), and (23)), is simply equal to a regular double integral plus a regular one-dimensional integral. Notice that no approximations have been introduced in the derivation of expression (27) from the original statement (16).

The terms containing $\hat{\rho}(\theta)$ takes into account the external shape of $R_s$, while the terms with $\beta(\theta)$ and $\gamma(\theta)$ account for the *distortion* of $\sigma_\epsilon$, which is introduced by the mapping of the original neighborhood $e_\epsilon$ (Figs. 3 and 4).

Since we selected a symmetric shape for $e_\epsilon$, we have in (27) that $\int_0^{2\pi} F_{-1}(\theta) \ln |\beta(\theta)| d\theta = 0$ and $\int_0^{2\pi} F_{-2}(\theta)[\gamma(\theta)/\beta^2(\theta)] d\theta = 0$. However, the same does not hold for more general shapes of $e_\epsilon$.

Both integrals in (27) are in polar coordinates defined in the parameter plane, which allows for a standard numerical implementation. As shown in Section 4 on numerical examples, standard Gaussian quadrature rules of low order provide very good accuracy.

Formula (27) is fully general. It holds for any kind of boundary elements employed. Moreover, a similar formula (which formally looks exactly the same) can be given for any hypersingular boundary integral equation, either for scalar or vector problems. As a matter of fact, all functions involved can be systematically obtained as shown in Appendix C.

If the singular point is shared by more than one element as in Fig. 2(*b*), formula (27) becomes

$$I = \sum_m \left\{ \int_{\theta_1^m}^{\theta_2^m} \int_0^{\hat{\rho}^m(\theta)} \left[ F^m(\rho, \theta) - \left( \frac{F_{-2}^m(\theta)}{\rho^2} + \frac{F_{-1}^m(\theta)}{\rho} \right) \right] d\rho d\theta \right.$$
$$+ \int_{\theta_1^m}^{\theta_2^m} \left[ F_{-1}^m(\theta) \ln \left| \frac{\hat{\rho}^m(\theta)}{\beta^m(\theta)} \right| \right.$$
$$\left. \left. - F_{-2}^m(\theta) \left( \frac{\gamma^m(\theta)}{(\beta^m(\theta))^2} + \frac{1}{\hat{\rho}^m(\theta)} \right) \right] d\theta \right\}, \quad (28)$$

where the index $m$ refers to one element around the collocation point at a time, and $\theta_1^m \le \theta \le \theta_2^m$ on the $m$th element. As mentioned before, the interpolation functions for $u$ on the elements must be $C^{1,\alpha}$-continuous at the collocation point (see also Hartmann, 1989, pp. 29, 263). However, this is not related to the specific method used. Yet, it must be true for the original statement (2) or (6) to be meaningful. Therefore, such continuity requirements have to be satisfied no matter what method of analysis is used, including all the other approaches to HBIE's mentioned in the Introduction.

## 4 Numerical Examples

The present method for the direct evaluation of surface integrals with hypersingular integrand is applied to two numerical examples. Eight-node quadrilateral elements were used because they are of sufficiently high order to test in full generality all the aspects of the proposed approach. Moreover, they allow curved surfaces to be represented. All the computations were performed in double-precision arithmetic with 16-digit accuracy.

**4.1 Plane Distorted Element.** The first tests were performed on a plane quadrilateral element $S_s$ with a high degree of distortion, as shown in Fig. 5. Due to the position of the nodes, *the Jacobian is neither constant nor even linear.* The singular point $\mathbf{y}$ was located at three different positions: (a) $\mathbf{y} = (0, 0)$; (b) $\mathbf{y} = (0.66, 0)$; and (c) $\mathbf{y} = (0.479226, 0.66)$, corresponding, respectively, to the intrinsic coordinates (0, 0), (0.66, 0), and (0.66, 0.66) in the parameter plane (Fig. 6).

Without loss of generality, the following hypersingular integral was considered (cf. (4)):

$$I=\lim_{\epsilon\to 0^+}\left\{\int\!\!\int_{(S_s-e_\epsilon)+s_\epsilon}-\frac{1}{r^3}\left[3r_{,3}\frac{\partial r}{\partial n}-n_3\right]dS_x\right\}$$

$$=\lim_{\epsilon\to 0^+}\left\{\int\!\!\int_{(S_s-e_\epsilon)}\frac{1}{r^3}\,dS_x-\frac{2\pi}{\epsilon}\right\}, \quad (29)$$

where $e_\epsilon$ was chosen (just for convenience) to be a *circle* centered at $\mathbf{y}$ and of radius $\epsilon$. The term subtracted in (29) is clearly affected by the selected shape of $e_\epsilon$.

This integral was chosen for the purpose of comparison since it can be integrated in closed form. Notice, however, that it shows the same relevant features of some typical hypersingular integrals in the BEM (cf. (4) and (16)).

Formula (27) was employed for the computation, with $F = (1/r^3)J\rho$. Standard Gauss formulae were used for both the double and the simple integrals in expression (27) (an $n \times n$ product rule, and a formula of order $n$, respectively). For the actual application of Gaussian formulae, the element was subdivided into four triangles with a common vertex at $\eta$, as usual.

Table 1 gives the numerical results as obtained for the three cases of Fig. 5 and $n$ = 4, 6, 8, and 10, together with the exact values. With order $n$ = 6, at least three significant digits are always exact. With order 10, the error is always lower than 0.004 percent. With less distorted elements, a better accuracy is obtained.

**4.2 Curved Boundary Element.** As a more practical example, a *curved* boundary element is considered (Fig. 7). It represents a 90-deg cylindrical panel (radius = 1, length = 2). As above, three positions for the singular point $\mathbf{y}$ are taken, corresponding to intrinsic coordinates (a) $\eta$ = (0, 0), (b) $\eta$ = (0.66, 0), and (c) $\eta$ = (0.66, 0.66), respectively.

In this case, the hypersingular kernel function for three-dimensional potential problems,

$$V_3=-\frac{1}{4\pi r^3}\left[3r_{,3}\frac{\partial r}{\partial n}-n_3(\mathbf{x})\right], \quad (30)$$

is integrated. It is interesting to note that this kernel is actually made up of the sum of a hypersingular term of order $r^{-3}$ and of a strongly singular term of order $r^{-2}$, as $\partial r/\partial n = O(r)$, on $S_s$. However, they must be considered together for the cancellation in (26) to occur. As in the previous example, the computation was performed according to formula (27), with $F = V_3J\rho$. Since the evaluation is performed in the parameter plane of intrinsic coordinates, there are no differences in the numerical implementation between a flat element and a curved one.

The results are reported in Table 2, for orders of the Gauss formulae from 4 to 10, for the three cases (a), (b), and (c) of Fig. 7. The results are remarkably stable. Although the exact values are not available, the convergence is sufficiently good to expect very good accuracy also in this case. Other examples with boundary elements of different shape always showed the same stability and convergence (Guiggiani et al., 1991). Apparently, this is the first time that integrals with hypersingular kernels are evaluated on curved boundary elements.

The implementation for, e.g., elastic problems would not have required a substantial higher effort, the only difference being in the expressions of $F_{-2}$ and $F_{-1}$ in (27). Appendix C provides full detail on the systematic derivation of these quantities.

## 5 Discussion and Conclusions

In the first part of the present paper the limiting process

**Table 1 Numerical evaluation of hypersingular integrals on a flat distorted element (Fig. 5)**

| order n | case (a) | case (b) | case (c) |
|---|---|---|---|
| 4 | -5.749091 | -9.222214 | -15.72221 |
| 6 | -5.749244 | -9.157439 | -15.30541 |
| 8 | -5.749236 | -9.154546 | -15.31768 |
| 10 | -5.749237 | -9.154525 | -15.32806 |
| exact | -5.749237 | -9.154585 | -15.32850 |

**Table 2 Numerical evaluation of hypersingular integrals on a *curved* element (Fig. 7)**

| order n | case (a) | case (b) | case (c) |
|---|---|---|---|
| 4 | -0.343645 | -0.496925 | -0.876300 |
| 6 | -0.343804 | -0.497091 | -0.877106 |
| 8 | -0.343807 | -0.497099 | -0.877203 |
| 10 | -0.343807 | -0.497099 | -0.877214 |

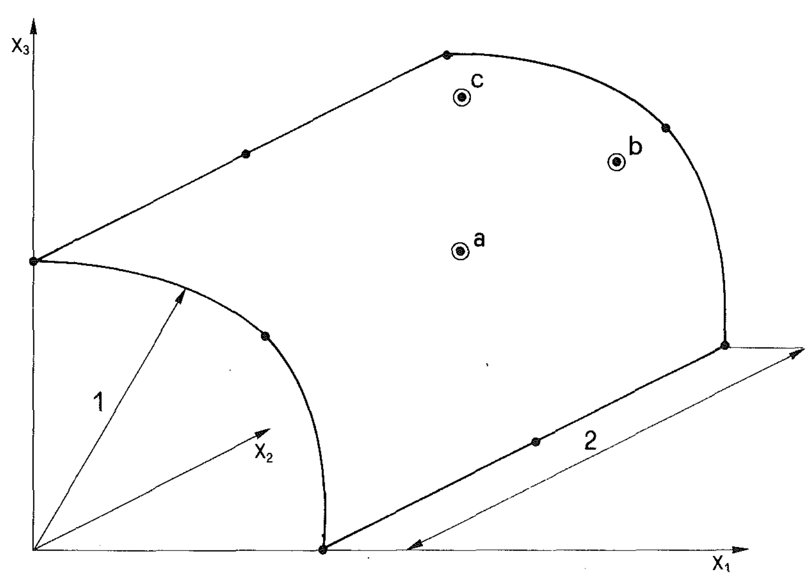


**Fig. 7 Curved boundary element and collocation points**

leading to hypersingular boundary integral equations has been thoroughly discussed. It shows that theoretical difficulties in dealing with HBIE's are only apparent. In fact, no unbounded quantities actually arise, provided the *limit is properly taken*. That essentially means that in the limit process, the integral on the whole boundary $(S - e_\epsilon) + s_\epsilon$ cannot be artificially divided into an integral on $(S - e_\epsilon)$ and an integral on $s_\epsilon$, unless the single parts exist independently. The analysis presented in the first part also shows that no special interpretation is really necessary to attach meaning to either hypersingular or strongly singular integrals, their existence being always guaranteed (whatever the shape of $v_\epsilon$) by the very nature of the kernels involved.

Equations (10) and (11) provide a rigorous, unambiguous form for any hypersingular boundary integral equations for scalar and vector problems, respectively. For clarity, the limits are still explicitly indicated. Equations in the form of (10) or (11) form the basis for the subsequent numerical work.

In the second part, a general approach to the evaluation of integrals with hypersingular kernels has been presented. In its derivation, special care has been exercised in preserving the features of the limiting process when the discretization of the geometry is introduced (cf. Eqs. (16), (18), and (20)). Also noteworthy is that all singular integrations are performed *directly* and *analytically*. The method can be applied on either closed or open surfaces (as, e.g., in crack analysis).

The final formulae (27) or (28) show that any hypersingular integral is equivalent to the sum of a double and a one-dimensional regular integrals. Since all integrals are expressed in the parameter plane of intrinsic coordinates, the actual computation requires only a straightforward application of standard quadrature rules. The same formulae for two-dimensional problems are given in Guiggiani (1992b).

Interestingly, the comparison of formula (28) in the present paper and formula (20*e*) in Guiggiani and Gigante (1990) shows that the latter is included as a special case in the former. Indeed, the two formulae coincide if $F_{-2} = 0$, i.e., if the integrand is only strongly singular instead of hypersingular. Moreover, if both $F_{-2}$ and $F_{-1}$ are equal to zero, formula (28) (or (27)) reduces to the familiar formula for weakly singular integrals in polar coordinates. Therefore, it is now available a unified method to the evaluation of singular integrals in the BEM.

The numerical results confirm the effectiveness of the proposed approach even on curved surface elements.


## Acknowledgments

This work was carried out while M. Guiggiani was visiting Iowa State University sponsored by Consiglio Nazionale delle Ricerche (CNR fellowship). Additional support to M. G. was provided by MURST. Partial support for F. J. Rizzo was provided by the Office of Naval Research under Contract No. N00014-89-K-0109.


## References


Beyer, W. H., ed., 1987, *CRC Standard Mathematical Tables*, 28th ed., CRC Press, Boca Raton, FL.

Bonnet, M., 1986, "Méthodes des Equations Intégrales Régularisées en Elastodynamique," Ph.D. Thesis, Ecole National des Ponts et Chaussées.

Bonnet, M., 1989, "Regular Boundary Integral Equations for Three-Dimensional Finite or Infinite Bodies With or Without Curved Cracks in Elastodynamics," *Boundary Element Techniques: Applications in Engineering*, C. A. Brebbia and N. Zamani, eds., Computational Mechanics Publications, Southampton, U.K., pp. 171–188.

Brockett, T. E., Kim, M.-H., and Park, J.-H., 1989, "Limiting Forms for Surface Singularity Distributions When the Field Point is on the Surface," *Journal of Engineering Mathematics*, Vol. 23, pp. 53–79.

Budreck, D. E., and Achenbach, J. D., 1988, "Scattering From Three-Dimensional Planar Cracks by the Boundary Integral Equation Method," ASME Journal of Applied Mechanics, Vol. 55, pp. 405–412.

Guiggiani, M., 1992a, "Computing Principal Value Integrals in 3D BEM for Time-Harmonic Elastodynamics—A Direct Approach," *Communications in Applied Numerical Methods*, Vol. 8, pp. 141–149.

Guiggiani, M., 1992b, "Direct Evaluation of Hypersingular Integrals in 2D BEM," *Notes in Numerical Field Mechanics*, Vol. 33, W. Hackbusch, ed., Vieweg, Braunschweig, pp. 23–34.

Guiggiani, M., and Gigante, A., 1990, "A General Algorithm for Multidimensional Cauchy Principal Value Integrals in the Boundary Element Method," ASME Journal of Applied Mechanics, Vol. 57, pp. 906–915.

Guiggiani, M., Krishnasamy, G., Rizzo, F. J., and Rudolphi, T. J., 1991, "Hypersingular Boundary Integral Equations: A New Approach to Their Numerical Treatment," *Boundary Integral Methods*, L. Morino and R. Piva, eds., Springer-Verlag, Berlin, pp. 211–220.

Hartmann, F., 1981, "The Somigliana Identity on Piecewise Smooth Surfaces," *Journal of Elasticity*, Vol. 11, No. 4, pp. 403–423.

Hartmann, F., 1989, *Introduction to Boundary Elements*, Springer-Verlag, Berlin.

Kellog, O. D., 1929, *Foundations of Potential Theory*, Frederick Ungar Publishing Company, New York.

Krishnasamy, G., Schmerr, L. W., Rudolphi, T. J., and Rizzo, F. J., 1990, "Hypersingular Boundary Integral Equations: Some Applications in Acoustic and Elastic Wave Scattering," ASME Journal of Applied Mechanics, Vol. 57, pp. 404–414.

Martin, P. A., and Rizzo, F. J., 1989, "On Boundary Integral Equations for Crack Problems," *Proc. Royal Soc. London*, Vol. A421, pp. 341–355.

Nishimura, N., and Kobayashi, S., 1989, "A Regularized Boundary Integral Equation Method for Elastodynamic Crack Problems," *Computational Mechanics*, Vol. 4, pp. 319–328.

Polch, E. Z., Cruse, T. A., and Huang, C.-J., 1987, "Traction BIE Solutions for Flat Cracks," *Computational Mechanics*, Vol. 2, pp. 253–267.

Rudolphi, T. J., Krishnasamy, G., Schmerr, L. W., and Rizzo, F. J., 1988, "On the Use of Strongly Singular Equations for Crack Problems," *Boundary Elements X*, Vol. 3, C. A. Brebbia, ed., Computational Mechanics Publications, Southampton, U.K., pp. 249–263.

Rudolphi, T. J., 1990, "Higher Order Elements and Element Enhancement by Combined Regular and Hypersingular Boundary Integral Equations," *Boundary Element Methods in Engineering*, B. S. Annigeri and K. Tseng, eds., Springer-Verlag, pp. 448–455.

Rudolphi, T. J., 1991, "The Use of Simple Solutions in the Regularization of Hypersingular Boundary Integral Equations," *Mathematical and Computer Modelling*, (special issue on BIEM/BEM), Vol. 15, pp. 269–278.

Sládek, V., and Sládek, J., 1984, "Transient Elastodynamic Three-Dimensional Problems in Cracked Bodies," *Applied Mathematical Modelling*, Vol. 8, pp. 2–10.

Zhang, Ch., and Achenbach, J. D., 1989, "A New Boundary Integral Equation Formulation for Elastodynamic and Elastostatic Crack Analysis," ASME Journal of Applied Mechanics, Vol. 56, pp. 284–290.


# APPENDIX A

## Free-Term Coefficients for Hypersingular Boundary Integral Equations

In this Appendix, the free-term coefficients $c_{ik}$ and $b_i$ associated to hypersingular boundary integral equations are derived. They are defined by expressions (8) and (9), respectively.

For simplicity, let us consider two-dimensional potential problems. The kernel functions in (8) and (9) are given by

$$W_i(\mathbf{y}, \mathbf{x}) = \frac{\partial U(\mathbf{y}, \mathbf{x})}{\partial y_i} = \frac{1}{2\pi r} r_{,i},$$

$$V_i(\mathbf{y}, \mathbf{x}) = \frac{\partial U(\mathbf{y}, \mathbf{x})}{\partial x_k \partial y_i} n_k(\mathbf{x}) = -\frac{1}{2\pi r^2}\left[2r_{,i}\frac{\partial r}{\partial n} - n_i(\mathbf{x})\right], \quad \text{(A1)}$$

where $r = |\mathbf{x} - \mathbf{y}|$, $r_{,i} = \partial r/\partial x_i$ and $U(\mathbf{y}, \mathbf{x}) = -(1/2\pi)\ln r$ is the familiar fundamental solution. Also, $\mathbf{y} = \{y_k\}$ is the source point, and $\mathbf{x} = \{x_k\}$ is the integration point. The outward unit normal at $\mathbf{x}$ is denoted by $\boldsymbol{n} = \{n_k\}$.

Figure A1 exemplifies the situation. For convenience, $s_\epsilon$ is assumed to be a circle centered at $\mathbf{y}$ and of radius $\epsilon$. The angle, with respect to a horizontal axis, is denoted by $\varphi$, so that, on $s_\epsilon$, $\varphi_1 \le \varphi \le \varphi_2$. Owing to the selected shape of $s_\epsilon$, the following simple relations hold when $\mathbf{x} \in s_\epsilon$:

$$\begin{aligned} &r = \epsilon, && \frac{\partial r}{\partial n} = -1, \\ &r_{,1} = \cos\varphi, && r_{,2} = \sin\varphi, \\ &n_1 = -\cos\varphi, && n_2 = -\sin\varphi, \\ &x_1 - y_1 = \epsilon\cos\varphi, && x_2 - y_2 = \epsilon\sin\varphi \end{aligned} \quad \text{(A2)}$$

and $dS_x = \epsilon d\varphi$. Moreover, the kernel functions become

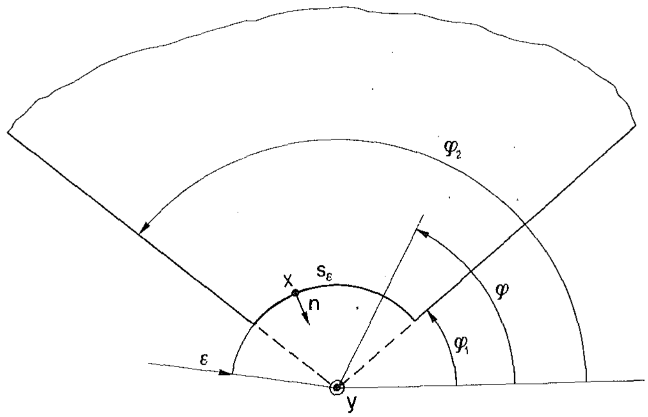


**Fig. A1 Definition of local geometry for free-term coefficients**

$$W_1=\frac{\cos\varphi}{2\pi\epsilon},\quad W_2=\frac{\sin\varphi}{2\pi\epsilon},$$
$$V_1=\frac{\cos\varphi}{2\pi\epsilon^2}=\frac{W_1}{\epsilon},\quad V_2=\frac{\sin\varphi}{2\pi\epsilon^2}=\frac{W_2}{\epsilon}. \tag{A3}$$

The integrations in (8) and (9) are now a straightforward matter. They are not much different from the derivation of the corresponding coefficients in the standard BIE (see Hartmann, 1981). For instance,

$$\frac{b_1(\mathbf{y})}{\epsilon}=\int_{s_\epsilon} V_1 dS_x=\frac{1}{2\pi}\int_{\varphi_1}^{\varphi_2}\frac{\cos\varphi}{\epsilon^2}\,\epsilon d\varphi=\frac{\sin\varphi_2-\sin\varphi_1}{2\pi}\frac{1}{\epsilon}. \tag{A4}$$

Note that $b_1=0$ if $\varphi_2=\varphi_1+2\pi$, that is if $\mathbf{y}$ is an internal point. Similar observations hold for $b_2$ which are given by

$$b_2=\frac{\cos\varphi_1-\cos\varphi_2}{2\pi}. \tag{A5}$$

However, these quantities do not need to be evaluated in actual computations.

An analogous treatment applies for coefficients $c_{ik}$. For instance,

$$c_{11}(\mathbf{y})=\int_{s_\epsilon}[V_1(x_1-y_1)-W_1n_1]dS_x=\frac{1}{2\pi}\int_{\varphi_1}^{\varphi_2}2\cos^2\varphi d\varphi$$
$$=\frac{1}{2\pi}\left[(\varphi_2-\varphi_1)+\frac{\sin(2\varphi_2)-\sin(2\varphi_1)}{2}\right]. \tag{A6}$$

Note that $c_{11}=0$ if $\mathbf{y}$ is an internal point, while $c_{11}=0.5$ if $\mathbf{y}$ is at a smooth boundary point, i.e., if $\varphi_2=\varphi_1+\pi$. The other coefficients are given by

$$c_{22}=\frac{1}{2\pi}\left[(\varphi_2-\varphi_1)-\frac{\sin(2\varphi_2)-\sin(2\varphi_1)}{2}\right], \tag{A7}$$

and

$$c_{12}=c_{21}=\frac{\sin^2\varphi_2-\sin^2\varphi_1}{2\pi}. \tag{A8}$$

At smooth boundary points, $c_{22}=0.5$, and $c_{12}=c_{21}=0$, as expected.

## APPENDIX B

### Hypersingular Kernel Functions for Elastic Problems

The well-known strongly singular kernels $T_{ij}$ in the standard BIE for elastostatic problems are given by

$$T_{ij}=-\frac{A}{r^\alpha}\left\{(1-2\nu)(n_ir_{,j}-n_jr_{,i})+[(1-2\nu)\delta_{ij}+\beta r_{,i}r_{,j}]\frac{\partial r}{\partial n}\right\}, \tag{B1}$$

where $\alpha=1, 2$ and $\beta=2, 3$ in two-dimensional and three-dimensional problems, respectively. The constant $A$ is equal to $1/[4\alpha\pi(1-\nu)]$.

The hypersingular kernels $V_{ikj}$ are therefore given by

$$V_{ikj}=\frac{\partial T_{ij}}{\partial y_k}=-\frac{A}{r^\beta}\{(1-2\nu)[\beta r_{,k}(n_ir_{,j}-n_jr_{,i})-n_i\delta_{jk}+n_j\delta_{ik}-n_k\delta_{ij}]-\beta n_kr_{,i}r_{,j}+\beta[(\alpha+3)r_{,i}r_{,j}r_{,k}+(1-2\nu)\delta_{ij}r_{,k}-\delta_{ik}r_{,j}-\delta_{jk}r_{,i}]\frac{\partial r}{\partial n}\right\}, \tag{B2}$$

where $r_{,i}=\partial r/\partial x_i$. The other kernel functions $W_{ikj}=\partial U_{ij}/\partial y_k$ are given by

$$W_{ikj}=\frac{A}{2Gr^\alpha}[\beta r_{,i}r_{,j}r_{,k}+(3-4\nu)\delta_{ij}r_{,k}-\delta_{ik}r_{,j}-\delta_{jk}r_{,i}]. \tag{B3}$$

## APPENDIX C

### Explicit Expressions of $F_{-2}(\theta)$, $F_{-1}(\theta)$, $\beta(\theta)$, and $\gamma(\theta)$

Before deriving in a systematic way the expressions of $F_{-2}(\theta)$, $F_{-1}(\theta)$, $\beta(\theta)$, and $\gamma(\theta)$, some more basic expansions are obtained. In particular, we are interested in Taylor series expansions about the source point $\mathbf{y}\in S_s$ of $(x_i-y_i)$, $r^3$, and $r_{,i}$.

As usual in the BEM, the coordinates of the generic point on the boundary element $S_s$ are given by a parametric representation in terms of shape functions $M^c(\xi_1, \xi_2)$, and nodal coordinates $x_i^c$,

$$x_i=\sum_c M^c(\xi_1, \xi_2)x_i^c,\quad i=1, 2, 3. \tag{C1}$$

Let us indicate, by $\boldsymbol{\eta}=(\eta_1, \eta_2)$, the image of the source point $\mathbf{y}$ so that $y_i=M^c(\eta_1, \eta_2)x_i^c$.

From (C1), the first and second derivatives can be easily obtained, i.e.,

$$\frac{\partial x_i}{\partial \xi_k}=\frac{\partial M^c}{\partial \xi_k}x_i^c, \tag{C2}$$

$$\frac{\partial^2 x_i}{\partial \xi_k^2}=\frac{\partial^2 M^c}{\partial \xi_k^2}x_i^c. \tag{C3}$$

By employing a Taylor expansion about the source point, it is easy to establish formulae of the form

$$x_i-y_i=\left[\frac{\partial x_i}{\partial \xi_1}\bigg|_{\xi=\eta}(\xi_1-\eta_1)+\frac{\partial x_i}{\partial \xi_2}\bigg|_{\xi=\eta}(\xi_2-\eta_2)\right]+\left[\frac{\partial^2 x_i}{\partial \xi_1^2}\bigg|_{\xi=\eta}\frac{(\xi_1-\eta_1)^2}{2}+\frac{\partial^2 x_i}{\partial \xi_1\partial\xi_2}\bigg|_{\xi=\eta}(\xi_1-\eta_1)(\xi_2-\eta_2)+\frac{\partial^2 x_i}{\partial \xi_2^2}\bigg|_{\xi=\eta}\frac{(\xi_2-\eta_2)^2}{2}\right]+\ldots \tag{C4}$$

where, as indicated, all derivatives are evaluated at $\boldsymbol{\eta}$.

If polar coordinates $(\rho, \theta)$, centered at $\eta$ are introduced in the parameter plane (see (19)), expansions (C4) become

$$x_i - y_i = \rho\left[\frac{\partial x_i}{\partial \xi_1}\bigg|_{\xi=\eta}\cos\theta + \frac{\partial x_i}{\partial \xi_2}\bigg|_{\xi=\eta}\sin\theta\right] + \rho^2\left[\frac{\partial^2 x_i}{\partial \xi_1^2}\bigg|_{\xi=\eta}\frac{\cos^2\theta}{2} + \frac{\partial^2 x_i}{\partial \xi_1 \partial \xi_2}\bigg|_{\xi=\eta}\cos\theta\sin\theta + \frac{\partial^2 x_i}{\partial \xi_2^2}\bigg|_{\xi=\eta}\frac{\sin^2\theta}{2}\right] + O(\rho^3), \quad \text{(C5)}$$

or, more concisely,

$$x_i - y_i = \rho A_i(\theta) + \rho^2 B_i(\theta) + O(\rho^3). \quad \text{(C6)}$$

Notice that $A_i(\theta)$ and $B_i(\theta)$ are just *simple trigonometric functions* of $\theta$.

Since the series expansion (21) for the singular function $F(\rho, \theta)$ involves two terms, the first two terms in the above Taylor expansions have been considered. This is a general rule. The higher the order of singularity, the more terms must be retained. In Guiggiani and Gigante (1990), only the first term was considered because the singularity was one order lower.

It is now convenient to define

$$A(\theta) = \left\{\sum_{k=1}^{3}[A_k(\theta)]^2\right\}^{1/2} > 0,$$

$$B(\theta) = \left\{\sum_{k=1}^{3}[B_k(\theta)]^2\right\}^{1/2} \geq 0. \quad \text{(C7)}$$

According to the previous results, the Taylor series expansions for the powers of $r = |\mathbf{x} - \mathbf{y}|$ are given by (repeated indicies imply summation)

$$r^n = \rho^n A^n\left(1 + n\rho\frac{A_k B_k}{A^2}\right) + O(\rho^{n+2}), \quad n = 1, 2, 3, \ldots. \quad \text{(C8)}$$

From (C7) and (C8) with $n = 1$, the expansions for the derivatives of $r$ can be obtained and are

$$r_{,i} = \frac{x_i - y_i}{r} = \frac{\rho A_i + \rho^2 B_i + O(\rho^3)}{\rho A\left(1 + \rho\frac{A_k B_k}{A^2}\right) + O(\rho^3)}$$

$$= \frac{A_i}{A} + \rho\left(\frac{B_i}{A} - A_i\frac{A_k B_k}{A^3}\right) + O(\rho^2)$$

$$= d_{i0}(\theta) + \rho d_{i1}(\theta) + O(\rho^2). \quad \text{(C9)}$$

Also important is the expansion for $r^{-3}$. It is obtained from (C8) with $n = 3$

$$\frac{1}{r^3} = \frac{1}{\rho^3 A^3\left[1 + 3\rho\frac{A_k B_k}{A^2} + O(\rho^2)\right]}$$

$$= \frac{1}{\rho^3 A^3} - \frac{3A_k B_k}{\rho^2 A^5} + O\left(\frac{1}{\rho}\right)$$

$$= \frac{S_{-3}(\theta)}{\rho^3} + \frac{S_{-2}(\theta)}{\rho^2} + O\left(\frac{1}{\rho}\right). \quad \text{(C10)}$$

Actually, the expansions of the inverse powers of $r$ can be obtained directly from (C8) with negative $n$.

It is worth noting that all the above expansions are valid for any kind of boundary elements.

The hypersingular integrand $F(\rho, \theta)$ is given by

$$F = V_i N^a J\rho = \frac{1}{r^3} Q_i N^a J\rho, \quad \text{(C11)}$$

where the Jacobian is given by $J = \{\Sigma_{k=1}^3 J_k^2\}^{1/2}$. An examination of the regular function $Q_i$ (see (4) and (B2)) reveals that every term in its expression is multiplied by a component $n_k$ of the unit normal vector. Therefore, the product $Q_i J$ in (C11) can be expressed only in terms of $r_{,k}$ and $J_k$, since we have that $J_k = n_k J$. This means that we need only the expansions of $J_k$ (besides those of $r_{,k}$, already obtained) and not of either $n_k$ and $J$.

$$J_k = J_k(\eta) + \rho\left[\frac{\partial J_k}{\partial \xi_1}\bigg|_{\xi=\eta}\cos\theta + \frac{\partial J_k}{\partial \xi_2}\bigg|_{\xi=\eta}\sin\theta\right] + O(\rho^2)$$

$$= J_{k0} + \rho J_{k1}(\theta) + O(\rho^2), \quad \text{(C12)}$$

where all derivatives are evaluated at $\eta$. The derivatives $\partial J_k/\partial \xi_j$ can be expressed in terms of the first and second derivatives of $x_i(\xi_1, \xi_2)$ as given in (C2) and (C3).

The last expansion we require is that of the shape function $N^a$

$$N^a = N^a(\eta) + \rho\left[\frac{\partial N^a}{\partial \xi_1}\bigg|_{\xi=\eta}\cos\theta + \frac{\partial N^a}{\partial \xi_2}\bigg|_{\xi=\eta}\sin\theta\right] + O(\rho^2)$$

$$= N_0^a + \rho N_1^a(\theta) + O(\rho^2). \quad \text{(C13)}$$

Notice that $J_{k0}$ and $N_0^a$ are just constants, and not functions of $\theta$.

The series expansions (C9), (C10), (C12), and (C13) are all we need to obtain $F_{-2}$ and $F_{-1}$ for *any* hypersingular integrand in the BEM.

For instance, let us consider the case of three-dimensional potential problem, whose kernels $V_i$ are given by expression (4). We have for the hypersingular integrand in (20)

$$F(\rho,\theta) = -\frac{1}{4\pi r^3}[3r_{,i}(r_{,k}J_k) - J_i]N^a\rho. \quad \text{(C14)}$$

From (C9) and (C12),

$$r_{,k}J_k = d_{k0}(\theta)J_{k0} + \rho[d_{k1}(\theta)J_{k0} + d_{k0}(\theta)J_{k1}(\theta)] + O(\rho^2)$$

$$= \rho(B_k J_{k0} + A_k J_{k1})/A + O(\rho^2) = \rho p_1(\theta) + O(\rho^2), \quad \text{(C15)}$$

since $A_k J_{k0} \equiv 0$. Hence, from (C9) and (C15),

$$r_{,i}(r_{,k}J_k) = \rho d_{i0}(\theta)p_1(\theta) + O(\rho^2)$$

$$= \rho(A_i/A^2)(B_k J_{k0} + A_k J_{k1}) + O(\rho^2)$$

$$= \rho g_{i1}(\theta) + O(\rho^2). \quad \text{(C16)}$$

Thus, from (C12) and (C16),

$$3r_{,i}(r_{,k}J_k) - J_i = -J_{i0} + \rho[3g_{i1}(\theta) - J_{i1}(\theta)] + O(\rho^2)$$

$$= b_{i0} + \rho b_{i1}(\theta) + O(\rho^2), \quad \text{(C17)}$$

where $b_{i0} = -J_{i0} = -J_i(\eta)$ is not a function of $\theta$. Then, from (C13) and (C17),

$$[3r_{,i}(r_{,k}J_k) - J_i]N^a = b_{i0}N_0^a + \rho[b_{i1}(\theta)N_0^a + b_{i0}N_1^a(\theta)] + O(\rho^2)$$

$$= a_{i0} + \rho a_{i1}(\theta) + O(\rho^2). \quad \text{(C18)}$$

Notice that $a_{i0} = 0$, if $N^a(\eta) = N_0^a = 0$. In that case, the integrand $F$ would be only strongly singular. Therefore, from the expansion (C10) of $r^{-3}$ and from (C18), the expansion of $F(\rho, \theta)$ can be obtained:

$$F(\rho, \theta) = -\frac{1}{4\pi}\rho\left[\frac{S_{-3}(\theta)}{\rho^3} + \frac{S_{-2}(\theta)}{\rho^2} + O\left(\frac{1}{\rho}\right)\right][a_{i0} + \rho a_{i1}(\theta) + O(\rho^2)]$$

$$= -\frac{1}{4\pi}\left[\frac{S_{-3}(\theta)a_{i0}}{\rho^2} + \frac{S_{-2}(\theta)a_{i0} + S_{-3}(\theta)a_{i1}(\theta)}{\rho} + O(1)\right]$$

$$= \frac{F_{-2}(\theta)}{\rho^2} + \frac{F_{-1}(\theta)}{\rho} + O(1), \quad \text{(C19)}$$

which defines the two required (real) functions $F_{-2}$ and $F_{-1}$. Notice that these functions are basically made up of combinations of elementary trigonometric functions of $\theta$. From inspection, it is easy to see that $F_{-2}(\theta) = F_{-2}(\theta + \pi)$, whereas

$F_{-1}(\theta) = -F_{-1}(\theta + \pi)$. These properties are shared by all hypersingular kernels in the BEM.

A similar procedure can be applied to any kernel, no matter how complicated its expression may appear. As a matter of fact, even in vector problems such as elasticity the kernels are given by a combination of simple terms, each one basically like the potential kernel considered here above (cf. (4) and (B2)). Furthermore, even in cases like time-harmonic elastodynamics or acoustics, where the kernels may seem very complicated, it just suffices to observe that their asymptotic behavior is exactly represented by their static counterpart (see, e.g., Bonnet (1986), Budreck and Achenbach (1988); or Guiggiani (1992a), in the context of direct evaluation of singular integrals). Therefore, the functions $F_{-2}$ and $F_{-1}$ are exactly the same for either static or dynamic problems. For instance, the expressions given in (C19) are also valid for steady-state acoustic problems (Helmholtz equation).

From the above results, the derivation of $\beta(\theta)$ and $\gamma(\theta)$ is quite easy.

The contour of the neighborhood $e_\epsilon$ of radius $\epsilon$ is given by (see expression (13))

$$\epsilon = r. \tag{C20}$$

In polar coordinates in the parameter plane it becomes (see (C8) with $n = 1$)

$$\epsilon = \rho A(\theta) + \rho^2 \frac{A_k B_k}{A} + O(\rho^3). \tag{C21}$$

By using the reversion of the above series (see, e.g., Beyer (1987), p. 297), we obtain the expansion in powers of $\epsilon$ of the equation in polar coordinates of the contour of $\sigma_\epsilon$ (the image of $e_\epsilon$) (Fig. 4)

$$\rho = \alpha(\epsilon, \theta) = \frac{\epsilon}{A(\theta)} - \epsilon^2 \frac{A_k B_k}{A^4} + O(\epsilon^3)$$
$$= \epsilon\beta(\theta) + \epsilon^2\gamma(\theta) + O(\epsilon^3), \tag{C22}$$

that defines $\beta(\theta)$ and $\gamma(\theta)$ (see (C7)). Notice that $\beta(\theta) = \beta(\theta + \pi)$, and $\gamma(\theta) = -\gamma(\theta + \pi)$.

# An Investigation of Dynamic Pulse Buckling of Thick Rings

**N. G. Pegg**
Defence Scientist,
Defence Research Establishment Atlantic,
Dartmouth, Nova Scotia, B2Y 3Z7, Canada

*The occurrence of dynamic buckling of thick rings responding to an impulse load is investigated by analytical and numerical solutions to the equation of motion and by nonlinear finite element analyses. An extension to the linearized analytical solution is made using a finite difference scheme which incorporates a nonlinear moment-curvature relationship to model the effects of elastoplastic behavior and strain-rate reversal on the buckle formation. The finite element solution to the problem is formulated with the nonlinear code, ADINA. A comparison of the results shows that the numerical solutions (and, in particular, the ADINA solution) predict a significant reduction in the amplitude of buckling response and an increase in the predominant wavelength of response with time, in comparison to the linear analytical solution. A limited comparison to published experimental results of dynamic pulse buckling of thick rings is also given.*

## Introduction

Dynamic buckling of a structure can be defined by excessive growth of flexural displacements during its response period. Perturbations to the structure's motion, resulting from initial imperfections in its geometry and/or loading, increase in amplitude to form a buckled mode shape. This type of failure was first investigated for rings subject to radial pulses by Abrahamson and Goodier (1962), whose theory is also described, along with subsequent studies of dynamic pulse buckling at Stanford Research Institute, in the summary collection of Lindberg and Florence (1987).

Analytical solutions for dynamic pulse buckling of rings and cylinders are limited to simple cases of axisymmetric pulses (Abrahamson and Goodier, 1962; Goodier and McIvor, 1964; Lindberg, 1964; Stuiver, 1965; Florence and Vaughan, 1968; and Lindberg and Florence, 1987). These solutions are also limited to linear material constitutive relationships of either plastic flow with strain hardening for thick rings and cylinders or elastic for thin rings and cylinders. Though limited to simple cases, these theories do give considerable insight into the characteristics of dynamic pulse buckling. Response to asymmetric pulses of complex spatial or temporal variation, cylinders of intermediate thickness, noncylindrical or nonuniform shells, or cylinders with nonlinear elastoplastic material constitutive relations are some examples of problems where these simple theories can no longer be applied. For these cases numerical solutions are required.

Lindberg and Kennedy (1975) applied an axisymmetric finite element analysis uncoupled in each circumferential harmonic of response to include a more complete theory of the shell response, and showed that the harmonics of predominant growth predicted by the simple theory for plastic flow buckling were too high. Their analysis included the effects of strain-rate reversal which caused the attenuation of higher order harmonics and allowed lower order harmonics to become predominant. More recently, Kirkpatrick and Holmes (1987) and Gefken, Kirkpatrick, and Holmes (1988) applied three-dimensional nonlinear finite element solutions to rings and finite length thin shells with good correlation to experimental results.

This paper presents an investigation of dynamic pulse buckling of thick rings (representative of infinite cylinders under plane strain conditions) which deform radially with considerable plastic strain before buckle amplitudes become significant. Three methods of solution are studied to examine the process of dynamic pulse buckling and to determine the effects of some nonlinear characteristics. The first method is the analytical plastic flow buckling solution of the equation of motion for a ring subject to a uniform initial velocity presented by Abrahamson and Goodier (1962), derived, in this case, for initial geometric imperfections. The second method is an extension to the analytical solution in which an explicit finite difference solution to the equation of motion is developed to model nonlinear moment-curvature behavior by including elastoplasticity and strain-rate reversal in the constitutive relation. The finite difference solution indicates a complex state of curvature-rate reversal in combination with strain-rate reversal as the buckling motion becomes well advanced, but is unable to carry the solution through this state due to limiting assumptions in the governing differential equation. A nonlinear finite element solution with the program ADINA (1987) was the third method used, which includes all of the material and geometric nonlinear effects and can be extended to more complex dynamic buckling problems. A parametric study of the modeling and solution requirements for ADINA is presented, as well as a comparison of the three solution methods and a limited comparison to some published experimental results.

Contributed by the Applied Mechanics Division of The American Society of Mechanical Engineers for publication in the ASME Journal of Applied Mechanics.

Discussion on this paper will be addressed to the Technical Editor, Professor Leon M. Keer, The Technological Institute, Northwestern University, Evanston, IL 60208, and will be accepted until four months after final publication of the paper itself in the Journal of Applied Mechanics.

Manuscript received by the ASME Applied Mechanics Division, Oct. 16, 1990; final revision, Feb. 11, 1991. Associate Technical Editor: A. K. Noor.

## Analytical Solution to the Equation of Motion

Abrahamson and Goodier's (1962) solution for the dynamic pulse buckling of infinite, thick cylindrical shells (or rings) relies on the basic assumption that the ring is in a state of plastic flow with continuously increasing compressive plane strain with no reversal of strain rate. Perturbations in extensional flexural modes, caused by an imperfect axisymmetric initial velocity, are superimposed on an unperturbed extensional hoop motion. Moments, produced by a stress differential through the thickness as a result of strain hardening, control the growth of the buckling perturbations. This theory is dependent upon the material having a nonzero plastic tangent modulus. The following discussion of this theory is for the case of initial shape imperfections, instead of the initial velocity imperfections used by Abrahamson and Goodier.

The equation of radial motion, $u$, for a ring with initial imperfect shape, $u_i$, in nondimensional form, is:

$$\frac{\partial^4 u}{\partial \theta^4}+(1+s^2)\frac{\partial^2 u}{\partial \theta^2}+s^2 u+\frac{\partial^2 u}{\partial \tau^2}=-s^2\left(1+u_i+\frac{\partial^2 u_i}{\partial \theta^2}\right) \quad (1)$$

where the nondimensional time is $\tau = 1/\sqrt{12}\sqrt{E_h/\rho}\, ht/a^2$ and the shell parameter is $s^2 = Sa^2/E_hI = 12\sigma_m a^2/E_h h^2$. The constant hoop force is $S = \sigma_m h$, $\sigma_m$ is the average flow stress, the moment of inertia of the ring cross-section is $I = h^3/12$, $E_h$ is the tangent or strain hardening modulus, $\rho$ is the shell density, $h$ is the shell thickness, $a$ is the shell radius, $\theta$ is the circumferential coordinate, and $t$ is real time. The parameters $a$, $h$, $E_h$, and $\sigma_m$ are assumed to be constant in this theory. The important assumption of linear plastic behavior (constant modulus $E_h$) allows a linear moment-curvature relationship, $M = E_hI\kappa$, which has been incorporated into Eq. (1).

For initial shape imperfections and response in the form of harmonic functions, the analytical solution to Eq. (1), for an initial nondimensional velocity, $v_o = \sqrt{12\rho/E_h}\, a/h\, V_o$, is (not including wave numbers greater than $s$):

$$u(\tau)=-1+\cos s\tau+\frac{v_o}{s}\sin s\tau + \sum_{n=2}^{s}\frac{s^2}{s^2-n^2}\frac{A_n}{a}(\cosh p_n\tau-1)\cos(n\theta+\phi_n) \quad (2)$$

where $p_n = \sqrt{(n^2-1)(s^2-n^2)}$, $n$ is the circumferential wave number, $A_n$ is the initial shape imperfection, and $\phi_n$ is the phase angle shift for wave number $n$.

By determining the critical point of the gradient of the perturbed motion with respect to $n$, an expression for the critical buckling wave number, $n_{cr}$, results:

$$n_{cr}^2=\frac{1}{2}(s^2+1). \quad (3)$$

Buckling is established by investigating Eq. (2) for a range of $n$ in the vicinity of $n_{cr}$ and setting a critical limit to the amplitude of modal growth. Lindberg and Florence (1987) present an approximate expression for the critical velocity to cause a 20-fold increase in the initial imperfection of the critical wave number as

$$V_{cr}=\sqrt{3}\left(\frac{hc}{a}\right)\sqrt{\frac{E_h}{E}} \quad (4)$$

where $c$ is the speed of sound in the shell material.

The occurrence of strain-rate reversal is a limitation to this theory. It causes the outer fibers of a buckle to unload elastically and give a much stiffer resistance to the further formation of the buckle. Strain-rate reversal occurs first in the buckles of shorter wavelength which have the highest curvature. The occurrence, but not the effect, of strain-rate reversal can be investigated by monitoring the strain at the outer fiber of the shell, $u \pm (h/2a)(\partial^2 u/\partial\phi^2)$, where $u$ is that of Eq. (2). Investigation of the occurrence of strain-rate reversal for the case of initial shape imperfections shows that it is dependent on the amplitude of initial shape imperfection, $A_n$, and, that for shape imperfections commonly used in other studies (e.g., $A_n = 0.01h$), strain-rate reversal occurs very early in the shell motion.

## Finite Difference Solution to the Equation of Motion

In order to include the effects of a full elastoplastic constitutive relationship with strain-rate reversal, the moment-curvature relationship can no longer be considered linear and must be numerically evaluated. The differential equation of motion (Eq. (1)) is rewritten to explicitly include the moment as

$$\frac{\partial^2 M}{\partial \theta^2}+s^2\frac{\partial^2 u}{\partial \theta^2}+s^2 u+\frac{\partial^2 u}{\partial \tau^2}=-s^2\left(1+u_i+\frac{\partial^2 u_i}{\partial \theta^2}\right) \quad (5)$$

where $M$ is the nondimensional moment, $M = a/E_hI\, m$. Using central differences and an explicit time-integration scheme, Eq. (5) is rewritten as:

$$\left[\frac{M_{j+1}-2M_j+M_{j-1}}{\Delta\theta^2}\right]^k+s^2\left[\frac{u_{j+1}-2u_j+u_{j-1}}{\Delta\theta^2}\right]^k + \frac{u_j^{k+1}-2u_j^k+u_j^{k-1}}{\Delta\tau^2}=-s^2\left[1+u_j^k+u_{i_j}+\frac{\partial^2 u_{i_j}}{\partial\theta}\right] \quad (6)$$

where $k$ is the time step, $j$ is the spatial distribution step, and the right-hand side is evaluated analytically for harmonic initial shape imperfections. The solution is for the radial displacement, $u_j^{k+1}$, with $s$ and $M_j$ being evaluated from the previous step. The shell parameter, $s$, is defined here as $\sigma_h ha^2/E_hI$ where the hoop stress, $\sigma_h$, is calculated from the hoop strain, $\epsilon_\theta^k = u^k$, using the complete elastoplastic constitutive relationship including strain-rate reversal.

$M_j^{k+1}$ is evaluated numerically by first determining the curvature at the ring cross-section, $\kappa_j = 1/a\,[(u_{j+1}-2u_j+u_{j-1})/\Delta\theta^2 + u_j]^k$, dividing the cross-section into a number of strips, and evaluating the total strain in each strip as, $\epsilon = \epsilon_\theta + z\kappa$ where $z$ is the distance from the neutral axis to the center of the strip. The stress is then calculated using the full elastoplastic material model and by tracking the strain history to include strain-rate reversal. Due to the nonlinear stress-strain model, an iterative procedure is required to find the location of the neutral axis to give force equilibrium in the cross-section. The force in each strip is a function of the total strain in the strip, which in turn depends on the position of the neutral axis. A considerable number of iterations are required when the strips are not all of the same modulus (in a state of elastoplastic transition or strain-rate reversal) and several schemes and variations in the number of strips and spatial and temporal step sizes were investigated to improve solution convergence. Once equilibrium is achieved to a given tolerance, the moment is calculated from the cross-section force distribution.

Despite its limitations, the linear analytical solution indicates several important characteristics which must be incorporated into the numerical finite difference and finite element solutions. The initial buckling modes occur in higher harmonics than for static buckling. Equation (3) shows that $n_{cr}$ is a direct function of the shell parameter, $s$, and is of the order of 10 to 50 for thick metal shells. This places two important requirements on the numerical solutions. First, a finely discretized geometric mesh is required to model response correctly in the higher wave numbers. Depending on the order of the element used, several elements (or node points) per wavelength may be needed, resulting in models with discretizations of one hundred to several hundred nodes circumferentially. Second, the time integration scheme used must be capable of incorporating motion at the frequencies associated with the higher wave numbers, which may be in the hundreds of kHz range. An additional factor, necessary for the investigation of the effects of an elastoplastic strain-rate reversal material model, is sufficient integration through the ring thickness to model the complex stress distribution. These factors result in CPU intensive analyses where a large number of times steps will be required for large matrices. As is the case in the analytical solution, initial imperfections are needed in the numerical models to initiate buckling growth. Kirkpatrick and Holmes (1987) used an idealized distribution of modal amplitude, $A_n$, based on the results of shell imperfection surveys for thin shells, of the form:

$$A_n = .05h, \text{ for } n \le 10$$
$$A_n = \frac{b}{n^{1.3}}, \text{ for } n > 10. \tag{7}$$

This distribution was adopted for part of the present thick shell finite element study. Equation (7) does, however, give imperfections which may in practice be too large for thick shells, and a second model for radial imperfections

$$A_n = .01h, \text{ for } n \le 10$$
$$A_n = \frac{h}{n^2}, \text{ for } n > 10 \tag{8}$$

was also used for comparison to analytical and experimental results. These imperfection amplitudes were used for all three solution methods: analytical, finite difference, and finite element, and were incorporated into the initial radial geometry, $a(\theta)$, by the harmonic summation

$$a(\theta) = a + \sum_{n=2}^{100} A_n \cos(n\theta + \phi_n), \tag{9}$$

where a random number generator was used for the phase angle, $\phi_n$.

## Finite Element Solution

Using the aforementioned numerical modeling considerations, ADINA was used to model planar rings of eight-node membrane elements in the $R$, $\theta$-plane to represent the plane-strain case of an infinite cylinder. ADINA, which has both explicit and implicit solution capability, was the only nonlinear code readily available to the author; no doubt other codes would also be suitable. A first set of analyses, with a half cosine initial velocity distribution (loaded on top half only), was used to investigate the various finite element solution parameters of element discretization, element integration order, integration time step, and initial model imperfections. A second set of analyses was then undertaken with uniform axisymmetric initial velocity distributions for comparison to the analytical and numerical solutions to the equation of motion and some published experimental results.

The finite element model used for the solution parameter study represented a cylinder of 6061-T6 aluminum with a mean radius of 152.4 mm and a thickness of 5.08 mm, to give a radius to thickness ratio of $a/h = 30$. The geometry was taken from a study by Lindberg and Kennedy (1975) in which experimental results of the radial motion of the shell were presented. Ishizaki and Bathe (1980), also used this test case for verifying the dynamic response (without buckling) of ADINA. The material parameters were modeled as a bilinear curve with Young's modulus = 69 GPa, Poisson's ratio = 0.33, yield stress = 285 MPa, tangent modulus = 900 MPa, and density = 2.7 grams/cm$^3$. Lindberg and Kennedy (1975) and Kirkpatrick and Holmes (1987), used similar bilinear material curves in their numerical studies.

As an initial test case for this current study, a "perfect" finite element model was analyzed with a half cosine initial velocity distribution of 103 ms$^{-1}$ amplitude. The finite element response showed no occurrence of buckling, with the ring deforming plastically and oscillating elastically as expected. A

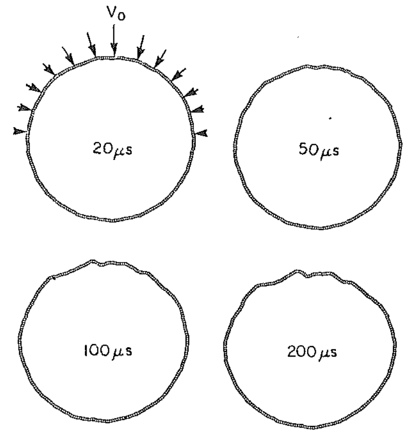


**Fig. 1 Buckling mode formation of parameter study model with half cosine initial velocity distribution**

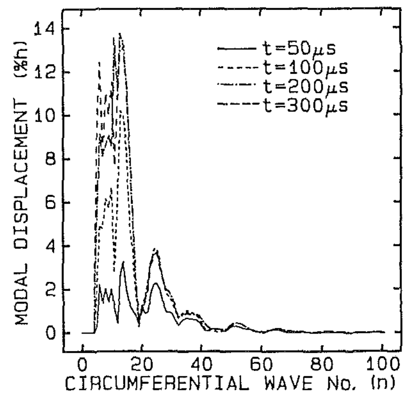


**Fig. 2 Modal growth for the parameter study model with 240 elements, 4 × 4 integration, $\Delta t$ = 1 $\mu$s, and imperfections in $n$ = 2–100**

solution time step of the order of 1 $\mu$s or less with implicit Newmark time integration gave good agreement with displacement results of the experiment and the analyses of the above references.

To investigate dynamic pulse buckling, the same model was reformulated using Eq. (9) with imperfections in the initial radial coordinates defined by Eq. (7). This planar ring model consisted of 240 eight-node membrane elements and used 4 × 4 Gauss integration. The deflected shape is shown at various time steps in Fig. 1. To investigate the growth of buckling modes, Fourier decomposition of the radial displacements was undertaken at several time steps. Figure 2 shows the growth of the Fourier components (wave numbers) as complex amplitudes (modal displacement as a percentage of the ring thickness) at four time steps. For this first model, the predominant wavelength of response can be seen to increase (decrease in wave number, $n$) with increasing time of response. Initially both wave numbers 14 and 25 grow rapidly, but $n$ = 25 ceases to grow past 100 $\mu$s, whereas $n$ = 14 continues to increase in amplitude until 200 $\mu$s where it reaches 14 percent of the ring thickness. This attenuation of the growth of the higher wave numbers is caused by the occurrence of strain-rate reversal and subsequent curvature rate and curvature reversal. The experimental results presented by Lindberg and Kennedy (1975) indicate predominant harmonics from $n$ = 14 to 21 for tests with varying initial velocity amplitudes. The experiments used a perturbed initial velocity and no data on initial shape imperfections are given.

The model was re-analyzed using an integration order of 6 × 6 with little difference occurring in mode shape or amplitude compared to the 4 × 4 model. An integration order of 2 × 2 was also investigated. The 2 × 2 integration order was not

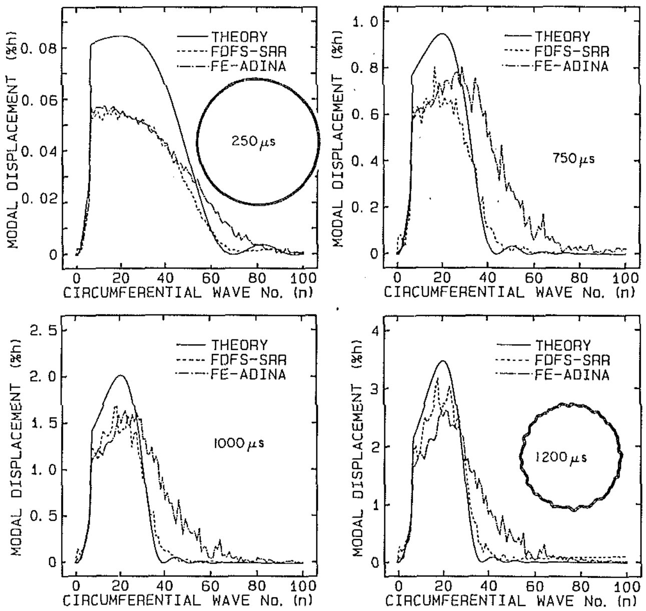


**Fig. 3 Comparison of modal growth for the analytical (THEORY), finite difference (FDFS-SRR) and finite element (FE-ADINA) solutions, and buckled mode shape (from ADINA)**

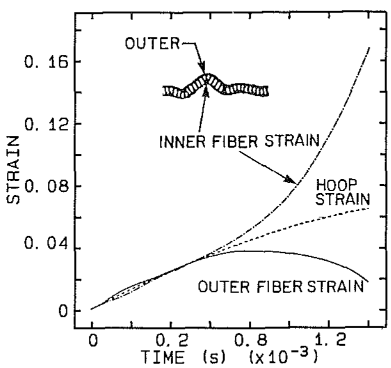


**Fig. 4 Time histories for outer and inner fiber and hoop strains from the finite difference solution**

as capable as the higher integration orders of modeling variation through the ring thickness, and thus the occurrence of strain-rate reversal is not modeled as effectively. This resulted in the higher numbered wavelengths having greater amplitudes and not being attenuated as quickly as they were in the higher integration order models. To investigate circumferential discretization, the number of elements was increased from 240 to 360 (uniformly distributed) with no appreciable difference in results.

To investigate the effect of solution time step on the response, the 360 element model was analyzed with a time step of $\Delta t = 0.1$ $\mu$s. This time step should allow response for this ring in wavelengths up to and in excess of $n = 100$. The modal growth results for $\Delta t = 0.1$ $\mu$s were in good agreement with the $\Delta t = 1.0$ $\mu$s results, even for early time when the amplification of higher wave numbers is most expected. It is interesting to note that both explicit central difference and implicit Newmark integration schemes were considered, and although explicit schemes are generally more efficient for impulse problems, this was not the case here due to instability in the explicit solutions caused by the very small natural periods of the small length finite elements. With larger radius models, and hence longer element lengths, the explicit schemes can be used with time steps which make them more efficient.

Since most of the response, even at early time, is in modes with $n < 50$, a 240 element model was created with initial imperfections in harmonics of $n = 2$ to 50. The modal growth plots for the $n = 2$ to 50 and the $n = 2$ to 100 models indicated little difference in buckling mode shape or amplitude.

## Comparison of Solutions

A thick ring model of radius = 1524.0 mm, thickness = 50.8 mm, steel bilinear material properties of $E = 207$ GPa, $\nu = 0.33$, $\sigma_y = 345$ MPa, and $E_h = 6900$ MPa with von Mises yield criterion and isotropic hardening, an initial axisymmetric velocity of 102 ms$^{-1}$ and initial shape imperfections modeled by Eqs. (8) and (9), was used to compare the three solution methods for dynamic pulse buckling discussed in this paper. It should be noted that the strain-rate insensitive, linear hardening model used for the numerical comparison is an assumption which may not truely represent steel cylinders. Figure 3 compares the modal growth plots of this model for four time steps for the three solution methods; the analytical solution from Abrahamson and Goodier's theory (labelled THEORY in figure), the finite difference solution to the equation of motion (FDFS-SRR) and the finite element solution (FE-ADINA). Figure 3 also shows the buckled shape (from the ADINA analysis) of the model at two time steps. The threshold between elastic and plastic behavior occurred at around 250 $\mu$s and significant occurrences of strain-rate reversal were noted by 750 $\mu$s. Figure 4 shows the outer and inner fiber and the hoop strains as a function of time at the zero degree (top) location on the ring. A reversal in curvature for this location is evident where the outer and inner strain curves cross at about 500 $\mu$s. Strain-rate reversal occurs at about 700 $\mu$s where the outer fiber strain line starts to decrease. This location is on a buckle whose radius of curvature is inside the ring (i.e., inside is under the highest compressive strain). These observations were made using the strain results from the finite difference solution which was easily modified to acquire detailed results. In fact, it was possible to monitor some stress, strain, and curvature results as the finite difference solution progressed, something which was not possible in the finite element solution with its much longer solution time and large volume of output requiring extensive postprocessing.

From Fig. 3, the finite difference and finite element solutions show reasonable agreement for the response of the most amplified harmonics up to about 1200 $\mu$s. Harmonics above $n = 30$ show poor agreement between the finite difference and finite element solutions, but good agreement between the finite difference and analytical solutions. It should be noted that for this model, the shell parameter, $s$, which defines the wave number where the solution of the differential equation (Eqs. (1) and (2)) changes from hyperbolic to sinusoidal form, is 28. Both the finite difference and analytical solutions indicate a rapid drop in modal amplitudes beyond $n = 30$.

The finite difference solution was only successful for a limited time past the occurrence of strain-rate reversal and started to break down by 1200 $\mu$s. Curvature reversal in combination with strain-rate reversal produces a complex strain state which violates the assumptions of plane sections remaining plane and the neglect of variations in the tangential displacement which are used in formulating the differential equation and solution. It should be noted, from Fig. 4, that by 1200 $\mu$s, the hoop strain has reached six percent and the inner fiber strain has reached 12 percent with considerable curvature occurring. The finite element method, which is not restricted by these assumptions, is required to further the solution.

The analytical solution predicts amplitudes greater than the numerical solutions because it does not model elastic behavior, strain-rate reversal or curvature reversal. Including these effects leads to a significant reduction in buckling amplitude and in the dominant wave number of the mode shape. Figure 5 shows the modal growth (for the same time steps) of the analytical ($a$) and finite element ($b$) solutions after significant

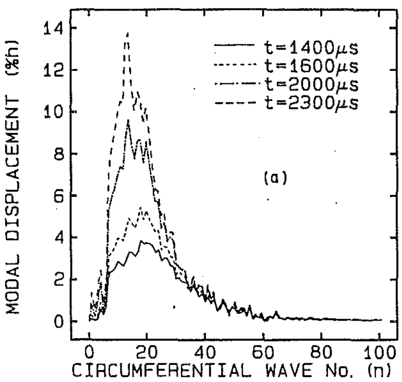


Fig. 5(*a*)

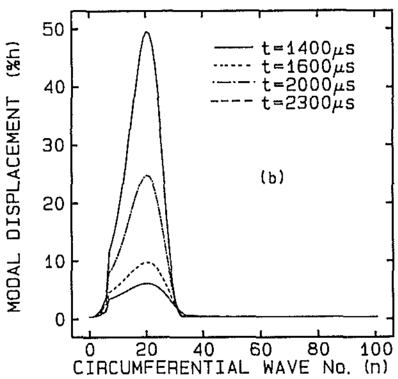


Fig. 5(*b*)

Fig. 5 Modal growth of finite element (*a*) and analytical (*b*) solutions to time of terminal

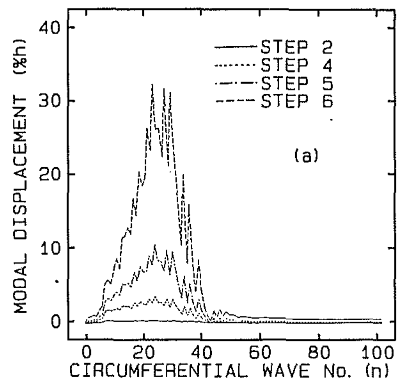


Fig. 7(*a*)

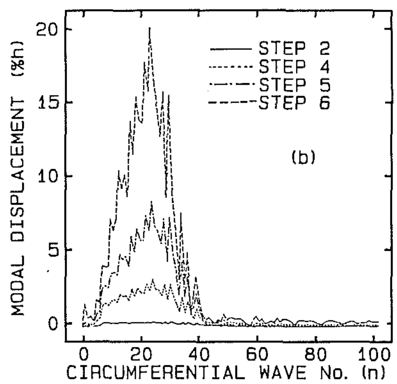


Fig. 7(*b*)

Fig. 7 Comparison of finite difference solutions without (*a*) and with (*b*) the effect of strain-rate reversal

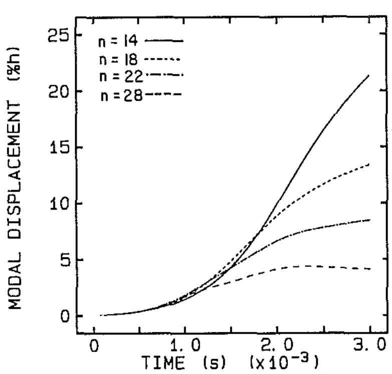


Fig. 6 Buckling growth of specific wave numbers from finite element solution

strain-rate reversal has occurred, until the theoretical time of terminal hoop motion (when the inward hoop velocity first reaches zero). The analytical solution remains in the theoretical critical mode of $n_{cr} = 20$ (Eq. (3)), and reaches an amplitude of 50 percent of the ring thickness. The finite element solution shows a drop in dominant mode to $n_{cr} = 14$ which reaches an amplitude of 14 percent. Figure 6 shows the growth of four predominant wave numbers with time (to 3ms) from the finite element solution. Initially, $n = 28$ is dominant, followed by $n = 22$, then $n = 18$, and finally $n = 14$ takes over as the dominant wave number.

In considering the analytical solution (Eq. (2)), it should be noted that the hoop mode ($n = 0$) is uncoupled from the flexural modes ($n \geq 2$) and hence no transfer of energy from the hoop mode can take place. As noted by Lindberg and Kennedy (1975), this causes a longer response time to terminal motion and allows the amplification functions of the analytical solution to expand for too long a time period producing unrealistically large buckling amplitudes. The finite element solution does allow this energy transfer between the modes and the initial energy is dissipated much quicker than for the analytical solution.

Figure 7 shows the effects of strain-rate reversal using the finite difference solution. Figure 7(*a*) is the finite difference solution neglecting the elastic unloading effects of strain-rate reversal where wave numbers 22, 28, and 32 are all amplified to over 30 percent of the ring thickness by time step 6. Figure 7(*b*) is the finite difference solution including the effects of strain-rate reversal where mode 22 only reaches 20 percent of the thickness and the higher wave numbers of $n = 28$ and $n = 32$ only reach 15 percent by time step 6. Figure 7 cannot be compared to the results of Figs. 3 to 6 as it is for a different model and loading.

## Comparison to Experimental Results

Abrahamson and Goodier (1962) present results of several pulse-buckling experiments. Comparison to these experimental results can only be qualitative as the initial geometric and axisymmetric shock load imperfections are unknown. Two of the experimental models, numbers 25 and 43, which were an aluminum cylinder of $a/h = 9.9$ and a steel cylinder of $a/h = 35.6$, respectively, were modeled with ADINA. The experiments were arranged to represent infinite cylinder, plane-strain cases and as such were modeled as two-dimensional rings. The experimental results are given as the observed number of crests and also as the average amplitude of the buckles (which is based on a different number of crests than the observed number). These quantities are used for comparison to the ADINA modal displacement results, although they are derived differently. Nominal initial velocities and material properties re-

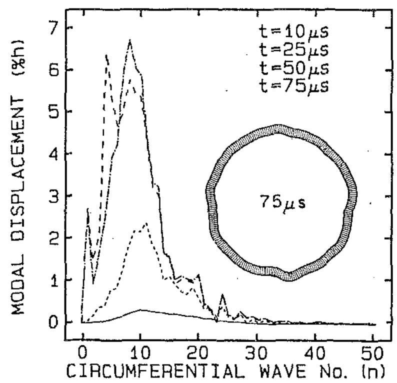


**Fig. 8 Modal growth and buckling mode shape for ADINA model of experimental cylinder number 25**

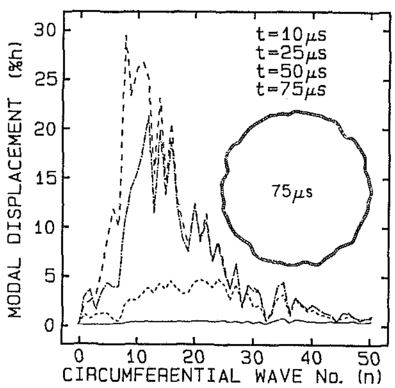


**Fig. 9 Modal growth and buckling mode shape for ADINA model of experimental cylinder number 43**

ported in the experimental study, and the imperfections of Eq. (8), were used in the ADINA analyses.

The finite element analysis modal growth plot and the buckled shape for cylinder number 25 is shown in Fig. 8. The experimental results given by Abrahamson and Goodier (1962) indicate an observed mode of nine waves and an average buckle amplitude of about 3.6 percent of the shell thickness (using seven waves in the average). The finite element results show predominant modal formation in $n$ = 7–10 and an average amplitude of about six percent. The analytical solution (Eqs. (2) and (3)) predicts the critical mode to be $n$ = 14 with an amplitude of 43 percent of the thickness by the time of terminal motion at 51 $\mu$s. Strain-rate reversal occurs much earlier than 51 $\mu$s for this model and is the most likely cause for the analytical solution overpredicting the critical mode and greatly overpredicting the amplitude of response. The finite element solution gives a reasonable prediction of the experimental results. The effects of axial strain in the experimental models, which were not truely infinite cylinders, the neglect of damping and the simplification of material properties in the finite element analysis, and the attraction of deformation energy to an imperfection produced by seams in the explosive and attenuator layers, may have been responsible for lower experimental buckling amplitude values.

The modal growth curves and the buckling mode shape for cylinder number 43 are shown in Fig. 9. The experimental results reported 28 as the observed number of waves in the response and gave an average amplitude of 10.7 percent of the shell thickness with 20 waves in the average. The dominant wave numbers of response in the finite element solution are $n$ = 20 with a final steady amplitude of about 12 percent of the thickness, $n$ = 16 at about 20 percent, $n$ = 12 at about 24 percent, and $n$ = 8 at about 30 percent. The finite element response in $n$ = 20 is in reasonable agreement with the experimental results for average amplitude over 20 waves, but lower numbered waves have higher buckling amplitudes. This model also shows the decrease in wave number with time, starting off with dominant wave numbers of $n$ = 20–24, dropping to $n$ = 16 and finishing with $n$ = 8 and 12. The analytical solution of Eqs. (2) and (3) predicts a critical wave number of $n$ = 58 with an amplitude of 53 percent in this mode at 25 $\mu$s and an impossibly large amplitude by the terminal motion time of 46 $\mu$s. Strain-rate reversal occurs very early in the motion of this model which explains the failure of the analytical solution.

## Discussion and Conclusions

The occurrence and fundamental characteristics of dynamic pulse buckling of thick rings (infinite cylinders) have been investigated using three different solution methods. The basic difference between behavior of thick rings as opposed to thinner rings is that significant strain levels are reached (well into the plastic flow regime) before appreciable buckling deformations occur. As the amplitudes and curvature of individual buckles increase, they reach the point of strain-rate reversal which causes elastic unloading. This greatly increases the moment across the ring thickness which retards the further growth of buckling waves. Longer wavelength buckles, which have less curvature for a given amplitude than shorter wavelength buckles, experience strain-rate reversal later in the motion and overtake the shorter wavelengths as the dominant wave numbers in the buckling response. The overtaking of short wavelengths by longer wavelengths results in reversals of curvature and curvature rate, which when in combination with strain-rate reversal and large values of strain, produces a very complex stress state in the ring.

There was roughly an order of magnitude between solution times for the three methods, with the analytical taking a few seconds, the finite difference a few minutes to an hour, and the finite element taking several hours; the numerical solution times depending on the spatial and temporal discretization levels.

The analytical solution presented by Abrahamson and Goodier (1962), reformulated for initial shape imperfections (Eqs. (1) and (2)), does not model elastoplastic behavior or strain-rate reversal and assumes continual plastic flow of all wavelengths. The critical wave number in the buckling mode shape (Eq. (3)) dominates the response throughout the motion. The analytical solution is valid before strain-rate reversal occurs (except for the omission of elastic behavior), but for rings with initial shape imperfections of reasonable amplitude (such as Eqs. (7) an (8)), strain-rate reversal occurs early in the ring motion, well before the time of terminal hoop motion (first occurrence of zero velocity in the hoop motion). The time of terminal motion is overestimated by the analytical solution as it does not model energy transfer from the hoop to the flexural modes. Solutions using Eq. (2) until terminal motion is reached can considerably overestimate the amplitudes and predominant wave numbers of response. Modifications to the analytical solution to include elastic behavior were considered (Lindberg and Florence, 1987) by numerically integrating the equation of motion with the hoop stress and the modulus as functions of time. This approach improves the early time performance of the analytical solution, but requires the entire ring to be of the same modulus at a given time; a restriction which the finite difference solution, via the strip integration, does not have.

The finite difference solution to the equation of motion allowed a limited investigation of elastoplastic and strain-rate reversal effects. This solution broke down at high strain levels in attempting to model the complex stress state resulting from curvature reversal producing a second occurrence of strain-rate reversal at a cross-section. The finite difference solution would require the inclusion of the tangential displacement variable and some additional nonlinear terms in the equation of motion to model further dynamic buckling response of the ring. This would considerably increase the difficulty and complexity of the solution which, in light of the success of the finite element method, would not be warranted. The relative simplicity of the finite difference solution in both solution time and ease of obtaining results at any point in the ring, proved to be very useful in determining the stress and strain state, until it reached its computational limits.

The ADINA finite element solutions proved to be successful and reasonably efficient in predicting dynamic buckling response. The complex stress state resulting from strain rate and curvature reversals was successfully modeled. The requirements of modeling initial shape imperfections to produce the buckling mode, time and geometry discretization to allow formation of the buckling mode, and sufficient variation of strain through the ring thickness (via integration points) to model strain-rate reversal, have been demonstrated. The latter requirement is especially important in thinner shells where strain-rate reversal occurs quickly and extensively and models using shell elements with single integration points through the thickness will not adequately model the proper response. There was reasonable agreement of the finite element results with the published experimental results, certainly much better than the analytical solutions provided.

The finite element solution to dynamic buckling can be extended to other types of structures and will lead to designs which can better resist the destructive results of impact loads. As discussed, the prediction of dynamic buckling requires a high level of finite element modeling, more so than what may be used for general stress analysis.

## Acknowledgments

In addition to the Defence Research Establishment Atlantic, who supported this work in the course of the author's employment as a Defence Scientist, the author also wishes to acknowledge the support of Dr. R. C. Gilkie and the late Dr. S. Malhotra of the Technical University of Nova Scotia and of Dr. D. L. Anderson of the University of British Columbia in their advisory roles in the author's doctoral thesis work, from which this paper is derived.

## References

Abrahamson, G. R., and Goodier, J. N., 1962, "Dynamic Plastic Flow Buckling of a Cylindrical Shell from Uniform Radial Impulse," *Proc. of the Fourth US National Congress of Applied Mechanics*, Vol. 2, pp. 939–950.

ADINA, 1987, "A Finite Element Program for Automatic Dynamic Incremental Nonlinear Analysis, User's Manual," ADINA Engineering, Watertown, Mass.

Florence, A., and Vaughan, H., 1968, "Dynamic Plastic Flow Buckling of Short Cylindrical Shells Due to Impulsive Loading," *J. Solids and Structures*, Vol. 4, pp. 741–756.

Gefken, P. R., Kirkpatrick, S. W., and Holmes, B. S., 1988, "Response of Impulsively Loaded Cylindrical Shells," *International Journal of Impact Engineering*, Vol. 7, No. 2, pp. 213–227.

Goodier, J. N., and McIvor, I. K., 1964, "The Elastic Cylindrical Shell Under Nearly Uniform Radial Impulse," ASME Journal of Applied Mechanics, pp. 259–266.

Kirkpatrick, S. W., and Holmes, B. S., 1987, "Structural Response of Thin Cylindrical Shells Subjected to Impulsive External Loads," *AIAA Journal*, Vol. 26, No. 1, pp. 96–103.

Lindberg, H. E., 1964, "Buckling of a Very Thin Cylindrical Shell Due to an Impulsive Pressure," ASME Journal of Applied Mechanics, pp. 267–272.

Lindberg, H. E., and Florence, A. L., 1987, *Dynamic Pulse Buckling*, Martinus Nihoff Publishers, Boston.

Lindberg, H. E., and Kennedy, T. C., 1975, "Dynamic Plastic Pulse Buckling Beyond Strain-Rate Reversal," ASME Journal of Applied Mechanics, pp. 411–416.

Ishizaki, T., and Bathe, K. J., 1980, "On Finite Element Large Displacement and Elastic-Plastic Dynamic Analysis of Shell Structures," *Computers and Structures*, Vol. 12, pp. 309–318.

Stuiver, W., 1965, "On the Buckling of Rings Subject to Impulsive Pressures," ASME Journal of Applied Mechanics, pp. 511–518.

Yilong Bai

Zhong Ling

Limin Luo

Fujiu Ke

Laboratory for Non-Linear Mechanics of Continuous Media, Institute of Mechanics, Chinese Academy of Sciences, Beijing 100080, China

# Initial Development of Microdamage Under Impact Loading[1]

*In this paper, the initial development of microdamage in material subjected to impulsive loading was investigated experimentally and analytically with controllable short-load duration. Based on a general solution to the statistical evolution of a one-dimensional system of ideal microcracks, a prerequisite to experimental investigation of nucleation of microcracks was derived. By counting the number of microcracks, the distribution of nucleation of microcracks was studied. The law of the nucleation rate of microcracks can be expressed as a separable function of stress and cracksize. It is roughly linear dependence on loading stress. The normalized number density of microcracks is in agreement with that of a second-phase particle.*

## 1 Introduction

Spallation, occurring in solids subjected to impact loading, usually results from accumulation of microdamage. Generally speaking, the microdamage is created by tensile stress waves, which form when compressive waves reflect at free surface, corners, or interfaces adjacent to media with low-wave impedance. Closeup observations have revealed that the microdamage is produced by means of nucleation, extension, and coalescence of microcracks or microvoids (Curran et al., 1987). The idea that coalescence of microcracks or microvoids should be responsible for complete spallation was suggested long ago. However, the evolution of microdamage, especially the transition from gradual accumulation of microdamage to complete failure of materials, has not been clearly interpreted yet, either experimentally or theoretically.

In a previous paper (Shen et al., 1986) it has been shown that the collapse of residual strength of damaged samples appears to be catastrophic at a certain level of microdamage. The specimens were cut from rolled aluminum alloy plate and tested under planar impact loading with a light gas gun. Then the central part of a half of an individual impacted specimen was statically tested to examine the residual ultimate strength of the damaged sample. Another half was sectioned, polished, and observed with a microscope to investigate corresponding microdamage. It seems that an abrupt loss of residual ultimate strength happens at $l'/l \sim 0.7$, where $l'$ is the total length of microcracks adjacent to a would be separation line and $l$ is the length of the observed section (Fig. 1). In this diagram the damage function is defined by $F = 1 - \sigma_r/\sigma_b$, where $\sigma_r$ and $\sigma_b$ are the residual ultimate tensile strength of impacted sample and the bulk strength of the virgin material, respectively. Clearly, the sharp loss of residual ultimate strength of damaged material manifests a critical state of microscopic damage. In this regard damage fracture transition represents a class of material instability.

For the sake of understanding the instability, it is necessary to determine the variables which can properly characterize the accumulation of microdamage. As the basis of the study, this paper restricts consideration to the initial development of microdamage, i.e., the nucleation of microcracks under planar impact loading, because spallation occurring under this condition causes planar penny-shaped microcracks parallel to each other. Thus, the configuration can simplify the problem as one-dimensional, since only one variable is needed to characterize the microcracks.

## 2 General Solution

A general framework concerning the statistical evolution of microdamage has been put forward in previous papers (Bai et al., 1988). Here, a brief introduction will be given, particularly for the case of a one-dimensional system of ideal microcracks.

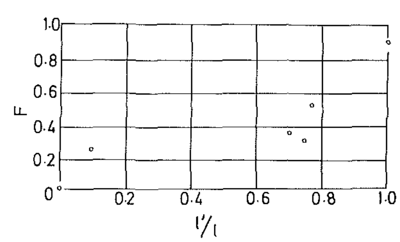


**Fig. 1 Relationship between macroscopic damage function $F = 1 - \sigma_r/\sigma_b$ and total length of microcracks by observed section length $l'/l$ (from Shen et al., 1986)**

[1]This work was supported in part by the Chinese Natural Science Foundation.

Contribution by the Applied Mechanics Division of THE AMERICAN SOCIETY OF MECHANICAL ENGINEERS for publication in the ASME JOURNAL OF APPLIED MECHANICS.

Discussion on this paper should be addressed to the Technical Editor, Professor Leon M. Keer, The Technological Institute, Northwestern University, Evaston, IL 60208, and will be accepted until four months after final publication of the paper itself in the JOURNAL OF APPLIED MECHANICS.

Manuscript received by the ASME Applied Mechanics Division, June 29, 1990; final revision, Feb. 6, 1991. Associate Technical Editor: J. W. Rudnicki.

Microcracks are termed as ideal provided they satisfy the following conditions: (1) nucleation and extension of microcracks are independent of each other and (2) nucleation and extension of an individual microcrack are governed by its microscopically local conditions. In addition, it is assumed that each microcrack can be characterized by a single variable in phase space. For example, a penny-shaped crack can be described by its area or radius. Obviously, this assumption can significantly simplify the formulation of laws of nucleation and extension of microcracks.

The governing equation of the statistical evolution of a one-dimensional system of ideal microcracks has been derived (Bai et al., 1988; Ke et al., 1990; Bai et al., 1991) in a phase space and can be written as

$$\frac{\partial n}{\partial t}+\frac{\partial(\dot{c}n)}{\partial c}=n_N \tag{1}$$

where $t$ is time; $c$ is the length scale variable of microcrack; $\dot{c}$ is the extension rate of an individual crack; $n$ is the number density of cracks, i.e., the number of cracks per unit physical volume per unit crack length; and $n_N$ is nucleation rate of number density of cracks, i.e., nucleating number of cracks per unit physical volume per unit crack length per unit time. The details of the derivation of Eq. (1) can be found in the paper of Ke et al. (1990) and Bai et al. (1991). Clearly, the dynamic laws for $n_N$ and $\dot{c}$ are dependent on loading stress $\sigma(t)$ and material properties in addition to the microcrack variable $c$, but are independent of the number density $n$, in the system of ideal microcracks:

$$n=n(c,\sigma(t),X_m) \tag{2}$$

$$\dot{c}=\dot{c}(c,\sigma(t),X_m) \tag{3}$$

where $X_m$ are material parameters.

The general solution to Eq. (1) has been obtained by Ke et al. (1990) and expressed in the following form:

$$n(c,t)=\begin{cases} n_N(c)t & c\le b \\ \dfrac{1}{A(c)}\displaystyle\int_{\eta(c,t)}^{c} n_N(c')dc' & c>b \end{cases} \tag{4}$$

provided the loading stress $\sigma$ remains constant. Hence, $\sigma$ and $X_m$ are not denoted explicitly in (4). Here, $\dot{c}$ is defined by

$$\dot{c}=\begin{cases} 0 & c\le b \\ A(c) & c>b \end{cases} \tag{5}$$

where $b$ denotes a size threshold of extension of microcrack and $\eta$ is defined in the following way:

$$t=\int_{\eta(c,t)}^{c}\frac{dc'}{A(c')}\,. \tag{6}$$

When $c \Rightarrow b$, the asymptotic behavior of extension rate $A(c)$ determines whether a stationary solution exists in the range of $b<c<c_0$, where $c_0$ is defined by

$$t=\int_{b}^{c_0(t)}\frac{dc'}{A(c')}\,.$$

The stationary solution to Eq. (1) manifests the saturation of the number density of microcracks (Ke et al., 1990). But in this paper we have to focus our discussion on the nucleation of microcracks. The readers, interested in the theoretical detail of the evolutionary solution to Eq. (1), can refer to the Ke et al. (1990) paper.

## 3 Experimental Procedure and Distribution Function

It was pointed out in the previous section that two dynamic laws, nucleation and extension of microcracks, can substantially affect the evolution of microcracks. There is a simple extension law derived by Berry (1960) for a crack in a linear elastic medium. Of course one cannot expect that the microcracks in the micrometer range are truly brittle. But before realistic models of microcracks are developed, Berry's formula can be adopted as an operational expression of an extension law.

On the other hand, nucleation laws of microcracks proposed hitherto are mostly indirect (Curran et al., 1987; McClintock, 1973; Batdorf, 1975). Due to the significance of the function $n_N$ in the evolution of microcracks, for example in expression (4), the determination of the nucleation function was thought to be a primary task in the experimental study. But extracting the information on the nucleation of microcracks from experimental observations is difficult because one cannot observe straightforwardly the nucleation of microcracks. In order to unveil the nucleation law of microcracks let us examine the solution (4)–(6) of the evolution of microcracks. The concrete aim is to guide the design of experiments.

For a very short stress pulse $\alpha(\delta t)$, the expression (6) can be rewritten as

$$\eta=c-A(c)\cdot\delta t. \tag{7}$$

In fact, $\eta=\eta(c,t)$ represents the size of microcracks at $t=0$, for the crack of length $c$ at time $t$ (Ke et al., 1990), if it could contract according to the same extension law (5). Substitution of (7) into (4) gives following approximate solution for a short stress pulse,

$$n(c,\delta t)=\begin{cases} n_N(c)\cdot\delta t & c<b \\ n_N(c-\theta\cdot A(c)\cdot\delta t)\cdot\delta t & c>b \end{cases} \tag{8}$$

where $\theta$ is a parameter $0<\theta<1$.

If we intend to express the nucleation rate $n_N(c)$ as

$$n_N(c)\doteq\frac{n(c,\delta t)}{\delta t}, \tag{9}$$

the following inequality should be satisfied:

$$c>>\theta\cdot A(c)\cdot\delta t. \tag{10}$$

The typical extension rate of microcrack $A(c)$ could be estimated by observing the length scale of microcracks in the

## Nomenclature

$A(c)$ = extension rate of individual crack when $c>b$

$b$ = threshold of extension of microcrack

$c$ = length scale variable of microcrack

$\dot{c}$ = extension rate of microcrack

$n$ = number density of microcrack, i.e., number of microcracks per unit physical volume per unit crack length

$n_N$ = nucleation rate of number density of microcracks, i.e., nucleating number of cracks per unit physical volume per unit crack length per unit time

$N$ = total number of microcracks per unit volume

$t$ = time

$X_m$ = material parameters

$\rho$ = normalized number density of microcracks

$\sigma$ = stress

**Subscripts**

$p$ = variable on sectioned surface

$N$ = variables describing nucleation of microcracks

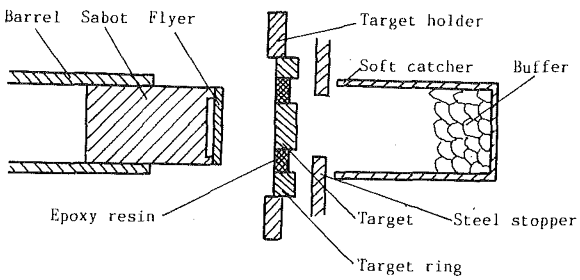


**Fig. 2 Set up of light gas gun**


**Fig. 3 Microcracks formed in specimen under short stress pulse loading**

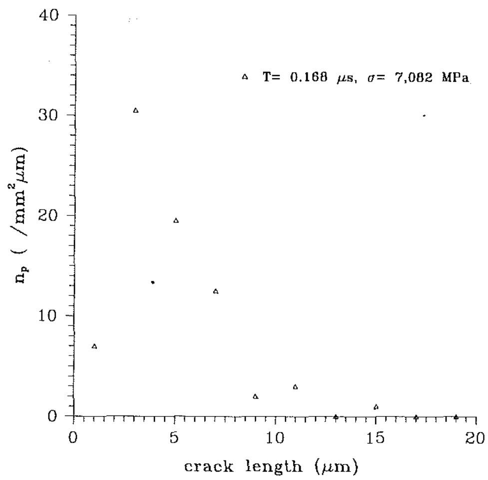


**Fig. 4 Typical distribution of microcracks**

specimen and loading duration. It is observed that the crack extension $\Delta c$ of about 10 $\mu$m was produced during loading time of about 1 $\mu$s. The typical extension rate, therefore, would be 10 $\mu$m/$\mu$s under the stress pulse loading.

Hence, if the tests for nucleation study are carried out with loading time of about 0.1 $\mu$s, the expression (10) leads to

$$c >> \theta \cdot A(c) \cdot \delta t \sim \theta \times 1 \mu\text{m}. \tag{11}$$

This is, if the nucleated size of microcracks is several micrometers, one can apply the observed number density of microcracks $n(c, \delta t)$ and expression (9) to obtain the nucleation rate of microcracks $n_N(c)$. Of course, the prerequisite is that the loading time must be submicrosecond.

An experimental method, i.e., the short stress pulse technique, was developed in our laboratory (Shen et al., 1985). A thin metal foil attached to a hollow projectile with low impedance support can create a one-dimensional stress pulse with a submicrosecond duration in target when impact between the target and the foil is conducted by making use of a light gas gun (Fig. 2). In the present study, stress pulses of about 100 ns duration were applied to examine the nucleation of microcracks. Figure 3 gives a picture of microcracks under the loading condition.

All the data listed in this paper were taken from a series of impact tests, in which a 0.1-mm thick nickel flyer strikes a 5-mm thick aluminium target. The details of material and testing procedure are given in the papers of Luo (1988) and Shen et al. (1991). The tested specimens were sectioned and polished carefully. The observations were conducted with an S-570 Scanning Electron Microscope and an Image Analysis System. Particularly, the statistics of microcracks, such as the visual length, orientation, number, etc., can be readily obtained by means of the instruments. Figure 4 shows a typical distribution of microcracks formed in the aluminum alloy target under the stress pulse loading with a duration of about 100 ns. The distribution of microcracks on a polished plane shows the following several distinct features with respect to visual length:

(1) there is a peak in the count at some crack length;
(2) the count tends to zero when crack becomes too long or too short; and
(3) the distribution curve is not symmetrical.

For comparison, the normalized distribution of the number density of microcracks $\rho$ (defined as $\rho_p(c) = n_p(c)/\int_0^\infty n_p(c)dc$) where subscript $p$ denotes the parameters on sectioned surface and also that of second-phase particles, on a polished section of the sample, are shown in Figs. 5 and 6.

The two distributions are qualitatively similar to each other. In addition, the locations of the two peaks in the two curves are in the same range, i.e., 2-5 $\mu$m. Furthermore, the value of crack length seems to be reasonable for the requirement for nucleation study, see expression (11). All of these offer corroborative evidence that the observed distribution is a proper representation of the nucleation of microcracks.

The data of the normalized distribution of number density of microcracks $\rho$ can be fitted to Weibull's function as

$$\rho_p(c) \sim c^{m-1} \cdot \exp(-c^m) \tag{12a}$$

or a function similar to Rayleigh's function

$$\rho_p(c) \sim c^m \cdot \exp(-c^2) \tag{12b}$$

(Fig. 5), where subscript $p$ denotes the quantities on a sectioned surface.

## 4 Law of Nucleation Rate

Before continuing, two points should be made. Since the difference between the number density of microcracks $n(c)$, i.e., the number of cracks in unit physical volume and unit phase space volume, and the corresponding variable on sectioned surface $n_p(c)$ depends on a integration with respect to crack length scale only, the prerequisite to the nucleation study, i.e., formulas (9) and (11) still works for $n_p(c)$. Secondly, we prefer to retain the obtained data on nucleation in its original form, namely the distribution function on a sectioned surface, because all simple transformations of surface counting into volume distribution are based on some further assumptions on cracks (Seaman et al., 1978). We believe that the original form of nucleation distribution function may be more helpful for further examination.

Now, we are quite convinced that the data obtained by short stress pulse technique are a fair representation of the nucleation of microcracks. However, in practice we need a concise expression of the law of nucleation rate. Then the question is how to determine the expression from obtained data. It has been observed that the cracking is mostly confined to the second-phase copper particles in the aluminum alloy. More importantly, for second-phase particles of all sizes, only part of them became debonded. To look for the stress dependence and size distribution of nucleation of microcracks, we should once more turn to examine the normalized distribution of the number density of microcracks. Figures 5($a$) ($\rho_p(c)$) presents the experimental normalized number density of microcracks where $n_p$ is the number density on a sectioned surface and $N$ is the sum of the microcracks. The loading duration ranges mainly from 0.14 $\mu$s to 0.17 $\mu$s and the stress amplitude from 2.5 to 7.5 GPa. Figures 5($b$) and 5($c$) present two fittings. We also provide a normalized cumulative measure, i.e., the cumulative number of cracks per unit area divided by the total number of cracks per unit area. This curve shows better fitting, but disguises some scatter and deviations (Figs. 5($b$), 5($c$), and 5($d$)). According to the definition of $\rho_p$ and the approximate solution (8) and (9), we can derive

$$\rho_p(c,t,\sigma)=\frac{n_p(c,t,\sigma)}{\int_0^\infty n_p(c,t,\sigma)dc}\cong\frac{n_{Np}(c,\sigma)\delta t}{N_{Np}(\sigma)\delta t}$$

$$=\frac{n_{Np}(c,\sigma)}{N_{Np}(\sigma)}=\rho_p(c,\sigma), \quad (13)$$

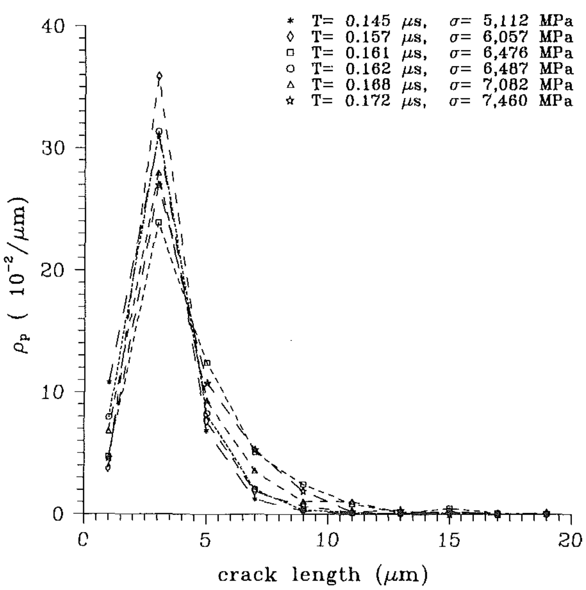

Fig. 5($a$) Experimental data

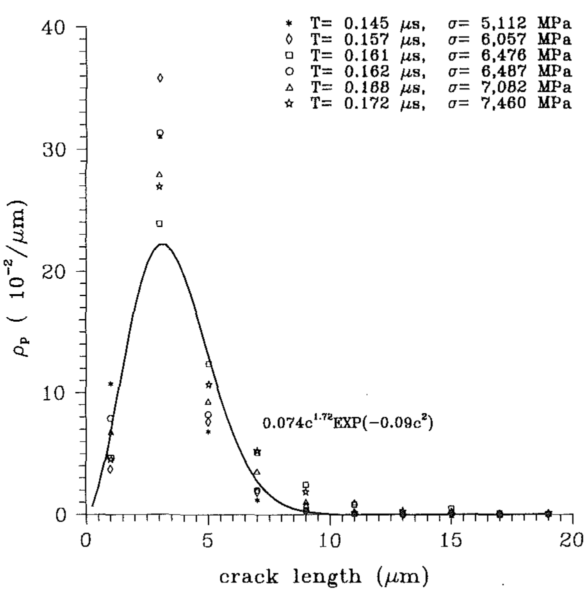

Fig. 5($b$) Fitting by $c^m \exp(-Bc^2)$, similar to Rayleigh's distribution

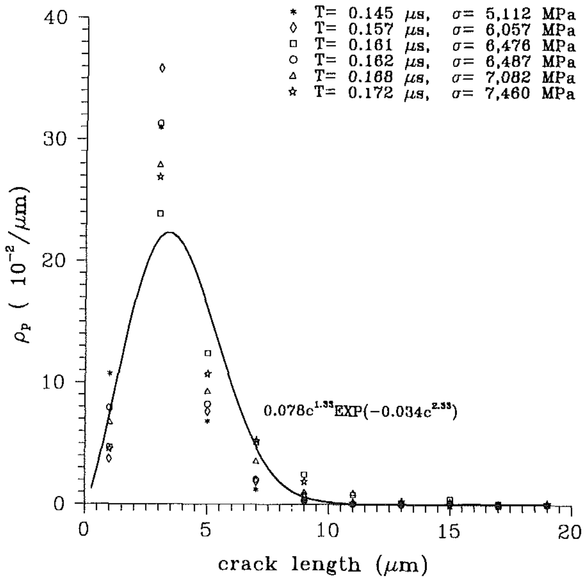

Fig. 5($c$) Fitting by Weibull's distribution, $c^{m-1}\exp(-Bc^m)$

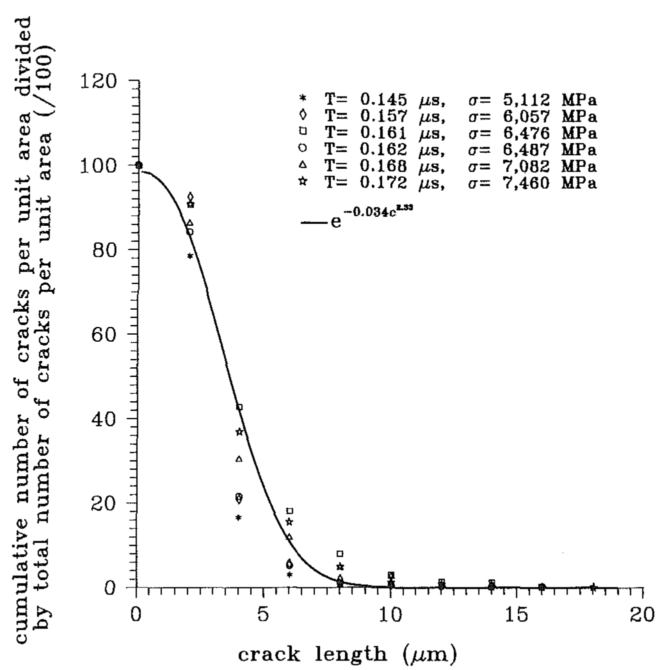

Fig. 5($d$) Cumulative size distribution of cracks

Fig. 5 Normalized distribution of number density of microcracks, $\rho_p$, showing $\rho_p(c,\sigma)$ is insensitive to loading stress, $\rho_p(c,\sigma)\sim\rho_p(c)$

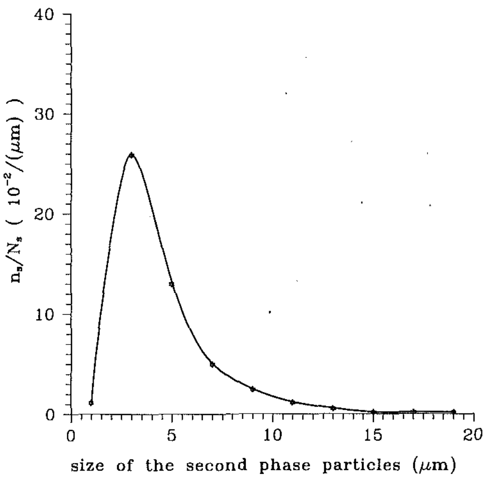


**Fig. 6 Distribution of the second-phase particles; $n_s$: number of the second-phase particles per unit area per unit particle length on the sectioned surface; $N_s$: total number of the second phase particles per unit area on the sectioned surface**

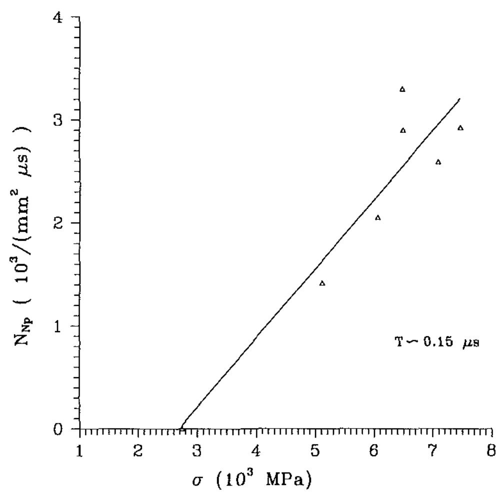


**Fig. 7 Relation between the nucleation of microcracks and the loading stress**

where

$$N_N(\sigma) = \int_0^\infty n_N(c, \sigma)\, dc. \tag{14}$$

Again, by examining Fig. 5 carefully, one can observe that $\rho_p$ can be expressed as a function of a single variable (crack length $c$) irrespective of stress $\sigma$ in the experimental range, namely

$$\rho_p(c, \sigma) \sim \rho_p(c). \tag{15}$$

Therefore, substitution of formula (15) into (13) gives the nucleation rate of microcracks $n_{Np}$

$$n_{Np}(c, \sigma) = N_{Np}(\sigma) \bullet \rho(c). \tag{16}$$

Furthermore, the data fitting of $N_{Np}(\sigma)$ gives a roughly linear stress dependence. See Fig. 7 ($N_{Np}(\sigma)$)

$$N_{Np}(\sigma) \sim \left(\frac{\sigma}{\sigma_0} - 1\right). \tag{17}$$

According to formulas (12), (13), (16), and (17), one can deduce

$$n_{Np}(c, \sigma) = K_0 \bullet \left(\frac{\sigma}{\sigma_0} - 1\right) \bullet \rho_p(c). \tag{18}$$

From (12) it follows that

$$n_{Np}(\sigma, c) = K \bullet \left(\frac{\sigma}{\sigma_0} - 1\right) \bullet c^{m-1} \exp(-B \bullet c^m) \tag{19a}$$

or

$$n_{Np}(\sigma, c) = K \bullet \left(\frac{\sigma}{\sigma_0} - 1\right) \bullet c^m \bullet exp(-B \bullet c^2) \tag{19b}$$

where $K_0$ and $K$ are coefficients. For our experimental range $\sigma = (2500 \sim 7500$ MPa), $t = (0.14 \sim 0.17\ \mu s)$. These results become

$$n_{Np} = K \bullet \left(\frac{\sigma}{\sigma_0} - 1\right) \left(\frac{c}{c_*}\right)^{m-1} \exp\left(-\left(\frac{c}{c_*}\right)^m\right), \tag{20a}$$

where

$$\begin{aligned} K &= 971 \quad \text{number}/(\text{mm}^2 \bullet \mu\text{m} \bullet \mu\text{s}) \\ \sigma_0 &= 2689 \quad \text{MPa} \\ c_* &= 4.27 \quad \mu m \\ m &= 2.33 \end{aligned}$$

or

$$n_{Np} = K \bullet \left(\frac{\sigma}{\sigma_0} - 1\right) \left(\frac{c}{c^*}\right)^m \exp\left(-\left(\frac{c}{c^*}\right)^2\right)$$

where

$$\begin{aligned} K &= 1042 \quad \text{number}/(\text{mm}^2 \bullet \mu\text{m} \bullet \mu\text{s}) \\ \sigma_0 &= 2689 \quad \text{MPa} \\ c_* &= 3.3 \quad \mu m \\ m &= 1.72. \end{aligned} \tag{20b}$$

The stress dependence (16) is consistent with macroscopic and empirical cumulative for incipient spallation (Luo, 1988)

$$\left(\frac{\sigma}{450} - 1\right)^{0.97} \Delta t = 1.21 \tag{21}$$

where the stress is in MPa and time is in $\mu$s. On the other hand, according to (17) and (18), the integration of solution (8), with respect to crack length $c$, can give a linear dependence of the total number of microcracks on tensile stress as well as on the loading time (Bai et al., 1991)

$$\left(\frac{\sigma}{\sigma_0} - 1\right) \Delta t \sim N_p, \tag{22}$$

where $N_p = \int_0^\infty n_p\, dc$ is the total number of microcracks over a unit area. Clearly, for incipient spallation, the macroscopic experimental criterion (21) and microscopic theoretical derivation (22) are in good agreement.

## 5 Disscussion

Complete spallation seems to be a sort of material instability, i.e., the evolution and then abrupt transition into large-scale coalesence of numerous microcracks. To understand this kind of micro-macroscopic material instability, the following preliminary and essential facts have been explored:

1 Based on a general solution to the statistical evolution of a one-dimensional system of ideal microcracks, the initial development of microdamage, under planar impacting load, can be analyzed. Moreover, a prerequisite to experimental investigation of nucleation of microcracks was derived.

2 A short stress pulse technique developed by means of a light gas gun was applied to meet the prerequisite and to obtain the data relevant to the nucleation of microcracks.

3 The normalized number density of microcracks was found to have a asymmetric distribution, which is in agreement with that of second-phase particles.

4 Furthermore, the normalized number density of microcracks shows approximate stress-independence in the experi-

mental range. Therefore, the law of nucleation rate of microcracks can be expressed as a separable function of stress and crack size.

5 The nucleation rate of microcracks was shown, to be, by experimental results, of roughly linear dependence on loading stress.

6 Above all, the nucleation rate of microcracks can be expressed in the form

$$n_{Np} = K \cdot \left(\frac{\sigma}{\sigma_0} - 1\right) \cdot f\left(\frac{c}{c^*}\right) .$$

An illustrative data fitting of the nucleation rate of microcracks on the sectioned surface in an aluminum alloy was given.

## References


Bai, Y., Ke, F., and Luo, L., 1988, "Statistical Modelling of Damage Evolution in Spallation," *J. de Physique*, Collque C3, Supplement, Vol. 49, No. 9, pp. C3-215.

Bai, Y., Ke, F., and Xia, M., 1991, "Formulation of Statistical Evolution of Microcracks in Solids," *Acta Mechanica Sinica*, Vol. 7, pp. 59–66.

Batdorf, S. B., 1975, "Fracture Statistics of Brittle Materials with Intergranular Cracks," *Nucl. Engng. and Design*, Vol. 35, pp. 349–360.

Berry, J. P., 1960, "Some Kinetic Considerations of the Griffith Criterion for Fracture—I: Equations of Motion at Constant Force," *J. Mech. Phys. Solids*, Vol. 8, pp. 194–216.

Curran, D. R., Seaman, L., and Shockey, D. A.; 1987, "Dynamic Failure of Solids," *Phys. Reports*, Vol. 147, pp. 253–388.

Ke, F., Bai, Y., and Xia, M., 1990, "Evolution of Ideal Microcracks System," *Scientia Sinica*, Series A, Vol. 33, pp. 1447–1459.

Luo, L., 1988, "Experimental Study of Nucleation Law and Simple Evolution of Spall Damage in An Aluminum Alloy," Master Thesis, Institute of Mechanics, CAS.

McClintock, F. A., 1973, *Fracture Mechanics of Ceramics*, Vol. 1, R. C. Bradt, D. P. H. Hassled, and F. F. Lange, eds., Plenum Press, New York, pp. 93–114.

Seaman, L., Curran, D. R., and Crewdson, R. C., 1978, "Transformation of Observed Crack Traces on A Section to True Crack Density for Fracture Calculation," *J. Appl. Phys.*, Vol. 49, pp. 5221–5229.

Shen, L., Bai, Y., and Zhao, S., 1986, "Experimental Study of Spall Damage in An Aluminum Alloy," *Proc. of Int. Symp. on Intense Dynamic Loading and Its Effects*, Science Press, Beijing, pp. 753–758.

Shen, L., Wu, S., Zhao, S., and Bai, Y., 1985, *Macro- and Micro-Mechanics of High Velocity Deformation and Fracture*, K. Kawata, and J. Shinier, eds., Springer-Verlag, Berlin, pp. 27–36.

Shen, L., Zhao, S., Bai, Y., and Luo, L., 1992, "Experimental Study on Criteria and Mechanism of Spallation in An Aluminum Alloy," submitted to *Int. J. Impact Engng*.

# ERRATUM

Erratum on "A Crack Terminating at a Slippage Interface Between Two Materials," by V. M. Gharpuray, J. Dundurs, and L. M. Keer, ASME JOURNAL OF APPLIED MECHANICS, Vol. 58, Dec. 1991, pp. 960–963.

Equation (15) should read as follows:

$$\Delta(\lambda;\alpha,\gamma)=2\lambda(2+\lambda)(1-\alpha)^2\sin^2\gamma[\lambda(2+\lambda)\sin^2\gamma-\cos 2\gamma]$$
$$+2\lambda(2+\lambda)(1+\alpha)^2\sin^2\gamma\cos^2\gamma$$
$$+2\lambda(2+\lambda)(1-\alpha)\sin^2\gamma\{\cos[2(1+\lambda)\gamma]+\cos[2\lambda\pi-2(1+\lambda)\gamma]\}$$
$$+\lambda(1+\alpha)\sin 2\gamma\{\sin[2(1+\lambda)\gamma]-\sin[2\lambda\pi-2(1+\lambda)\gamma]\}$$
$$-4\sin[(2+\lambda)\gamma]\sin[\lambda\pi-(2+\lambda)\gamma]\{\cos\lambda\pi+\alpha\cos[\lambda(\pi-2\gamma)]\} \quad (15)$$

# A Theory for Transverse Deflection of Poroelastic Plates

**Larry A. Taber**
Department of Mechanical Engineering,
University of Rochester,
Rochester, NY 14627
Mem. ASME

*A theory is presented for the bending of fluid-saturated poroelastic plates. The governing equations, based on linear consolidation theory, reduce to a single fourth-order integro-partial-differential equation to be solved for the transverse displacement of the middle surface. This equation resembles the classical plate equation but has an added convolution integral, which represents the viscous losses due to the flow of fluid relative to the solid. Laplace transform and perturbation solution methods are presented. The Laplace-transformed poroelastic plate equation and the first-order equation of the perturbation expansion have the forms of the standard plate equation. Results are given for a simply-supported rectangular plate with a time-dependent surface pressure.*

## Introduction

Recently, interest has intensified concerning the influence of poroeleasticity on the mechanical behavior of biological tissues. In general, poroelastic analyses have been based on three-dimensional mixture theory (Bowen, 1976) or three-dimensional consolidation theory (Biot, 1941, 1955, 1962, 1972). Many biological structures, however, are fluid-saturated membranes, beams, plates, or shells. Examples include arteries, hearts, diaphragms, skin, bones, and bladders. One and two-dimensional poroelasticity theories would be useful for these and other related mechanics problems.

To date, few papers have addressed sub-three-dimensional theories for poroelastic media. Using the linear consolidation theory, Biot (1964) examined the problem of cylindrical bending and buckling of a porous plate due to end loads, and Nowinski and Davis (1972) presented a poroelastic beam theory for application to bones. These linear theories are necessary prerequisites to the development of nonlinear theories, which are even more scarce. Using the mixture theory, Rajagopal et al. (1983) presented possibly the only nonlinear theory for poroelastic spherical membranes.

This paper extends the analysis of Biot (1964) to obtain a linear poroelastic plate theory. The development considers quasi-static transverse displacement of a porous, rectangular elastic plate of dimensions $a \times b$ and uniform thickness $h \ll (a, b)$ that is saturated with a viscous fluid (Fig. 1). Interconnected pores contribute to the porosity $\phi$, the ratio of pore volume to total volume. Transverse pressures $\bar{p} = \bar{p}_1(x, y, t)$ and $\bar{p} = \bar{p}_2(x, y, t)$ act on the upper ($z = -h/2$) and lower ($z = h/2$) plate surfaces, respectively.

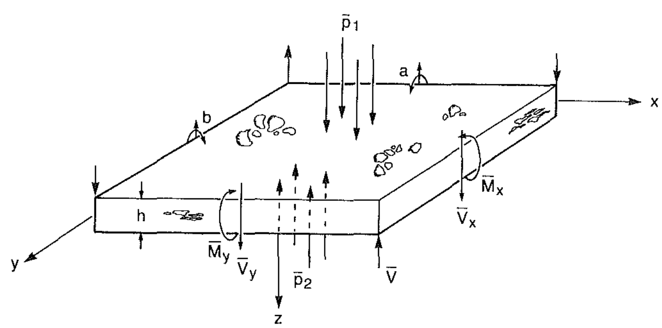


**Fig. 1 Poroelastic plate geometry**

Governing equations are developed using the methods of the classical linear theory for bending of thin elastic plates (Szilard, 1974). Except for the boundary conditions, which are found from the principle of virtual work, the equations are developed on mechanical grounds. This approach enhances physical insight while laying the foundation for future nonlinear theories, including those for large strain. The present theory is based on the following assumptions:

1 Normals to the middle surface of the solid skeleton ($z = 0$) remain straight and normal during deformation.
2 The plate is in a state of approximate plane stress, i.e., the *total* stress $\tau_z = 0$.
3 In-plane fluid-velocity *gradients* relative to the solid are small compared to the transverse fluid-velocity gradient.

The first two assumptions are the well-known Kirchhoff hypotheses (Szilard, 1974) and the third is a consequence of the transverse resistance to flow being much smaller than the resistance parallel to the middle surface.

The primary product of this study is a single fourth-order integro-partial-differential equation to be solved for the mid-

Contributed by the Applied Mechanics Division of THE AMERICAN SOCIETY OF MECHANICAL ENGINEERS for publication in the ASME JOURNAL OF APPLIED MECHANICS.

Discussion on this paper should be addressed to the Technical Editor, Professor Leon M. Keer, The Technological Institute, Northwestern University, Evanston, IL 60208, and will be accepted until four months after final publication of the paper itself in the JOURNAL OF APPLIED MECHANICS.

Manuscript received by the ASME Applied Mechanics Division, Oct. 3, 1990; final revision, Jan. 30, 1991. Associate Technical Editor: J. W. Rudnicki.

dle-surface transverse displacement $w_0$. This poroelastic plate equation has the same form as the classical plate equation with an added convolution integral, which is coupled to the time derivative of $w_0$ and represents the resistance due to the flow of fluid relative to the solid.

We investigate two methods for solving the equation: Laplace transforms and perturbation series. Taking the Laplace transform puts the poroelastic plate equation into the form of the standard plate equation, with the transform of $w_0$ entering only as the argument of the biharmonic operator. The first-order perturbation equation also has this form. Results are presented for a simply supported rectangular plate with a time-dependent surface pressure.

## Geometric Relations

Let $\mathbf{u}^s(x, y, z, t) = u^s\mathbf{e}_x + v^s\mathbf{e}_y + w^s\mathbf{e}_z$ and $\mathbf{u}^f(x, y, z, t) = u^f\mathbf{e}_x + v^f\mathbf{e}_y + w^f\mathbf{e}_z$ be the solid and fluid displacements, respectively, at time $t$ relative to the Cartesian coordinates $(x, y, z)$. The transverse displacement of the middle surface is $w_0(x, y, t) \equiv w^s(x, y, 0, t)$. Then, assumption (1) gives the in-plane solid displacements

$$u^s = -zw_{0,x}, \quad v^s = -zw_{0,y} \tag{1}$$

and the solid strains

$$\epsilon_x^s = u_{,x}^s = z\kappa_x, \quad \epsilon_y^s = v_{,y}^s = z\kappa_y, \quad \epsilon_{xy}^s = \frac{1}{2}\,(u_{,y}^s + v_{,x}^s) = z\kappa_{xy}$$
$$\epsilon_z^s = w_{,z}^s, \quad \epsilon_{xz}^s = \epsilon_{yz}^s = 0 \tag{2}$$

where the middle-surface curvatures are

$$\kappa_x = -w_{0,xx}, \quad \kappa_y = -w_{0,yy}, \quad \kappa_{xy} = -w_{0,xy}. \tag{3}$$

In this paper, a comma denotes differentiation with respect to the follower coordinate, and the components of fluid strain do not enter the analysis directly.

Like the classical plate theory, the present poroelastic plate theory ignores the stretching of normals in geometric considerations ($\epsilon_z^s = 0$) but relaxes this constraint in the analysis of stress, including the fluid pressure. For a thin plate, this inconsistency produces small errors.

## Equilibrium

In Biot's (1941, 1955, 1962) linear consolidation theory for poroelastic media, the *total* stresses per unit area of bulk material are

$$\tau_x = \sigma_x - \phi p_f, \quad \tau_y = \sigma_y - \phi p_f, \quad \tau_z = \sigma_z - \phi p_f$$
$$\tau_{xy} = \sigma_{xy}, \quad \tau_{xz} = \sigma_{xz}, \quad \tau_{yz} = \sigma_{yz} \tag{4}$$

where the $\sigma_i$ and $\sigma_{ij}$ are partial stresses acting on the solid component and $p_f$ is the pore pressure. With body and inertial forces neglected, the equilibrium equations are

$$\begin{aligned} &\tau_{x,x} + \tau_{xy,y} + \tau_{xz,z} = 0 \\ &\tau_{xy,x} + \tau_{y,y} + \tau_{yz,z} = 0 \\ &\tau_{xz,x} + \tau_{yz,y} + \tau_{z,z} = 0. \end{aligned} \tag{5}$$

On the faces of the plate, the total stresses must satisfy the boundary conditions

$$\begin{aligned} z = -\frac{h}{2}: &\quad \tau_z = -\bar{p}_1, \quad \tau_{xz} = \tau_{yz} = 0 \\ z = \frac{h}{2}: &\quad \tau_z = -\bar{p}_2, \quad \tau_{xz} = \tau_{yz} = 0. \end{aligned} \tag{6}$$

Integrating Eqs. (5) across the plate thickness and satisfying the boundary conditions (6) yields

$$\begin{aligned} &N_{x,x} + N_{xy,y} = 0 \\ &N_{xy,x} + N_{y,y} = 0 \\ &Q_{x,x} + Q_{y,y} = -p_0 \end{aligned} \tag{7}$$

where $p_0 \equiv \bar{p}_1 - \bar{p}_2$. In addition, multiplying Eq. $(5)_{1,2}$ by $z$ and integrating over the thickness gives

$$\begin{aligned} M_{x,x} + M_{xy,y} = Q_x \\ M_{xy,x} + M_{y,y} = Q_y \end{aligned} \tag{8}$$

in which Eqs. (6) again have been used. In these equations, the stress and moment resultants are

$$\begin{aligned} (N_x, N_y, N_{xy}, Q_x, Q_y) &= \int (\tau_x, \tau_y, \tau_{xy}, \tau_{xz}, \tau_{yz})dz \\ (M_x, M_y, M_{xy}) &= \int (\tau_x, \tau_y, \tau_{xy})z\,dz \end{aligned} \tag{9}$$

per unit length of the middle surface, where $\int \equiv \int_{-h/2}^{h/2}$.

## Constitutive Relations

The constitutive relations for a fluid-saturated poroelastic solid are (Biot and Willis, 1957)

$$\begin{aligned} \tau_x &= 2\mu\epsilon_x^s + \lambda\epsilon^s - \alpha p_f \\ \tau_y &= 2\mu\epsilon_y^s + \lambda\epsilon^s - \alpha p_f \\ \tau_z &= 2\mu\epsilon_z^s + \lambda\epsilon^s - \alpha p_f \\ \tau_{xy} &= 2\mu\epsilon_{xy}^s \\ p_f &= F(\zeta - \alpha\epsilon^s) \end{aligned} \tag{10}$$

where $\lambda$ and $\mu$ are the Lamé constants for the solid skeleton, and $\alpha$ and $F$ are constants which can be determined from compressibility tests. Furthermore,

$$\zeta \equiv \phi(\epsilon^s - \epsilon^f) \tag{11}$$

where

$$\epsilon^s = \nabla\cdot\mathbf{u}^s = \epsilon_x^s + \epsilon_y^s + \epsilon_z^s, \quad \epsilon^f = \nabla\cdot\mathbf{u}^f \tag{12}$$

are the solid and fluid dilatations. Note that since transverse shear strains are neglected, the stress-strain relations for $\tau_{xz}$ and $\tau_{yz}$ are omitted.

After substitution of Eq. $(12)_1$ into $(10)_3$, the plane stress condition $\tau_z = 0$ (assumption (2)) gives

$$\epsilon_z^s = A^{-1}[\alpha p_f - \lambda(\epsilon_x^s + \epsilon_y^s)] \tag{13}$$

where

$$A = \lambda + 2\mu \tag{14}$$

is the aggregate elastic modulus. Inserting Eq. (13) into Eq. $(10)_{1,2}$ then yields

$$\begin{aligned} \tau_x &= \frac{E}{1-\nu^2}\,(\epsilon_x^s + \nu\epsilon_y^s) - B\alpha p_f \\ \tau_y &= \frac{E}{1-\nu^2}\,(\epsilon_y^s + \nu\epsilon_x^s) - B\alpha p_f \end{aligned} \tag{15}$$

where

$$\frac{E}{1-\nu^2} = \frac{4\mu(\lambda+\mu)}{A}, \quad \nu = \frac{\lambda}{2(\lambda+\mu)}, \quad B = \frac{2\mu}{A} = \frac{1-2\nu}{1-\nu}, \tag{16}$$

in which $E$ and $\nu$ are the Young's modulus and Poisson's ratio, respectively, for the solid skeleton with $p_f = 0$. Next, substituting Eq. (13) into Eq. $(12)_1$ gives

$$\epsilon^s = \alpha p_f/A + B(\epsilon_x^s + \epsilon_y^s), \tag{17}$$

and putting this expression into Eq. $(10)_5$ yields

$$\zeta = \beta p_f + \alpha B(\epsilon_x^s + \epsilon_y^s) \tag{18}$$

where

$$\beta = \alpha^2/A + 1/F. \tag{19}$$

Finally, after substitution of Eqs. (2), $(10)_4$, and (15) into (9), integration over the shell thickness provides the poroelastic plate constitutive relations

$$N_x = N_y = B\alpha N,\ N_{xy} = 0$$

$$M_x = D(\kappa_x + \nu\kappa_y) + B\alpha M$$

$$M_y = D(\kappa_y + \nu\kappa_x) + B\alpha M$$

$$M_{xy} = D(1-\nu)\kappa_{xy} \quad (20)$$

where

$$D = \frac{Eh^3}{12(1-\nu^2)} \quad (21)$$

is the flexural rigidity of the plate solid skeleton. In addition,

$$N = -\int p_f dz,\ M = -\int p_f z\ dz \quad (22)$$

are the effective stress resultant and bending moment due to the variation in pore pressure across the plate thickness. For a solid plate, $\alpha = 0$ and Eqs. (20) reduce to the constitutive relations of classical plate theory.

## Fluid Flow

In the consolidation theory of Biot (1941, 1962), the flow of viscous fluid through a porous elastic solid is governed by Darcy's law

$$\frac{k}{\mu_f} \nabla p_f = \phi(\dot{\mathbf{u}}^s - \dot{\mathbf{u}}^f) \quad (23)$$

$$\xi = \begin{cases} \bar{p}_1(x,y,t)\left(\frac{1}{2} - \frac{z}{h}\right) + \bar{p}_2(x,y,t)\left(\frac{1}{2} + \frac{z}{h}\right) & \text{for BC (A1)–(B1)} \quad (\#1) \\ \bar{p}_1(x,y,t) & \text{for BC (A1)–(B2)} \quad (\#2). \\ 0 & \text{for BC (A2)–(B2)} \quad (\#3) \end{cases} \quad (29)$$

where $k$ is the permeability, $\mu_f$ is the fluid viscosity, $\nabla \equiv \mathbf{e}_x(\partial/\partial x) + \mathbf{e}_y(\partial/\partial y) + \mathbf{e}_z(\partial/\partial z)$, and dot denotes differentiation with respect to time. Taking the divergence of Eq. (23) and using Eq. (12) gives

$$\frac{k}{\mu_f} \nabla^2 p_f = \dot{\zeta} \quad (24)$$

with $\zeta$ defined by Eq. (11). Since relative in-plane fluid-velocity gradients are neglected (assumption (3)), Eq. (23) implies that $(|p_{f,xx}|, |p_{f,yy}|) \ll |p_{f,zz}|$. Then, substitution of Eqs. (2), (3), and (18) into (24) yields

$$Kp_{f,zz} = \dot{p}_f + \dot{\eta} \quad (25)$$

in which the effective plate permeability is

$$K = k/\mu_f\beta \quad (26)$$

**Table 1 Eigenvalues and eigenfunctions**

| BC | $\lambda_n$ | $\phi_0$ | $\phi_n$ |
|---|---|---|---|
| 1 | $\frac{n\pi}{h}$ | 0 | $\sin\frac{\lambda_n h}{2}\cos\lambda_n z + \cos\frac{\lambda_n h}{2}\sin\lambda_n z$ |
| 2 | $\frac{(2n-1)\pi}{2h}$ | 0 | $\sin\frac{\lambda_n h}{2}\cos\lambda_n z + \cos\frac{\lambda_n h}{2}\sin\lambda_n z$ |
| 3 | $\frac{n\pi}{h}$ | 1 | $\cos\frac{\lambda_n h}{2}\cos\lambda_n z + \sin\frac{\lambda_n h}{2}\sin\lambda_n z$ |

and the forcing term is

$$\eta(x,y,z,t) = -cz\nabla_0^2 w_0(x,y,t) \quad c = \alpha B/\beta \quad (27)$$

where $\nabla_0^2 \equiv (\partial^2/\partial x^2) + (\partial^2/\partial y^2)$. Equation (25) couples the mean plate curvature to the pore pressure. Since strong transverse gradients in pore pressure can occur, we solve Eq. (25) in its three-dimensional form, rather than integrating it over the plate thickness.

In this paper, we consider combinations of the following boundary conditions:

$$z = -\frac{h}{2}: \quad p_f = \bar{p}_1(x,y,t) \quad \text{(A1)}$$

$$p_{f,z} = 0 \quad \text{(A2)}$$

$$z = \frac{h}{2}: \quad p_f = \bar{p}_2(x,y,t) \quad \text{(B1)}$$

$$p_{f,z} = 0 \quad \text{(B2)}. \quad (28)$$

Conditions (A1) and (B1) correspond to permeable plate surfaces, while (A2) and (B2) give impermeable surfaces ($\dot{w}^s = \dot{w}^f$, see Eq. (23)).

A separation of variables solution to Eq. (25) can be found in the form

$$p_f(x,y,z,t) = \xi(x,y,z,t) + \sum_{n=0}^{\infty} A_n(x,y,t)\phi_n(z)$$

Table 1 gives the eigenfunctions $\phi_n$ and the corresponding eigenvalues $\lambda_n$ for various combinations of the boundary conditions (28). In addition,

$$A_0(x,y) = c_0(x,y)$$

$$A_n(x,y,t) = c_n(x,y)G_n(t) + \int_0^t G_n(t-\tau)\dot{a}_n(x,y,\tau)d\tau,\ n = 1,2,\ldots \quad (30)$$

where the dot denotes differentiation with respect to $\tau$, the $c_n(x,y)$ are functions to be determined by the initial conditions,

$$G_n(t) = e^{-K\lambda_n^2 t} \quad (31)$$

is the relaxation function, and

$$a_n(x,y,t) = -\frac{2}{h}\int [\eta(x,y,z,t) + \xi(x,y,z,t)]\phi_n(z)dz. \quad (32)$$

Given the boundary conditions, Eq. (32) can be integrated using Eqs. (27) and $(29)_2$ and Table 1. The result can be expressed in the form

$$a_n(x,y,t) = \eta_n\nabla_0^2 w_0(x,y,t) + \xi_n[\bar{p}_1(x,y,t), \bar{p}_2(x,y,t)] \quad (33)$$

where

**Table 2 Terms of pore pressure solution**

| BC | $\xi_n$ | $\Phi_{n;0}$ | $\Phi_{n;1}$ | $\Psi_0$ | $\Psi_1$ |
|---|---|---|---|---|---|
| 1 | $(2\Phi_{n;1} - \Phi_{n;0})\bar{p}_1 - (2\Phi_{n;1} + \Phi_{n;0})\bar{p}_2$ | $2(\lambda_n^*)^{-1}s^2$ | $(\lambda_n^*)^{-2}c(2s - \lambda_n^* c)$ | $\frac{1}{2}(\bar{p}_1 + \bar{p}_2)$ | $\frac{1}{12}(\bar{p}_2 - \bar{p}_1)$ |
| 2 | $-2\Phi_{n;0}\bar{p}_1$ | $2(\lambda_n^*)^{-1}s^2$ | $-(\lambda_n^*)^{-2}s(2s - \lambda_n^* c)$ | $\bar{p}_1$ | 0 |
| 3 | 0 | 0 | $(\lambda_n^*)^{-2}s(2s - \lambda_n^* c)$ | 0 | 0 |

$\lambda_n^* \equiv \lambda_n h;\ s \equiv \sin(\lambda_n^*/2),\ c \equiv \cos(\lambda_n^*/2)$

$$\eta_n = 2ch\Phi_{n;1}. \tag{34}$$

The quantities $\xi_n$ and (for $k = 0, 1$)

$$\Phi_{n;k} \equiv h^{-(k+1)} \int \phi_n z^k dz, \tag{35}$$

are listed in Table 2 for specified boundary conditions on the upper and lower plate surfaces. Thus, given $\overline{p}_1$ and $\overline{p}_2$, $a_n$ is an explicit function of $w_0$. Then, on substitution of Eqs. (30) and (33), Eqs. (29) provide $p_f$ in terms of a hereditary integral (Eq. $(30)_2$) involving $w_0$ and the unknown functions $c_n$.

According to Eqs. $(7)_{1,2}$ and $(20)_1$, $N_{,x} = N_{,y} = 0$ for $N = N(t)$. Then, Eq. $(22)_1$ gives $p_f = p_f(z, t)$, which is consistent with assumption (3). The present theory, however, allows for dependency of $p_f$ also on $x$ and $y$ (Eq. (29)). This inconsistency is not unlike that of classical plate theory, where the Kirchhoff assumption $\epsilon_z = 0$ is not consistent with the plane stress assumption $\tau_z = 0$. If the fluid pressure varies slowly with $x$ and $y$, then this approximation should not lead to serious errors.

Finally, with $p_f$ known, $N$ and $M$ can be computed. Substitution of Eqs. (29) into (22) and noting (35) yields

$$N = -h\left[\sum_{n=0}^{\infty} A_n \Phi_{n;0} + \Psi_0\right]$$

$$M = -h^2\left[\sum_{n=0}^{\infty} A_n \Phi_{n;1} + \Psi_1\right] \tag{36}$$

where the

$$\Psi_k \equiv h^{-(k+1)} \int \xi z^k dz \tag{37}$$

are given in Table 2. Using these equations, along with (30), (31), (33), and (34) and the expressions in Table 2, we can express the force and moment resultants (Eqs. (20)) in terms of $w_0$.

## The Poroelastic Plate Equation

This section combines the equations of the previous sections into a single equation for $w_0$. First, substituting Eqs. (8) for $Q_x$ and $Q_y$ into $(7)_3$ yields

$$M_{x,xx} + 2M_{xy,xy} + M_{y,yy} = -p_0. \tag{38}$$

Then, inserting Eqs. (3) into the moments of Eqs. (20) and the results into (38) leads to

$$D\nabla_0^4 w_0 = p_0 + B\alpha \nabla_0^2 M \tag{39}$$

which, with $\nabla_0^4 \equiv \nabla_0^2 \nabla_0^2$ is the governing equation of linear poroelastic plate theory. With $M$ expressed in terms of $w_0$ (Eqs. (30), (33), and $(36)_2$), Eq. (39) becomes a single equation to be solved for $w_0$. For a solid plate, $\alpha = 0$ and Eq. (39) reduces to the classical plate equation (Szilard, 1974).

Note the strong resemblance of Eq. (39) to the thermoelastic plate equation given in Chapter 12 of Boley and Weiner (1960). This is not unexpected since consolidation theory is analogous to *coupled* thermoelasticity (Biot, 1964). However, as is usually done, Boley and Weiner ignore the coupling between temperature and deformation, so the thermal bending moment (analogous to $M$) can be computed *a priori*. The present theory retains the coupling between fluid flow and deformation.

## Boundary Conditions

The principle of virtual work provides the appropriate boundary conditions for the poroelastic plate problem. Consider the rectangular plate in Fig. 1 with applied surface pressure ($\overline{p}$), edge shear forces ($\overline{V}_x$, $\overline{V}_y$), edge bending moments ($\overline{M}_x$, $\overline{M}_y$), and corner forces $\overline{V}$. The principle of virtual work takes the form

$$\delta W_i + \delta W_f = \delta W_e + \delta W_s \tag{40}$$

where $\delta W_i$ is the internal virtual work for the fluid-solid system, $\delta W_f$ is the energy dissipated through relative viscous fluid flow, and $\delta W_e$ and $\delta W_s$ represent the virtual work done by the edge and surface loads, respectively.

For a plate of bulk volume $\Omega$ and middle-surface area $S$, the first two terms in Eq. (40) can be written (Biot, 1962, 1972)

$$\delta W_i = \int_\Omega (\tau_x \delta\epsilon_x^s + \tau_y \delta\epsilon_y^s + 2\tau_{xy}\delta\epsilon_{xy}^s + p_f \delta\zeta) d\Omega \tag{41}$$

$$\delta W_f = \int_\Omega (\mu_f / k)\dot{\omega}\delta\omega d\Omega \tag{42}$$

where

$$\omega \equiv \phi(w^s - w^f),\ \delta\zeta = \delta\omega_{,z}. \tag{43}$$

The expression for $\delta\zeta$ follows from Eqs. (23) and (24) and assumption (3), which yield $\dot{\zeta} \cong (k/\mu_f)p_{f,zz} = \phi(\dot{w}^s - \dot{w}^f)_{,z}$. The applied loading terms are

$$\delta W_s = -\int_S [\overline{p}(1-\phi)\delta w^s + \overline{p}\phi\delta w^f] dS \tag{44}$$

$$\delta W_e = \int_0^b [\overline{V}_x \delta w_0 - \overline{M}_x \delta w_{0,x}]_0^a dy + \int_0^a [\overline{V}_y \delta w_0 - \overline{M}_y \delta w_{0,y}]_0^b dx - [\overline{V}\delta w_0]\,|_0^a|_0^b \tag{45}$$

where $[\ ] \equiv [\ ]_{-h/2}^{h/2}$ if limits are not specified.

Manipulation of Eqs. (41)-(45) follows standard procedures. First, after substitution of Eqs. (2) and $(43)_2$ into (41), integrating over the plate thickness and noting Eqs. (9) yields

$$\delta W_i = \int_S (M_x \delta\kappa_x + M_y \delta\kappa_y + 2M_{xy}\delta\kappa_{xy} + [p_f \delta\omega]) dS - \int_\Omega p_{f,z}\delta\omega d\Omega. \tag{46}$$

Moreover, since $\delta\omega = \phi(\delta w^s - \delta w^f)$, $\delta w^s \cong \delta w_0$ ($\epsilon_z^s \cong 0$), and $[\overline{p}] = \overline{p}_2 - \overline{p}_1 = -p_0$, Eq. (44) can be written

$$\delta W_s = \int_S (p_0 \delta w_0 + [\overline{p}\ \delta\omega]) dS. \tag{47}$$

Next, inserting Eqs. (3) into (46), integrating by parts to remove derivatives of $\delta w_0$, and combining the result with Eqs. (40), (42), (45), and (47) yields

$$\begin{aligned}
&-\int_S (M_{x,xx} + 2M_{xy,xy} + M_{y,yy} + p_0)\delta w_0 dS \\
&+ \int_\Omega (\mu_f \dot{\omega}/k - p_{f,z})\delta\omega d\Omega + \int_S [(p_f - \overline{p})\delta\omega] dS \\
&+ \int_0^b [(V_x - \overline{V}_x)\delta w_0 - (M_x - \overline{M}_x)\delta w_{0,x}]_0^a dy \\
&+ \int_0^a [(V_y - \overline{V}_y)\delta w_0 - (M_y - \overline{M}_y)\delta w_{0,y}]_0^b dy \\
&- [(2M_{xy} - \overline{V})\delta w_0]\,|_0^a|_0^b = 0.
\end{aligned} \tag{48}$$

where

$$V_x = Q_x + M_{xy,y}, \quad V_y = Q_y + M_{xy,x} \tag{49}$$

with $Q_x$ and $Q_y$ given by Eqs. (8). The first two integrals imply Eq. (38) and the normal component of Eq. (23), respectively. The other terms give the boundary conditions

$$\begin{aligned}
z = \pm\frac{h}{2}:&\qquad p_f = \overline{p} \quad \text{or } \delta\omega = 0 \\
x = 0, a:&\qquad V_x = \overline{V}_x \quad \text{or } \delta w_0 = 0 \\
&\qquad M_x = \overline{M}_x \quad \text{or } \delta w_{0,x} = 0
\end{aligned}$$

$$y=0,\ b: \qquad V_y=\overline{V}_y \quad \text{or } \delta w_0=0$$
$$M_y=\overline{M}_y \quad \text{or } \delta w_{0,y}=0$$
$$x=0,a;\ y=0,b:\ 2M_{xy}=\overline{V} \text{ or } \delta w_0=0 \tag{50}$$

where Eqs. (3) and (20) give $M_{xy}$ in terms of $w_0$. The first set of boundary conditions correspond to the fluid conditions of Eqs. (28), while the others have the same form as those of classical plate theory. Differences, however, are contained implicitly in the fluid contribution to the bending moments (see Eqs. (20)). Furthermore, the in-plane stress resultants $N_x$ and $N_y$ are neglected at the edges.

## Solution Methods

This section first considers a solution of the poroelastic plate equation by Lapalce transforms, which are often used in poroelasticity problems. Since inverting Laplace transforms is not always easy, we also present a peturbation solution method.

**Laplace Transform.** Taking the Laplace transform of Eq. (39) with respect to time yields

$$D\nabla_0^4\hat{w}_0(x,y,s)=\hat{p}_0(x,y,s)+B\alpha\nabla_0^2\hat{M}(x,y,s) \tag{51}$$

where hat denotes a transformed variable and $s$ is the transform parameter. Equations $(36)_2$, (30), (31), and (33), respectively, give

$$\hat{M}(x,y,s)=-h^2\left[\sum_{n=0}^{\infty}\hat{A}_n(x,y,s)\Phi_{n;1}+\hat{\Psi}_1(x,y,s)\right]$$
$$\hat{A}_n(x,y,s)=c_n(x,y)\hat{G}_n(s)+s\hat{G}_n(s)\hat{a}_n(x,y,s)$$
$$\hat{G}_n(s)=(s+K\lambda_n^2)^{-1}$$
$$\hat{a}_n(x,y,s)=\eta_n\nabla_0^2\hat{w}_0(x,y,s)+\hat{\xi}_n(x,y,s). \tag{52}$$

Substituting Eqs. (52) into (51) and rearranging terms leads to

$$\hat{D}_p(s)\nabla_0^4\hat{w}_0(x,y,s)=\hat{p}(x,y,s) \tag{53}$$

where

$$\hat{D}_p(s)=D+B\alpha h^2 s\sum_{n=0}^{\infty}\hat{G}_n(s)\Phi_{n;1}\eta_n \tag{54}$$

is the equivalent transformed flexural rigidity and

$$\hat{p}(x,y,s)=\hat{p}_0(x,y,s)-B\alpha h^2\nabla_0^2\left\{\sum_{n=0}^{\infty}\hat{G}_n(s)\Phi_{n;1}[c_n(x,y)+s\hat{\xi}_n(x,y,s)]+\hat{\Psi}_1(x,y,s)\right\} \tag{55}$$

is the equivalent transformed pressure loading.

The initial conditions give the $c_n$ and, with the surface loads specified, the quantities $\hat{\xi}_n$ and $\hat{\Psi}_1$ can be computed (see Table 2). Then, with care taken to satisfy the correct boundary conditions, standard techniques (Szilard, 1974) can be used to solve Eq. (53) for $\hat{w}_0(x,y,s)$ with $s$ as a parameter. Finally, taking the inverse Laplace transform provides $w_0(x,y,t)$.

**Perturbation.** For the following analysis, we introduce the nondimensional quantities

$$\epsilon=h/a,\ a^*=a/b,\ (w_0^*,\ W_0^*)=(w_0,\ W_0)/h$$
$$x^*=x/a,\ y^*=y/b,\ z^*=z/h,\ t^*=Kt/h^2$$
$$\lambda_n^*=\lambda_n h,\ \eta_n^*=\eta_n a^2/Eh^3$$
$$(p_0^*,\ P_0^*,\ \overline{p}_1^*,\ \overline{p}_2^*,\ p_f^*,\ A_n^*,\ a_n^*,\ \xi^*,\ \xi_n^*,\ \Psi_k^*)$$
$$=(p_0,\ P_0,\ \overline{p}_1,\ \overline{p}_2,\ p_f,\ A_n,\ a_n,\ \xi,\ \xi_n,\ \Psi_k)a^4/Eh^4$$
$$(M_x^*,\ M_y^*)=(M_x,\ M_y)a^2/Eh^4,\ M^*=Ma^4/Eh^6$$
$$D^*=D/Eh^3=[12(1-\nu^2)]^{-1},\ c^*=ca^2/Eh^2$$
$$\nabla_0^{*2}=\frac{\partial^2}{\partial x^{*2}}+a^{*2}\frac{\partial^2}{\partial y^{*2}} \tag{56}$$

where $\epsilon$ is the perturbation parameter. Then, Eqs. (39), (25) and (27), and $(22)_2$, respectively, become

$$D^*\nabla_0^{*4}w_0^*=p_0^*+B\alpha\epsilon^2\nabla_0^{*2}M^*$$
$$\frac{\partial^2 p_f^*}{\partial z^{*2}}=\frac{\partial}{\partial t^*}(p_f^*-c^*z^*\nabla_0^{*2}w_0^*)$$
$$M^*=-\int_{-1/2}^{1/2}p_f^*z^*dz^* \tag{57}$$

with $\nabla_0^{*4}=\nabla_0^{*2}\nabla_0^{*2}$.

The dependent variables are expanded in series of the form

$$v^*=v^{(0)}+\epsilon^2 v^{(1)}+\ldots \tag{58}$$

where $v^*=(w_0^*,p_f^*,M^*)$. Substituting Eq. (58) into (57) and equating like powers of $\epsilon$ gives, in the order needed for computation,

$$D^*\nabla_0^{*4}w_0^{(0)}=p_0^*$$
$$\frac{\partial^2 p_f^{(0)}}{\partial z^{*2}}=\frac{\partial}{\partial t^*}(p_f^{(0)}-c^*z^*\nabla_0^{*2}w_0^{(0)})$$
$$M^{(0)}=-\int_{-1/2}^{1/2}p_f^{(0)}z^*dz^*$$
$$D^*\nabla_0^{*4}w_0^{(1)}=B\alpha\nabla_0^{*2}M^{(0)}$$
$$\frac{\partial^2 p_f^{(1)}}{\partial z^{*2}}=\frac{\partial}{\partial t^*}(p_f^{(1)}-c^*z^*\nabla_0^{*2}w_0^{(1)})$$
$$M^{(1)}=-\int_{-1/2}^{1/2}p_f^{(1)}z^*dz^*. \tag{59}$$

Given $p_0^*$ and the boundary and initial conditions on the $v^{(k)}$, these equations can be solved successively for $w_0^{(0)}$, $p_f^{(0)}$, $M^{(0)}$, $w_0^{(1)}$, $p_f^{(1)}$, and $M^{(1)}$ to provide a second-order solution. Note that the first relation is the governing equation for the drained plate.

## Example

Consider a rectangular plate ($a\times b$) that is simply supported on all edges, so the boundary conditions on the edges are

$$x^*=0,\ 1:\ w_0^*=M_x^*=0$$
$$y^*=0,\ 1:\ w_0^*=M_y^*=0. \tag{60}$$

A pressure load

$$p_0^*(x^*,y^*,t^*)=P_0^*(t^*)\Theta(x^*,y^*) \tag{61}$$

is applied to the upper surface only, where

$$P_0^*(t^*)=\dot{P}_0^*t^*$$
$$\Theta(x^*,y^*)=\sin\pi x^*\sin\pi y^*, \tag{62}$$

with $\dot{P}_0^*=dP_0^*/dt^*$ being a constant loading rate. Since the applied load is zero at $t^*=0$, all of the dependent variables are also zero initially. Thus, Eqs. (30) and (36) and Table 2 show that $c_n(x,y)=0$ $(n=0,1,2,\ldots)$.

**Laplace Transform Solution.** Equations (3), (20), (30), (33), $(36)_2$, (61), and (62) and Table 2 show that the boundary conditions (60) are satisfied by

$$w_0^*(x^*,y^*,t^*)=W_0^*(t^*)\Theta(x^*,y^*) \tag{63}$$

where $W_0^*$ is to be determined. Then, substituting the Laplace transforms of the dimensional forms of Eqs. (61), (62), and (63) into (53) and setting

$$\hat{p}(x,y,s)=\hat{P}(s)\Theta(x,y) \tag{64}$$

yields

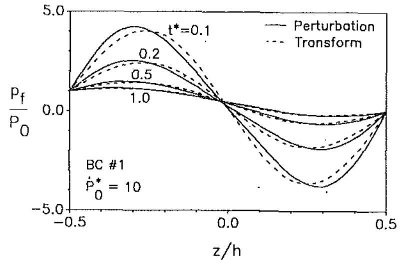


Fig. 2(*a*)

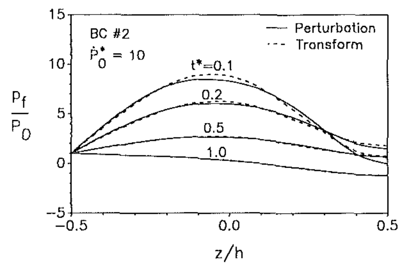


Fig. 2(*b*)

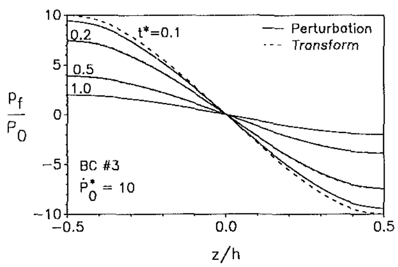


Fig. 2(*c*)

**Fig. 2 Pore pressure distributions for (*a*) permeable upper and lower surfaces, (*b*) permeable upper and impermeable lower surface, and (*c*) impermeable upper and lower surfaces**

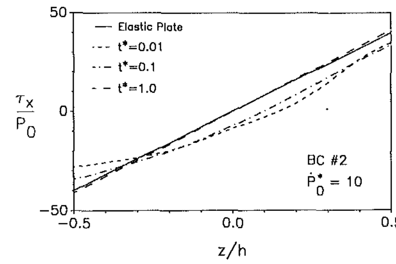


**Fig. 3 Total stress distributions for permeable upper and impermeable lower surface (perturbation solution)**

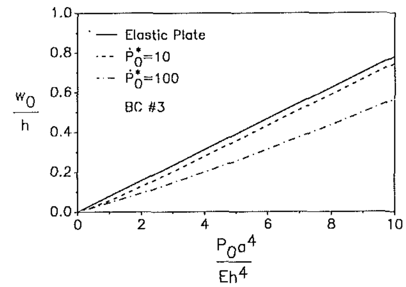


**Fig. 4 Deflection-load curves for impermeable upper and lower surfaces (perturbation solution)**

$$\hat{W}_0(s) = \frac{\hat{P}(s)}{\hat{D}_p(s)\left[\left(\frac{\pi}{a}\right)^2 + \left(\frac{\pi}{b}\right)^2\right]^2}. \qquad (65)$$

For this problem, inserting Eqs. (54) and (55) into (53) gives $\hat{W}_0(s)$ as a ratio of two polynomials in $s$, which can be inverted by a standard method (Greenberg, 1988). ($\Theta$ cancels out since only even spatial derivatives appear in the equations.)

**Perturbation Solution.** To solve Eqs. (59), we assume

$$v^{(k)}(x^*, y^*, t^*) = V^{(k)}(t^*)\Theta(x^*, y^*) \qquad (66)$$

where $v^{(k)} = (w_0^{(k)}, p_f^{(k)}, M^{(k)}, A_n^{(k)}, a_n^{(k)})$ and $V^{(k)}$ is the corresponding amplitude function. Substituting Eq. (58) for $p_f^*$ into the boundary conditions (28) provides the conditions on the $p_f^{(k)}$, and Eqs. (29), $(36)_2$, (59), and (66) give

$$w_0^{(0)} = \frac{p_0^*}{D^*\pi^4(1+a^{*2})^2},\ w_0^{(1)} = \frac{-B\alpha M^{(0)}}{D^*\pi^2(1+a^{*2})}$$

$$p_f^{(0)} = \xi^* + \sum_{n=1}^{\infty} A_n^{(0)}\phi_n,\ p_f^{(1)} = \sum_{n=1}^{\infty} A_n^{(1)}\phi_n,$$

$$M^{(0)} = -\left[\sum_{n=1}^{\infty} A_n^{(0)}\Phi_{n;1} + \Psi_1^*\right],\ M^{(1)} = -\left[\sum_{n=1}^{\infty} A_n^{(1)}\Phi_{n;1}\right] \qquad (67)$$

where

$$A_n^{(k)} = \int_0^{t^*} G_n(t^* - \tau^*)\dot{a}_n^{(k)} d\tau^*$$

$$G_n(t^*) = e^{-\lambda_n^{*2} t^*}$$

$$a_n^{(0)} = \eta_n^* \nabla_0^{*2} w_0^{(0)} + \xi_n^*$$

$$a_n^{(1)} = \eta_n^* \nabla_0^{*2} w_0^{(1)}$$

$$\eta_n^* = 2c^*\Phi_{n;1}. \qquad (68)$$

Also, $\xi_n^*$ and $\Psi_1^*$ are obtained by placing asterisks on the pressures in Table 2.

**Results.** Results are presented for the center ($x^* = y^* = 0.5$) of a poroelastic plate with the following parameter values:

$$a^* = 0.5,\ \epsilon = 0.1,\ \nu = 0.1,\ c^* = 50,\ \alpha = 1.$$

The value for $\epsilon$ represents a moderately thick plate, and the value of $\alpha$ is restricted to the bounds $\phi \le \alpha \le 1$ (Biot and Willis, 1957), with $\alpha \cong 1$ corresponding to a nearly incompressible solid. To see the meaning of the value chosen for $c^*$, we note that since $A/E = (1-\nu)/[(1+\nu)(1-2\nu)]$, Eqs. (16), (19), (27), and (56) give

$$c^* = \frac{\alpha A}{\epsilon^2 E}\left(\frac{1-2\nu}{1-\nu}\right)\left(\frac{F}{A+\alpha^2 F}\right) = \frac{\alpha}{(1+\nu)\epsilon^2}\left(\alpha^2 + \frac{A}{F}\right)^{-1}. \qquad (69)$$

Thus, for $\alpha = 1$ and $A/F = O(1)$, $c^* = O(\epsilon^{-2})$ as specified above. The Laplace transform results are based on three terms in the pore-pressure series (see Eq. (29)), and, since the algebra involved in the perturbation expansion is less tedious, the perturbation solution is based on five terms.

Pore pressure distributions (Fig. 2) show good agreement between the two solutions. For small $t^*$, strong transverse pressure gradients occur, but as the fluid approaches equilibrium relative to the solid, the gradients decrease toward the elastic plate solution, with $p_f$ acting as a hydrostatic pressure. The positive bending causes compression for $z < 0$ and tension for $z > 0$, as illustrated by the total stress distributions (Fig. 3). For symmetric surface boundary conditions (BCs #1 and #3 of Eq. (29), Figs. 2(*a*, *c*)), this leads to positive fluid pressures in the upper half of the plate and negative pressures in the lower half, inducing flow primarily from top to bottom. The other (asymmetric) boundary condition (BC #2, Fig. 2(*b*)) gives positive pore pressures throughout for short times, forcing the fluid from the center toward both plate surfaces.

For short times, the total bending stresses (Fig. 3) deviate significantly from those given by the elastic plate solution. In the example shown (BC #2), a boundary layer appears near the permeable upper surface ($z/h = -0.5$). In addition, for BC #3 at high loading rates, the deflection at a given load is significantly lower than the deflection for an elastic plate (Fig. 4). This difference is less for the other boundary conditions.

Finally, to check assumption (3), we computed the ratio $|p_{f,xx}/p_{f,zz}|$ (not shown). For BCs #1 and #2, this ratio remains less than about 0.05 throughout the plate except near $z = 0$, where values up to 0.3 occur, and near the permeable surfaces, where very large values appear. For BC #3, the ratio is small except within a narrow zone near $z = 0$, where it grows very large. The large values are due to a very small $p_{f,zz}$ rather than a large $p_{f,xx}$, so they do not necessarily indicate that the in-plane flow is important. Thus, assumption #3 appears to be valid for a thin plate.

## Acknowledgment

This work was supported by NIH grant NRSA HL08199.

## References

Biot, M. A., 1941, "General Theory of Three-Dimensional Consolidation," *Journal of Applied Physics*, Vol. 12, pp. 155-164.

Biot, M. A., 1955, "Theory of Elasticity and Consolidation for a Porous Anisotropic Solid," *Journal of Applied Physics*, Vol. 26, pp. 182-185.

Biot, M. A., 1962, "Mechanics of Deformation and Acoustic Propagation in Porous Media," *Journal of Applied Physics*, Vol. 33, pp. 1482-1498.

Biot, M. A., 1964, "Theory of Buckling of a Porous Slab and Its Thermoelastic Analogy," ASME Journal of Applied Mechanics, Vol. 31, pp. 194-198.

Biot, M. A., 1972, "Theory of Finite Deformations of Porous Solids," *Indiana University Mathematics Journal*, Vol. 21, pp. 597-620.

Biot, M. A., and Willis, D. G., 1957, "The Elastic Coefficients of the Theory of Consolidation," ASME Journal of Applied Mechanics, Vol. 24, pp. 594-601.

Boley, B. A., and Weiner, J. H., 1960, *Theory of Thermal Stresses*, John Wiley and Sons, New York.

Bowen, R. M., 1976, "Theory of Mixtures," *Continuum Physics*, A. C. Eringen, ed., Academic Press, New York, pp. 1-127.

Greenberg, M. D., 1988, *Advanced Engineering Mathematics*, Prentice-Hall, Englewood Cliffs, N.J.

Nowinski, J. L., and Davis, C. F., 1972, "The Flexure and Torsion of Bones Viewed as Anisotropic Poroelastic Bodies," *International Journal of Engineering Science*, Vol. 10, pp. 1063-1079.

Rajagopal, K. R., Wineman, A. S., and Shi, J. J., 1983, "The Diffusion of a Fluid Through a Highly Elastic Spherical Membrane," *International Journal of Engineering Science*, Vol. 21, pp. 1171-1183.

Szilard, R., 1974, *Theory and Analysis of Plates*, Prentice-Hall, Englewood Cliffs, N.J.

**Yu Wang**
Asst. Professor,
Department of Mechanical Engineering,
University of Maryland,
Baltimore, MD 21228
Mem. ASME

**Matthew T. Mason**
Assoc. Professor,
School of Computer Science,
Carnegie Mellon University,
Pittsburgh, PA 15213

# Two-Dimensional Rigid-Body Collisions With Friction

*This paper presents an analysis of a two-dimensional rigid-body collision with dry friction. We use Routh's graphical method to describe an impact process and to determine the frictional impulse. We classify the possible modes of impact, and derive analytical expressions for impulse, using both Poisson's and Newton's models of restitution. We also address a new class of impacts,* tangential impact, *with zero initial approach velocity. Some methods for rigid-body impact violate energy conservation principles, yielding solutions that increase system energy during an impact. To avoid such anomalies, we show that Poisson's hypothesis should be used, rather than Newton's law of restitution. In addition, correct identification of the contact mode of impact is essential.*

## 1 Introduction

Although planar rigid-body impact has been studied for centuries, and is discussed in almost all dynamics texts, there are still unresolved difficulties:

- There are two competing laws governing the coefficients of restitution: *Newton's law* and *Poisson's hypothesis*. When do they give the same system behavior? Is one law preferable to the other?
- Some methods, for instance in Whittaker (1944), can result in an increase in total energy, violating basic energy conservation principles (Keller 1986; Brach 1984). How can we avoid such anomalies?

This paper resolves these difficulties by adopting Poisson's hypothesis of restitution and by using Routh's method (Routh 1860) to determine the resultant impulsive forces. The Routh-Poisson analysis gives an impulse consistent with Coulomb's law, without an increase in total energy. An interesting dividend is that the Routh-Poisson analysis admits a new class of impact, called *tangential impact*, defined as an impact with zero initial approach velocity.

Routh's method is a simple graphical technique for analyzing frictional impact in the plane. Using Coulomb's law of dry friction, and either Newton or Poisson restitution, Routh's method readily predicts the total impulse. We can also use Routh's method to distinguish several different types of contact, to identify cases where relative sliding either ceases or reverses, and to identify the cases where Newton and Poisson restitution differ in their predictions. Although this geometrical approach is restricted to planar problems, Keller (1986) develops an analytical method that extends the fundamental concepts to three-dimensional problems. Han and Gilmore (1989) apply the same approach to multiple-contact impact.

The choice between Newton's law of restitution, and Poisson's hypothesis, is particularly important. Newton prescribes the final normal velocity, while Poisson prescribes the normal forces applied during restitution, a difference which leads Kilmister and Reeve (1966) to argue that Poisson's hypothesis is philosophically superior to Newton's law. In the simplest cases, the two methods give identical results, but generally they do not. Although Newton's law of restitution is the more commonly applied method, we show that the violations of energy principles can be attributed to Newton's law of restitution.

Section 2 reviews the classical impact model of collision and the definitions of restitution and friction. Section 3 describes the equations of motion and introduces Routh's graphical technique. Sections 3.4 and 3.5 identify the different classes of impact and derive solutions for each class. Sections 4 and 5 derive expressions for system energy change and compare Newton's law of restitution and Poisson's hypothesis. Section 6 presents some examples using both Routh-Poisson and Routh-Newton. Finally, Section 7 contains a few concluding remarks. Some of results were previously presented in (Wang, 1986; Wang and Mason, 1987; Mason and Wang, 1988).

## 2 Rigid-Body Model of Collision

The sudden, short-term encounter between two colliding bodies is a very complicated event. The major characteristics are the very brief duration and the large magnitudes of the forces generated. Other phenomena include vibration waves propagating through the bodies, local deformations produced in the vicinity of the contact area, and frictional and plastic dissipation of mechanical energy. The complexity of the process leads to serious difficulties in the mathematical analysis of the problem. By introducing the rigid-body assumption and Coulomb's law, we simplify the analysis while retaining a fair approximation of a significant class of real systems.

Contributed by the Applied Mechanics Division of THE AMERICAN SOCIETY OF MECHANICAL ENGINEERS for publication in the ASME JOURNAL OF APPLIED MECHANICS.

Discussion on this paper should be addressed to the Technical Editor, Professor Leon M. Keer, The Technological Institute, Northwestern University, Evanston, IL 60208 and will be accepted until four months after final publication of the paper itself in the JOURNAL OF APPLIED MECHANICS.

Manuscript received by the ASME Applied Mechanics Division, Mar. 26, 1990; final revision, Jan. 7, 1991. Associate Technical Editor: P. D. Spanos.

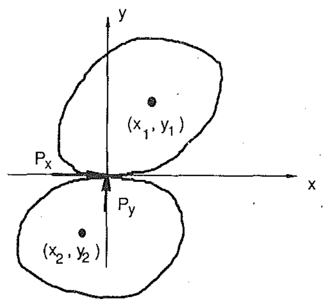


**Fig. 1** Two colliding rigid bodies in a plane. The normal impulse and tangential impulse acting on the body 1 are shown as $P_y$ and $P_x$.

For the collision of two rigid bodies (Fig. 1), the primary simplifying assumption is a postulated deformation history. This deformation history is assumed to consist of two periods: the period of compression and the period of restitution. The compression period extends from the instant of contact to the point of maximum compression, when the approach velocity becomes zero. The period of restitution then begins, lasting to the instant of separation. The time interval of the contact is assumed to be very small and the interaction forces are high. These postulates permit some further assumptions. (1) The collision process is instantaneous, and linear and angular velocities of the bodies have discontinuous changes. (2) Interactive forces are impulsive, and all other finite forces are negligible. (3) No displacements occur during the collision.

**2.1 Coefficient of Restitution.** During the brief period of contact, a normal force $F$ acts along the common normal between the two bodies.[1] Since the contact duration is sufficiently small, the contact force may be represented by Dirac's delta function.

$$P=\lim_{\Delta t\to 0}\int F(t)dt. \tag{1}$$

It is called *impulse* and is defined to be finite.

The magnitude of the normal impulse consists of two parts, $P_c$ and $P_r$, corresponding to the periods of compression and restitution, respectively. The total impulse is the sum of the two parts

$$P_y=P_c+P_r. \tag{2}$$

If we adopt *Poisson's hypothesis* (Beer and Johnston, 1984), it is further postulated that the ratio of $P_r$ to $P_c$ is determined,

$$e=\frac{P_r}{P_c}. \tag{3}$$

This constant $e$ is called the *coefficient of restitution*, and is assumed to depend solely on the materials of the bodies (Goldsmith, 1960). The coefficient describes the degree of plasticity of the collision, and its value is always between zero and one. When $e = 0$, the impact is said to be perfectly plastic; when $e = 1$, it is said to be perfectly elastic.

Poisson's hypothesis immediately suggests a model based on a hysteretic spring or other passive elements. The coefficient of restitution may, however, be put in another form, known as *Newton's law of restitution*, which cannot be modeled in this way. Newton's law of restitution states

$$e=-\frac{C^+}{C^-} \tag{4}$$

where $C^-$ and $C^+$ are the normal components of relative velocity at the contact point before and after the collision, respectively.

Both Poisson's hypothesis and Newton's law have been adopted by the scientific community to describe the energy dissipation. However, they do not in general produce consistent solutions. In this paper, we discuss both definitions and their solutions of impact. Section 5 shows that Newton's law can lead to violation of energy conservation.

## 3 The Two-Dimensional Collision Problem

This section analyzes the process of two planar rigid bodies with friction. First, we present Routh's method. Then, we use Routh's method to classify the different kinds of impact and derive solutions for each class.

**3.1 Equations of Motion.** When two bodies collide, impulses in the normal direction $P_y$ and in the tangential direction $P_x$ at the contact point are produced. These impulses will change the object's motions. In the coordinate system shown in Fig. 1, the initial translational and rotational velocity components of the first object are $\dot{x}_{1o}$, $\dot{y}_{1o}$, and $\dot{\theta}_{1o}$. The origin of the coordinates is chosen at the point of contact. The coordinate axes $x$ and $y$ are in the directions tangential and normal to the contact surfaces. At any instant during the impact, the motion of the object is governed by the linear and angular impulse-momentum laws, which provide the following relations:

$$m_1(\dot{x}_1-\dot{x}_{1o})=P_x \tag{5}$$

$$m_1(\dot{y}_1-\dot{y}_{1o})=P_y \tag{6}$$

$$m_1\rho_1^2(\dot{\theta}_1-\dot{\theta}_{1o})=P_xy_1-P_yx_1 \tag{7}$$

where $m_1$ is the mass, $\rho_1$ is the radius of gyration of inertia, and $x_1$ and $y_1$ are the coordinates of the center of mass for the first object.

The velocity of the point of contact on the first object consists of two components, $\dot{x}_{1c}$ and $\dot{y}_{1c}$. These two components are given by

$$\dot{x}_{1c}=\dot{x}_1+\dot{\theta}_1y_1 \tag{8}$$

$$\dot{y}_{1c}=\dot{y}_1-\dot{\theta}_1x_1. \tag{9}$$

Similarly, we obtain the dynamic equations for the second object

$$m_2(\dot{x}_2-\dot{x}_{2o})=-P_x \tag{10}$$

$$m_2(\dot{y}_2-\dot{y}_{2o})=-P_y \tag{11}$$

$$m_2\rho_2^2(\dot{\theta}_2-\dot{\theta}_{2o})=-P_xy_2+P_yx_2 \tag{12}$$

$$\dot{x}_{2c}=\dot{x}_2+\dot{\theta}_2y_2 \tag{13}$$

$$\dot{y}_{2c}=\dot{y}_2-\dot{\theta}_2x_2 \tag{14}$$

where $m_2$ is the mass, $\rho_2$ is the radius of gyration of inertia, and $x_2$ and $y_2$ are the coordinates of the center of mass for the second object.

From Eqs. (8), (9), (13), and (14), the tangential component of relative velocity of the points in contact is called *sliding velocity* and is given as

$$\begin{aligned}S&=\dot{x}_{1c}-\dot{x}_{2c}\\&=(\dot{x}_1+\dot{\theta}_1y_1)-(\dot{x}_2+\dot{\theta}_2y_2)\end{aligned} \tag{15}$$

and the normal component of relative velocity is called *compression velocity* and is given as

$$\begin{aligned}C&=\dot{y}_{1c}-\dot{y}_{2c}\\&=(\dot{y}_1-\dot{\theta}_1x_1)-(\dot{y}_2-\dot{\theta}_2x_2).\end{aligned} \tag{16}$$

Substituting the dynamic Eqs. (5)–(7) and (10)–(12) into these kinematic equations, we find that

$$S=S_o+B_1P_x-B_3P_y \tag{17}$$

$$C=C_o-B_3P_x+B_2P_y \tag{18}$$

[1]If one of the contact points is a vertex, the common normal is defined as the normal of the other body's surface. We do not consider the case of two vertices in contact.

where

$$B_1=\frac{1}{m_1}+\frac{1}{m_2}+\frac{y_1^2}{m_1\rho_1^2}+\frac{y_2^2}{m_2\rho_2^2} \tag{19}$$

$$B_2=\frac{1}{m_1}+\frac{1}{m_2}+\frac{x_1^2}{m_1\rho_1^2}+\frac{x_2^2}{m_2\rho_2^2} \tag{20}$$

$$B_3=\frac{x_1y_1}{m_1\rho_1^2}-\frac{x_2y_2}{m_2\rho_2^2} \tag{21}$$

and

$$S_o=\dot{x}_{1co}-\dot{x}_{2co}$$
$$=(\dot{x}_{1o}+\dot{\theta}_{1o}y_1)-(\dot{x}_{2o}+\dot{\theta}_{2o}y_2) \tag{22}$$
$$C_o=\dot{y}_{1co}-\dot{y}_{2co}$$
$$=(\dot{y}_{1o}-\dot{\theta}_{1o}x_1)-(\dot{y}_{2o}-\dot{\theta}_{2o}x_2). \tag{23}$$

Note that $S_o$ and $C_o$ are the initial values of sliding and compression velocities. $B_1$, $B_2$, and $B_3$ are constants, dependent on the geometry and mass properties of the system, with $B_1$ and $B_2$ always positive. In all cases, $B_1B_2 > B_3^2$, which will be useful in later sections.

**3.2 Restitution and Friction.** The algebraic Eqs. (17) and (18) give the relative velocity ($S$, $C$) as a function of total accumulated impulse ($P_x$, $P_y$). Routh's method also requires that we express the laws governing restitution and friction in terms of the total accumulated impulse ($P_x$, $P_y$).

*3.2.1 Coefficient of Restitution.* By assumption, object deformation consists of two phases: compression and restitution. At the end of the compression phase, the normal component of the relative velocity of the points in contact is zero ($C = 0$). Substituting Eq. (18), we obtain a linear relationship between the impulse components at maximum compression:

$$C_o-B_3P_x+B_2P_y=0. \tag{24}$$

In the ($P_x$, $P_y$) space, this equation defines a straight line called the *line of maximum compression.*

After the point of maximum compression, the restitution phase begins, lasting to the end of the collision. Under Newton's law, the collision ends when the normal velocity $C$ is $-e$ times the initial normal velocity $C_0$. That is

$$e=-\frac{C(t_f)}{C(t_o)} \tag{25}$$

where $t_o$ is the initial collision time and $t_f$ is the termination time. Substituting this into Eq. (24), we obtain

$$(1+e)C_o-B_3P_x+B_2P_y=0 \quad (t=t_f). \tag{26}$$

Again, we obtain a line in the ($P_x$, $P_y$) space, called the *line of termination.* When using Newton's law of restitution, the total impulse will always fall on the line of termination.

But under Poisson's hypothesis, the collision ends when the total normal impulse $P_y$ is $(1+e)$ times that value of $P_y$ at maximum compression. That is

$$\frac{P_y(t_f)}{P_y(t_c)}=1+e \tag{27}$$

where $t_c$ denotes the instant of maximum compression. Unlike Newtonian restitution, Poisson's hypothesis does not yield a line of termination.

*3.2.2 Coefficient of Friction.* Friction causes an impulsive force in the tangential direction at the contact point. We adopt Coulomb's law to determine the force of dry friction. The law states that the magnitude of the (tangential) frictional force $F_x$ depends only on the magnitude of the normal force $F_y$ and the materials in contact, and its direction is always opposite that of relative tangential motion. This law is commonly expressed as

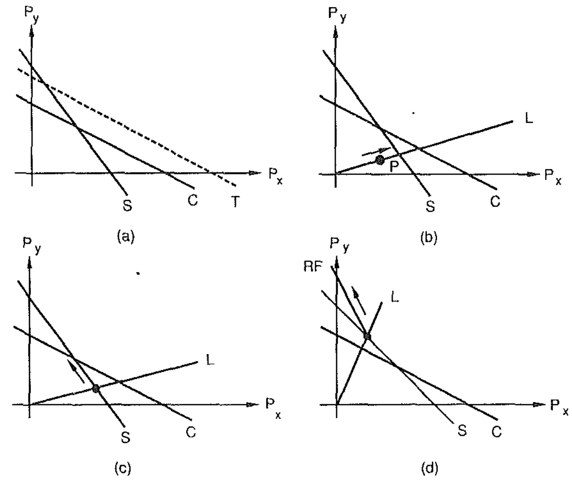


**Fig. 2 Impact process diagram. The lines of sticking, lines of maximum compression, and lines of termination are labeled, respectively, with S, C, and T. The lines of limiting friction and the line of reversed limiting friction are labeled with L and RF, respectively. The point P is the representative point.**

$$|F_x|\le\mu F_y \tag{28}$$

where $\mu$ is the *coefficient of friction* and is an empirical constant. In this paper, we do not distinguish between static and dynamic friction and we take the values for corresponding noncollision processes.

Coulomb's law includes two different cases: sticking and sliding. Since differential impulse is force, these cases are expressed as

$$|dP_x|<\mu dP_y \text{ for sticking}$$
$$|dP_x|=\mu dP_y \text{ for sliding.}$$

In the sticking case, the tangential component of relative velocity vanishes ($S = 0$). Again we can substitute Eq. (17), obtaining a linear relation between the components of impulse ($P_x$, $P_y$),

$$S_o+B_1P_x-B_3P_y=0. \tag{29}$$

This gives a straight line in the ($P_x$, $P_y$) space, called the *line of sticking.*

**3.3 Impact Process Diagram.** To solve an impact problem, we employ Routh's graphical technique to determine the total impulse. Figure 2 shows an example. We construct *impulse space* with coordinate axes $P_x$ and $P_y$, and plot the accumulating impulse $P$. When the impact begins, $P$ is at the origin. During the impact, the normal impulse $P_y$ increases monotonically until the restitution law, which could be either Poisson or Newton, says that the impact is finished.

$P_x$ also accumulates, in accordance with Coulomb's law. Assuming initial sliding, the impulse increases along a *line of limiting friction* (Fig. 2($b$)) satisfying Coulomb's law:

$$P_x=-\mu sP_y \tag{30}$$

where $s$ is the sign of the initial sliding velocity $S_o$,

$$s=\frac{S_o}{|S_o|} \text{ if } S_o\neq 0.$$

If the point reaches the line of sticking, the sliding will end and the frictional impulse will exhibit a change. There are two possibilities:

1 If the friction necessary to prevent sliding is less than the limiting friction, the point $P$ will follow the line of sticking until the process terminates (Fig. 2($c$)).
2 If the limiting friction is too small to prevent sliding, then $P$ will cross the line of sticking, and the tangential force will

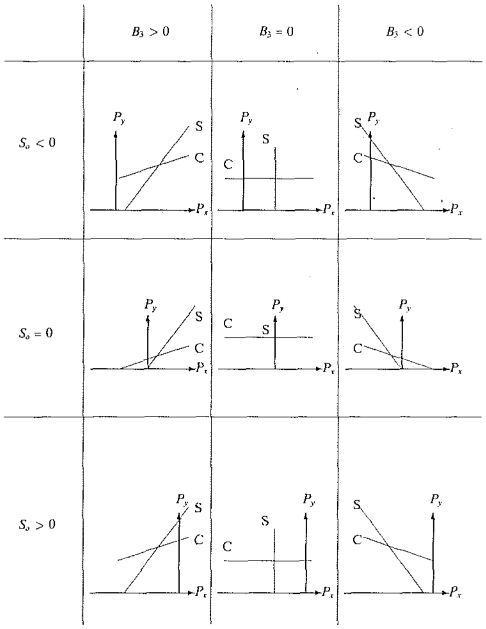


Fig. 3 All possible cases of meeting impact in the ($P_x$, $P_y$) space. The lines of sticking and maximum compression are labeled S and C.

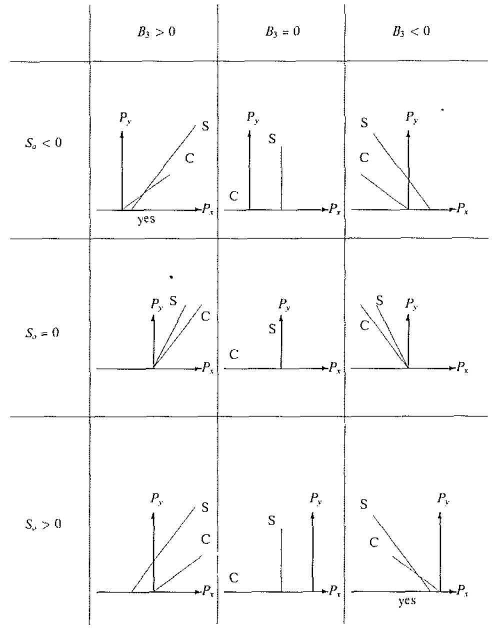


Fig. 4 There are two possible cases of tangential impact in the ($P_x$, $P_y$) space, which are labeled "yes." The lines of sticking and maximum compression are labeled S and C.

change sign, so that $P$ now travels along the *line of reversed limiting friction* given by (Fig. 2 ($d$))

$$dP_x = \mu s dP_y.$$

Eventually, point $P$ will cross the line of maximum compression. A perfectly plastic collision terminates at that point. By Poisson's hypothesis, a perfectly elastic collision continues until the normal impulse $P_y$ is doubled. Intermediate cases, with coefficients of restitution between 0 and 1, terminate when the normal impulse is $(1 + e)$ times the value of $P_y$ obtained at maximum compression. By Newton's law of restitution, the collision terminates when the point $P$ reaches the line of termination.

The entire process can be summarized in a few lines. To recapitulate:

1 $P$ moves initially along the line of limiting friction.
2 If $P$ reaches the line of sticking, $S = 0$, then $P$ switches to either the line of sticking, or the line of reversed limiting friction, whichever is steeper.
3 Termination occurs when:
 ($a$) Newton: $P$ reaches the line of termination.
 ($b$) Poisson: $P_y$ reaches a value $(1 + e)$ times its value at the line of maximum compression.

This procedure solves the impact problem by constructing the total impulse, from which we can immediately determine the resulting body motions.

**3.4 Classes of Impact and Contact Modes.** Routh's procedure, described above, is a graphical solution of impact problems. It can also be used to derive an analytic solution of impact problems. In this section we identify the different cases that must be considered. In the following section we derive analytic solutions of impact for each case using both Poisson's and Newton's methods.

*3.4.1 Direct and Oblique, Central and Eccentric, Tangential and Meeting Impacts.* Collision problems are classified first by the locations of the line of sticking and the line of maximum compression, which depend primarily on the signs of $B_3$, $S_0$, and $C_0$. Figures 3 and 4 show all possible combinations of the linear relationships, and thereby classifies all possible impacts. Figure 3 takes the case $C_0 < 0$, and plots all nine combinations for the signs of $B_2$ and $S_0$. The rows indicate the direction of the sliding velocity while the columns indicate the impact configuration. There are two special classes. If the initial sliding velocity is zero ($S_0 = 0$), the impact is called a *direct impact*, represented by the middle row in the figure. If $B_3 = 0$, the impact is called a *generalized central impact*, represented by the middle column. (Central impact, where the body centers of mass lie on the contact normal, is subsumed by generalized central impact.) Impacts which are neither direct, nor generalized central impacts, are called *eccentric oblique impacts*.

Figure 4 shows a new class of impacts, which we will call *tangential impacts*, which can occur when $C_0 = 0$. Previous work has only considered collisions with finite approach velocities, $C_0 < 0$, which we might term *meeting impacts*. Perhaps this reflects a bias towards finite force solutions. Indeed, Kilmister and Reeve (1966) even adopt a *principle of constraints* stating:

> constraints shall be maintained by forces, so long as this is possible; otherwise, and only otherwise, by impulses.

However, there are problems with zero initial compression velocity for which only impulsive forces will maintain the kinematic constraints. An example is presented in Section 6. So, even if we adopt the principle of constraints, tangential collisions are sometimes the only solution available.

Only two of the cases shown in Fig. 4 yield feasible tangential impacts: $S_0 < 0$ and $B_3 > 0$; or $S_0 > 0$ and $B_3 < 0$. In these two cases, and with a large enough coefficient of friction, the line of limiting friction passes immediately below the line of maximum compression, yielding a compressive phase followed by a restitution phase as in ordinary meeting impacts.

It is also natural to consider admitting collisions with positive compression velocities $C_0 > 0$, which we might term *parting impacts*. It is possible to view the restitution phase of a meeting impact as a parting impact, but otherwise we see no necessity for admitting parting impacts.

*3.4.2 Contact Modes.* The contact mode can be determined by a few simple comparisons. We consider the case with $S_o < 0$ and $B_3 < 0$ (Fig. 5). Other cases are similar. In Fig. 5, the line of sticking intersects the line of maximum compression at point $Q$ and the line of termination at point $D$. The

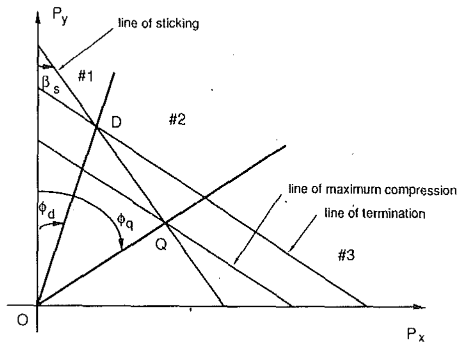


**Fig. 5 Three regions in impulse space. In region 1, sticking never occurs; in region 2 and region 3, either a sticking or a reversed sliding contact occurs.**

$(P_x, P_y)$ space is divided into three regions by the lines $OD$ and $OQ$. If the limiting friction line lies in region 1, the impact will be terminated before the representative point $P$ reaches the line of sticking. The friction continues the limiting value throughout the process, so that the objects slide continuously. In this case Poisson and Newton give identical results, so the impact terminates at the line of termination.

If the limiting friction line lies in region 2, it reaches the line of maximum compression first, then reaches the line of sticking. If the limiting friction line lies in region 3, it reaches the line of sticking first. In either of regions 2 or 3, after intersecting with the line of sticking, it either continues sticking until termination or changes to reversal sliding.

These regions can be used to classify contact modes of impact. For an oblique impact, there are five contact modes: (1) sliding, (2) sticking in compression phase (C-sticking), (3) sticking in restitution phase (R-sticking), (4) reversed sliding in compression phase (C-reversed sliding), and (5) reversed sliding in restitution phase (R-reversed sliding). The classification depends on the values of $\mu$, $\mu_d$, $\mu_q$, $\mu_s$, $P_d$, and $P_q$ given by

$$\mu = \tan\alpha \tag{31}$$

$$\mu_d = \tan \phi_d = \frac{(1+e)B_3C_o + B_2S_o}{(1+e)B_1C_o + B_3S_o} \tag{32}$$

$$\mu_q = \tan \phi_q = \frac{B_3C_o + B_2S_o}{B_1C_o + B_3S_o}. \tag{33}$$

$$\mu_s = \tan \beta_s = -\frac{B_3}{B_1} \tag{34}$$

$$P_d = (B_2 + s\mu B_3)sS_o \tag{35}$$

$$P_q = (\mu B_1 + sB_3)(-C_o). \tag{36}$$

The contact modes are summarized in Table 1. Note that the reversed sliding contact modes require that $S_oB_3 > 0$.

For a direct impact ($S_o = 0$), the line of sticking passes through the origin (Fig. 3). Region 2 vanishes and $\mu_d$ and $\mu_q$ have the same value as $\mu_s$. Only two contact modes are possible, sticking (in compression phase) or sliding. Reversed sliding will never occur. As discussed by Routh, the representative point will follow either the line of limiting friction or the line of sticking throughout the entire process, depending on the following conditions:

$$\mu < |\mu_s| \text{ for sliding} \tag{37}$$

$$\mu > |\mu_s| \text{ for sticking.} \tag{38}$$

Wang and Mason (1987) and Han and Gilmore (1989) present similar results.

**3.5 Analytical Solutions of Impulse.** Once the contact mode is determined, we can solve for the impulses and object motions. If we define the sign function of initial sliding velocity $S_o$ to be of value one when $S_o = 0$, the resulting impulses for both direct impact and oblique impact can be expressed in a unified form.

**Table 1 Contact modes of impact, where $\mu$ is the friction coefficent and $s$ is the sign function of $S_o$ if $S_o \neq 0$**

| | $\mu > \lvert\mu_s\rvert$ | $\mu < \lvert\mu_s\rvert$ |
|---|---|---|
| $P_d > (1+e)P_q$ | Sliding | |
| $P_q < P_d < (1+e)P_q$ | R-Sticking | R-Reversed Sliding |
| $P_d < P_q$ | C-Sticking | C-Reversed Sliding |

For Poisson's method, the impulses are given by contact mode:

- *sliding:*

$$P_x = -s\mu P_y \tag{39}$$

$$P_y = -(1+e)\frac{C_o}{B_2 + s\mu B_3} \tag{40}$$

- C-sticking:

$$P_x = \frac{B_3P_y - S_o}{B_1} \tag{41}$$

$$P_y = -(1+e)\frac{B_1C_o + B_3S_o}{B_1B_2 - B_3^2} \tag{42}$$

- R-sticking:

$$P_x = \frac{B_3P_y - S_o}{B_1} \tag{43}$$

$$P_y = -(1+e)\frac{C_o}{B_2 + s\mu B_3} \tag{44}$$

- C-reversed sliding:

$$P_x = s\mu\left[P_y - \frac{2S_o}{B_3 + s\mu B_1}\right] \tag{45}$$

$$P_y = -\frac{1+e}{B_2 - s\mu B_3}\left[C_o + \frac{2s\mu B_3S_o}{B_3 + s\mu B_1}\right] \tag{46}$$

- R-reversed-sliding:

$$P_x = s\mu\left[P_y - \frac{2S_o}{B_3 + s\mu B_1}\right] \tag{47}$$

$$P_y = -(1+e)\frac{C_o}{B_2 + s\mu B_3} \tag{48}$$

where

$$s = \begin{cases} \dfrac{S_o}{|S_o|} & \text{if } S_o \neq 0 \\ 1 & \text{if } S_o = 0. \end{cases} \tag{49}$$

If we use Newton's law of restitution, the conditions for contact modes remain the same. However, whether sticking occurs in the restitution phase or in the compression phase does not affect the resulting impulses. The impulses are:

- sliding:

$$P_x = -s\mu P_y \tag{50}$$

$$P_y = -(1+e)\frac{C_o}{B_2 + s\mu B_3} \tag{51}$$

- sticking (C-sticking or R-sticking):

$$P_x = -\frac{B_2S_o + (1+e)C_oB_3}{B_1B_2 - B_3^2} \tag{52}$$

$$P_y = -\frac{B_3 S_o + (1+e) C_o B_1}{B_1 B_2 - B_3^2} \tag{53}$$

- reversed sliding (C-reversed sliding or R-reversed sliding):

$$P_x = s\mu \left[ P_y - \frac{2S_o}{B_3 + s\mu B_1} \right] \tag{54}$$

$$P_y = -\frac{1}{B_2 - s\mu B_3} \left[ (1+e) C_o + \frac{2s\mu B_3 S_o}{B_3 + s\mu B_1} \right] \tag{55}$$

where $s$ is defined by Eq. (49).

Note that for sticking (in compression or in restitution) contact, the solutions are independent of the value of the coefficient of friction. As long as the friction is sufficient to prevent sliding, further increases do not matter. These expressions also appear in Wang (1989). Han and Gilmore (1989) present a similar analysis.

## 4 Energy Loss

Since some methods for rigid-body impact violate energy conservation principles, we develop expressions for the total energy loss during the impact. Due to the existence of friction and inelasticity, the system must lose some mechanical energy during the collision. The change in kinetic energy equals work done by the impulse. If $T_1$ and $T_2$ are the kinetic energies of body 1 and body 2, respectively, then the system energy change is (Routh 1860),

$$\Delta T = (T_1(t_f) + T_2(T_f)) - (T_1(t_o) + T_2(t_o))$$

$$= \frac{1}{2} [\mathbf{P}^T(\mathbf{V}_c + \mathbf{V}_{co})] \tag{56}$$

where, $\mathbf{P} = [P_x, P_y]^T$, $\mathbf{V}_c = [S\ C]^T$, and $\mathbf{V}_{co} = [S_o\ C_o]^T$. Substituting Eqs. (17) and (18) the energy change is

$$\Delta T = \frac{1}{2} (\mathbf{P}^T \mathbf{B} \mathbf{P} + 2\mathbf{V}_{co}^T \mathbf{P}) \tag{57}$$

where

$$\mathbf{B} = \begin{bmatrix} B_1 & -B_3 \\ -B_3 & B_2 \end{bmatrix}.$$

Conservation of energy requires that

$$\Delta T \le 0. \tag{58}$$

This gives a geometrical constraint in the impulse space: The total impulse must remain within an ellipse.

## 5 Poisson's Hypothesis Versus Newton's Law

By comparing the solutions of impulse presented in Section 3.5, we can identify the conditions under which Poisson's hypothesis and Newton's law give the same solution:

1 The collision is a direct impact, where the initial velocities of the contact points are directly along the common normal ($S_o = 0$) (Kilmister and Reeve (1966).
2 The collision is a generalized central impact ($B_3 = 0$).
3 The surfaces of the bodies are perfectly smooth and frictionless (Beer and Johnston, 1984).
4 The surfaces of the bodies are perfectly plastic ($e = 0$) (Wang, 1989).
5 The impact is of sliding contact, if friction between the bodies exists (Keller, 1986).

Now let us check energy conservation for the two models. We need examine only the perfect elastic case ($e = 1$), since any degree of plasticity will result in more energy loss. Under Poisson's hypothesis, an energy gain is impossible, which is verified by substituting the solutions of Section 3.5 into Eq. (56) (see Appendix). However, Newton's law of restitution sometimes produces energy gains. An example is given in the next section.

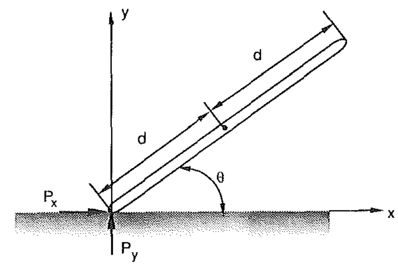


Fig. 6 A rigid rod colliding a frictional surface. In all cases, $m = 1$, length $d = 1/2$, $m\rho^2 = 1/12$, $\theta = 45$ deg, and initial angular velocity $\omega = 0$.

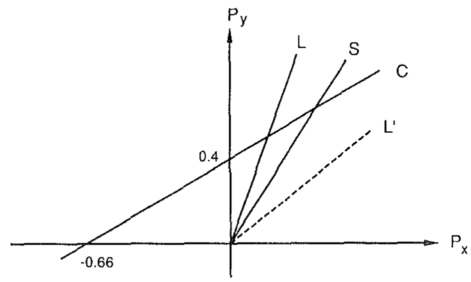


Fig. 7 Impact process diagram of the falling rod for case 1. Initial compression velocity $C_o = -1$ and initial sliding velocity $S_o = 0$. $L$ and $L'$ denote the lines of limiting friction for $\mu < 0.6$ and $\mu > 0.6$, respectively.

From both philosophical and practical points of view, Poisson's hypothesis is preferable to Newton's law of restitution. The philosophical reason, as argued by Kilmister and Reeve (1966), is that Poisson's hypothesis is expressed as a dynamic law, rather than as a kinematic constraint. The practical reason is that Poisson's hypothesis is consistent with energy conservation. This seems also to be consistent with Routh's original work where only Poisson's method is used.

## 6 Examples

This section illustrates our results with the example of a rod colliding with an immobile object (Fig. 6). This example has been used on many occasions to illustrate paradoxes in the mechanics of friction and impact (Goldsmith, 1960; Lotstedt, 1981; Brach, 1989; Erdmann, 1984). We assume point contact with Coulomb friction. The rod's initial orientation is $\theta = 45$ deg, and the initial angular velocity is zero $\omega(t_o) = 0$. The rod has unit mass and unit length ($m_1 = 1$, $\rho_1^2 = 1/12$). Note that $m_2 \to \infty$ and $m_2\rho_2^2 \to \infty$ and $B_1 = 2.5$, $B_2 = 2.5$, $B_3 = 1.5$, and $\mu_s = -0.6$.

By varying the initial velocity, we obtain four cases that illustrate the results of the paper.

**Case 1: Direct Impact ($C_o = -1$ and $S_o = 0$).** Since $S_o = 0$, this is a direct impact. The impact process diagram is shown in Fig. 7. From Eqs. (37) and (38), we find that if $\mu < 0.6$, sliding contact occurs and the rod's tip has a negative final tangential velocity; otherwise ($\mu > 0.6$), sticking contact occurs and the final tangential tip velocity is zero. These results agree with those in (Brach, 1989).

**Case 2: Reversed Sliding ($C_o = -1.0$ and $S_o = 0.6$).** If the initial tangential velocity is 0.6 (Fig. 8), then we will have reversed sliding for $\mu < 0.6$ and sticking for $\mu > 0.6$. Assuming the sticking contact, $\mu > 0.6$, with Newton's law of restitution, there is a net gain in energy. The impulses and resultant motions are

$$P_x = 0.375\ e$$

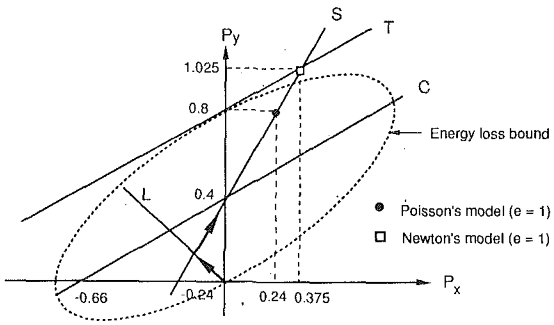


**Fig. 8 Impact process diagram of the falling rod for case 2. Initial compression velocity $C_o = -1.0$ and initial sliding velocity $S_o = 0.6$. The ellipse denotes the boundary of the region of energy loss. The line of termination $T$ is tangent to the ellipse.**

$$P_y = 0.4 + 0.0625\ e$$
$$S = 0$$
$$C = e$$

and the energy gain of the system is

$$\Delta T = \frac{1}{2}\ (0.625\ e^2 - 0.4).$$

Therefore, for all values $e > 0.8$, the rod gains energy instead of losing energy. In order to lose energy, the final impulse must lie within the ellipse plotted in Fig. 8. For $e = 1$, the rod gains energy for any $\mu > 0$.

The difficulty does not occur if we use Poisson's hypothesis instead, giving

$$P_x = 0.24\ e$$
$$P_y = 0.4(1+e)$$
$$S = 0$$
$$C = 0.64\ e$$

with a corresponding energy increase

$$\Delta T = \frac{1}{2}\ (0.256\ e^2 - 0.4)$$

which is always negative for $0 \le e \le 1$. Poisson's model results in both kinematically and dynamically valid solutions.

Brach (1989) uses the same example, with Newton's law of restitution, and resolves the increase in energy in a very different manner. He does not treat $\mu$ (or $e$) as predetermined parameters. For this example, he disallows nonzero $\mu$, because it would lead to energy gains.

**Case 3: Forward Sliding; Sticking ($C_o = -1.0$ and $S_o = -1.0$).** For initial conditions of $S_o = C_o = -1.0$, Fig. 9 shows the impact process diagram. The critical values of $\mu$ are $\mu_d = (3(1+e)+5)/(5(1+e)+3)$ and $\mu_q = 1.0$. If $\mu < \mu_d$, the tip keeps forward sliding in the collision; if $\mu_d < \mu < 1.0$, sticking in restitution occurs; and if $\mu > 1.0$, sticking in compression occurs.

**Case 4: Tangential Impact ($C_o = 0$ and $S_o = -0.2$).** The final example involves tangential impact, which was defined and discussed in Section 3.4. Initially the rod is sliding along the surface with zero normal velocity. We begin by considering a finite-force approach to the problem. We also modify the problem slightly: We introduce a gravitational field. The surprising result is that no solution exists: Every contact force consistent with Coulomb's law will violate the kinematic constraint. If the contact force were zero, the gravitational force would accelerate the tip downward. For positive contact forces, and with $\mu > 1.666$, the rod's physical parameters have been chosen so that the angular acceleration, accelerating the tip downward, dominates the linear acceleration, which would

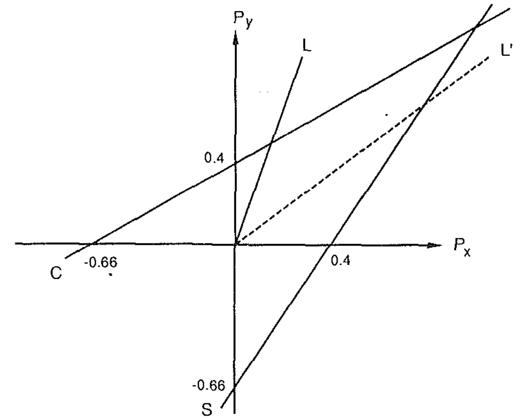


**Fig. 9 Impact process diagram of the falling rod for case 3. Initial compression velocity $C_o = -1.0$ and initial sliding velocity $S_o = -1.0$. $L$ and $L'$ denote the lines of limiting friction for $\mu < \mu_d$ and $\mu > \mu_d$, respectively.**

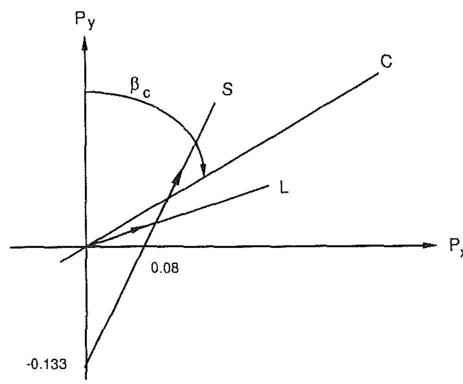


**Fig. 10 Impact process diagram of the falling rod for case 4. Initial compression velocity $C_o = 0$ and initial sliding velocity $S_o = -0.2$**

accelerate the tip upward. Mason and Wang (1988) and Wang (1989) present a more detailed analysis of the problem. Previous work, neglecting the possibility of an impact solution, present this example and variations to demonstrate the inconsistency of rigid-body mechanics (Lotstedt, 1981; Erdmann, 1984; Beghin, 1923–1924; Klein, 1909; Painleve, 1895; Hamel, 1949).

Now we apply the Routh-Poisson method to derive impulsive forces. In the impact process diagram (Fig. 10), the line of maximum compression $C$ passes the origin with an angle $\beta_c = \tan^{-1} 1.666$. For $\mu > 1.666$, an impact solution with sticking contact exists, and both nonzero tangential and normal impulses are obtained. If $\mu < 1.666$, then compression cannot occur, so impulsive forces will be zero. An impact solution exists in exactly those cases where the finite solution does not exist.

How does Newton's law of restitution relate to tangential impact? Since the normal velocity is zero, the final velocity would also be zero, no matter what value for the coefficient of restitution. Hence, any difference between plastic and elastic behavior cannot be expressed using Newton's law.

## 7 Summary and Conclusion

This paper derives solutions for frictional planar rigid-body collisions, using Routh's impact process diagrams, for both Newtonian and Poisson restitution. We apply the graphical method of Routh to describe an analytical solution to the collision problem. The contact mode determines how the body velocities change during the course of impact. If the contact mode of impact is not properly identified, solutions sometimes violate energy conservation. Using Routh's method, we characterize all possible contact modes of impact, and then derive analytical solutions for impulses and motions of the bodies.

An important observation regards the definition of the coefficient of restitution. We have presented solutions using both Poisson's hypothesis and Newton's law of restitution. Poisson's hypothesis, relating the normal impulses during two postulated phases of compression and restitution, guarantees energy conservation principles, but Newton's law of restitution, relating the initial and final normal velocities, cannot. As a dynamic law, Poisson's hypothesis is superior to Newton's law of restitution which is an artificial kinematic relationship and is not always applicable.

There are alternative methods to resolve the violation of energy conservation. Rather than blaming the definition of restitution, it is possible to blame the definition of friction. Brach (1989) takes this approach, and adopts a coefficient of friction that is lowered to prevent energy gains, and also to prevent reversal of tangential tip velocity. In the most extreme cases, the only value of $\mu$ that satisfies these constraints is zero. We view Poisson restitution as preferable to a law that determines $\mu$ after the fact. In addition, Poisson's hypothesis works nicely with tangential impact. Stronge (1990) proposes an alternative law of restitution which also appears to resolve the energy conservation problem.

As Routh indicated, the extension of his approach to the general three-dimensional rigid-body impact problem is not by any means straightforward. Keller (1986) provides an analytical extension to three dimensions, and also gives a fundamental development of the method. However, the simplicity of Routh's graphical approach does not extend to three dimensions. No algebraic relationships in impulse space can be found to describe limiting friction. Differential descriptions are necessary, and an analytical solution would be difficult at best.

## Acknowledgment

We would like to thank Randy Brost, Ken Goldberg, and Michael Peshkin for their many useful suggestions. Special thanks to J. B. Keller for his constructive comments on an earlier report of the work. This work was supported under grants from the System Development Foundation and the National Science Foundation under grant DMC-8520475.

## References

Beer, F. P., and Johnston, Jr., E. R., 1984, *Vector Mechanics for Engineers*, 4th ed., McGraw-Hill, New York, pp. 624–631.

Beghin, H., 1923–1924, "Sur Certain problemes de frottement," *Nouvelles Annales, 5e (Serie 2)*, pp. 305–312.

Brach, R. M., 1984, "Friction, Restitution, and Energy Loss in Planar Collisions," ASME JOURNAL OF APPLIED MECHANICS, Vol. 51, pp. 164–170.

Brach, R. M., 1989, "Rigid Body Collisions," ASME JOURNAL OF APPLIED MECHANICS, Vol. 56, pp. 133–138.

Erdmann, M. A., 1984, "On Motion Planning with Uncertainty," Technical Report 810, M.I.T. Artificial Intelligence Laboratory, Cambridge, MA.

Goldsmith, W., 1960, *Impact: The Theory and Physical Behavior of Colliding Solids*, Edward Arnold Publishers Ltd., London, pp. 5–19.

Hamel, G., 1949, *Theoretische Mechanik*. Springer, Berlin, pp. 393–402; 543–549.

Han, I., and Gilmore, B. J., 1989, "Impact Analysis for Multiple-Body Systems with Friction and Sliding Contact," In *Flexible Assembly Systems*, D. P. Sathyadev, ed., New York, pp. 99–108.

Keller, J. B., 1986, "Impact with Friction," ASME JOURNAL OF APPLIED MECHANICS, Vol. 53, pp. 1–4.

Kilmister, C. W., and Reeve, J. E., 1966, *Rational Mechanics*, Elsevier, New York, p. 189.

Klein, F., 1909, "Zu Painleves Kritik der Coulombschen Rebungsgesetze," *Z.f. Math. und. Phys.*, Vol. 58, pp. 186–191.

Lotstedt, P., 1981, "Coulomb Friction in Two-Dimensional Rigid Body Systems," *Zeitschrift fur Angewandte Mathematik und Mechanik*, Vol. 61, No. 12, pp. 605–615.

Mason, M., and Wang, Y., 1988, "On the Inconsistency of Rigid-Body Frictional Planar Mechanics," *IEEE International Conference on Robotics and Automation*, Philadelphia, PA, pp. 524–528.

Painlevé, P., 1895, "Sur les lois du frottement de glissement," *Comptes Rendus de l'Academie des Sciences*, Vol. 121, pp. 112–115.

Routh, E. J., 1860, *Dynamics of a System of Rigid Bodies: Elementary Part*, 7th ed., Macmillan, London; also, Dover Publications, New York, 1905, pp. 126–162.

Stronge, W. J., 1990, "Rigid Body Collisions with Friction," *Proceedings of Royal Society of London*, Vol. A431, pp. 169–181.

Wang, Y., 1986, "On Impact Dynamics of Robotic Operations," CMU-RI-TR-86-14, The Robotic Institute, Carnegie-Mellon University.

Wang, Y., 1989, "Dynamic Analysis and Simulation of Mechanical Systems With Intermittent Constraints," Ph.D. Thesis, Department of Mechanical Engineering, Carnegie-Mellon University.

Wang, Y., and Mason, M. T., 1987, "Modeling Impact Dynamics for Robotic Operations," *1987 IEEE International Conference on Robotics and Automation*, Raleigh, NC, pp. 678–685.

Whittaker, E. T., 1944, *A Treatise on the Analytical Dynamics of Particles and Rigid Bodies*, 4th Ed., Dover Publications, New York, p. 232.

## APPENDIX

We verify energy conservation for Poisson's hypothesis for the perfect elastic case ($e = 1$). It is useful to note that $P_y \geq 0$, $B_1 > 0$, $B_2 > 0$, and $B_1B_2 - B_3^2 > 0$. The energy losses are given by contact mode:

- sliding:

$$2\Delta T = -s\mu P_y(S+S_o).$$

Note that $S$ remains the same sign with $S_o$ and $s(S+S_o) \geq 0$. Therefore, $\Delta T \leq 0$.

For the remaining contact modes, if we solve for $S_o$ and $C_o$ from the solutions of impulse given in Section 3.5 and substitute them in Eq. (57), then the energy change is a quadratic form of variables of impulses ($P_x$ $P_y$) can be examined to determine its sign.

- C-sticking:

$$2\Delta T = -\frac{1}{B_1}(B_1P_x - B_3P_y)^2 \leq 0.$$

- R-sticking:

$$2\Delta T = -(B_1P_x^2 + s\mu B_3P_y^2).$$

There are two cases, $sB_3 \geq 0$ (therefore, $\Delta T \leq 0$) and $sB_3 < 0$. In the second case, the quadratic form is hyperbolic and $\Delta T \leq 0$ requires that $|P_x| \geq \sqrt{\mu|\mu_s|}P_y$, where $\mu_s = -B_3/B_1$ (Table 1). The conditions of the contact mode (Table 1) can be written as

$$-sP_x \geq \frac{1}{2}(\mu + |\mu_s|)P_y \text{ and } -sP_s \leq \mu P_y.$$

Since $\mu \geq |\mu_s|$ and $\mu \geq 1/2(\mu + |\mu_s|) \geq \sqrt{\mu|\mu_s|}$, it is evident that within these constraints the energy change $\Delta T \leq 0$ is true.

- C-reversed sliding:

$$2\Delta T = -\left[\frac{sB_3}{\mu}P_x^2 - (B_3 + s\mu B_1)P_xP_y + s\mu B_3P_y^2\right].$$

The conditions for the contact mode are $sB_3 > 0$ and $\mu \leq |\mu_s|$, where $\mu_s = -B_3/B_1$.

The determinant of the quadratic form is found to be

$$\Delta = B_3^2\left[1 - \frac{1}{4}(1 + \mu/|\mu_s|)^2\right] \geq 0.$$

Therefore, $\Delta T \leq 0$.

- R-reversed sliding:

$$2\Delta T = -\left[\frac{sB_3}{\mu}P_x^2 + (B_3 - s\mu B_1)P_xP_y + s\mu B_3P_y^2\right].$$

Considering the conditions $sB_3 > 0$ and $0 < \mu \leq |\mu_s|$, we found the determinant of the quadratic form to be

$$\Delta = B_3^2\left[1 - \frac{1}{4}(1 - \mu/|\mu_s|)^2\right] \geq 0$$

yielding $\Delta T \leq 0$.

# A Projection Method Approach to Constrained Dynamic Analysis[1]

**W. Blajer**[2]

Institute B of Mechanics,
University of Stuttgart,
Pfaffenwaldring 9,
7000 Stuttgart 80,
Germany

*The paper presents a unified approach to the dynamic analysis of mechanical systems subject to (ideal) holonomic and/or nonholonomic constraints. The approach is based on the projection of the initial (constraint reaction-containing) dynamical equations into the orthogonal and tangent subspaces; the orthogonal subspace which is spanned by the constraint vectors, and the tangent subspace which complements the orthogonal subspace in the system's configuration space. The tangential projection gives the reaction-free (or purely kinetic) equations of motion, whereas the orthogonal projection determines the constraint reactions. Simplifications due to the use of independent variables are indicated, and examples illustrating the concepts are included.*

## 1 Introduction

Over the years several methods for obtaining *constraint reaction-free* (or purely kinetic) equations of motion for systems subject to constraints have been introduced and compared to each other with respect to algebraic complexity and ease of practical applications. Lagrange-type equations, Gibbs-Appell equations, Kane's equations, Maggi's equations, and Boltzmann-Hamel equations may serve as examples of these methods. The equations are derived usually by using the *virtual formalism*, e.g. the concepts of virtual displacement and virtual work. Although it is an efficient and reliable mathematical technique, geometrical insight into the problems solved is very often missing. This causes that a reader encountering the presentation of the methods may find them difficult to be interpreted and, in a way, artificial. Moreover, the methods, aimed at automatic elimination of constraint forces, usually do not answer the problem of how to determine the constraint reactions (which may be of importance in practical applications). The user of a particular method (the Lagrange's equations for instance) does not often define the constraints at all, and may be unaware of the constraint idealness being postulated. Furthermore, the cases of systems subject to holonomic (geometrical) and nonholonomic (nonintegrable kinematical) constraints are usually treated seperately. The same refers to the problem of derivation of dynamical equations of motion in generalized coordinates and quasi-coordinates (quasi-velocities).

The objective of this paper is an attempt to give a unified and compact approach to the aforementioned topics. The formulation proposed originates mostly from the idea of the "projection method" formulated by Scott (1988). To introduce the technique, let us consider a particle motion on a smooth surface. The solution proposed by Scott consists of resolving forces and accelerations along the tangent and normal directions to the particle path. In other words, Newton's laws are projected onto the local tangent plane to the constraint surface at the location of the particle, and the direction orthogonal to the plane there. The tangential projection gives the kinetic equations of motion, whereas the orthogonal projection determines the constraint reaction. The concept is generalized to a many-particle system characterized by an independent set of generalized coordinates. The Scott's approach is then extended by Storch and Gates (1989) to a many particle system with linear nonholonomic constraints, and the equivalence of that formulation and Kane's equations is reported.

The content of this paper generalizes Scott's approach considerably and comprises the well-known orthogonal complement technique, Kane's form of Appell's equations, and Maggi's equations. For reasons of generality, the starting point of the present analysis are the governing equations of an $n$-degree-of-freedom *unconstrained* system. In other words, the analysis is carried out in the $n$-dimensional (configuration) space, and the system's motion in the space is interpreted as the motion of a generalized particle having $n$ coordinates. If $m$ independent constraints are imposed on the system, the associated constraint vectors span an $m$-dimensional subspace. Appealing to the example of particle moving on a smooth surface, let us call the $m$-subspace an *orthogonal subspace*, and its $k$-dimensional $(k=n-m)$ complement in the $n$-space—a *tangent subspace*. The projection of the initial dynamical equations into the orthogonal and tangent subspaces is the key of the approach proposed. The tangential projection gives the *constraint reaction-free* (or purely kinetic) equations of motion, and the orthogonal projection serves for determination of the constraint reactions.

In the projection method formulation reported in this paper, holonomic and nonholonomic constraints are given equal

---

[1]This work was supported in part by the Alexander von Humboldt Foundation, Bonn-Bad Godesberg, Germany.

[2]On leave form the Technical University of Random, Department of Mechanics, ul. Malczewskiego 29, 26-600 Radom, Poland.

Contributed by the Applied Mechanics Division of THE AMERICAN SOCIETY OF MECHANICAL ENGINEERS for publication in the ASME JOURNAL OF APPLIED MECHANICS.

Discussion on this paper should be addressed to the Technical Editor, Professor Leon M. Keer, The Technological Institute, Northwestern University, Evanston, IL 60208, and will be accepted until four months after final publication of the paper itself in the JOURNAL OF APPLIED MECHANICS.

Manuscript received by the ASME Applied Mechanics Division, Aug. 1, 1990; final revision, Dec. 17, 1990. Associate Technical Editor: R. L. Huston.

treatment, and the analysis starts from the constraint equations transformed to the second-order kinematical form. However, some simplifications due to the use of independent coordinates and/or velocities are indicated. In these cases, the projection method is shown to lead to slightly modified, and in a way generalized, Kane's form of Appell's equations and Maggi's equations, respectively. The theoretical considerations are illustrated through practical applications.

## 2 Problem Formulation

As a means of introduction, consider a mechanical system characterized by $n$ generalized coordinates $x=[x_1, \ldots, x_n]^T$. The equations of motion of the system can be written in the following matrix form

$$M\dot{v}=h^*, \tag{1a}$$

$$\dot{x}=Av+a_0, \tag{1b}$$

where $M(x, t)$ is an $n\times n$ symmetric positive-definite matrix, $v=[v_1, \ldots, v_n]^T$ is a column matrix representation of kinematical parameters, $A(x, t)$ is an $n\times n$ invertible (tranformation) matrix, $h^*(v, x, t)$ and $a_v(x, t)$ are $n\times 1$ matrices, and $t$ is the time. On the other hand, from the point of view of the vector space and tensor algebra analyses, $M$ can be interpreted as the metric tensor matrix of the base $e_v=[e_{v1}, \ldots, e_{vn}]^T$, $M=e_v e_v^T$; $v$ and $x$ are the contravariant representations of the vectors $\mathbf{v}$ and $\mathbf{x}$ in the bases $e_v$ and $e_x$, respectively, $\mathbf{v}=v^T e_v$ and $\mathbf{x}=x^T e_x$; and $h^*$ is the covariant representation of the applied and centrifugal force vector in the base $\overset{*}{e}_v$, $\mathbf{h}=h^{*T}\overset{*}{e}_v$. The superscript (*) denotes here the covariant representations of vectors and contravariant base vectors, e.g., $e_v=M\overset{*}{e}_v$, and $\dot{v}^*=M\dot{v}$ ($\dot{v}^*$ denotes the representation of inertial forces). Note that all the position, velocity, and acceleration vectors are represented by contravariant components, whereas the force vectors are represented by covariant components. The distinction between the contravariant and covariant components of vectors is essential in the following formulation as they transform differently when reference frames are changed, see, e.g., Sokolnikoff (1951).

Equations (1) are meant here as the initial governing equations of the *unconstrained* system. For generality, this will apply, however, not only to the usual meaning of the unconstrained system, that is a system being an assembly of unconstrained particles and/or bodies, but also to a system whose dynamics has been previously formulated in the independent coordinates by any method. This meets, for instance, the reaction-free equations of motion of interconnected body systems.

Equation (1$b$) describes a transformation between the generalized velocities $\dot{x}$ and the kinematical parameters $v$ which are often introduced in practical applications. The kinematical parameters are either new generalized velocities when adequate components of

$$v=B\dot{x}+b_0, \tag{2}$$

where $B=A^{-1}$ and $b_0=-A^{-1}a_0$, are integrable, or quasi-velocities when the components are not integrable. In particular, for $b_{0i}=0$, the $i$th component of (2), $v_i=B^{(i)}\dot{x}$, where $B^{(i)}$ is the $i$th row of $B$, is a new generalized velocity if the Jacobian $\partial B^{(i)}/\partial x$ is a symmetric matrix, e.g., $\partial B_j^{(i)}/\partial x_k=\partial B_k^{(i)}/\partial x_j$, $j$, $k$ = 1, ..., $n$, for details refer to Nejmark and Fufajev (1967, Chap. I.7). Otherwise, $v_i$ is a quasi-velocity. For brevity in the following, $v$ will be called the vector of quasi-velocities.

Assume then that $m$-independent constraints are imposed on the system, and introduce the constraint equations in the second-order kinematical form

$$C_\lambda\dot{v}+\overset{*}{c}_{\lambda 0}=0 \tag{3}$$

where $C_\lambda(v, x, t)$ is an $m\times n$ constraint matrix of maximal rank, and the so-called *constraint vectors* (Kamman and Huston, 1984) are contained in $C_\lambda^T$ as columns; and $\overset{*}{c}_{\lambda 0}(v, x, t)$ is an $m\times 1$ matrix. Since $C_\lambda\dot{v}$ can be interpreted as dot products of the constraint vectors and the acceleration vector $\dot{\mathbf{v}}$, the columns of $C_\lambda^T$ are the covariant representations of the constraint vectors in the base $\overset{*}{e}_v$. If there are geometrical, $f(x, t)=0$, and/or first-order kinematical; $\varphi(v, x, t)=0$, constraints on the system, they are to be transformed to the form (3) by differentiating with respect to time twice or once, respectively. In these cases, $C_\lambda$ and $\overset{*}{c}_{\lambda 0}$ are

$$c_\lambda=\begin{cases}\dfrac{\partial f}{\partial x}A & \text{for } f(x, t)=0 \qquad (4a)\\[2ex] \dfrac{\partial\varphi}{\partial v} & \text{for } \varphi(v, x, t)=0 \qquad (4b)\end{cases}$$

$$\overset{*}{c}_{\lambda 0}=\begin{cases}\left(\dfrac{\partial f}{\partial x}A\right)^{\cdot}v+\left(\dfrac{\partial f}{\partial x}a_0+\dfrac{\partial f}{\partial t}\right)^{\cdot} & \text{for } f(x, t)=0 \qquad (5a)\\[2ex] \dfrac{\partial\varphi}{\partial x}(Av+a_0)+\dfrac{\partial\varphi}{\partial t} & \text{for } \varphi(v, x, t)=0. \qquad (5b)\end{cases}$$

Evidently, the transformation of $f=0$ and $\varphi=0$ into the form (3) yields appropriate conditions imposed on the initial values $v_0$ and $x_0$.

The constraints (3) imposed on the system introduce reactions which must occur in the dynamic Eq. (1$a$). A class of ideal constraints will be considered here, which yields that constraint reactions are postulated to be collinear with the associated constraint vectors. Hence, the constraining generalized forces applied to the system due to the constraints (3) can be represented in the directions of $v$ as follows:

$$r^*=\sum_{i=1}^{m}r_i^*=\sum_{i=1}^{m}\overset{*}{c}_{\lambda i}\lambda_i=C_\lambda^T\lambda, \tag{6}$$

where $\lambda=[\lambda_1, \ldots, \lambda_m]^T$ is the vector of undetermined multipliers, and $\overset{*}{c}_{\lambda i}$ is the $i$th column of $C_\lambda^T$.

The form (6) of the constraining forces $r^*$ may also be derived by using the Gauss' principle of least constraint. In the sense of that principle, ideal constraint reactions minimize a Gauss'/Gibbs'/Appell's functional (an acceleration energy function) (for details see Nejmark and Fufajev (1967), Pars (1961))

$$Z=\frac{1}{2}\dot{v}^T(M\dot{v}-h^*-r^*)=0. \tag{7}$$

The stationary condition is equivalent to the following demand

$$\delta Z=\delta\dot{v}^T(M\dot{v}-h^*-r^*)=0. \tag{8}$$

Since for the *unconstrained* system $\delta\dot{v}^T(m\dot{v}-h^*)=0$, the ideal constraint reactions must satisfy the condition

$$\delta\dot{v}^T r^*=0, \tag{9}$$

which compared with the condition of constraints (3)

$$C_\lambda\delta\dot{v}=0 \qquad \text{or} \qquad \delta\dot{v}^T C_\lambda^T=0, \tag{10}$$

yields that $r^*$ must be collinear with the constraint vectors. Hence, the relationship (6) is evident.

Since $\delta\dot{v}=[\delta\dot{v}_1, \ldots, \delta\dot{v}_n]^T$ must satisfy the conditions (10), only $k=n-m$ components of $\delta\dot{v}$ are independent. Hence, the values of $\lambda$ at every instant of the system's motion must be fitted such that the coefficients accompanied in (8), the dependent components of $\delta\dot{v}$, be equal zero. This leads to the following set of governing equations of motion for a system with ideal constraints:

$$M\dot{v}=h^*+C_\lambda^T\lambda, \tag{11a}$$

$$\dot{x}=Av+a_0, \tag{11b}$$

$$C_\lambda\dot{v}+\overset{*}{c}_{\lambda 0}=0. \tag{11c}$$

## 3 Projection Method Formulation

Denote the column matrix representation of constraint vectors by $e_\lambda = [\overset{*}{e}_{\lambda 1}, \ldots, e_{\lambda m}]^T$, the covariant components of which in the base $\overset{*}{e}_v$ are contained in $C_\lambda^T$ as columns. In principle, $e_\lambda$ are independent (rank($C_\lambda$) = max = $m$), hence, a set of $k = n - m$ independent vectors $e_\tau = [e_{\tau 1}, \ldots, e_{\tau k}]^T$, assume orthogonal to $e_\lambda$, exist. Noting that $e_\tau$ are represented by cotravariant components in the base $e_v$ which are contained in $C_\tau^T$ as columns ($C_\tau(v, x, t)$ is a $k \times n$ matrix of maximal rank), the orthogonality condition can be written as

$$C_\tau C_\lambda^T = 0 \quad \text{or} \quad C_\lambda C_\tau^T = 0, \tag{12}$$

( $= C_\tau$ is an orthogonal complement of $C_\lambda$ in the $n$-dimensional space). On the other hand, (12) represents the dot products, $e_\tau e_\lambda^T$ or $e_\lambda e_\tau^T$ of orthogonal vectors (recall that $e_\lambda$ are represented in $C_\lambda^T$ by covariant components, whereas $e_\tau$ are represented in $C_\tau^T$ by contravariant components).

Since the vectors $e' = [e_\lambda^T, e_\tau^T]^T$ are linearly independent, they form a new base in the $n$-dimensional space. Hence, the following formula for the transformation of the base vectors can be written

$$e' = \begin{bmatrix} e_\lambda \\ e_\tau \end{bmatrix} = \begin{bmatrix} C_\lambda M^{-1} \\ C_\tau \end{bmatrix} e_v = T e_v, \tag{13}$$

where $e_v$ and $e'$ are covariant base vectors here. Since the dynamical Eqs. (11$a$) are represented in covariant components, the (covariant) representation of the equations in the base $e'^*$ is equivalent to the left-sided multiplication of (11$a$) by the transformation matrix $T$. Noting that $e_\lambda$ span an *orthogonal subspace*, and $e_\tau$ span a *tangent subspace*, the resulting dynamic equations in the base $e'^*$ can be decomposed (= projected into the two subspaces) as follows:

$$C_\lambda \dot{v} = C_\lambda M^{-1} h^* + C_\lambda M^{-1} C_\lambda^T \lambda, \tag{14a}$$

$$C_\tau M \dot{v} = C_\tau h^*. \tag{14b}$$

Now, (11$c$), (14$b$), and (11$b$) form a new set of governing equations which can be written as

$$TM\dot{v} = h'^*, \tag{15a}$$

$$\dot{x} = Av + a_0, \tag{15b}$$

where $h'^* = [-\overset{*}{c}{}_{\lambda 0}^T, (C_\tau h^*)^T]^T$. Note that the dimension of (15) is reduced to $2n$ as compared with the dimension of (11) which equals $2n + m$. Note also that the tangential projection (14$b$), as well as the governing Eqs. (15), are conceptually equivalent to the results obtained by Hemami and Weimer (1981) by using the *orthogonal complement method*, and then expanded upon by others, e.g., Kamman and Huston (1984), Kim and Vanderploeg (1986), Liang and Lance (1987), and Angeles and Lee (1988).

The orthogonal projection (14$a$) may serve for explicit determination of undetermined multiplier values, and then for determination of constraint reactions. Namely, after considering (11$c$) it follows from (14$a$) that

$$\lambda = -M_\lambda^{-1}(\overset{*}{c}_{\lambda 0} + C_\lambda M^{-1} h^*) = \lambda(v, x, t), \tag{16}$$

where $M_\lambda(v, x, t) = C_\lambda M^{-1} C_\lambda^T$ is an $m \times m$ matrix (= metric tensor of the orthogonal subspace). Then, the $i$th constraint reaction can be found as

$$\overset{*}{r}_i = \overset{*}{c}_{\lambda i} \lambda_i = \overset{*}{r}_i(v, x, t), \tag{17}$$

where $\overset{*}{c}_{\lambda i}$ is the $i$th column of $C_\lambda^T$.

If the constraint Eqs. (3) ((11$c$), the first $m$ equations of (15$a$)) are the transformed forms of lower-order constraint equations, direct integration of (15) may yield the constraint violation due to the integration numerical errors. There are at least two fundamental approaches aimed at avoiding the constraint violation. The first approach is to apply special integration techniques based on monitoring the constraint violation at every step of integration and aimed at reducing the violation, and in fact, the methods minimize the constraint violations only. The Baumgarte's constraint violation stabilization method (see Baumgarte (1972) and Nikravesh (1984)) may serve as an example of the approach. The second approach are methods based on expressing the dynamic equations in the independent variables chosen so that all the constraint conditions be satisfied. Kane's form of Appell's equations (Kane and Levinson, 1980, 1985), Maggi's equations (Nejmark and Fufajev, 1967, Chap. II. 4; Papastavridis, 1990), Gibbs-Appell equations (Desloge, 1988; Papastavridis, 1988), and the coordinate partitioning technique (Wehage and Haug, 1982) are application of the approach. An additional advantage of the approach is the reduction of dimension of the resulting dynamical equations. In this paper the second approach will be discussed and extended from the point of view of the projection method. However, prior to the presentation of the formulation, some mathematical relationships will be introduced which will be of some use in the further analysis.

The metric tensor matrix $M'$ of the base $e'$ is

$$M' = TMT^T = \begin{bmatrix} C_\lambda M^{-1} C_\lambda^T & 0 \\ 0 & C_\tau M C_\tau^T \end{bmatrix} = \begin{bmatrix} M_\lambda & 0 \\ 0 & M_\tau \end{bmatrix}, \tag{18}$$

where $M_\lambda$ and $M_\tau$ are the metric tensor matrices of the orthogonal and tangent subspaces, respectively. From (18) it comes evidently that the subspaces complement each other.

Using (18), an inverse of the transformation matrix $T$ can be found as

$$T^{-1} = MT^T(M')^{-1} = MT^T \begin{bmatrix} M_\lambda^{-1} & 0 \\ 0 & M_\tau^{-1} \end{bmatrix}. \tag{19}$$

Now, let us define the vector of independent quasi-accelerations $\dot{u} = [\dot{u}, \ldots, \dot{u}_k]^T$, and choose them such that they be not represented in the orthogonal subspace. In other words, (3) may be treated as a set of $m$ quasi-accelerations which, due to the constraints imposed, are always equal to zero. Hence, there are only $k(= n - m)$ independent quasi-accelerations. Mathematically, it may be stated as

$$M' \begin{bmatrix} 0 \\ \dot{u} \end{bmatrix} = \begin{bmatrix} 0 \\ M_\tau \dot{u} \end{bmatrix} = \begin{bmatrix} C_\lambda \dot{v} + \overset{*}{c}_{\lambda 0} \\ C_\tau M \dot{v} + \overset{*}{c}_{\tau 0} \end{bmatrix} = TM\dot{v} + \begin{bmatrix} \overset{*}{c}_{\lambda 0} \\ \overset{*}{c}_{\tau 0} \end{bmatrix}, \tag{20}$$

where $\overset{*}{c}_{\tau 0}(v, x, t)$ is a $k$-dimensional vector the meaning of which will be made precise later on. From (20), after considering (18), it comes to

$$\dot{v} = T^T(M')^{-1}\left(M' \begin{bmatrix} 0 \\ \dot{u} \end{bmatrix} - \begin{bmatrix} \overset{*}{c}_{\lambda 0} \\ \overset{*}{c}_{\tau 0} \end{bmatrix}\right) =$$

$$= C_\tau^T \dot{u} - (M^{-1} C_\lambda M_\lambda^{-1} \overset{*}{c}_{\lambda 0} + C_\tau^T M_\tau^{-1} \overset{*}{c}_{\tau 0}) = C_\tau^T \dot{u} + c_{u0}, \tag{21}$$

and the substitution of (21) into (15$a$) yields

$$M' \begin{bmatrix} 0 \\ \dot{u} \end{bmatrix} - \begin{bmatrix} \overset{*}{c}_{\lambda 0} \\ \overset{*}{c}_{\tau 0} \end{bmatrix} = \begin{bmatrix} -\overset{*}{c}_{\lambda 0} \\ C_\tau h^* \end{bmatrix}. \tag{22}$$

The first $m$ equations of (22) give the identity $-\overset{*}{c}_{\lambda 0} = -\overset{*}{c}_{\lambda 0}$, and the remaining $k$ equations are the dynamical equations in the independent quasi-accelerations, and are represented in the tangent subspace

$$M_\tau \dot{u} = C_\tau h^* + \overset{*}{c}_{\tau 0} = h_\tau^*. \tag{23}$$

## 4 Holonomic Case

Assume that the $m$ constraints imposed on the system are geometrical (holonomic) constraints of the form

$$f(x, t) = 0. \tag{24}$$

The constraints are assumed to be independent, hence, (24) can be treated as a set of $m$ curvilinear coordinates which, due to the constraints imposed, equal zero at every instant of system's motion. Then, the position of the system can be explicitly expressed by $k(=n-m)$ independent coordinates $q=[q_1, \ldots, q_k]^T$. The independent coordinates can be chosen as

$$\begin{bmatrix} 0 \\ q \end{bmatrix} = \begin{bmatrix} f(x, t) \\ g(x, t) \end{bmatrix}, \tag{25}$$

where $g$ is a twice differentiable function chosen such that $[f^T, g^T]^T$ describes the coordinate transformation, rank $((\partial f/\partial x)^T, (\partial g/\partial x)^T) = \max = n$. Hence, at least theoretically, an inverse relation to (25) exists, that is

$$x = x(q, t). \tag{26}$$

In fact, the relation (26) is usually formulated a priori without mentioning (25). Introduce, then, the vector of independent quasi-velocities $u=[u_1, \ldots, u_k]^T$, and define a relation corresponding to $(1b)$, i.e.,

$$\dot{q} = Du + d_0, \tag{27}$$

where $D(q, t)$ is a $k \times k$ invertible (transformation) matrix, and $d_0(q, t)$ is a $k$-dimensional vector.

Differentiating twice with respect to time the relation (26), and considering $(15b)$ and (27), one can obtain

$$\dot{v} = A^{-1}JD\dot{u} + c_{u0}, \tag{28}$$

where $J = \partial x/\partial q$ is the $n \times k$ Jacobian matrix, and $c_{u0} = (A^{-1}JD)^{\cdot}u + [A^{-1}(Jd_0 + \partial x/\partial t - a_0)]^{\cdot}$. Comparing (21) and (28), it is evident that

$$C_\tau^T = A^{-1}JD, \tag{29}$$

and taking $A(x(q, t))$, $C_\tau$ in (29) can be expressed as dependent on $q$ and $t$. Similarly, $c_{u0}$ in (28) can be expressed as a function of $u$, $q$, and $t$.

One can easily deduce that $C_\tau$ defined by (29) is really an orthogonal complement of $C_\lambda$ defined by $(4a)$. Namely, the dynamic constraint conditions (3) yield $C_\lambda \delta\dot{v} = 0$, and from (28) it follows that $\delta\dot{v} = A^{-1}JD\delta\dot{u}$, hence, $C_\lambda(A^{-1}JD)\delta\dot{u} = 0$. Since $\delta\dot{u}$ are independent, $C_\lambda(A^{-1}JD) = C_\lambda C_\tau^T = 0$, which expresses the orthogonality condition.

Now, after substituting (28) into $(15a)$, the reduced-dimension dynamic equations, equivalent to (23), can be found as

$$M_\tau \dot{u} = (A^{-1}JD)^T(h^* - Mc_{u0}) = h_\tau^*, \tag{30}$$

where $M_\tau = (A^{-1}JD)^TM(A^{-1}JD)$, and $-(A^{-1}DJ)^TMc_{u0}$ refers to $\overset{*}{c}_{\rho 0}$ from (20) and (23). Considering that $M_\rho = M_\tau(q, t)$ and $h_\tau = h_\tau(u, q, t)$, the set of new governing equations of motion, (30) and (27), is equivalent to the initial governing equations (1) of the *unconstrained* system. The dimension of the new set of governing equations is reduced to $2k$.

Due to the known a priori relation (26), the formulation provided in this section does not require the determination of $C_\tau$ as an orthogonal complement of $C_\lambda$, which may be a cumbersome task in practical applications. Moreover, the analytical formulation of the imposed constraints is not necessary for obtaining the tangent dynamical Eqs. (30) either. Note also that $f(x(q, t), t)) \equiv 0$.

When the constraint reactions are to be found, $C_\lambda$ and $\overset{*}{c}_{\lambda 0}$ must be determined according to $(4a)$ and $(5a)$. Then after substituting $x = x(q, t)$ and $v = v(u, x, t)$, the undetermined multipliers and the constraint reactions can be found from (16) and (17) as functions of $u$, $q$, and $t$.

The tangent dynamical Eqs. (30) are a generalized form of Kane's form of Appell's equations (Kane and Levinson, 1980, 1985). Using the nomenclature of Kane's approach, $C_\tau^T = A^{-1}JD = \partial v/\partial u = \partial\dot{v}/\partial\dot{u} = \ldots$, corresponds to the matrix of so-called partial velocities. Hence, Kane's formulation

$$\frac{\partial v}{\partial u}(-M\dot{v} + h^*) = 0 \tag{31}$$

is also a projection of the dynamical equations of *unconstrained* system into the tangent subspace relative the constraints imposed.

## 5 Nonholonomic Case

Assume now that the system is subjected to $m$ first-order kinematical (nonholonomic) constraints

$$\varphi(v, x, t) = 0, \tag{32}$$

where $\varphi = [\varphi_1, \ldots, \varphi_m]^T$ are at least once differentiable functions, and the maximal rank of the Jacobian matrix $\partial\varphi/\partial v$ is demanded. Most often linear nonholonomic constraints are encountered, see Nejmark and Fufajev (1967, Chap. I.1), i.e.,

$$\varphi = Ev + \overset{*}{e}_0 = 0, \tag{33}$$

where $E(x, t)$ is an $m \times n$ constraint matrix of maximal rank, and $\overset{*}{e}_0(x, t)$ is an $m$-dimensional vector. As opposed do the kinematical (= differentiated) form of geometrical constraints, (33) are assumed to be nonintegrable (see the comments following (3) in Section 3 of this paper).

By analogy to the holonomic case formulation of Section 4, the nonholonomic constraint equations, (32) or (33), may be interpreted as $m$ new quasi-velocities which, due to the constraints imposed, remain zero. Hence, $k(=n-m)$ independent quasi-velocities $u = [u_1, \ldots, u_k]^T$ can be constructed as follows (note that nonholonomic constraints do not reduce the number of generalized coordinates describing the system's position in the $n$-dimensional space):

$$\begin{bmatrix} 0 \\ u \end{bmatrix} = \begin{bmatrix} \varphi(v, x, t) \text{ or } Ev + \overset{*}{e}_0 \\ \gamma(v, x, t) \end{bmatrix}. \tag{34}$$

Now, assuming that rank $((\partial\varphi/\partial v)^T, (\partial\gamma/\partial v)^T) = \max = n$, the following (inverse) relation exists (at last theoretically):

$$v = v(u, x, t). \tag{35}$$

In practical applications, however, the relation (35) is usually difficult to be formulated a priori. Hence, for nonlinear nonholonomic equations, a general projection method provided in Section 3 is recommended. For linear constraints, Maggi's approach may be used; which will be shown to be equivalent to the projective approach.

In the case of linear constraints (33), the independent quasi-velocities are easy to be defined as (compare with (20))

$$M'\begin{bmatrix} 0 \\ u \end{bmatrix} = \begin{bmatrix} 0 \\ M_\tau u \end{bmatrix} = \begin{bmatrix} Ev + \overset{*}{e}_0 \\ C_\tau Mv \end{bmatrix} = TMv + \begin{bmatrix} \overset{*}{e}_0 \\ 0 \end{bmatrix}, \tag{36}$$

where $C_\tau$ is an orthogonal complement of $E$, that is $C_\tau E^T = 0$, and $M_\tau$ is defined by (18). Differentiation with respect to time transforms the relation (36) to the form (20), where

$$C_\lambda = E, \tag{37a}$$

$$\overset{*}{c}_{\lambda 0} = \dot{E}v + \dot{\overset{*}{e}}_0 \tag{37b}$$

$$\overset{*}{c}_{\tau 0} = (C_\tau M)^{\cdot}v - \dot{M}_\tau u. \tag{37c}$$

Since from (36) it follows that

$$v = C_\tau^T u - M^{-1}C_\lambda^T M_\lambda^{-1}\overset{*}{e}_0, \tag{38}$$

the final governing equations of motion can be expressed as follows (compare with (23))

$$M_\tau(x, t)\dot{u} = h_\tau^*(u, x, t), \tag{39a}$$

$$\dot{x} = A(x, t)C_\tau^T(x, t)u + \tilde{a}_0(x,t), \tag{39b}$$

where $\tilde{a}_0 = a_0 - M^{-1}C^TM_\lambda^{-1}\overset{*}{e}_0$. Note that the dimension of (39) is reduced to $2n - m = k + n$, and the solution of (39) assures that the constraints (33) are satisfied in principle.

As mentioned previously, the mathematical formulation of (38)–(39) is equivalent to the Maggi's approach (refer, for instance, to Nejmark and Fufajev (1967) and Papastavridis (1990)). Here the approach has been slightly modified and, in a way, generalized. Following (16) and (17), and considering the present meaning of the relations, the reactions of the non-

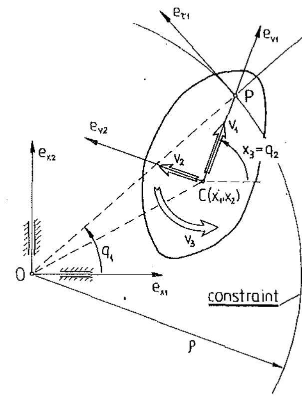


**Fig. 1 Holonomic case illustration: a rigid body plane motion with a point constrained to slide along a circle**

holonomic constraints can be determined as functions of current values of $u$, $x$, and $t$.

## 6 Some Applications

**Example 1.** Consider a plane motion of a rigid body of mass $m$ and (central) moment of inertia $J$. Expressing the dynamical equations of motion in a central body-fixed reference frame, the initial governing equations of the (unconstrained) body motion can be written in the following form, which corresponds to (1),

$$\begin{bmatrix} m & 0 & 0 \\ 0 & m & 0 \\ 0 & 0 & J \end{bmatrix} \begin{bmatrix} \dot{v}_1 \\ \dot{v}_2 \\ \dot{v}_3 \end{bmatrix} = \begin{bmatrix} m v_3 v_2 + F_{x1}\cos x_3 + F_{x2}\sin x_3 \\ -m v_3 v_1 - F_{x1}\sin x_3 + F_{x2}\cos x_3 \\ M_{x3} \end{bmatrix}, \tag{40a}$$

$$\begin{bmatrix} \dot{x}_1 \\ \dot{x}_2 \\ \dot{x}_3 \end{bmatrix} = \dot{x} = \begin{bmatrix} \cos x_3 & -\sin x_3 & 0 \\ \sin x_3 & \cos x_3 & 0 \\ 0 & 0 & 1 \end{bmatrix} \begin{bmatrix} \dot{v}_1 \\ \dot{v}_2 \\ \dot{v}_3 \end{bmatrix} = Av, \tag{40b}$$

where $x_1$ and $x_2$ are the position coordinates of the body mass center in the inertial reference frame, $x_3$ is the angle of the body angular orientation (see Fig. 1), $v_1$ and $v_2$ are the projections of the body linear velocity onto the axes of the body-fixed reference frame, and $v_3$ is the body angular velocity (note that $v_1$ and $v_2$ are quasi-velocities whereas $v_3$ is a generalized velocity). The external forces applied to the body are represented by the resultant force components $F_{x1}$ and $F_{x2}$ along the inertial frame axes, and the torque $M_{x3}$ of the forces in relation to the body mass center $C$.

Assume then that a point $P$ of the body $\overline{CP} = s$, is constrained to slide along a circle of radius $\rho$, and the friction effects are neglected. Choosing the body-fixed reference frame such that $P$ belongs to the first axis of the frame, and coinciding the origin of the inertial frame with the center of the constraint circle, the (holonomic) constraint equation can be written as follows (see Fig. 1):

$$f = \frac{1}{2}(x_1 + s\cos x_3)^2 + (x_2 + s\sin x_3)^2 - \rho^2) = 0 \tag{41}$$

The geometrical constraint (41) can be transformed to the form (3), i.e., $C_\lambda \dot{v} + \overset{*}{c}_{\lambda 0} = 0$. Namely, twice differentiation of (41) with respect to time yields

$$C_\lambda^T = \begin{bmatrix} x_1\cos x_3 + x_2\sin x_3 + s \\ -x_1\sin x_3 + x_2\cos x_3 \\ s(-x_1\sin x_3 + x_2\cos x_3) \end{bmatrix}, \tag{42}$$

$$\overset{*}{c}_{\lambda 0} = v_1 v_2(-x_1\sin x_3 + x_2\cos x_3) - (v_2 v_3 + v_3^2 s)\ (x_1\cos x_3 + x_2\sin x_3) + v_1^2 + v_2^2 + v_2 v_3 s. \tag{43}$$

Using (42) and (43), the initial governing equations of the constrained motion in the form (11) can be easily constructed. Then, following the projection method formulation of Section 3, the matrix $C_\tau$ (an orthogonal complement of $C_\lambda$) may be found as

$$C_\tau^T = \begin{bmatrix} -(-x_1\sin x_3 + x_2\cos x_3 & 0 \\ x_1\cos x_3 + x_2\sin x_3 + s & -s \\ 0 & 1 \end{bmatrix}. \tag{44}$$

Now, the transformation matrix $T$ can be formulated according to the definition given in (13), and the reaction-free governing equations of the form (15) can be derived easily (for brevity, these equations will not be reported here). It is worth noting, however, that the solution of the equations demands that appropriate initial conditions must be given, that is $f(x_0, 0) = 0$, and $\dot{f}(f(v_0, x_0, 0) = 0$.

One may ascertain that the governing equations in the form (15) obtained by using the general approach of the projection method are rather complicated, and the same refers to the problem of determination of the constraint reaction via (16) and (17). As stated in Section 3, and amplified in Section 4, a more convenient approach is to use independent coordinates. For the case at hand, there are two such coordinates, and a reasonable choice of them is $q = [q_1, q_2]^T$, where $q_1$ is the angle of point $P$ position on the constraint circle (see Fig. 1), and $q_2 = x_3$. Then, the vector of independent quasi-velocities $u = [u_1, u_2]^T$ can be stated as $u = \dot{q}$ ($u$ are generalized velocities here).

Now, the relation (26) expressing the transformation from independent coordinates $q$ to the initial coordinates $x$ is

$$\begin{bmatrix} x_1 \\ x_2 \\ x_3 \end{bmatrix} = \begin{bmatrix} \rho\cos q_1 - s\cos q_2 \\ \rho\sin q_1 - s\sin q_2 \\ q_2 \end{bmatrix} \tag{45}$$

and the Jacobian matrix of the coordinate transformation is

$$\frac{\partial x}{\partial q} = \begin{bmatrix} -\rho\sin q_1 & -s\sin q_2 \\ \rho\cos q_1 & -s\cos q_2 \\ 0 & 1 \end{bmatrix}. \tag{46}$$

Using (45), (46), and (40b), the relation (28) can be derived as

$$\begin{bmatrix} \dot{v}_1 \\ \dot{v}_2 \\ \dot{v}_3 \end{bmatrix} = \begin{bmatrix} \rho\sin(q_2 - q_1) & 0 \\ \rho\cos(q_2 - q_1) & -s \\ 0 & 1 \end{bmatrix} \begin{bmatrix} \dot{u}_1 \\ \dot{u}_2 \end{bmatrix} + \begin{bmatrix} u_1(u_2 - u_1)\cos(q_2 - q_1) \\ -\rho u_1(u_2 - u_1)\sin(q_2 - q_1) \\ 0 \end{bmatrix}. \tag{47}$$

Formulating the metric tensor matrix $M_\tau$ of the tangent subspace spanned by the directions of $u$, the final reduced-dimension dynamical equations of motion of the considered constrained system are

$$\begin{bmatrix} m\rho^2 & -m\rho s\cos(q_2-q_1) \\ -m\rho s\cos(q_2-q_1) & ms^2+J \end{bmatrix} \begin{bmatrix} \dot{u}_1 \\ \dot{u}_2 \end{bmatrix}$$

$$= \begin{bmatrix} -m\rho s u_2^2 \sin(q_2-q_1) - F_{x1}\rho\sin q_1 + F_{x2}\rho\cos q_1 \\ m\rho s u_1^2 \sin(q_2-q_1) + F_{x1}s\sin q_2 - F_{x2}s\cos q_2 + M_{x3} \end{bmatrix}. \quad (48)$$

Then, following Eqs. (16) and (17), and introducing the independent coordinates $q$ and velocities $u$, the multiplier $\lambda$ and the constraint reaction $r^*$ associated the realization of the constraint (41) are

$$\lambda = -\frac{\kappa}{\rho}F_\lambda, \quad (49)$$

$$r^* = C_\lambda \lambda = \begin{bmatrix} \cos(q_2-q_1) \\ -\sin(q_2-q_1) \\ -s\sin(q_1-q_1) \end{bmatrix} \kappa F_\lambda, \quad (50)$$

where $\kappa = J/(J + ms^2\sin^2(q_2 - q_1))$, and $F_\lambda = msu_1^2 - msu_2^2\cos(q_2 - q_1) + F_{x1}\cos q_1 + F_{x2}\sin q_1$. Note that (50) expresses (covariant) components of the constraint reaction vector in the base $\overset{*}{e}_v$. Since $\overset{*}{e}_{v1}$ and $\overset{*}{e}_{v2}$ are orthogonal and have the same magnitude, from (50) it comes that $\kappa F_\lambda$ is the constraint reaction value.

**Example 2.** Consider now a well-studied problem of knife-edged motion, (see, e.g., Nejmark and Fufajev (1967), and Papastavridis (1988, 1990)). On the assumption that the knife's blade remains perpendicular to the motion plane, the initial governing equations of the unconstrained system can be taken as in (40). Then, assuming that the knife's mass center overlaps its edge, and choosing the body-fixed reference frame such that the knife's contact point $P$ belongs to the first axis of the frame (see Fig. 2), the (nonholonomic) constraint equation can be written in the following form

$$\varphi = v_2 + sv_3 = 0, \quad (51)$$

which expresses the demand of collinearity of the velocity vector of point $P$ and the knife's edge.

Following the mathematical formulation of Section 3;

$$C_\lambda = [0 \quad 1 \quad s], \quad (52)$$

$$\overset{*}{c}_{\lambda 0} = 0, \quad (53)$$

and the matrix $C_\tau$ can be constructed as

$$C_\tau = \begin{bmatrix} 0 & -s & 1 \\ 1 & 0 & 0 \end{bmatrix}. \quad (54)$$

Using this, Eqs. (15*a*) are

$$\begin{bmatrix} 0 & 1 & s \\ 0 & -ms & J \\ m & 0 & 0 \end{bmatrix} \begin{bmatrix} \dot{v}_1 \\ \dot{v}_2 \\ \dot{v}_3 \end{bmatrix} = \begin{bmatrix} 0 \\ s(mv_1v_2 + F_{x1}\sin x_3 - F_{x2}\cos x_3) + M_{x3} \\ mv_2v_3 + F_{x1}\cos x_3 + F_{x2}\sin x_3 \end{bmatrix}, \quad (55)$$

which, completed with (40*b*), form the reaction-free governing equations of the knife's motion. Then, following (16) and (17), $\lambda$ and $r^*$ (expressed in the base $\overset{*}{e}_v$) are

$$\lambda = -\kappa F_\lambda, \quad (56)$$

$$r^* = C_\lambda^T \lambda = \begin{bmatrix} 0 \\ 1 \\ s \end{bmatrix} \kappa F_\lambda, \quad (57)$$

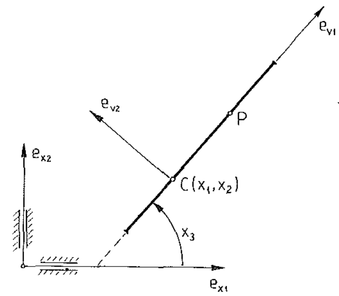


**Fig. 2 Nonholonomic case illustration: a knife-edge problem**

where $\kappa = J/(J + ms^2)$, and $F_\lambda = -mv_1v_2 + F_{x1}\sin x_3 + F_{x2}\cos x_3 + ms/J + M_{x3}$. One may easy ascertain that $\kappa F_\lambda$ is the constraint reaction value.

Let us follow now the formulation given in Section 5, that is, try to find independent quasi-velocities and express (55)-(57) by means of them. According to (36), the independent quasi-velocities may be defined as

$$\begin{bmatrix} \frac{J+ms^2}{mJ} & 0 & 0 \\ 0 & J+ms^2 & 0 \\ 0 & 0 & m \end{bmatrix} \begin{bmatrix} 0 \\ u_1 \\ u_2 \end{bmatrix} = \begin{bmatrix} 0 & 1 & s \\ 0 & -ms & J \\ m & 0 & 0 \end{bmatrix} \begin{bmatrix} v_1 \\ v_2 \\ v_3 \end{bmatrix} \quad (58)$$

which leads to the inverse relation, equivalent to (38)

$$\begin{bmatrix} v_1 \\ v_2 \\ v_3 \end{bmatrix} = \begin{bmatrix} 0 & 1 \\ -s & 0 \\ 1 & 0 \end{bmatrix} \begin{bmatrix} u_1 \\ u_2 \end{bmatrix}. \quad (59)$$

Then the final reduced-dimension governing equations in the form (39) may be formulated for the case at hand as

$$\begin{bmatrix} J+ms^2 & 0 \\ 0 & m \end{bmatrix} \begin{bmatrix} \dot{u}_1 \\ \dot{u}_2 \end{bmatrix} = \begin{bmatrix} s(mu_1u_2 + F_{x1}\sin x_3 - F_{x1}\cos x_3) + M_{x3} \\ -msu_1^2 + F_{x1}\cos x_3 + F_{x2}\sin x_3 \end{bmatrix}, \quad (60)$$

$$\begin{bmatrix} \dot{x}_1 \\ \dot{x}_2 \\ \dot{x}_3 \end{bmatrix} = \begin{bmatrix} s\sin x_3 & \cos x_3 \\ -s\cos x_3 & \sin x_3 \\ 1 & 0 \end{bmatrix} \begin{bmatrix} u_1 \\ u_2 \end{bmatrix}. \quad (61)$$

Using the independent quasi-coordinates $u$, $\lambda$ and $r^*$ defined in (56) and (57) can be expressed as functions of $u$ and $x$.

## Conclusion

Compact mathematical formulation, unified treatment of holonomic and nonholonomic system cases, and intuitive appeal as a generalization of simple dynamics problems are the main advantages of the proposed projective approach to the analysis of constrained systems. The method affords an interesting and useful geometrical insight into the problems which clarifies the mathematical transformations and makes them more comprehensible. The language of vector spaces is used, and tensor algebra is applied. The latter enables one to shorten the mathematical formulation and supplies the method with a reliable mathematical background.

## References


Angeles, J., and Lee, S. K., 1988, "The Formulation of Dynamical Equations of Holonomic Mechanical Systems Using a Natural Orthogonal Complement," ASME JOURNAL OF APPLIED MECHANICS, Vol. 55, pp. 243–244.

Baumgarte, J., 1972, "Stabilization of Constraints and Integrals of Motion in Dynamical Systems," *Computer Methods in Applied Mechanics and Mathematics*, Vol. 1, pp. 1-16.

Desloge, E. A., 1988, "The Gibbs-Appell Equations of Motion," *American Journal of Physics*, Vol. 56, pp. 841-846.

Hemami, H., and Weimer, F. C., 1981, "Dynamics of Nonholonomic Dynamic Systems with Applications," ASME JOURNAL OF APPLIED MECHANICS, Vol. 48, pp. 177-182.

Kamman, J. W., and Huston, R. L., 1984, "Dynamics of Constrained Multibody Systems," ASME JOURNAL OF APPLIED MECHANICS, Vol. 51, pp. 899-903.

Kane, T. R., and Levinson, D. A., 1980, "Formulation of Equations of Motion for Complex Spacecraft," *AIAA Journal of Guidance and Control*, Vol. 3, pp. 99-112.

Kane, T. R., and Levinson, D. A., 1985, *Dynamics: Theory and Applications*, McGraw-Hill, New York.

Kim, S. S., and Vanderploeg, M. J., 1986, "QR Decomposition for State Space Representation of Constrained Mechanical Dynamic Systems," ASME *Journal of Mechanisms, Transmissions, and Automation in Design*, Vol. 108, pp. 183-188.

Liang, C. G., and Lance, G. M., 1987, "A Differentiable Null Space Method for Constrained Dynamic Analysis," ASME *Journal of Mechanisms, Transmissions, and Automation in Design*, Vol. 109, pp. 405-411.

Nejmark, J. I., and Fufajev, N. A., 1967, *Dynamics of Nonholonomic Systems*, (in Russian), Nauka, Moscow.

Nikravesh, P. E., 1984, *Some Methods for Dynamic Analysis of Constrained Mechanical Systems: A Survey* (NATO ASI Series), Vol. F9, Springer-Verlag, Berlin-Heidelberg, pp. 351-368.

Papastavridis, J. G., 1987, "On the Nonlinear Appell's Equations and the Determination of Generalized Reaction Forces," *International Journal of Engineering Sciences*, Vol. 25, pp. 609-625.

Papastavridis, J. G., 1990 "Maggi's Equations of Motion and the Determination of Constraint Reactions," *AIAA Journal of Guidance, Control, and Dynamics*, Vol. 13, pp. 213-220.

Pars, L. A., 1965, *A Treatise on Analytical Mechanics*, Heinemann, London.

Scott, D., 1988, "Can a Projection Method of Obtaining Equations of Motion Compete with Lagrange's Equations?" *American Journal of Physics*, Vol. 56, pp. 451-456.

Sokolnikoff, I. S., 1962, *Tensor Analysis: Theory and Applications*, John Wiley and Sons, London.

Storch, J., and Gates, S., 1989, "Motivating Kane's Method for Obtaining Equations of Motion for Dynamic Systems," *AIAA Journal of Guidance, Control, and Dynamics*, Vol. 12, pp. 593-595.

Wehage, R. A., and Haug, E. J., 1982, "Generalized Coordinate Partitioning for Dimension Reduction in Analysis of Constrained Dynamic Systems," ASME *Journal of Mechanical Design*, Vol. 104, pp. 247-255.

# Eigenvalue Inclusion Principles for Distributed Gyroscopic Systems

**B. Yang**
Asst. Professor,
Department of Mechanical Engineering,
University of South California,
Los Angeles, CA 90089-1453
Assoc. Mem. ASME

*In his famous treatise* The Theory of Sound, *Rayleigh enunciated an eigenvalue inclusion principle for the discrete, self-adjoint vibrating system under a constraint. According to this principle, the natural frequencies of the discrete system without and with the constraint are alternately located along the positive real axis. Although it is commonly believed that the same rule also applied for distributed vibrating systems, no proof has been given for the distributed gyroscopic system. This paper presents several eigenvalue inclusion principles for a class of distributed gyroscopic systems under pointwise constraints. A transfer function formulation is proposed to describe the constrained system. Five types of nondissipative constraints and their effects on the system natural frequencies are studied. It is shown that the transfer function formulation is a systematic and convenient way to handle constraint problems for the distributed gyroscopic system.*

## 1 Introduction

In his famous treatise *The Theory of Sound*, Rayleigh (1945) enunciated the so-called inclusion principle, which may be stated as follows:

**Theorem 1.** *For a linear, discrete, self-adjoint vibrating system whose natural frequencies are* $\omega_k$, *arranged in ascending order of magnitude, if a spring is attached to the system or if one point of the system is fixed, the natural frequencies* $\Omega_k$ *of the constrained system are such that*

$$\omega_k \le \Omega_k \le \omega_{k+1}, \quad k=1, 2, \ldots .$$

Vibration and dynamics of distributed gyroscopic systems have been extensively studied by Ziegler (1968), Mote (1972), Hagedorn (1975), Huseyin (1978), Meirovitch (1980), D'Eleuterio and Hughes (1984), and many others. Although it is commonly believed that Theorem 1 is also valid for general vibrating continua, no proof has been given for distributed gyroscopic systems. Meirovitch and Hale (1978) investigated the relationship between the eigenvalues of different discretized models for distributed gyroscopic systems. They showed that the eigenvalues of a discretized model alternate with those of the same model modified with an added term in discretization. This result, while useful in discretization and numerical analysis, does not deal with distributed gyroscopic systems with physical constraints. Recently, the author (Yang, 1991) studied several eigenvalue inclusion principles for discrete gyroscopic systems with physical constraints. It is found that the natural frequencies of a constrained system alternate with those of the corresponding unconstrained system. Nonetheless, no work has addressed inclusion principles for physically constrained distributed gyroscopic systems.

This paper prevents several inclusion principles for a class of distributed gyroscopic systems under pointwise constraints. In Section 2, a Green's function is derived to predict the response of the unconstrained system. The constraint problem is formulated in the $s$ domain in Section 3. The unconstrained system is an open loop; the distributed gyroscopic system under a constraint is a closed loop with the constraint as a feedback controller. The closed-loop transfer function is determined based on the system Green's function. In Section 4, five types of nondissipative constraints and their effects on the system natural frequencies are studied through investigation of the poles of the closed loop. The inclusion principles developed are illustrated on the axially moving string in Section 5.

## 2 System Description

Consider the linear, distributed gyroscopic system described by

$$w_{tt}(x,t) + Gw_t(x,t) + Kw(x,t) = f(x, t), \; x \in E, \; t>0 \quad (1)$$

$$w(x,t)\,|_{t=0} = a(x) \quad w_t(x,t)_{t=0} = b(x), \; x \in E \quad (2)$$

$$\Gamma w(x,t) = 0, \; x \in \partial E, \; t>0 \quad (3)$$

which relate the displacement $w(x,t)$ to the external force $f(x,t)$ and the initial conditions $a(x)$ and $b(x)$. Here, $E$ is a bounded, open region in $R^n$, $n=1$, 2, or 3 with boundary $\partial E$, $(\,)_t$ denotes partial derivative of ( ) with respect to $t$, $G$ is a skew-symmetric,[1] spatial differential operator normally evolving from Coriolis acceleration or mass transport, $K$ is a symmetric, positive definite, spatial differential operator describing

Contributed by the Applied Mechanics Division of THE AMERICAN SOCIETY OF MECHANICAL ENGINEERS for publication in the ASME JOURNAL OF APPLIED MECHANICS.

Discussion on this paper should be addressed to the Technical Editor, Professor Leon M. Keer, The Technological Institute, Northwestern University, Evanston, IL 60208 and will be accepted until four months after final publication of the paper itself in the JOURNAL OF APPLIED MECHANICS.

Manuscript received by the ASME Applied Mechanics Division, July 17, 1991; final revision, Mar. 1, 1991. Associate Technical Editor: D. J. Inman.

[1] The operator $G$ is skew symmetric if $\langle w_1, Gw_2\rangle = -\langle Gw_1, w_2\rangle$, where $\langle \cdot,\cdot \rangle$ is an inner product, and $w_1$ and $w_2$ are admissible functions (Meirovitch and Silverberg, 1985).

the elastic restoring forces of the system, and $\Gamma$ is a linear operator reflecting boundary conditions. For $G=0(1)$ is a classical self-adjoint system.

The eigenvalue problem associated with (1)

$$(\lambda_k^2+\lambda_k G+K)\nu_k(x)=0 \qquad (4)$$

has eigensolutions of the form

$$\lambda_{\pm k}=\pm i\omega_k \quad \nu_{\pm k}(x)=\nu_k^R\pm i\nu_k^I(x),\ k=1,\ 2,\ \ldots \qquad (5)$$
$$\nu_k^R,\ \nu_k^I \in R \quad \omega_k>0\ i\equiv\sqrt{-1}.$$

The $\omega_k$ and $\omega_k(x)$ are the frequency and eigenfunction of the $k$th mode of vibration. For nonzero $G$, $\nu_k(x)$ are usually nonorthogonal; the system response $w(x,t)$ can not be evaluated by the classical model analysis. Nevertheless, $w(x,t)$ can still be expressed by a series of $\nu_k(x)$ (Yang and Mote, 1991a), which is briefly described as follows.

Equation (1) is transformed into an equivalent state space equation

$$z_t=Az+Q,\ z|_{t=0}=z_0(x) \qquad (6a)$$

where

$$z(x,t)=\begin{pmatrix} w_t(x,t)\\ w(x,t)\end{pmatrix}\quad A=\begin{bmatrix}-G & -K\\ 1 & 0\end{bmatrix}\quad Q(x,t)=\begin{pmatrix} f(x,t)\\ 0\end{pmatrix}\quad z_0(x)=\begin{pmatrix} b(x)\\ a(x)\end{pmatrix}. \qquad (6b)$$

The state vector $z$ belongs to a Hilbert space. The eigenvalue problem associated with Eq. (6a)

$$A\phi_k(x)=\gamma_k\phi_k(x) \qquad (7)$$

has eigensolutions of the form

$$\gamma_k=\lambda_k \quad \phi_k(x)=\begin{pmatrix}\lambda_k\nu_k(x)\\ \nu_k(x)\end{pmatrix},\ k=\pm 1,\ \pm 2,\ \ldots \qquad (8)$$

where $\lambda_k$ and $\nu_k(x)$ are given in (5). The adjoint eigenvalue problem to (7) is

$$A^*\psi_k=\bar{\lambda}_k\psi_k$$

with the adjoint operator given by

$$A^*=\begin{bmatrix} G & 1\\ -K & 0\end{bmatrix}.$$

The eigenfunctions of the adjoint problem are

$$\psi_k(x)=\begin{pmatrix}\lambda_k\nu_k(x)\\ K\nu_k(x)\end{pmatrix},\ k=\pm 1,\ \pm 2,\ \ldots. \qquad (9)$$

where $K$ is the operator from (1). The $\phi_k$ and $\psi_k$ satisfy the bi-orthogonality conditions

$$\langle\psi_j,\phi_k\rangle=2\delta_{jk}\quad \langle\psi_j,A\phi_k\rangle=2\lambda_j\delta_{jk} \qquad (10)$$

where the inner product is defined by $\langle z_1,z_2\rangle=\int_E \bar{z}_1^T z_2 dz$ with $\bar{z}_1^T$ denoting the conjugate transpose of $z_1$. Assume that the sets $\{\phi_k\}$ and $\{\psi_k\}$ are complete in the Hilbert space. With the orthogonality conditions (10), the state vector $z(x,t)$ under the $Q(x,t)$ and $z_0(x)$ is determined as

$$z(x,t)=\int_E S(x,\xi,t)z_0(x)d\xi+\int_0^t\int_E S(x,\xi,t-\tau)Q(\xi,\tau)d\xi d\tau \qquad (11)$$

where the two-by-two function matrix

$$S(x,\xi,t)\equiv\begin{bmatrix} g_{11}(x,\xi,t) & g_{12}(x,\xi,t)\\ g_{21}(x,\xi,t) & g_{22}(x,\xi,t)\end{bmatrix}=\frac{1}{2}\sum_{k=\pm1}^{\pm\infty}e^{\lambda_k t}\begin{bmatrix}\omega_k^2\nu_k(x)\bar{\nu}_k(\xi) & \lambda_k\nu_k(x)K\bar{\nu}_k(\xi)\\ \bar{\lambda}_k\nu_k(x)\bar{\nu}_k(\xi) & \nu_k(x)K\bar{\nu}_k(\xi)\end{bmatrix} \qquad (12)$$

and the super bar denotes complex conjugation. With (4) and (12) it is shown that

$$g_{22}(x,\xi,t)=\frac{\partial}{\partial t}g_{21}(x,\xi,t)-Gg_{21}(x,\xi,t). \qquad (13)$$

By (6) and (11)–(13), the response of the distributed gyroscopic system under external and initial disturbances is expressed by

$$w(x,t)=\int_E\{g(x,\xi,t)[Ga(\xi)+b(\xi)]+g_t(x,\xi,t)a(\xi)\}d\xi+\int_0^t\int_E g(x,\xi,t-\tau)f(\xi,\tau)d\xi d\tau \qquad (14)$$

where the Green's function is given by

$$g(x,\xi,t)\equiv g_{21}(x,\xi,t)=\frac{1}{2}\sum_{k=\pm1}^{\pm\infty}e^{\lambda_k t}\bar{\lambda}_k\nu_k(x)\bar{\nu}_k(\xi). \qquad (15)$$

The presence of the skew-symmetric operator $G$ makes the system (1) nonself adjoint; the system response $w(x,t)$ can not be evaluated by the classical modal analysis. The explicit representation of the bi-orthogonal eigenfunctions $\phi_k$ and $\psi_k$ in terms of the modes of vibration ($\omega_k$, $\nu_k$), however, makes it possible to express $w(x,t)$ in a modal expansion form.

## 3 Transfer Function Formulation

The distributed gyroscopic system (1) under a pointwise constraint is considered as a feedback control system. The system (1) without the constraint is an open-loop system. The system (1) with the constraint is a closed-loop system with the constraint as a feedback controller. Both the open-loop and closed-loop transfer functions are obtained, based on which the eigenvalues of unconstrained and constrained systems can be evaluated.

**Open Loop: The Unconstrained System.** The Laplace transform of (1) with respect to $t$ gives

$$(s^2+sG+K)\bar{w}(x,s)=\bar{f}(x,s)+Ga(x)+b(x)+sa(x) \qquad (16)$$

where $\bar{w}(\cdot,s)$ and $\bar{f}(\cdot,s)$ are the Laplace transforms of $w(\cdot,t)$ and $f(\cdot,t)$, respectively. The solution of (16) is given by the Laplace transform of (14), i.e.,

$$\bar{w}(x,s)=\int_E W_o(x,\xi,s)\{\bar{f}(\xi,s)+Ga(\xi)+b(\xi)+sa(\xi)\}d\xi \qquad (17)$$

where the open-loop transfer function $W_o(x,\xi,s)$ is the Laplace transform of the Green's function $g(x,\xi,t)$ and is given by

$$W_o(x,\xi,s)=\frac{1}{2}\sum_{k=\pm1}^{\pm\infty}\frac{-\lambda_k}{s-\lambda_k}\nu_k(x)\bar{\nu}_k(\xi). \qquad (18)$$

The poles of $W_o(x,\xi,t)$ are the eigenvalues of $\lambda_k$ of the unconstrained gyroscopic system.

**Closed Loop: The Constrained System.** Assume that a constraint is imposed on the system (1) at $x_c\in E$. The constraint force is considered as the control force from a feedback controller that has a sensor and an actuator both located at $x_c$. The constraint force in consideration takes two forms:

$$\bar{f}_c(x,s)=\delta(x-x_c)C(s)\bar{w}(x_c,s) \qquad (19a)$$

if the displacement $w(x_c,t)$ is constrained, or

$$\bar{f}_c(x,s)=-D_\eta\delta(x-x_c)C(s)D_\eta\bar{w}(x_c,s) \qquad (19b)$$

if the slope $D_\eta w(x_c,t)$ is constrained. Here $\bar{f}_c(x,s)$ is the Laplace transform of the constraint force, $C(s)$ is the transfer function of the constraint (the controller) in the form

$$C(s)=\mu\frac{N(s)}{D(s)} \qquad (20)$$

where $N(s)$ and $D(s)$ are polynomials in $s$, $\mu>0$ is a gain parameter, and $D_\eta(\ )$ is the directional derivative of ( ) in the direction $\eta$. For a one-dimensional region $E$, $D_\eta = \partial/\partial x$; for an $n$-dimensional region $E$, $x=(x_1, \ldots, x_n)$, $\eta=(\eta_1, \ldots, \eta_n)$, $D_\eta = \Sigma_{j=1}^n \eta_j \, \partial/\partial x_j$, $n=2$ or 3. Note that $\bar{f}_c(x,s)$ in (19b) physically represents a pointwise moment at $x_c$.

The total external force $\bar{f}(x,s) = \bar{f}_c(x,s) + \bar{f}_e(x,s)$, where $\bar{f}_e(x,s)$ is the Laplace transform of other external disturbance. Substituting the above expression into (17) and using (19), (20) gives

$$\overline{w}(x,s) = W_o(x,x_c,s)\mu\frac{N(s)}{D(s)}\overline{w}(x_c,s) + \int_E W_o(x,\xi,s)\bar{f}_{el}(\xi,s)d\xi \quad (21a)$$

for the displacement constraint (19a), and

$$\overline{w}(x,s) = D_\eta^\xi W_o(x,x_c,s)\mu\frac{N(s)}{D(s)}D_\eta^x\overline{w}(x_c,s) + \int_E W_o(x,\xi,s)\bar{f}_{el}(\xi,s)d\xi \quad (21b)$$

for the slope constraint (19b), where $\bar{f}_{el}(\xi,s) = \bar{f}_e(\xi,s) + Ga(\xi) + b(\xi) + sa(\xi)$, $D_\eta^\xi$ and $D_\eta^x$ are the operator $D_\eta$ acting on $\xi$ and $x$, respectively. Solving (21) for $\overline{w}(x_c,s)$ and $D_\eta^x(x_c,s)$ and substituting for them in (21) leads to

$$\overline{w}(x,s) = \int_E W_{cl}(x,\xi,s)\bar{f}_{el}(\xi,s)d\xi \quad (22)$$

where the closed-loop transfer function

$$W_{cl}(x,\xi,s) = \frac{N_{cl}(x,\xi,s)}{D_{cl}(s)} \quad (23)$$

with

$$N_{cl}(x,\xi,s) = D(s)W_o(x,\xi,s) + \mu N(s)[W_o(x,x_c,s)W_o(x_c,\xi,s) - W_o(x,\xi,s)W_o(x_c,x_c,s)] \quad (24a)$$

$$D_{cl}(s) = D(s) - \mu N(s)W_o(x_c,x_c,s)$$

for the displacement constraint (19a), and

$$N_{cl}(x,\xi,s) = D(s)W_o(x,\xi,s) + \mu N(s)[D_\eta^\xi W_o(x,x_c,s)D_\eta^x W_o(x_c,\xi,s) - W_o(x,\xi,s)D_\eta^x D_\eta^\xi W_o(x_c,x_c,s)] \quad (24b)$$

$$D_{cl}(s) = D(s) - \mu N(s)D_\eta^x D_\eta^\xi W_o(x_c,x_c,s)$$

for the slope constraint (19b). The eigenvalues of the constrained gyroscopic system are the poles of $W_{cl}(x,\xi,s)$.

**Theorem 2.** *The eigenvalues of the distributed gyroscopic system (1) under the displacement constraint (19a) (the slope constraint (19b)) are the roots of $D_{cl}(s)=0$ and $\lambda_l$ for some $l$ if $\nu_l(x_c)=0$ ($D_\eta\nu_l(x_c)=0$) or $N(\lambda_l)=0$.*

**Proof:** See Appendix A.

Theorem 2 relates to controllability of the distributed gyroscopic system (1) (Yang and Mote, 1991b). If the constraint is away from the nodal points of all modes of vibration, and has no pole-zero cancellation, the gyroscopic system is controllable for all modes; the constraint will change all the system eigenvalues. If the constraint is at a nodal point of the $k$th mode or has a zero cancelling the $k$th eigenvalue $\lambda_k$, the gyroscopic system is not controllable for the $k$th mode; the constraint will not influence $\lambda_k$. Here the "nodal" points in the slope constraint case are the roots of $D_\eta\nu_k(x)=0$, $k=1, 2, \ldots$.

## 4 Inclusion Principles

With the closed-loop transfer function $W_{cl}(x,\xi,s)$, eigenvalue inclusion principles are developed for the distributed gyroscopic system (1) under pointwise nondissipative constraints. Assume that the natural frequencies $\omega_k$ of the unconstrained system are distinct. (The case of repeated eigenvalues will be discussed later in this section.) For the gyroscopic system (1) under a nondissipative constraint, its eigenvalues have the form $i\Omega_k$, where $\Omega_k$ are the natural frequencies of the constrained system. In the following analyses the $\omega_k$ and $\Omega_k$ are arranged in ascending order of magnitude.

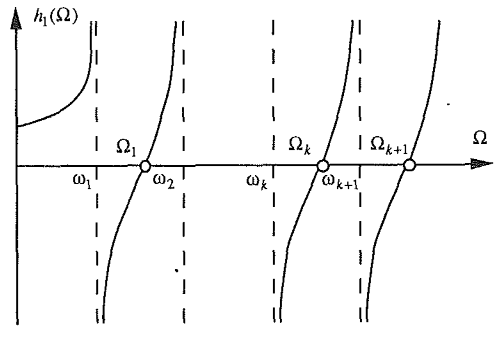


**Fig. 1 Natural frequencies of the gyroscopic system (1) under Constraint 1, $B\nu_k(x_c)\neq 0$ for all $k$**

**Constraint 1: A Spring Attached to the Gyroscopic System.** A spring of coefficient $\mu$ is attached to the system (1) at $x_c$. Two kinds of springs are considered: the linear spring constraining the displacement $w(x_c,t)$, and the rotational spring constraining the slope $D_\eta w(x_c,t)$. The constraint force of the linear spring has the form (19a); the constraint force of the rotational spring has the form (19b). The transfer functions of the springs are both given by

$$C(s) = -\mu, \quad N(s) = -1, \quad D(s) = 1. \quad (25)$$

If $x_c$ is not a nodal point of any mode of the unconstrained system, according to Theorem 2 and (24), (25) the natural frequencies $\Omega_k$ of the constrained system are the roots of

$$h_1(\Omega) \equiv D_{cl}(i\Omega) = 1 + \mu\sum_{k=1}^{+\infty}\frac{\omega_k^2}{-\Omega^2+\omega_k^2}|B\nu_k(x_c)|^2 = 0 \quad (26)$$

where $B=1$ for the linear spring and $B=D_\eta$ for the rotational spring. It is easy to see that

$$h_1(0)>0, \lim_{\Omega\to\omega_k-0} h_1(\Omega) = +\infty \text{ and } \lim_{\Omega\to\omega_k+0} h_1(\Omega) = -\infty \text{ for all } k$$

$$\frac{d}{d\Omega}h_1(\Omega)>0 \text{ at } \Omega\epsilon(0,+\infty) \text{ and } \Omega\neq\omega_k,\ k=1, 2, \ldots.$$

Because $h_1(\Omega)$ is continuous and monotonically increasing on $(\omega_k, \omega_{k+1})$ and because $h_1(\omega_k+0)$ and $h_1(\omega_{k+1}-0)$ have different signs, there is one and only one root $\Omega_k$ of (26) in $(\omega_k, \omega_{k+1})$. No root falls in $(0, \omega_1)$ because $h_1(0)>0$. These indicate that $\omega_k<\Omega_k<\omega_{k+1}$; see Fig. 1.

If the point $x_c$ is a node of the $l$th mode of the unconstrained system, i.e., $B\nu_l(x_c)=0$, $h_1(\omega_l)$ is finite. By Theorem 2, $\omega_l$ is a natural frequency of the constrained system. Because $h_1(\Omega)$ is continuous and monotonically increasing on $(\omega_{l-1}, \omega_{l+1})$ and because $h_1(\omega_{l-1}+0)$ and $h_1(\omega_{l+1}-0)$ have different signs, (26) has one and only one root in $(\omega_{l-1}, \omega_{l+1})$. This implies that the constrained system has two natural frequencies, $\Omega_{l-1}$ and $\Omega_l$, in $(\omega_{l-1}, \omega_{l+1})$. The locations of these two natural frequencies depend on the value of $h_1(\omega_l)$ (see Fig. 2):

(a) $\omega_{l-1}<\Omega_{l-1}\leq\omega_l=\Omega_l<\omega_{l+1}$ for $h_1(\omega_l)>0$;

(b) $\omega_{l-1}<\Omega_{l-1}=\omega_l=\Omega_l<\omega_{l+1}$ for $h_1(\omega_l)=0$;

(c) $\omega_{l-1}<\Omega_{l-1}=\omega_l<\Omega_l<\omega_{l+1}$ for $h_1(\omega_l)<0$.

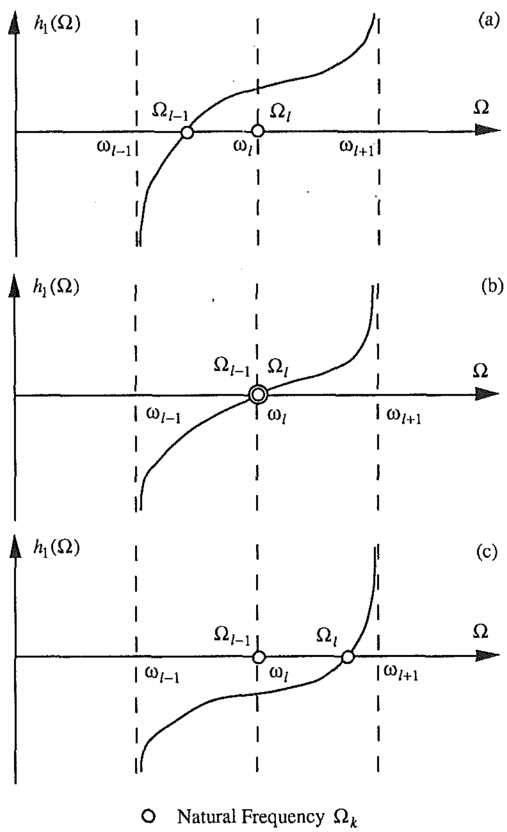


**Fig. 2 Natural frequencies of the gyroscopic system (1) under Constraint 1, $B\nu_l(x_c)=0$: (a) $h_1(\omega_l)>0$; (b) $h_1(\omega_l)=0$; (c) $h_1(\omega_l)<0$**

Note that the constrained system may have repeated eigenvalues even if the unconstrained system has distinct eigenvalues. Thus, a statement is given below.

**Theorem 3.** *If a spring (linear or rotational) is attached to the distributed gyroscopic system (1) whose natural frequencies are $\omega_k$, the natural frequencies $\Omega_k$ of the constrained system are such that*

$$\omega_k \le \Omega_k \le \omega_{k+1},\ k=1,\ 2,\ \ldots . \tag{27}$$

For the unconstrained gyroscopic system with distinct natural frequencies, i.e., $\omega_k<\omega_{k+1}$, at most one equality holds in (27) for a given $k$.

**Constraint 2: A Mass Attached to the Gyroscopic System.** A lumped mass $\mu$ is attached to the system (1) at $x_c$. The displacement of the mass is the same as $w(x_c,t)$. The constraint force has the form (19*a*) with the transfer function

$$C(s)=-\mu s^2,\quad N(s)=-s^2,\quad D(s)=1. \tag{28}$$

According to Theorem 2 and (24*a*), (28), the natural frequencies $\Omega_k$ of the constrained system are the roots of

$$h_2(\Omega)\equiv D_{cl}(i\Omega)=1-\mu\Omega^2\sum_{k=1}^{+\infty}\frac{\omega_k^2}{-\Omega^2+\omega_k^2}\,|\nu_k(x_c)|^2=0 \tag{29}$$

and $\omega_l$ for some $l$ if $\nu_l(x_c)=0$. The function $h_2(\Omega)$ has the following properties:

$$h_2(0)>0,\ \lim_{\Omega\to\omega_k-0}h_2(\Omega)=-\infty \ \text{ and } \lim_{\Omega\to\omega_k+0}h_2(\Omega)=+\infty \ \text{ for all } k$$

$$\frac{d}{d\Omega}h_2(\Omega)<0 \text{ at } \Omega\epsilon(0,+\infty) \ \text{ and } \ \Omega\ne\omega_k,\ k=1,\ 2,\ \ldots .$$

With the same arguments as in Constraint 1 it can be shown that if $x_c$ is not a nodal point of any mode of the unconstrained system, $0<\Omega_k<\omega_k<\Omega_{k+1}$, and that if $x_c$ is a node of the $l$th mode of the unconstrained system, i.e., $\nu_l(x_c)=0$, the constrained system has two natural frequencies, $\Omega_l$ and $\Omega_{l+1}$, in $(\omega_{l-1},\ \omega_{l+1})$:

(*a*) $\omega_{l-1}<\Omega_l=\omega_l<\Omega_{l+1}<\omega_{l+1}$ for $h_2(\omega_l)>0$;

(*b*) $\omega_{l-1}<\Omega_l=\omega_l=\Omega_{l+1}<\omega_{l+1}$ for $h_2(\omega_l)=0$;

(*c*) $\omega_{l-1}<\Omega_l<\omega_l=\Omega_{l+1}<\omega_{l+1}$ for $h_2(\omega_l)<0$.

The results are summarized as follows:

**Theorem 4.** *If a lumped mass is attached to the distributed gyroscopic system (1) whose natural frequencies are $\omega_k$, the natural frequencies $\Omega_k$ of the constrained system are such that*

$$\Omega_k\le\omega_k\le\Omega_{k+1},\ \Omega_1>0,\ k=1,\ 2,\ \ldots . \tag{30}$$

**Constraint 3: Zero Displacement or Zero Slope at a Point.** The constraints

$$w(x_c,t)=0 \ \text{ and } \ D_\eta w(x_c,t)=0 \tag{31}$$

often appear in, but are not limited to, boundary conditions for strings, bars, beams, membranes, and plates. These constraints can be considered as the limiting cases of Constraint 1 when the spring coefficient $\mu$ approaches infinity. According to Appendix B, the natural frequencies $\Omega_k$ of the constrained system are the roots of

$$h_3(\Omega)\equiv\sum_{k=1}^{+\infty}\frac{\omega_k^2}{-\Omega^2+\omega_k^2}\,|B\nu_k(x_c)|^2=0 \tag{32}$$

and $\omega_l$ for some $l$ if $B\nu_l(x_c)=0$, where $B=1$ for the displacement constraint, and $B=D_\eta$ for the slope constraint. The properties of $h_3(\Omega)$ are similar to those of $h_1(\Omega)$. Therefore, the following conclusion is given without proof.

**Theorem 5.** *If zero displacement or zero slope is imposed at a point of the distributed gyroscopic system (1) whose natural frequencies are $\omega_k$, the natural frequencies $\Omega_k$ of the constrained system are such that*

$$\omega_k\le\Omega_k\le\omega_{k+1},\ k=1,\ 2,\ \ldots . \tag{33}$$

For the unconstrained gyroscopic system with distinct natural frequencies, i.e., $\omega_k<\omega_{k+1}$, at most one equality holds in (33) for a given $k$.

**Constraint 4: A Mass Connected to the Gyroscopic System by a Spring.** A lumped mass $m$ is connected to the system (1) at $x_c$ by a spring of coefficient $\mu$. The displacement $\xi(t)$ of $m$ is in the direction of the displacement $w(x_c,t)$. The motion of the constrained system is described by

$$w_{tt}(x,t)+Gw_t(x,t)+Kw(x,t)=\mu[\xi(t)-w(x_c,t)]\,\delta(x-x_c)+f_e(x,t)\quad m\ddot{\xi}(t)+\mu[\xi(t)-w(x_c,t)]=0 \tag{34}$$

where $f_e(x,t)$ is the external force. The Laplace transform of (34) and elimination of $\xi$ gives

$$(s^2+sG+K)\overline{w}(x,s)=-\mu\frac{ms^2}{ms^2+\mu}\overline{w}(x_c,s)\delta(x-x_c)+\overline{f}_{eI}(x,s)+F_{I\xi}(s)\delta(x-x_c)$$

where $F_{I\xi}(s)$ contains the initial conditions of the mass $m$. It is seen that the constraint force has the form (19*a*) with the transfer function

$$C(s)=-\mu\frac{s^2}{s^2+\alpha^2},\ \alpha^2=\frac{\mu}{m}. \tag{35}$$

By Theorem 2, (24*a*), and (35), the natural frequencies $\Omega_k$ of the constrained system are the roots of

$$D_{cl}(i\Omega)=-\Omega^2+\alpha^2-\mu\Omega^2\sum_{k=1}^{+\infty}\frac{\omega_k^2}{-\Omega^2+\omega_k^2}\,|\nu_k(x_c)|^2=0 \tag{36}$$

and $\omega_l$ if $\nu_l(x_c)=0$ for some $l$. Rewrite (36) as

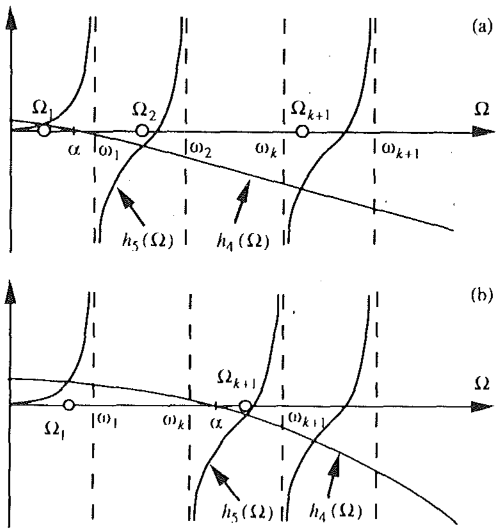



○ Natural Frequency $\Omega_k$

**Fig. 3 Natural frequencies of the gyroscopic system (1) under Constraint 4: (*a*) $\alpha\epsilon(0,\omega_1)$; (*b*) $\alpha\epsilon(\omega_k,\omega_{k+1})$ and $h_5(\alpha)<0$**

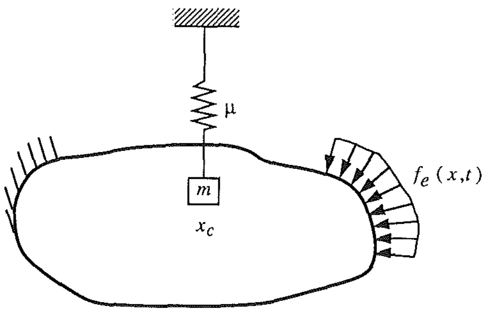



Distributed Gyroscopic System

**Fig. 4 The gyroscopic system (1) with an attached mass-spring system**

$$h_4(\Omega)=h_5(\Omega) \tag{37}$$

where

$h_4(\Omega)\equiv-\Omega^2+\alpha^2$

$$h_5(\Omega)\equiv\mu\Omega^2\sum_{k=1}^{+\infty}\frac{\omega_k^2}{-\Omega^2+\omega_k^2}\,|\,\nu_k(x_c)\,|^2=0. \tag{38}$$

The roots of (36) are determined by the intersections of $h_4(\Omega)$ and $h_5(\Omega)$. With the properties

$$h_4(\Omega)>0 \text{ for } \Omega\epsilon[0,\alpha),\ h_4(\alpha)=0,\ h_4(\Omega)<0 \text{ for } \Omega\epsilon(\alpha,+\infty)$$

$$\lim_{\Omega\to\omega_k-0}h_5(\Omega)=+\infty \text{ and } \lim_{\Omega\to\omega_k+0}h_5(\Omega)=-\infty \text{ for all } k$$

$$\frac{d}{d\Omega}h_5(\Omega)>0 \text{ at } \Omega\epsilon(0,+\infty) \text{ and } \Omega\neq\omega_k,\ k=1,\,2,\,\ldots$$

the following result can be shown.

**Theorem 6.** *If a spring connects a lumped mass to the distributed gyroscopic system* (1) *whose natural frequencies are $\omega_k$, the distribution of the natural frequencies $\Omega_k$ of the constrained system depends on the parameter $\alpha=\sqrt{\mu/m}$ (see Fig. 3):*

(*a*) for $\alpha\epsilon(0,\omega_1)$

$$0<\Omega_1<\alpha<\omega_1\leq\Omega_2\leq\cdots\leq\omega_k\leq\Omega_{k+1}\leq\omega_{k+1}\leq\cdots; \tag{39a}$$

(*b*) for $\alpha\epsilon(\omega_k,\omega_{k+1})$

$$0<\Omega_1\leq\omega_1\leq\cdots\leq\Omega_k\leq\omega_k,\ \omega_{k+1}\leq\Omega_{k+2}\leq\omega_{k+2}\leq\cdots \tag{39b}$$

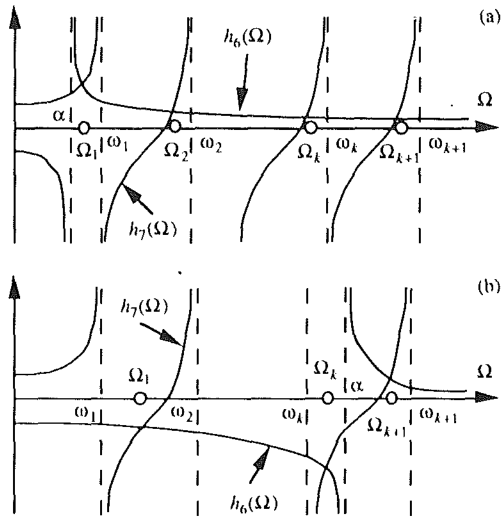



○ Natural Frequency $\Omega_k$

**Fig. 5 Natural frequencies of the gyroscopic system (1) under Constraint 5: (*a*) $\alpha\epsilon(0,\omega_1)$; (*b*) $\alpha\epsilon(\omega_k,\omega_{k+1})$**

with

$$\omega_k\leq\Omega_{k+1}<\alpha<\omega_{k+1} \quad \text{if } h_5(\alpha)>0$$
$$\omega_k<\alpha=\Omega_{k+1}<\omega_{k+1} \quad \text{if } h_5(\alpha)=0$$
$$\omega_k<\alpha<\Omega_{k+1}\leq\omega_{k+1} \quad \text{if } h_5(\alpha)<0;$$

(*c*) for $\alpha=\omega_k$

$$0<\Omega_1\leq\omega_1\leq\cdots\leq\Omega_k\leq\alpha=\omega_k\leq\Omega_{k+1}\leq\omega_{k+1}\leq\cdots. \tag{39c}$$

There are two extreme cases. First, when the spring coefficient $\mu$ goes to infinity, the mass $m$ is rigidly connected to the system (1); (35) becomes $C(s)=-ms^2$, Constraint 2. Second, when the mass $m$ approaches infinity, its displacement $\xi(t)$ vanishes rendering the spring attached to the system (1); (35) reduces to (25), Constraint 1.

**Constraint 5: A Mass-Spring System Attached to the Gyroscopic System.** The mass-spring system in Fig. 4 consists of a lumped mass $m$ attached to the system (1) at the point $x_c$, and a spring of coefficient $\mu$ connecting the mass and a point in a fixed reference. The displacement of the attached mass is assumed to be equal to that of the gyroscopic system at $x_c$, $w(x_c,t)$. One example of the constrained system is the rotating disk with an attached mass-spring system, which is a modal of guided circular saws (D'Angelo et al., 1985). The constraint has the form (19*a*) with the transfer function

$$C(s)=-\mu\frac{s^2+\alpha^2}{\alpha^2},\ N(s)=-s^2-\alpha^2,\ D(s)=\alpha^2;\ \alpha^2=\frac{\mu}{m}. \tag{40}$$

According to Theorem 2, (24*a*), and (40), the natural frequencies $\Omega_k$ of the constrained system are the roots of

$$D_{cl}(i\Omega)=\alpha^2-\mu(\Omega^2-\alpha^2)\sum_{k=1}^{+\infty}\frac{\omega_k^2}{-\Omega^2+\omega_k^2}\,|\,\nu_k(x_c)\,|^2=0 \tag{41}$$

and $\omega_l$ for some $l$ if $\nu_l(x_c)=0$ or $N(i\omega_l)=0$. Note that $\Omega=\alpha$ is not a root of (41) since $D_{cl}(i\alpha)=\alpha^2$. So, (41) is equivalent to

$$h_6(\Omega)=h_7(\Omega) \tag{42}$$

where

$$h_6(\Omega)\equiv\frac{\alpha^2}{\Omega^2-\alpha^2}\quad h_7(\Omega)\equiv\mu\sum_{k=1}^{+\infty}\frac{\omega_k^2}{-\Omega^2+\omega_k^2}\,|\,\nu_k(x_c)\,|^2. \tag{43}$$

The roots of (41) are the intersections of $h_6(\Omega)$ and $h_7(\Omega)$. With the properties

$$h_6(\Omega)<0 \text{ for } \Omega\in[0,\alpha),\ h_6(\Omega)>0 \text{ for } \Omega\in(\alpha,+\infty),\ h_6(\alpha\pm 0)=+\infty$$

$$h_7(0)>0,\ \lim_{\Omega\to\omega_k-0} h_7(\Omega)=+\infty \text{ and } \lim_{\Omega\to\omega_k+0} h_7(\Omega)=-\infty \text{ for all } k$$

$$\frac{d}{d\Omega}h_7(\Omega)>0 \text{ at } \Omega\in(0,+\infty) \text{ and } \Omega\neq\omega_k,\ k=1,2,\ldots$$

the following theorem can be proven.

**Theorem 7.** *If the mass-spring system (40) is attached to the distributed gyroscopic system (1) whose natural frequencies are $\omega_k$, the distribution of the natural frequencies $\Omega_k$ of the constrained system depends on the parameter $\alpha=\sqrt{\mu/m}$. (see Fig. 5):*

(*a*) for $\alpha\in(0,\omega_1)$

$$0<\alpha<\Omega_1\le\omega_1\le\Omega_2\le\omega_2\le\cdots; \quad (44a)$$

(*b*) for $\alpha\in(\omega_k,\omega_{k+1})$

$$\omega_1\le\Omega_1\le\cdots\le\omega_k\le\Omega_k<\alpha<\Omega_{k+1}\le\omega_{k+1}\le\Omega_{k+2}\le\omega_{k+2}\le\cdots; \quad (44b)$$

(*c*) for $\alpha=\omega_k$

$$\omega_1\le\Omega_1\le\cdots\le\omega_{k-1}\Omega_{k-1}<\omega_k=\Omega_k=\alpha<\Omega_{k+1}\le\omega_{k+1}\le\cdots. \quad (44c)$$

When $\alpha$, the natural frequency of the mass-spring system, is less than the first natural frequency $\omega_1$ of the unconstrained gyroscopic system, the whole spectrum of the constrained system shifts downward showing the dominant inertia effect of the constraint; see (44*a*). When $\alpha$ is larger than $\omega_1$, the system spectrum is divided into two parts (see (44*b*)): below $\alpha$, all natural frequencies shift upwards due to the dominant spring effect of the constraint; above $\alpha$, all natural frequencies shift downwards due to the dominant inertia effect of the constraint. When $\alpha$ coincides with the $k$th natural frequency $\omega_k$, the constraint (40) has a zero cancelling the eigenvalue $\lambda_k$, and therefore has no influence on the $k$th natural frequency; see (44*c*).

Five types of constraints have been studied. Many other constraints can be treated in a similar manner. Also, the idea presented in this paper can be easily extended to distributed gyroscopic systems with repeated eigenvalues. In this case the eigenvalue problem associated with (1) is

$$(\lambda_k^2+\lambda_k G+K)\nu_{kl}(x)=0,\ \ \lambda_k=i\omega_k,\ \ k=1,2,\ldots,\ l=1,2,\ldots r_k$$

where $\lambda_k$ and $\nu_{kl}(x)$ are the eigensolutions with $r_k$ multiplicity of $\lambda_k$. It can be shown that the open-loop transfer function

$$W_o(x,\xi,s)=\frac{1}{2}\sum_{k=\pm1}^{\pm\infty}\sum_{l=1}^{r_k}\frac{-\lambda_k}{s-\lambda_k}\nu_{kl}(x)\bar{\nu}_{kl}^T(\xi).$$

Analyses of the natural frequencies of the constrained system follow the same steps as in Sections 3 and 4. Results similar to Theorems 3 to 7 are expected.

## 5 Example

The results in the previous section are illustrated on the axially moving string. For a uniform axially moving string travelling at a constant velocity between two fixed eyelets separated by a unit length, its transverse displacement $w(x,t)$ (Skutch, 1897) is described by

$$w_{tt}(x,t)+2c\frac{\partial}{\partial x}w_t(x,t)-(1-c^2)\frac{\partial^2}{\partial x^2}w(x,t)=f(x,t),$$
$$x\in(0,1),\ t>0;\ w(0,t)=0\ w(1,t)=0,\ t>0 \quad (45)$$

where $c<1$ is the dimensionless transport speed of the string, and $x$ is the coordinate of the point of the string measured in a fixed reference. The differential operators in (1) for the system are

$$G=2c\frac{\partial}{\partial x}\ \ K=-(1-c^2)\frac{\partial^2}{\partial x^2}.$$

The solutions of the eigenvalue problem (Mote, 1972)

$$\left\{\lambda^2+2c\lambda\frac{\partial}{\partial x}-(1-c^2)\frac{\partial}{\partial x^2}\right\}\nu(x)=0,\ \nu(0)=\nu(1)=0$$

are

$$\lambda_k=i\omega_k=ik\pi(1-c^2),\ \nu_k(x)=a_k\sin k\pi x\, e^{ik\pi cx},\quad i=\sqrt{-1},\ k=1,2,\ldots \quad (46)$$

where $a_k$ are constants.

Attach a spring of coefficient $\mu$ to the string at $x=x_c$; i.e.,

$$\frac{\partial}{\partial x}w(x_c+0,t)-\frac{\partial}{\partial x}w(x_c-0,t)=\mu w(x_c,t). \quad (47)$$

The characteristic equation of the string (45) under the constraint (47) is

$$1+\frac{\mu}{1-c^2}\frac{\sin\beta x_c\sin\beta(1-x_c)}{\beta\sin\beta}=0,\ \beta=\frac{\Omega}{1-c^2}. \quad (48)$$

The natural frequencies of the constrained system are $\Omega_k=\beta_k(1-c^2)$, $k=1,2,\ldots$, where $\beta_k$ are the nonzero roots of (48). Theorem 3 predicts that

$$\omega_k\le\Omega_k\le\omega_{k+1},\ k=1,2,\ldots$$

which can be shown using (46) and (48).

Now, let the spring coefficient $\mu$ go to infinity; i.e., a third eyelet is imposed at the point $x_c$

$$w(x_c,t)=0. \quad (49)$$

The characteristic equation of the string (45) under the constraint (49) is

$$\sin\beta x_c\sin\beta(1-x_c)=0,\ \beta=\frac{\Omega}{1-c^2} \quad (50)$$

which gives

$$\Omega_k=k\pi\frac{(1-c^2)}{x_c}\ \text{ and }\ k\pi\frac{(1-c^2)}{1-x_c},\ k=1,2,\ldots \quad (51)$$

Comparison of (46) and (51) gives

$$\omega_k\le\Omega_k\le\omega_{k+1},\ k=1,2,\ldots$$

which is (33).

## 6 Conclusion

Several inclusion principles have been presented for distributed gyroscopic systems under pointwise, nondissipative constraints. When a distributed gyroscopic system is modified with an added spring (or a lumped mass), its natural frequencies will increase (or decrease), and alternate with those of the unmodified system. With the transfer function formulation, many other constraint problems for distributed gyroscopic systems can be investigated in a systematic and convenient way. The inclusion principles obtained can be used to develop algorithms for computing eigenvalues of modified vibrating systems, and to estimate the bounds of natural frequencies of structures.


## Acknowledgment

This research is sponsored by Charles Lee Powell Foundation. Also, the author wishes to acknowledge the reviewers for the helpful suggestions and comments with the presentation.

## References

D'Angelo, C., III, Alvarado, N. T., Wang, K. W., and Mote, C. D., Jr., 1985, "Current Research on Circular Saw and Band Saw Vibration and Stability," *The Shock and Vibration Digest*, Vol. 17, No. 5, pp. 11-23.

D'Eleuterio, G. M. T., and Hughes, P. C., 1984, "Dynamics of Gyroelastic Continua," ASME Journal of Applied Mechanics, Vol. 51, pp. 415-422.

Hagedorn, P., 1975, "Uber Due Instabilitat Konservativer Systeme Mit Gyroskopischen Kraften," *Arch. Rat. Mech. Anal.*, Vol. 58, pp. 1-9.

Huseyin, K., 1978, *Vibration and Stability of Multiple Parameter Systems*, Noordholl International Publishing.

Meirovitch, L., 1980, *Computational Methods in Structural Dynamics*, Sijthoff and Noordhoff.

Meirovitch, L., and Hale, A. L., 1978, "Synthesis and Dynamic Characteristics of Large Structures with Rotating Substructures," *Proceedings of the IUTAM Symposium on Dynamics of Multibody Systems*, K. Magnus, ed., Springer-Verlag, New York.

Meirovitch, L., and Silverberg, L. M., 1985, "Control on Non-Self-Adjoint Distributed-Parameter Systems," *Journal of Optimization Theory and Applications*, Vol. 47, No. 1, pp. 77-90.

Mote, C. D., Jr., 1972, "Dynamic Stability of Axially Moving Materials," *The Shock and Vibration Digest*, Vol. 4, No. 4, pp. 2-11.

Rayleigh, J. W. S., 1945, *The Theory of Sound*, Vol. 1, Dover, New York, p. 119.

Skutch, R., 1897, "Uber die Bewegung Eines Gespannten Fadens, Weicher Gezwungun ist, Durch Zwei Feste Punkte, mit Einer Constanten Geschwindigkeit zu gehen, und Zwischen denselben in Transversal Schwingungen von gerlinger Amplitude Versetzt Wird," *Annalen der Physik Chemie*, Vol. 61, pp. 190-195.

Yang, B., 1991, "Eigenvalue Inclusion Principles for Discrete Gyroscopic Systems," ASME Journal of Applied Mechanics, Vol. 59, No. 2, Pt. 2, pp. S278-S283.

Yang, B., and Mote, C. D., Jr., 1991a, "Frequency-Domain Vibration Control of Distributed Gyroscopic Systems," ASME *Journal of Dynamic Systems, Measurement, and Control*, Vol. 113, pp. 18-25.

Yang, B., and Mote, C. D., Jr., 1991b, "Controllability and Observability of Distributed Gyroscopic Systems," ASME *Journal of Dynamic Systems, Measurement, and Control*, Vol. 113, pp. 11-17.

Ziegler, H., 1968, *Principles of Structural Stability*, Blaisdel Publishing Company, London, U.K.


## APPENDIX A

### Proof of Theorem 2.

Consider the limit of $W_{cl}(x,\xi,s)$ as $s\to\lambda_k$ for a given $k$. Write $s-\lambda_k=\epsilon e^{i\theta}$, $\epsilon>0$. If $\nu_k(x_c)=0$ or $D_\eta\nu_k(x_c)=0$, by (18) and (24), as $s\to\lambda_k$, $\epsilon\to 0$ and

$$W_{cl}(x,\xi,s)\to\frac{e^{-i\theta}}{\epsilon}A_1(x,\xi)$$
$$0<\rho_1\le|A_1(x,\xi)|,\ \forall x,\ \xi\epsilon E. \tag{A1}$$

The limit in (A1) is unbounded indicating that $\lambda_k$ is a pole of $W_{cl}(x,\xi,s)$. If $\nu_k(x_c)\neq 0$ or $D_\eta\nu_k(x_c)\neq 0$, by (18) and (24), as $s\to\lambda_k$, $\epsilon\to 0$, and

$$W_{cl}(x,\xi,s)\to\frac{1}{\mu\lambda_k N(\lambda_k+\epsilon e^{i\theta})\,|\nu_k(x_c)|^2}A_2(x,\xi)$$
$$0<\rho_2\le|A_2(x,\xi)|\le\rho_3<+\infty,\ \forall x,\ \xi\epsilon E. \tag{A2}$$

Recall that $\mu>0$ and $\omega_k>0$. The limit in (A2) has two possibilities:

(i) $N(\lambda_k)=0$, the limit in (A2) is unbounded; $\lambda_k$ is a pole of $W_{cl}(x,\xi,s)$.
(ii) $N(\lambda_k)\neq 0$, the limit in (A2) is determinate and finite; $\lambda_k$ is not a pole of $W_{cl}(x,\xi,s)$.

Note that $N_{cl}(x,\xi,s)$ in (24) has no singular points in the complex plane other than $\lambda_k$. Besides those $\lambda_k$ which are the poles of $W_{cl}(x,\xi,s)$, all other poles of the closed-loop transfer function can only be the roots of $D_{cl}(s)=0$.

## APPENDIX B

### Eigenvalues of the System (1) Under Constraint 3

Constraint 3 can be considered as the limiting case of Constraint 1 as the spring coefficient $\mu$ goes to infinity. By (23)–(25), as $\mu\to+\infty$, the closed-loop transfer function becomes

$$W_{cl}(x,\xi,s)=\frac{N_{cl}^{\infty}(x,\xi,s)}{D_{cl}^{\infty}(s)} \tag{B1}$$

where

$$N_{cl}^{\infty}(x,\xi,s)=W_o(x,\xi,s)\,W_o(x_c,x_c,s)-W_o(x,x_c,s)\,W_o(x_c,\xi,s)$$
$$D_{cl}^{\infty}(s)=\sum_{k=1}^{+\infty}\frac{\omega_k^2}{s^2+\omega_k^2}\,|\nu_k(x_c)|^2$$

for the displacement constraint (31$a$), and

$$N_{cl}^{\infty}(x,\xi,s)=W_o(x,\xi,s)D_\eta^x D_\eta^\xi W_o(x_c,x_c,s)-D_\eta^\xi W_o(x,x_c,s)D_\eta^x W_o(x_c,\xi,s)$$
$$D_{cl}^{\infty}(s)=\sum_{k=1}^{+\infty}\frac{\omega_k^2}{s^2+\omega_k^2}\,|D_\eta\nu_k(x_c)|^2$$

for the slope constraint (31$b$). With a similar argument to that in Appendix A, it can be shown that the poles of $W_{cl}(x,\xi,s)$ in (B1) are the roots of

$$\sum_{k=1}^{+\infty}\frac{\omega_k^2}{-\Omega^2+\omega_k^2}\,|B\nu_k(x_c)|^2=0 \tag{B2}$$

and $\omega_l$ for some $l$ if $B\nu_l(x_c)=0$, where $B=1$ for the constraint (31$a$), and $B=D_\eta$ for the constraint (31$b$).

# Auto and Cross-Bispectral Analysis of a System of Two Coupled Oscillators With Quadratic Nonlinearities Possessing Chaotic Motion

**Charles Pezeshki**
Department of Mechanical and Materials Engineering.

**Steve Elgar**
Department of Electrical and Computer Engineering.

**R. Krishna**
Department of Mechanical and Materials Engineering.

**T. D. Burton**
Department of Mechanical and Materials Engineering.

Washington State University,
Pullman, WA 99164-2920

*Auto and cross-bispectral analyses of a two-degree-of-freedom system with quadratic nonlinearities having two-to-one internal (autoparametric) resonance are presented. Following the work of Nayfeh (1987), the method of multiple scales is used to obtain a first-order uniform expansion yielding four first-order nonlinear ordinary differential equations governing the modulation of the amplitudes and phases of the two modes. The particular case of parametric resonance of the first mode considered in this paper admits Hopf bifurcations and a pure period doubling route to chaos. Auto bicoherence spectra isolate the phase coupling between increasing numbers of triads of Fourier components for a pure period doubling route to chaos for the individual degrees-of-freedom. Cross-bicoherence spectra, on the other hand, yield information about the phase coupling between the two degrees-of-freedom. The results presented here confirm the capacity of bispectral techniques to identify a quadratically nonlinear mechanical system that possesses chaotic motions. For the chaotic case, cross-bicoherence spectra indicate that most of the nonlinear energy transfer between the modes is owing to cross-coupling between phase modulations rather than between amplitude modulations.*

## 1 Introduction

Polyspectral methods present detailed information about the nonlinear modal couplings present in a given system. Bispectral analysis has been used to study a wide variety of quadratic nonlinear systems, including fluid (Yeh et al., 1973; Li et al., 1976; Helland et al., 1977; Van Atta, 1979; Kim et al., 1980; Ritz et al., 1988; Choi et al., 1984), mechanical (Sato et al., 1977), and a quantum mechanical systems (Miller, 1986). Nikias and Raghuveer (1987) provide a recent review. These higher-order spectral analysis techniques provide information about a chaotic system complementary to that obtained with other methods of dynamical system analyses, such as fractal dimension (Farmer et al., 1983) and Lyapunov exponent calculations (Wolf et al., 1985).

Power spectral techniques are adequate for the analyses of linear systems, but do not, however, provide information about nonlinear interactions between Fourier components in a nonlinear system. Higher-order spectra, on the other hand, can isolate and quantify the phase coupling between nonlinearly interacting Fourier components. Bispectral analyses of the quadratic interactions that produce a pure period-doubling sequence to chaos in the Rossler equations resulted in successful identification of this system for both nonchaotic and chaotic cases (Pezeshki et al., 1990). Further application to mechanical systems, such as the magnetically buckled beam governed by a Duffing equation was useful for parameter ranges where period doubling and other quadratic phenomena dominated the dynamics. In the chaotic regime the bicoherence completely vanished, consistent with the cubic nonlinearity that dominated the system during chaos. The present study presents results of bispectral analyses of quadratically nonlinear mechanical systems with two degrees-of-freedom. Such systems govern the response of many elastic systems such as ships, elastic pendulums, beams, arches, composite plates, and shells (Haddow et al., 1984; Nayfeh, 1986). The bispectrum provides detailed information about the nonlinear mode couplings on a frequency by frequency basis, thus identifying the quadratically interacting Fourier components.

The equations of a system of two coupled oscillators with quadratic nonlinearities which govern the response of a ship whose motion is constrained to pitch and roll are presented in

Contributed by the Applied Mechanics Division of The American Society of Mechanical Engineers for publication in the ASME Journal of Applied Mechanics.

Discussion on this paper should be addressed to the Technical Editor, Professor Leon M. Keer, The Technological Institute, Northwestern University, Evanston, IL 60208, and will be accepted until final publication of the paper itself in the Journal of Applied Mechanics.

Manuscript received by the ASME Applied Mechanics Division, Sept. 5, 1989; final revision, June 4, 1990. Associate Technical Editor: P. D. Spanos.

Section 2. Following the work of Nayfeh (1983, 1983b), averaged equations are obtained by the method of multiple scales for the case of parametric resonance of the first mode. Trajectories of the modulation equations for the pure period-doubling route to chaos are also presented in Section 2. Definitions of the relevant bispectral quantities and details of the numerics are considered in Section 3. Auto and cross-bicoherence spectra of the two degrees-of-freedom are presented in Section 4. The quadratic interactions resulting in the pure period doubling sequence to chaos are isolated by the auto and cross-bispectra. Conclusions follow in Section 5.

## 2 The Coupled Oscillator

Comprehensive analyses of coupled oscillators with quadratic nonlinearities possessing internal resonances have been considered by numerous authors (Sethna, 1965; Nayfeh and Zavodney, 1986). Froude (1863) observed that ships have undesirable roll characteristics when subjected to internal (autoparametric) resonance. Mook et al. (1974), Nayfeh et al. (1973) and Nayfeh (1983a) provide a detailed analysis of a coupled oscillator with quadratic nonlinearities that governs the response of a ship that is restrained to pitch and roll. Miles (1985) showed that Hopf bifurcations do not exist for the case of an internally resonant, perfectly tuned, pendulum when the lower mode is excited by a principal parametric resonance. Nayfeh (1987) relaxed this assumption, and subsequently found Hopf bifurcations and calculated responses with period multiplying bifurcations leading to chaos.

Following the work of Nayfeh (1987), let $u_1$ and $u_2$ be two generalized coordinates which describe the motion of the system. Formulating Lagrange's equations and considering simultaneous harmonic parametric and external excitations, yields

$$\begin{aligned}\ddot{u}_1+\omega_1^2u_1+\epsilon[2\mu_1\dot{u}_1+\delta_1u_1^2+\delta_2u_1u_2+\delta_3u_2^2+\delta_4\dot{u}_1^2\\ +\delta_5\dot{u}_1\dot{u}_2+\delta_6\dot{u}_2^2+\delta_7u_1\ddot{u}_1+\delta_8u_2\ddot{u}_1+\delta_9u_1\ddot{u}_2\\ +\delta_{10}u_2\ddot{u}_2+(f_{11}u_1+f_{12}u_2)\cos\,\Omega_1t]=F_1\cos\,(\Omega_2t+\tau_1)\end{aligned} \tag{1}$$

$$\begin{aligned}\ddot{u}_2+\omega_2^2u_2+\epsilon[2\mu_2\dot{u}_2+\alpha_1u_1^2+\alpha_2u_1u_2+\alpha_3u_2^2+\alpha_4\dot{u}_1^2\\ +\alpha_5\dot{u}_1\dot{u}_2+\alpha_6\dot{u}_2^2+\alpha_7u_1\ddot{u}_1+\alpha_8u_2\ddot{u}_1+\alpha_9u_1\ddot{u}_2\\ +\alpha_{10}u_2\ddot{u}_2+(f_{21}u_1+f_{22}u_2)\cos\,(\Omega_1t\\ +\tau)]=F_2\cos\,(\Omega_2t+\tau_2)\end{aligned} \tag{2}$$

where $\mu_1$ and $\mu_2$ are the damping coefficients. The $F_n, f_{mn}, \Omega_n, \tau_n, \delta_n$, and $\alpha_n$ are constants and $\omega_1$ and $\omega_2$ are natural frequencies. $F_1$, $\Omega_1$ and $F_2$, $\Omega_2$ are the amplitudes and frequencies of the parametric and external excitations, respectively. The parameter $\epsilon$ is a small dimensionless parameter which has been used as a bookkeeping device in the perturbation analysis. If $\delta_1=\delta_3=\delta_4=\phi_6=\delta_7=\delta_{10}=\alpha_2=\alpha_5=\alpha_8=\alpha_9=0$, the equations that govern the response of a ship constrained to pitch and roll are recovered. Using the method of multiple scales (Nayfeh and Mook, 1979), $u_1$ and $u_2$ are expanded as

$$u_1(t;\epsilon)=u_{10}(T_0,\,T_1)+\epsilon u_{11}(T_0,\,T_1) \tag{3}$$

$$u_2(t;\epsilon)=u_{20}(T_0,\,T_1)+\epsilon u_{21}(T_0,\,T_1) \tag{4}$$

where $T_0$ is a fast time scale on which the main oscillatory behavior occurs and $T_n (n\geq 1)$ are scales on which amplitude and phase modulations take place.

Time derivatives are given by

$$\frac{d}{dt}=D_0+\epsilon D_1+\ldots,\ \frac{d^2}{dt^2}=D_0^2+2\epsilon D_0D_1+\ldots \tag{5}$$

where $D_n=\dfrac{\partial}{\partial T_n}$.

Substituting Eqs. (3)–(5) into Eqs. (1) and (2), equating like powers of $\epsilon$ and solving for $O(\epsilon^0)$ yields

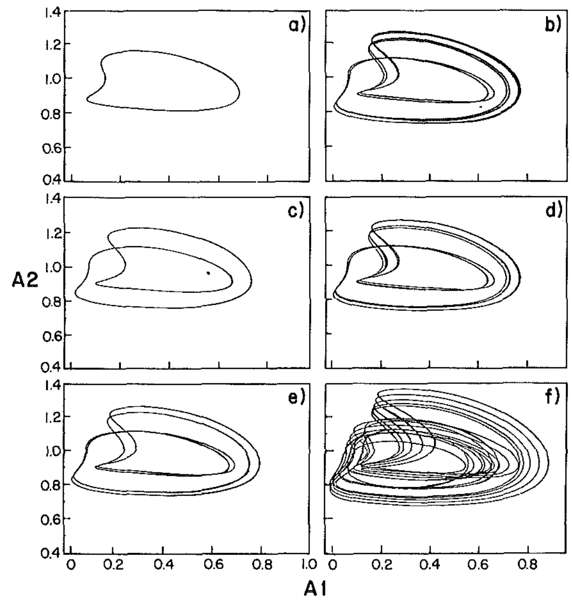


**Fig. 1 Projection of the modulation equations on $a_1-a_2$ plane for $\mu_n/f=0.02$, $\sigma_2/f=0.16$; (a) period 1 motion, $\sigma_1/f=0.205$; (b) period 2 motion, $\sigma_1/f=0.2025$; (c) period 4 motion, $\sigma_1/f=0.2014$; (d) period 8 motion, $\sigma_1/f=0.2013$; (e) period 16 motion, $\sigma_1/f=0.20126$; (f) chaotic motion, $\sigma_1/f=0.200$**

$$u_{10}=A_1(T_1)e^{i\omega_1T_0}+cc \tag{6}$$

$$u_{20}=A_2(T_1)e^{i\omega_2T_0}+cc \tag{7}$$

where $cc$ is the complex conjugate of the preceding terms. $A_n$ can be represented by

$$A_n=1/2a_ne^{i\beta_n}\quad\text{for}\quad n=1,2 \tag{8}$$

where $a_n$ and $\beta_n$ are the amplitude and phase of the $n$th mode, respectively. The particular case of parametric resonance of the first mode given by

$$\Omega_1=2\omega_1+\epsilon\sigma_2\quad\text{and}\quad\omega_2=2\omega_1+\epsilon\sigma_1 \tag{9}$$

is studied here, where $\sigma_1$ and $\sigma_2$ are detuning parameters. Substituting Eqs. (6)–(9) into $O(\epsilon^1)$ equations and annulling the resultant secular term gives

$$2i(A_1'+\mu_1A_1)+4\Lambda_1A_2\bar{A}_1e^{i\sigma_1T_1}+2f\bar{A}_1e^{i\sigma_2T_1}=0 \tag{10}$$

$$2i(A_2'+\mu_2A_2)+4\Lambda_2A_1^2e^{i\sigma_1T_1}=0 \tag{11}$$

where the prime denotes $\dfrac{d}{dT_1}$ and $f_{11}=4\omega_1f$. $\Lambda_1$ and $\Lambda_2$ are defined by

$$4\omega_1\Lambda_1=\delta_2+\delta_5\omega_1\omega_2-\delta_8\omega_1^2-\delta_9\omega_2^2 \tag{12}$$

$$4\omega_2\Lambda_2=\alpha_1-\alpha_4\omega_1^2-\alpha_7\omega_1^2. \tag{13}$$

Substituting Eq. (8) into Eqs. (10) and (11) and separating real and imaginary parts yields

$$a_1'=-\mu_1a_1-\Lambda_1a_1a_2\sin\gamma_2 \tag{14}$$

$$a_2'=-\mu_2a_2-\Lambda_2a_1^2\sin\gamma_1 \tag{15}$$

$$\beta_1'=\Lambda_1a_2\cos\gamma_1+f\cos\gamma_2 \tag{16}$$

$$\beta_2'=\Lambda_2\frac{a_1^2}{a_2}\cos\gamma_1 \tag{17}$$

where

$$\gamma_1=\sigma_1T_1+\beta_2-2\beta_1\quad\text{and}\quad\gamma_2=\sigma_2T_1-2\beta_1. \tag{18}$$

Equations (14)–(17) were numerically integrated using a fourth-order Runge-Kutta subroutine with a time step of 0.05. (Tests with larger and smaller time steps indicated that 0.05 was sufficient for numerical accuracy and stability.) $\mu_n/f$ was fixed at 0.02 and $\sigma_2/f$ = 0.16. Varying the value of $\sigma_1/f$ produces a period doubling sequence leading to chaos, as illustrated in Fig. 1.

Although the averaged equations demonstrate chaotic behavior, an analysis of the original equations has not been performed for the chaotic regime. Indeed, this is not the purpose of the present work. Further work is needed to confirm whether the multiple scales analysis actually represents the physical system in the chaotic regime.

## 3 Spectral Analysis and Numerical Details

Consider a discretely sampled time series $\eta_m(t)$ with the Fourier representation

$$\eta_m(t) = \sum_n A_m(\omega_n)e^{i\omega_n t} + A_m^*(\omega_n)e^{-i\omega_n t} \tag{19}$$

where the subscript $m$ = 1, 2 refers to each degree-of-freedom and the asterisk indicates complex conjugation. The power spectrum of mode $m$ is defined as

$$P_m(\omega_1) = E[A_m(\omega_1)A_m^*(\omega_1)] \tag{20}$$

where $E[\ ]$ is the expected value. The auto bispectrum of mode $m$ and the cross-bispectrum between modes $m$ and $n$ are defined, respectively, as

$$B_m(\omega_1,\omega_2) = E[A_m(\omega_1)A_m(\omega_2)A_m^*(\omega_1+\omega_2)] \tag{21}$$

$$XB_{m,n}(\omega_1,\omega_2) = E[A_m(\omega_1)A_m(\omega_2)A_n^*(\omega_1+\omega_2)]. \tag{22}$$

The normalized magnitude of the bispectrum, known as the squared bicoherence, is given by

$$b_m^2(\omega_1,\omega_2) = \frac{|B_m(\omega_1,\omega_2)|^2}{P_m(\omega_1)P_m(\omega_2)P_m(\omega_1+\omega_2)} \tag{23}$$

and the normalized magnitude of the squared cross-bicoherence is given by

$$xb_{m,n}^2(\omega_1,\omega_2) = \frac{|B_{m,n}(\omega_1,\omega_2)|^2}{P_m(\omega_1)P_m(\omega_2)P_n(\omega_1+\omega_2)}. \tag{24}$$

The squared bicoherence represents the fraction of power at the sum frequency ($\omega_1 + \omega_2$) of the triad owing to quadratic interactions between the two other Fourier components ($\omega_1$ and $\omega_2$).

The time series produced by the numerical integrations of Eqs. (14)–(17) were sampled (in dimensional units) at 1 Hz, and subdivided in 32 segments, each of 128 s duration for processing, resulting in a frequency resolution of 0.0078 Hz and 64 statistical degrees-of-freedom. Bicoherence values of $b$ > 0.40 are statistically significant at the 95 percent level for 64 degrees-of-freedom (Haubrich, 1979). Although higher frequency resolution was possible, the associated decrease in statistical stability of bispectral estimates was deemed unacceptable. The frequency resolution used here is sufficient to resolve the power spectral primary peak, its super harmonics, and one subharmonic. Finer frequency resolution does not alter any of the conclusions that will be presented as follows.

## 4 Results

Phase-plane portraits of the period-doubling route to chaos are shown in Fig. 1. Power spectra for the first and second degree-of-freedom motions corresponding to period one, two, four, eight, sixteen, and chaotic motions are presented in Figs. 2 and 3, respectively. The harmonic structure is clearly displayed in the power spectra. For period-one motion, the spectrum is dominated by a primary spectral peak at $f$ = 0.045 Hz and its higher harmonics for the first-degree-of-freedom motion (Fig. 2$a$). For period two and subsequent period-doubled motion, the subharmonic ($f$ = 0.0215) is excited (Fig. 2($b$)–2($f$). The subharmonics for period four, eight, and sixteen are not resolved owing to the frequency resolution used, as discussed above. Owing to the quadratic nonlinearities, the spectrum contains peaks at frequencies corresponding to sum interactions between the subharmonic, the primary, and their harmonics. For the second degree-of-freedom motion shown in Fig. 3, intermediate frequencies, in addition to the subharmonic, the primary, and their harmonics, are excited by the cross-couplings of both the degrees-of-freedom. Bicoherence spectra quantify the coupling of and energy exchange between triads of Fourier components as the system progresses toward chaos as $\sigma_1/f$ is decreased from $\sigma_1/f$ = 0.205 to $\sigma_1/f$ = 0.200. Auto-bicoherence spectra for the first and second degree-of-freedom motions are presented in Figs. 4 and 5, respectively. For periodic motions, the coupling is centered about the dominant frequencies composing the limit cycles. Through the period doubling cascade up to period 16 motion (Figs. 4($a$)–4($d$) and 5($a$)–5($d$), additional Fourier components are nonlinearly excited by quadratic interactions between the dominant frequency and itself, as well as smaller interactions among the superharmonics and subharmonics.

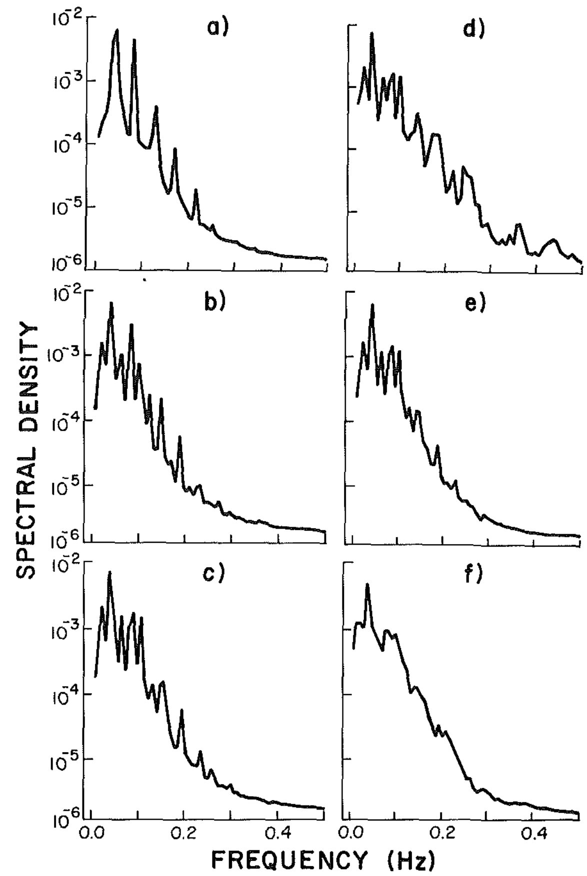


**Fig. 2 Power spectra of the first-mode amplitude modulations; ($a$) period 1 motion; ($b$) period 2 motion; ($c$) period 4 motion; ($d$) period 8 motion; ($e$) period 16 motion; ($f$) chaotic motion. The units of power are arbitrary.**

The spread of nonlinear interactions to include more Fourier components as $\sigma_1/f$ is reduced from 0.205 to 0.2014 is shown by the increasing number of triads with high auto-bicoherence in Figs. 4($a$)–4($d$), 5($a$)–5($d$). For $\sigma_1/f$ corresponding to 0.2013 and less, the superharmonics decrease in level (Figs. 2($e$)–2($f$) and Figs. 3($e$)–3($f$)) as do the bicoherence of triads containing these superharmonics (Figs. 4($e$)–4($f$); 5($e$)–5($f$)).

Figure 6 shows the Fourier component couplings of the first degree-of-freedom motion to those of the second ($m$ = 1, $n$ = 2). Figure 7, on the other hand, shows couplings between frequencies of the second degree-of-freedom motion to the first ($m$ = 2, $n$ = 1). Both the figures display the cross-coupling owing to amplitude modulations of the respective degree-of-freedom motion. The cross-bicoherence increases steadily up to period 8 with the reduction of $\sigma_1/f$ from 0.205 to 0.2013 (Fig. 6($a$)-6($d$); Fig. 7($a$)-7($d$)). For $\sigma_{1/f} < 0.2013$, the superharmonics are suppressed, resulting in the reduction of the cross-bicoherence (Figs. 6($e$)-6($f$) and 7($e$)-7($f$)). The auto and cross-bicoherence spectra suggest that there is very little nonlinear energy transfer between amplitude modulations during chaos; in other words, there is very little cross-coupling owing to amplitude modulations in the chaotic regime. If both the modes are decoupled (i.e., if $\omega_2 \neq \omega_1$), then the system of averaged equations cannot exhibit chaos, as is true for a second-order homogeneous system. Consequently, in order to admit chaos, there must be a strong cross-coupling between the phase and amplitude modulations or between the phase modulations of the two modes. Cross-bispectra between amplitude and phase modulations are small (Figs. 8($a$), 8($b$)), thus negating the first possibility. On the other hand, there is very strong cross-coupling of the phase modulations, as demonstrated by high values (as great as $xb = 0.8$) of cross-bicoherence between the phases of the two modes of motion (Fig. 8($a$)-8($c$)). Thus, the entire source of coupling, or the nonlinear energy transfer is through the cross-coupling of phase modulations in the chaotic regime.

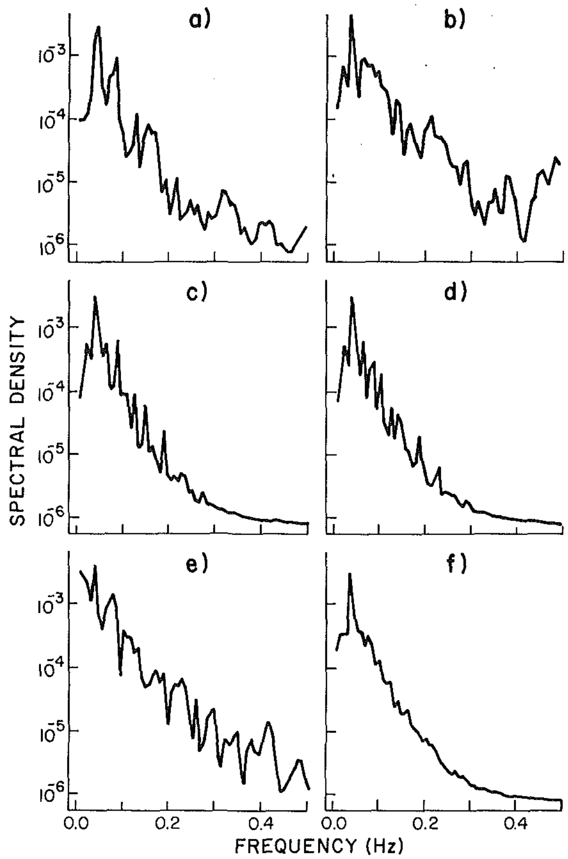


Fig. 3 Power spectra of the second-mode amplitude modulations; ($a$) period 1 motion; ($b$) period 2 motion; ($c$) period 4 motion; ($d$) period 8 motion; ($e$) period 16 motion; ($f$) chaotic motion. The units of power are arbitrary.

## 5 Conclusions

Auto and cross-bicoherence calculations were performed for a system of two coupled oscillators with quadratic nonlinearities possessing chaotic motions. Since the nonlinear interactions among the Fourier components are quadratically nonlinear, they are characterized by the auto and cross-bicoherence both outside and inside the chaotic regime. The period one, two, four, eight, sixteen, and chaotic trajectories all possessed strong auto bicoherence, originating primarily from interactions involving the fundamental frequency of oscillation. There is negligible cross-bicoherence between the amplitude modulations in the chaotic regime. On the other hand, there is a strong cross-coupling of the phases. In the averaged equations, the cross-couplings of both the amplitude and phase modulations must be assessed (e.g., with bispectral analysis) in order to understand the dynamics of nonlinear energy transfer.

The different bispectral analyses presented here clearly show the coupling mechanisms responsible for chaotic motion of

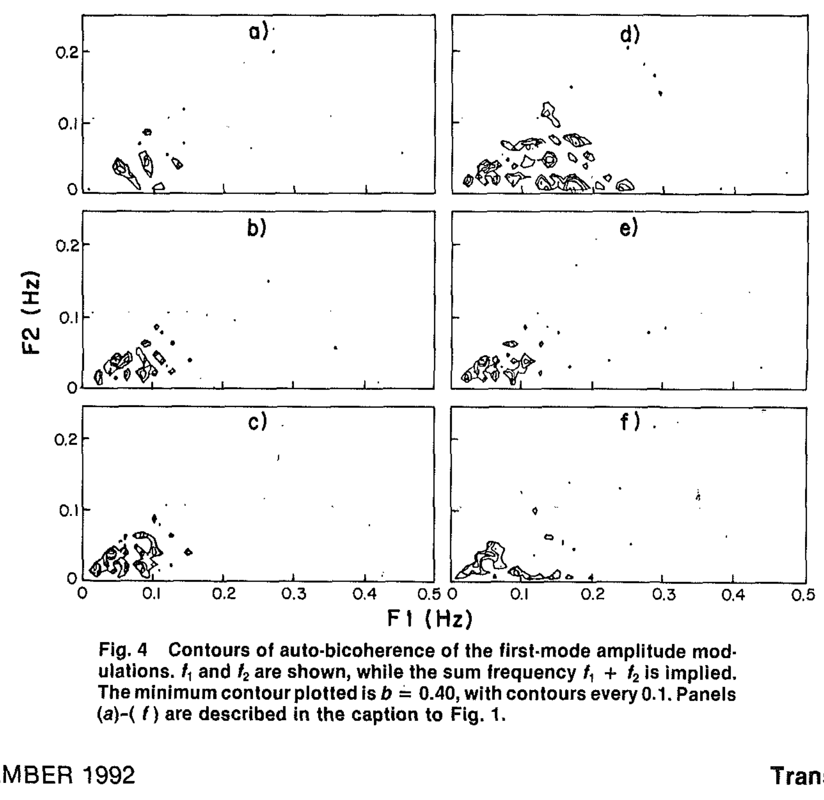


Fig. 4 Contours of auto-bicoherence of the first-mode amplitude modulations. $f_1$ and $f_2$ are shown, while the sum frequency $f_1 + f_2$ is implied. The minimum contour plotted is $b = 0.40$, with contours every 0.1. Panels ($a$)-($f$) are described in the caption to Fig. 1.

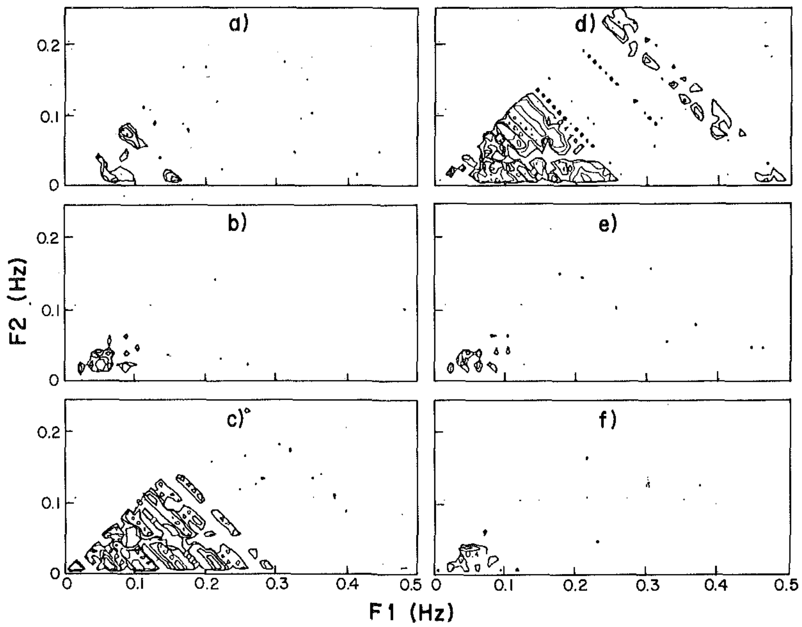


**Fig. 5 Contours of auto-bicoherence of the second-mode amplitude modulations. The format is the same as Fig. 4.**

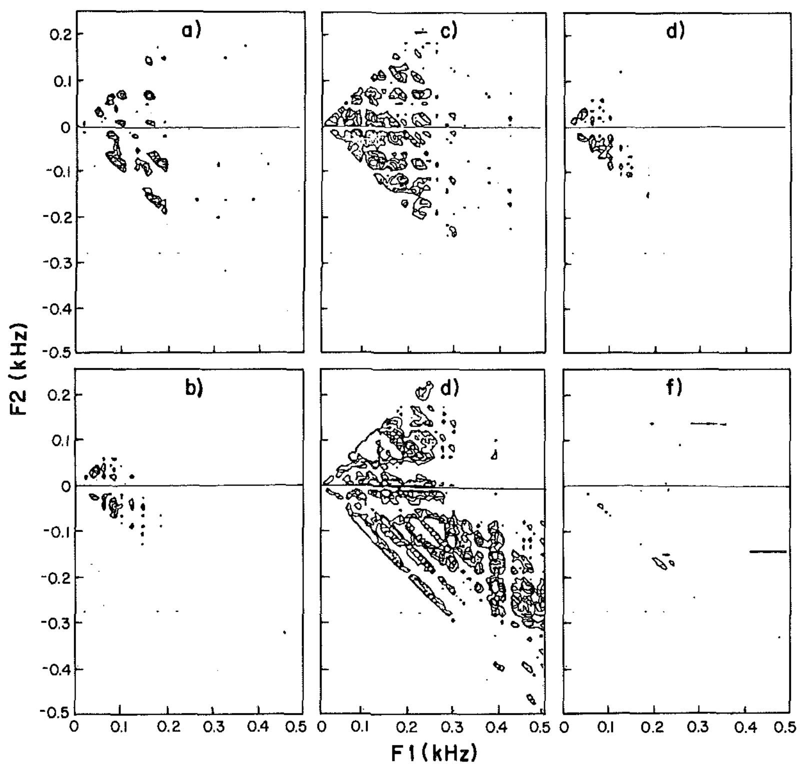


***Fig. 6 Contours of cross-bicoherence between the first-mode amplitude modulations ($f_1$, $f_2$) and the second-mode amplitude modulations ($f_1 + f_2$). The minimum contour plotted is $xb = 0.4$, with contours every 0.1. The panels (a)–(f) are described in the caption to Fig. 1.***

this oscillator. Moreover, since they illustrate the wave coupling mechanisms and the resulting chaotic transitions, bispectra provide a powerful tool for understanding other nonlinear, quadratic systems, including those possessing chaotic motion. These methods operate solely on time series information, and thus, they offer a way to distinguish chaotic motion from linear random motion because the bicoherence of a linear random time series is zero.


## Acknowledgments

Charles Pezeshki's research is supported by a grant from Washington State University's OGRD Program. Steve Elgar's research is supported by the Office of Naval Research (Coastal Science) and the National Science Foundation (Physical Oceanography). The governing equations and the perturbation analysis was procured from lectures delivered in *Perturbation*

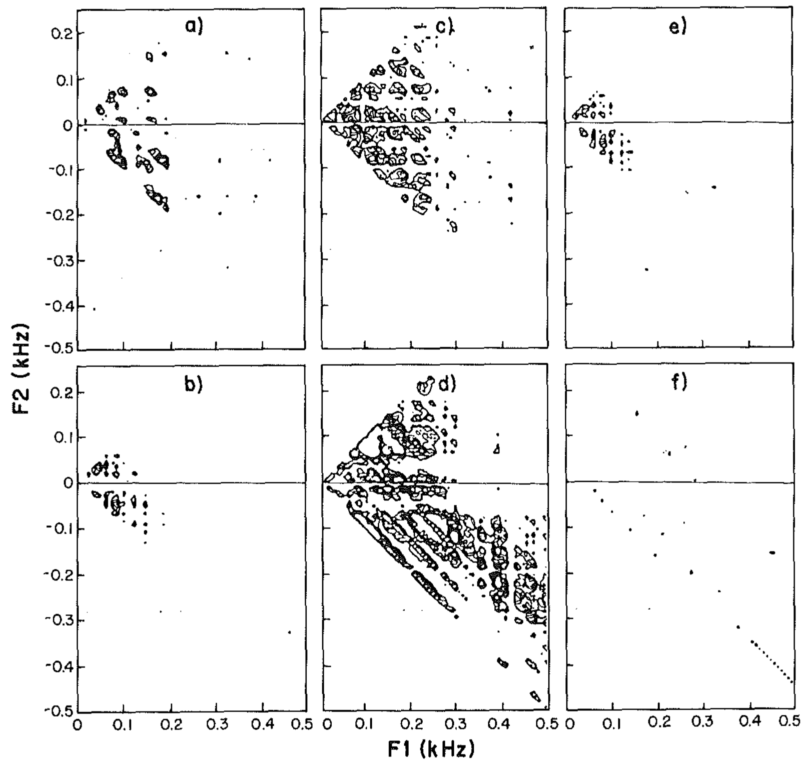


**Fig. 7 Contours of cross-bicoherence between the second-mode amplitude modulations ($f_1$, $f_2$) and the first-mode amplitude modulations ($f_1$ + $f_2$). The format is the same as Fig. 6.**

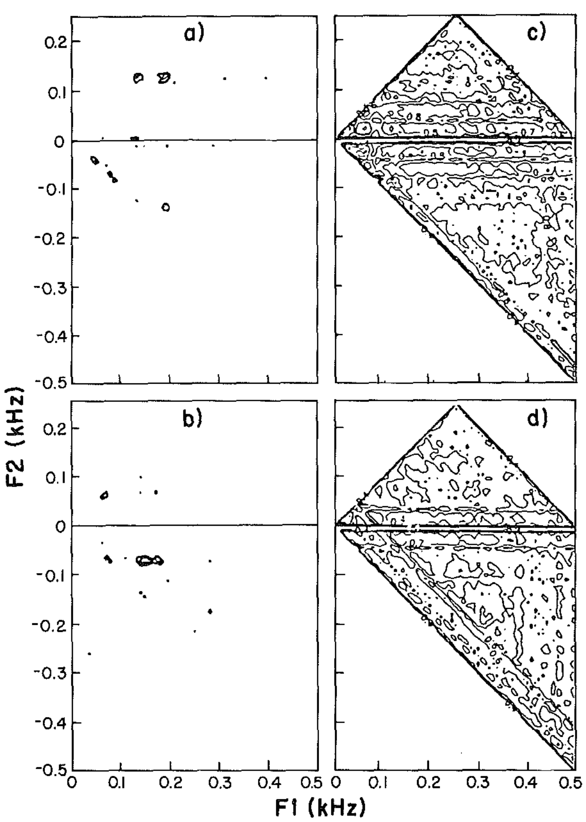


**Fig. 8 Contours of cross-bicoherence between; (*a*) first-mode amplitude modulations ($f_1$, $f_2$) and second-mode phase modulations ($f_1$ + $f_3$); (*b*) second-mode amplitude modulations ($f_1$, $f_2$) and first-mode phase modulations ($f_1$ + $f_2$); (c) first-mode phase modulations ($f_1$, $f_2$) and second-mode phase modulations ($f_1$ + $f_2$); (*d*) second-mode phase modulations ($f_1$, $f_2$) and first-mode phase modulations ($f_1$ + $f_2$). The minimum contour plotted is $xb$ = 0.4 with contours every 0.1.**

*Methods* by Prof. A. H. Nayfeh at VPI&SU, whose ideas and discussions are gratefully acknowledged. Signal processing computations were performed at the San Diego Supercomputer Center (supported by NSF).

## References

Choi, D., Chang, J. H., Stearman, R., and Powers, E., 1984, "Bispectral Identification of Nonlinear Mode Interactions," *Proc. 2nd Int. Modal Analysis Conference*, Vol. II, pp. 3–12.

Farmer, J., Ott, E., and Yorke, J., 1983, "The Dimension of Chaotic Attractors," *Physica D*, Vol. 7, pp. 153–179.

Froude, W., 1863, "Remarks on Mr. Scott-Russel's paper on Rolling," *Transactions of the Institute of Naval Architecture*, Vol. 4, p. 232.

Haddow, A. G., Barr, A. D. S., and Mook, D. T., 1984, "Theoretical and Experimetnal Study of Modal Interaction in a Two-Degree-of-Freedom Structure," *Journal of Sound and Vibration*, Vol. 97, p. 451.

Haubrich, R. A., 1979, "Earth Noises, 5 to 500 Millicycles Per Second," *Journal of Geophysical Research*, Vol. 70, p. 1415.

Helland, K. N., Van Atta, C. W., and Stegun, G. N., 1977, "Spectral Energy Transfer in High Reynolds Number Turbulence," *Journal of Fluid Mechanics*, Vol. 79, pp. 337–359.

Kim, Y. C., Beall, J. M., Powers, E. J., and Miksad, R. W., 1980, "Bispectrum and Nonlinear Wave Coupling," *Physics of Fluids*, Vol. 23, pp. 258–263.

Lii, K. S., Rosenblatt, M., and Van Atta, C., 1976, "Bispectral Measurements in Turbulence," *Journal of Fluid Mechanics*, Vol. 77, pp. 45–62.

Miles, J., 1985, "Parametric Excitation of an Internally Resonant Double Pendulum," *Journal of Applied Mathematical Physics* (*SAMP*), Vol. 36, p. 337.

Miller, M., 1986, "Bispectral Analysis of the Driven Sine-Gordon Chain," *Physical Review B*, Vol. 34, pp. 6326–6333.

Mook, D. T., Marshall, L. R., and Nayfeh, A. H., 1974, "Subharmonic and Superharmonic Resonances in the Pitch and Roll Modes of Ship Motions," *Journal of Hydronautics*, Vol. 8, p. 32.

Nayfeh, A. H., 1983a, "The Response of Two-Degree-of-Freedom Systems with Quadratic Non-linearities to a Parametric Excitation," *Journal of Sound and Vibration*, Vol. 88, p. 547.

Nayfeh, A. H., 1983b, "The Response of Multidegree-of-Freedom Systems with Quadratic Non-Linearities to a Harmonic Parametric Resonance," *Journal of Sound and Vibration*, Vol. 88, p. 237.

Nayfeh, A. H., 1988, "On the Undesirable Roll Characteristics of Ships in Regular Seas," *Journal of Ship Research*, Vol. 32, No. 2, pp. 92–100.

Nayfeh, A. H., 1987, "Parametric Excitation of Two Internally Resonant

Oscillators," *Journal of Sound and Vibration*, Vol. 119, No. 1, pp. 95-109.
Nayfeh, A. H., and Mook, D. T., 1979, *Nonlinear Oscillations*, John Wiley and Sons, New York.
Nayfeh, A. H., Mook, D. T., and Marshall, L. R., 1973, "Nonlinear Coupling of Pitch and Roll Modes in Ship Motions," *Journal of Hydronautics*, Vol. 7, p. 145.
Nayfeh, A. H., and Zavodney, L. D., 1986, "The Response of Two-Degree-of-Freedom Systems with Quadratic Nonlinearities," *Journal of Sound and Vibration*, Vol. 107, p. 329.
Nikias, C. L., and Raghuveer, M. R., 1987, "Bispectrum Estimation: A Digital Signal Processing Framework," *IEEE Proceedings*, Vol. 75, No. 7, pp. 869-891.
Pezeshki, C., Elgar, S., and Krishna, R. C., 1990, "Bispectral Analysis of Systems Possessing Chaotic Motion," *Journal of Sound and Vibration*, Vol. 137, No. 3, pp. 357-369.
Ritz, Ch., Powers, E., Miksad, R., and Solis, R., 1988, "Nonlinear Spectral Dynamics of a Transitioning Flow," *Physics of Fluids*, Vol. 31, pp. 3577-3588.
Sato, T., Sasaki, K., and Nakamura, Y., 1977, "Real-time Bispectral Analysis of Gear Noise and Its Application to Contactless Diagnostics," *Journal of the Acoustical Society of America*, Vol. 62, No. 2, pp. 382-387.
Sethna, P. R., 1965, "Vibrations of Dynamical Systems with Quadratic Nonlinearities," ASME Journal of Applied Mechanics, Vol. 32, p. 576.
Van Atta, C.W., 1979, "Inertial Range Bispectra in Turbulence," *Physics of Fluids*, Vol. 22, pp. 1440-1443.
Wolf, A., Swift, J. B., Swinney, H. L., and Vastano, J. A., 1985, "Determining Lyapunov Exponents from a Time Series," *Physica D*, Vol. 16, pp. 285-317.
Yeh, T. T., and Van Atta, C. W., 1973, "Spectral Transfer of Scales and Velocity Fields in Heated-Grid Turbulence," *Journal of Fluid Mechanics*, Vol. 58, pp. 233-261.

# Lyapunov Exponents and Stochastic Stability of Coupled Linear Systems Under Real Noise Excitation

**S. T. Ariaratnam**
Professor.

**Wei-Chau Xie**
Asst. Professor.

Solid Mechanics Division,
Faculty of Engineering,
University of Waterloo,
Waterloo, Ontario N2L 3G1
Canada

*The almost-sure asymptotic stability of a class of coupled multi-degrees-of-freedom systems subjected to parametric excitation by an ergodic stochastic process of small intensity is studied. Explicit asymptotic expressions for the largest Lyapunov exponent for various values of the system parameters are obtained by using a combination of the method of stochastic averaging and a well-known procedure due to Khas'minskii, from which the asymptotic stability boundaries are determined. As an application, the example of the flexural-torsional instability of a thin elastic beam acted upon by a stochastically fluctuating load at the central cross-section of the beam is investigated.*

## 1 Introduction

Lyapunov exponents play an important role in the modern theory of nonlinear structural dynamics. They characterize the exponential rates of change of the response of dynamical systems. The vanishing of the largest Lyapunov exponent implies a change in the stability property of the response.

A formulation for the exact evaluation of the largest Lyapunov exponent of linear systems of Itô stochastic differential equations was given by Khas'minskii (1967) and has been successfully employed to determine numerically Lyapunov exponents and stochastic stability conditions for certain two-dimensional systems (Mitchell and Kozin, 1974). Asymptotic expressions for Lyapunov exponents for such systems subjected to weak excitations were obtained by Auslender and Mil'stein (1983), Arnold et al. (1986), Wedig (1988), Pardoux and Wihstutz (1988), and Ariaratnam and Xie (1989). The direct use of Khas'minskii's method to higher dimensional systems has not met with much success, because of the difficulty of studying diffusion processes occurring on surfaces of unit hyperspheres in higher dimensional Euclidean spaces.

In this paper, the stability of a class of coupled multi-degrees-of-freedom systems subjected to parametric excitation by an ergodic stochastic process of small intensity and short correlation time is considered. The motivation for the study stems from certain problems in the dynamic stability of elastic systems subjected to stochastically fluctuating loads. The *stochastic moment stability* of such systems was examined previously by Ariaratnam and Srikantaiah (1978) using the method of stochastic averaging. In the present study, the almost-sure stability of the same class of problems is studied using a combination of the method of averaging and the technique of Khas'minskii (1967). Explicit asymptotic expressions for the largest Lyapunov exponent for various values of the system parameters are obtained. The result for single-degree-of-freedom systems is obtained in the special case when the coupling parameters are set equal to zero. As an application, the example of the flexural-torsional instability of a thin elastic beam acted upon by a stochastically fluctuating load at the central cross-section of the beam is considered.

This paper is an extension to real noise excitation of a previous report (Ariaratnam et al., 1990) that dealt with the case of white noise excitation.

## 2 Formulation

The systems considered are described by stochastic differential equations of the form

$$\ddot{q}_i + 2\sum_{j=1}^{n} \beta_{ij}\dot{q}_j + \omega_i^2 q_i + \omega_i \xi(t) \sum_{j=1}^{n} k_{ij} q_j = 0, \quad i = 1,2,\ldots,n, \tag{1}$$

where the $q_i$ are generalized coordinates, $\beta_{ij}$ are damping constants, $\omega_i$ are natural frequencies, and $k_{ij}$ are constants. The excitation is represented by $\xi(t)$, which is taken to be an ergodic stochastic process with zero mean value and a sufficiently small correlation time. Equations (1) describe exactly the parametrically excited motion of certain nongyroscopic, discrete, linear elastic systems with $n$ degrees-of-freedom about the equilibrium configuration $q_i(t) = 0$. They also describe approximately the motion of certain continuous elastic structures whose equations of motion have been discretized by some suitable technique such as Rayleigh-Ritz, Galerkin, finite differences,

Contributed by the Applied Mechanics Division of THE AMERICAN SOCIETY OF MECHANICAL ENGINEERS for publication in the ASME JOURNAL OF APPLIED MECHANICS.

Discussion on this paper should be addressed to the Technical Editor, Prof. Leon M. Keer, The Technological Institute, Evanston, IL 60208 and will be accepted until four months after final publication of the paper itself in the JOURNAL OF APPLIED MECHANICS.

Manuscript received by the ASME Applied Mechanics Division, Oct. 3, 1990; final revision, Apr. 29, 1991. Associate Technical Editor: D. J. Inman.

or finite elements. It will be seen later that small cross-damping terms such as $\beta_{ij}$, $i \neq j$ have no effect on the solution in the first approximation.

When the parametric excitation is a deterministic harmonic function of time, i.e., $\xi(t) = \epsilon \cos\omega t$, it is well known (see, e.g., Mettler, 1968) that the instability of the trivial solution $\mathbf{q} = \dot{\mathbf{q}} = \mathbf{0}$ occurs when the excitation frequency $\omega$ is in the neighborhood of $\omega = \omega_0/m$, where $m$ is a positive integer determining the *order* of the instability and $\omega_0$ depends on the nature of the coupling coefficients $k_{ij}$. For $\omega_0 = 2\omega_i$, the regions are referred to as instability regions of the *first kind* and correspond to parametric resonance of the *subharmonic* type in which only the particular mode $q_i$ is excited into motion. Instability regions of the *second kind* are found for

$$\begin{aligned}\omega_0 &= \omega_i + \omega_j \ (i \neq j), \quad \text{if } k_{ij}k_{ji} > 0\\ &= |\omega_i - \omega_j| \ (i \neq j), \quad \text{if } k_{ij}k_{ji} < 0.\end{aligned}$$

The instabilities occurring when $\omega_0 = |\omega_i \pm \omega_j|$ are referred to as *combination resonances* since the excitation frequency $\omega$ is in the vicinity of fractions of the sum and difference combinations of the natural frequencies. In combination resonance, a pair of modes is excited into motion while the remaining modes are at rest.

In Eq. (1), the generalized coordinates $q_i(t)$ and velocities $\dot{q}_i(t)$ are transformed to polar coordinates by means of the relations

$$q_i = a_i \cos\Theta_i, \quad \dot{q}_i = -a_i\omega_i \sin\Theta_i, \quad \Theta_i = \omega_i t + \theta_i, \ i = 1, 2, \ldots, n. \tag{2}$$

Then, one obtains the equations of motion in terms of $a_i(t)$ and $\theta_i(t)$:

$$\dot{a}_i = -\frac{2}{\omega_i}\sum_{j=1}^{n} \beta_{ij} a_j \omega_j \sin\Theta_j \sin\Theta_i + \xi(t) \sum_{j=1}^{n} k_{ij} a_j \cos\Theta_j \sin\Theta_i,$$

$$\dot{\theta}_i = -\frac{2}{a_i\omega_i}\sum_{j=1}^{n} \beta_{ij} a_j \omega_j \sin\Theta_j \cos\Theta_i + \frac{1}{a_i}\xi(t)\sum_{j=1}^{n} k_{ij} a_j \cos\Theta_j \cos\Theta_i. \tag{3}$$

It is supposed that the damping constants and the stochastic perturbation are small, i.e., $\beta_{ij} = O(\epsilon)$, $S(\omega) = O(\epsilon)$, $\Psi(\omega) = O(\epsilon)$, $0 < |\epsilon| << 1$, where $S(\omega)$ and $\Psi(\omega)$ denote the cosine and sine power spectral densities of the stochastic process $\xi(t)$, defined by

$$S(\omega) + i\Psi(\omega) = 2\int_0^\infty E[\xi(t)\xi(t+\tau)]e^{i\omega\tau} d\tau,$$

$E[\cdot]$ denoting the expectation operation. Under these conditions, the method of stochastic averaging (Stratonovich, 1963; Khas'minskii, 1966) may be applied to Eqs. (3) to yield the following Itô equations for the averaged amplitudes $a_i$ and phase angles $\theta_i$, whose solutions provide a uniformly valid first approximation to the exact values (Ariaratnam and Srikantaiah, 1978):

$$\begin{aligned}da_i &= m_{a_i} dt + \sum_{j=1}^{n} \sigma_{ij} dW_j,\\ d\theta_i &= m_{\theta_i} dt + \sum_{j=1}^{n} \mu_{ij} dB_j,\end{aligned} \tag{4}$$

where $W_j(t), B_j(t), j = 1, 2, \ldots, n$ are mutually independent unit Wiener processes and the drift coefficients $m_{a_i}$, $m_{\theta_i}$ and the diffusion coefficients $\sigma_{ij}$, $\mu_{ij}$ are given by

$$m_{a_i} = \left[-\beta_{ii} + \frac{3}{16}k_{ii}^2 S(2\omega_i) + \frac{1}{8}\sum_{\substack{j=1\\ j\neq i}}^{n} k_{ij}k_{ji} S_{ij}^{-}\right] a_i + \frac{1}{16}\sum_{\substack{j=1\\ j\neq i}}^{n} k_{ij}^2 S_{ij}^{+} \frac{a_j^2}{a_i},$$

$$m_{\theta_i} = \frac{1}{8}\sum_{j=1}^{n} k_{ij}k_{ji}\Psi_{ij}^{-}\left(1 + \frac{a_j}{a_i}\right) - \frac{1}{4}\sum_{j=1}^{n} k_{ij}^2 \Psi_{ij}^{+} \frac{a_j^2}{a_i^2},$$

$$[\sigma\sigma^T]_{ii} = \frac{1}{8}k_{ii}^2 S(2\omega_i) a_i^2 + \frac{1}{8}\sum_{\substack{j=1\\ j\neq i}}^{n} k_{ij}^2 S_{ij}^{+} a_j^2,$$

$$[\sigma\sigma^T]_{ij} = \frac{1}{8}k_{ij}k_{ji}S_{ij}^{-} a_i a_j, \quad (i \neq j),$$

$$[\mu\mu^T]_{ii} = \frac{1}{8}k_{ii}^2[2S(0) + S(2\omega_i)] + \frac{1}{8}\sum_{\substack{j=1\\ j\neq i}}^{n} k_{ij}^2 S_{ij}^{+} a_j^2,$$

$$[\mu\mu^T]_{ij} = \frac{1}{4}k_{ii}k_{jj}S(0) + \frac{1}{8}k_{ij}k_{ji}S_{ij}^{+}, \quad (i \neq j),$$

$$[\sigma] = [\sigma_{ij}], \quad [\mu] = [\mu_{ij}].$$

In the above expressions, the functions $S^+$, $S^-$, $\Psi^+$, $\Psi^-$ are defined by

$$S_{ij}^{\pm} = S(\omega_i + \omega_j) \pm S(\omega_i - \omega_j), \quad \Psi_{ij}^{\pm} = \Psi(\omega_i + \omega_j) \pm \Psi(\omega_i - \omega_j).$$

The $n$-degrees-of-freedom system given by Eq. (1) is difficult to study in its general form. Hence, the discussion from now on will be restricted to two-degrees-of-freedom systems described by the equations:

$$\begin{aligned}\ddot{q}_1 + 2\beta_{11}\dot{q}_1 + 2\beta_{12}\dot{q}_2 + \omega_1^2 q_1 + \omega_1(k_{11}q_1 + k_{12}q_2)\xi(t) &= 0,\\ \ddot{q}_2 + 2\beta_{21}\dot{q}_1 + 2\beta_{22}\dot{q}_2 + \omega_2^2 q_2 + \omega_2(k_{21}q_1 + k_{22}q_2)\xi(t) &= 0,\end{aligned} \tag{5}$$

in which, by a suitable scaling of coordinates, it is always possible to take $k_{12} = \pm k_{21} = k > 0$, without loss of generality. The product $|k_{12}k_{21}| = k^2$, however, remains invariant under scaling. The results derived for the two-degrees-of-freedom system may be generalized to $n$-degrees-of-freedom systems ($n > 2$) under certain conditions on the spectral density distribution of the parametric excitation (see Section 6).

For the two-degrees-of-freedom system, the amplitude equations of (4) become

$$\begin{aligned}da_1 &= m_1 dt + \sigma_{11}dW_1 + \sigma_{12}dW_2,\\ da_2 &= m_2 dt + \sigma_{21}dW_1 + \sigma_{22}dW_2,\end{aligned} \tag{6}$$

where

$$m_1 = \left[-\beta_1 + \frac{3}{16}k_{11}^2 S(2\omega_1) + \frac{1}{8}k_{12}k_{21}S^-\right] a_1 + \frac{1}{16}k_{12}^2 S^+ \frac{a_2^2}{a_1},$$

$$m_2 = \left[-\beta_2 + \frac{3}{16}k_{22}^2 S(2\omega_2) + \frac{1}{8}k_{12}k_{21}S^-\right] a_2 + \frac{1}{16}k_{21}^2 S^+ \frac{a_1^2}{a_2},$$

$$[\sigma\sigma^T]_{11} = \frac{1}{8}k_{11}^2 S(2\omega_1) a_1^2 + \frac{1}{8}k_{12}^2 S^+ a_2^2,$$

$$[\sigma\sigma^T]_{22} = \frac{1}{8}k_{22}^2 S(2\omega_2) a_2^2 + \frac{1}{8}k_{21}^2 S^+ a_1^2,$$

$$[\sigma\sigma^T]_{12} = [\sigma\sigma^T]_{21} = \frac{1}{8}k_{12}k_{21}S^- a_1 a_2,$$

$$S^{\pm} = S(\omega_1 + \omega_2) \pm S(\omega_1 - \omega_2), \quad \beta_1 = \beta_{11}, \quad \beta_2 = \beta_{22}.$$

It may be noted that the averaged amplitude vector $(a_1, a_2)$ is a two-dimensional diffusion process and that the coefficients of the right-hand side terms of Eqs. (6) are homogeneous in $a_1$, $a_2$ of degree one. Hence, the procedure of Khas'minskii (1967) may be employed to derive an expression for the largest Lyapunov exponent of the amplitude process (Ariaratnam, 1977). To this end a further logarithmic polar transformation is applied:

$$\rho=\frac{1}{2}\log(a_1^2+a_2^2),\quad \phi=\mathrm{Tan}^{-1}\left(\frac{a_2}{a_1}\right),\quad 0\le\phi\le\frac{1}{2}\pi,$$

and, by the use of Itô's differential rule or otherwise, the following pair of Itô equations governing $\rho$, $\phi$ are obtained:

$$d\rho=Q(\phi)dt+\Sigma(\phi)dW,$$
$$d\phi=\Phi(\phi)dt+\Psi(\phi)dW, \qquad (7)$$

where $W(t)$ is a Wiener process of unit intensity and

$$Q(\phi)=\lambda_1\cos^2\phi+\lambda_2\sin^2\phi\pm\frac{1}{8}k^2S^-+\Psi^2(\phi),$$

$$\Phi(\phi)=-\frac{1}{2}(\lambda_1-\lambda_2)\sin2\phi+\frac{1}{16}[2(\lambda_1+\lambda_2+\beta_1+\beta_2)-k^2S(\omega_1\pm\omega_2)]\sin4\phi+\frac{1}{8}k^2S^+\cot2\phi,$$

$$\Sigma^2(\phi)=(\lambda_1+\beta_1)\cos^4\phi+(\lambda_2+\beta_2)\sin^4\phi+\frac{1}{8}k^2S(\omega_1\pm\omega_2)\sin^22\phi,$$

$$\Psi^2(\phi)=\frac{1}{8}k^2S^++\frac{1}{8}[2(\lambda_1+\lambda_2+\beta_1+\beta_2)-k^2S(\omega_1\pm\omega_2)]\sin^22\phi, \qquad (8)$$

in which the upper sign is taken when $k_{12}=k_{21}=k$, and the lower sign when $k_{12}=-k_{21}=k$. The constants $\lambda_1$, $\lambda_2$ are defined by

$$\lambda_1=-\beta_1+\frac{1}{8}k_{11}^2S(2\omega_1),\quad \lambda_2=-\beta_2+\frac{1}{8}k_{22}^2S(2\omega_2), \qquad (9)$$

which, as will be seen later, are the Lyapunov exponents of the two uncoupled single-degree-of-freedom systems that result when the coupling coefficients $k_{12}$, $k_{21}$ are set equal to zero.

From the second of Eqs. (7), it is clear that the $\phi$-process is itself a diffusion on the first quadrant of the unit circle. If $\Psi(\phi)$ vanishes in $[0, \pi/2]$, the diffusion process is *singular*, otherwise it is *nonsingular*. From the last of (8), $\Psi^2(\phi)$ can be rewritten as

$$\Psi^2(\phi)=\begin{cases}\frac{1}{8}k^2[S(\omega_1-\omega_2)+S(\omega_1+\omega_2)\cos^22\phi]\\ \qquad +\frac{1}{4}(\lambda_1+\lambda_2+\beta_1+\beta_2)\sin^22\phi, & k_{12}k_{21}>0,\\ \frac{1}{8}k^2[S(\omega_1+\omega_2)+S(\omega_1-\omega_2)\cos^22\phi]\\ \qquad +\frac{1}{4}(\lambda_1+\lambda_2+\beta_1+\beta_2)\sin^22\phi, & k_{12}k_{21}<0.\end{cases} \qquad (10)$$

Since $\lambda_1+\lambda_2+\beta_1+\beta_2=[k_{11}^2S(2\omega_1)+k_{22}^2S(2\omega_2)]/8\ge 0$, it is clear that $\Psi(\phi)$ vanishes at $\phi=\phi_0=\pi/4$ only when

(i) for $k_{12}k_{21}>0$, $k_{11}=k_{22}=0$, $S(\omega_1-\omega_2)=0$;

(ii) for $k_{12}k_{21}<0$, $k_{11}=k_{22}=0$, $S(\omega_1+\omega_2)=0$.

In the following sections, the evaluation of the largest Lyapunov exponent of the averaged system (7) will be examined in detail for both nonsingular and singular cases.

## 3 Nonsingular Case

Suppose that $\Psi(\phi)$ does not vanish in $0\le\phi\le\pi/2$. Then the diffusion is nonsingular, the density $\mu(\phi)$ of the invariant measure being governed by the Fokker-Planck equation

$$\frac{1}{2}\frac{d^2}{d\phi^2}[\Psi^2(\phi)\mu(\phi)]-\frac{d}{d\phi}[\Phi(\phi)\mu(\phi)]=0. \qquad (11)$$

The general solution of Eq. (11) is

$$\mu(\phi)=\frac{C}{\Psi^2(\phi)U(\phi)}-\frac{G}{\Psi^2(\phi)U(\phi)}\int^{\phi}U(t)dt, \qquad (12)$$

where $C$, $G$ are integration constants and

$$U(\phi)=\exp\left[-2\int^{\phi}\{\Phi(t)\Psi^{-2}(t)\}dt\right]=\frac{1}{\sin2\phi}\exp\left[\frac{\lambda_2-\lambda_1}{2a}\int^{\cos2\phi}\frac{dt}{1-bt^2/a}\right], \qquad (13)$$

the constants $a$, $b$ being given by

$$a=\frac{1}{8}[2(\lambda_1+\lambda_2+\beta_1+\beta_2)+k^2S(\omega_1\mp\omega_2)],$$

$$b=\frac{1}{8}[2(\lambda_1+\lambda_2+\beta_1+\beta_2)-k^2S(\omega_1\pm\omega_2)].$$

It can be shown (Appendix) that the boundaries $\phi=0$, $\phi=\pi/2$ are both *entrance points*[1] in the sense of Feller (1952), and hence the stationary probability flux represented by $G$ is zero. Thus, there is no accumulation of probability mass at the boundaries, and the $\phi$-process is ergodic throughout the interval $0\le\phi\le\pi/2$. The invariant density $\mu(\phi)$ is therefore given by

$$\mu(\phi)=\frac{C}{\Psi^2(\phi)U(\phi)}, \qquad (14)$$

$C$ being the normalizing constant. Since the constant $a$ is always positive, the form of the integral in Eq. (13) depends on the sign of the constant $b$.

For $b>0$, i.e., $\lambda_1+\lambda_2+\beta_1+\beta_2>k^2S(\omega_1\pm\omega_2)/2$, the invariant density $\mu(\phi)$ is of the form

$$\mu(\phi)=\frac{C\sin2\phi}{\Psi^2(\phi)}\exp\left[\frac{\lambda_1-\lambda_2}{2\sqrt{\Delta}}\tanh^{-1}\frac{b\cos2\phi}{\sqrt{\Delta}}\right],\quad (b>0), \qquad (15a)$$

where $C$ is determined from the normalization condition and is found to be

$$C=\frac{1}{2}(\lambda_1-\lambda_2)\mathrm{csch}\left(\frac{\lambda_1-\lambda_2}{2\sqrt{\Delta}}\tanh^{-1}\frac{b}{\sqrt{\Delta}}\right),\quad (b>0). \qquad (15b')$$

The constant $\Delta$ is defined by $\Delta=ab$.

For $b<0$, the hyperbolic term in (15) is to be replaced appropriately by its trigonometric counterpart, while, for $b=0$, the right-hand side of (15) is replaced by its limit as $b\to 0$. Stated explicitly, these expressions are

$$\mu(\phi)=\frac{C\sin2\phi}{\Psi^2(\phi)}\exp\left[-\frac{\lambda_1-\lambda_2}{2\sqrt{-\Delta}}\tan^{-1}\frac{b\cos2\phi}{\sqrt{-\Delta}}\right],\quad (b<0), \qquad (15a)$$

$$C=\frac{1}{2}(\lambda_1-\lambda_2)\mathrm{csch}\left[\frac{\lambda_1-\lambda_2}{2\sqrt{-\Delta}}\tan^{-1}\frac{b}{\sqrt{-\Delta}}\right],\quad (b<0), \qquad (15b')$$

and

$$\mu(\phi)=\frac{C\sin2\phi}{\Psi^2(\phi)}\exp\left[\frac{(\lambda_1-\lambda_2)\cos2\phi}{2a}\right],\quad (b=0), \qquad (15c)$$

$$C=\frac{1}{2}(\lambda_1-\lambda_2)\mathrm{csch}\left(\frac{\lambda_1-\lambda_2}{2a}\right),\quad (b=0). \qquad (15c')$$

A typical plot of the density $\mu(\phi)$ for the case $b<0$ is shown in Fig. 1 together with the result obtained from a digital simulation of the Itô differential Eq. (7) governing $\phi(t)$.

[1]Physically, it is clear that unless the coupling coefficients $k_{12}$ and $k_{21}$ in Eq. (5) are both zero, it is not possible to have a solution with either $a_1(t)\equiv 0$ or $a_2(t)\equiv 0$. Since $\phi=0$ implies $a_2=0$ and $\phi=\pi/2$ implies $a_1=0$, there can be no accumulation of probability mass at these points.

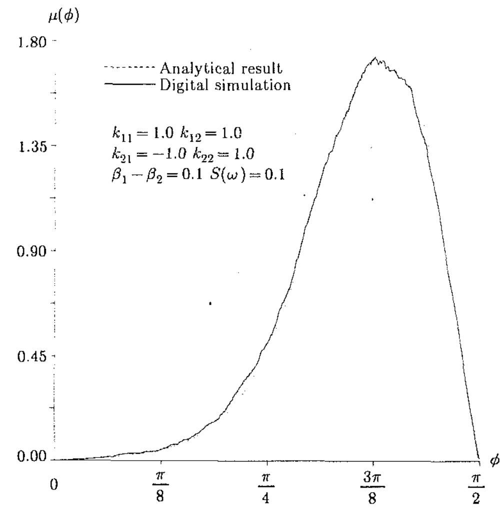


**Fig. 1 Probability density $\mu(\phi)$**

Employing Khas'minskii's (1967) formulation (see also Ariaratnam and Xie, 1990), the largest Lyapunov exponent of system (6) is given by

$$\lambda = E[Q(\phi)] = \int_0^{\pi/2} Q(\phi)\mu(\phi)d\phi. \qquad (16)$$

Substituting from Eqs. (8) and (15) into Eq. (16) and performing the indicated integration yields the following expression for the Lyapunov exponent:

$$\lambda = \frac{1}{2}\left[(\lambda_1+\lambda_2)+(\lambda_1-\lambda_2)\coth\left(\frac{\lambda_1-\lambda_2}{2\sqrt{\Delta}}\tanh^{-1}\frac{b}{\sqrt{\Delta}}\right)\right] \pm \frac{1}{8}k^2S^-, \quad (b>0). \qquad (17a)$$

Again, when $b < 0$, the corresponding trigonometric form is substituted in the right-hand side of Eq. (17$a$) to give:

$$\lambda = \frac{1}{2}\left\{(\lambda_1+\lambda_2)+(\lambda_1-\lambda_2)\coth\left[\frac{\lambda_1-\lambda_2}{2\sqrt{-\Delta}}\tan^{-1}\frac{-b}{\sqrt{-\Delta}}\right]\right\} \pm \frac{1}{8}k^2S^-, \quad (b<0), \qquad (17b)$$

In the exceptional case when $b = 0$, the limiting form of (17$a$) is

$$\lambda = \frac{1}{2}\left[(\lambda_1+\lambda_2)+(\lambda_1-\lambda_2)\coth\frac{4(\lambda_1-\lambda_2)}{k^2S^+}\right] \pm \frac{1}{8}k^2S^-, \quad (b=0). \qquad (17c)$$

Since

$$\Delta = ab = \frac{1}{(32)^2}[k_{11}^2S(2\omega_1)+k_{22}^2S(2\omega_2)\pm 4k^2S(\omega_1-\omega_2)] \cdot [k_{11}^2S(2\omega_1)+k_{22}^2S(2\omega_2)\mp 4k^2S(\omega_1+\omega_2)],$$

it is easy to show that, for $b > 0$,

$$\sqrt{\Delta} = \frac{1}{32}[K^2-4k^4(S^+)^2]^{1/2},$$

where $K = k_{11}^2S(2\omega_1) + k_{22}^2S(2\omega_2) \mp 2k^2S^-$. Let $\gamma$ be defined by

$$\tanh\gamma = \frac{b}{\sqrt{\Delta}} = \left(\frac{b}{a}\right)^{1/2}, \quad (b>0).$$

Since $0 < \sqrt{b/a} < 1$, $0 < \tanh\gamma < 1$, and therefore $0 < \gamma < \infty$. Using an appropriate identity for hyperbolic functions, one obtains

$$\cosh 2\gamma = \frac{k_{11}^2S(2\omega_1)+k_{22}^2S(2\omega_2)\mp 2k^2S^-}{2k^2S^+}.$$

Hence, the Lyapunov exponent (17) can be written as, after defining $\Delta_0 = 16\Delta$,

$$\lambda = \frac{1}{2}\left[(\lambda_1+\lambda_2)+(\lambda_1-\lambda_2)\coth\left(\frac{\lambda_1-\lambda_2}{\Delta_0^{1/2}}\alpha\right)\right] \pm \frac{1}{8}k^2S^-, \quad (b>0),$$

where

$$\alpha = 2\gamma = \cosh^{-1}\left(\frac{K}{2k^2S^+}\right), \quad \Delta_0 = \frac{1}{64}[K^2-4k^4(S^+)^2].$$

For the case $b < 0$, let $\tan\gamma = -b/\sqrt{-\Delta} = \sqrt{-b/a}$, ($b < 0$), which implies that $0 < \gamma < \pi/2$. But $\tan 2\gamma = 2\sqrt{-\Delta}/(a+b)$, which can be positive or negative. The sign of $\tan 2\gamma$, or $\cos 2\gamma$, is determined by the sign of $a + b$. Since $a + b = K/16$, one notes that $\mathrm{sgn}(\cos 2\gamma) = \mathrm{sgn}(\tan 2\gamma) = \mathrm{sgn}(K)$ and therefore $\cos 2\gamma = K/2k^2S^+$. The expression for the largest Lyapunov exponent (17$b$) thus becomes

$$\lambda = \frac{1}{2}\left\{(\lambda_1+\lambda_2)+(\lambda_1-\lambda_2)\coth\left[\frac{\lambda_1-\lambda_2}{(-\Delta_0)^{1/2}}\alpha\right]\right\} \pm \frac{1}{8}k^2S^-, \quad (b<0),$$

where $\alpha = \cos^{-1}(K/2k^2S^+)$.

In summary, taking note of the fact that $k^2 = |k_{12}k_{21}|$, the largest Lyapunov exponent for system (6) is

(i) if $k_{11}^2S(2\omega_1) + k_{22}^2S(2\omega_2) > 4|k_{12}k_{21}|S(\omega_1 \pm \omega_2)$; i.e., $\Delta_0 > 0$,

$$\lambda = \frac{1}{2}\left[(\lambda_1+\lambda_2)+(\lambda_1-\lambda_2)\coth\left(\frac{\lambda_1-\lambda_2}{\Delta_0^{1/2}}\alpha\right)\right] + \frac{1}{8}k_{12}k_{21}S^-, \quad (b>0), \qquad (18a)$$

where $\alpha = \cosh^{-1}(K/2|k_{12}k_{21}|S^+)$;

(ii) if $k_{11}^2S(2\omega_1) + k_{22}^2S(2\omega_2) < 4|k_{12}k_{21}|S(\omega_1 \pm \omega_2)$; i.e., $\Delta_0 < 0$,

$$\lambda = \frac{1}{2}\left\{(\lambda_1+\lambda_2)+(\lambda_1-\lambda_2)\coth\left[\frac{\lambda_1-\lambda_2}{(-\Delta_0)^{1/2}}\alpha\right]\right\} + \frac{1}{8}k_{12}k_{21}S^-, \quad (b<0), \qquad (18b)$$

where $\alpha = \cos^{-1}(K/2|k_{12}k_{21}|S^+)$.

(iii) if $k_{11}^2S(2\omega_1) + k_{22}^2S(2\omega_2) = 4|k_{12}k_{21}|S(\omega_1 \pm \omega_2)$; i.e., $\Delta_0 = 0$,

$$\lambda = \frac{1}{2}\left\{(\lambda_1+\lambda_2)+(\lambda_1-\lambda_2)\coth\left[\frac{4(\lambda_1-\lambda_2)}{|k_{12}k_{21}|S^+}\right]\right\} + \frac{1}{8}k_{12}k_{21}S^-, \quad (b=0). \qquad (18c)$$

The constants $K$ and $\Delta_0$ are defined as

$$K = k_{11}^2S(2\omega_1)+k_{22}^2S(2\omega_2)-2k_{12}k_{21}S^-,$$

$$\Delta_0 = \frac{1}{64}[K^2-4k_{12}^2k_{21}^2(S^+)^2].$$

In conditions (i), (ii), (iii), the upper (plus) sign is to be taken when $k_{12}k_{21} > 0$, and the lower (minus) sign when $k_{12}k_{21} < 0$.

The Lyapunov exponent for a single-degree-of-freedom system, which was first obtained by Stratonovich and Romanov-

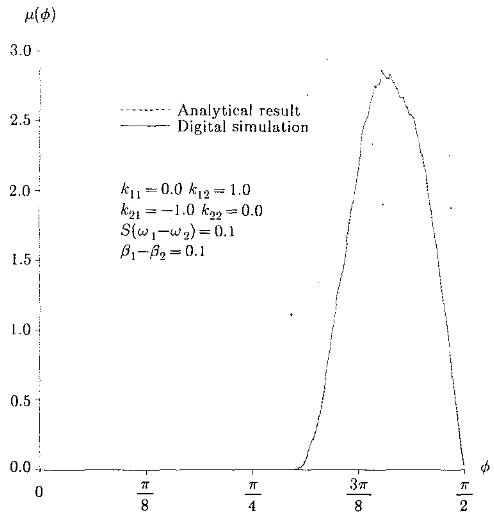

Fig. 2 Probability density $\mu$ ($\phi$)

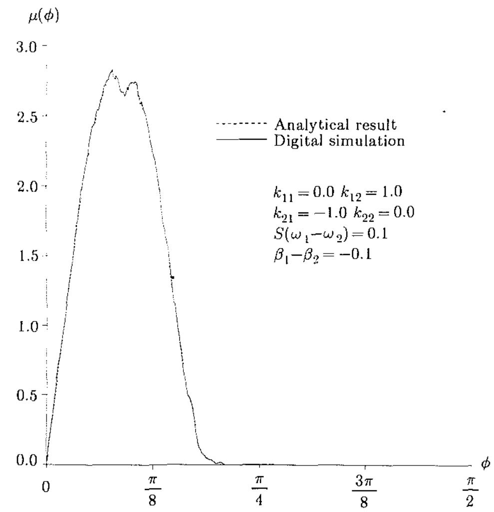

Fig. 3 Probability density $\mu$ ($\phi$)

skii (1958), may be deduced from Eq. (18). Thus, setting the coupling coefficients $k_{12}$, $k_{21}$ to zero, it is evident that $\Delta_0 > 0$, $\alpha \to +\infty$, and Eq. (18*a*) then gives $\lambda = \lambda_1$ if $\lambda_1 > \lambda_2$ and $\lambda = \lambda_2$ if $\lambda_2 > \lambda_1$, confirming that the expression (18) is, in fact, the largest Lyapunov exponent of the system.

The trivial solution $\mathbf{q}(t) = \mathbf{0}$ of Eq. (1) is asymptotically stable w.p.1 if $\lambda$ is negative and unstable w.p.1 if $\lambda$ is positive.

## 4 Singular Case

It was found in Section 2 that $\Psi(\phi)$ vanishes at $\phi_0 = \pi/4$ when

(i) $k_{12}k_{21} > 0$, $k_{11} = k_{22} = 0$, $S(\omega_1 - \omega_2) = 0$,
(ii) $k_{12}k_{21} < 0$, $k_{11} = k_{22} = 0$, $S(\omega_1 + \omega_2) = 0$.

In both cases, $\phi_0 = \pi/4$ is a singular point. To determine the nature of the singular point, the sign of the drift coefficient $\Phi(\phi)$ at this point has to be checked. From Eq. (8), one obtains (see, e.g., Mitchell and Kozin, 1974):

(i) if $\beta_1 > \beta_2$, then $\Phi(\pi/4) > 0$; the singular point $\phi_0 = \pi/4$ is therefore a *right* or *forward shunt*;
(ii) if $\beta_2 > \beta_1$, then $\Phi(\pi/4) < 0$; the singular point $\phi_0 = \pi/4$ is therefore a *left* or *backward shunt*;
(iii) if $\beta_2 = \beta_1 = \beta$, then $\Phi(\pi/4) = 0$; the singular point $\phi_0 = \pi/4$ is therefore a *trap*.

In the following, these three cases will be discussed in some detail.

(*a*) $\beta_1 > \beta_2$. For $\beta_1 > \beta_2$, the singular point $\phi_0 = \pi/4$ is a right shunt. This means that even if an initial point $\phi$ is in the left-half interval $(0, \pi/4)$, it will eventually be shunted across to the right-half interval $(\pi/4, \pi/2)$ and remain there forever. Hence, the probability density $\mu(\phi)$ is concentrated in the right half of the interval $0 \le \phi \le \pi/2$. The density $\mu(\phi)$ of the invariant measure is governed by the Fokker-Planck Eq. (11), whose solution is now of the form

$$\mu(\phi) = \begin{cases} 0, & 0 \le \phi \le \frac{1}{4}\pi, \\ \dfrac{C}{\Psi^2(\phi)U(\phi)}, & \frac{1}{4}\pi < \phi \le \frac{1}{2}\pi, \end{cases} \tag{19}$$

where

$$U(\phi) = \exp\left[-2\int^{\phi} \Phi(t)\Psi^{-2}(t)dt\right] = \frac{1}{\sin 2\phi}\exp\left[-\frac{4(\beta_1-\beta_2)}{k^2S(\omega_1 \pm \omega_2)}\sec 2\phi\right]. \tag{20}$$

The constant $C$ in Eq. (19) is determined by the normalization condition and is found to be

$$C = (\beta_1 - \beta_2)\exp\left[\frac{4(\beta_1-\beta_2)}{k^2S(\omega_1 \pm \omega_2)}\right].$$

A typical plot of the density $\mu(\phi)$ is shown in Fig. 2 together with the result obtained from a digital simulation of the Itô differential Eq. (7) governing $\phi(t)$.

Substituting from Eqs. (8) and (19) in Eq. (16) and performing the indicated integration results in, after replacing $k^2$ by $|k_{12}k_{21}|$,

$$\lambda = -\beta_2 + \frac{1}{8}|k_{12}k_{21}|S(\omega_1 \pm \omega_2), \quad \beta_1 > \beta_2, \tag{21}$$

where the upper sign is taken when $k_{12}k_{21} > 0$, and the lower sign when $k_{12}k_{21} < 0$.

(*b*) $\beta_2 > \beta_1$. For $\beta_2 > \beta_1$, the singular point $\phi = \pi/4$ is a left shunt and the invariant probability density of the $\phi$-process is now concentrated in the left half of the interval $0 \le \phi \le \pi/2$. The density $\mu(\phi)$ of the invariant measure is given by

$$\mu(\phi) = \begin{cases} \dfrac{C}{\Psi^2(\phi)U(\phi)}, & 0 \le \phi < \frac{1}{4}\pi, \\ 0, & \frac{1}{4}\pi \le \phi \le \frac{1}{2}\pi, \end{cases} \tag{22}$$

where $U(\phi)$ is given by Eq. (20). The constant $C$ determined by the normalization condition is

$$C = (\beta_2 - \beta_1)\exp\left[\frac{4(\beta_2-\beta_1)}{k^2S(\omega_1 \pm \omega_2)}\right].$$

Again, to confirm the correctness of the analysis, a typical plot of the density $\mu(\phi)$ along with the result obtained from simulation of the Itô Eq. (7) governing $\phi(t)$ is shown in Fig. 3.

Substituting from Eq. (8) and (22) in Eq. (16), one obtains the largest Lyapunov exponent as

$$\lambda = -\beta_1 + \frac{1}{8}|k_{12}k_{21}|S(\omega_1 \pm \omega_2), \quad \beta_2 > \beta_1. \tag{23}$$

(*c*) $\beta_1 = \beta_2 = \beta$. For $\beta_1 = \beta_2 = \beta$, the singular point $\phi_0 = \pi/4$ is a trap. This means that regardless of where the initial point $\phi$ is situated, it will eventually be attracted to the point $\phi_0 = \pi/4$ and remain there forever. The density $\mu(\phi)$ of the invariant measure is the Dirac delta function concentrated at $\pi/4$:

$$\mu(\phi)=\delta\left(\phi-\frac{1}{4}\pi\right), \quad 0\le\phi\le\frac{1}{2}\pi. \tag{24}$$

From Eqs. (8), (16), and (24), the largest Lyapunov exponent is found to be:

$$\lambda=\int_0^{\pi/2} Q(\phi)\delta\left(\phi-\frac{1}{4}\pi\right)d\phi=Q\left(\frac{1}{4}\pi\right)$$

$$=-\beta+\frac{1}{8}|k_{12}k_{21}|S(\omega_1\pm\omega_2), \quad \beta_1=\beta_2=\beta. \tag{25}$$

It may be noted that the result (25) can also be obtained from either (24) or (23) by taking $\beta_1 = \beta_2 = \beta$.

Again, in Eqs. (21), (23), and (25), the upper sign is to be taken when $k_{12}k_{21} > 0$ and the lower sign when $k_{12}k_{21} < 0$.

## 5 White Noise Excitation

Suppose that the excitation in system (5) represented by $\xi(t)$ is taken to be a wide-band stationary stochastic process with a nearly constant spectral density $S$ over a wide range of frequencies which includes $\omega_1$ and $\omega_2$. Then $\xi(t)$ may be approximated by a white noise process having the spectral density function $S(\omega) = S =$ constant, for all $\omega$. For a white noise process, therefore, $S^+ = 2S$, $S^- = 0$, and Eqs. (8) become

$$Q(\phi)=\lambda_1\cos^2\phi+\lambda_2\sin^2\phi+\Psi^2(\phi),$$

$$\Phi(\phi)=\frac{1}{2}(\lambda_1-\lambda_2)\sin2\phi+\frac{S}{64}[(k_{11}^2+k_{22}^2)\sin4\phi + 16(k_{12}^2\sin^4\phi+k_{21}^2\cos^4\phi)\cot2\phi],$$

$$\Sigma^2(\phi)=\frac{S}{16}[2(k_{11}^2\cos^4\phi+k_{22}^2\sin^4\phi)+(k_{12}^2+k_{21}^2)\sin^22\phi],$$

$$\Psi^2(\phi)=\frac{S}{32}[(k_{11}^2+k_{22}^2)\sin^22\phi+8(k_{12}^2\sin^4\phi+k_{21}^2\cos^4\phi)], \tag{26}$$

where $\lambda_1 = -\beta_1 + Sk_{11}^2/8$, $\lambda_2 = -\beta_2 + Sk_{22}^2/8$.

Since $\Psi(\phi)$ does not vanish in $0 \le \phi \le 1/2\pi$, the diffusion is nonsingular, so that the results obtained in Section 3 can be applied. The largest Lyapunov exponent for system (6) under white noise excitation is found to be:

(i) if $k_{11}^2 + k_{22}^2 > 4|k_{12}k_{21}|$; i.e., $\Delta_0 > 0$,

$$\lambda=\frac{1}{2}\left[(\lambda_1+\lambda_2)+(\lambda_1-\lambda_2)\coth\left(\frac{\lambda_1-\lambda_2}{\Delta_0^{1/2}}\alpha\right)\right], \tag{27a}$$

where $\alpha = \cosh^{-1}(k_{11}^2 + k_{22}^2/4|k_{12}k_{21}|)$;

(ii) if $k_{11}^2 + k_{22}^2 < 4|k_{12}k_{21}|$; i.e., $\Delta_0 < 0$,

$$\lambda=\frac{1}{2}\left[(\lambda_1+\lambda_2)+(\lambda_1-\lambda_2)\coth\left(\frac{\lambda_1-\lambda_2}{(-\Delta_0)^{1/2}}\alpha\right)\right], \tag{27b}$$

where $\alpha = \cos^{-1}(k_{11}^2 + k_{22}^2/4|k_{12}k_{21}|)$;

(iii) if $k_{11}^2 + k_{22}^2 = 4|k_{12}k_{21}|$; i.e., $\Delta_0 = 0$,

$$\lambda=\frac{1}{2}\left\{(\lambda_1+\lambda_2)+(\lambda_1-\lambda_2)\coth\left[\frac{2(\lambda_1-\lambda_2)}{|k_{12}k_{21}|S}\right]\right\}. \tag{27c}$$

The constant $\Delta_0$ is defined as $\Delta_0 = S^2[(k_{11}^2 + k_{22}^2)^2 - 16k_{12}^2k_{21}^2]/64$.

The Lyapunov exponents given by expressions (27) are seen to be the same as those obtained by Ariaratnam et al. (1990). Here they are obtained as a special case of the results for systems under a more general form of excitation.

## 6 Generalization to Multi-Degrees-of-Freedom Systems

Consider now the $n$-degrees-of-freedom system

$$\ddot{q}_i+2\sum_{j=1}^{n}\beta_{ij}\dot{q}_j+\omega_i^2q_i+\omega_i\xi(t)\sum_{j=1}^{n}k_{ij}q_j=0, \ i=1,2,\ldots,n. \tag{1}$$

Suppose the spectral density $S(\omega)$ of $\xi(t)$ has significant values only over a bandwidth $\Delta\omega_0$ around a frequency $\omega_0$ and is zero outside this band, and $S(\omega) = O(\epsilon)$, $0 < |\epsilon| \ll 1$. Then the correlation time $\tau_c$ of the process $\xi(t)$ is $O(1/\Delta\omega_0)$ while the relaxation time $\tau_r$ of the response process $\mathbf{q}(t)$ is $O(1/\epsilon)$. The correlation time $\tau_c$ characterizes the size of the time interval over which significant correlation extends between values of the process $\xi(t)$, while the relaxation time $\tau_r$ measures approximately the time scale over which a significant change of the amplitude of the response process may be observed. Hence, if $\Delta\omega_0 \gg \epsilon$, then $\tau_c \ll \tau_r$. Under this condition, the stochastic averaging procedure used in Section 2 is justified (Stratonovich, 1963).

From the results of the previous sections, the largest Lyapunov exponents for the $n$-degrees-of-freedom system (1) may be deduced:

(a) $k_{ij}k_{ji} > 0$.

If $\omega_0 = \omega_i + \omega_j$,

$$\lambda=-\min(\beta_i,\beta_j)+\frac{1}{8}k_{ij}k_{ji}S(\omega_i+\omega_j), \tag{28}$$

where $\beta_i = \beta_{ii}$.

If $\omega_0 = |\omega_i - \omega_j|$,

$$\lambda=-\frac{1}{2}(\beta_i+\beta_j)-\frac{1}{8}k_{ij}k_{ji}S(\omega_i-\omega_j) +\frac{1}{2}(\beta_i-\beta_j)\coth\left[\frac{4(\beta_i-\beta_j)}{k_{ij}k_{ji}S(\omega_i-\omega_j)}\right]. \tag{29}$$

(b) $k_{ij}k_{ji} < 0$.

If $\omega_0 = |\omega_i - \omega_j|$,

$$\lambda=-\min(\beta_i,\beta_j)-\frac{1}{8}k_{ij}k_{ji}S(\omega_i-\omega_j), \tag{30}$$

If $\omega_0 = \omega_i + \omega_j$,

$$\lambda=-\frac{1}{2}(\beta_i+\beta_j)+\frac{1}{8}k_{ij}k_{ji}S(\omega_i+\omega_j) -\frac{1}{2}(\beta_i-\beta_j)\coth\left[\frac{4(\beta_i-\beta_j)}{k_{ij}k_{ji}S(\omega_i+\omega_j)}\right]. \tag{31}$$

(c) $\omega_0 = 2\omega_i$.

$$\lambda=\lambda_i=-\beta_i+\frac{1}{8}k_{ii}^2S(2\omega_i). \tag{32}$$

This last result can also be obtained from Eq. (28) or (31) by taking $i = j$.

## 7 Application: Flexural-Torsional Stability of a Rectangular Beam

As an application, the flexural-torsional stability of a simply supported, uniform, narrow, rectangular, elastic beam of length $L$ subjected to a stochastically varying concentrated load $P(t)$ acting at the center of the beam cross-section as shown in Fig. 4 is considered. Both *non-follower* and *follower* loading cases are studied.

### 7.1 Formulation.

***Non-Follower Force Case.*** For non-follower force, the lateral deflection $u(t)$ and the angle of twist $\psi(t)$ of a transverse cross-section $z =$ constant are governed by the equations of motion (see, e.g., Bolotin (1964) and Fu and Nemat-Nasser (1972)):

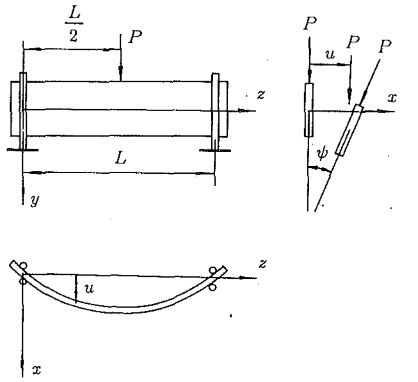


Fig. 4 Loaded rectangular strip in flexural-torsional deformation

$$EI_y \frac{\partial^4 u}{\partial z^4} + \frac{\partial^2 (M_x \psi)}{\partial z^2} + m \frac{\partial^2 u}{\partial t^2} + D_u \frac{\partial u}{\partial t} = 0,$$
$$- GJ \frac{\partial^2 \psi}{\partial z^2} + M_x \frac{\partial^2 u}{\partial z^2} + mr^2 \frac{\partial^2 \psi}{\partial t^2} + D_\psi \frac{\partial \psi}{\partial t} = 0, \quad (33)$$

where

$$M_x = \begin{cases} \frac{1}{2} Pz, & 0 \le z \le \frac{1}{2} L, \\ \frac{1}{2} P(L-z), & \frac{1}{2} L \le z \le L, \end{cases}$$

and $EI_y$, $GJ$ denote the relevant flexural and torsional rigidities of the cross-section, $D_u$, $D_\psi$ the viscous damping coefficients, $m$ the mass per unit length, and $r$ the polar radius of gyration of the cross-section.

The conditions of simple support at the ends imply the boundary conditions:

$$u(0,t) = u(L,t) = u''(0,t) = u''(L,t) = 0,$$
$$\psi(0,t) = \psi(L,t) = 0. \quad (34)$$

Considering the fundamental mode, the above boundary conditions are satisfied by taking

$$u(z,t) = Krq_1(t) \sin \frac{\pi z}{L}, \quad \psi(z,t) = q_2(t) \sin \frac{\pi z}{L}. \quad (35)$$

Substituting (35) in the equations of motion (33) and employing the Galerkin method lead to

$$\ddot{q}_1 + 2\beta_1 \dot{q}_1 + \omega_1^2 q_1 - \frac{1}{K} \omega_1 \omega_2 \xi(t) q_2 = 0,$$
$$\ddot{q}_2 + 2\beta_2 \dot{q}_2 + \omega_2^2 q_2 - K \omega_1 \omega_2 \xi(t) q_1 = 0, \quad (36)$$

where

$$\omega_1^2 = \frac{EI_y}{m} \left(\frac{\pi}{L}\right)^4, \quad \omega_2^2 = \frac{GJ}{mr^2} \left(\frac{\pi}{L}\right)^2, \quad 2\beta_1 = \frac{D_u}{m},$$
$$2\beta_2 = \frac{D_\psi}{mr^2}, \quad \xi(t) = \frac{P(t)}{P_{cr}}, \quad P_{cr} = \frac{8mrL\omega_1\omega_2}{4+\pi^2}.$$

Here, $P_{cr}$ is the value of the critical non-follower force at which static buckling will occur. By choosing the constant $K = -(\omega_2/\omega_1)^{1/2}$, one obtains

$$\ddot{q}_1 + 2\beta_1 q_1 + \omega_1^2 q_1 + \omega_1 k_{12} \xi(t) q_2 = 0,$$
$$\ddot{q}_2 + 2\beta_2 q_2 + \omega_2^2 q_2 + \omega_2 k_{21} \xi(t) q_1 = 0, \quad (37)$$

where $k_{12} = k_{21} = (\omega_1\omega_2)^{1/2} = k_N$. Equations (37) are of the form (5) with $k_{11} = k_{22} = 0$.

*Follower Force Case.* For follower force case, the equations of motion governing the lateral deflection $u(z, t)$ and the angle of twist $\psi(z, t)$ are

$$EI_y \frac{\partial^4 u}{\partial z^4} + \frac{\partial^2 (M_x \psi)}{\partial z^2} + P\psi_m \delta\left(z - \frac{1}{2} L\right) + m \frac{\partial^2 u}{\partial t^2} + D_u \frac{\partial u}{\partial t} = 0,$$
$$- GJ \frac{\partial^2 \psi}{\partial z^2} + M_x \frac{\partial^2 u}{\partial z^2} + mr^2 \frac{\partial^2 \psi}{\partial t^2} + D_\psi \frac{\partial \psi}{\partial t} = 0, \quad (38)$$

where $\psi_m$ is the value of $\psi(z, t)$ at $z = L/2$, $\delta(z - L/2)$ is the Dirac delta function centered at $z = L/2$, and $M_x$ is the same as for non-follower force.

Substituting the fundamental mode (35) in the equations of motion (38), and applying the Galerkin method results in

$$\ddot{q}_1 + 2\beta_1 q_1 + \omega_1^2 q_1 + \omega_1 K_{12} \xi(t) q_2 = 0,$$
$$\ddot{q}_2 + 2\beta_2 q_2 + \omega_2^2 q_2 + \omega_2 K_{21} \xi(t) q_1 = 0, \quad (39)$$

where

$$\omega_1^2 = \frac{EI_y}{m} \left(\frac{\pi}{L}\right)^4, \quad \omega_2^2 = \frac{GJ}{mr^2} \left(\frac{\pi}{L}\right)^2, \quad 2\beta_1 = \frac{D_u}{m}, \quad 2\beta_2 = \frac{D_\psi}{mr^2},$$

$$\xi(t) = \frac{P(t)}{P_{cr}}, \quad P_{cr} = \frac{4mrL|\omega_1^2 - \omega_2^2|}{[(12-\pi^2)(4+\pi^2)]^{1/2}},$$

$$K_{12} = \frac{|\omega_1^2 - \omega_2^2|}{2K\omega_1} \left(\frac{12-\pi^2}{4+\pi^2}\right)^{1/2}, \quad K_{21} = -\frac{K|\omega_1^2 - \omega_2^2|}{2\omega^2} \left(\frac{4+\pi^2}{12-\pi^2}\right)^{1/2}.$$

Here, $P_{cr}$ is the value of the critical follower force at which static buckling will occur. Choosing the constant

$$K = \left(\frac{\omega_2}{\omega_1} \frac{12-\pi^2}{4+\pi^2}\right)^{1/2},$$

the equations of motion are again of the form of (5), in which

$$k_{12} = -k_{21} = \frac{|\omega_1^2 - \omega_2^2|}{2(\omega_1\omega_2)^{1/2}} = k_F, \quad k_{11} = k_{22} = 0.$$

**7.2 Lyapunov Exponent and Stochastic Stability.** If the stochastic process $\xi(t)$ is stationary, with mean zero, the results obtained in Sections 3 and 4 may be used to obtain the largest Lyapunov exponent of the system and hence the condition for almost-sure asymptotic stability.

*Non-Follower Force Case.* For the non-follower force case, $k_{11} = k_{22} = 0$, $k_{12} = k_{21} = k_N = (\omega_1\omega_2)^{1/2}$, so that

$$\lambda_1 = -\beta_1, \quad \lambda_2 = -\beta_2, \quad \Delta_0 = -\frac{1}{16} k_{12}^2 k_{21}^2 [(S^+)^2 - (S^-)^2] < 0.$$

Substituting these values in Eq. (18$b$) leads to

$$\lambda = -\frac{1}{2}\Bigg\{(\beta_1 + \beta_2) - (\beta_1 - \beta_2) \coth\left[\frac{4(\beta_1 - \beta_2)}{k_{12}k_{21}[(S^+)^2 - (S^-)^2]^{1/2}} \alpha\right]\Bigg\} + \frac{1}{8} k_{12}k_{21}S^-, \quad (40)$$

where $\alpha = \cos^{-1}[-(S^-/S^+)]$.

The boundary of almost-sure stability is obtained by setting $\lambda = 0$, which is found to be

$$-\frac{\beta_1 + \beta_2}{k_{12}k_{21}S^+} + \frac{\beta_1 - \beta_2}{k_{12}k_{21}S^+} \coth\left\{\frac{4(\beta_1 - \beta_2)}{k_{12}k_{21}S^+} \times \frac{1}{[1-(S^-/S^+)]^{1/2}} \cos^{-1}\left(-\frac{S^-}{S^+}\right)\right\} + \frac{1}{4}\frac{S^-}{S^+} = 0.$$

By defining

$$\beta_i^* = \frac{1}{[1-(S^-/S^+)]^{1/2}} \cos^{-1}\left(-\frac{S^-}{S^+}\right) \left(\frac{8\beta_i}{k_{12}k_{21}S^+} - \frac{S^-}{S^+}\right), \quad i = 1,2,$$

the stability boundary may be expressed in the form

$$\beta_1^* e^{-\beta_1^*} = \beta_2^* e^{-\beta_2^*}. \quad (41)$$

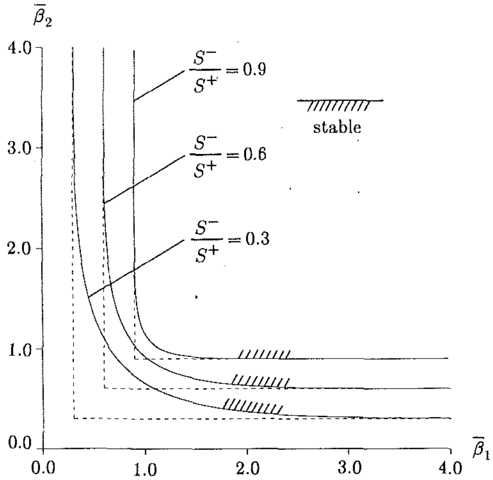


Fig. 5(*a*) Stability boundaries for non-follower force case $k_{12}k_{21} > 0$

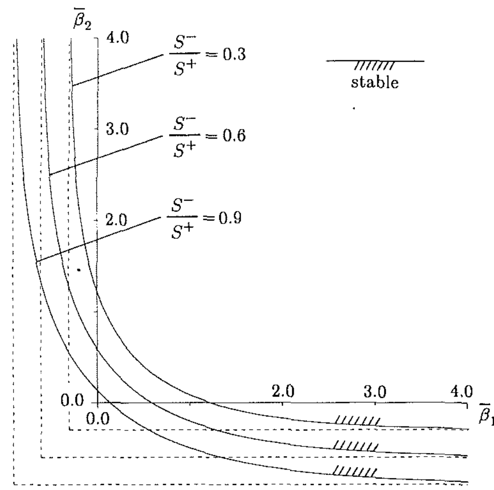


Fig. 6(*a*) Stability boundaries for follower force case $k_{12}k_{21} < 0$

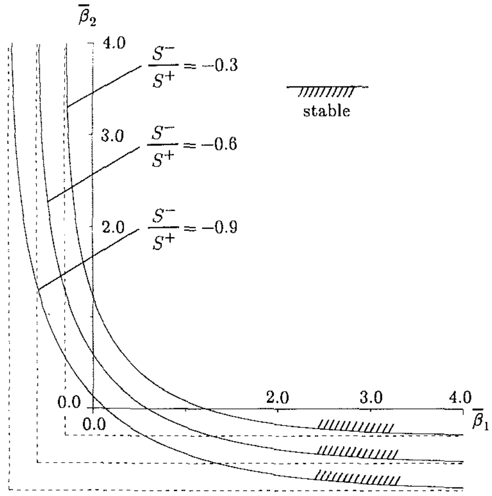


Fig. 5(*b*) Stability boundaries for non-follower force case $k_{12}k_{21} > 0$

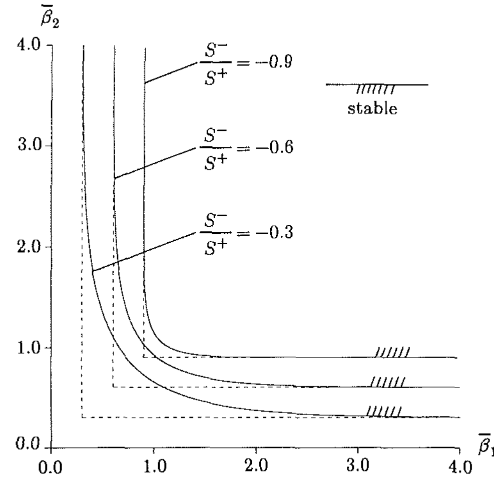


Fig. 6(*b*) Stability boundaries for follower force case $k_{12}k_{21} < 0$

By solving Eq. (41), the stability boundary is obtained in terms of $\beta_1^*$ and $\beta_2^*$, or in terms of $\bar\beta_1$ and $\bar\beta_2$, where

$$\bar\beta_i=\frac{8\beta_i}{k_{12}k_{21}S^+}=\frac{S^-}{S^+}+\frac{[1-(S^-/S^+)]^{1/2}}{\cos^{-1}(-S^-/S^+)}\,\beta_i^*,\quad i=1,2. \tag{42}$$

Typical plots are shown in Figs. 5(*a*) and (*b*) for $S^-$ positive and negative, respectively. It can be seen that if $S^- < 0$, the effect of the stochastic disturbance can be stabilizing, while if $S^- > 0$, the stochastic excitation always destabilizes the system.

*Follower Force Case.* For the follower force case, $k_{11} = k_{22} = 0$, $k_{12} = -k_{21} = k_F = |\omega_1^2 - \omega_2^2|/2(\omega_1\omega_2)^{1/2}$, so that

$$\lambda_1=-\beta_1,\quad \lambda_2=-\beta_2,\quad \Delta_0=-\frac{1}{16}\,k_{12}^2k_{21}^2[(S^+)^2-(S^-)^2]<0.$$

Substituting these values in Eq. (18*b*) leads to

$$\lambda=-\frac{1}{2}\Bigg\{(\beta_1+\beta_2)$$
$$-(\beta_1-\beta_2)\coth\left[\frac{4(\beta_1-\beta_2)}{|k_{12}k_{21}|[(S^+)^2-(S^-)^2]^{1/2}}\,\alpha\right]\Bigg\}+\frac{1}{8}\,k_{12}k_{21}S^-, \tag{43}$$

where $\alpha = \cos^-(S^-/S^+)$.

Following the procedure as for the non-follower force, the boundary of almost-sure stability is found by setting $\lambda = 0$ and is given by Eq. (41) in which $\beta_1^*$ and $\beta_2^*$ are

$$\beta_i^*=\frac{1}{[1-(S^-/S^+)]^{1/2}}\cos^{-1}\left(-\frac{S^-}{S^+}\right)\times\left(\frac{8\beta_i}{|k_{12}k_{21}|S^+}+\frac{S^-}{S^+}\right),\quad i=1,2.$$

After solving the transcendental equation for the stability boundary in terms of $\beta_1^*$, $\beta_2^*$, one can obtain the stability boundaries in terms of $\bar\beta_1$, $\bar\beta_2$ for different values of $S^-/S^+$, where

$$\bar\beta_i=\frac{8\beta_i}{|k_{12}k_{21}|S^+}=-\frac{S^-}{S^+}+\frac{[1-(S^-/S^+)]^{1/2}}{\cos^{-1}(-S^-/S^+)}\,\beta_i^*,\quad i=1,2. \tag{44}$$

Some typical curves are shown in Figs. 6(*a*) and (*b*) for $S^-$ positive and negative, respectively. It may be noted that if $S^- > 0$, the effect of the stochastic disturbance can be stabilizing, while if $S^- < 0$, the stochastic excitation always destabilizes the system, which are opposite to those found in the case of non-follower force.

In the special case when the stochastic process $\xi(t)$ is stationary, with mean zero, and possesses a constant spectral density $S$ over a sufficiently wide band of frequencies, it can

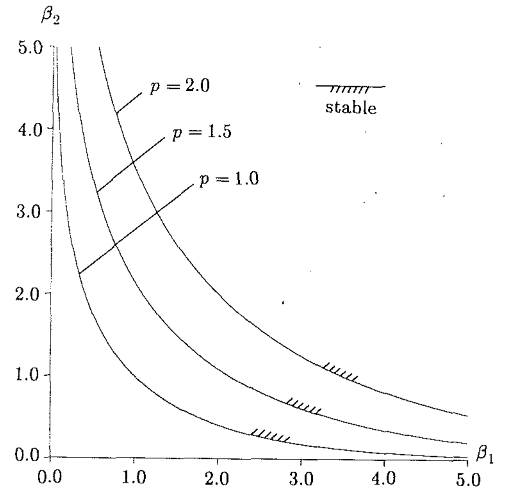


**Fig. 7 Stability boundaries under white noise excitation**

be approximated by a white noise process. For white noise excitation, the expression for the largest Lyapunov exponent is of the same form for both non-follower and follower forces, and is, from Eq. (27), given by

$$\lambda = -\frac{1}{2}\left[(\beta_1+\beta_2)-(\beta_1-\beta_2)\coth\frac{\pi(\beta_1-\beta_2)}{|k_{12}k_{21}|S}\right]. \qquad (45)$$

By making $S \to 0$ in Eq. (45), the results for the deterministic case may be recovered; thus, if $\beta_1 > \beta_2$, $\lambda \to -\beta_2$ and if $\beta_2 > \beta_1$, $\lambda \to -\beta_1$ as expected.

The boundary of almost-sure stability obtained by setting $\lambda = 0$ is found to be given by Eq. (41) in terms of $\beta_1^*$ and $\beta_2^*$, where $\beta_i^* = (1/p)\beta_i$, $i = 1, 2$, $p = |k_{12}k_{21}|S/2\pi$. Hence, after solving Eq. (41) for the stability boundary in terms of $\beta_1^*$, $\beta_2^*$, one can determine the stability boundaries in terms of $\beta_1$, $\beta_2$, which are shown in Fig. 7 for different values of the excitation parameter $p$.

## 8 Conclusion

A method of calculating the Lyapunov exponents of a class of two-degrees-of-freedom systems subjected to random parametric excitation has been presented. Explicit expressions for the largest Lyapunov exponent, valid in the first approximation, have been obtained and applied to an example in the stochastic stability of elastic structures. The method has also been extended to certain multi-degrees-of-freedom linear systems.


## Acknowledgment

This research was supported by the Natural Sciences and Engineering Research Council of Canada through Grant No. A-1815.


## References


Ariaratnam, S. T., 1977, Discussion to paper by Kozin and Sugimoto, *Stochastic Problems in Dynamics*, B. L. Clarkson, ed., Pitman Press, p. 34.

Ariaratnam, S. T., and Srikantaiah, T. K., 1978, "Parametric Instabilities in Elastic Structures Under Stochastic Loading," *Journal of Structural Mechanics*, Vol. 6, No. 4, pp. 349–365.

Ariaratnam, S. T., Tam, D. S. F., and Xie, Wei-Chau, 1990; "Lyapunov Exponents and Stochastic Stability of Coupled Linear Systems," *Probabilistic Engineering Mechanics*, Vol. 6, No. 2, pp. 51–56.

Ariaratnam, S. T., and Xie, Wei-Chau, 1989, "Stochastic Perturbation of Pitchfork Bifurcations," *Structural Safety*, Vol. 6, pp. 205–210.

Ariaratnam, S. T., and Xie, Wei-Chau, 1990, "Lyapunov Exponent and Rotation Number of a Two-Dimensional Nilpotent Stochastic System," *Dynamics and Stability of Systems*, Vol. 5, No. 1, pp. 1–9.

Arnold, L., Papanicolaou, G., and Wihstutz, V., 1986, "Asymptotic Analysis of the Lyapunov Exponent and Rotation Number of the Random Oscillator and Applications," *SIAM Journal of Applied Mathematics*, Vol. 46, No. 3, pp. 427–450.

Auslender, E. I., and Mil'shtein, G. N., 1983, "Asymptotic Expansions of the Lyapunov Index for Linear Stochastic Systems with Small Noise," *Journal of Applied Mathematics and Mechanics* (*PMM*), Vol. 46, pp. 277–283 (English translation).

Bolotin, V. V., 1964, *The Dynamic Stability of Elastic Systems*, Holden-Day, Inc.

Fu, F. C. L., and Nemat-Nasser, S., 1972, "On the Stability of Steady-State Response of Certain Nonlinear Dynamic Systems Subjected to Harmonic Excitations," *Ingeneur-Archiv*, Vol. 41, No. 6, pp. 407–420.

Gikhman, I. I., and Skorokhod, A. V., 1972, *Stochastic Differential Equations*, Springer-Verlag, New York.

Karlin, S., and Taylor, H., 1981, *A Second Course in Stochastic Processes*, Academic Press, New York.

Khas'minskii, R. Z., 1966, "A Limit Theorem for the Solutions of Differential Equations with Random Right-Hand Sides," *Theory of Probability and Its Applications*, Vol. 11, pp. 309–406 (English translation).

Khas'minskii, R. Z., 1967, "Necessary and Sufficient Conditions for the Asymptotic Stability of Linear Stochastic Systems," *Theory of Probability and Its Applications*, Vol. 12, pp. 144–147 (English translation).

Mettler, E., 1968, "Combination Resonances in Mechanical Systems Under Harmonic Excitation," *Proceedings of the 4th Conference on Nonlinear Oscillation*, Academia Publication House, pp. 51–70.

Mitchell, R. R., and Kozin, F., 1974, "Sample Stability of Second-Order Linear Differential Equations with Wide-Band Noise Coefficients," *SIAM Journal of Applied Mathematics*, Vol. 27, No. 4, pp. 571–604.

Pardoux, E., and Wihstutz, V., 1988, "Lyapunov Exponent and Rotation Number of Two-Dimensional Linear Stochastic Systems with Small Diffusion," *SIAM Journal of Applied Mathematics*, Vol. 48, No. 2, pp. 442–457.

Stratonovich, R. L., and Romanovskii, Yu.M., 1958, "Parametric Effect of a Random Force on Linear and Non-Linear Oscillatory Systems," *Nauchnye doklady vysshei shkoly fiziko-mat. nauk.*, Vol. 3, (reprinted in *Non-Linear Transformations of Stochastic Processes*, P. I. Kuznetsov, R. L. Stratonovich, and V. I. Tikhonov, eds., Pergamon Press, pp. 322–326, English translation).

Wedig, W., 1988, "Lyapunov Exponents of Stochastic Systems and Related Bifurcation Problems," *Stochastic Structural Dynamics—Progress in Theory and Applications*, S. T. Ariaratnam, G. I. Schuëller, and I. Elishakoff, eds., Elsevier Applied Science, pp. 315–327.


## APPENDIX

The procedure described by Karlin and Taylor (1981) is followed to establish the nature of the boundaries $\phi = 0$, $\phi = \pi/2$ of the diffusion process $\phi(t)$ defined by the second equation of (7).

The scale density $U(\phi)$ is as given by Eq. (13)

$$U(\phi) = \exp\left[-2\int^{\phi}\Phi(\theta)\Psi^{-2}(\theta)d\theta\right]$$

$$= \begin{cases} \dfrac{1}{\sin 2\phi}\exp\left[-\dfrac{\lambda_1-\lambda_2}{2\sqrt{\Delta}}\tanh^{-1}\dfrac{b\cos 2\phi}{\sqrt{\Delta}}\right], & b>0, \\[2ex] \dfrac{1}{\sin 2\phi}\exp\left[\dfrac{\lambda_1-\lambda_2}{2\sqrt{-\Delta}}\tan^{-1}\dfrac{b\cos 2\phi}{\sqrt{-\Delta}}\right], & b<0, \\[2ex] \dfrac{1}{\sin 2\phi}\exp\left[-\dfrac{(\lambda_1-\lambda_2)\cos 2\phi}{2a}\right], & b=0. \end{cases}$$

Hence, there exist positive constants $K_1$, $K_2$ such that

$$K_1\operatorname{cosec} 2\phi \le U(\phi) \le K_2\operatorname{cosec} 2\phi.$$

The scale measure $S[\phi_1, \phi_2]$ of the $\phi$-process is defined by

$$S[\phi_1, \phi_2] = \int_{\phi_1}^{\phi_2} U(\phi)d\phi.$$

Hence, if $0 < \phi < \pi/2$,

$$S(0,\phi] = \int_0^{\phi} U(\phi)d\phi \geq \int_0^{\phi} K_1 \mathrm{cosec} 2\phi d\phi = \infty,$$

and

$$S\left[\phi, \frac{1}{2}\pi\right) = \int_{\phi}^{1/2\pi} U(\phi)d\phi \geq \int_{\phi}^{1/2\pi} K_1 \mathrm{cosec} 2\phi d\phi = \infty.$$

These boundaries are therefore *natural* under the Gikhman-Skorokhod classification (Gikhman and Skorokhod, 1972).

To further determine whether they are also entrance boundaries as defined by Feller it is necessary to consider the speed measure defined by

$$M[\phi_1,\phi_2] = \int_{\phi_1}^{\phi_2} \frac{1}{\Psi^2(\phi)U(\phi)} d\phi,$$

and the integrals

$$N(0) = \int_0^{\phi} U(\theta)M(0,\theta]d\theta,$$

and

$$N\left(\frac{1}{2}\pi\right) = \int_{\phi}^{1/2\pi} U(\theta)M\left[\theta, \frac{1}{2}\pi\right)d\theta.$$

The quantities $N(0)$ and $N(\pi/2)$ approximately measure the time it takes to reach an interior point $\phi$, $0 < \phi < \pi/2$, starting at the boundary points $\phi = 0$ and $\phi = \pi/2$, respectively. If these times are finite, then the boundaries are classified as entrance boundaries. It is found that

$$M[\phi_1,\phi_2]$$
$$= \begin{cases} -\dfrac{1}{\lambda_1-\lambda_2}[e^u]_{\phi_1}^{\phi_2}, & u = \dfrac{\lambda_1-\lambda_2}{2\sqrt{\Delta}}\tanh^{-1}\dfrac{b\cos 2\phi}{\sqrt{\Delta}}, \quad b>0, \\ \dfrac{1}{\lambda_1-\lambda_2}[e^u]_{\phi_1}^{\phi_2}, & u = \dfrac{\lambda_1-\lambda_2}{2\sqrt{-\Delta}}\tan^{-1}\dfrac{b\cos 2\phi}{\sqrt{-\Delta}}, \quad b<0, \\ -\dfrac{1}{\lambda_1-\lambda_2}[e^u]_{\phi_1}^{\phi_2}, & u = \dfrac{(\lambda_1-\lambda_2)\cos 2\phi}{2a}, \quad b=0. \end{cases}$$
$$= K[e^{u(\phi_2)} - e^{u(\phi_1)}] \geq 0.$$

Hence,

$$N(0) = \int_0^{\phi} U(\theta)M(0,\theta]d\theta$$
$$\leq \int_0^{\phi} \frac{KK_2}{\sin 2\theta}[e^{u(\theta)} - e^{u(0)}]d\theta,$$

and since

$$\lim_{\epsilon\to 0^+} \frac{e^{u(\epsilon)} - e^{(0)}}{\sin 2\epsilon} = \lim_{\epsilon\to 0^+} \frac{u'(\epsilon)e^{u(\epsilon)}}{2\cos 2\epsilon} < \infty,$$

(i.e., positively bounded),

the integral is a positively bounded function in $[0, \phi]$, so that $N(0) < \infty$. Therefore, $\phi = 0$ is an *entrance* boundary in the sense of Feller. Similar arguments can be applied to $N(\pi/2)$ to confirm that $\phi = \pi/2$ is an entrance boundary.

Journal of Applied Mechanics

# Brief Notes

A Brief Note is a short paper that presents a specific solution of technical interest in mechanics but which does not necessarily contain new general methods or results. A Brief Note should not exceed 1500 words *or equivalent* (a typical one-column figure or table is equivalent to 250 words; a one line equation to 30 words). Brief Notes will be subject to the usual review procedures prior to publication. After approval such Notes will be published as soon as possible. The Notes should be submitted to the Technical Editor of the JOURNAL OF APPLIED MECHANICS. Discussions on the Brief Notes should be addressed to the Editorial Department, ASME, United Engineering Center, 345 East 47th Street, New York, N. Y. 10017, or to the Technical Editor of the JOURNAL OF APPLIED MECHANICS. Discussions on Brief Notes appearing in this issue will be accepted until two months after publication. Readers who need more time to prepare a Discussion should request an extension of the deadline from the Editorial Department.

## A Follower Load Buckling Problem for Rectangular Plates

**Eric Reissner**[1] **and Frederic Y. M. Wan**[2]

### Introduction

In what follows, we consider a rectangular elastic plate with two opposite edges simply supported and with the other two edges acted upon by a uniform distribution of equal and opposite in-plane normal edge stress resultants. In order to determine the buckling values of these edge stress resultants, it is necessary to stipulate their direction during the process of buckling. One possible assumption is that they remain parallel to the plane of the unbuckled plate, the same as in the determination of the Euler load for a cantilever beam. The solution for this "non-follower" edge load plate problem has been given by Woinowsky-Krieger (1951).

An alternate stipulation for the applied edge loads is that they are of the follower type, with their directions remaining tangent to the plate surface during the process of buckling. It is well known that there is no static buckling load for the corresponding follower load cantilever *beam* buckling problem. The follower load plate buckling problem with which we are concerned here is mentioned in Woinowsky-Krieger (1951), with a statement which reads in free translation: *"It would not be difficult to show that there are no static follower type buckling loads for this plate problem, similar to the corresponding result for the cantilever beam buckling problem."* The results in Woinowsky-Krieger (1951) for the non-follower load problem are reproduced in Timoshenko and Gere (1961) without mention of the possibility, or impossibility, of follower load instabilities.

In this Note we show that the indicated static follower load problem—which may be of intrinsic rather than of practical interest—is in fact associated with finite buckling loads, and we determine numerical values and asymptotic expressions for these loads.

[1]Department of Applied Mechanics and Engineering Sciences, University of California, San Diego, La Jolla, CA 92093. Fellow ASME.

[2]Department of Applied Mathematics, University of Washington, Seattle, WA 98195. Fellow ASME.

Manuscript received by the ASME Applied Mechanics Division, Sept. 6, 1990; final revision, Mar. 18, 1991. Associate Technical Editor: J. G. Simmonds.

### Differential Equations and Boundary Conditions

We consider a uniform isotropic plate with midplane coordinates $x$ and $y$, with simply supported edges $x = 0$, $a$ and with the edges $y = \pm b/2$ acted upon by uniform thrusts $N$. The differential equation for this plate buckling problem is

$$D\nabla^2\nabla^2 w + Nw_{,yy} = 0. \tag{1}$$

The associated conditions of simple support are

$$x=0,\ a: \quad w=0, \quad D(w_{,xx}+\nu w_{,yy})=0. \tag{2}$$

The conditions at the loaded edges of the plate are

$$y=\pm\frac{b}{2}: \begin{cases} D(w_{,yy}+\nu w_{,xx})=0 \\ D[w_{,yyy}+(2-\nu)w_{,yxx}]+\epsilon N w_{,y}=0. \end{cases} \tag{3}$$

In these equations, $D$ is the plate-bending stiffness factor, $\nu$ is Poisson's ratio, and $\epsilon$ has the value 0 or 1. When $\epsilon = 1$, we have the non-follower load case with the edge loads $N$ remaining parallel to the undeflected midplane of the plate. When $\epsilon = 0$, we have the follower load case, with the edge loads remaining tangent to the deflected midsurface of the plate. We do not, in this Note, concern ourselves with problems corresponding to other values of $\epsilon$.

### The Condition of Buckling

We satisfy (1) and (2) by stipulating

$$w(x,y) = \sin(\pi x/a) f(\pi y/a). \tag{4}$$

With $\pi y/a = \xi$ and $(\,)_{,y} = (\pi/a)(\,)_{,\xi} \equiv (\pi/a)(\,)'$ we then obtain from (1), as a differential equation for $f(\xi)$,

$$f'''' - (2-k)f'' + f = 0, \tag{5}$$

where $k = Na^2/\pi^2 D$.

The boundary conditions at $y = \pm b/2$ become conditions for $\xi = \pm(\pi/2)(b/a) \equiv \pm\lambda$, of the form

$$f''(\pm\lambda) - \nu f(\pm\lambda) = f'''(\pm\lambda) - \rho f'(\pm\lambda) = 0 \tag{6}$$

where $\rho = 2 - \nu - \epsilon k$.

The solution of (5) can be written in the form

$$f = c_o \sinh(r\xi) + \bar{c}_o \sinh(\bar{r}\xi) + c_e \cosh(r\xi) + \bar{c}_e \cosh(\bar{r}\xi) \tag{7}$$

where (—) denotes the complex conjugate of ( ) and

$$r^2 = 1 - \frac{1}{2}k + i\sqrt{1-\left(1-\frac{1}{2}k\right)^2}. \tag{8}$$

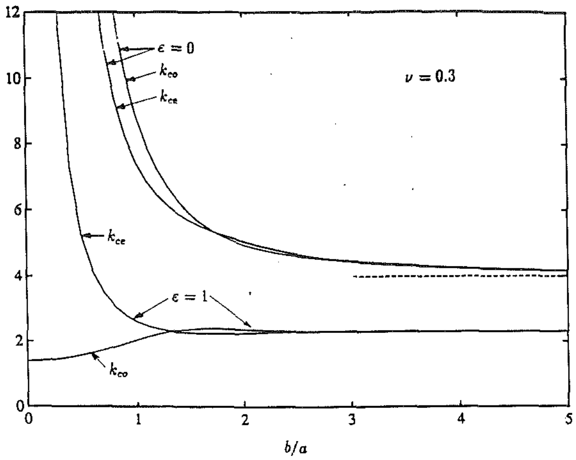


Fig. 1 The dependence of the critical loads $k_{ce}$ and $k_{co}$ on the aspect ratio $b/a$ for $\nu = 0.3$

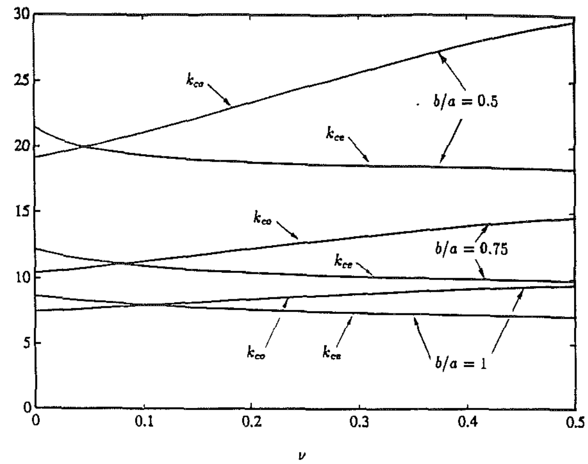


Fig. 3 The dependence of the critical loads $k_{ce}$ and $k_{co}$ on Poisson's ratio $\nu$ for $b/a = 0.5, 0.75$, and $1.0$

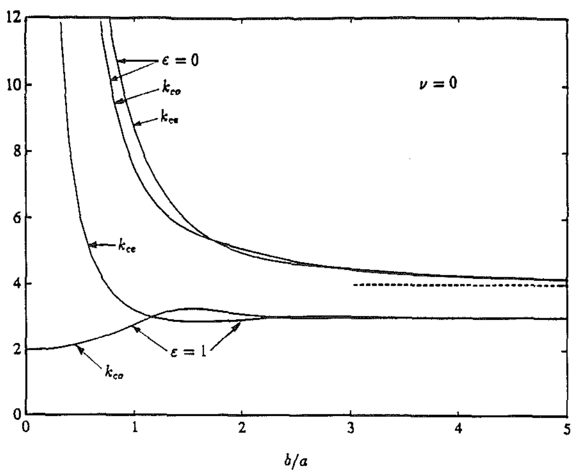


Fig. 2 The dependence of the critical loads $k_{ce}$ and $k_{co}$ on the aspect ratio $b/a$ for $\nu = 0$

When $4 < k$, which turns out to be the range of $k$-values of interest here, it is preferable to write

$$f = c_{1o}\sin({}_1\xi) + c_{2o}\sin(p_2\xi) + c_{1e}\cos(p_1\xi) + c_{2e}\cos(p_2\xi) \tag{9}$$

where

$$\begin{pmatrix} p_1^2 \\ p_2^2 \end{pmatrix} = \frac{1}{2}k - 1 \pm \sqrt{\left(\frac{1}{2}k - 1\right)^2 - 1}. \tag{10}$$

Introduction of (9) into (6) and a separate consideration of the even and odd buckling modes give the following conditions for the determination of the critical values of $k$ in the range $4 < k$. For the even modes, we have

$$\begin{aligned} G_e(k) \equiv 2 &\begin{vmatrix} (p_1^2+\nu)\cos(\lambda p_1) & (p_2^2+\nu)\cos(\lambda p_2) \\ (p_1^3+\rho p_1)\sin(\lambda p_1) & (p_2^3+\rho p_2)\sin(\lambda p_2) \end{vmatrix} \\ &= \sqrt{k-4}\,[(1-\nu)^2 - \nu k - \epsilon(1-\nu)k]\,\sin(\lambda\sqrt{k}) \\ &\quad - \sqrt{k}\,[(1-\nu)(3+\nu) + \nu k - \epsilon(1+\nu)k]\,\sin(\lambda\sqrt{k-4}) = 0. \end{aligned} \tag{11}$$

The corresponding condition for the odd modes[3] comes out to be

$$\begin{aligned} G_o(k) \equiv \sqrt{k}\,&[(3+\nu)(1-\nu) + \nu k - \epsilon(1+\nu)k]\,\sin(\lambda\sqrt{k-4}) \\ &+ \sqrt{k-4}\,[(1-\nu)^2 - \nu k - \epsilon(1-\nu)k]\,\sin(\lambda\sqrt{k}) = 0. \end{aligned} \tag{12}$$

Similarly, introduction of (7) into (6) gives as the condition for the determination of the even-mode critical values of $k$ in the range $0 < k < 4$

$$\begin{aligned} F_e(k) \equiv 2i &\begin{vmatrix} (r^2-\nu)\cosh(\lambda r) & (\bar{r}^2-\nu)\cosh(\lambda\bar{r}) \\ (r^3-\rho r)\sinh(\lambda r) & (\bar{r}^3-\rho\bar{r})\sinh(\lambda\bar{r}) \end{vmatrix} \\ &= \sqrt{k}\,[(3+\nu)(1-\nu) + \nu k - \epsilon k(1+\nu)]\,\sinh(\lambda\sqrt{4-k}) \\ &\quad - \sqrt{4-k}\,[(1-\nu)^2 - \nu k - \epsilon k(1-\nu)]\,\sin(\lambda\sqrt{k}) = 0 \end{aligned} \tag{13}$$

and for the odd-mode critical values,

$$\begin{aligned} F_o(k) \equiv \sqrt{k}\,&[(3+\nu)(1-\nu) + \nu k - \epsilon k(1+\nu)]\,\sinh(\lambda\sqrt{4-k}) \\ &+ \sqrt{4-k}\,[(1-\nu)^2 - \nu k - \epsilon k(1-\nu)]\,\sin(\lambda\sqrt{k}) = 0. \end{aligned} \tag{14}$$

Equations (11), (13), and, in less explicit form (14), with $\epsilon = 1$, have previously been derived in Woinowsky-Krieger (1951). The equation corresponding to (12) for $\epsilon = 1$ is omitted there.

## The Buckling Load for the Follower Load Case

The numerical determination of the critical values of $k$ for the three conditions (11), (13), and (14) for the non-follower load case with $\epsilon = 1$ has been carried out in Woinowsky-Krieger (1951). We limit ourselves here to the evaluation of the follower load case $\epsilon = 0$. While we do not find follower buckling loads in the range $0 \le k < 4$ as $F_e(k)$ and $F_o(k)$ do not change sign in this range of $k$, we do find follower buckling loads in the range $4 < k$ on the basis of Eqs. (11) and (12). Graphs of $G_e(k)$ and $G_o(k)$ give us estimates of the critical values $k_c$. Newton's iteration is then employed to obtain $k_c$ accurate to four significant figures. Our numerical results are shown in Figs. 1 and 2 for the range $0 < b/a < 5$. The corresponding previously known results for the non-follower load case $\epsilon = 1$ are also shown for comparison.

As might be expected, $k_c$ decreases as $b/a$ increases and appears to be asymptotic to the value 4 as $b/a$ approaches infinity. As might also be expected, for a given value of $b/a$, the values of $k_c$ are larger for the follower load case than for the non-follower load case. The results for the two cases differ in the range by at most not much more than a factor of two, $2 < b/a$.

## Asymptotic Behavior for Large and Small Aspect Ratios

The numerical results for sufficiently large values of $b/a$

[3]These odd modes are also the buckling modes for a plate with sides $a$ and $b/2$ and three simply-supported edges.

Table 1 Variation of the computed $k_{co}/k_{ce}$ ratio with aspect ratio and Poisson's ratio

| $b/a$ \ $\nu$ | 0.5 | 0.3 | 0 |
|---|---|---|---|
| 0.5 | 1.614... | 1.379... | 0.8896... |
| 0.3 | 1.664... | 1.404... | 0.9451... |
| 0 | 1.685... | 1.404... | 1 |

indicate that $k_c$ approaches the value four from above as $\lambda$ tends to infinity. Setting in (11) and (12)

$$k_c \approx 4 + \frac{c^2}{\lambda^2}, \tag{15}$$

we find that these equations effectively reduce to the form sin$c$ = 0 with the smallest positive root $c = \pi$, and therewith

$$k_{ce} \approx k_{co} \approx 4\left(1+\frac{a^2}{b^2}\right) \tag{16}$$

for sufficiently large values of $b/a$.

In the range $b/a \ll 1$, it is suggested by the form of (11) and (12) that

$$k_c \approx \frac{c^2}{\lambda^2}. \tag{17}$$

However, we now find that the results for Eqs. (11) and (12) differ from each other. Introduction of (17) into the even-mode formula (11), in conjunction with stipulating $\lambda \ll 1$, leads again to the simple relation sin$c$ = 0, so that in this range

$$k_{ce} \approx \frac{\pi^2}{\lambda^2} = \frac{4a^2}{b^2}. \tag{18}$$

Introduction of (17) into the odd-mode formula (12) leads to a somewhat less simple asymptotic result. We find, on the basis of the two terms with $\nu k$ here having opposite signs, that the coefficient $c^2$ in (17) is now determined by the relation

$$(2-\nu)\sin c = \nu c \cos c. \tag{19}$$

Evidently, we have $k_{co} = k_{ce}$ when $\nu = 0$. For $\nu > 0$, however, we have $c = c(\nu) > \pi$ and therewith the asymptotic values of $\kappa_{co}$ are larger than the corresponding values of $k_{ce}$. Specifically, we have $k_{co} \approx 1.404\, k_{ce}$ for $\nu = 0.3$ and $k_{co} \approx 1.685\, k_{ce}$ for $\nu = 0.5$.

The above asymptotic results are (as they must be) consistent with our numerical results for the effect of Poisson's ratio on the values of $k_{ce}$ and $k_{co}$ as may be seen from Table 1.

## Acknowledgment

The research of F. Y. M. Wan is supported by NSF Grant DMS-8904845. The authors were ably assisted by Ms. Zhu Dantong in the machine computation and computer graphics for this paper.

## References

Timoshenko, S. P., and Gere, J. M., 1961, *Theory of Elastic Stability*, 2nd ed., McGraw-Hill, New York, pp. 370–373.

Woinowsky-Krieger, S., 1951, "Uber die Beulsicherheit von Rechteckplatten mit querverschieblichen Rändern," *Ing. Arch.*, Vol. 19, pp. 200–207.

# Instability of Generalized Equilibria of Pseudodissipative Systems

J. A. Walker[4]

In Walker (1988), criteria were obtained for stability and instability of the generalized equilibria of nonlinear pseudodissipative systems. It has since been found that the results on instability can be both improved and further simplified. By making more use of nonuniqueness for the pair $(U,D)$ in the definition of a pseudodissipative system (Walker, 1988), we can produce extensions of both the basic instability result (Theorem 3.2) and its simplification (Corollary 3.2). These extensions then lead to a new and much simpler criterion for instability, stated here as Corollary 3.3.

In the basic definition of a pseudodissipative system, Definition 2.1 of (Walker, 1988), the pair $(U,D)$ is far from unique. If $f_i\ \mathcal{O}\to\mathbb{R}^n$ are $n$ arbitrary $C^1$-smooth functions $(i=1,2,\ldots,n)$, the pair $(U,D)$can be replaced by an alternative pair $(\hat{U},\hat{D})$,

$$\hat{U}(t,q,u) \equiv U(t,q,u) + \sum_{i=1}^{n} u_i f_i(q), \tag{1}$$

$$\hat{D}_j(t,q,u) \equiv D_j(t,q,u) - \sum_{i=1}^{n} u_i\left[\frac{\partial}{\partial q_i} f_j(q) - \frac{\partial}{\partial q_j} f_i(q)\right], \tag{2}$$

$(j = 1,2,\ldots,n)$ which also satisfies Definition 2.1. Consequently, the pair $(L,D)$ can be replaced by $(\hat{L},\hat{D})$, with $\hat{L} \equiv T-\hat{U}$. This replacement has no effect on the basic stability result (Theorem 3.1) of (Walker, 1988) for a generalized equilibrium $(q^e, 0) \in \mathbb{R}^n \times \mathbb{R}^n$, since the function $G$ is not changed, and its sole effect on the basic instability result (Theorem 3.2) is to permit replacement of the function $R$ by

$$\hat{R}(\tilde{q},u) \equiv R(\tilde{q},u) + \sum_{i=1}^{n}\sum_{j=1}^{n} \gamma_{ij} u_i[-f_j(q)+f_j(q^e)]$$
$$-\sum_{i=1}^{n}\sum_{j=1}^{n}\gamma_{ij}(q_i-q_i^e)\sum_{k=1}^{n} u_k\left[2\frac{\partial}{\partial q_j} f_k(q) - \frac{\partial}{\partial q_k} f_j(q)\right] \tag{3}$$

in conditions (d)–(e) of Theorem 3.2 (Walker, 1988). Since all $f_i$ are arbitrary, the replacement of $R$ by $\hat{R}$ amounts to a further extension of Theorem 3.2.

Identifying $n$-tuples with column matrices, we may choose $f(q) \equiv S^T q$, where $S$ is any real $n \times n$ matrix. It follows that $S$ in Corollary 3.2 (Walker, 1988) may be any matrix, provided that we redefine

$$P(\mu,\nu,\Gamma,S) \equiv \begin{bmatrix} \nu K - \Gamma K - K\Gamma^T & \Gamma(B-S^T-C)+(B-S)\Gamma^T \\ (B-S^T-C)^T\Gamma^T + \Gamma(B-S)^T & \nu M + \Gamma M + M\Gamma^T + 2\mu\overline{C} \end{bmatrix}; \tag{4}$$

see the proof of Corollary 3.2 in (Walker, 1988). Since $S$ need no longer be chosen symmetric, Corollary 3.2 has been extended.

[4]Department of Mechanical Engineering, Northwestern University, Evanston, IL 60208.

Manuscript received by the ASME Applied Mechanics Division, Sept. 27, 1990; final revision, May 6, 1991. Associate Technical Editor: P. D. Spanos.

Table 1 Variation of the computed $k_{co}/k_{ce}$ ratio with aspect ratio and Poisson's ratio

| $b/a$ \ $\nu$ | 0.5 | 0.3 | 0 |
|---|---|---|---|
| 0.5 | 1.614... | 1.379... | 0.8896... |
| 0.3 | 1.664... | 1.404... | 0.9451... |
| 0 | 1.685... | 1.404... | 1 |

indicate that $k_c$ approaches the value four from above as $\lambda$ tends to infinity. Setting in (11) and (12)

$$k_c \approx 4 + \frac{c^2}{\lambda^2}, \tag{15}$$

we find that these equations effectively reduce to the form $\sin c = 0$ with the smallest positive root $c = \pi$, and therewith

$$k_{ce} \approx k_{co} \approx 4\left(1 + \frac{a^2}{b^2}\right) \tag{16}$$

for sufficiently large values of $b/a$.

In the range $b/a \ll 1$, it is suggested by the form of (11) and (12) that

$$k_c \approx \frac{c^2}{\lambda^2}. \tag{17}$$

However, we now find that the results for Eqs. (11) and (12) differ from each other. Introduction of (17) into the even-mode formula (11), in conjunction with stipulating $\lambda \ll 1$, leads again to the simple relation $\sin c = 0$, so that in this range

$$k_{ce} \approx \frac{\pi^2}{\lambda^2} = \frac{4a^2}{b^2}. \tag{18}$$

Introduction of (17) into the odd-mode formula (12) leads to a somewhat less simple asymptotic result. We find, on the basis of the two terms with $\nu k$ here having opposite signs, that the coefficient $c^2$ in (17) is now determined by the relation

$$(2-\nu)\sin c = \nu c \cos c. \tag{19}$$

Evidently, we have $k_{co} = k_{ce}$ when $\nu = 0$. For $\nu > 0$, however, we have $c = c(\nu) > \pi$ and therewith the asymptotic values of $\kappa_{co}$ are larger than the corresponding values of $k_{ce}$. Specifically, we have $k_{co} \approx 1.404\ k_{ce}$ for $\nu = 0.3$ and $k_{co} \approx 1.685\ k_{ce}$ for $\nu = 0.5$.

The above asymptotic results are (as they must be) consistent with our numerical results for the effect of Poisson's ratio on the values of $k_{ce}$ and $k_{co}$ as may be seen from Table 1.

## Acknowledgment

The research of F. Y. M. Wan is supported by NSF Grant DMS-8904845. The authors were ably assisted by Ms. Zhu Dantong in the machine computation and computer graphics for this paper.

## References

Timoshenko, S. P., and Gere, J. M., 1961, *Theory of Elastic Stability*, 2nd ed., McGraw-Hill, New York, pp. 370–373.

Woinowsky-Krieger, S., 1951, "Uber die Beulsicherheit von Rechteckplatten mit querverschieblichen Rändern," *Ing. Arch.*, Vol. 19, pp. 200–207.

# Instability of Generalized Equilibria of Pseudodissipative Systems

J. A. Walker[4]

In Walker (1988), criteria were obtained for stability and instability of the generalized equilibria of nonlinear pseudodissipative systems. It has since been found that the results on instability can be both improved and further simplified. By making more use of nonuniqueness for the pair $(U,D)$ in the definition of a pseudodissipative system (Walker, 1988), we can produce extensions of both the basic instability result (Theorem 3.2) and its simplification (Corollary 3.2). These extensions then lead to a new and much simpler criterion for instability, stated here as Corollary 3.3.

In the basic definition of a pseudodissipative system, Definition 2.1 of (Walker, 1988), the pair $(U,D)$ is far from unique. If $f_i\ \mathcal{O}\to\mathbb{R}^n$ are $n$ arbitrary $C^1$-smooth functions $(i=1,2,\ldots,n)$, the pair $(U,D)$can be replaced by an alternative pair $(\hat{U},\hat{D})$,

$$\hat{U}(t,q,u) \equiv U(t,q,u) + \sum_{i=1}^{n} u_i f_i(q), \tag{1}$$

$$\hat{D}_j(t,q,u) \equiv D_j(t,q,u) - \sum_{i=1}^{n} u_i \left[\frac{\partial}{\partial q_i} f_j(q) - \frac{\partial}{\partial q_j} f_i(q)\right], \tag{2}$$

$(j = 1,2,\ldots,n)$ which also satisfies Definition 2.1. Consequently, the pair $(L,D)$ can be replaced by $(\hat{L},\hat{D})$, with $\hat{L} \equiv T-\hat{U}$. This replacement has no effect on the basic stability result (Theorem 3.1) of (Walker, 1988) for a generalized equilibrium $(q^e, 0) \in \mathbb{R}^n \times \mathbb{R}^n$, since the function $G$ is not changed, and its sole effect on the basic instability result (Theorem 3.2) is to permit replacement of the function $R$ by

$$\hat{R}(\tilde{q},u) \equiv R(\tilde{q},u) + \sum_{i=1}^{n}\sum_{j=1}^{n} \gamma_{ij} u_i[-f_j(q) + f_j(q^e)] - \sum_{i=1}^{n}\sum_{j=1}^{n} \gamma_{ij}(q_i - q_i^e)\sum_{k=1}^{n} u_k\left[2\frac{\partial}{\partial q_j} f_k(q) - \frac{\partial}{\partial q_k} f_j(q)\right] \tag{3}$$

in conditions (d)–(e) of Theorem 3.2 (Walker, 1988). Since all $f_i$ are arbitrary, the replacement of $R$ by $\hat{R}$ amounts to a further extension of Theorem 3.2.

Identifying $n$-tuples with column matrices, we may choose $f(q) \equiv S^T q$, where $S$ is any real $n \times n$ matrix. It follows that $S$ in Corollary 3.2 (Walker, 1988) may be any matrix, provided that we redefine

$$P(\mu,\nu,\Gamma,S) \equiv \begin{bmatrix} \nu K - \Gamma K - K\Gamma^T & \Gamma(B-S^T-C) + (B-S)\Gamma^T \\ (B-S^T-C)^T\Gamma^T + \Gamma(B-S)^T & \nu M + \Gamma M + M\Gamma^T + 2\mu\bar{C} \end{bmatrix}; \tag{4}$$

see the proof of Corollary 3.2 in (Walker, 1988). Since $S$ need no longer be chosen symmetric, Corollary 3.2 has been extended.

[4]Department of Mechanical Engineering, Northwestern University, Evanston, IL 60208.

Manuscript received by the ASME Applied Mechanics Division, Sept. 27, 1990; final revision, May 6, 1991. Associate Technical Editor: P. D. Spanos.

The actual stability properties of a generalized equilibrium do not depend upon the manner in which Definition 2.1 is used, so there should be a "best choice" for $S$, a choice which does not sacrifice generality for simplicity. $S$ is no longer required to be symmetric, and experience has convinced the author that little or no generality is lost by choosing

$$4S \equiv 2(B+B^T) + (C-C^T). \tag{5}$$

Unless $C = 0$, this choice differs from the choice suggested in Comment 3.2 of (Walker, 1988). The choice (5) leads to

$$P(\mu,\nu,\Gamma,S) = \hat{P}(\mu,\nu,\Gamma) - \begin{bmatrix} 0 & \Gamma\overline{C} \\ \overline{C}\Gamma^T & 0 \end{bmatrix} \tag{6}$$

where

$$\hat{P}(\mu,\nu,\Gamma) \equiv \begin{bmatrix} \nu K - \Gamma K - K\Gamma^T & \Gamma X - (\Gamma X)^T \\ (\Gamma X)^T - \Gamma X & \nu M + \Gamma M + M\Gamma^T + 2\mu\overline{C} \end{bmatrix}, \tag{7}$$

$$2\overline{C} \equiv C + C^T \leq 0,\ 4X \equiv (2B-C) - (2B-C)^T = -4X^T. \tag{8}$$

As $\overline{C} = \overline{C}^T \geq 0$, $P$ is positive definite for some $\mu \geq 0$ if and only if $\hat{P} > 0$ for some other (possibly larger) $\mu \geq 0$. Hence, the foregoing extension of Corollary 3.2 (Walker, 1988) leads to the following simplification:

**Corollary 3.3:** Let the generalized force be pseudodissipative with pseudopotential $U$ and dissipative part $D$. Suppose that $(q^e, 0) \in \mathcal{R}^n \times \mathcal{R}^n$ is a generalized equilibrium and the following conditions hold:

(a) There exists $h > 0$ such that $\mathcal{C}(t) \supset \mathcal{N}_h$ for all $t \geq t_o$.

(b) The Lagrangian $L: \mathcal{R} \times \mathcal{O} \times \mathcal{R}^n \rightarrow \mathcal{R}^R$ is time-invariant and $C^2$-smooth, the dissipative part $D$: $\mathcal{R} \times \mathcal{O} \times \mathcal{R}^n \rightarrow \mathcal{R}^n$ is time-invariant and $C^1$-smooth, and $D(t_o, q, 0) = D(t_o, q^e, 0)$ for all $q \in \mathcal{O}$.

(c) det $(K) \neq 0$ but $K$ is not positive definite.

(d) There exist real numbers $\mu \geq 0$, $\nu \geq 0$, and a real $n \times n$ matrix $\Gamma$ such that $\hat{P}(\mu, \nu, \Gamma)$ is positive definite.

Then $(q^e, 0)$ is *unstable.*

Corollary 3.3 is much simpler than Corollary 3.2 of (Walker, 1988). Not only has the $n \times n$ parameter matrix $S$ been chosen, but $X = 0$ if $2B-C$ is symmetric, which implies that $\hat{P}$ is "matrix-diagonal." The matrices $M = M^T \geq 0$, $K = K^T$, $B$, $C$, and $\overline{C} \geq 0$ were defined in (Walker, 1988). Notice that the arbitrary substitutions (1)–(2) affect $B$ and $C$, which appear directly in Corollary 3.2, but they do *not* affect the matrices $M$, $K$, $\overline{C}$, and $X$ which appear directly in the new Corollary 3.3. This desirable property motivated our choice (5) for $S$, and it suggests that (5) might always be the "best choice" for $S$ in our extended Corollary 3.2. That is, the much simpler Corollary 3.3 may be fully equivalent to the extended Corollary 3.2. There is as yet no evidence that it is not.

If $M > 0$ and condition (c) is met, there exist $\nu$ and $\Gamma$ such that both of the diagonal submatrices in $\hat{P}$ are positive definite with $\mu = 0$; hence, if *either* $\overline{C} > 0$ or $2B$-$C$ is symmetric ($X = 0$), we find that condition (d) is met. Condition (d) is difficult to verify only if $\overline{C}$ is *not* positive definite *and* $2B$-$C$ is *not* symmetric. That is, condition (d) becomes difficult *only* when there is a chance of "gyroscopic stabilization" in the "linearized system,"

$$M\ddot{x}(t) + (\overline{C} - 2X)\dot{x}(t) + Kx(t) = 0. \tag{9}$$

See Eq. (25) in (Walker, 1988), and notice that $B^T - B + C = \overline{C} - 2X$. The instability results of (Walker, 1988) and Corollary 3.3 are applicable to any generalized equilibrium $(q^e, 0)$ of any (nonlinear) pseudodissipative system, so they are also applicable to the equilibrium (0, 0) of the linear system (9).

If $\overline{C} = 0$ and $X^T = -X \neq 0$, then (9) describes the "linear conservative gyroscopic system" considered in (Hagedorn, 1975) and (Walker, 1991). In Hagedorn (1975), instability is concluded if $M = I$, $\overline{C} = 0$, and $X^T X + K < 0$; this result follows from Corollary 3.3 with $\nu \equiv 0$, $\Gamma \equiv I$. Theorem II in (Walker, 1991) improves upon this result, but it too follows from Corollary 3.3 with $\nu \equiv 0$, $\Gamma \equiv (I - \lambda K)^{-1}$.

All instability results obtained for the (nonlinear) example in Walker (1988) also follow from Corollary 3.3, for the same choice of $(\mu,\nu,\Gamma)$. The advantage of not having to select the $n \times n$ matrix $S$ in Collorary 3.2 becomes very significant as $n$ increases.

## References


Hagedorn, P., 1975, "Uber Die Instabitat Konservativer Systeme Mit Gyroskopischen Kraften," *Archieve for Rational Mechanics and Analysis*, Vol. 58, pp. 1-9.

Walker, J. A., 1988, "Pseudodissipative Systems I: Stability of Generalized Equilibria," ASME JOURNAL OF APPLIED MECHANICS, Vol. 55, pp. 681-686.

Walker, J. A., 1991, "Stability of Linear Conservative Gyroscopic Systems," ASME JOURNAL OF APPLIED MECHANICS, Vol. 58, pp. 229-232.


# A Note on Determining the Initial Velocity of a Modal Field


**Q. Zhou[5], T. G. Zhang[6], and T. X. Yu[7]**


## 1 Introduction

The modal solution method first developed by Martin and Symonds (1966), is an effective approximate method to pursue the dynamic plastic response of structures. The use of a fundamental mode simplifies a complex infinite degree-of-freedom system to a simple one-degree-of-freedom system. In fact, for a rigid-plastic structure, it merely refers to the later modal response and neglects the early instantaneous response of the structures under impulsive loadings.

Among the few methods for determining the initial velocity value of the modal field from the true initial velocity field of structures, the one widely applied is the so-called minimum $\Delta_0$ technique (Martin and Symonds, 1966), which has been proved appropriate in solving engineering problems. According to Martin and Symonds (1966), $\Delta_0$ is defined as the difference at the initial instant between the true kinetic energy of structure and the kinetic energy of the modal field chosen. Making $\Delta_0$ minimum to determine the initial velocity value of the modal field is called the minimum $\Delta_0$ technique.

Let $\mathbf{V}_0 = \mathbf{V}(\mathbf{x},0)$ be a true initial velocity field and $\mathbf{V}_0^* = \boldsymbol{\phi}(\mathbf{x})V_0^*$ modal initial velocity field, where $\boldsymbol{\phi}(\mathbf{x})$ is the shape function of the mode. Martin and Symonds (1966) defined $\Delta_0$ as

$$\Delta_0(V_0^*) = \frac{1}{2}\int_v \rho(\mathbf{V}_0 - V_0^*\boldsymbol{\phi})\cdot(\mathbf{V}_0 - V_0^*\boldsymbol{\phi})dv, \tag{1}$$


[5]Department of Ocean Engineering, Massachusetts Institute of Technology, Cambridge, MA 02139.

[6]Taiyuan University of Technology, Taiyuan, China.

[7]Department of Mechanics, Peking University, Beijing, China.



Manuscript received by the ASME Applied Mechanics Division, July 17, 1990; final revision, Nov. 29, 1990. Associate Technical Editor: R. L. Huston.

The actual stability properties of a generalized equilibrium do not depend upon the manner in which Definition 2.1 is used, so there should be a "best choice" for $S$, a choice which does not sacrifice generality for simplicity. $S$ is no longer required to be symmetric, and experience has convinced the author that little or no generality is lost by choosing

$$4S \equiv 2(B+B^T)+(C-C^T). \tag{5}$$

Unless $C = 0$, this choice differs from the choice suggested in Comment 3.2 of (Walker, 1988). The choice (5) leads to

$$P(\mu,\nu,\Gamma,S)=\hat{P}(\mu,\nu,\Gamma)-\begin{bmatrix} 0 & \Gamma\overline{C} \\ \overline{C}\Gamma^T & 0 \end{bmatrix} \tag{6}$$

where

$$\hat{P}(\mu,\nu,\Gamma)\equiv\begin{bmatrix} \nu K-\Gamma K-K\Gamma^T & \Gamma X-(\Gamma X)^T \\ (\Gamma X)^T-\Gamma X & \nu M+\Gamma M+M\Gamma^T+2\mu\overline{C} \end{bmatrix}, \tag{7}$$

$$2\overline{C}\equiv C+C^T\le 0,\ 4X\equiv(2B-C)-(2B-C)^T=-4X^T. \tag{8}$$

As $\overline{C} = \overline{C}^T \geq 0$, $P$ is positive definite for some $\mu \geq 0$ if and only if $\hat{P} > 0$ for some other (possibly larger) $\mu \geq 0$. Hence, the foregoing extension of Corollary 3.2 (Walker, 1988) leads to the following simplification:

**Corollary 3.3:** Let the generalized force be pseudodissipative with pseudopotential $U$ and dissipative part $D$. Suppose that $(q^e, 0) \in \mathcal{R}^n \times \mathcal{R}^n$ is a generalized equilibrium and the following conditions hold:

(a) There exists $h > 0$ such that $\mathcal{C}(t) \supset \mathfrak{N}_h$ for all $t \geq t_o$.

(b) The Lagrangian $L: \mathcal{R} \times \mathcal{O} \times \mathcal{R}^n \to \mathcal{R}^R$ is time-invariant and $C^2$-smooth, the dissipative part $D$: $\mathcal{R} \times \mathcal{O} \times \mathcal{R}^n \to \mathcal{R}^n$ is time-invariant and $C^1$-smooth, and $D(t_o, q, 0) = D(t_o, q^e, 0)$ for all $q \in \mathcal{O}$.

(c) det $(K) \neq 0$ but $K$ is not positive definite.

(d) There exist real numbers $\mu \geq 0$, $\nu \geq 0$, and a real $n \times n$ matrix $\Gamma$ such that $\hat{P}(\mu, \nu, \Gamma)$ is positive definite.

Then $(q^e, 0)$ is *unstable.*

Corollary 3.3 is much simpler than Corollary 3.2 of (Walker, 1988). Not only has the $n \times n$ parameter matrix $S$ been chosen, but $X = 0$ if $2B-C$ is symmetric, which implies that $\hat{P}$ is "matrix-diagonal." The matrices $M = M^T \geq 0$, $K = K^T$, $B$, $C$, and $\overline{C} \geq 0$ were defined in (Walker, 1988). Notice that the arbitrary substitutions (1)–(2) affect $B$ and $C$, which appear directly in Corollary 3.2, but they do *not* affect the matrices $M$, $K$, $\overline{C}$, and $X$ which appear directly in the new Corollary 3.3. This desirable property motivated our choice (5) for $S$, and it suggests that (5) might always be the "best choice" for $S$ in our extended Corollary 3.2. That is, the much simpler Corollary 3.3 may be fully equivalent to the extended Corollary 3.2. There is as yet no evidence that it is not.

If $M > 0$ and condition (c) is met, there exist $\nu$ and $\Gamma$ such that both of the diagonal submatrices in $\hat{P}$ are positive definite with $\mu = 0$; hence, if *either* $\overline{C} > 0$ or $2B$-$C$ is symmetric ($X = 0$), we find that condition (d) is met. Condition (d) is difficult to verify only if $\overline{C}$ is *not* positive definite *and* $2B$-$C$ is *not* symmetric. That is, condition (d) becomes difficult *only* when there is a chance of "gyroscopic stabilization" in the "linearized system,"

$$M\ddot{x}(t)+(\overline{C}-2X)\dot{x}(t)+Kx(t)=0. \tag{9}$$

See Eq. (25) in (Walker, 1988), and notice that $B^T - B + C = \overline{C} - 2X$. The instability results of (Walker, 1988) and Corollary 3.3 are applicable to any generalized equilibrium $(q^e, 0)$ of any (nonlinear) pseudodissipative system, so they are also applicable to the equilibrium (0, 0) of the linear system (9).

If $\overline{C} = 0$ and $X^T = -X \neq 0$, then (9) describes the "linear conservative gyroscopic system" considered in (Hagedorn, 1975) and (Walker, 1991). In Hagedorn (1975), instability is concluded if $M = I$, $\overline{C} = 0$, and $X^T X + K < 0$; this result follows from Corollary 3.3 with $\nu \equiv 0$, $\Gamma \equiv I$. Theorem II in (Walker, 1991) improves upon this result, but it too follows from Corollary 3.3 with $\nu \equiv 0$, $\Gamma \equiv (I - \lambda K)^{-1}$.

All instability results obtained for the (nonlinear) example in Walker (1988) also follow from Corollary 3.3, for the same choice of $(\mu,\nu,\Gamma)$. The advantage of not having to select the $n \times n$ matrix $S$ in Collorary 3.2 becomes very significant as $n$ increases.

## References


Hagedorn, P., 1975, "Uber Die Instabitat Konservativer Systeme Mit Gyroskopischen Kraften," *Archieve for Rational Mechanics and Analysis*, Vol. 58, pp. 1-9.

Walker, J. A., 1988, "Pseudodissipative Systems I: Stability of Generalized Equilibria," ASME Journal of Applied Mechanics, Vol. 55, pp. 681-686.

Walker, J. A., 1991, "Stability of Linear Conservative Gyroscopic Systems," ASME Journal of Applied Mechanics, Vol. 58, pp. 229-232.


# A Note on Determining the Initial Velocity of a Modal Field

**Q. Zhou[5], T. G. Zhang[6], and T. X. Yu[7]**

## 1 Introduction

The modal solution method first developed by Martin and Symonds (1966), is an effective approximate method to pursue the dynamic plastic response of structures. The use of a fundamental mode simplifies a complex infinite degree-of-freedom system to a simple one-degree-of-freedom system. In fact, for a rigid-plastic structure, it merely refers to the later modal response and neglects the early instantaneous response of the structures under impulsive loadings.

Among the few methods for determining the initial velocity value of the modal field from the true initial velocity field of structures, the one widely applied is the so-called minimum $\Delta_0$ technique (Martin and Symonds, 1966), which has been proved appropriate in solving engineering problems. According to Martin and Symonds (1966), $\Delta_0$ is defined as the difference at the initial instant between the true kinetic energy of structure and the kinetic energy of the modal field chosen. Making $\Delta_0$ minimum to determine the initial velocity value of the modal field is called the minimum $\Delta_0$ technique.

Let $\mathbf{V}_0 = \mathbf{V}(\mathbf{x},0)$ be a true initial velocity field and $\mathbf{V}_0^* = \boldsymbol{\phi}(\mathbf{x}) V_0^*$ modal initial velocity field, where $\boldsymbol{\phi}(\mathbf{x})$ is the shape function of the mode. Martin and Symonds (1966) defined $\Delta_0$ as

$$\Delta_0(V_0^*)=\frac{1}{2}\int_v \rho(\mathbf{V}_0-V_0^*\boldsymbol{\phi})\cdot(\mathbf{V}_0-V_0^*\boldsymbol{\phi})dv, \tag{1}$$


[5]Department of Ocean Engineering, Massachusetts Institute of Technology, Cambridge, MA 02139.

[6]Taiyuan University of Technology, Taiyuan, China.

[7]Department of Mechanics, Peking University, Beijing, China.


Manuscript received by the ASME Applied Mechanics Division, July 17, 1990; final revision, Nov. 29, 1990. Associate Technical Editor: R. L. Huston.

while the minimum $\Delta_0$ technique requires

$$\frac{\partial \Delta_0}{\partial V_0^*}=0. \tag{2}$$

Accordingly, the initial velocity value of the modal field $V_0^*$ is determined by (Martin and Symonds, 1966)

$$V_0^*=\frac{\int_v \rho \mathbf{V}_0 \cdot \phi dv}{\int_v \rho \phi \cdot \phi dv}. \tag{3}$$

The characteristics of this method is making the difference between the true initial velocity and the modal initial velocity minimum in the sense of least square.

A universal procedure for determining the initial velocity of a modal field is proposed in this paper in the light of Lagrange's equation of impulsive motion. It will degenerate to the minimum $\Delta_0$ technique developed by Martin and Symonds (1966) if the system has a continuous distribution of mass.

## 2 Lagrange's Equation of Impulsive Motion and Modal Initial Velocity

The fundamental mode of a structure is actually a one-degree-of-freedom system with scleronomic nonideal constraints. If the internal forces at the plastic deforming zones, i.e., the fully plastic moments at the plastic hinges, are regarded as active forces, it will be a one-degree-of-freedom system with scleronomic ideal constraints. Suppose the system can be described by the generalized coordinates $q^*$ and the true initial velocity $\dot{q}^*$, and it consists of $n$ particles with the mass $m_j$ and the true initial velocity $\mathbf{V}_j^0$ ($j=1, 2, \ldots, n$), respectively. The distribution of $\mathbf{V}_j^0$ is usually different from the specified modal velocity field. To determine the initial velocity value of the modal field, suppose the system is static at the initial instant and it is subjected to impulse $\mathbf{S}_j=m_j\mathbf{V}_j^0$ in a very short duration. Consequently, it acquires the modal initial velocity $\dot{q}_0^*$.

Because the loadings duration is very short, it may be reasonable to assume that the displacement of the system and the nonimpulsive forces, such as the active forces, i.e., fully plastic moments, can be neglected during the impulsive loading process.

Lagrange's equation of impulsive motion indicates (refer to Rosenberg, 1977)

$$\Delta\left(\frac{\partial T}{\partial \dot{q}^*}\right)=I, \tag{4}$$

where $T$ is the kinetic energy of the system and $I$ is the generalized impulse caused by the momentum $\mathbf{S}_j$. $\Delta(\partial T/\partial \dot{q}^*)$ represents the difference between the generalized momentum prior to impacting and that after impacting. Since the former is zero, Eq. (4) can be rewritten as

$$\frac{\partial T_0}{\partial \dot{q}_0^*}=I, \tag{5}$$

where $T_0$ is the initial kinetic energy of the modal velocity field.

Because the system has merely one degree-of-freedom, the vector of the $j$th particle $\mathbf{r}_j$ is the function of generalized coordinates $q^*$, and its expression does not include the time $t$ as the constraints are scleronomic. That is,

$$\mathbf{r}_j=\mathbf{r}_j(q^*). \tag{6}$$

Hence, the velocity of the $j$th particle is

$$\mathbf{V}_j=\frac{d\mathbf{r}_j}{dt}=\frac{\partial \mathbf{r}_j}{\partial q^*}\dot{q}^*, \tag{7}$$

where

$$\frac{\partial \mathbf{r}_j}{\partial q^*}=\phi \tag{8}$$

is exactly the shape function of the mode. Thus, the kinetic energy of the system is found to be

$$T=\sum_{j=1}^{n}\frac{1}{2}m_j\mathbf{V}_j\cdot\mathbf{V}_j=\sum_{j=1}^{n}\frac{1}{2}m_j\left(\frac{\partial \mathbf{r}_j}{\partial q^*}\right)\cdot\left(\frac{\partial \mathbf{r}_j}{\partial q^*}\right)\dot{q}^{*2}. \tag{9}$$

It follows that

$$\frac{\partial T_0}{\partial \dot{q}_0^*}=\sum_{j=1}^{n}m_j\left(\frac{\partial \mathbf{r}_j}{\partial q_0^*}\right)\cdot\left(\frac{\partial \mathbf{r}_j}{\partial q_0^*}\right)\dot{q}_0^*. \tag{10}$$

Caused by momentum $\mathbf{S}_j$, the generalized impulse should be

$$I=\sum_{j=1}^{n}\mathbf{S}_j\cdot\frac{\partial \mathbf{r}_j}{\partial q_0^*}=\sum_{j=1}^{n}m_j\mathbf{V}_j^0\cdot\frac{\partial \mathbf{r}_j}{\partial q_0^*}. \tag{11}$$

By substituting (10) and (11) into (5), the modal initial velocity value can be solved

$$\dot{q}_0^*=\frac{\Sigma_{j=1}^{n}m_j\mathbf{V}_j^0\cdot\frac{\partial \mathbf{r}_j}{\partial q_0^*}}{\Sigma_{j=1}^{n}m_j\left(\frac{\partial \mathbf{r}_j}{\partial q_0^*}\right)\cdot\left(\frac{\partial \mathbf{r}_j}{\partial q_0^*}\right)}. \tag{12}$$

The foregoing expression is more universal than formula (3), and it possesses a clear mechanics background.

The particle system can be transformed into a continuum body of volume $v$ and mass density $\rho$, provided that $m_j=\rho dv$, $\dot{q}_0^*=V_0^*$, while the sum is changed into integration. By using (8), expression (12) is changed into

$$V_0^*=\frac{\int_v \rho \mathbf{V}_0 \cdot \phi dv}{\int_v \rho \phi \cdot \phi dv}, \tag{13}$$

which is exactly the same as expression (3) obtained by the minimum $\Delta_0$ technique.

While using the aforementioned procedure, formula (5) may be convenient because it represents the conservation of angular momentum in some cases. In fact, when the modal velocity field of a structure results in a movement of one degree-of-freedom, at least a part of the structure rotates about a fixed axis rotation (see the second example that follows). Formula (5) indicates that, with respect to the same fixed axis, the modal initial velocity field and the true one have equal angular momentum. This explanation reflects the mechanics significance of the minimum $\Delta_0$ technique.

## 3 Examples

**Example 1.** As shown in Fig. 1, a quadrantal circular beam is subjected to a radial impact at its tip by a rigid mass $G$. The rigid-plastic complete solution, the modal solution, and the finite element solution were all given by Yu, Symonds, and Johnson (1985). The modal shape in their solution is a rotation about the fixed root $A$. The conservation of angular momentum with respect to $A$ results in

$$J\omega_0^*=RGV_0, \tag{14}$$

where $J$ is the moment of inertia of the beam and rigid mass $G$ with respect to $A$, $\omega_0^*$ is the modal initial angular velocity, and $R$ is the radius of the qaudrantal circle. Here, $\omega_0^*$, determined by (14), is exactly the same as that determined by the minimum $\Delta_0$ technique (Yu, Symonds, and Johnson, 1985). In this example, only the component $V_0/\sqrt{2}$ (of the true velocity), which is perpendicular to $AB$, makes contribution to the modal solution.

**Example 2.** In Fig. 2, when one column of a portal frame is subjected to a uniformly distributed impulsive loading, a

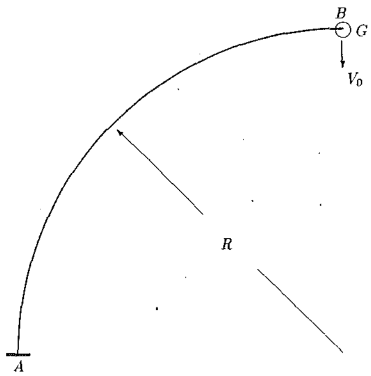


Fig. 1

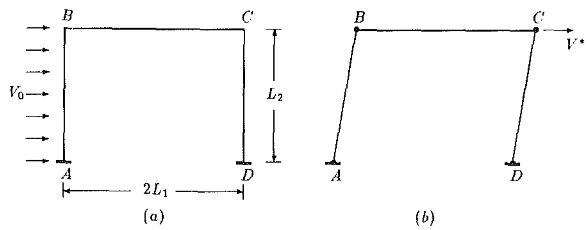


Fig. 2

four-hinged mode (Fig. 2(*b*)) may be taken as a modal shape. With the help of conservation of angular momentum with respect to $A$, we can easily find that the modal initial velocity at characteristic point $C$ (and $B$) is

$$V_0^* = \frac{3L_2V_0}{4L_2+12L_1}. \qquad (15)$$

This example illustrates that a one-degree-of-freedom system may also include other movements besides a rotation about a fixed axis.

## 4 Conclusions

If the modal velocity field of a structure under impulsive loadings results in a one-degree-of-freedom movement, its initial velocity value can be determined from the true initial velocity field by the Lagrange's equation of impulsive motion. When the system mass distribution is continuous, this procedure will degenerate to the minimum $\Delta_0$ technique suggested by Martin and Symonds (1966). In addition, from the view of mechanics, both procedures imply the conservation of angular momentum. In general, however, the initial kinetic energy and the initial momentum of the modal solution are smaller, respectively, than those carried by the true initial conditions.

### References

Martin, J. B., 1966, "A Note on the Uniqueness of Solutions for Dynamically Loaded Rigid-Plastic and Rigid-Viscoplastic Continuum," ASME Journal of Applied Mechanics, Vol. 33, pp. 207-209.

Martin, J. B., and Symonds, P. S., 1966, "Mode Approximations for Impulsively Loaded Rigid-Plastic Structures," *Proc. ASCE*, Vol. 92, No. EM5, pp. 43-66.

Rosenberg, R. M., 1977, *Analytical Dynamics of Discrete System*, Plenum Pres, New York.

Yu, T. X., Symonds, P. S., and Johnson, W., 1985, "A Quadrantal Circular Beam Subjected to Radial Impact in Its Own Plane at Its Tip by a Rigid Mass," *Proc. R. Soc. Lond.*, Vol. A400, pp. 19-36.

# On the Bending of Rectangular Plates With Two Opposite Edges Simply Supported

James R. Hutchinson[8]

### Introduction

It has recently been brought to my attention that several authors, when seeking exact solutions to plate bending problems, have relied on the solution given on pages 208–210 in the "Theory of Plates and Shells" by Timoshenko and Woinowsky-Kreiger (1959). That series solution is for the uniformly loaded rectangular plate with two opposite edges simply supported, one edge free and the other edge clamped. Unfortunately, the form of solution as given is incapable of producing accurate results, or at least results accurate enough for comparison purposes. The series solution in Timoshenko and Woinowsky-Kreiger (1959), while being theoretically convergent is extremely imprecise when using a finite number of digits for computation. The lack of precision comes from the fact that the solution form involves small differences of large numbers. The imprecision occurs after about three terms in the series for the number of digits that are carried in most computers. While the results produced from three terms are accurate enough for most engineering purposes, they are not as precise as one would like for comparison purposes. Of course the accuracy of the bending moments is worse than that of the displacement since the moments are formed from second derivatives of the displacement. Wu and Altiero (1979) and Burgess and Mahajerin (1985) used the solution of Timoshenko and Woinowsky-Kreiger (1959) as an *exact* solution for a basis of comparison with their approximate techniques. Burgess and Mahajerin (1985) pointed out that the *exact* solution of Wu and Altiero (1979) was in error because of convergence problems in calculation of the bending moments. Burgess and Mahajerin tried to correct the problem by calculating the bending moments by finite differences of the displacement function. The correction of Burgess and Mahajerin was still in error. Accurate solutions can be obtained by either changing the coordinate system or the solution forms as shown in the formulation which follows.

### Formulation

For the plate with the coordinate system shown in Fig. 1(*a*), Timoshenko and Woinowsky-Kreiger use the solution form

$$w = \frac{4qa^4}{\pi^5 D} \sum_{n=1,3,5,\ldots}^{\infty} \left[ \frac{1}{n^5} + A_n \cosh \alpha_n y + B_n \alpha_n y \sinh \alpha_n y \right.$$
$$\left. + C_n \sinh \alpha_n y + D_n \alpha_n y \cosh \alpha_n y \right] \sin \alpha_n x \qquad (1)$$

where $\alpha_n = n\pi/a$, and other notation is as in Timoshenko and Woinowsky-Kreiger (1959). Numerical difficulties arise when using the solution form in Eq. (1) for the origin placement shown in Fig. 1(*a*). The hyperbolic terms are all small at $y=0$ and large at $y=b$, and the terms become increasingly large with increasing $n$. Satisfying the boundary conditions leads to $A_n \approx -B_n \approx -C_n \approx D_n$ for large $n$. For example, for $n=5$, the differences in the magnitude of the coefficients $A_n$, $B_n$, $C_n$, and $D_n$ are in the eighth significant figure. Taking as a typical case, $y=b=a$, $\cosh\alpha_n y$ and $\sinh\alpha_n y$ differ in the thirteenth significant figure for $n=5$. Thus, one needs to carry eight

[8]Civil Engineering Department, University of California, Davis, CA 95616. Mem. ASME.

Manuscript received by the ASME Applied Mechanics Division, Sept. 18, 1990; final revision, Aug. 8, 1991. Associate Technical Editor: L. M. Keer.

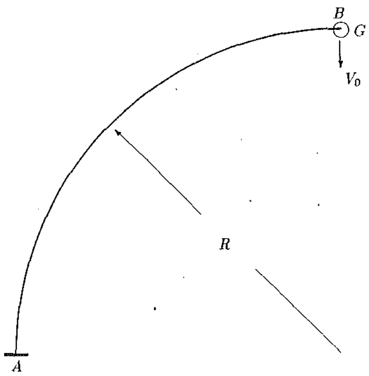


Fig. 1

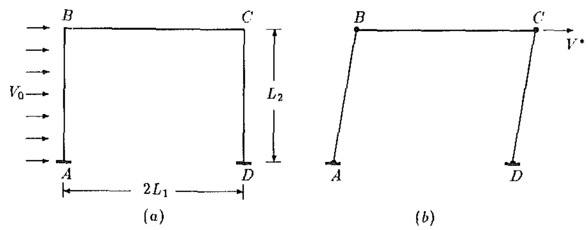


Fig. 2

four-hinged mode (Fig. 2($b$)) may be taken as a modal shape. With the help of conservation of angular momentum with respect to $A$, we can easily find that the modal initial velocity at characteristic point $C$ (and $B$) is

$$V_0^* = \frac{3L_2V_0}{4L_2 + 12L_1}. \tag{15}$$

This example illustrates that a one-degree-of-freedom system may also include other movements besides a rotation about a fixed axis.

## 4 Conclusions

If the modal velocity field of a structure under impulsive loadings results in a one-degree-of-freedom movement, its initial velocity value can be determined from the true initial velocity field by the Lagrange's equation of impulsive motion. When the system mass distribution is continuous, this procedure will degenerate to the minimum $\Delta_0$ technique suggested by Martin and Symonds (1966). In addition, from the view of mechanics, both procedures imply the conservation of angular momentum. In general, however, the initial kinetic energy and the initial momentum of the modal solution are smaller, respectively, than those carried by the true initial conditions.

### References

Martin, J. B., 1966, "A Note on the Uniqueness of Solutions for Dynamically Loaded Rigid-Plastic and Rigid-Viscoplastic Continuum," ASME Journal of Applied Mechanics, Vol. 33, pp. 207-209.

Martin, J. B., and Symonds, P. S., 1966, "Mode Approximations for Impulsively Loaded Rigid-Plastic Structures," *Proc. ASCE*, Vol. 92, No. EM5, pp. 43-66.

Rosenberg, R. M., 1977, *Analytical Dynamics of Discrete System*, Plenum Pres, New York.

Yu, T. X., Symonds, P. S., and Johnson, W., 1985, "A Quadrantal Circular Beam Subjected to Radial Impact in Its Own Plane at Its Tip by a Rigid Mass," *Proc. R. Soc. Lond.*, Vol. A400, pp. 19-36.

# On the Bending of Rectangular Plates With Two Opposite Edges Simply Supported

James R. Hutchinson[8]

## Introduction

It has recently been brought to my attention that several authors, when seeking exact solutions to plate bending problems, have relied on the solution given on pages 208–210 in the "Theory of Plates and Shells" by Timoshenko and Woinowsky-Kreiger (1959). That series solution is for the uniformly loaded rectangular plate with two opposite edges simply supported, one edge free and the other edge clamped. Unfortunately, the form of solution as given is incapable of producing accurate results, or at least results accurate enough for comparison purposes. The series solution in Timoshenko and Woinowsky-Kreiger (1959), while being theoretically convergent is extremely imprecise when using a finite number of digits for computation. The lack of precision comes from the fact that the solution form involves small differences of large numbers. The imprecision occurs after about three terms in the series for the number of digits that are carried in most computers. While the results produced from three terms are accurate enough for most engineering purposes, they are not as precise as one would like for comparison purposes. Of course the accuracy of the bending moments is worse than that of the displacement since the moments are formed from second derivatives of the displacement. Wu and Altiero (1979) and Burgess and Mahajerin (1985) used the solution of Timoshenko and Woinowsky-Kreiger (1959) as an *exact* solution for a basis of comparison with their approximate techniques. Burgess and Mahajerin (1985) pointed out that the *exact* solution of Wu and Altiero (1979) was in error because of convergence problems in calculation of the bending moments. Burgess and Mahajerin tried to correct the problem by calculating the bending moments by finite differences of the displacement function. The correction of Burgess and Mahajerin was still in error. Accurate solutions can be obtained by either changing the coordinate system or the solution forms as shown in the formulation which follows.

## Formulation

For the plate with the coordinate system shown in Fig. 1($a$), Timoshenko and Woinowsky-Kreiger use the solution form

$$w = \frac{4qa^4}{\pi^5 D} \sum_{n=1,3,5,\ldots}^{\infty} \left[ \frac{1}{n^5} + A_n \cosh \alpha_n y + B_n\, \alpha_n y \sinh \alpha_n y \right.$$
$$\left. + C_n \sinh \alpha_n y + D_n\, \alpha_n y \cosh \alpha_n y \right] \sin \alpha_n x \tag{1}$$

where $\alpha_n = n\pi/a$, and other notation is as in Timoshenko and Woinowsky-Kreiger (1959). Numerical difficulties arise when using the solution form in Eq. (1) for the origin placement shown in Fig. 1($a$). The hyperbolic terms are all small at $y=0$ and large at $y=b$, and the terms become increasingly large with increasing $n$. Satisfying the boundary conditions leads to $A_n \approx -B_n \approx -C_n \approx D_n$ for large $n$. For example, for $n=5$, the differences in the magnitude of the coefficients $A_n$, $B_n$, $C_n$, and $D_n$ are in the eighth significant figure. Taking as a typical case, $y=b=a$, $\cosh\alpha_n y$ and $\sinh\alpha_n y$ differ in the thirteenth significant figure for $n=5$. Thus, one needs to carry eight

[8]Civil Engineering Department, University of California, Davis, CA 95616. Mem. ASME.

Manuscript received by the ASME Applied Mechanics Division, Sept. 18, 1990; final revision, Aug. 8, 1991. Associate Technical Editor: L. M. Keer.

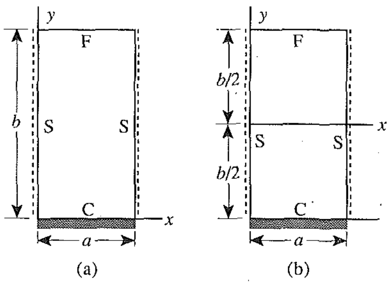


**Fig. 1 SCSF plate with different origins**

significant figures to produce the third term ($n=5$) to one significant figure. For the fourth term ($n=7$), eleven significant figures must be carried to produce a fourth term to 1 significant figure and for the fifth term ($n=9$), fourteen significant figures are needed.

The solution form in Eq. (1) would work well for the coordinate system shown in Fig. 1($b$), whereas for the coordinate system shown in Fig. 1($a$), the form should be

$$w=\frac{4qa^4}{\pi^5 D}\sum_{n=1,3,5,\ldots}^{\infty}\left[\frac{1}{n^5}+A_n\exp(-\alpha_n y)+B_n\,\alpha_n y\exp(-\alpha_n y)\right.$$
$$+C_n\exp[-\alpha_n(b-y)]$$
$$\left.+D_n\,\alpha_n y\exp[-\alpha_n(b-y)]\right]\sin\alpha_n x. \quad (2)$$

In this Brief Note the form shown in Eq. (1) will be applied to the coordinate system shown in Fig. 1($b$). The computation of the hyperbolic functions can lead to very large numbers and hence to computer overflow problems. Computer overflow and underflow refer to the attempt to store numbers which are too large or too small in the computer (eg., for the VAX used in these computations, overflow in single precision occurs when the number is greater than approximately $10^{38}$ and underflow when the number is less than approximately $10^{-38}$). To obviate this problem, the hyperbolic functions are replaced with the modified hyperbolic functions defined as follows:

$$\mathrm{Sh}(\alpha y)=2\sinh(\alpha y)/\exp(\alpha b/2)=\exp[-\alpha(b/2-y)]$$
$$-\exp[-\alpha(b/2+y)] \quad (3)$$

$$\mathrm{Ch}(\alpha y)=2\cosh(\alpha y)/\exp(\alpha b/2)=\exp[-\alpha(b/2-y)]$$
$$+\exp[-\alpha(b/2+y)]. \quad (4)$$

The modified hyperbolic functions (Sh and Ch) differentiate in the same way as the hyperbolic functions, but have maxima in the region of interest of the order of one. Computer overflow is avoided by computing the functions using the last form shown in Eq. (3) and (4). Computer underflow is avoided by computing the arguments of the exponential functions first. If the arguments are negative numbers large enough to cause underflow in the computation of the exponential functions, the exponential functions are returned as zero.

The solution forms identically satisfy the governing differential equations for a uniformly loaded thin plate and the simply-supported boundary conditions on the two opposite edges ($x=0$ and $x=a$). For the SCSF plate shown in Fig. 1($b$), the boundary conditions at $y=-b/2$ are $w=0$ and $w_{,y}=0$, and at $y=b/2$ are $M_y=0$ and $V_y=0$. The functions $w_{,y}$, $M_y$, and $V_y$ are expressed as

$$w_{,y}=\frac{4qa^4}{\pi^5 D}\sum_{n=1,3,5,\ldots}^{\infty}\alpha_n\{A_n\,\mathrm{Sh}(\alpha_n y)+B_n[\alpha_n y\,\mathrm{Ch}(\alpha_n y)$$
$$+\mathrm{Sh}(\alpha_n y)]+C_n\,\mathrm{Ch}(\alpha_n y)+D_n[\alpha_n y\,\mathrm{Sh}(\alpha_n y)$$
$$+\mathrm{Ch}(\alpha_n y)]\}\sin\alpha_n x \quad (5)$$

**Table 1 Deflections and bending moments for a uniformly loaded SCSF plate; $\nu=0.3$**

| | $x=a/2,\ y=b/2$ | | $x=a/2, y=-b/2$ |
|---|---|---|---|
| $b/a$ | $w_{max}$ | $M_x$ | $M_y$ |
| 0 | 0.125000000 $qb^4/D$ | 0.000000000 $qa^2$ | -0.500000000 $qb^2$ |
| 1/3 | 0.093979265 $qb^4/D$ | 0.007820037 $qa^2$ | -0.427943638 $qb^2$ |
| 1/2 | 0.058226695 $qb^4/D$ | 0.029263071 $qa^2$ | -0.318974533 $qb^2$ |
| 2/3 | 0.033543373 $qb^4/D$ | 0.055854598 $qa^2$ | -0.226910373 $qb^2$ |
| 1 | 0.011235939 $qb^4/D$ | 0.097184565 $qa^2$ | -0.118406669 $qb^2$ |
| 3/2 | 0.014147801 $qa^4/D$ | 0.123332401 $qa^2$ | -0.123734805 $qa^2$ |
| 2 | 0.014949099 $qa^4/D$ | 0.130529073 $qa^2$ | -0.124665721 $qa^2$ |
| 3 | 0.015203454 $qa^4/D$ | 0.132813522 $qa^2$ | -0.124975003 $qa^2$ |
| ∞ | 0.015219156 $qa^4/D$ | 0.132954545 $qa^2$ | -0.125000000 $qa^2$ |

**Table 2 Deflections and bending moments for a uniformly loaded SSSF plate; $\nu=0.3$**

| | $x=a/2,\ y=b/2$ | | $x=a/2,\ y=0$ | |
|---|---|---|---|---|
| $b/a$ | $w_{max}$ | $M_x$ | $M_x$ | $M_y$ |
| 1/2 | 0.007094143 $qa^4/D$ | 0.060158549 $qa^2$ | 0.038486816 $qa^2$ | 0.022324240 $qa^2$ |
| 2/3 | 0.009679443 $qa^4/D$ | 0.083244614 $qa^2$ | 0.055105422 $qa^2$ | 0.030231695 $qa^2$ |
| 1/1.4 | 0.010287565 $qa^4/D$ | 0.088691703 $qa^2$ | 0.059337263 $qa^2$ | 0.032017834 $qa^2$ |
| 1/1.3 | 0.010918482 $qa^4/D$ | 0.094347155 $qa^2$ | 0.063916242 $qa^2$ | 0.033829516 $qa^2$ |
| 1/1.2 | 0.011564421 $qa^4/D$ | 0.100140760 $qa^2$ | 0.068856712 $qa^2$ | 0.035630251 $qa^2$ |
| 1/1.1 | 0.012214176 $qa^4/D$ | 0.105971327 $qa^2$ | 0.074168268 $qa^2$ | 0.037369785 $qa^2$ |
| 1 | 0.012852415 $qa^4/D$ | 0.111700549 $qa^2$ | 0.079853586 $qa^2$ | 0.038980893 $qa^2$ |
| 1.1 | 0.013405953 $qa^4/D$ | 0.116670604 $qa^2$ | 0.085340074 $qa^2$ | 0.040260990 $qa^2$ |
| 1.2 | 0.013834358 $qa^4/D$ | 0.120517639 $qa^2$ | 0.090130665 $qa^2$ | 0.041133265 $qa^2$ |
| 1.3 | 0.014164209 $qa^4/D$ | 0.123479891 $qa^2$ | 0.094323408 $qa^2$ | 0.041690010 $qa^2$ |
| 1.4 | 0.014417184 $qa^4/D$ | 0.125751839 $qa^2$ | 0.098001539 $qa^2$ | 0.042005741 $qa^2$ |
| 1.5 | 0.014610598 $qa^4/D$ | 0.127488916 $qa^2$ | 0.101234791 $qa^2$ | 0.042139803 $qa^2$ |
| 2 | 0.015069210 $qa^4/D$ | 0.131607828 $qa^2$ | 0.112480515 $qa^2$ | 0.041412940 $qa^2$ |
| 3 | 0.015210665 $qa^4/D$ | 0.132878286 $qa^2$ | 0.121655007 $qa^2$ | 0.039063965 $qa^2$ |
| ∞ | 0.015219156 $qa^4/D$ | 0.132954545 $qa^2$ | 0.125000000 $qa^2$ | 0.037500000 $qa^2$ |

**Table 3 Deflections and bending moments for a uniformly loaded SFSF plate; $\nu=0.3$**

| | $x=a/2,\ y=b/2$ | | $x=a/2,\ y=0$ | |
|---|---|---|---|---|
| $b/a$ | $w_{max}$ | $M_x$ | $M_x$ | $M_y$ |
| 0.1 | 0.014326860 $qa^4/D$ | 0.125134615 $qa^2$ | 0.124932693 $qa^2$ | 0.000576920 $qa^2$ |
| 0.3 | 0.014456216 $qa^4/D$ | 0.126175323 $qa^2$ | 0.124415537 $qa^2$ | 0.005043400 $qa^2$ |
| 0.5 | 0.014644623 $qa^4/D$ | 0.127812536 $qa^2$ | 0.123642359 $qa^2$ | 0.012147577 $qa^2$ |
| 0.7 | 0.014821944 $qa^4/D$ | 0.129390877 $qa^2$ | 0.122994213 $qa^2$ | 0.019166737 $qa^2$ |
| 0.8 | 0.014895912 $qa^4/D$ | 0.130053091 $qa^2$ | 0.122773859 $qa^2$ | 0.022192335 $qa^2$ |
| 0.9 | 0.014958835 $qa^4/D$ | 0.130617260 $qa^2$ | 0.122626314 $qa^2$ | 0.024826733 $qa^2$ |
| 1 | 0.015011257 $qa^4/D$ | 0.131087659 $qa^2$ | 0.122545398 $qa^2$ | 0.027078215 $qa^2$ |
| 1.2 | 0.015089110 $qa^4/D$ | 0.131786619 $qa^2$ | 0.122545663 $qa^2$ | 0.030564510 $qa^2$ |
| 1.5 | 0.015157062 $qa^4/D$ | 0.132396867 $qa^2$ | 0.122806077 $qa^2$ | 0.033862386 $qa^2$ |
| 2 | 0.015202171 $qa^4/D$ | 0.132801999 $qa^2$ | 0.123467772 $qa^2$ | 0.036388775 $qa^2$ |
| 3 | 0.015218060 $qa^4/D$ | 0.132944703 $qa^2$ | 0.124452197 $qa^2$ | 0.037499828 $qa^2$ |
| ∞ | 0.015219156 $qa^4/D$ | 0.132954545 $qa^2$ | 0.125000000 $qa^2$ | 0.037500000 $qa^2$ |

$$M_y=\frac{4qa^4}{\pi^5 D}\sum_{n=1,3,5,\ldots}^{\infty}\alpha_n^2\left\{-\frac{\nu}{n^5}+A_n(1-\nu)\,\mathrm{Ch}(\alpha_n y)\right.$$
$$+B_n[\alpha_n y(1-\nu)\,\mathrm{Sh}(\alpha_n y)+2\,\mathrm{Ch}(\alpha_n y)]+C_n(1-\nu)\,\mathrm{Sh}(\alpha_n y)$$
$$\left.+D_n[(1-\nu)\alpha_n y\,\mathrm{Ch}(\alpha_n y)+2\,\mathrm{Sh}(\alpha_n y)]\right\}\sin\alpha_n x \quad (6)$$

$$V_y=\frac{4qa^4}{\pi^5 D}\sum_{n=1,3,5,\ldots}^{\infty}-\alpha_n^3\{A_n(1-\nu)\,\mathrm{Sh}(\alpha_n y)$$
$$+B_n[(1-\nu)\,\alpha_n y\,\mathrm{Ch}(\alpha_n y)-(1+\nu)\,\mathrm{Sh}(\alpha_n y)]$$
$$+C_n(1-\nu)\,\mathrm{Ch}(\alpha_n y)+D_n[(1-\nu)\alpha_n y\,\mathrm{Sh}(\alpha_n y)$$
$$-(1+\nu)\,\mathrm{Ch}(\alpha_n y)]\}\sin\alpha_n x \quad (7)$$

Applying the boundary conditions at $y=\pm b/2$ yields a four-by-four system of equations for the unknowns $A_n$, $B_n$, $C_n$, and $D_n$ for each $n$. Other boundary conditions are handled in a similar manner. When the boundary conditions are such that the displacement will be symmetric, the constants $C_n$ and $D_n$ will go to zero, as in the case of an SFSF plate.

## Results

Accurate results are given for the SSSF and the SFSF case as well as the SCSF case. Table 1 is the for the SCSF case and corresponds to Table 39 in Timoshenko and Woinowsky-Kreiger (1959). Table 2 is for the SSSF case and corresponds to Table 42 in Timoshenko and Woinowsky-Kreiger (1959). Table 3 is the for SFSF case and is similar to the Tables 1 and 2 in that it considers a few key values at various $b$ to $a$ ratios. Every effort was made to ensure that the results are good to the number of significant figures shown in the tables. While this type of accuracy is not required for engineering design, it is extremely valuable as an accurate comparison to newly developed approximate methods such as those of Wu and Altiero (1979) and Burgess and Mahajerin (1985). The results in Tables 1 and 2 show that the Tables 39 and 42 in Timoshenko and Woinowsky-Kreiger (1959) are correct but are limited to only a few significant figures. It is hoped that the accurate results presented in this Note can be of use in future comparisons.

## References

Burgess, G., and Mahajerin, E., 1985, "A Numerical Method for Laterally Loaded Thin Plates," *Computer Methods in Applied Mechanics and Engineering*, Vol. 49, pp. 1–15.

Timoshenko, S., and Woinowsky-Kreiger, S., 1958, *Theory of Plates and Shells*, 2nd ed., McGraw-Hill, New York.

Wu, B. C., and Altiero, N. J., 1979, "A Boundary Integral Method Applied to Plates of Arbitrary Plan Form and Arbitrary Boundary Conditions," *Computers and Structures*, Vol. 10, pp. 703–707.

# Energy Dissipated in Planar Collision

**W. J. Stronge**[9]

Compact solid bodies that collide at low or moderate impact speeds suffer negligible deformation outside a small region surrounding the point of contact. During collision, the reaction forces on colliding bodies decrease the sum of their kinetic energies in an initial phase of compression. Then elastic strain energy from the deformed region drives the bodies apart and restores some kinetic energy in a succeeding period of restitution. The energy dissipated in collision is the difference between the initial and final kinetic energies.

For partly elastic collision of "rigid" bodies, the kinetic energy that is dissipated $D$ is equal to the negative of work done by reaction forces on the colliding bodies. This work can be calculated by considering changes in relative velocity across the small deforming region that surrounds the contact point. If the deforming region is infinitesimal, the reaction forces across this region are equal but opposite. Thus, during the brief period of a "rigid body" collision, changes in relative velocity $v_i(t)$ across the deforming region can be found as a function of impulse. At any time during collision the energy dissipated in changing the velocity of the rigid bodies on either side of the deforming region depends on work $W(t)$ done by the reaction forces $F_i(t)$;

$$D(t) = -W(t) = -\int_o^t F_i v_i dt' \qquad (1)$$

[9]Department of Engineering, University of Cambridge, Cambridge, CB2 1PZ, U.K. Mem. ASME.

Contributed by the Applied Mechanics Division of THE AMERICAN SOCIETY OF MECHANICAL ENGINEERS. Manuscript received by the ASME Applied Mechanics Division, Nov. 15, 1990; final revision, May 15, 1991. Associate Technical Editor: C. Horgan.

where repeated subscripts imply summation over the set of spatial coordinates. Impact reactions are large in comparison with body forces so the only forces that do work during a "rigid body" collision are reactions at points of contact with neighboring bodies.

The reaction impulse $P_i(t)$ is the integral of force. Since $dP_i = F_i dt$, work done by the reaction can be expressed as

$$W(t) = \int_o^{P_i(t)} v_i dP_i'. \qquad (2)$$

Equation (2) is readily evaluated for a period of unidirectional slip since changes in relative velocity are proportional to changes in reaction impulse if the direction of $F_i$ is constant. The direction of $F_i$, however, has a tangential component (friction) that is always opposed to the tangential component of $v_i$ (slip). If small initial slip is halted or reversed before collision terminates, both $F_i$ and $dP_i$ change direction the instant slip vanishes. Consequently, for somewhat rough bodies the integration of (2) must be divided into separate periods before and after slip vanishes. In any case, the terminal impulse at separation $P_i(t_f)$ can be related to energy dissipated by irreversible internal deformation; this relationship is provided by Stronge's (1990) definition for the energetic coefficient of restitution $e_*$.

A useful method of calculating energy dissipation in a collision is to use the following theorem for each separate period of slip and then sum the results for the period of collision.

> Work done by reaction forces on colliding bodies during any period of unidirectional slip $\Delta t = t_2 - t_1$, equals the scalar product of the reaction impulse $\Delta P_i$ and half the sum of the initial and final relative velocities across the contact point; i.e., $\Delta W = \Delta P_i[v_i(t_2) + v_i(t_1)]/2$ where $\Delta P_i = P_i(t_2) - P_i(t_1)$.

To prove this theorem, consider a triad of mutually perpendicular unit vectors $n_i$ aligned such that $n_n$ is the normal to the common tangent plane through the point of contact $CP$ and $n_t$ is the incident direction of slip. For any period of unidirectional slip $\Delta t = t_2 - t_1$, the Amonton-Coulomb law of friction relates the tangential and normal components of impulse by a limiting friction coefficient $\mu$;

$$\Delta P_t = -\mu \Delta P_n \mathrm{sgn}(u) \qquad (3)$$

where $u = v_i n_t$ depends on the direction of slip for the contact point of the other body.

Across the contact point of colliding bodies separated by an infinitesimal deforming element, changes in relative velocity are obtained from the laws of motion,

$$v_i(t) = v_i(t_1) - m_{ij}^{-1} \Delta P_j(t), \quad t > t_1 \qquad (4)$$

where $m_{ij}$ is the effective mass for $CP$. Elements of $m_{ij}$ are dependent only on the mass of each colliding body and the distribution of mass relative to CP. If components of $\Delta P_j$ are related by the friction law (3), then during any period of unidirectional slip, Eq. (2) yields

$$\Delta W = \Delta P_i v_i(t_1) - m_{ij}^{-1} \Delta P_j \Delta P_i / 2. \qquad (5)$$

With (4), this can be expressed as

$$\Delta W = \Delta P_i [v_i(t_1) + v_i(t_2)]/2. \qquad (6)$$

This is a generalization of a theorem by Thomson and Tait (1879); their statement is valid only for collision of smooth (frictionless) bodies. It is noteworthy that the theorem does not apply to nonplanar phases of frictional collision; if changes in velocity are nonplanar, the direction of friction changes continuously during collision. (A previous statement without proof by Stronge (1987) did not point out that the general theorem is restricted to periods of unidirectional slip.) The separation into periods of unidirectional slip is required if

## Results

Accurate results are given for the SSSF and the SFSF case as well as the SCSF case. Table 1 is the for the SCSF case and corresponds to Table 39 in Timoshenko and Woinowsky-Kreiger (1959). Table 2 is for the SSSF case and corresponds to Table 42 in Timoshenko and Woinowsky-Kreiger (1959). Table 3 is the for SFSF case and is similar to the Tables 1 and 2 in that it considers a few key values at various $b$ to $a$ ratios. Every effort was made to ensure that the results are good to the number of significant figures shown in the tables. While this type of accuracy is not required for engineering design, it is extremely valuable as an accurate comparison to newly developed approximate methods such as those of Wu and Altiero (1979) and Burgess and Mahajerin (1985). The results in Tables 1 and 2 show that the Tables 39 and 42 in Timoshenko and Woinowsky-Kreiger (1959) are correct but are limited to only a few significant figures. It is hoped that the accurate results presented in this Note can be of use in future comparisons.

## References

Burgess, G., and Mahajerin, E., 1985, "A Numerical Method for Laterally Loaded Thin Plates," *Computer Methods in Applied Mechanics and Engineering*, Vol. 49, pp. 1-15.

Timoshenko, S., and Woinowsky-Kreiger, S., 1958, *Theory of Plates and Shells*, 2nd ed., McGraw-Hill, New York.

Wu, B. C., and Altiero, N. J., 1979, "A Boundary Integral Method Applied to Plates of Arbitrary Plan Form and Arbitrary Boundary Conditions," *Computers and Structures*, Vol. 10, pp. 703-707.

# Energy Dissipated in Planar Collision

**W. J. Stronge**[9]

Compact solid bodies that collide at low or moderate impact speeds suffer negligible deformation outside a small region surrounding the point of contact. During collision, the reaction forces on colliding bodies decrease the sum of their kinetic energies in an initial phase of compression. Then elastic strain energy from the deformed region drives the bodies apart and restores some kinetic energy in a succeeding period of restitution. The energy dissipated in collision is the difference between the initial and final kinetic energies.

For partly elastic collision of "rigid" bodies, the kinetic energy that is dissipated $D$ is equal to the negative of work done by reaction forces on the colliding bodies. This work can be calculated by considering changes in relative velocity across the small deforming region that surrounds the contact point. If the deforming region is infinitesimal, the reaction forces across this region are equal but opposite. Thus, during the brief period of a "rigid body" collision, changes in relative velocity $v_i(t)$ across the deforming region can be found as a function of impulse. At any time during collision the energy dissipated in changing the velocity of the rigid bodies on either side of the deforming region depends on work $W(t)$ done by the reaction forces $F_i(t)$;

$$D(t) = -W(t) = -\int_o^t F_i v_i dt' \tag{1}$$

where repeated subscripts imply summation over the set of spatial coordinates. Impact reactions are large in comparison with body forces so the only forces that do work during a "rigid body" collision are reactions at points of contact with neighboring bodies.

The reaction impulse $P_i(t)$ is the integral of force. Since $dP_i = F_i dt$, work done by the reaction can be expressed as

$$W(t) = \int_o^{P_i(t)} v_i dP_i'. \tag{2}$$

Equation (2) is readily evaluated for a period of unidirectional slip since changes in relative velocity are proportional to changes in reaction impulse if the direction of $F_i$ is constant. The direction of $F_i$, however, has a tangential component (friction) that is always opposed to the tangential component of $v_i$ (slip). If small initial slip is halted or reversed before collision terminates, both $F_i$ and $dP_i$ change direction the instant slip vanishes. Consequently, for somewhat rough bodies the integration of (2) must be divided into separate periods before and after slip vanishes. In any case, the terminal impulse at separation $P_i(t_f)$ can be related to energy dissipated by irreversible internal deformation; this relationship is provided by Stronge's (1990) definition for the energetic coefficient of restitution $e_*$.

A useful method of calculating energy dissipation in a collision is to use the following theorem for each separate period of slip and then sum the results for the period of collision.

> Work done by reaction forces on colliding bodies during any period of unidirectional slip $\Delta t = t_2 - t_1$, equals the scalar product of the reaction impulse $\Delta P_i$ and half the sum of the initial and final relative velocities across the contact point; i.e., $\Delta W = \Delta P_i[v_i(t_2) + v_i(t_1)]/2$ where $\Delta P_i = P_i(t_2) - P_i(t_1)$.

To prove this theorem, consider a triad of mutually perpendicular unit vectors $n_i$ aligned such that $n_n$ is the normal to the common tangent plane through the point of contact $CP$ and $n_t$ is the incident direction of slip. For any period of unidirectional slip $\Delta t = t_2 - t_1$, the Amonton-Coulomb law of friction relates the tangential and normal components of impulse by a limiting friction coefficient $\mu$;

$$\Delta P_t = -\mu \Delta P_n \mathrm{sgn}(u) \tag{3}$$

where $u = v_i n_t$ depends on the direction of slip for the contact point of the other body.

Across the contact point of colliding bodies separated by an infinitesimal deforming element, changes in relative velocity are obtained from the laws of motion,

$$v_i(t) = v_i(t_1) - m_{ij}^{-1} \Delta P_j(t), \quad t > t_1 \tag{4}$$

where $m_{ij}$ is the effective mass for $CP$. Elements of $m_{ij}$ are dependent only on the mass of each colliding body and the distribution of mass relative to CP. If components of $\Delta P_j$ are related by the friction law (3), then during any period of unidirectional slip, Eq. (2) yields

$$\Delta W = \Delta P_i v_i(t_1) - m_{ij}^{-1} \Delta P_j \Delta P_i / 2. \tag{5}$$

With (4), this can be expressed as

$$\Delta W = \Delta P_i[v_i(t_1) + v_i(t_2)]/2. \tag{6}$$

This is a generalization of a theorem by Thomson and Tait (1879); their statement is valid only for collision of smooth (frictionless) bodies. It is noteworthy that the theorem does not apply to nonplanar phases of frictional collision; if changes in velocity are nonplanar, the direction of friction changes continuously during collision. (A previous statement without proof by Stronge (1987) did not point out that the general theorem is restricted to periods of unidirectional slip.) The separation into periods of unidirectional slip is required if

[9]Department of Engineering, University of Cambridge, Cambridge, CB2 1PZ, U.K. Mem. ASME.

Contributed by the Applied Mechanics Division of THE AMERICAN SOCIETY OF MECHANICAL ENGINEERS. Manuscript received by the ASME Applied Mechanics Division, Nov. 15, 1990; final revision, May 15, 1991. Associate Technical Editor: C. Horgan.

tangential impulse is obtained from the Amonton-Coulomb friction law.

The general theorem is particularly useful for relating losses of energy to separate frictional and internal hysteresis sources of dissipation. This separation is explicit if the contact points have negligible tangential compliance.

## References


Stronge, W. J., 1987, "The Domino Effect: A Wave of Destabilizing Collisions in a Periodic Array," *Proc. Roy. Soc. Lond.*, Vol. A409, pp. 199–208.

Stronge, W. J., 1990, "Rigid Body Collisions with Friction," *Proc. Roy. Soc. Lond.*, Vol. A431, pp. 169–181.

Thomson, W., and Tait, P. G., 1879, *Treatise on Natural Philosophy*, Vol. 1, Part I, Cambridge University Press, Cambridge, U.K.


# Unilateral Contract of a Springboard and a Fulcrum


**M. Kuipers[10] and A. A. F. van de Ven[11]**



*A springboard, as commonly used in diving, is considered. It is hinged at the rear end and rests free on a rubber fulcrum at the middle of the board. If an excentric load is applied to its front end, then due to torsion it is possible that the board is lifted away from the fulcrum along a certain distance. This problem is investigated for a static load. Although a linear small displacement theory is applied, the problem is nonlinear due to the unknown length of noncontact.*


## 1 Introduction

Springboards used in diving are hinged at the rear end and rest free on a movable fulcrum close at midspan. Those presently in use at international contests are extremely flexible, but also vulnerable to overloading, causing fatigue (aluminium) or internal buckling of fibers (wood).

Although the demands put to the strength of a springboard are excessively high, specifications with respect to the allowable amount of torsion are neither prescribed by the F.I.N.A. (Federation International de Natation Amateur), nor given by the producers of springboards. We feel that a simple static test, in which a board is loaded by an excentric force, would be of some value to qualify the springboard. This paper has been written to evaluate the results of such a test quantitatively. Hence, in what follows, we shall analyse the deformation of the board and, specifically, we shall concentrate on the distribution of the reaction forces at the fulcrum in the presence of a possible detachment of the board from the latter. In doing so, we shall assume that the fulcrum behaves as a linear foundation of the so called Winkler type, which gives rise to a line load along the contact line between board and fulcrum. Throughout the analysis we apply linear field equations ensuing from a small displacement beam theory. However, in view of the unilateral characteristics of the contact between board and fulcrum, the problem is essentially a nonlinear one.

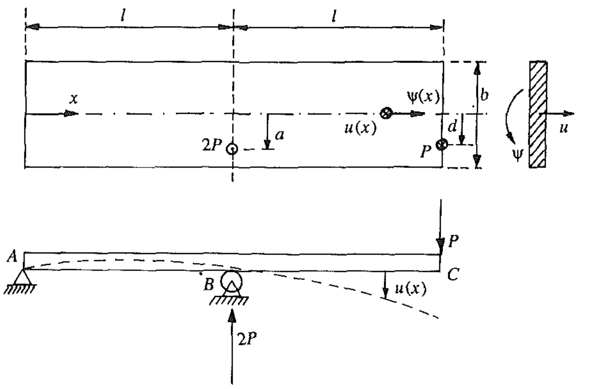


Fig. 1 The springboard *ABC* is loaded by a force *P* applying excentrically at the front end *C*

## 2 Mathematical Analysis

We consider a springboard *ABC* of length $2l$ and width $b$ (Fig. 1). The hinge is at the rear end $A$ and the fulcrum is placed in the middle $B$ of the board. Until further notice we shall assume that the board has a uniform cross-section, so that its bending and torsional stiffnesses are constants. We note that usually springboards are tapered; therefore, we shall return to this point in the sequel. The board is loaded by a static force $P$ applied at a distance $d$ from the center of the front end $C$, as shown in Fig. 1 ($0 \le d \le b/2$). In what follows we shall neglect the effect of the anticlastic bending of the board. Although for a beam of homogeneous material this anticlastic effect can be quite strong, we nevertheless think that the neglect of this effect is justified here. The reason for this is in the special construction of springboards, which are constructed such as to keep the lateral contraction as small as possible. In the absence of anticlastic bending, any cross-section of the board remains straight and may show only a translation and a rotation. Then, as for the contact of board and fulcrum, we have to distinguish between a rigid fulcrum and a resilient one. In the event of a rigid fulcrum, kinematical contact along the full width of the fulcrum without rotation of the cross-section at $B$ about the longitudinal axis of the board exists. Then the whole part $AB$ of the board is free from torsion. We note that these findings hold irrespective of the magnitude of $P$ and of the torsional stiffness of the board. In what follows we shall return to this point.

Next, we consider a resilient fulcrum, modeled as a linear elastic foundation, modulus $c$ (defined as the magnitude of the reaction of the foundation measured per unit of length along the fulcrum if the deflection is equal to unity). Here we have to distinguish between full and partial contact. Designating the displacement and the torsion angle of the cross-section at $B$ by $u(l)$ and $\psi(l)$, respectively, we note that full contact exists if for every $\eta$ satisfying $|\eta| \le b/2$

$$u(l)+\eta\psi(l)=\frac{2P}{cb}+\frac{dPl\eta}{\alpha_t+\frac{1}{12}cb^3l}\ge 0, \tag{1}$$

where $\alpha_t$ is the torsional stiffness of the board.

From this we readily find

$$D\ge 3\bar{d}-2, \tag{2}$$

where the dimensionless torsional stiffness $D$ and the dimensionless excentricity $\bar{d}$ follow from

$$D=\frac{24\alpha_t}{cb^3l}, \text{ and } \bar{d}=\frac{2d}{b}, \tag{3}$$

so that $0 \le \bar{d} \le 1$.

[10] Professor, Faculty of Mathematics and Physical Science, Department of Mathematics and Computing Science, University of Groningen, 9700 AV Groningen, The Netherlands.

[11] Associate Professor, Faculty of Mathematics and Computing Science, Eindhoven University of Technology, 5600 MD Eindhoven, The Netherlands.


Contributed by the Applied Mechanics Division of THE AMERICAN SOCIETY OF MECHANICAL ENGINEERS. Manuscript received by the ASME Applied Mechanics Division, Aug. 1, 1990; final revision, Apr. 8, 1991. Associate Technical Editor: J. G. Simmonds.

tangential impulse is obtained from the Amonton-Coulomb friction law.

The general theorem is particularly useful for relating losses of energy to separate frictional and internal hysteresis sources of dissipation. This separation is explicit if the contact points have negligible tangential compliance.

## References


Stronge, W. J., 1987, "The Domino Effect: A Wave of Destabilizing Collisions in a Periodic Array," *Proc. Roy. Soc. Lond.*, Vol. A409, pp. 199–208.

Stronge, W. J., 1990, "Rigid Body Collisions with Friction," *Proc. Roy. Soc. Lond.*, Vol. A431, pp. 169–181.

Thomson, W., and Tait, P. G., 1879, *Treatise on Natural Philosophy*, Vol. 1, Part I, Cambridge University Press, Cambridge, U.K.


# Unilateral Contract of a Springboard and a Fulcrum


**M. Kuipers[10] and A. A. F. van de Ven[11]**



*A springboard, as commonly used in diving, is considered. It is hinged at the rear end and rests free on a rubber fulcrum at the middle of the board. If an excentric load is applied to its front end, then due to torsion it is possible that the board is lifted away from the fulcrum along a certain distance. This problem is investigated for a static load. Although a linear small displacement theory is applied, the problem is nonlinear due to the unknown length of noncontact.*


## 1 Introduction

Springboards used in diving are hinged at the rear end and rest free on a movable fulcrum close at midspan. Those presently in use at international contests are extremely flexible, but also vulnerable to overloading, causing fatigue (aluminium) or internal buckling of fibers (wood).

Although the demands put to the strength of a springboard are excessively high, specifications with respect to the allowable amount of torsion are neither prescribed by the F.I.N.A. (Federation International de Natation Amateur), nor given by the producers of springboards. We feel that a simple static test, in which a board is loaded by an excentric force, would be of some value to qualify the springboard. This paper has been written to evaluate the results of such a test quantitatively. Hence, in what follows, we shall analyse the deformation of the board and, specifically, we shall concentrate on the distribution of the reaction forces at the fulcrum in the presence of a possible detachment of the board from the latter. In doing so, we shall assume that the fulcrum behaves as a linear foundation of the so called Winkler type, which gives rise to a line load along the contact line between board and fulcrum. Throughout the analysis we apply linear field equations ensuing from a small displacement beam theory. However, in view of the unilateral characteristics of the contact between board and fulcrum, the problem is essentially a nonlinear one.


[10]Professor, Faculty of Mathematics and Physical Science, Department of Mathematics and Computing Science, University of Groningen, 9700 AV Groningen, The Netherlands.

[11]Associate Professor, Faculty of Mathematics and Computing Science, Eindhoven University of Technology, 5600 MD Eindhoven, The Netherlands.



Contributed by the Applied Mechanics Division of THE AMERICAN SOCIETY OF MECHANICAL ENGINEERS. Manuscript received by the ASME Applied Mechanics Division, Aug. 1, 1990; final revision, Apr. 8, 1991. Associate Technical Editor: J. G. Simmonds.


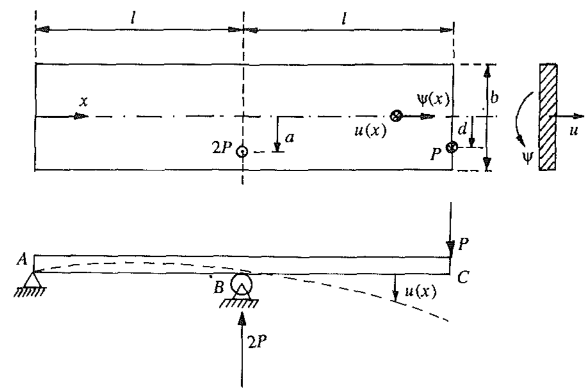


Fig. 1 The springboard *ABC* is loaded by a force *P* applying excentrically at the front end *C*

## 2 Mathematical Analysis

We consider a springboard $ABC$ of length $2l$ and width $b$ (Fig. 1). The hinge is at the rear end $A$ and the fulcrum is placed in the middle $B$ of the board. Until further notice we shall assume that the board has a uniform cross-section, so that its bending and torsional stiffnesses are constants. We note that usually springboards are tapered; therefore, we shall return to this point in the sequel. The board is loaded by a static force $P$ applied at a distance $d$ from the center of the front end $C$, as shown in Fig. 1 ($0 \leq d \leq b/2$). In what follows we shall neglect the effect of the anticlastic bending of the board. Although for a beam of homogeneous material this anticlastic effect can be quite strong, we nevertheless think that the neglect of this effect is justified here. The reason for this is in the special construction of springboards, which are constructed such as to keep the lateral contraction as small as possible. In the absence of anticlastic bending, any cross-section of the board remains straight and may show only a translation and a rotation. Then, as for the contact of board and fulcrum, we have to distinguish between a rigid fulcrum and a resilient one. In the event of a rigid fulcrum, kinematical contact along the full width of the fulcrum without rotation of the cross-section at $B$ about the longitudinal axis of the board exists. Then the whole part $AB$ of the board is free from torsion. We note that these findings hold irrespective of the magnitude of $P$ and of the torsional stiffness of the board. In what follows we shall return to this point.

Next, we consider a resilient fulcrum, modeled as a linear elastic foundation, modulus $c$ (defined as the magnitude of the reaction of the foundation measured per unit of length along the fulcrum if the deflection is equal to unity). Here we have to distinguish between full and partial contact. Designating the displacement and the torsion angle of the cross-section at $B$ by $u(l)$ and $\psi(l)$, respectively, we note that full contact exists if for every $\eta$ satisfying $|\eta| \leq b/2$

$$u(l)+\eta\psi(l)=\frac{2P}{cb}+\frac{dPl\eta}{\alpha_t+\frac{1}{12}cb^3l}\geq 0, \tag{1}$$

where $\alpha_t$ is the torsional stiffness of the board.

From this we readily find

$$D \geq 3\bar{d}-2, \tag{2}$$

where the dimensionless torsional stiffness $D$ and the dimensionless excentricity $\bar{d}$ follow from

$$D=\frac{24\alpha_t}{cb^3l}, \text{ and } \bar{d}=\frac{2d}{b}, \tag{3}$$

so that $0 \leq \bar{d} \leq 1$.

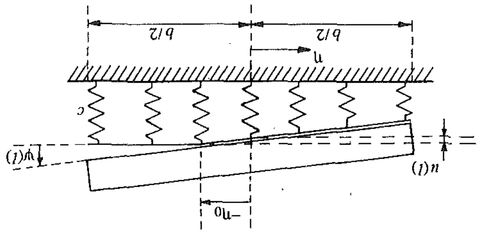

Fig. 2 The point $\eta = \eta_0$ separates the intervals of contact and noncontact

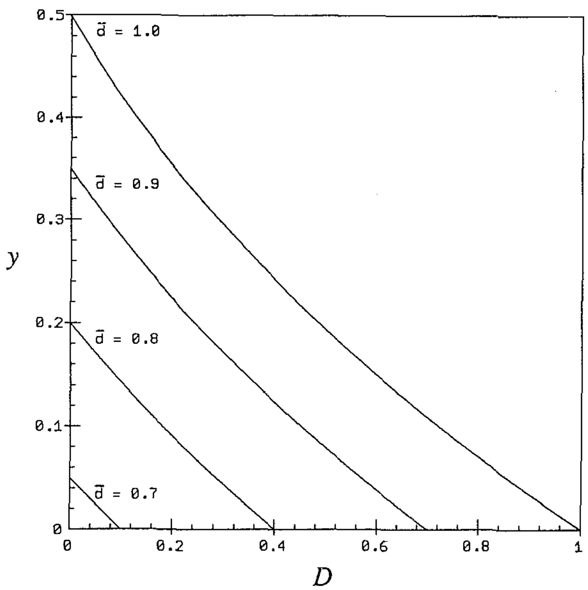


Fig. 3 The dimensionless noncontact length $y$ as a function of the dimensionless torsional stiffness $D$ for several values of the dimensionless excentricity $\bar{d}$

We see that for $\bar{d} < 2/3$, the inequality (2) is satisfied automatically. However, if $\bar{d} \geq 2/3$, then for too small values of $D$, it is not compiled with. In that case full contact is not possible, and part of the fulcrum becomes unstuck. At first sight this looks plausible, since a very small torsional stiffness will give rise to a large twist detaching one side of the board from the fulcrum. On the other hand, however, there is a seeming discrepancy with the finding that in the case of a rigid fulcrum, full contact develops irrespective of the value of the torsional stiffness. How things are becomes clear if we consider the case of partial contact.

As sketched in Fig. 2, we suppose that contact between board and fulcrum exists only for $\eta > \eta_0$, where $\eta_0 > -b/2$. The relation $u(l) + \eta_0\psi(l) = 0$ and the equilibrium of forces and moments, from the latter of which $u(l)$ has been eliminated, yield the following three equations:

$$U - 2(1-y)\Psi = 0, \tag{4}$$

$$(U + y\Psi)(2-y) = p, \quad \left(p = \frac{16P}{cb^2}\right), \tag{5}$$

$$\Psi\left\{-D + \frac{1}{2}\left(\frac{3}{2}\bar{d} - 1 - y\right)(2-y)^2\right\} = 0, \tag{6}$$

respectively, for the three unknown dimensionless quantities

$$U = \frac{4}{b}\,u(l),\ \Psi = \psi(l),\ y = 1 + \frac{2\eta_0}{b}. \tag{7}$$

Since $\Psi \neq 0$, we can formally solve $y$ from (6) as a function of $D$, after which (4) and (5) yield

$$U = \frac{2(1-y)p}{(2-y)^2},\ \Psi = \frac{p}{(2-y)^2}. \tag{8}$$

## 3 Discussion and Numerical Results

Before proceeding to the numerical evaluation of the results obtained so far, we first note the following: From (6) we can calculate $D$ as a function of $y$ yielding

$$D = \frac{1}{2}\left(\frac{3}{2}\bar{d} - 1 - y\right)(2-y)^2, \tag{9}$$

and from this we find positive values of $D$ only if

$$y < \frac{3}{2}\bar{d} - 1. \tag{10}$$

Since, a priori, $-b/2 \leq \eta \leq b/2$ or, equivalently, $0 \leq y \leq 2$, $(3)^2$ and (10) yield

$$\frac{2}{3} \leq \bar{d} \leq 1, \tag{11}$$

so that $y \in [0, 1/2]$ or, equivalently,

$$\eta_0 \in \left[-\frac{b}{2}, -\frac{b}{4}\right]. \tag{12}$$

Evidently, the maximal length of noncontact is $b/4$, and it occurs if $\bar{d} = 1$, or $d = b/2$, as is to be expected. Moreover, from (9), (10), and (11) it follows that

$$0 \leq D \leq 3\bar{d} - 2, \tag{13}$$

and this result is in agreement with (2) pertaining to full contact. Figure 3 shows $y$ as a function of $D$, computed from (9) for some values of $\bar{d}$.

For strength considerations it is interesting to know the maximal value $q_{max}$ of the line load on the board at the cross-section $B$. For this value we readily find, for the cases of

(i) *full contact* ($y = 0$)

$$0 \leq \bar{d} \leq \frac{2}{3}.\ D \text{ arbitrary, or } \frac{2}{3} \leq \bar{d} \leq 1,\ D \geq 3\bar{d} - 2,$$

$$q_{max} = \frac{cbp}{8}\left(1 + \frac{3\bar{d}}{D+2}\right), \tag{14}$$

(ii) *partial contact* ($0 < y \leq 1/2$)

$$\frac{2}{3} < \bar{d} \leq 1,\ D < 3\bar{d} - 2,$$

$$q_{max} = \frac{cbp}{2(2-y)}. \tag{15}$$

As is to be expected, the greatest stress concentration occurs for $\bar{d} = 1$, showing a concentration factor $\gamma$ of

$$\gamma = \frac{8}{3} \cong 2.67. \tag{16}$$

If one performs a static torsion test at a springboard, the twist angle $\psi(2l)$ at the front end $C$ will be measured. From the foregoing, it follows:

$$\psi(2l) = \Psi + \frac{3p\bar{d}}{4D}, \tag{17}$$

holding for every $\bar{d}$ and $D$.

Next, we turn to the seeming discrepancy mentioned in the preceding section following formula (2). In this respect we note that for very large values of $c$, the value of $D$ approaches zero, leading to a case of partial contact with the limit $y \to 1/2$. However, $p$ becomes very small as well, yielding $U \to 0$ and $\Psi \to 0$. This means that in the event of a very stiff fulcrum the noncontact length formally may remain finite. However, the play vanishes. Hence, from a physical point of view, there is no question of any discrepancy.

Finally, we note that real springboards are tapered from the fulcrum toward the ends, whereas we have assumed that the board has a uniform cross-section. However, by inspection we find that the results obtained here still hold if we use for $\alpha_t$ the harmonic mean $\overline{\alpha}_t$ of the torsional stiffness, i.e.,

$$\overline{\alpha}_t = \frac{1}{\frac{1}{2l}\int_0^{2l} \frac{dx}{\alpha_t(x)}}. \tag{18}$$

Apart from that, it is easy to see that for tapered boards the error resulting from the neglect of the anticlastic bending in this paper will be smaller than for boards with a uniform cross-section. Also, for boards consisting of a plate provided with separate longitudinal stiffeners, the effect of the anticlastic bending is small. However, in the latter case the deformation of the cross-section in its plane will come into play.

**Acknowledgment**

The authors gratefully acknowledge the stimulating discussions with Prof. Dr. D. J. Gerritsen on the optimal design of springboards. The present problem emerged from these talks.

## Slewing Motion Control of a Very Flexible Elastic Beam

**J. W. Eischen[12,13], L. Silverberg[12,13], and H. L. Wang[13]**

### 1 Introduction

This Note presents a novel approach to the slewing of beams that are permitted to undergo large combined rigid-body/elastic motions. The problem addressed is a classical noncollocated beam control problem in which a slewing torque is applied at the beam root and sensor measurements are taken at the beam root and the beam tip. Cannon and Schmitz (1984) proposed one of the first feedback control algorithms for such a problem, and as well provided experimental verification. Juang, Turner, and Chun (1985) developed closed-form expressions for control gains that resulted in fuel optimal slewing. Skaar and Tucker (1987) developed classical open-loop and closed-loop control strategies making use of transfer functions. Bayo (1987) employed a structural finite element technique to solve the inverse dynamics problem (open-loop control) for a slewing beam. In each of these investigations, beam motions were restricted to small elastic deflections.

In contrast, this Note presents a strategy well suited for beams undergoing large elastic motions described by nonlinear partial differential equations of motion. The associated torque is governed by a slewing control algorithm consisting of open-loop and closed-loop components. The open-loop component produces the desired overall rigid-body motion of the beam, while the closed-loop component suppresses the elastic vibrational motion relative to a shadow beam. The shadow beam is a fictitious beam whose motion is prescribed by the designer. This concept of a shadow structure was developed by Silverberg and Foster (1990) for maneuvering flexible spacecraft. In the present work, the shadow beam is essentially a straight line that remains tangent to the beam at its root. The closed-loop control component is expressed as a function of three parameters; the collocation gain, the angular displacement gain, and the angular rate gain. The angular displacement gain provides the beam with artificial stiffness and the angular rate gain provides the beam with artificial damping as described by Silverberg and Morton (1989) for this class of structures. The collocation gain provides torque smoothing as well as a means of controlling the degree of sensor/actuator collocation.

The approach introduced in this Note has the potential to apply to a broad class of nonlinear control problems. In view of this, Section 2 reviews general nonlinear beam kinematics. The slewing control algorithm is developed in Section 3. Then Section 4 discusses the efficient numerical integration of the associated equations of motion by an enhanced Newmark (1959) algorithm. Finally, Section 5 presents simulation results.

### 2 Beam Kinematics

Consider a very flexible beam, subject to a slewing torque applied through a hinge point at the root (see Fig. 1). The beam undergoes arbitrarily large elastic bending, axial, and transverse shear deformations. All motions occur in the horizontal plane absent gravitational effects. No restriction is placed on the magnitude of displacement of points along the elastic axis or on cross-section rotations. Figure 1 shows the flexible beam in an intermediate configuration as well as the associated shadow beam. The angle of rotation of the cross-section at the root is denoted $\theta_1$. This angle defines the orientation of the shadow beam. The inertial displacement components at the beam tip are designated by $u_1$ and $u_2$. Longitudinal and transverse displacements at the beam tip relative to the shadow beam are designated by $u$ and $v$. The connecting angle $\theta$ defines the orientation of the line joining the beam root and beam tip. The unstretched length of the beam is $L$.

The tip displacements relative to the shadow beam are expressed in terms of $u_1$, $u_2$, $\theta_1$, and $L$ as follows:

$$-u=[-u_1-L(1-\cos\theta_1)]\cos\theta_1-[u_2-L\sin\theta_1]\sin\theta_1 \tag{1}$$

$$v=[-u_1-L(1-\cos\theta_1)]\sin\theta_1+[u_2-L\sin\theta_1]\cos\theta_1. \tag{2}$$

The time derivatives of $u$ and $v$ are easily expressed in terms of $u_1$, $u_2$, $\dot{u}_1$, $\dot{u}_2$, $\theta_1$, and $\dot{\theta}_1$. The connecting angle is simply

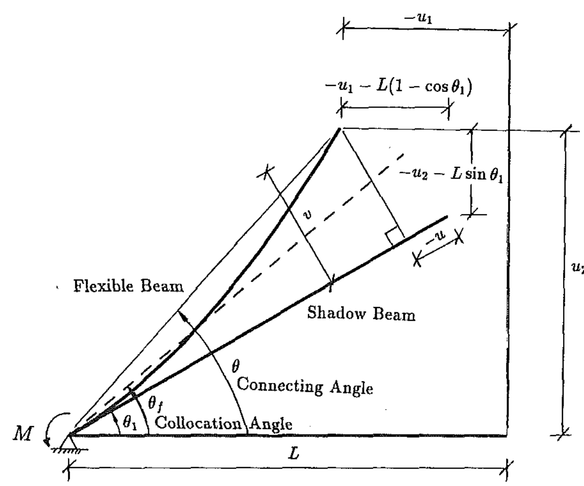


Fig. 1 Geometry and deformation measures for the elastic beam

[12]Mem. ASME.

[13]Department of Mechanical and Aerospace Engineering, North Carolina State University, Raleigh, NC 27695-7910.

Contributed by the Applied Mechanics Division of The American Society of Mechanical Engineers. Manuscript received by the ASME Applied Mechanics Division, Nov. 20, 1990; final revision, Apr. 30, 1991. Associate Technical Editor: D. J. Inman.

the play vanishes. Hence, from a physical point of view, there is no question of any discrepancy.

Finally, we note that real springboards are tapered from the fulcrum toward the ends, whereas we have assumed that the board has a uniform cross-section. However, by inspection we find that the results obtained here still hold if we use for $\alpha_t$ the harmonic mean $\bar{\alpha}_t$ of the torsional stiffness, i.e.,

$$\bar{\alpha}_t = \frac{1}{\dfrac{1}{2l}\displaystyle\int_0^{2l} \frac{dx}{\alpha_t(x)}}. \tag{18}$$

Apart from that, it is easy to see that for tapered boards the error resulting from the neglect of the anticlastic bending in this paper will be smaller than for boards with a uniform cross-section. Also, for boards consisting of a plate provided with separate longitudinal stiffeners, the effect of the anticlastic bending is small. However, in the latter case the deformation of the cross-section in its plane will come into play.

**Acknowledgment**

The authors gratefully acknowledge the stimulating discussions with Prof. Dr. D. J. Gerritsen on the optimal design of springboards. The present problem emerged from these talks.

## Slewing Motion Control of a Very Flexible Elastic Beam

**J. W. Eischen[12,13], L. Silverberg[12,13], and H. L. Wang[13]**

### 1 Introduction

This Note presents a novel approach to the slewing of beams that are permitted to undergo large combined rigid-body/elastic motions. The problem addressed is a classical noncollocated beam control problem in which a slewing torque is applied at the beam root and sensor measurements are taken at the beam root and the beam tip. Cannon and Schmitz (1984) proposed one of the first feedback control algorithms for such a problem, and as well provided experimental verification. Juang, Turner, and Chun (1985) developed closed-form expressions for control gains that resulted in fuel optimal slewing. Skaar and Tucker (1987) developed classical open-loop and closed-loop control strategies making use of transfer functions. Bayo (1987) employed a structural finite element technique to solve the inverse dynamics problem (open-loop control) for a slewing beam. In each of these investigations, beam motions were restricted to small elastic deflections.

In contrast, this Note presents a strategy well suited for beams undergoing large elastic motions described by nonlinear partial differential equations of motion. The associated torque is governed by a slewing control algorithm consisting of open-loop and closed-loop components. The open-loop component produces the desired overall rigid-body motion of the beam, while the closed-loop component suppresses the elastic vibrational motion relative to a shadow beam. The shadow beam is a fictitious beam whose motion is prescribed by the designer. This concept of a shadow structure was developed by Silverberg and Foster (1990) for maneuvering flexible spacecraft. In the present work, the shadow beam is essentially a straight line that remains tangent to the beam at its root. The closed-loop control component is expressed as a function of three parameters; the collocation gain, the angular displacement gain, and the angular rate gain. The angular displacement gain provides the beam with artificial stiffness and the angular rate gain provides the beam with artificial damping as described by Silverberg and Morton (1989) for this class of structures. The collocation gain provides torque smoothing as well as a means of controlling the degree of sensor/actuator collocation.

The approach introduced in this Note has the potential to apply to a broad class of nonlinear control problems. In view of this, Section 2 reviews general nonlinear beam kinematics. The slewing control algorithm is developed in Section 3. Then Section 4 discusses the efficient numerical integration of the associated equations of motion by an enhanced Newmark (1959) algorithm. Finally, Section 5 presents simulation results.

### 2 Beam Kinematics

Consider a very flexible beam, subject to a slewing torque applied through a hinge point at the root (see Fig. 1). The beam undergoes arbitrarily large elastic bending, axial, and transverse shear deformations. All motions occur in the horizontal plane absent gravitational effects. No restriction is placed on the magnitude of displacement of points along the elastic axis or on cross-section rotations. Figure 1 shows the flexible beam in an intermediate configuration as well as the associated shadow beam. The angle of rotation of the cross-section at the root is denoted $\theta_1$. This angle defines the orientation of the shadow beam. The inertial displacement components at the beam tip are designated by $u_1$ and $u_2$. Longitudinal and transverse displacements at the beam tip relative to the shadow beam are designated by $u$ and $v$. The connecting angle $\theta$ defines the orientation of the line joining the beam root and beam tip. The unstretched length of the beam is $L$.

The tip displacements relative to the shadow beam are expressed in terms of $u_1$, $u_2$, $\theta_1$, and $L$ as follows:

$$-u = [-u_1 - L(1-\cos\theta_1)]\cos\theta_1 - [u_2 - L\sin\theta_1]\sin\theta_1 \tag{1}$$

$$v = [-u_1 - L(1-\cos\theta_1)]\sin\theta_1 + [u_2 - L\sin\theta_1]\cos\theta_1. \tag{2}$$

The time derivatives of $u$ and $v$ are easily expressed in terms of $u_1$, $u_2$, $\dot{u}_1$, $\dot{u}_2$, $\theta_1$, and $\dot{\theta}_1$. The connecting angle is simply

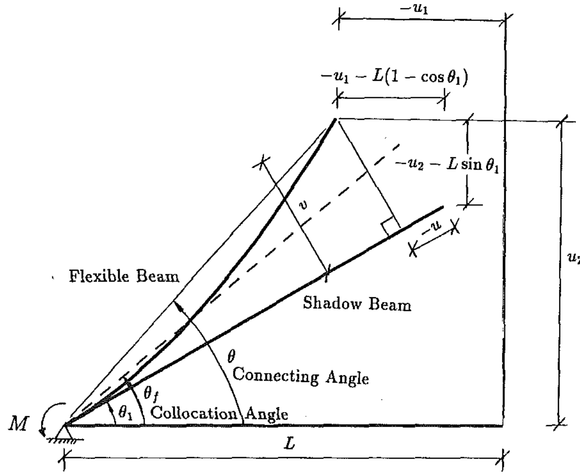


Fig. 1 Geometry and deformation measures for the elastic beam

[12]Mem. ASME.

[13]Department of Mechanical and Aerospace Engineering, North Carolina State University, Raleigh, NC 27695-7910.

Contributed by the Applied Mechanics Division of The American Society of Mechanical Engineers. Manuscript received by the ASME Applied Mechanics Division, Nov. 20, 1990; final revision, Apr. 30, 1991. Associate Technical Editor: D. J. Inman.

$$\theta = \tan^{-1}\left[\frac{u_2}{L+u_1}\right] \text{ for } L+u_1 \geq 0 \tag{3}$$

$$\theta = \pi + \tan^{-1}\left[\frac{u_2}{L+u_1}\right] \text{ for } L+u_1 < 0. \tag{4}$$

The time derivative of $\theta$ is easily expressed in terms of $u_1$, $u_2$, $\dot{u}_1$, and $\dot{u}_2$.

## 3 Beam Control

The proposed slewing control algorithm is an implicit function of inertial measurements of displacements and velocities at the beam tip: $u_1$, $u_2$, $\dot{u}_1$, $\dot{u}_2$, and also makes explicit use of the root angle $\theta_1$, the connecting angle $\theta$ and their time derivatives. Furthermore, two additional quantities are introduced to aid in the development of the slewing algorithm. The two quantities are a desired path angle $\theta_0(t)$ and a collocation angle $\theta_f(t)$. The desired path angle is expressed in the polynomial form

$$\theta_0(t) = a_0 + a_1 t + a_2 t^2 + a_3 t^3 + a_4 t^4 + a_5 t^5 \quad t \leq T \tag{5}$$

where $T$ is the slewing time. The coefficients $a_0$ through $a_5$ are determined by appropriate initial and final states. In the numerical example presented here, the beam is slewed 90 deg counterclockwise in a rest-to-rest maneuver. The initial and final states are

$$\theta_0(0) = 0 \quad \dot{\theta}_0(0) = 0 \quad \ddot{\theta}_0(0) = 0 \tag{6}$$

$$\theta_0(T) = \frac{\pi}{2} \quad \dot{\theta}_0(T) = 0 \quad \ddot{\theta}_0(T) = 0. \tag{7}$$

For a slewing time $T = 5$, the coefficients for $t \leq T$ are

$$a_0 = a_1 = a_2 = 0,\ a_3 = 0.12566371,$$
$$a_4 = -0.03769911,\ a_5 = 0.00301593 \tag{8}$$

and for $t > T$ are

$$a_0 = \frac{\pi}{2},\ a_1 = a_2 = a_3 = a_4 = a_5 = 0. \tag{9}$$

The slewing torque is expressed as

$$M(t) = M_0(t) + M_c(t) \tag{10}$$

where $M_0$ represents an open-loop torque and $M_c$ represents a closed-loop torque. The open-loop torque controls gross overall slewing motion, while the closed-loop torque controls elastic motions relative to the desired nominal path. The open-loop torque $M_0$ is simply the torque required to maneuver a rigid beam along the desired path. Thus,

$$M_0 = I_m \ddot{\theta}_0 \tag{11}$$

where $I_m = mL^2/3$ is the mass moment of inertia of the rigid beam about the hinge point and $m$ is the total mass of the beam. The closed-loop torque is defined as

$$M_c = -(\alpha_1^2 + \alpha_2^2) I_m (\theta_f - \theta_0) - 2\alpha_1 I_m (\dot{\theta}_f - \dot{\theta}_0) \tag{12}$$

where $\theta_f$ represents a collocation angle defined here as

$$\theta_f \equiv \theta_1 + \beta_c(\theta - \theta_1). \tag{13}$$

The parameters $\alpha_1$, $\alpha_2$, and $\beta_c$ are selected by the designer. The parameter $\alpha_1$ controls damping of the beam motions, $\alpha_2$ controls the frequency of oscillation, and $\beta_c$ represents a torque smoothing parameter. The quantity $\beta_c$ may also be interpreted as a collocation parameter, and enables the introduction of the collocation angle $\theta_f$, as shown in Eq. (13). As $\beta_c$ varies between 0 and 1, the collocation angle varies continuously between $\theta_1$ and $\theta$. When $\beta_c = 0$, $\theta_f = \theta_1$ and the feedback control is collocated, i.e., the sensor ($\theta_1$, $\dot{\theta}_1$) is collocated with the actuator ($M(t)$). If the beam were absolutely rigid, $\alpha_1$ would be identical to the damping rate, and $\alpha_2$ would be equal to the closed-loop frequency. When $\beta_c > 0$, then the sensor and actuator are noncollocated, i.e., when $\beta_c = 1$, $\theta_f = \theta$.

## 4 Dynamic Finite Element Analysis

The slewing motions of very flexible beams under the influence of control torques are governed by nonlinear partial differential equations (PDE's) of motion. The derivation of these PDE's and their efficient numerical solution by a finite element discretization procedure was proposed by Simo and Vu-Quoc (1986). The beam is effectively divided into a series of finite elements, joined at nodal points whose positions are selected by the analyst. The spatially discretized equations of motion for the large deformation beam theory proposed by Simo and Vu-Quoc (1986) are conveniently presented in a form commonly encountered in nonlinear structural dynamics,

$$\mathbf{Ma} + \mathbf{P}(\mathbf{d}) = \mathbf{F}^c(\mathbf{d}, \mathbf{v}) \tag{14}$$

where $\mathbf{d}$ is a vector containing nodal displacements and cross-section rotations, $\mathbf{v}$ is a vector containing nodal velocities and cross-section angular velocities, and $\mathbf{a}$ is a vector containing nodal accelerations and cross-section angular accelerations. $\mathbf{M}$ is the symmetric system mass matrix. The mass matrix is time invariant here because kinematic quantities are referred to an inertial reference frame, i.e., there are no rotating reference frames. $\mathbf{P}(\mathbf{d})$ is the nonlinear internal force vector and $\mathbf{F}^c(\mathbf{d}, \mathbf{v})$ is the system control force vector. Details regarding the numerical solution of Eq. (14) in which $\mathbf{F}^c(\mathbf{d}, \mathbf{v}) = \mathbf{0}$ are given in the paper by Simo and Vu-Quoc (1986). The computational procedure developed by Simo and Vu-Quoc (1986) is summarized briefly as follows, along with an extension that incorporates the control force.

Essentially, the computational task is to advance an equilibrium solution from known values of $\mathbf{d}_n$, $\mathbf{v}_n$, and $\mathbf{a}_n$ at time $t = t_n$ to values $\mathbf{d}_{n+1}$, $\mathbf{v}_{n+1}$, and $\mathbf{a}_{n+1}$ at $t = t_{n+1}$. This can be accomplished by combining the Newton-Raphson method for solving nonlinear systems of equations with the Newmark (1959) method for solving second-order systems of ordinary differential equations. The key steps in the solution algorithm are described as:

**Displacement/Velocity Predictors:**

$$\tilde{\mathbf{d}}_{n+1}^{(i)} = \mathbf{d}_n + \Delta t \mathbf{v}_n + \frac{\Delta t^2}{2}(1 - 2\beta)\mathbf{a}_n \tag{15}$$

$$\tilde{\mathbf{v}}_{n+1}^{(i)} = \mathbf{v}_n + \Delta t (1 - \gamma)\mathbf{a}_n. \tag{16}$$

The superscript $^{(i)}$ is an iteration counter, initially set to 0. Note that $\mathbf{a}_{n+1}^{(0)} = 0$. Newmark parameters are indicated by $\beta$ and $\gamma$. These adjustable parameters control the stability and accuracy of the Newmark algorithm. For this work, $\beta = 1/4$ and $\gamma = 1/2$, corresponding to the trapezoidal rule. The following linear system of algebraic equations is then solved to generate the incremental acceleration $\Delta\mathbf{a}$,

$$\left[\mathbf{M} - \gamma\Delta t \frac{\partial \mathbf{F}^c(\tilde{\mathbf{d}}_{n+1}^{(i)}, \tilde{\mathbf{v}}_{n+1}^{(i)})}{\partial \mathbf{v}} + \beta \Delta t^2 \left(\frac{\partial \mathbf{P}(\tilde{\mathbf{d}}_{n+1}^{(i)})}{\partial \mathbf{d}} - \frac{\partial \mathbf{F}^c(\tilde{\mathbf{d}}_{n+1}^{(i)}, \tilde{\mathbf{v}}_{n+1}^{(i)})}{\partial \mathbf{d}}\right)\right]\Delta\mathbf{a} = \mathbf{F}^c(\tilde{\mathbf{d}}_{n+1}^{(i)}, \tilde{\mathbf{v}}_{n+1}^{(i)}) - \mathbf{P}(\tilde{\mathbf{d}}_{n+1}^{(i)}) \tag{17}$$

or

$$\mathbf{M}^* \Delta\mathbf{a} = \mathbf{R}_{n+1}^{(i)} \tag{18}$$

where $\mathbf{M}^*$ is the effective mass matrix, and $\mathbf{R}_{n+1}^{(i)}$ is referred to as the residual.

**Displacement/Velocity/Acceleration Updates:** After solving for the acceleration $\Delta\mathbf{a}$ in Eq. (18), calculate

$$\tilde{\mathbf{d}}_{n+1}^{(i+1)} = \tilde{\mathbf{d}}_{n+1}^{(i)} + \beta\Delta t^2 \Delta\mathbf{a} \tag{19}$$

$$\tilde{\mathbf{v}}_{n+1}^{(i+1)} = \tilde{\mathbf{v}}_{n+1}^{(i)} + \gamma\Delta t \Delta\mathbf{a} \tag{20}$$

$$\tilde{\mathbf{a}}_{n+1}^{(i+1)} = \tilde{\mathbf{a}}_{n+1}^{(i)} + \Delta\mathbf{a}. \tag{21}$$

A convergence check is performed at this stage by forming the ratio $\|\mathbf{R}_{n+1}^{(i+1)}\| / \|\mathbf{R}_{n+1}^{(0)}\|$. If this ratio is greater than a pre-

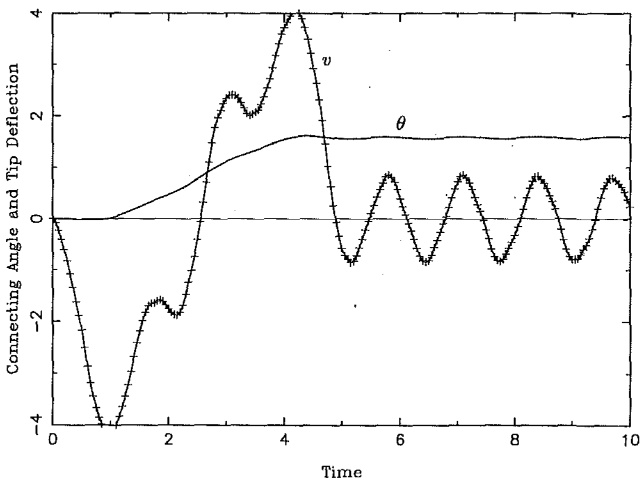


Fig. 2 Open-loop response ($\alpha_1$ = 0.0, $\alpha_2$ = 0.0, $\beta_c$ = 0.0)

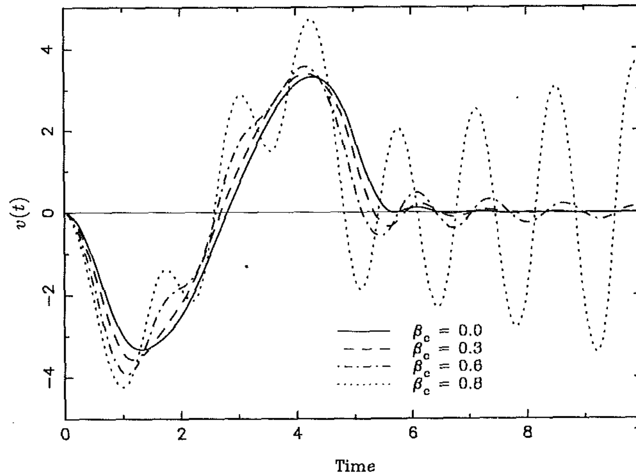


Fig. 4 Closed-loop response sensitivity to control parameter $\beta_c$ ($\alpha_1$ = 0.2, $\alpha_2$ = 0.2)

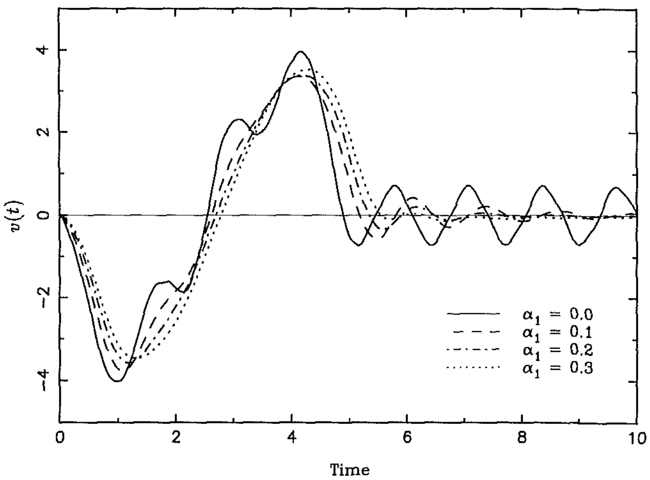


Fig. 3 Closed-loop response sensitivity to control parameter $\alpha_1$ ($\alpha_2$ = 0.2, $\beta_c$ = 0.3)

specified error tolerance, Eq. (18) is solved again using the new updated kinematic quantities. If this ratio is less than the user-specified tolerance ($1.0 \times 10^{-8}$ in our work), convergence is achieved and the desired kinematic quantities at $t = t_{n+1}$ are

$$\mathbf{d}_{n+1} = \tilde{\mathbf{d}}_{n+1}^{(i+1)} \quad \mathbf{v}_{n+1} = \tilde{\mathbf{v}}_{n+1}^{(i+1)} \quad \mathbf{a}_{n+1} = \tilde{\mathbf{a}}_{n+1}^{(i+1)} \tag{22}$$

Explicit expressions for $\mathbf{M}$, $\mathbf{P}$, and $\partial\mathbf{P}/\partial\mathbf{d}$ (tangent stiffness) are contained in the paper by Simo and Vu-Quoc (1986). The term $\partial\mathbf{F}^c/\partial\mathbf{d}$ involves derivatives of the control moment with respect to certain finite element nodal kinematical quantities. In the present control algorithm, these quantities are the cross-section rotation and angular velocity at the hinge point and the inertial displacements and velocities at the beam tip. The partial derivatives $\partial M/\partial\theta_1$, $\partial M/\partial u_1$, $\partial M/\partial u_2$ are calculated and added properly to the $\mathbf{M}^*$ matrix above. These quantities clearly depend on $\partial\theta/\partial u_1$, $\partial\theta/\partial u_2$, $\partial\dot{\theta}/\partial u_1$, and $\partial\dot{\theta}/\partial u_2$, which are calculated from Eq. (3). Likewise, the tangent damping matrix $\partial\mathbf{F}^c/\partial\mathbf{v}$ involves the derivatives $\partial M/\partial\dot{\theta}_1$, $\partial M/\partial\dot{u}_1$, $\partial M/\partial\dot{u}_2$, which in turn depend on $\partial\dot{\theta}/\partial\dot{u}_1$ and $\partial\dot{\theta}/\partial\dot{u}_2$.

## 5 Simulation Results

The flexible beam is discretized with ten finite elements. The following physical parameters were selected:

$L = 10$ (total length)

$E = 10{,}000$ (elastic modulus)

$G = 12{,}000$ (shear modulus)

$A = 1$ (cross-sectional area)

$I = 1/10$ (second moment of area)

$\rho = 1$ (mass density).

Figure 2 shows the response of the connecting angle $\theta$ and the tip deflection $v$ for open-loop control ($\alpha_1 = \alpha_2 = 0$). In the case of open-loop control, the connecting angle $\theta$ is identical to the desired path angle $\theta_0$ if the beam is rigid. Since the simulations performed here are representative of a very flexible beam, oscillations associated with the fundamental bending vibration mode are detected, and after the maneuver period ($T = 5$), the connecting angle oscillates about the desired value $\theta_0 = \pi/2$. The tip deflection oscillates about zero with no damping. Note the very large transverse bending deflections of $\pm 4$ compared to the beam length $L = 10$. This and subsequent simulations use an integration time step $\Delta t = 0.5$. The fundamental period $T_f$ for the bending mode calculated from classical linear vibration theory (pinned-free beam) is $T_f = 2\pi/(3.926602)^2\ (EI/\rho AL^4)^{-1/2} = 1.289$. The simulation agrees well with this result.

Figure 3 shows the tip deflection response for the case $\alpha_2 = 0.2$ and $\beta_c = 0.3$. For $0 \le \alpha_1 \le 0.3$, the response is clearly stable, and the elastic motion of the beam is slowly damped in time. As the control parameter $\alpha_1$ increases, the damping rate increases. For $\alpha_1 = 0.3$, the elastic motions are suppressed after a few oscillations beyond the maneuver time $T = 5$. Figure 4 shows the time response of the tip deflection $v(t)$ as a function of the parameter $\beta_c$, holding $\alpha_1$ and $\alpha_2$ constant. This figure highlights the effect of the noncollocated control on the response in the presence of altered stiffness characteristics. Figure 5 shows the region of stability corresponding to the physical parameters listed above. Instability arises as the collocation parameter increases beyond critical levels. Figure 6 shows the fuel consumption $F_{ul}$ defined by $F_{ul} = \int_0^\infty |M| dt$ for a range of values of the parameters $\alpha_1$ and $\beta_c$, holding $\alpha_2 = 0$. It is significant to note that the fuel consumption is maximum for collocated control ($\beta_c = 0$), and decreases as the collocation parameter increases.

## 6 Conclusions

A simple method has been proposed to control the slewing motion of a very flexible elastic beam. The control system

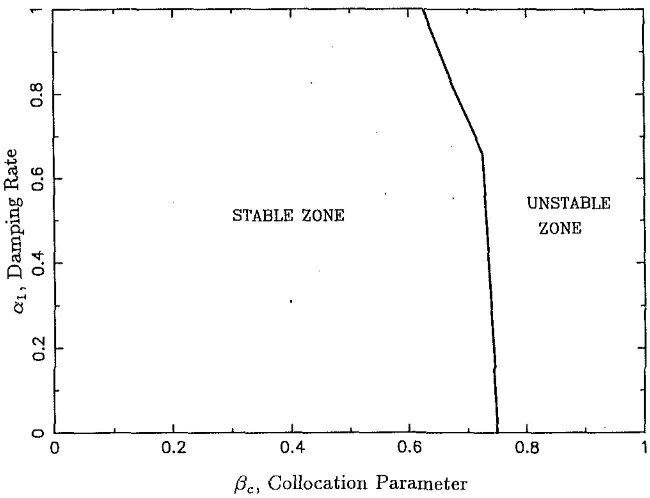


**Fig. 5 Control system stability plot**

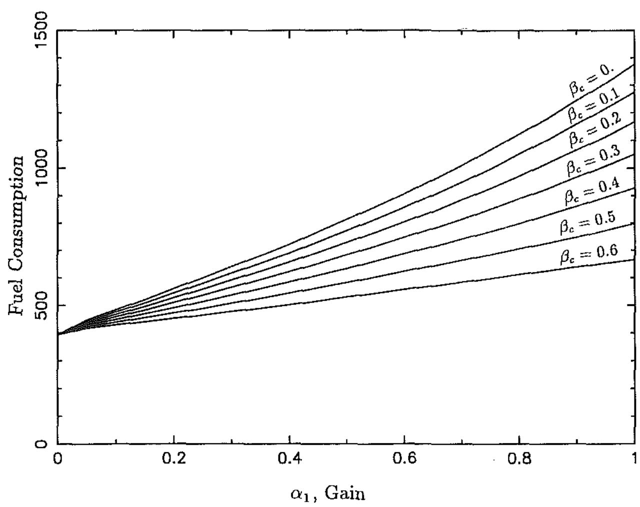


**Fig. 6 Fuel consumption versus $\alpha_1$ and $\beta_c$ ($\alpha_2 = 0.0$)**

relies on sensing position and velocity information at the beam tip together with angular position and rate at the beam root. Simulations demonstrate that the control system performs very well for a large angle slewing maneuver for a beam that experiences large elastic bending deformations. Furthermore, it is shown how the fuel consumption decreases as the sensors become noncollocated with the actuators.

### References


Bayo, E., 1987, "A Finite Element Approach to Control the End-Point Motion of a Single-Link Flexible Robot," *Journal of Robotic Systems*, Vol. 4, No. 1, pp. 63–75.

Cannon, R. H., and Schmitz, E., 1984, "Initial Experiments on the End-Point Control of a Flexible One-Link Robot," *The International Journal of Robotics Research*, Vol. 3, No. 3, pp. 62–75.

Juang, J. N., Turner, J. D., and Chun, H. M., 1985, "Closed-Form Solutions of Control Gains for a Terminal Controller," *Journal of Guidance, Control, and Dynamics*, Vol. 8, pp. 38–43.

Newmark, N. M., 1959, "A Method of Computation for Structural Dynamics," *ASCE Journal of the Engineering Mechanics Division*, pp. 67–94.

Simo, J. C., and Vu-Quoc, L., 1986, "On the Dynamics of Flexible Beams Under Large Overall Motions—The Plane Case: Parts I and II," ASME Journal of Applied Mechanics, Vol. 53, No. 4, pp. 849–863.

Skaar, S. B., and Tucker, D., 1986, "Point Control of a One-Link Flexible Manipulator," ASME Journal of Applied Mechanics, Vol. 53, pp. 23–27.

Silverberg, L., and Foster, L. A., 1990, "Decentralized Feedback Maneuver of Flexible Spacecraft," *Journal of Guidance, Control, and Dynamics*, Vol. 13, No. 2, pp. 258–264.

Silverberg, L., and Morton, M., 1989, "On the Nature of Natural Control," *Journal of Vibration, Stress, and Reliability in Design*, Vol. 111, pp. 412–422.


## Absence of One Nodal Diameter Critical Speed Modes in an Axisymmetric Rotating Disk


**Anthony A. Renshaw,[14,16] and C. D. Mote, Jr.[15,16]**


### Introduction

Numerically computed eigenvalues of an axisymmetric, rotating disk suggest that the natural vibration frequencies with one nodal diameter are bounded below by the rotation frequency of the disk. This Brief Note proves the existence of this bound for a large class of axisymmetric stress fields and boundary conditions.

The bound bears directly on the critical speed instability of rotating disks. The critical speed of a rotating disk is the lowest rotation speed at which the propagation speed of a backward traveling circumferential wave equals the rotation speed. At critical speed the propagating wave is stationary in the nonrotating reference frame and is excited to resonance by a stationary, transverse force. Since the 1920's, both numerical and experimental results on centrally clamped, spinning disks have never found a critical speed mode with zero or one nodal diameters (e.g., Lamb and Southwell, 1921; Southwell, 1922; Tobias and Arnold, 1957; Mote, 1970; Iwan and Moeller, 1976). The zero nodal diameter mode can be critical only if its eigenvalue is zero; this is not possible if the Rayleigh Quotient is positive definite. The one nodal diameter mode, however, is critical when its eigenfrequency equals the rotation frequency. Although previous studies noted the absence of one nodal diameter critical speed modes for their specific cases, no general conditions under which this would occur were set forth.

The proof that one nodal diameter natural frequencies are bounded by the rotation frequency rests on two observations. First, equilibrium under a centripetally induced stress field ensures that the completely free rotating disk has an eigenfunction whose eigenfrequency exactly equals the rotation frequency. This eigenfunction corresponds to rigid-body tilting of the disk about the nodal diameter. Second, although the method of multiplicative variation is typically useful only for nonvanishing eigenfunctions (Courant and Hilbert, 1957), it can be used with one nodal diameter eigenfunctions provided that the stresses and boundary conditions are axisymmetric. If the vibration problem is asymmetric, then the nodal lines of the resulting vibration modes cannot be predicted in advance and the proof is not valid.

### Eigenvalue Problem and Stress Field

Eigensolutions for the transverse displacement of a uniform, axisymmetric disk satisfy the self-adjoint, dimensionless equation

$$\nabla^4 w - \frac{1}{r}(r\sigma_r w_{,r})_{,r} - \frac{1}{r^2}\sigma_\theta w_{,\theta\theta} = \lambda^2 w \tag{1}$$

plus appropriate boundary conditions, where $w(r,\theta)$ is the transverse displacement, $\sigma_r$ and $\sigma_\theta$ are the radial and hoop stresses, $\nabla^4$ is the biharmonic operator, a comma denotes partial differentiation, $\lambda^2$ is the eigenvalue, and $\lambda$ is the natural frequency. Solutions to (1) render the Rayleigh Quotient, $J$, stationary with $J = \lambda^2$:

[14]Graduate Student.

[15]FANUC Chair in Mechanical Systems and Vice Chancellor. Fellow ASME.

[16]Department of Mechanical Engineering, University of California, Berkeley, CA 94720.


*Contributed by the Applied Mechanics Division of* The American Society of Mechanical Engineers. Manuscript received by the ASME Applied Mechanics Division, Dec. 18, 1990; final revision, Apr. 2, 1991. Associate Technical Editor: D. J. Inman.

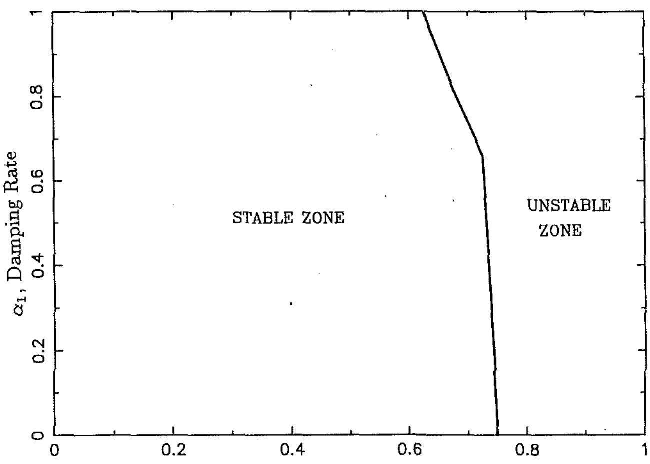


Fig. 5 Control system stability plot

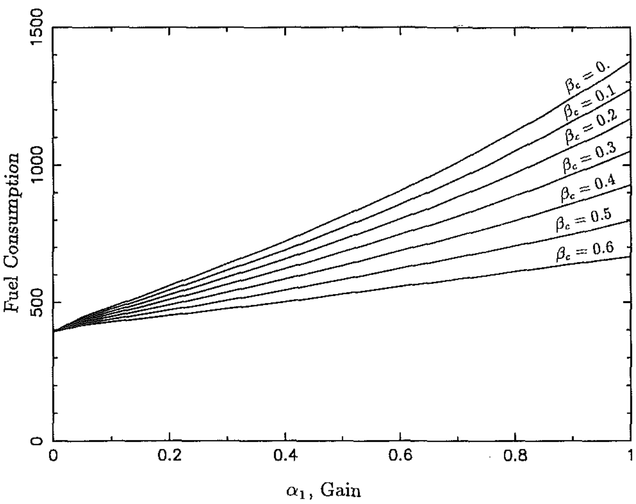


Fig. 6 Fuel consumption versus $\alpha_1$ and $\beta_c$ ($\alpha_2$ = 0.0)

relies on sensing position and velocity information at the beam tip together with angular position and rate at the beam root. Simulations demonstrate that the control system performs very well for a large angle slewing maneuver for a beam that experiences large elastic bending deformations. Furthermore, it is shown how the fuel consumption decreases as the sensors become noncollocated with the actuators.

### References

Bayo, E., 1987, "A Finite Element Approach to Control the End-Point Motion of a Single-Link Flexible Robot," *Journal of Robotic Systems*, Vol. 4, No. 1, pp. 63–75.

Cannon, R. H., and Schmitz, E., 1984, "Initial Experiments on the End-Point Control of a Flexible One-Link Robot," *The International Journal of Robotics Research*, Vol. 3, No. 3, pp. 62–75.

Juang, J. N., Turner, J. D., and Chun, H. M., 1985, "Closed-Form Solutions of Control Gains for a Terminal Controller," *Journal of Guidance, Control, and Dynamics*, Vol. 8, pp. 38–43.

Newmark, N. M., 1959, "A Method of Computation for Structural Dynamics," *ASCE Journal of the Engineering Mechanics Division*, pp. 67–94.

Simo, J. C., and Vu-Quoc, L., 1986, "On the Dynamics of Flexible Beams Under Large Overall Motions—The Plane Case: Parts I and II," ASME JOURNAL OF APPLIED MECHANICS, Vol. 53, No. 4, pp. 849–863.

Skaar, S. B., and Tucker, D., 1986, "Point Control of a One-Link Flexible Manipulator," ASME JOURNAL OF APPLIED MECHANICS, Vol. 53, pp. 23–27.

Silverberg, L., and Foster, L. A., 1990, "Decentralized Feedback Maneuver of Flexible Spacecraft," *Journal of Guidance, Control, and Dynamics*, Vol. 13, No. 2, pp. 258–264.

Silverberg, L., and Morton, M., 1989, "On the Nature of Natural Control," *Journal of Vibration, Stress, and Reliability in Design*, Vol. 111, pp. 412–422.

# Absence of One Nodal Diameter Critical Speed Modes in an Axisymmetric Rotating Disk

**Anthony A. Renshaw,**[14,16] **and C. D. Mote, Jr.**[15,16]

## Introduction

Numerically computed eigenvalues of an axisymmetric, rotating disk suggest that the natural vibration frequencies with one nodal diameter are bounded below by the rotation frequency of the disk. This Brief Note proves the existence of this bound for a large class of axisymmetric stress fields and boundary conditions.

The bound bears directly on the critical speed instability of rotating disks. The critical speed of a rotating disk is the lowest rotation speed at which the propagation speed of a backward traveling circumferential wave equals the rotation speed. At critical speed the propagating wave is stationary in the nonrotating reference frame and is excited to resonance by a stationary, transverse force. Since the 1920's, both numerical and experimental results on centrally clamped, spinning disks have never found a critical speed mode with zero or one nodal diameters (e.g., Lamb and Southwell, 1921; Southwell, 1922; Tobias and Arnold, 1957; Mote, 1970; Iwan and Moeller, 1976). The zero nodal diameter mode can be critical only if its eigenvalue is zero; this is not possible if the Rayleigh Quotient is positive definite. The one nodal diameter mode, however, is critical when its eigenfrequency equals the rotation frequency. Although previous studies noted the absence of one nodal diameter critical speed modes for their specific cases, no general conditions under which this would occur were set forth.

The proof that one nodal diameter natural frequencies are bounded by the rotation frequency rests on two observations. First, equilibrium under a centripetally induced stress field ensures that the completely free rotating disk has an eigenfunction whose eigenfrequency exactly equals the rotation frequency. This eigenfunction corresponds to rigid-body tilting of the disk about the nodal diameter. Second, although the method of multiplicative variation is typically useful only for nonvanishing eigenfunctions (Courant and Hilbert, 1957), it can be used with one nodal diameter eigenfunctions provided that the stresses and boundary conditions are axisymmetric. If the vibration problem is asymmetric, then the nodal lines of the resulting vibration modes cannot be predicted in advance and the proof is not valid.

## Eigenvalue Problem and Stress Field

Eigensolutions for the transverse displacement of a uniform, axisymmetric disk satisfy the self-adjoint, dimensionless equation

$$\nabla^4 w - \frac{1}{r}(r\sigma_r w,_r),_r - \frac{1}{r^2}\sigma_\theta w,_{\theta\theta} = \lambda^2 w \tag{1}$$

plus appropriate boundary conditions, where $w(r,\theta)$ is the transverse displacement, $\sigma_r$ and $\sigma_\theta$ are the radial and hoop stresses, $\nabla^4$ is the biharmonic operator, a comma denotes partial differentiation, $\lambda^2$ is the eigenvalue, and $\lambda$ is the natural frequency. Solutions to (1) render the Rayleigh Quotient, $J$, stationary with $J = \lambda^2$:

[14]Graduate Student.

[15]FANUC Chair in Mechanical Systems and Vice Chancellor. Fellow ASME.

[16]Department of Mechanical Engineering, University of California, Berkeley, CA 94720.

*Contributed by the Applied Mechanics Division of* THE AMERICAN SOCIETY OF MECHANICAL ENGINEERS. Manuscript received by the ASME Applied Mechanics Division, Dec. 18, 1990; final revision, Apr. 2, 1991. Associate Technical Editor: D. J. Inman.

$$J[w] = \frac{J_N[w]}{J_D[w]} \qquad (2)$$

$$J_N[w] = \int_\tau \Bigg[ (\nabla^2 w)^2 - (1-\nu)L[w,w] + \sigma_r (w,_r)^2 + \frac{1}{r^2}\sigma_\theta (w,_\theta)^2 \Bigg] d\tau \qquad (3a)$$

$$J_D[w] = \int_\tau (w^2)d\tau. \qquad (3b)$$

$\tau$ is the area of the plate, $\nu$ is Poisson's ratio, and the bilinear operator $L$ for any $a$ and $b$ is

$$L[a,\ b] = a,_{rr}\left(\frac{1}{r}\,b,_r + \frac{1}{r^2}\,b,_{\theta\theta}\right) - 2\left(\frac{1}{r}\,a,_\theta\right),_r\left(\frac{1}{r}\,b,_\theta\right),_r + \left(\frac{1}{r}\,a,_r + \frac{1}{r^2}\,a,_{\theta\theta}\right)b,_{rr}. \qquad (4)$$

The stress field of the disk is assumed to be axisymmetric. Circumferential equilibrium is identically satisfied and radial equilibrium requires

$$\frac{1}{r}\,(r\sigma_r),_r - \frac{1}{r}\,\sigma_\theta = -\Omega^2 r \qquad (5)$$

where $\Omega$ is the rotation frequency. It is assumed that $\sigma_r$ vanishes on any edge where the displacement, $w$, is not zero, and that $\sigma_r$ is non-negative and vanishes only at isolated radii. No assumptions are made on $\sigma_\theta$. This class of stress fields includes those induced by rotation as specific examples.

## Bounding the One Nodal Diameter Eigenvalues

Modal decomposition of (1) or (2) uses the separable form $w(r,\ \theta) = R(r)\cos(n\theta)$ where $n$ is the number of nodal diameters. Because of radial equilibrium (5), the one nodal diameter mode of a disk with free boundaries has the rigid-body eigenfunction $w = r\cos\theta$ with eigenvalue $\lambda^2 = \Omega^2$. This eigenfunction describes tilting of the disk without flexural deformation.

Axisymmetry gives all one nodal diameter modes at least the same zeros as the rigid-body eigenfunction. Hence, any one nodal diameter comparison function $\phi$ can be formed by multiplicatively varying the rigid-body mode by some function $\eta(r)$:

$$\phi(r,\theta) = \eta(r) r\cos\theta. \qquad (6)$$

$J$ is then bounded by splitting $J_N[\phi]$ into two parts such that $J_N = J_{N1} + J_{N2}$. $J_{N1}$ includes the terms derived from the bending stiffness of the disk and is non-negative for all $\phi$:

$$J_{N1}[\phi] = \int_\tau \{(\nabla^2\phi)^2 - (1-\nu)L[\phi,\ \phi]\}d\tau \qquad (7a)$$

$$\geq \int_\tau \left\{\left[\,|\phi,_{rr}| - \left|\left(\frac{1}{r}\,\phi,_r + \frac{1}{r^2}\,\phi,_{\theta\theta}\right)\right|\,\right]^2 + 2(1-\nu\left[\left(\frac{1}{r}\,\phi,_\theta\right),_r\right]^2\right\}d\tau \geq 0. \qquad (7b)$$

$J_{N2}$ includes the stress-related terms and provides the bound to the eigenvalues:

$$J_{N2}[\phi] = \int_\tau \left\{\sigma_r(\phi,_r)^2 + \frac{1}{r^2}\,\sigma_\theta(\phi,_\theta)^2\right\}d\tau \qquad (8a)$$

$$= \int_\tau \left\{\sigma_r(r^2\eta,_r^2 + 2r\eta\eta,_r + \eta^2)\cos^2\theta + \sigma_\theta\eta^2\sin^2\theta\right\}d\tau. \qquad (8b)$$

Noting that $2\eta\eta,_r = (\eta^2),_r$ and that by assumption either $\eta = 0$ or $\sigma_r = 0$ at the edge of the disk, integration of (8b) by parts followed by use of radial equilibrium (5) gives

$$J_{N2}[\phi] = \pi\int[\Omega^2 r^3\eta^2 + \sigma_r r^3\eta,_r^2]dr \qquad (9a)$$

$$\geq \Omega^2\int_\tau \phi^2 d\tau = \Omega^2 J_D[\phi]. \qquad (9b)$$

Equality in (9b) occurs only for $\eta = constant$. Therefore, for disks with axisymmetric boundary conditions which constrain the rigid body mode from the space of comparison functions with one nodal diameter, $J[\phi] > \Omega^2$. Boundary conditions satisfying these conditions include, but are not limited to, clamped, pinned, and sliding edges, as well as other axisymmetric restraints on the interior of the disk. The bound also holds when the bending stiffness of the disk is zero.

## References

Courant, R., and Hilbert, D., 1957, *Methods of Mathematical Physics*, John Wiley and Sons, New York.

Iwan, W. D., and Moeller, T. L., 1976, "The Stability of a Spinning Elastic Disk with a Transverse Load System," ASME JOURNAL OF APPLIED MECHANICS, Vol. 43, pp. 485–490.

Lamb, H., and Southwell, R. V., 1921, "The Vibrations of a Spinning Disk," *Proceedings of the Royal Society of London*, Vol. A99, No. 699, pp. 272–280.

Mote, Jr., C. D., 1970, "Stability of Circular Plates Subjected to Moving Loads," *Journal of the Franklin Institute*, Vol. 290, No. 4, pp. 329–344.

Southwell, R. V., 1922, "On the Free Transverse Vibrations of a Uniform Circular Disc Clamped at its Centre; and on the Effects of Rotation," *Proceedings of the Royal Society of London*, Vol. 101, pp. 133–153.

Tobias, S. A., and Arnold, R. N., 1957, "The Influence of Dynamic Imperfections on the Vibrations of Rotating Disks," *Proceedings of the Institute of Mechanical Engineers*, Vol. 171, pp. 669–690.

# Nonuniqueness in Elastoplastic Frames

**W. A. M. Alwis**[17]

*Lack of uniqueness of the kinematic solution of elastoplastic flexural frames is studied by deriving a general solution for nonholonomic behavior. A singular hinge set is defined as a collection of plastic hinges that would form a mechanism if they were replaced by mechanical hinges. It is shown that whenever singular subsets can be found among active plastic hinges, the kinematic solution may become nonunique. The rate of work done by the load rates on the contributing mechanisms must be zero if a prevailing nonuniqueness is to sustain.*

## 1 Introduction

Researchers have known since the early days of the theory of plasticity that the strain rates in elastoplastic solids need not be unique (Koiter, 1960), a well-known instance being plastic collapse. Kinematic nonuniqueness may occur even when the structure is still safe from the danger of collapse. Potential hazards of ignoring or being unaware of nonuniqueness has been pointed out by Smith and Munro (1978) referring to safety analysis for concrete frames and by Hodge and his co-workers (Hodge and White, 1980; White and Hodge, 1980; Hodge, Bathe, and Dvorkin, 1986) referring to the use of finite element computer programs.

To the author's knowledge, a general theory or a method of comprehensive analysis of nonuniqueness in elastoplastic frames or other structures is not available in the literature.

[17]Department of Civil Engineering, National University of Singapore, Kent Ridge, 0511 Singapore.

Contributed by the Applied Mechanics Division Oct. 3, 1990; final revision, Apr. 30, 1991. Associate Technical Editor: M. E. Fourney.

$$J[w]=\frac{J_N[w]}{J_D[w]} \tag{2}$$

$$J_N[w]=\int_\tau\left[(\nabla^2 w)^2-(1-\nu)L[w,w]\right.$$
$$\left.+\sigma_r(w,_r)^2+\frac{1}{r^2}\sigma_\theta(w,_\theta)^2\right]d\tau \tag{3a}$$

$$J_D[w]=\int_\tau (w^2)d\tau. \tag{3b}$$

$\tau$ is the area of the plate, $\nu$ is Poisson's ratio, and the bilinear operator $L$ for any $a$ and $b$ is

$$L[a,\,b]=a,_{rr}\left(\frac{1}{r}\,b,_r+\frac{1}{r^2}\,b,_{\theta\theta}\right)-2\left(\frac{1}{r}\,a,_\theta\right),_r\left(\frac{1}{r}\,b,_\theta\right),_r$$
$$+\left(\frac{1}{r}\,a,_r+\frac{1}{r^2}\,a,_{\theta\theta}\right)b,_{rr}. \tag{4}$$

The stress field of the disk is assumed to be axisymmetric. Circumferential equilibrium is identically satisfied and radial equilibrium requires

$$\frac{1}{r}\,(r\sigma_r),_r-\frac{1}{r}\,\sigma_\theta=-\Omega^2 r \tag{5}$$

where $\Omega$ is the rotation frequency. It is assumed that $\sigma_r$ vanishes on any edge where the displacement, $w$, is not zero, and that $\sigma_r$ is non-negative and vanishes only at isolated radii. No assumptions are made on $\sigma_\theta$. This class of stress fields includes those induced by rotation as specific examples.

### Bounding the One Nodal Diameter Eigenvalues

Modal decomposition of (1) or (2) uses the separable form $w(r,\,\theta)=R(r)\cos(n\theta)$ where $n$ is the number of nodal diameters. Because of radial equilibrium (5), the one nodal diameter mode of a disk with free boundaries has the rigid-body eigenfunction $w=r\cos\theta$ with eigenvalue $\lambda^2=\Omega^2$. This eigenfunction describes tilting of the disk without flexural deformation.

Axisymmetry gives all one nodal diameter modes at least the same zeros as the rigid-body eigenfunction. Hence, any one nodal diameter comparison function $\phi$ can be formed by multiplicatively varying the rigid-body mode by some function $\eta(r)$:

$$\phi(r,\theta)=\eta(r)r\cos\theta. \tag{6}$$

$J$ is then bounded by splitting $J_N[\phi]$ into two parts such that $J_N=J_{N1}+J_{N2}$. $J_{N1}$ includes the terms derived from the bending stiffness of the disk and is non-negative for all $\phi$:

$$J_{N1}[\phi]=\int_\tau \{(\nabla^2\phi)^2-(1-\nu)L[\phi,\,\phi]\}d\tau \tag{7a}$$

$$\geq\int_\tau\left\{\left[\,|\phi,_{rr}|-\left|\left(\frac{1}{r}\,\phi,_r+\frac{1}{r^2}\,\phi,_{\theta\theta}\right)\right|\,\right]^2\right.$$
$$\left.+2(1-\nu\left[\left(\frac{1}{r}\,\phi,_\theta\right),_r\right]^2\right\}d\tau\geq 0. \tag{7b}$$

$J_{N2}$ includes the stress-related terms and provides the bound to the eigenvalues:

$$J_{N2}[\phi]=\int_\tau\left\{\sigma_r(\phi,_r)^2+\frac{1}{r^2}\,\sigma_\theta(\phi,_\theta)^2\right\}d\tau \tag{8a}$$

$$=\int_\tau\left\{\sigma_r(r^2\eta,_r^2+2r\eta\eta,_r+\eta^2)\cos^2\theta+\sigma_\theta\eta^2\sin^2\theta\right\}d\tau. \tag{8b}$$

Noting that $2\eta\eta,_r=(\eta^2),_r$ and that by assumption either $\eta=0$ or $\sigma_r=0$ at the edge of the disk, integration of (8$b$) by parts followed by use of radial equilibrium (5) gives

$$J_{N2}[\phi]=\pi\int[\Omega^2 r^3\eta^2+\sigma_r r^3\eta,_r^2]dr \tag{9a}$$

$$\geq\Omega^2\int_\tau\phi^2 d\tau=\Omega^2 J_D[\phi]. \tag{9b}$$

Equality in (9$b$) occurs only for $\eta=constant$. Therefore, for disks with axisymmetric boundary conditions which constrain the rigid body mode from the space of comparison functions with one nodal diameter, $J[\phi]>\Omega^2$. Boundary conditions satisfying these conditions include, but are not limited to, clamped, pinned, and sliding edges, as well as other axisymmetric restraints on the interior of the disk. The bound also holds when the bending stiffness of the disk is zero.

### References


Courant, R., and Hilbert, D., 1957, *Methods of Mathematical Physics*, John Wiley and Sons, New York.

Iwan, W. D., and Moeller, T. L., 1976, "The Stability of a Spinning Elastic Disk with a Transverse Load System," ASME JOURNAL OF APPLIED MECHANICS, Vol. 43, pp. 485–490.

Lamb, H., and Southwell, R. V., 1921, "The Vibrations of a Spinning Disk," *Proceedings of the Royal Society of London*, Vol. A99, No. 699, pp. 272–280.

Mote, Jr., C. D., 1970, "Stability of Circular Plates Subjected to Moving Loads," *Journal of the Franklin Institute*, Vol. 290, No. 4, pp. 329–344.

Southwell, R. V., 1922, "On the Free Transverse Vibrations of a Uniform Circular Disc Clamped at its Centre; and on the Effects of Rotation," *Proceedings of the Royal Society of London*, Vol. 101, pp. 133–153.

Tobias, S. A., and Arnold, R. N., 1957, "The Influence of Dynamic Imperfections on the Vibrations of Rotating Disks," *Proceedings of the Institute of Mechanical Engineers*, Vol. 171, pp. 669–690.


## Nonuniqueness in Elastoplastic Frames

**W. A. M. Alwis**[17]

*Lack of uniqueness of the kinematic solution of elastoplastic flexural frames is studied by deriving a general solution for nonholonomic behavior. A singular hinge set is defined as a collection of plastic hinges that would form a mechanism if they were replaced by mechanical hinges. It is shown that whenever singular subsets can be found among active plastic hinges, the kinematic solution may become nonunique. The rate of work done by the load rates on the contributing mechanisms must be zero if a prevailing nonuniqueness is to sustain.*

### 1 Introduction

Researchers have known since the early days of the theory of plasticity that the strain rates in elastoplastic solids need not be unique (Koiter, 1960), a well-known instance being plastic collapse. Kinematic nonuniqueness may occur even when the structure is still safe from the danger of collapse. Potential hazards of ignoring or being unaware of nonuniqueness has been pointed out by Smith and Munro (1978) referring to safety analysis for concrete frames and by Hodge and his co-workers (Hodge and White, 1980; White and Hodge, 1980; Hodge, Bathe, and Dvorkin, 1986) referring to the use of finite element computer programs.

To the author's knowledge, a general theory or a method of comprehensive analysis of nonuniqueness in elastoplastic frames or other structures is not available in the literature.

[17]Department of Civil Engineering, National University of Singapore, Kent Ridge, 0511 Singapore.

Contributed by the Applied Mechanics Division Oct. 3, 1990; final revision, Apr. 30, 1991. Associate Technical Editor: M. E. Fourney.

Smith and Munro (1978) have tackled the case of nonholonomic frame analysis; Hodge et al. (1986) have studied a truss example that exhibits nonuniqueness; and Tin-Loi and Wong (1989) have developed a computer method of elastoplastic analysis of frames which can detect an encounter with a nonunique solution without determining the complete solution. In this paper, a general theoretical basis that describes nonuniqueness in nonholonomic elastoplastic frames is derived using a matrix formulation.

## 2 Governing Equations

The following simplifying assumptions are made regarding the frame that is being considered. Equilibrium equations are not affected by geometrical changes (first-order theory); bending moment is the only active internal force that produces deformation and yielding; and moment-curvature relationship is linearly elastic/perfectly plastic. The frame is discretized into straight uniform members joined at nodes where equivalent joint loads are applied. Under such conditions, plastic hinges would form only at member extremities.

Adopting the matrix approach pioneered by Maier (1970), the governing equation can be expressed as follows by stating that the total stress is the sum of elastic and residual stresses.

$$\mathbf{Q}=\mathbf{Y}\mathbf{F}+\mathbf{Z}\mathbf{p} \tag{1}$$

where $\mathbf{Q}$ is the $\mu \times 1$ bending moment vector, $\mathbf{F}$ is the $\nu \times 1$ load vector, and $\mathbf{p}$ is the $\mu \times 1$ plastic hinge rotation vector; $\mathbf{Y}$ and $\mathbf{Z}$ are influence coefficient matrices of elastic moment-load and residual moment-hinge rotation; $\mu$ = number of unknown bending moments at member extremities and $\nu$ = number of degrees-of-freedom. $\mathbf{Z}$ is symmetric and negative semi-definite; the number of linearly independent rows (or columns) in $\mathbf{Z}$ is $\rho$, where $\rho$ is the degree of redundancy in the frame.

The development of hinge rotations through plastic deformation is formalized by describing the yield constraints which specify that

$$\mathbf{K}^{-} \leq \mathbf{Q} \leq \mathbf{K}^{+} \tag{2}$$

where $\mathbf{K}^-$ and $\mathbf{K}^+$ are the vectors of plastic moments in negative and positive bending, respectively. The associated flow rule stipulates that $\dot{p}_i > 0$ only if $Q_i = K_i^+$ and $\dot{Q}_i = 0$; and similarly, $\dot{p}_i < 0$ only if $Q_i = K_i^-$ and $\dot{Q}_i = 0$; whereas $\dot{p}_i$ can assume zero under all circumstances. Here $(\dot{\ })$ denotes the rate of change with respect to an arbitrary time scale in this quasi-static analysis.

Accordingly, the behavior of the frame is governed in phases by sets of linear equations. The initial phase is up to the point of first yield and the following phases span between plastic events (i.e., formation of plastic hinges or plastic unloading of hinges to the elastic range).

## 3 Kinematic Solution

Consider the incremental form of Eq. (1):

$$\mathbf{Q}=\mathbf{Y}\dot{\mathbf{F}}+\mathbf{Z}\dot{\mathbf{p}}. \tag{3}$$

According to the uniqueness theorem of stress rates (Melan, 1938), for a given $\dot{\mathbf{F}}$ the resulting $\dot{\mathbf{Q}}$ is unique. It follows that the residual moment vector $\mathbf{Z}\dot{\mathbf{p}}$ is also unique. The presentation here focuses on $\dot{\mathbf{p}}$ which may have multiple solutions.

As only $\rho$ columns of $\mathbf{Z}$ are linearly independent, the relation that expresses a linear dependency among columns of $\mathbf{Z}$ can be stated in the form

$$\mathbf{Z}\dot{\mathbf{c}}_k=\mathbf{o} \tag{4}$$

where $\mathbf{o}$ denotes a null vector. It can be readily identified that $\dot{\mathbf{c}}_k$ is the vector of relative hinge rotation rates of a mechanism of instability. The set of mechanical hinges that has to be introduced to generate the mechanism $\dot{\mathbf{c}}_i$ is denoted by $s_k$ and referred to as a *singular hinge set* in this paper. There will be $(\mu - \rho)$ independent mechanisms in the frame. In view of (4), the general solution for $\dot{\mathbf{p}}$ can be expressed in the form

$$\dot{\mathbf{p}}=\dot{\mathbf{p}}^{*}+\mathbf{C}\boldsymbol{\alpha} \tag{5}$$

where $\dot{\mathbf{p}} = \dot{\mathbf{p}}^*$ is a solution that satisfies (3) such that $\dot{Q}_i = 0$ at the plastic hinges; $\mathbf{C}$ is the matrix of mechanisms formed by collecting a complete set of linearly independent column vectors $\dot{\mathbf{c}}_k$; and $\boldsymbol{\alpha} = \{\alpha_k\}$ is a vector of multipliers which scale the mechanisms. The flow rule introduces bounds on these multipliers.

Let the set of active plastic hinges in the frame at a certain point in time be $S$. If $s_k \subseteq S$, then $\dot{\mathbf{c}}_k$ would be admitted to the solution by virtue of having a nonzero $\alpha_k$, as the flow rule does not restrict the magnitude of total rotation at a hinge. The mechanisms that cannot be admitted have their multipliers forced to zero by the flow rule.

If any of the bounds of $\alpha_k$ is infinite in magnitude, then the contribution of $\dot{\mathbf{c}}_k$ can be arbitrarily scaled resulting in uncontained plastic deformation. This is the well-known case of plastic collapse, the collapse mechanism being defined by $\dot{\mathbf{c}}_k$ together with the sign of that infinite bound. Over-complete collapse results if there are more than one contributing mechanism with uncontained multipliers.

The last term of (5) provides a continuous range of options for competing kinematic solutions within the limits allowed by the flow rule. However, once the frame assumes one of the possible deformed shapes, "bifurcation" to another competing deformed shape under constant load is not permitted, since the flow rule does not allow a reduction in the magnitude of rotation once a plastic hinge has rotated. Hence, the free movement of "limited mechanisms" (Maier et al., 1979) that occur in holonomic structures is not permitted in this nonholonomic case. Plastic collapse is an exception where it is possible to assume other deformation options under constant load with monotonically increasing magnitudes of hinge rotations.

The solution would become unique again if some plastic hinges get unloaded such that no singular subset remains. By applying the principle of virtual work to the compatible system $(\dot{\mathbf{u}}_k, \dot{\mathbf{c}}_k)$ and the $(\mathbf{F}, \dot{\mathbf{Q}})$ system in equilibrium, one obtains

$$\mathbf{F}^{t}\dot{\mathbf{u}}_k=\dot{\mathbf{Q}}^{t}\dot{\mathbf{c}}_k \tag{6}$$

where $\dot{\mathbf{u}}_k$ is the vector of velocities of the mechanism $\dot{\mathbf{c}}_k$ and $(\ )^t$ denotes matrix transpose. Whenever $s_k \subseteq S$ the term on the right-hand side of (6) becomes zero because the bending moments at active hinges remain constant. Thus, if $\dot{\mathbf{c}}_k$ is to remain as a contributor to the solution it is necessary that the load rate $\dot{\mathbf{F}}$ satisfies

$$\dot{\mathbf{F}}^{t}\dot{\mathbf{u}}_k=0. \tag{7}$$

In geometric terms, this result states that in the Cartesian space of load/displacement the difference between any two com-

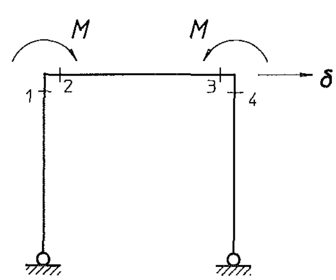


Fig. 1 Example frame

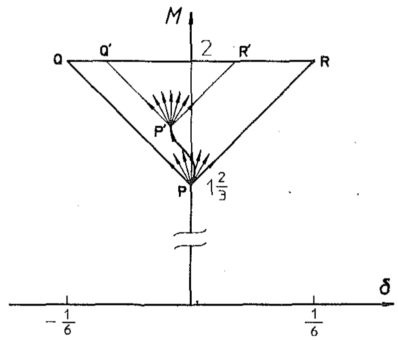


Fig. 2 Load-horizontal displacement curve

peting solutions is normal to the planes of equilibrium equations defined by mechanisms as given by (6).

## 4 Illustrative Example

Consider the frame shown in Fig. 1. Each of the three members are of unit length, flexural rigidity, and plastic moment. The singular hinge sets are $s_1 = \{1, 2\}$, $s_2 = \{3, 4\}$, and $s_3 = \{1, 4\}$, arising from the mechanisms given by $\dot{\mathbf{c}}_1^t = (1, 1, 0, 0)$, $\dot{\mathbf{c}}_2^t = (0, 0, 1, 1)$ and $\dot{\mathbf{c}}_3^t = (1, 0, 0, 1)$, respectively. (Sign convention adopted is that counterclockwise moments at member ends are positive.) Let the frame be loaded as shown by two equal and opposite moments of magnitude $M$. The horizontal displacement $\delta$ of the beam is observed under monotonically increasing load. The solution for the initial elastic phase is given by $\dot{\mathbf{Q}} = \dot{M}(-0.6, -0.4, 0.4, 0.6)^t$; $\dot{\mathbf{p}} = \mathbf{o}$; and $\dot{\delta} = 0$. Note that the problem, and hence the elastic solution, is symmetric.

At $M = 5/3$, the elastic phase terminates as plastic hinges form at locations 1 and 4. The solution of the second phase can be expressed as $\dot{\mathbf{Q}} = \dot{M}(0, -1, 1, 0)^t$; $\dot{\mathbf{p}} = \dot{M}(-0.5, 0, 0, 0.5)^t + \alpha\dot{\mathbf{c}}_3$; $-0.5\dot{M} \le \alpha \le 0.5\dot{M}$; and $\dot{\delta} = \alpha$. This is a nonunique solution. As shown in Fig. 2, the $M \sim \delta$ curve has multiple options at each instant as the load increases. At the beginning of this phase the frame can choose to arrive at any point within $PQR$, but after having chosen the path $PP'$, the scope narrows to $P'Q'R'$. Note that the deformation behavior is not symmetric in general. The second phase terminates at $M = 2$ as plastic hinges form at locations 2 and 3. A further analysis of will show that plastic collapse occurs then.

## References

Hodge, P. G., Jr., and White, D. L., 1980, "Nonuniqueness in Contained Plastic Deformation," ASME JOURNAL OF APPLIED MECHANICS, Vol. 47, pp. 273–277.

Hodge, P. G., Jr., Bathe, K. J., and Dvorkin, E. N., 1986, "Causes and Consequences of Nonuniqueness in an Elastic/Perfectly-Plastic Truss," ASME JOURNAL OF APPLIED MECHANICS, Vol. 53, pp. 235–241.

Koiter, W. T., 1060, "General Theorems for Elastic-Plastic Solids," *Progress in Solid Mechanics I*, I. N. Sneddon and R. Hills, eds., North-Holland, Amsterdam, pp. 167–221.

Maier, G., 1970, "A Matrix Structural Theory of Piecewise Linear Elasto Plasticity With Interacting Yield Planes," *Meccanica*, Vol. 5, pp. 54–66.

Maier, G., Giacomini, S., and Paterlini, F., 1979, "Combined Elastoplastic and Limit Analysis via Restricted Basis Linear Programming," *Computer Methods in Applied Mechanics and Engineering*, Vol. 19, pp. 21–48.

Melan, E, 1938, "Zur Plastizität des räumlichen Kontinuums," *Ingenieur-Archiv*, Vol. 9, pp. 116–126.

Smith, D. L., and Munro, J., 1978, "On Uniqueness in the Elastoplastic Analysis of Frames," *Journal of Structural Mechanics*, Vol. 6, pp. 85–106.

Tin-Loi, F., and Wong, M. B., 1989, "Non-Uniqueness in Elastoplastic Analysis," *Mechanics of Structures and Machines*, Vol. 16, pp. 423–437.

White, D. L., and Hodge, P. G., Jr., 1980, "Computation of Non-unique Solutions of Elastic-Plastic Trusses," *Computers and Structures*, Vol. 12, pp. 769–774.

# Some Remarks on the Solutions of a Concentrated Torque and Double Forces on an Elastic Half-Space

T. Chen[18]

## 1 Introduction

Exact solutions for a concentrated force in an infinite or half-space linearly elastic medium are very useful in various applications, for example in boundary integral method or in fracture mechanics. In particular, it is advantageous to have analytical expressions for the stress and displacement fields. Such point force fundamental fields can be superposed to obtain solutions of other boundary value problems.

Recently, Chowdhury (1983) studied the boundary value problem of a homogeneous isotropic elastic half-space subjected to a concentrated torque normal to its surface by similarity transformations. Chow and Yang (1990) employed Hankel transforms to the same problem but in an orthotropic medium. In this study, we are concerned with the isotropic medium. It is shown that the solution of the above problem is equivalent to superposition of solutions of the Cerruti problem (1882). The approach followed is to use a well-known limiting process which leads to a significant simplification in the formulation. The process is extended to a similar problem under two pairs of double forces without moment. Such loading may be referred as a singularity of "center of compression or dilatation" (Love, 1944). These two kinds of loadings considered relate to the stresses $\sigma_{\phi Z}$ and $\sigma_{rz}$ (see Fig. 1) acting on a single point, respectively. Other types of singularities can be synthesized as well.

## 2 Solutions of Cerruti's Problems

Consider a homogeneous isotropic elastic half-space and define a Cartesian coordinate system $\{O; x_1, x_2, x_3\}$ with the plane $x_1 = 0$ coinciding with the surface of the half-space (Fig. 1). Exact solutions of the field variables in the half-space due to a tangential force $P$ acting at the origin of the coordinate system in the direction of $x_q$, $q \neq 1$, were originally due to Cerruti (1882). A lucid exposition is given in the treatise by Westergaard (1952). The corresponding stress and displacement components for a point force acting in the direction of $x_3$ (Fig. 1) are recorded in the following:

$$\sigma_1 = -\frac{3Px_1^2x_3}{2\pi R^5},\ \sigma_2 = -\frac{3Px_2^2x_3}{2\pi R^5} + \frac{P(1-2\nu)x_3}{2\pi(R+x_1)^2R^3}\left(3R^2 - x_3^2 - \frac{2Rx_3^2}{R+x_1}\right),$$

$$\sigma_3 = -\frac{3Px_3^3}{2\pi R^5}, + \frac{P(1-2\nu)x_3}{2\pi(R+x_1)^2R^3}\left(R^2 - x_2^2 - \frac{2Rx_2^2}{R+x_1}\right),$$

$$\sigma_{13} = -\frac{3Px_1x_3^2}{2\pi R^5},$$

$$\sigma_{23} = -\frac{3Px_2x_3^2}{2\pi R^5} - \frac{P(1-2\nu)x_2}{2\pi(R+x_1)^2R^3}\left(R^2 - x_3^2 - \frac{2Rx_3^2}{R+x_1}\right),$$

[18]Department of Civil Engineering, Rensselaer Polytechnic Institute, Troy, NY 12180-3590. Currently at the Department of Civil Engineering, National Cheng Kung University, Tainan, Taiwan.

Manuscript received by the ASME Applied Mechanics Division, Nov. 28, 1990; final revision, July 20, 1991. Associate Technical Editor: C. Horgan.

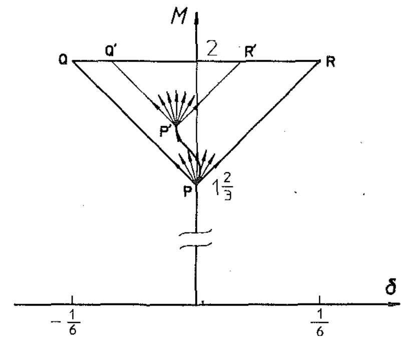


Fig. 2 Load-horizontal displacement curve

peting solutions is normal to the planes of equilibrium equations defined by mechanisms as given by (6).

## 4 Illustrative Example

Consider the frame shown in Fig. 1. Each of the three members are of unit length, flexural rigidity, and plastic moment. The singular hinge sets are $s_1 = \{1, 2\}$, $s_2 = \{3, 4\}$, and $s_3 = \{1, 4\}$, arising from the mechanisms given by $\dot{\mathbf{c}}_1^t = (1, 1, 0, 0)$, $\dot{\mathbf{c}}_2^t = (0, 0, 1, 1)$ and $\dot{\mathbf{c}}_3^t = (1, 0, 0, 1)$, respectively. (Sign convention adopted is that counterclockwise moments at member ends are positive.) Let the frame be loaded as shown by two equal and opposite moments of magnitude $M$. The horizontal displacement $\delta$ of the beam is observed under monotonically increasing load. The solution for the initial elastic phase is given by $\dot{\mathbf{Q}} = \dot{M}(-0.6, -0.4, 0.4, 0.6)^t$; $\dot{\mathbf{p}} = \mathbf{o}$; and $\dot{\delta} = 0$. Note that the problem, and hence the elastic solution, is symmetric.

At $M = 5/3$, the elastic phase terminates as plastic hinges form at locations 1 and 4. The solution of the second phase can be expressed as $\dot{\mathbf{Q}} = \dot{M}(0, -1, 1, 0)^t$; $\dot{\mathbf{p}} = \dot{M}(-0.5, 0, 0, 0.5)^t + \alpha\dot{\mathbf{c}}_3$; $-0.5\dot{M} \leq \alpha \leq 0.5\dot{M}$; and $\dot{\delta} = \alpha$. This is a nonunique solution. As shown in Fig. 2, the $M \sim \delta$ curve has multiple options at each instant as the load increases. At the beginning of this phase the frame can choose to arrive at any point within $PQR$, but after having chosen the path $PP'$, the scope narrows to $P'Q'R'$. Note that the deformation behavior is not symmetric in general. The second phase terminates at $M = 2$ as plastic hinges form at locations 2 and 3. A further analysis of will show that plastic collapse occurs then.

## References

Hodge, P. G., Jr., and White, D. L., 1980, "Nonuniqueness in Contained Plastic Deformation," ASME JOURNAL OF APPLIED MECHANICS, Vol. 47, pp. 273–277.

Hodge, P. G., Jr., Bathe, K. J., and Dvorkin, E. N., 1986, "Causes and Consequences of Nonuniqueness in an Elastic/Perfectly-Plastic Truss," ASME JOURNAL OF APPLIED MECHANICS, Vol. 53, pp. 235–241.

Koiter, W. T., 1060, "General Theorems for Elastic-Plastic Solids," *Progress in Solid Mechanics I*, I. N. Sneddon and R. Hills, eds., North-Holland, Amsterdam, pp. 167–221.

Maier, G., 1970, "A Matrix Structural Theory of Piecewise Linear Elasto Plasticity With Interacting Yield Planes," *Meccanica*, Vol. 5, pp. 54–66.

Maier, G., Giacomini, S., and Paterlini, F., 1979, "Combined Elastoplastic and Limit Analysis via Restricted Basis Linear Programming," *Computer Methods in Applied Mechanics and Engineering*, Vol. 19, pp. 21–48.

Melan, E, 1938, "Zur Plastizität des räumlichen Kontinuums," *Ingenieur-Archiv*, Vol. 9, pp. 116–126.

Smith, D. L., and Munro, J., 1978, "On Uniqueness in the Elastoplastic Analysis of Frames," *Journal of Structural Mechanics*, Vol. 6, pp. 85–106.

Tin-Loi, F., and Wong, M. B., 1989, "Non-Uniqueness in Elastoplastic Analysis," *Mechanics of Structures and Machines*, Vol. 16, pp. 423–437.

White, D. L., and Hodge, P. G., Jr., 1980, "Computation of Non-unique Solutions of Elastic-Plastic Trusses," *Computers and Structures*, Vol. 12, pp. 769–774.

# Some Remarks on the Solutions of a Concentrated Torque and Double Forces on an Elastic Half-Space

T. Chen[18]

## 1 Introduction

Exact solutions for a concentrated force in an infinite or half-space linearly elastic medium are very useful in various applications, for example in boundary integral method or in fracture mechanics. In particular, it is advantageous to have analytical expressions for the stress and displacement fields. Such point force fundamental fields can be superposed to obtain solutions of other boundary value problems.

Recently, Chowdhury (1983) studied the boundary value problem of a homogeneous isotropic elastic half-space subjected to a concentrated torque normal to its surface by similarity transformations. Chow and Yang (1990) employed Hankel transforms to the same problem but in an orthotropic medium. In this study, we are concerned with the isotropic medium. It is shown that the solution of the above problem is equivalent to superposition of solutions of the Cerruti problem (1882). The approach followed is to use a well-known limiting process which leads to a significant simplification in the formulation. The process is extended to a similar problem under two pairs of double forces without moment. Such loading may be referred as a singularity of "center of compression or dilatation" (Love, 1944). These two kinds of loadings considered relate to the stresses $\sigma_{\phi Z}$ and $\sigma_{rz}$ (see Fig. 1) acting on a single point, respectively. Other types of singularities can be synthesized as well.

## 2 Solutions of Cerruti's Problems

Consider a homogeneous isotropic elastic half-space and define a Cartesian coordinate system $\{O; x_1, x_2, x_3\}$ with the plane $x_1 = 0$ coinciding with the surface of the half-space (Fig. 1). Exact solutions of the field variables in the half-space due to a tangential force $P$ acting at the origin of the coordinate system in the direction of $x_q$, $q \neq 1$, were originally due to Cerruti (1882). A lucid exposition is given in the treatise by Westergaard (1952). The corresponding stress and displacement components for a point force acting in the direction of $x_3$ (Fig. 1) are recorded in the following:

$$\sigma_1 = -\frac{3Px_1^2x_3}{2\pi R^5},\ \sigma_2 = -\frac{3Px_2^2x_3}{2\pi R^5} + \frac{P(1-2\nu)x_3}{2\pi(R+x_1)^2R^3}\left(3R^2 - x_3^2 - \frac{2Rx_3^2}{R+x_1}\right),$$

$$\sigma_3 = -\frac{3Px_3^3}{2\pi R^5}, + \frac{P(1-2\nu)x_3}{2\pi(R+x_1)^2R^3}\left(R^2 - x_2^2 - \frac{2Rx_2^2}{R+x_1}\right),$$

$$\sigma_{13} = -\frac{3Px_1x_3^2}{2\pi R^5},$$

$$\sigma_{23} = -\frac{3Px_2x_3^2}{2\pi R^5} - \frac{P(1-2\nu)x_2}{2\pi(R+x_1)^2R^3}\left(R^2 - x_3^2 - \frac{2Rx_3^2}{R+x_1}\right),$$

[18]Department of Civil Engineering, Rensselaer Polytechnic Institute, Troy, NY 12180-3590. Currently at the Department of Civil Engineering, National Cheng Kung University, Tainan, Taiwan.

Manuscript received by the ASME Applied Mechanics Division, Nov. 28, 1990; final revision, July 20, 1991. Associate Technical Editor: C. Horgan.

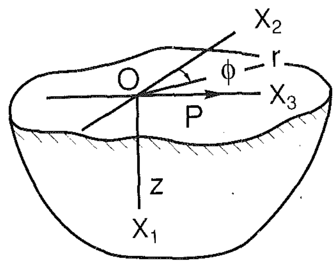


**Fig. 1 Cerruti's problem**

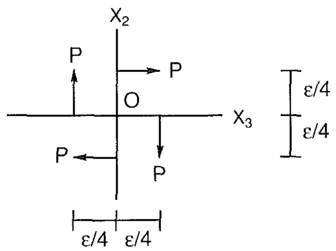


**Fig. 2 A schematic representation of a concentration torque applied at origin**

$$\sigma_{12}=-\frac{3Px_1x_2x_3}{2\pi R^5},$$

$$u_1=\frac{P}{4\pi\mu}\left[\frac{x_1x_3}{R^3}+\frac{(1-2\nu)x_3}{R(R+x_1)}\right],\ u_2=\frac{P}{4\pi\mu}\left[\frac{x_2x_3}{R^3}-\frac{(1-2\nu)x_2x_3}{R(R+x_1)^2}\right],$$

$$u_3=\frac{P}{4\pi\mu}\left\{\frac{1}{R}+\frac{x_3^2}{R^3}+(1-2\nu)\left[\frac{1}{R+x_1}-\frac{x_3^2}{R(R+x_1)^2}\right]\right\}. \tag{1}$$

When Poisson's ratio $\nu$ is 1/2, the above solutions due to a point force acting in the $x_q$ direction, $q\in\{2,3\}$, can be expressed in a coincise form:

$$\sigma_{ij}=-\frac{3Px_ix_jx_q}{2\pi R^5},\ i,j=1,2,3,$$

$$u_i=\frac{Px_ix_q}{4\mu\pi R^3},\ i\neq q,$$

$$u_q=\frac{P}{4\mu\pi}\left(\frac{1}{R}+\frac{x_q^2}{R^3}\right), \tag{2}$$

where $\mu$ is the shear modulus of the solid and $R$ is given as

$$\sqrt{x_1^2+x_2^2+x_3^2}.$$

## 3 A Concentrated Torque Acting at Origin

The boundary conditions of a concentrated torque applied at origin are equivalent to

$$\lim_{z\to 0}\sigma_{\phi z}=0,\ r\neq 0,\ \lim_{z\to 0}\int_0^\infty 2\pi\sigma_{\phi z}r^2dr+T=0, \tag{3}$$

where $T$ is the applied torque. It is illustrated in Fig. 2 that such a concentration torque can be represented by two pairs of equal and opposite forces applied in the neighborhood of the origin. As the distance $\epsilon$ diminishes indefinitely, the product

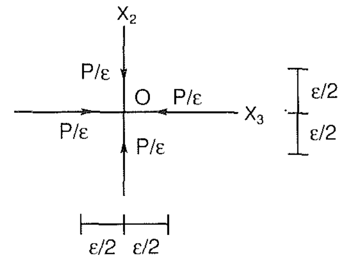


**Fig. 3 A point defect of "center of compression" at origin**

$P\epsilon$ can be regarded as a concentrated torque applied normal to its surface at origin. Therefore, we can write the stresses and displacements in the form:

$$\sigma_{ij}=\lim_{\epsilon\to 0}\left\{{}^3\sigma_{ij}\left(x_1,\ x_2-\frac{1}{4}\epsilon, x_3\right)-{}^3\sigma_{ij}\left(x_1,\ x_2+\frac{1}{4}\epsilon, x_3\right)\right.$$
$$\left.+{}^2\sigma_{ij}\left(x_1,\ x_2,\ x_3+\frac{1}{4}\epsilon\right)-{}^2\sigma_{ij}\left(x_1,\ x_2,\ x_3-\frac{1}{4}\epsilon\right)\right\}, \tag{4}$$

$$u_i=\lim_{\epsilon\to 0}\left\{{}^3u_i\left(x_1,\ x_2-\frac{1}{4}\epsilon, x_3\right)-{}^3u_i\left(x_1,\ x_2+\frac{1}{4}\epsilon, x_3\right)\right.$$
$$\left.+{}^2u_i\left(x_1,\ x_2,\ x_3+\frac{1}{4}\epsilon\right)-{}^2u_i\left(x_1,\ x_2,\ x_3-\frac{1}{4}\epsilon\right)\right\}, \tag{5}$$

where the superscript $k$ in ${}^k\sigma_{ij}$, ${}^ku_i$ assume the solutions of Cerutti's problem with point force acting in the $x_k$ direction. When $\epsilon$ is very small, the corresponding stress and displacement components can be expanded in a series with respect to ($x_1$, $x_2$, $x_3$) as

$${}^k\sigma_{ij}\left(x_1,\ x_2\pm\frac{1}{4}\epsilon,\ x_3\right)$$
$$={}^k\sigma_{ij}(x_1,\ x_2,\ x_3)\pm\frac{1}{4}\epsilon\frac{\partial({}^k\sigma_{ij})}{\partial x_2}+O(\epsilon^2)+\ldots,$$

$${}^k\sigma_{ij}\left(x_1,\ x_2,\ x_3\pm\frac{1}{4}\epsilon\right)$$
$$={}^k\sigma_{ij}(x_1,\ x_2,\ x_3)\pm\frac{1}{4}\epsilon\frac{\partial({}^k\sigma_{ij})}{\partial x_3}+O(\epsilon^2)+\ldots,$$

$${}^ku_i\left(x_1,\ x_2\pm\frac{1}{4}\epsilon,\ x_3\right)={}^ku_i(x_1,\ x_2,\ x_3)\pm\frac{1}{4}\epsilon\frac{\partial({}^ku_i)}{\partial x_2}+O(\epsilon^2)+\ldots,$$

$${}^ku_i\left(x_1,\ x_2,\ x_3\pm\frac{1}{4}\epsilon\right)={}^ku_i(x_1,\ x_2,\ x_3)\pm\frac{1}{4}\epsilon\frac{\partial({}^ku_i)}{\partial x_3}+O(\epsilon^2)+\ldots, \tag{6}$$

and Eqs. (4) and (5) reduce to

$$\sigma_{ij}=\frac{1}{2}\epsilon\left[\frac{\partial({}^2\sigma_{ij})}{\partial x_3}-\frac{\partial({}^3\sigma_{ij})}{\partial x_2}\right], \tag{7}$$

$$u_i=\frac{1}{2}\epsilon\left[\frac{\partial({}^2u_i)}{\partial x_3}-\frac{\partial({}^3u_i)}{\partial x_2}\right]. \tag{8}$$

With the concentrated torque $T$ being denoted by $P\epsilon$, one can derive the solutions for the stresses as:

$$\sigma_{11}=0.,\ \sigma_{22}=\frac{3Tx_2x_3}{2\pi R^5},\ \sigma_{33}=-\frac{3Tx_2x_3}{2\pi R^5},$$

$$\sigma_{12}=\frac{3Tx_1x_3}{4\pi R^5},\quad \sigma_{13}=-\frac{3Tx_1x_2}{4\pi R^5},\quad \sigma_{23}=\frac{3T(x_3^2-x_2^2)}{4\pi R^5}, \tag{9}$$

and for the displacements as:

$$u_1=0,\ u_2=-\frac{Tx_3}{4\mu\pi R^3},\ u_3=\frac{Tx_2}{4\mu\pi R^3}. \tag{10}$$

These can be expressed in a cylindrical coordinate system (with $z$-axis in the direction of $x_1$) and the nonvanishing quantities are:

$$\sigma_{\phi z}=-\frac{3T}{4\pi}\frac{rz}{R^5},\ \sigma_{r\phi}=-\frac{3T}{4\pi}\frac{r^2}{R^5},\ u_\phi=\frac{T}{4\pi\mu}\frac{r}{R^3}. \tag{11}$$

Equation (11) recovers the results by Chowdhury (1983) and by Chow and Yang (1990). As pointed out by the latter, there is a misprint of $\mu$ in the stress components of Chowdhury (1983).

## 4 Double Forces Without Moment Acting at Origin

In this section, we consider two pairs of forces acting at the origin which do not induce a moment. Let a force $\epsilon^{-1}P$ be applied at the point $(0, -\epsilon/2, 0)$ in the direction of $x_2$ and let an equal and opposite force be applied at $(0, \epsilon/2, 0)$; also, let $\epsilon\to 0$ at constant $P$. The same pair of forces is applied at the corresponding points in the neighborhood of the origin but in the direction of $x_3$ (as shown in Fig. 3). After superposition, the stresses and displacements are

$$\sigma_{ij}=\lim_{\epsilon\to 0}\left\{-{}^3\sigma_{ij}\left(x_1, x_2, x_3-\frac{1}{2}\epsilon\right)+{}^3\sigma_{ij}\left(x_1, x_2, x_3+\frac{1}{2}\epsilon\right)\right.$$
$$\left.-{}^2\sigma_{ij}\left(x_1, x_2-\frac{1}{2}\epsilon, x_3\right)+{}^2\sigma_{ij}\left(x_1, x_2+\frac{1}{2}\epsilon, x_3\right)\right\} \tag{12}$$

$$u_i=\lim_{\epsilon\to 0}\left\{-{}^3u_i\left(x_1, x_2, x_3-\frac{1}{2}\epsilon\right)+{}^3u_i\left(x_1, x_2, x_3+\frac{1}{2}\epsilon\right)\right.$$
$$\left.-{}^2u_i\left(x_1, x_2-\frac{1}{2}\epsilon, x_3\right)+{}^2u_i\left(x_1, x_2+\frac{1}{2}\epsilon, x_3\right)\right\}. \tag{13}$$

The limiting process can be applied as $\epsilon\to 0$ and the results are

$$\sigma_{ij}=\epsilon\left[\frac{\partial({}^2\sigma_{ij})}{\partial x_2}+\frac{\partial({}^3\sigma_{ij})}{\partial x_3}\right],\ u_i=\epsilon\left[\frac{\partial({}^2u_i)}{\partial x_2}+\frac{\partial({}^3u_i)}{\partial x_3}\right]. \tag{14}$$

Explicit forms of the above solutions are quite complicated. Simplified solutions are obtained for the case when Poisson's ratio is equal to 1/2. The nonvanishing stresses and displacements are:

$$\sigma_{rr}=\frac{Pr^2(15r^2-12R^2)}{2\pi R^7},$$
$$\sigma_{zz}=\frac{Pz^2(15r^2-6R^2)}{2\pi R^7},\quad \sigma_{rz}=\frac{Prz(15r^2-9R^2)}{2\pi R^7}, \tag{15}$$
$$u_r=\frac{Pr(2R^2-3r^2)}{4\pi\mu R^5},\quad u_z=\frac{Pz(2R^2-3r^2)}{4\pi\mu R^5}. \tag{16}$$

### Acknowledgment

The author gratefully acknowledges the encouragement of Prof. George J. Dvorak at Rensselaer.

### References

Cerutti, V., 1882, Roma, Acc. Lincei, Mem. fis. mat.

Chow, C. L., and Yang, F., 1990, "On the Solution of a Concentrated Torque on an Orthotropic Half-Space," *Int. J. Engng. Sci.*, Vol. 28, pp. 871–874.

Chowdhury, K. L., 1983, "Solutions of the Problem of a Concentrated Torque on a Semi-Space by Similarity Transformations," *J. Elasticity*, Vol. 13, pp. 87–90.

Love, A. E. H., 1944, *A Treatise on the Mathematical Theory of Elasticity*, Dover, New York.

Westergarrd, H. M., 1952, *Theory of Elasticity and Plasticity*, John Wiley and Sons, New York.

# Configuration of a Bent Tape of Curved Cross-Section

K. Schulgasser[19]

## Introduction

We consider an originally straight tape of curved cross-section, as is found for instance in measuring tapes or Venetian blind slats. The radius of curvature of the cross-section is denoted by $R$. When a bending moment, $M$, is applied at the ends of such a strip, it is found that at some critical moment, the cross-section of a portion of the strip will flatten and this portion (AB in Fig. 1) will go over into a circular arc while the remainder of the strip remains straight. The problem is to determine the radius, $r$, of the section AB. Although this problem was proposed nearly 70 years ago (see Calladine, 1988), it was not until many years later that a solution was given by Rimrott (1970). He found, as is observed experimentally, that

$$r=R. \tag{1}$$

This solution subsumes that the elastic properties of the strip are the same in the longitudinal and perpendicular directions. It is our purpose to generalize the solution to the case when the strip is anisotropic. If the Young's modulus in the longitudinal direction is $E_L$ and in the cross-direction is $E_C$, then we will show that the radius $r$ is given by

$$r=\left(\frac{E_L}{E_C}\right)^{1/2}R. \tag{2}$$

We follow very closely the development in Calladine (1988) and use his notation, only distinguishing between elastic properties in the two directions.

## Analysis

Consider Fig. 1. We identify three zones: (a) the curved region AB, (b) the nearly straight regions with the original undeformed cross-section, and (c) a transition region lying between (a) and (b). We examine the energy stored in the curved region (a) with its flattened cross-section; its radius $r$ is the unknown of the problem. Let $b$ be the transverse width of the flattened tape, which is taken to be somewhat smaller than $R$. Then the surface area of the tape in the region AB is $b\psi r$ where the angle $\psi$ is defined in the figure. We will calculate the strain energy in this region of the tape. First we note that the principle curvatures in the straight regions (b) and in the curved region (a) are given by

$$\text{Straight region:}\quad (\kappa_x, \kappa_y)=\left(0, \frac{1}{R}\right)$$
$$\text{Curved region:}\quad (\kappa_x, \kappa_y)=\left(\frac{1}{r}, 0\right). \tag{3a,b}$$

Here, $x$ and $y$ refer to the longitudinal and transverse directions in the tape surface, respectively. The changes in curvature when the tape deforms from straight to curved is thus

$$(\Delta\kappa_x, \Delta\kappa_y)=\left(-\frac{1}{r}, \frac{1}{R}\right). \tag{4}$$

The strain energy of bending per unit area, $U$, is given by

[19]Pearlstone Center for Aeronautical Engineering, Department of Mechanical Engineering, Ben-Gurion University of the Negev, Beer Sheva, Israel.

Contributed by the Applied Mechanics Division of The American Society of Mechanical Engineers for publication in the ASME Journal of Applied Mechanics. Manuscript received by the Applied Mechanics Division, February 20, 1991; final revision, September 30, 1991. Associate Technical Editor: W. N. Sharpe, Jr.

$$u_1=0,\ u_2=-\frac{Tx_3}{4\mu\pi R^3},\ u_3=\frac{Tx_2}{4\mu\pi R^3}. \tag{10}$$

These can be expressed in a cylindrical coordinate system (with $z$-axis in the direction of $x_1$) and the nonvanishing quantities are:

$$\sigma_{\phi z}=-\frac{3T}{4\pi}\frac{rz}{R^5},\ \sigma_{r\phi}=-\frac{3T}{4\pi}\frac{r^2}{R^5},\ u_\phi=\frac{T}{4\pi\mu}\frac{r}{R^3}. \tag{11}$$

Equation (11) recovers the results by Chowdhury (1983) and by Chow and Yang (1990). As pointed out by the latter, there is a misprint of $\mu$ in the stress components of Chowdhury (1983).

## 4 Double Forces Without Moment Acting at Origin

In this section, we consider two pairs of forces acting at the origin which do not induce a moment. Let a force $\epsilon^{-1}P$ be applied at the point $(0, -\epsilon/2, 0)$ in the direction of $x_2$ and let an equal and opposite force be applied at $(0, \epsilon/2, 0)$; also, let $\epsilon\to 0$ at constant $P$. The same pair of forces is applied at the corresponding points in the neighborhood of the origin but in the direction of $x_3$ (as shown in Fig. 3). After superposition, the stresses and displacements are

$$\sigma_{ij}=\lim_{\epsilon\to 0}\left\{-{}^3\sigma_{ij}\left(x_1, x_2, x_3-\frac{1}{2}\epsilon\right)+{}^3\sigma_{ij}\left(x_1, x_2, x_3+\frac{1}{2}\epsilon\right)\right.$$
$$\left.-{}^2\sigma_{ij}\left(x_1, x_2-\frac{1}{2}\epsilon, x_3\right)+{}^2\sigma_{ij}\left(x_1, x_2+\frac{1}{2}\epsilon, x_3\right)\right\} \tag{12}$$

$$u_i=\lim_{\epsilon\to 0}\left\{-{}^3u_i\left(x_1, x_2, x_3-\frac{1}{2}\epsilon\right)+{}^3u_i\left(x_1, x_2, x_3+\frac{1}{2}\epsilon\right)\right.$$
$$\left.-{}^2u_i\left(x_1, x_2-\frac{1}{2}\epsilon, x_3\right)+{}^2u_i\left(x_1, x_2+\frac{1}{2}\epsilon, x_3\right)\right\}. \tag{13}$$

The limiting process can be applied as $\epsilon\to 0$ and the results are

$$\sigma_{ij}=\epsilon\left[\frac{\partial({}^2\sigma_{ij})}{\partial x_2}+\frac{\partial({}^3\sigma_{ij})}{\partial x_3}\right],\ u_i=\epsilon\left[\frac{\partial({}^2u_i)}{\partial x_2}+\frac{\partial({}^3u_i)}{\partial x_3}\right]. \tag{14}$$

Explicit forms of the above solutions are quite complicated. Simplified solutions are obtained for the case when Poisson's ratio is equal to 1/2. The nonvanishing stresses and displacements are:

$$\sigma_{rr}=\frac{Pr^2(15r^2-12R^2)}{2\pi R^7},$$
$$\sigma_{zz}=\frac{Pz^2(15r^2-6R^2)}{2\pi R^7},\quad \sigma_{rz}=\frac{Prz(15r^2-9R^2)}{2\pi R^7}, \tag{15}$$

$$u_r=\frac{Pr(2R^2-3r^2)}{4\pi\mu R^5},\quad u_z=\frac{Pz(2R^2-3r^2)}{4\pi\mu R^5}. \tag{16}$$

### Acknowledgment

The author gratefully acknowledges the encouragement of Prof. George J. Dvorak at Rensselaer.

### References

Cerutti, V., 1882, Roma, Acc. Lincei, Mem. fis. mat.

Chow, C. L., and Yang, F., 1990, "On the Solution of a Concentrated Torque on an Orthotropic Half-Space," *Int. J. Engng. Sci.*, Vol. 28, pp. 871–874.

Chowdhury, K. L., 1983, "Solutions of the Problem of a Concentrated Torque on a Semi-Space by Similarity Transformations," *J. Elasticity*, Vol. 13, pp. 87–90.

Love, A. E. H., 1944, *A Treatise on the Mathematical Theory of Elasticity*, Dover, New York.

Westergarrd, H. M., 1952, *Theory of Elasticity and Plasticity*, John Wiley and Sons, New York.

## Configuration of a Bent Tape of Curved Cross-Section

**K. Schulgasser**[19]

### Introduction

We consider an originally straight tape of curved cross-section, as is found for instance in measuring tapes or Venetian blind slats. The radius of curvature of the cross-section is denoted by $R$. When a bending moment, $M$, is applied at the ends of such a strip, it is found that at some critical moment, the cross-section of a portion of the strip will flatten and this portion (AB in Fig. 1) will go over into a circular arc while the remainder of the strip remains straight. The problem is to determine the radius, $r$, of the section AB. Although this problem was proposed nearly 70 years ago (see Calladine, 1988), it was not until many years later that a solution was given by Rimrott (1970). He found, as is observed experimentally, that

$$r=R. \tag{1}$$

This solution subsumes that the elastic properties of the strip are the same in the longitudinal and perpendicular directions. It is our purpose to generalize the solution to the case when the strip is anisotropic. If the Young's modulus in the longitudinal direction is $E_L$ and in the cross-direction is $E_C$, then we will show that the radius $r$ is given by

$$r=\left(\frac{E_L}{E_C}\right)^{1/2}R. \tag{2}$$

We follow very closely the development in Calladine (1988) and use his notation, only distinguishing between elastic properties in the two directions.

### Analysis

Consider Fig. 1. We identify three zones: (a) the curved region AB, (b) the nearly straight regions with the original undeformed cross-section, and (c) a transition region lying between (a) and (b). We examine the energy stored in the curved region (a) with its flattened cross-section; its radius $r$ is the unknown of the problem. Let $b$ be the transverse width of the flattened tape, which is taken to be somewhat smaller than $R$. Then the surface area of the tape in the region AB is $b\psi r$ where the angle $\psi$ is defined in the figure. We will calculate the strain energy in this region of the tape. First we note that the principle curvatures in the straight regions (b) and in the curved region (a) are given by

$$\text{Straight region:}\quad (\kappa_x, \kappa_y)=\left(0, \frac{1}{R}\right)$$
$$\text{Curved region:}\quad (\kappa_x, \kappa_y)=\left(\frac{1}{r}, 0\right). \tag{3a,b}$$

Here, $x$ and $y$ refer to the longitudinal and transverse directions in the tape surface, respectively. The changes in curvature when the tape deforms from straight to curved is thus

$$(\Delta\kappa_x, \Delta\kappa_y)=\left(-\frac{1}{r}, \frac{1}{R}\right). \tag{4}$$

The strain energy of bending per unit area, $U$, is given by

[19]Pearlstone Center for Aeronautical Engineering, Department of Mechanical Engineering, Ben-Gurion University of the Negev, Beer Sheva, Israel.

Contributed by the Applied Mechanics Division of The American Society of Mechanical Engineers for publication in the ASME Journal of Applied Mechanics. Manuscript received by the Applied Mechanics Division, February 20, 1991; final revision, September 30, 1991. Associate Technical Editor: W. N. Sharpe, Jr.

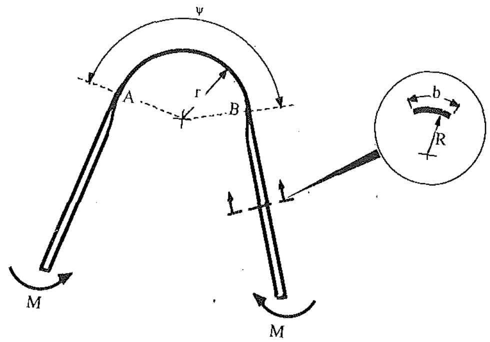


Fig. 1 Configuration of a bent curved tape showing (inset) the cross-section of the tape when straight

$$U=\frac{1}{2}\left[D_{11}\{\Delta\kappa_x\}^2+D_{22}\{\Delta\kappa_y\}^2+2D_{12}(\Delta\kappa_x)(\Delta\kappa_y)\right] \qquad (5)$$

where $D_{11}$ is the flexural rigidity of the strip in the longitudinal direction, $D_{22}$ is the flexural rigidity in the transverse direction, and $D_{12}$ is the cross-term.

Then using (4) we have

$$U=\frac{b\psi}{2}\left[\frac{1}{r^2}D_{11}+\frac{1}{R^2}D_{22}-\frac{2}{rR}D_{12}\right]. \qquad (6)$$

Multiplying by the total area of region (a); i.e., $b\psi r$, we obtain a simple expression for the total strain energy, $U_T$, in this region:

$$U_T=\frac{b\psi}{2}\left[\frac{1}{r}D_{11}+\frac{r}{R^2}D_{22}-\frac{2}{R}D_{12}\right]. \qquad (7)$$

The key observation of Rimrott was that we may ignore the transition region in seeking a solution to the present problem. This is so since the transition region is a more or less constant feature of the problem in the sense that it is independent of $r$. Additionally, the length of the transition region is observed to be approximately equal to the width of the tape, and this is small compared to the length of the region (a) which is $\psi r$. Hence, we expect the amount of elastic energy stored in this region to be small compared to that stored in region (a). We may also neglect the elastic energy stored in the nearly straight regions. Then the total energy in the system, which varies with $r$, is given in Eq. (7), and this expression must be a minimum with respect to $r$ for the equilibrium configuration. Putting

$$\frac{dU_T}{dr}=0, \qquad (8)$$

we obtain

$$\frac{r}{R}=\sqrt{\frac{D_{11}}{D_{22}}}, \qquad (9)$$

which is Eq. (2) when we recognize that the ratio of the flexural rigidities is simply the ratio of the Young's moduli.

## An Experiment

We now describe an interesting and extremely simple experiment to which Eq. (2) can be applied. Machine-made paper is an anisotropic (orthotropic) elastic material. Typically, for instance, photocopy paper has an elastic modulus in one (the "machine") direction about two times that in the other ("cross") direction. We take two sheets of such paper, and lay one over the other with one sheet turned 90 degrees with respect to the second. We then roll the two sheets together into a tube of diameter approximately 30 mm, and place a band around the tube so that it will not open. Now place the rolled tube into an oven at about 125°C for approximately ten minutes. Remove the tube from the oven and permit it to cool. When the band is removed the tube will very nearly maintain its restrained diameter due to viscoelastic relaxation of the natural polymers at the elevated temperature. Now cut a strip of width about 10 mm from each of the sheets in the rolled tube along the longitudinal direction of the tube. Perform the experiment indicated in Fig. 1 on each of the strips. If we denote by $E_{MD}$ the Young's modulus of the sheet of paper in the machine direction and by $E_{CD}$ the Young's modulus of the sheet of paper in the cross-direction, then application of equation (2) in the instances of each of the two strips gives

$$\frac{r_{MD}}{r_{CD}}=\frac{E_{MD}}{E_{CD}} \qquad (10)$$

where $r_{MD}$ and $r_{CD}$ are the radii which will be formed, respectively, for the strip cut in the machine direction and the cross-direction of the paper. If for each of the two strips we maintain the straight sections of the strips parallel we readily perceive the 2:1 ratio.

## References

Calladine, C. R., 1988, "The Theory of Thin Shell Structures 1888–1988," *Proc. Instn. Mech. Engrs.*, Vol. 202, pp. 1–9.

Rimrott, F. P. J., 1970, "Querschnittsverformung bei Torsion offener Profile," *ZAMM*, Vol. 50, pp. 775–778.

# The Dynamics of a Nonharmonically Excited System Having Rigid Amplitude Constraints

**Pi-Cheng Tung**[20]

*We consider the dynamic response of a single-degree-of-freedom system having two-sided amplitude constraints. The model consists of a piecewise-linear oscillator subjected to nonharmonic excitation. A simple impact rule employing a coefficient of restitution is used to characterize the almost instantaneous behavior of impact at the constraints. In this paper periodic and chaotic motions are found. The amplitude and stability of the periodic responses are determined and bifurcation analysis for these motions is carried out. Chaotic motions are found to exist over ranges of forcing periods.*

## 1 Introduction

Motions of systems with two-sided constraints have been studied in the context of the impact damper by several authors (see, for example, Masri, 1972; Nigm and Shabana, 1983; Shaw and Shaw, 1989). Also, Shaw (1985a, b) studied bilinear system using analytical method with harmonically periodic excitation. In this paper a system having two-sided constraints is considered, and method from dynamical systems and bifurcation theory are employed in order to study the dynamic behavior of our model.

Consider the simple system having nonsymmetrically placed rigid stops and subjected to nonharmonically periodic excitation shown in the Fig. 1. The left stop is placed right at the equilibrium position of the mass. The nondimensional equation of motion can be written as follows:

$$\ddot{x}+2\alpha\dot{x}+x=F(t);\ 0<x<1, \qquad (1)$$

where the definition of $F(t)$ in one period $T$ is

[20]Department of Mechanical Engineering, National Central University, Chung-Li, Taiwan 32054, Republic of China.

Manuscript received by the ASME Applied Mechanics Division, Feb. 14, 1991; final revision, May 20, 1991. Associate Technical Editor: D. J. Inman.

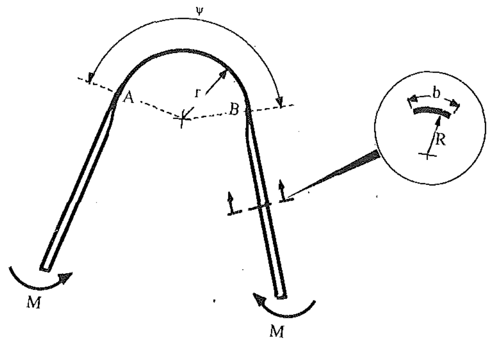


**Fig. 1 Configuration of a bent curved tape showing (inset) the cross-section of the tape when straight**

$$U=\frac{1}{2}\left[D_{11}\{\Delta\kappa_x\}^2+D_{22}\{\Delta\kappa_y\}^2+2D_{12}(\Delta\kappa_x)(\Delta\kappa_y)\right] \qquad (5)$$

where $D_{11}$ is the flexural rigidity of the strip in the longitudinal direction, $D_{22}$ is the flexural rigidity in the transverse direction, and $D_{12}$ is the cross-term.

Then using (4) we have

$$U=\frac{b\psi}{2}\left[\frac{1}{r^2}D_{11}+\frac{1}{R^2}D_{22}-\frac{2}{rR}D_{12}\right]. \qquad (6)$$

Multiplying by the total area of region (a); i.e., $b\psi r$, we obtain a simple expression for the total strain energy, $U_T$, in this region:

$$U_T=\frac{b\psi}{2}\left[\frac{1}{r}D_{11}+\frac{r}{R^2}D_{22}-\frac{2}{R}D_{12}\right]. \qquad (7)$$

The key observation of Rimrott was that we may ignore the transition region in seeking a solution to the present problem. This is so since the transition region is a more or less constant feature of the problem in the sense that it is independent of $r$. Additionally, the length of the transition region is observed to be approximately equal to the width of the tape, and this is small compared to the length of the region (a) which is $\psi r$. Hence, we expect the amount of elastic energy stored in this region to be small compared to that stored in region (a). We may also neglect the elastic energy stored in the nearly straight regions. Then the total energy in the system, which varies with $r$, is given in Eq. (7), and this expression must be a minimum with respect to $r$ for the equilibrium configuration. Putting

$$\frac{dU_T}{dr}=0, \qquad (8)$$

we obtain

$$\frac{r}{R}=\sqrt{\frac{D_{11}}{D_{22}}}, \qquad (9)$$

which is Eq. (2) when we recognize that the ratio of the flexural rigidities is simply the ratio of the Young's moduli.

## An Experiment

We now describe an interesting and extremely simple experiment to which Eq. (2) can be applied. Machine-made paper is an anisotropic (orthotropic) elastic material. Typically, for instance, photocopy paper has an elastic modulus in one (the "machine") direction about two times that in the other ("cross") direction. We take two sheets of such paper, and lay one over the other with one sheet turned 90 degrees with respect to the second. We then roll the two sheets together into a tube of diameter approximately 30 mm, and place a band around the tube so that it will not open. Now place the rolled tube into an oven at about 125°C for approximately ten minutes. Remove the tube from the oven and permit it to cool. When the band is removed the tube will very nearly maintain its restrained diameter due to viscoelastic relaxation of the natural polymers at the elevated temperature. Now cut a strip of width about 10 mm from each of the sheets in the rolled tube along the longitudinal direction of the tube. Perform the experiment indicated in Fig. 1 on each of the strips. If we denote by $E_{MD}$ the Young's modulus of the sheet of paper in the machine direction and by $E_{CD}$ the Young's modulus of the sheet of paper in the cross-direction, then application of equation (2) in the instances of each of the two strips gives

$$\frac{r_{MD}}{r_{CD}}=\frac{E_{MD}}{E_{CD}} \qquad (10)$$

where $r_{MD}$ and $r_{CD}$ are the radii which will be formed, respectively, for the strip cut in the machine direction and the cross-direction of the paper. If for each of the two strips we maintain the straight sections of the strips parallel we readily perceive the 2:1 ratio.

## References


Calladine, C. R., 1988, "The Theory of Thin Shell Structures 1888–1988," *Proc. Instn. Mech. Engrs.*, Vol. 202, pp. 1–9.

Rimrott, F. P. J., 1970, "Querschnittsverformung bei Torsion offener Profile," *ZAMM*, Vol. 50, pp. 775–778.


# The Dynamics of a Nonharmonically Excited System Having Rigid Amplitude Constraints

**Pi-Cheng Tung**[20]

*We consider the dynamic response of a single-degree-of-freedom system having two-sided amplitude constraints. The model consists of a piecewise-linear oscillator subjected to nonharmonic excitation. A simple impact rule employing a coefficient of restitution is used to characterize the almost instantaneous behavior of impact at the constraints. In this paper periodic and chaotic motions are found. The amplitude and stability of the periodic responses are determined and bifurcation analysis for these motions is carried out. Chaotic motions are found to exist over ranges of forcing periods.*

## 1 Introduction

Motions of systems with two-sided constraints have been studied in the context of the impact damper by several authors (see, for example, Masri, 1972; Nigm and Shabana, 1983; Shaw and Shaw, 1989). Also, Shaw (1985a, b) studied bilinear system using analytical method with harmonically periodic excitation. In this paper a system having two-sided constraints is considered, and method from dynamical systems and bifurcation theory are employed in order to study the dynamic behavior of our model.

Consider the simple system having nonsymmetrically placed rigid stops and subjected to nonharmonically periodic excitation shown in the Fig. 1. The left stop is placed right at the equilibrium position of the mass. The nondimensional equation of motion can be written as follows:

$$\ddot{x}+2\alpha\dot{x}+x=F(t);\ 0<x<1, \qquad (1)$$

where the definition of $F(t)$ in one period $T$ is

[20]Department of Mechanical Engineering, National Central University, Chung-Li, Taiwan 32054, Republic of China.

Manuscript received by the ASME Applied Mechanics Division, Feb. 14, 1991; final revision, May 20, 1991. Associate Technical Editor: D. J. Inman.

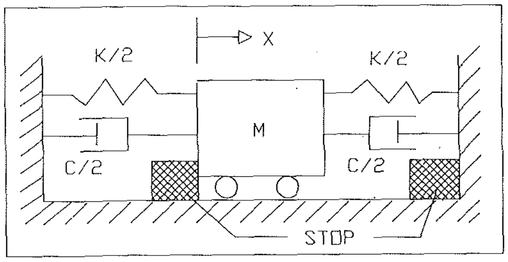


Fig. 1 The physical model

$$F(t)=\begin{cases}\beta & 0<t<D\\ 0 & D<t<T\end{cases}$$

with $\alpha$, $\beta$, and $D$ are the dimensionless damping constant, forcing amplitude, and the duration of a square pulse, respectively. Impacts occur at $x=1$ and at $x=0$ whereupon

$$\dot{x}(t^+)=-r\dot{x}(t^-) \text{ with } (t^+-t^-)\rightarrow 0. \tag{2}$$

## 2 The Poincare Maps

In periodically forced systems, a Poincare map is often used which stroboscopically samples $(x, y)$ points at time values $t=nT$, where $n=1, 2, \ldots$.. and $T$ is the forcing period. The Poincare section is then defined as

$$\Sigma^{t_0}=\{(x,y,t)\,|\,t=t_0 \bmod(T)\} \tag{3}$$

and the Poincare map is defined as

$$P^{t_0}:\Sigma^{t_0}\rightarrow\Sigma^{t_0} \text{ or } (x_{i+1},y_{i+1})=P^{t_0}(x_i,y_i). \tag{4}$$

Here, $t_0$ simple represents the particular phase of the periodic forcing at which the pulse is applied.

Referring to Eqs. (1) and (2), we see that nonlinearity occurs at $x=1$ and at $x=0$. Similar to the methods described in Shaw and Holmes (1983) and Shaw (1985a, b, 1986), a different type of Poincare map can be used to study the dynamics of this system, the Poincare section is taken to be

$$\Sigma_1 \epsilon R^+\times S^1=\{(x,y,t)\,|\,x=1, y>0\} \tag{5}$$

or to be

$$\Sigma_1 \epsilon R^+\times S^1=\{(x,y,t)\,|\,x=0, y<0\}. \tag{6}$$

This section is defined as those points in the phase space which correspond to states at which the mass hits the stops. This section and map exploit the piecewise linear nature of the system. However, due to our nonharmonically forced system, we need to use both Poincare sections, and their associated maps, in the analysis (see Tung and Shaw (1988) for details).

## 3 Existence of Periodic Motions

There exist many possible types of periodic motions involving impacts at $x=0$ and $x=1$. In this section we consider only the period-one double-impact motion in which the mass $m$ repeats its motion after one impact at $x=0$ and $x=1$ each during which one cycle of the forcing passes and an impact does not occur at $x=1$ during the applied force. Note that by considering only one type of periodic motion may limit the generality of the analysis.

In order to obtain explicit conditions for the existence of periodic motions, we may exploit the piecewise linear nature of our model. The analysis involves the piecing together of several trajectory pieces in such a manner that the motion is repetitive, i.e., periodic. A computer-generated plot of the resonance curve of the periodic point $\bar{y}$ versus forcing period $T$ is shown in Fig. 2. On the curve, the solid line represents stable motions and the dotted line represents unstable motions. The values shown correspond to the $\bar{y}$ component of the periodic points on the Poincare section of Eq. (5). The response curves shown in Fig. 2 were generated by a numerical solution of the matching problem (Tung and Shaw, 1988).

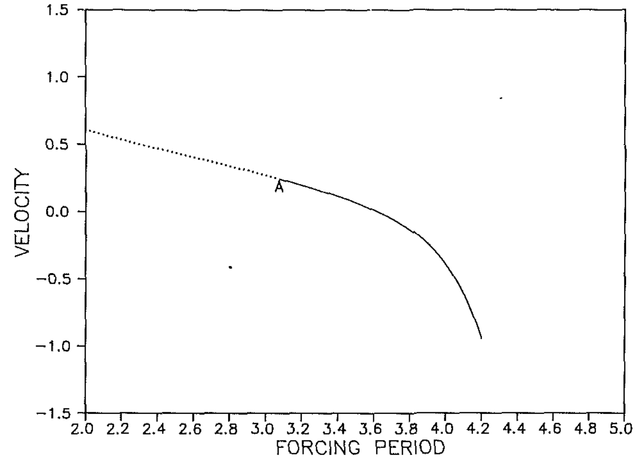


Fig. 2 Frequency response curve, velocity versus forcing period, $r=0.9$, $\alpha=0.1$, $\beta=3.0$, $D=1.0$

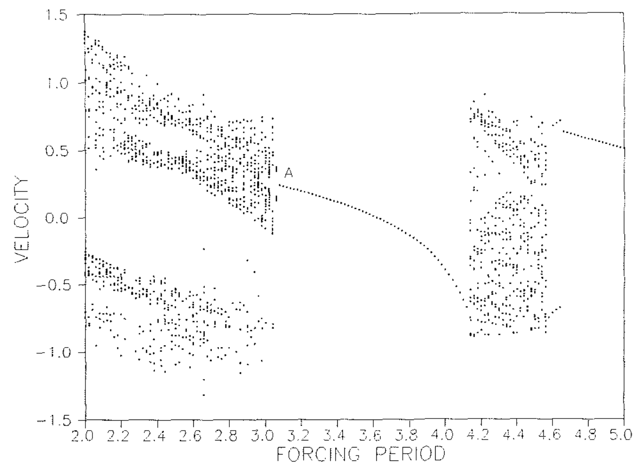


Fig. 3 Phase portrait with double impacts per forcing, $r=0.9$, $\alpha=0.1$, $\beta=3.0$, $D=1.0$, $T=3.2$

## 4 Stability of Periodic Motions

Referring to Fig. 3, it is seen that there are four pieces of a periodic trajectory which form one cycle. Hence, $DP$ can be written using the chain rule as

$$DP=\left[\frac{\partial(x_0,y_0)}{\partial(t_5,y_5)}\right]\left[\frac{\partial(t_5,y_5)}{\partial(t_4,y_4)}\right]\left[\frac{\partial(t_4,y_4)}{\partial(x_3,y_3)}\right]\left[\frac{\partial(x_3,y_3)}{\partial(t_2,y_2)}\right]$$
$$\times\left[\frac{\partial(t_2,y_2)}{\partial(t_1,y_1)}\right]\left[\frac{\partial(t_1,y_1)}{\partial(x_0,y_0)}\right]. \tag{7}$$

Performing the matrix multiplication of Eq. (7) and using the periodic points obtained in the above section, we can obtain the matrix $DP$ evaluated on the periodic point. Then the eigenvalues of $DP$ can be written in terms of $\bar{D}$, the determinant of $DP$ and $\bar{T}$, and the trace of $DP$ as

$$\lambda_{1,2}=\frac{\bar{T}}{2}\pm\sqrt{(\bar{T}/2)^2-\bar{D}} \tag{8}$$

which determine the stability of $(x_0, y_0)$ and the corresponding periodic motion. Similar calculations of $DP$ can be found in Tung and Shaw (1988).

From the curves shown in Fig. 2, as the forcing period $T$ is varied, the eigenvalues corresponding to a periodic point

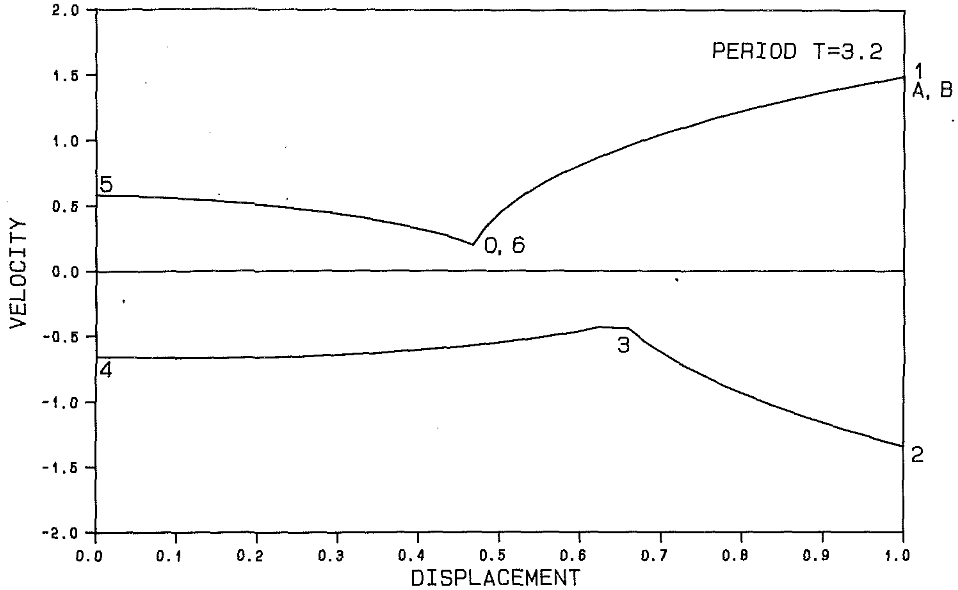


**Fig. 4 Frequency response by digital simulation, $r=0.9$, $\alpha=0.1$, $\beta=3.0$, $D=1.0$**

change. At point $A$, one of the eigenvalues will be equal to $-1$, in our case, and a period doubling bifurcation occurs. The periodic point $y$ of point $A$ is called a bifurcation point and is denoted by $y_{bif}$.

## 5 Simulations

Using results of digital simulations we can check the validity of our solution to the equations of motion, periodic points, and bifurcation points. Also, chaotic motions and other responses can be explored through simulation. Figure 3 shows the plot of phase portraits with two impacts per forcing cycle which is generated by digital simulations of Eqs. (1)-(2). The simulations can easily be performed by piecing together the solution from each piecewise linear equation and solving the boundary conditions, i.e., the crossing time and crossing velocity at $x=0$ and $x=1$ by using Newton-Raphson method. The time step should be as small as possible when impact is about to occur. Simulation trouble may occur due to the fact that the applied force may be about to start or to cease at the moment. Figure 4 shows the frequency response of velocity at the point at which a pulse is applied versus forcing period $T$ by using digital simulation. At point $A$ the motion begins to undergo a succession of period doubling or flip bifurcations, which results in chaotic motions. It is noted that Fig. 4 matches very nicely with Fig. 2.

## 6 Conclusions

In this paper the dynamics of a single-degree-of-freedom system subjected to nonharmonic excitation have been studied. The periodic motions and their stability are determined analytically and local bifurcations are considered. The frequency response curves shown in Fig. 2 indicate that there exist regions in parameter space for which there exist no stable periodic orbits. Local bifurcation analysis shows that period-doubling bifurcation occurs near the stability boundary which result in chaotic motions. These motions are irregular, bounded response to periodic excitation. Chaotic motions are found to exist over ranges of forcing periods.

As forcing period $T$ is increased past $T^*=4.14$, as shown in Fig. 4, the stable periodic motion suddenly changes to a chaotic motion. It has been conjectured that almost all sudden changes in chaotic motion are due to either tangent bifurcation or crises (Grebogi et al., 1982). However, from stability analysis none of the eigenvalues at parameter value $T^*=4.14$ are equal to $+1$. In our case, this is due to the fact that a degenerate impact occurs, i.e., the mass hits the stops with zero impact velocity and causes a sudden change in response structure to chaos without passing through other types of stable motions or bifurcation. However, it is not necessary that a degenerate impact always results in chaotic motions but involves response structure change. In Shaw and Holmes (1983), a degenerate impact occurred during period cascades and led to another type of stable motion.

## Acknowledgment

The author is grateful to Chin-Liang Lin for assistance with the computing.

## References

Grebogi, C., Ott, E., and Yorke, J. A., 1982, "Chaotic Attractors in Crisis," *Physical Review Letters*, Vol. 48, No. 22, pp. 1507–1510.

Masri, S. F., 1972, "Theory of the Dynamic Vibration Neutralizer with Motion-Limiting Stops," ASME JOURNAL OF APPLIED MECHANICS, Vol. 39, pp. 563–568.

Nigm, M. M., and Shabana, A. A., 1983, "Effect of an Impact Damper on a Multi-Degree-of-Freedom System," *Journal of Sound and Vibration*, Vol. 89, No. 4, pp. 541–557.

Shaw, S. W., and Holmes, P. J., 1983, "A Periodically Forced Piecewise Linear Oscillator," *Journal of Sound and Vibration*, Vol. 90, pp. 129–155.

Shaw, S. W., 1985a, "The Dynamics of a Harmonically Excited System Having Rigid Amplitude Constraints, Part I: Subharmonic Motions and Local Bifurcations," ASME JOURNAL OF APPLIED MECHANICS, Vol. 52, pp. 453–458.

Shaw, S. W., 1985b, "The Dynamics of a Harmonically Excited System Having Rigid Amplitude Constraints, Part II: Chaotic Motions and Global Bifurcations," ASME JOURNAL OF APPLIED MECHANICS, Vol. 52, pp. 459–464.

Shaw, S. W., 1986, "On the Dynamic Response of a System with Dry Friction," *Journal of Sound and Vibration*, Vol. 115, pp. 309–319.

Shaw, J., and Shaw, S. W., 1989, "The Onset of Chaos in a Two-Degree-of-Freedom Impacting System," ASME JOURNAL OF APPLIED MECHANICS, Vol. 56, pp. 168–174.

Tung, P. C., and Shaw, S. W., 1988, "The Dynamic of an Impact Print Hammer," *ASME Journal of Vibration, Acoustics, Stress, and Reliability in Design*, Vol. 110, No. 2, pp. 193–200.

# Viscoelastic Damping Calculations Using a *p*-Type Finite Element Code

C. J. Wilson,[21] P. Carnevali,[22] R. B. Morris,[22] and Y. Tsuji[22]

*Damping factors of viscoelastically damped structures can be calculated using the modal strain energy method, implemented with a sequence of undamped modal analysis computations. There are significant advantages in performing these calculations using* p*-type finite element codes. These include ease of mesh design, an indicator of degree of solution convergence, modest computation time, and an insensitivity to element aspect ratio. Capitalizing on these advantages an algorithm is defined, which is effective in solving for the natural frequencies and modal loss factors of damped structures. The algorithm is demonstrated using a sandwiched cantilevered beam as an example.*

## Introduction

The application of surface damping treatments to small mechanical structures for the purpose of controlling their frequency response to external loads or vibrations is of growing interest. For example, in the computer industry, by controlling the frequency response of components in a hard disk drive the possibility of head/disk crashes, as well as track misregistration problems, can be reduced. Since the components are small a weight effective method, such as constrained layer damping, should be used. In this method, an elastomer is fixed between two plates and flexural vibrations produce a shearing strain in the core. Due to the damping properties of the viscoelastic layer vibrations are reduced and natural frequencies are altered.

Methods of analyzing all types of damping, including closed-form solution techniques, have been developed over the past 20 years. A review of the literature on damping is given in Nakra (1976, 1981, 1984). These analytical models have many restrictions and difficulties are encountered when trying to work with complex geometries. Even for simple structures both algebraic and numerical solutions of the equations of motion tend to be time consuming. Thus, for the real world problems this type of extensive analysis is not practical. However, finite element methods have proven successful in overcoming these obstacles.

Current finite element methods for the analysis of damped structures can be classified into three categories: (1) complex eigenvalue method, (2) direct frequency response method, and (3) modal strain energy method. These methods are described in detail in Johnson and Kienholz (1982), Johnson et al. (1981), and Nashif et al. (1985). The modal strain energy method (MSE) and its application to finite element analysis, which was introduced in Johnson et al. (1981), is an economical way of making damping predictions which are useful, but not necessarily exact. In this method, a normal modes analysis, using the frequency-dependent material properties of the viscoelastic layer, is performed. The calculation yields the damped natural frequencies and modal loss factors of each of the modes of vibration.

Previously, MSE has been implemented using an *h*-version finite element code, such as MSC/NASTRAN (Schaeffer, 1984). An alternative to this is the *p*-version finite element method (Babuska et al., 1981). The *p*-type method has at least three distinct advantages over an *h*-version in connection with a MSE analysis. The first of these is that the convergence of the numerical solution can be monitored as the order of approximation is successively incremented. Second, the *p*-version code is relatively insensitive to mesh design. In the *p*-type method, a simple, relatively coarse mesh design can yield accurate numerical results. A third advantage is that there is rapid convergence of the method even with elements having large aspect ratios (see Carnevali et al. (1992) for a discussion of performance aspects). This makes it especially good to use with the constrained layer analysis, since damping layers are usually very thin. In particular, a *p*-type finite element code has been used previously to evaluate shearing stresses along material interfaces of laminate structures (Schiermeier, 1987).

This paper describes an algorithm by which MSE is combined with the *p*-version finite element method to estimate the damping properties of structures. The method is illustrated using a cantilevered beam with constrained layer damping as an example. Advantages of combining MSE with a *p*-version finite element code instead of an *h*-version are emphasized.

## Modal Strain Energy Method

A convenient measure of structural damping used in the analysis of system resonance is the loss factor. Simply stated, the loss factor is the ratio of the energy lost in a cycle to the energy stored in the system during that cycle. The loss factor, $\eta$, is defined as: $\eta = D/(2\pi W)$, where $D$ denotes the energy dissipated per cycle and $W$ denotes the total energy associated with the vibration cycle. In order to compute $\eta$, knowledge of the material parameters is required. For viscoelastic materials, Young's modulus and Poisson's ratio are frequency dependent. The variation of Young's modulus with frequency is available from nomograms for numerous materials (Nashif et al., 1985). However, since little information is available on Poisson's ratio as a function of frequency, it is often chosen to be constant.

In the modal strain energy approach (Johnson et al., 1981) the system modal loss factors are calculated using the loss factor of the viscoelastic material and the ratio of the strain energy stored in the damping layer to the strain energy stored in the composite structure. Strain energies are calculated using real normal modes of the undamped system. The mathematical statement for MSE is

$$\frac{\eta_S}{\eta_V} = \frac{SE_V}{SE} \tag{1}$$

where $\eta_S$ is the loss factor of the $n$th mode of the composite structure, $\eta_V$ is the material loss factor of the viscoelastic material, $SE_V$ is the elastic strain energy stored in the viscoelastic material when the structure deforms in its $n$th undamped mode shape, and $SE$ is the elastic strain energy of the entire composite structure in the $n$th mode shape. It was demonstrated in Johnson and Kienholz (1982) that the modal loss factors, $\eta_S$, obtained from Eq. (1) are good approximations to the computationally more expensive complex stiffness eigenvalue results. It is also shown in Wilson et al. (1990) that for the case of small damping MSE is equivalent to a first-order approximation of the complex eigenvalue problem.

Since MSE uses undamped normal modes, a constant-coefficient eigenvalue problem is solved. The frequency-dependent properties of the viscoelastic material are accommodated using an iterative procedure. For each natural frequency, the material properties are determined and the eigenvalue problem is solved. Each solution is valid only at the specific frequency for which the material properties apply, so the eigenvalue problem must be solved separately for each natural frequency.

[21]Computer Mechanics Laboratory, Department of Mechanical Engineering, Berkeley, CA 94720.

[22]IBM Research Division, Almaden Research Center, San Jose, CA 95120-6099.

Manuscript received by the ASME Applied Mechanics, Mar. 6, 1990; final revision, Dec. 10, 1990.

### Finite Element Analysis

In the $p$-version of the finite element method, successively higher order local basis functions are used to approximate the solution until numerical convergence is reached (Babuska et al., 1981). The implementation used in this study is described in Carnevali et al. (1992) and includes both static and dynamic (normal modes) analyses for three-dimensional problems with an element library of solid bricks (8 nodes), wedges (6 nodes), and tetrahedra (4 nodes).

Solid brick elements were used to model a sandwiched cantilevered beam. Typically, for $h$-type codes, shell elements are used to discretize the constraining layers and either solid or shear panel elements are used to discretize the viscoelastic layer (Johnson and Kienholz, 1982; Lalanne et al., 1975). This is done to reduce the number of degrees-of-freedom used in the calculation. There is, however, an incompatibility in the number of degrees-of-freedom per node for the different elements; the shell element has six, whereas the solid and shear panel elements have only three. As pointed out in Soni (1981), not all structures can be modeled easily using this combination of solid and shell elements, especially those with multiple layers. In the case of the $p$-version finite element code used here (Carnevali et al., 1991), which only uses solid elements, these difficulties are avoided. Since all the elements are of the same type, compatibility of displacements at the element interfaces is assured. This eliminates the need for additional constraints to be imposed on the system, and multiple layers can be modeled easily.

In most of the computations, the eigenvalues of the model were extracted using a subspace iteration method (Bathe, 1982), but when the aspect ratio of the elements was large, the Lanczos algorithm (Cullum and Willoughby, 1985) was used.

### Application and Discussion

The problem investigated (a simple cantilevered beam) has been studied extensively with both closed-form solution methods and finite element methods. The geometry and material properties are the same as in Soni (1981). This particular formulation has been studied in Johnson et al. (1981) and Soni (1981). The results are compared with those presented in Soni (1981) which included experimental data from Drake and Turborg (1980). The complex eigenvalue problem is not solved in Soni (1981). Instead, MAGNA-D, an $h$-type finite element code, combined with a method to predict the structural modal loss factors (Unger and Kerwin, 1962) was used by these authors for their calculations. Several versions of the model were examined. The number of elements was varied from a total of 42 (14 elements per layer) to 3 (one element per layer). The results are essentially independent of the number of elements used, provided the polynomial order is chosen to ensure the solution has converged. The $p$-version code easily handled the large aspect ratios (up to 1:1400) involved.

A block diagram of the solution algorithm is given in Fig. 1. The process is initialized by analyzing an all-metal cantilevered beam (Block 1 and 2). Convergence of the natural frequencies is compared for each successive polynomial order (Block 3). Once the change in all the frequencies between two consecutive polynomial orders is less than ten percent, the latter polynomial order is chosen to be used for the damping calculations (Block 4). This loose criterion is justified since there is a large amount of scatter present in the material property data obtained from the nomogram (Soni, 1981), and there is considerable variation from one batch of viscoelastic material to another.

Due to the variational formulation of the finite element method, as the convergence of the model is approached (polynomial order increased) the computed frequencies decrease monotonically. This implies that there are two possible sources for frequency changes: (1) material damping and (2) variational convergence of the finite element method. These are two independent effects and should not be confused. Therefore, once a polynomial order is chosen, it should be used for the entire iterative procedure (Block 4, Fig. 1).

With this polynomial order fixed, the iterative process for the damping analysis is initiated. For a particular frequency of interest, the Young's modulus and material loss factor for

**Table 1 Damped natural frequencies (Hz) and modal loss factors (in parentheses)**

| Mode | $N_{el}=42$ $p=8$ | $N_{el}=21$ $p=10$ | $N_{el}=12$ $p=12$ | $N_{el}=3$ $p=15$ | MAGNA-D | Exp. |
|---|---|---|---|---|---|---|
| 1 | 82.66 (.0053) | 82.66 (.0052) | 82.67 (.0053) | 82.79 (.0052) | 82. (.0049) | |
| 2 | 510.3 (.0093) | 510.3 (.0093) | 510.4 (.0093) | 511.1 (.0093) | 505. (.0101) | 510. (.006) |
| 3 | 1408. (.0097) | 1406. (.0109) | 1408. (.0097) | 1409. (.0109) | 1394. (.0123) | 1402. (.009) |
| 4 | 2694. (.0134) | 2697. (.0136) | 2695. (.0134) | 2698. (.0134) | 2690. (.0148) | 2699. (.014) |
| 5 | 4326. (.0169) | 4334. (.0159) | 4334. (.0159) | 4333. (.0162) | 4375. (.017) | 4380. (.018) |

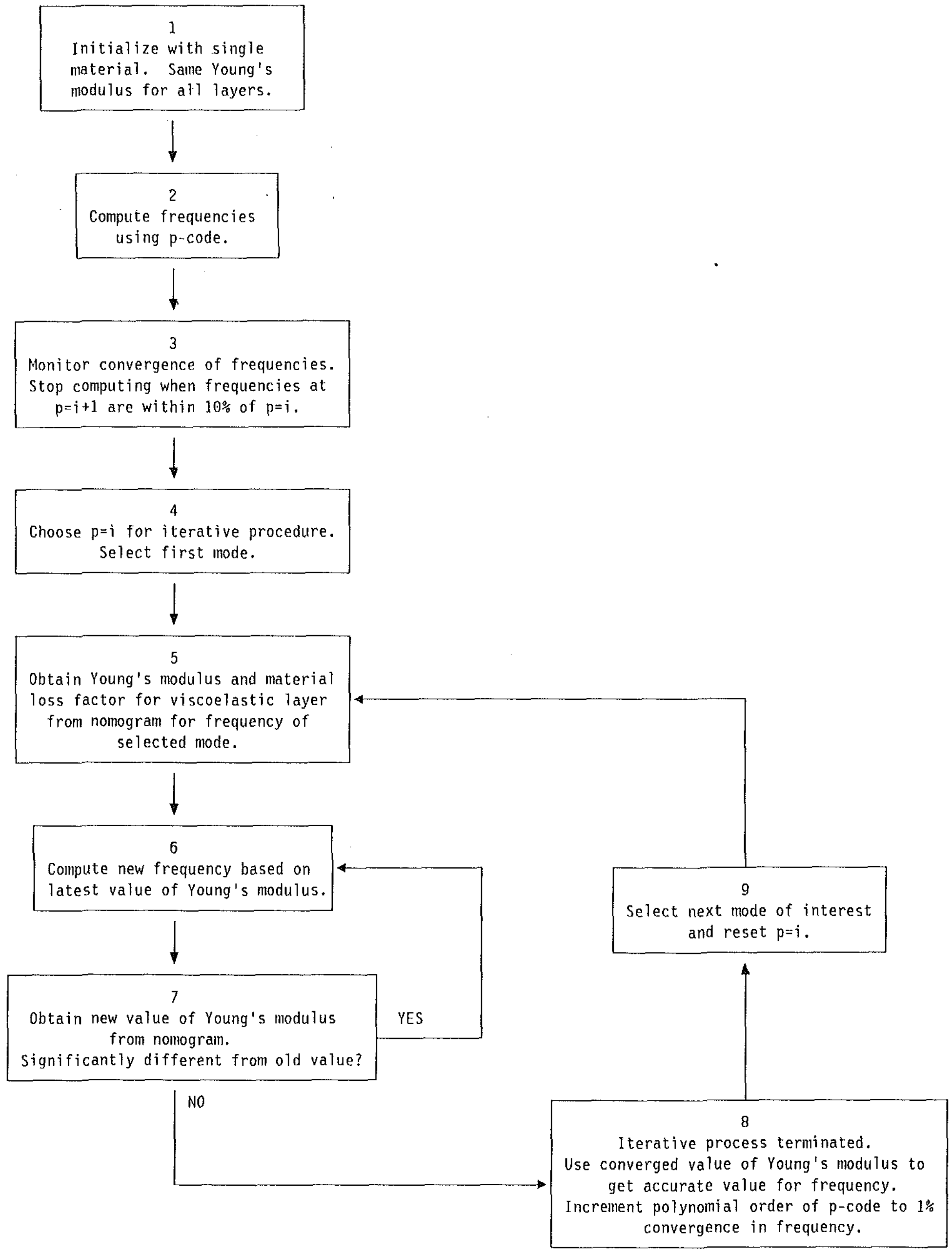


**Fig. 1 Flowchart representing solution algorithm**

the viscoelastic material are obtained from the nomogram (Block 5). A normal modes analysis at the chosen polynomial order is then used to compute the natural frequencies of the damped structure (Block 6). A new Young's modulus corresponding to the new frequency is obtained from the nomogram (Block 7). If the difference between the new and previous values of the Young's modulus (Block 7) is greater than that of the error in reading the nomogram, the new Young's modulus is used to compute new damped natural frequencies. Otherwise, the iterative process is terminated (Block 8). The converged value of the Young's modulus is then used to obtain a precise value of the damped natural frequency. This is achieved by incrementing the polynomial order in the $p$-version code until the frequencies have converged to within one percent (Block 8). The entire process is repeated for each frequency (Block 9). Thus, the $p$-type code implemented in the manner described can be used to create an efficient iterative process whereby natural frequencies and modal loss factors of damped structures can be determined.

The damped natural frequencies and corresponding modal loss factors of the converged solutions have been computed, for illustration purposes, using different numbers of elements and polynomial orders as in Table 1. As the number of elements is decreased, the polynomial order must be increased to obtain similar accuracy for each of the models. Table 1 also includes data from Soni (1981) for comparison in the last two columns.

Within the accuracy of the material properties as obtained from the nomogram, the values of the damped resonance frequencies from the $p$-version code are in good agreement with those from both MAGNA-D (Soni, 1981) and the experimental results (Drake and Turborg, 1980). The values of the modal loss factors also agree well except at very low damping. As stated in Soni (1981), this discrepancy may be attributed to errors in the measurement; with small damping, the sharpness of the amplitude-frequency response curve makes it difficult to locate the half-power bandwidth points.

## Conclusion

This paper demonstrates the attractive features of combining the modal strain energy method with the $p$-version finite element method to estimate damping in structures. It has been shown that since a $p$-type code is not as sensitive to element aspect ratio as an $h$-type code, far fewer elements can be used in the analysis. The $p$-version code can be used with a low polynomial order to create an efficient iterative process for use with the modal strain energy method; for the $h$-version, the entire structure must be modeled to full accuracy (many elements). These advantages imply less user involvement and can result in shorter design cycle times. A simple example of a cantilevered beam with constrained layer damping was studied, and good agreement was obtained with known solutions of damped natural frequencies and modal loss factors. However, the same process can be applied to more complicated, realistic structures.

## References


Babuska, I., Szabo, B. A., and Katz, I. N., 1981, "The $p$-Version of the Finite Element Method," *SIAM Journal of Numerical Analysis*, Vol. 18, pp. 515–545.

Bathe, K., 1982, *Finite Element Procedures in Engineering Analysis*, Prentice-Hall, Englewood Cliffs, NJ.

Carnevali, P., Morris, R. B., Tsuji, Y., and Taylor, G., 1992, "New Basic Functions and Computational Procedures for $p$-Type Finite Element Analysis," IBM Research Division, Research Report RJ 8710.

Cullum, J. K., and Willougby, R. A., 1985, *Lanczos Algorithms for Large Symmetric Eigenvalue Computations*, Vols. 1 and 2, Birkhauser, Boston.

Drake, M. L., and Turborg, G. E., 1980, "Polymeric Materials Testing Procedures to Determine the Damping Properties and the Result of Selected Commercial Materials," University of Dayton, Report UDTR-80-40.

Johnson, C. D., and Kienholz, D. A., 1982, "Finite Element Prediction of Damping in Structures With Constrained Viscoelastic Layers," *American Institute of Aeronautics and Astronautics Journal*, Vol. 20, pp. 1284–1290.

Johnson, C. D., Kienholz, D. A., and Rogers, L. C., 1981, "Finite Element Prediction of Damping in Beams with Constrained Viscoelastic Layers," *Shock and Vibration Bulletin*, Vol. 51, Pt. 1, pp. 71–81.

Lalanne, M., Paulard, P., and Trompette, P., 1975, "Response of Thick Structures Damped by Viscoelastic Material With Application to Layered Beams and Plates," *Shock and Vibration Bulletin*, Vol. 45, pp. 65–71.

Nakra, B. C., 1976, "Vibration Control With Viscoelastic Materials," *The Shock and Vibration Digest*, Vol. 8, pp. 3–12.

Nakra, B. C., 1981, "Vibration Control With Viscoelastic Materials, II," *The Shock and Vibration Digest*, Vol. 13, pp. 17–20.

Nakra, B. C., 1984, "Vibration Control With Viscoelastic Materials, III," *The Shock and Vibration Digest*, Vol. 16, pp. 17–22.

Nashif, A. D., Jones, D. I. G., and Henderson, J. P., 1985, *Vibration Damping*, John Wiley and Sons, New York.

Schaeffer, H. G., 1984, *MSC/NASTRAN Primer*, Wallace Press, Milford, NH.

Schiermeier, J., 1987, "Finite Element Analysis of Composites," *Advanced Materials and Processes*, Vol. 132, pp. 36–43.

Soni, M. L., 1981, "Finite Element Analysis of Viscoelastically Damped Sandwich Structures," *Shock and Vibration Bulletin*, Vol. 51, Pt. 1, pp. 97–108.

Unger, E. E., and Kerwin, E. M., 1962, "Loss Factors of Viscoelastic Systems in Terms of Energy Concepts," *The Journal of the Acoustical Society of America*, Vol. 34, pp. 954–957.

Wilson, C. J., Carnevali, P., Morris, R. B., and Tsuji, Y., 1990, "Viscoelastic Damping Calculations Using a $p$-Type Finite Element Code," IBM Research Division, Report RJ 7360 (68841).

Journal of Applied Mechanics

# Discussion

## Predicting Rebounds Using Rigid-Body Dynamics[1]

**Raymond M. Brach.**[2] In a recent paper, Smith (1991) presents comments related to specific items from the works of Brach (1984, 1989). In particular, Smith says:

(1) the statement of Brach (1989) that the kinematic coefficient of restitution is bounded by 0 and 1, that is $0 \leq e \leq 1$, is incorrect or at least unsupported,
(2) Eq. (19) in Brach (1984) for the energy loss of a collision of two particles is incorrect, and
(3) if the quantity, $\kappa$, in the denominator of Smith's expression (unnumbered) for the change in kinetic energy $\Delta K$ were replaced by 1, Smith's results would agree with Brach's energy loss expression.

The work of Stronge (1990) clearly points out that an energetic coefficient of restitution, $E^2$, is bounded by 0 and 1, that is, $0 \leq E^2 \leq 1$. Since the kinematic coefficient, $e$, and energetic coefficient, $E^2$, are generally different, Smith's criticism of Brach's bounds as summarized in item 1 above is justified.

Equation (19) for the energy loss of a planar particle collision is Brach (1984) follows directly from Newton's laws of particle dynamics as applied to collisions. This is demonstrated clearly in Brach (1984) and by a different method in Brach (1991). Consequently, Smith's claim in item 2 above is itself incorrect.

With reference to item 3 above, if the quantity $\kappa$ is replaced by 1, the appropriate expressions of Brach and Smith have the same *form*, however, there exists a subtle and important difference. In Smith's equation for $\Delta K$, $\mu$ is a coefficient of friction whereas in Brach's Eq. (19) $\mu$ is an impulse ratio. These can be equal, but only under certain conditions. Smith's equation will give a negative energy loss (which is physically unrealistic) for relatively small initial tangential contact velocities and relatively large coefficients of friction. Brach uses the impulse ratio specifically to avoid this problem.

[1] By Charles E. Smith and published in the September 1991 issue of the JOURNAL OF APPLIED MECHANICS, Vol. 58, pp. 754–758.

[2] Department of Aerospace and Mechanical Engineering, University of Notre Dame, Notre Dame, IN 46556-5637.

### References

Brach, R. M., 1984, "Friction, Restitution and Energy Loss in Planar Collisions," ASME JOURNAL OF APPLIED MECHANICS, Vol. 51, pp. 164–170.

Brach, R. M., 1989, "Rigid Body Collisions," ASME JOURNAL OF APPLIED MECHANICS, Vol. 56, pp. 133–138.

Brach, R. M., 1991, *Mechanical Impact Dynamics*, John Wiley and Sons, New York.

Smith, Charles E., 1991, "Predicting Rebounds Using Rigid-Body Dynamics," ASME JOURNAL OF APPLIED MECHANICS, Vol. 58, pp. 754–758.

Stronge, W. J., 1990, "Rigid Body Collisions with Friction," *Proceedings of the Royal Society, London*, Vol. A431, pp. 169–181.

### Author's Closure[3]

Introducing the concept of *particles* to an analysis of collisions with friction brings the need to resolve the following issue: To permit the definition of friction and normal components of the interactive forces, the bodies must have nonzero dimensions. This means that, except for peculiar shapes or special combinations of configuration and relative velocities, there will be moments about the centers of mass and corresponding changes in angular velocities. These changes are implied to be zero in "Newton's laws of particle dynamics as applied to collisions," to which the discussion refers. The contributions to change in kinetic energy from changes in angular velocities and from changes in velocities of the mass centers can be compared by examining expressions resulting from a rigid-body analysis.

One such expression is Eq. (26) of Brach (1989), which is followed by the statement, "This suitably reduces to the point mass results of Brach (1984)." However, reduction of this equation or the unnumbered equation of item 3 of the discussion to Eq. (19) of Brach (1984) requires that the ratio of body dimension to central radius of gyration approach zero. This is not a "suitable" reduction.

The unnumbered equation of Smith (1991) will *not* predict an increase in kinetic energy, unless the delimiter ($a > 1$), which appears immediately before the equation, is ignored.

The distinction between coefficient of friction and impulse ratio might be subtle to some because of Brach's unfortunate choice of the symbol $\mu$ to represent the latter, but the discrepancy under discussion remains independent of this distinction.

[3] Charles E. Smith, Professor, Department of Mechanical Engineering, Oregon State University, Corvallis, OR 97331.